Transactions of the ASME®

Journal of Heat Transfer

Published Bimonthly by The American Society of Mechanical Engineers

VOLUME 123 • NUMBER 5 • OCTOBER 2001

Transactions of the ASME, Journal of Heat Transfer (ISSN 0022-1481) is published bi-monthly (Feb., Apr., June, Aug., Oct., Dec.) by The American Society of Mechanical Engineers, Three Park Avenue, New York, NY 10016. Periodicals postage paid at New York, NY and additional mailing offices. POSTMASTER: Send address changes to Transactions of the ASME, Journal of Heat Transfer, c/o THE AMERICAN SOCIETY OF MECHANICAL ENGINEERS, 22 Law Drive, Box 2300, Fairfield, NJ 07007-2300. **CHANGES OF ADDRESS** must be received at Society headquarters seven weeks before they are to be effective. Please send old label and new address.
 INDEXED by Applied Mechanics Reviews and Engineering Information, Inc. Canadian Goods & Services Tax Registration #126148048.

TECHNICAL PAPERS

(Contents continued on inside back cover)

This journal is printed on acid-free paper, which exceeds the ANSI Z39.48-1992 specification for permanence of paper and library materials. ♾™
♻ 85% recycled content, including 10% post-consumer fibers.

(Contents continued)

TECHNICAL NOTE

ANNOUNCEMENTS

(Contents continued on facing page)

2000 Max Jacob Memorial Award Lecture

Thermal Deformation: From Thermodynamics to Heat Transfer

Vedat S. Arpacı
Professor
ASME Fellow
e-mail: arpaci@umich.edu
Department of Mechanical Engineering,
The University of Michigan,
2142 G. G. Brown,
2350 Hayward,
Ann Arbor, MI 48109-2125

An infinitesimal change in heat flux Q is shown, in terms of entropy flux $\Psi = Q/T$ to have two parts, $dQ = Td\Psi + \Psi dT$, the first part being the thermal displacement and the second part being the thermal deformation. Only the second part dissipates into internal energy and generates entropy. This generation is shown to be $d\Pi = (\Psi/T)dT$. Thermodynamic arguments are extended to transport phenomena. It is shown that a part of local rate of entropy generation is related to local rate of thermal deformation by $s''' = -\psi_i/T(\partial T/\partial x_i)$, where $\psi_i = q_i/T, q_i$ being the rate of heat flux.
[DOI: 10.1115/1.1379953]

I Introduction

One gets used to thermodynamics rather than learning it.
Planck

The concept of entropy production is now assumed to be well-understood (see, for example, Bird et al. [1], Arpacı [2–6], Bejan [7–9]). Recent interest in the topic has been primarily aimed at a variety of engineering applications (see Bejan [10] for an extensive review). An inspection of the literature, however, reveals a need for further studies on the Second Law. Specifically, in classical thermodynamics, the reversible entropy change in a system comprising a bath at temperature T_1 separated by a partition from another bath at temperature T_2 is given by

$$S_2 - S_1 = Q\left(\frac{1}{T_2} - \frac{1}{T_1}\right), \quad T_1 > T_2, \tag{1}$$

Q being the heat flux through the partition (Fig. 1). An interpretation of the right-hand side of Eq. (1) for an irreversible process appears to have been overlooked in classical thermodynamics and is the motivation of the lecture. Note that a finite temperature drop cannot exist across a partition of no appreciable thickness. Actually, one needs to replace the ideal model of Fig. 1 dealt in thermodynamics with an actual model which involves a partition of finite thickness l separating two baths (Fig. 2). In this model, the bath in equilibrium at temperature T_1 transfers heat via an irreversible process over a distance l to the bath in equilibrium at temperature T_2.

First note the following remarks on the notation to be used in this lecture. As is well-known, the efficiency of a Carnot cycle, coupled with the definition of Kelvin absolute temperature, leads to

$$\oint \frac{dQ}{T} = \frac{Q_1}{T_1} - \frac{Q_2}{T_2} = \sum \frac{Q}{T}, \tag{2}$$

where the left-hand notation was used in Fermi [11], as well as most of the texts on classical thermodynamics, while the right-hand notation was used in Planck [12]. The Carnot cycle introduces the concept of entropy flux

$$\Psi = \frac{Q}{T}, \tag{3}$$

and any reversible process related to this cycle introduces the concept of (internal) entropy S as a thermal property. For any finite (reversible or irreversible) process, the Second Law states that

$$S_2 - S_1 \geqslant \Psi, \tag{4}$$

Ψ being the net entropy flux through the boundaries. In terms of the concept of entropy production, Π, as a measure for the irreversibility of a process, the Second Law becomes

$$S_2 - S_1 = \Psi + \Pi, \tag{5}$$

or, for an infinitesimal process,

$$dS = d\Psi + d\Pi, \tag{6}$$

which may be expressed in terms of the heat flux as

$$dS = \frac{1}{T}\left[dQ - \left(\frac{Q}{T}\right)dT\right] + d\Pi. \tag{7}$$

Note that Eq. (7) clearly defines Q and dQ according to the rules of differential calculus. For a T-Constant reversible process, Eq. (6) is reduced to the well-known relation,

$$dS = \frac{dQ}{T}. \tag{8}$$

For a Q-Constant reversible process, however, it is reduced to

$$dS = -Q\left(\frac{dT}{T^2}\right). \tag{9}$$

Between two equilibrium states, Eq. (9) yields

$$S\Big|_1^2 = Q\left(\frac{1}{T}\right)\Big|_1^2, \tag{10}$$

which is identical to Eq. (1).

For a T-Constant process, now consider an irreversible process between two reservoirs which are separated by a distance l (Fig. 3). First, assume the process to be infinitesimally (or locally) reversible. The entropy change relative to a reference state S_0 for heat Q received by an infinitesimal system is

$$S - S_0 = \frac{Q}{T}, \tag{11}$$

the entropy change within the system for heat $(Q + dQ)$ lost is

$$S_0 - (S + dS) = -\frac{Q + dQ}{T}, \tag{12}$$

Contributed by the Heat Transfer Division for publication in the JOURNAL OF HEAT TRANSFER. Manuscript received by the Heat Transfer Division February 8, 2000; revision received February 20, 2001. Editor: V. K. Dhir.

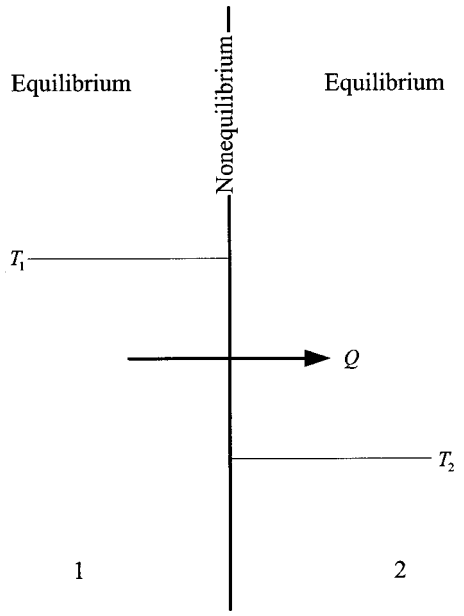

Fig. 1 Ideal partition

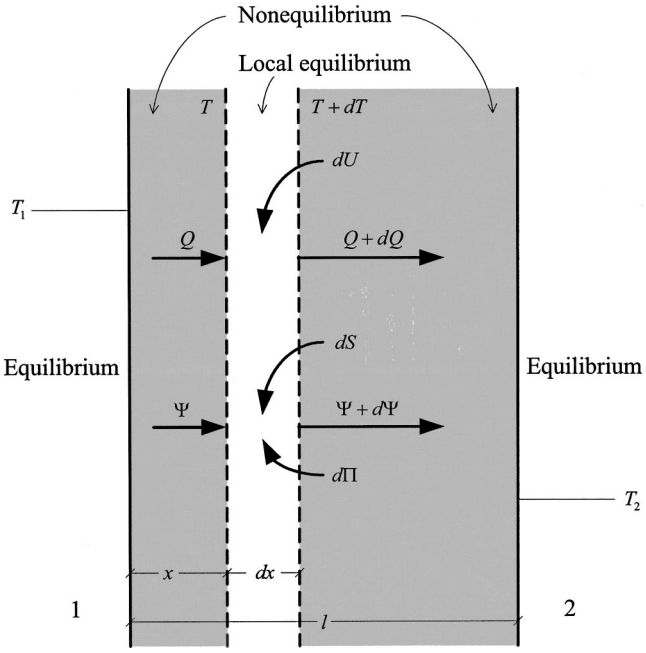

Fig. 3 Local equilibrium

and the net entropy change within the system is the familiar result

$$dS=\frac{dQ}{T}, \tag{8}$$

dQ being algebraic.

For an infinitesimally irreversible process,

$$dS=d\Psi+d\Pi, \tag{6}$$

and the First Law is

$$dU=dQ, \tag{13}$$

which is unaffected by the nature of the process. An alternative form of the First Law, rearranged in terms of the entropy flux, is

$$dU=Td\Psi+\Psi dT, \tag{14}$$

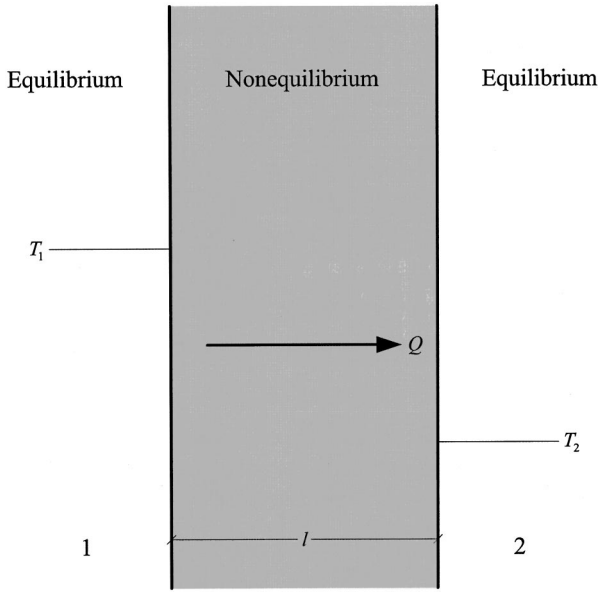

Fig. 2 Real partition

and the energy equivalent of the Second Law, obtained by multiplying it with temperature, is

$$TdS=T(d\Psi+d\Pi). \tag{15}$$

The difference between Eqs. (14) and (15) gives

$$dU-TdS=\Psi dT-Td\Pi. \tag{16}$$

Under the assumed local reversibility, the left-hand side of Eq. (16) is naught because of Eqs. (8) and (13). Then, the right-hand side yields

$$d\Pi=\left(\frac{\Psi}{T}\right)dT=\left(\frac{Q}{T^2}\right)dT. \tag{17}$$

For Q-Constant (recall Fig. 2), the integration of Eq. (17) between two reservoirs gives

$$\Pi|_1^2=-Q\left(\frac{1}{T}\right)\Bigg|_1^2. \tag{18}$$

A comparison of Eqs. (10) and (18) reveals that

$$S|_1^2+\Pi|_1^2=0, \tag{19}$$

that is, the reversible entropy change in the two reservoirs is balanced by the (irreversible) entropy production in the matter separating them.

This lecture consists of four sections: following this introduction, Section II introduces thermal deformation into classical thermodynamics, Section III extends the concept into transport phenomena, Section IV concludes the study.

II Thermal Deformation

Following Arpacı [6], consider the First Law applied to the control volume shown in Fig. 4,

$$dH^0=dQ-dW, \tag{20}$$

where

$$H^0=U+pV+U_K+U_P \tag{21}$$

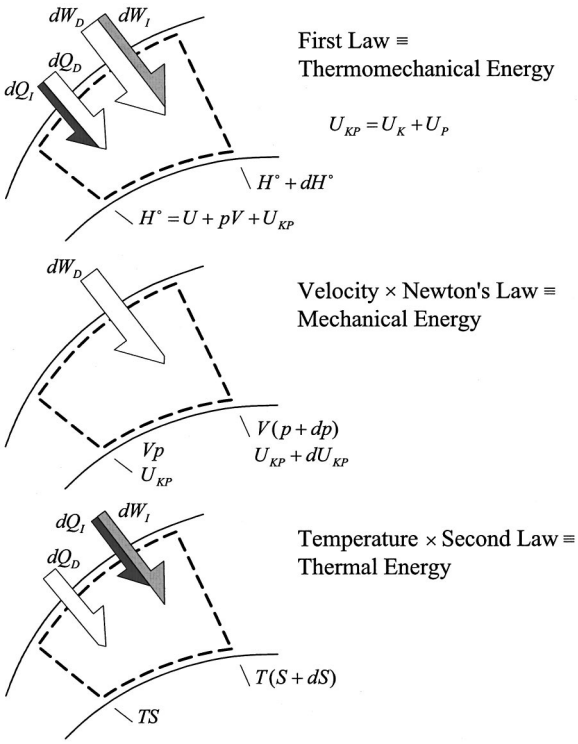

Fig. 4 Thermomechanical deformation

is the stagnation enthalpy, V the volume, U_K and U_P the kinetic and potential energies. Now, recall the definition of entropy flux (Eq. 3) and, express heat flux in terms of entropy flux,

$$dQ = d(\Psi T) = Td\Psi + \Psi dT, \tag{22}$$

or, with a short-hand notation,

$$dQ = dQ_D + dQ_I, \tag{23}$$

where $dQ_D = Td\Psi$ is the part of heat flux due to thermal displacement and $dQ_I = \Psi dT$ is the part of heat flux due to thermal deformation[1]. Only the latter part dissipates into internal energy and produces entropy. Although the concepts of displacement and deformation are well-known in mechanics, they are apparently overlooked in thermal science and are the motivation of this lecture. After a sign change (reflecting the opposite sign convention for pressure and stress related work), let the stress related (displacement plus deformation) work be split as[2]

$$dW = -(dW_D + dW_I), \tag{24}$$

where dW_D is the displacement work and is the work involved with the mechanical energy balance, and dW_I is the deformation work which dissipates into internal energy. Eq. (20) becomes, in terms of Eqs. (21), (23), and (24),

$$d(U + U_K + U_P) = d(Q_D + Q_I) - d(pV) + d(W_D + W_I). \tag{25}$$

The mechanical energy balance, obtained either by eliminating thermal effects from Eq. (25) or from the mechanical energy associated with Newton's Law is

$$d(U_K + U_P) = -Vdp + dW_D. \tag{26}$$

[1]Clearly, a deformation (involving species, momentum, heat, electromagnetic, and nuclear transport) dissipates into internal (thermal) energy. Less known is the fact that the deformation may have a diffusive or hysteretic origin, the diffusion being directional and the hysteresis being cyclical. However, except for a few cases (such as strain hardening and electromagnetic saturation), the majority of deformation processes, including the deformation of radiation, are diffusive in nature and are the concerns of this undertaking.

[2]The explicit tensorial form of dW is left to Section III.

Note that pdV and dW_I are the only work terms reversibly and irreversibly affecting the internal (thermal) energy. As is well-known, a special case of Eq. (26) is the Bernoulli equation for steady, incompressible, and inviscid flow.

Now, for a thermomechanical process, consider the energy difference

$$\text{First Law} - \text{Mechanical Energy} - T(\text{Second Law}),$$

or

$$(\text{Total} - \text{Mechanical} - \text{Thermal})\ \text{Energy}$$

which, in terms of Eqs. (25), (26), and (6) yields

$$dU + pdV - TdS = dQ_I + dW_I - Td\Pi, \tag{27}$$

or

$$dG = dQ_I + dW_I - Td\Pi, \tag{28}$$

where

$$G = U + pV - TS, \tag{29}$$

is the Gibbs function. Under local equilibrium,

$$dG = 0, \tag{30}$$

or, because of locally uniform p and T,

$$dU + pdV - TdS = 0, \tag{31}$$

and

$$d\Pi = \frac{1}{T}(dQ_I + dW_I). \tag{32}$$

Finally, let the internal energy, heat, and work associated with gas radiation (including infrared as well as visible spectra) be U^R, Q^R, W^R, respectively. In the case of negligible relativistic effects,

$$U^R \ll U, \quad Q^R \sim Q^K, \quad W^R \ll W, \tag{33}$$

provided the characteristic transport velocity remains much less than the velocity of light. Then, under the influence of radiation,

$$Q = Q^K + Q^R, \tag{34}$$

Q^K and Q^R respectively being the heat flow by conduction and radiation.

Next, the thermal deformation discussed in this section is extended to transport phenomena which require as well consideration of the momentum balance.

III Rate of Thermal Deformation

An Illustrative Example. Consider a fully developed steady flow between two parallel plates in relative motion (Fig. 5).

The local momentum balance for this flow is

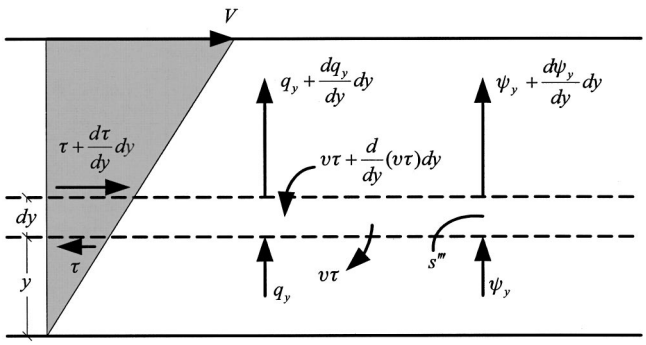

Fig. 5 Couette flow

$$0=\frac{d\tau}{dy} \tag{35}$$

and the rate of mechanical energy associated with the momentum is

$$0=v\left(\frac{d\tau}{dy}\right). \tag{36}$$

The rate of local thermomechanical energy conservation is

$$0=-\frac{dq_y}{dy}+\frac{d}{dy}(v\tau), \tag{37}$$

where

$$\frac{d}{dy}(v\tau)=v\left(\frac{d\tau}{dy}\right)+\tau\left(\frac{dv}{dy}\right), \tag{38}$$

the terms on the right-hand side respectively denote the rates of mechanical displacement and deformation energy.

In a similar manner, the heat flux can be expressed in terms of the entropy flux,

$$\frac{dq_y}{dy}=\frac{d}{dy}(T\psi_y)=T\left(\frac{d\psi_y}{dy}\right)+\psi_y\left(\frac{dT}{dy}\right) \tag{39}$$

where the terms on the right-hand side respectively denote the rates of thermal displacement and deformation energy. Also, the rate of entropy balance is

$$0=-\frac{d\psi_y}{dy}+s''' \tag{40}$$

and the rate of thermal energy associated with this balance is

$$0=T\left(-\frac{d\psi_y}{dy}+s'''\right). \tag{41}$$

Now, Eq. (37) expanded in terms of Eqs. (38) and (39) yields, in view of Eqs. (36) and (41),

$$s'''=\frac{1}{T}\left(-\psi_y\frac{dT}{dy}+\tau\frac{dv}{dy}\right), \tag{42}$$

where the right-hand side terms respectively denote the rate of entropy production resulting from thermal and mechanical deformations. Next, the foregoing one-dimensional example is extended to an unsteady multi-dimensional continuum which will be assumed a Stokesean fluid.

Multi-Dimensional Continua. For a Stokesean fluid, the momentum balance in terms of the usual nomenclature is

$$\rho\frac{Dv_i}{Dt}=-\frac{\partial p}{\partial x_i}+\frac{\partial\tau_{ij}}{\partial x_j}+\rho f_i, \tag{43}$$

where f_i includes all body forces. In terms of the rate of entropy flux,

$$\psi_i=\frac{q_i}{T}, \tag{44}$$

the entropy balance (the rate of Second Law balanced by the rate of local entropy production) is

$$\rho\frac{Ds}{Dt}=-\frac{\partial\psi_i}{\partial x_i}+s''', \tag{45}$$

where s''' denotes the local entropy production. Also, the conservation of total energy (or the rate of First Law) including the rate of heat flux expressed in terms of the rate of entropy flux,

$$\frac{\partial q_i}{\partial x_i}\equiv\frac{\partial}{\partial x_i}(\psi_i T)=T\frac{\partial\psi_i}{x_i}+\psi_i\frac{\partial T}{x_i}, \tag{46}$$

is

$$\rho\frac{D}{Dt}\left(u+\frac{1}{2}v_i^2\right)=-\frac{\partial}{\partial x_i}(\psi_i T)-\frac{\partial}{\partial x_i}(pv_i)+\frac{\partial}{\partial x_j}(\tau_{ij}v_i)+f_i v_i+u''', \tag{47}$$

where u''' denotes dissipation of non-thermomechanical energy into internal energy. Now, the fundamental difference of power,

Rate of Total Energy$-$(Momentum)$_i v_i-$(Rate of Entropy)T

or,

Rate of (Total$-$Mechanical$-$Thermal)Energy

leads, in terms of Eqs. (43), (45), (47), and the conservation of mass,

$$\frac{D\rho}{Dt}+\rho\frac{\partial v_i}{\partial x_i}=0, \tag{48}$$

to

$$\rho\left(\frac{Du}{Dt}-T\frac{Ds}{Dt}+p\frac{Dv}{Dt}\right)=-\psi_i\frac{\partial T}{\partial x_i}+\tau_{ij}s_{ij}+u'''-Ts''', \tag{49}$$

where s_{ij} is the rate of mechanical deformation. For a reversible process, all forms of deformation vanish, and

$$\frac{Du}{Dt}-T\frac{Ds}{Dt}+p\frac{Dv}{Dt}=0 \tag{50}$$

which is the Gibbs Thermodynamic relation. For an irreversible process, Eq. (50) continues to hold provided the process can be assumed in local equilibrium. Then, Eq. (49) gives the rate of local entropy production

$$s'''=\frac{1}{T}\left[-\psi\left(\frac{\partial T}{\partial x_i}\right)+\tau_{ij}s_{ij}+u'''\right], \tag{51}$$

where the first and second terms in brackets respectively denote the dissipation of thermal and mechanical energy into internal energy, and the third term denotes the dissipation of any energy (except for thermomechanical) into internal energy.

As an illustration of non-thermomechanical dissipation, consider Joulean dissipation of electromagnetic power. For a plasma flow prescribed by the MHD approximation (see, for example, Shercliff [13], Mitchner and Kruger [14]), the electromagnetic body force involved with Eq. (47) becomes

$$f_i^e=(\mathbf{J}\times\mathbf{B})_i, \tag{52}$$

where **J** and **B** respectively denote the electrical current density (A/m^2) and the magnetic field $(V.s)$, and **J** is given by Ohm's Law,

$$\mathbf{J}=\sigma(\mathbf{E}+\mathbf{V}\times\mathbf{B}), \tag{53}$$

σ being the electrical conductance (Ω^{-1}/m) and $v_i=(\mathbf{V})_i$ the flow velocity (m/s). For electromagnetic power, consider the dot product of Eq. (53) with **J**,

$$\mathbf{J}\cdot\mathbf{J}=\sigma(\mathbf{E}+\mathbf{V}\times\mathbf{B})\cdot\mathbf{J}, \tag{54}$$

which may be rearranged as[3]

$$\mathbf{J}\cdot\mathbf{J}/\sigma=\mathbf{E}\cdot\mathbf{J}+(\mathbf{V}\times\mathbf{B})\cdot\mathbf{J}, \tag{55}$$

or, in terms of

$$(\mathbf{V}\times\mathbf{B})\cdot\mathbf{J}=-(\mathbf{J}\times\mathbf{B})\cdot\mathbf{V}, \tag{56}$$

as

[3]Clearly, $\mathbf{J}\cdot\mathbf{J}=J^2$, but J is used only for the intensity of radiation.

$$\mathbf{E}\cdot\mathbf{J}=(\mathbf{J}\times\mathbf{B})\cdot\mathbf{V}+\mathbf{J}\cdot\mathbf{J}/\sigma, \tag{57}$$

or, by the notation of this manuscript,

$$E_iJ_i=f_i^e v_i+u''', \tag{58}$$

E_iJ_i being the total electromagnetic power, $f_i^e v_i$ and $\mathbf{J}\cdot\mathbf{J}/\sigma$ respectively the displaced and deformed (dissipated) electromagnetic power.

Also, note the total mechanical power

$$\frac{\partial}{\partial x_i}(\tau_{ij}v_i)=v_i\frac{\partial\tau_{ij}}{\partial x_j}+\tau_{ij}s_{ij}, \tag{59}$$

the first and second right-hand terms respectively denoting displaced and deformed mechanical power.

Including radiation, q_i now denotes the total heat flux involving the sum of conductive and radiative fluxes,

$$q_i=q_i^K+q_i^R. \tag{60}$$

Now, consider the usual conductive constitution

$$q_i^K=-k\frac{\partial T}{\partial x_i} \tag{61}$$

and, following Arpacı [6], introduce the radiative constitution

$$q_i^R=-\frac{\eta}{\alpha_M}\frac{\partial\Pi_{ij}}{\partial x_j}, \tag{62}$$

where

$$\Pi_{ij}=\frac{4}{3}E_b\delta_{ij}+4\sum_{n=1}^{\infty}\frac{1}{\alpha_M^{2n}}\left(M_{ijpq\ldots}\frac{\partial}{\partial x_p}\frac{\partial}{\partial x_q}\right)E_b \tag{63}$$

with

$$M_{ijpq\ldots}=\frac{1}{4\pi}\int_\Omega(l_il_jl_pl_q\ldots)d\Omega. \tag{64}$$

Here l_i is the specular unit vector, $E_b=\sigma T^4$ the Stefan-Boltzmann law for black body emissive power, $\alpha_M=(\alpha_P\alpha_R)^{1/2}$ the mean absorption coefficient, $\eta=(\alpha_P/\alpha_R)^{1/2}$ the degree of nongrayness, and α_P and α_R, respectively, the Planck and Rosseland means of the absorption coefficient. A procedure for evaluation of Eq. (64) in terms of the Wallis Integrals is described in Unno and Spiegel [15]. After lengthy manipulations, the procedure leads to

$$\Pi_{ij}=4\sum_{n=0}^{\infty}\frac{\nabla^{2n-2}(2n\partial_i\partial_j+\nabla^2\delta_{ij})E_b}{\alpha_M^{2n}(2n+1)(2n+3)}, \tag{65}$$

where $\partial_i\equiv\partial/\partial x_i$ and $\partial_i\equiv\partial/\partial x_j$ are used for notational convenience. The same result may be found also in earlier works (see, for example, Milne [16]). The formal similarity of Eq. (65) to the Hookean constitution for elastic solids should be noted.

For an alternative form of this stress, first consider the trace of Π_{ij},

$$\Pi_{kk}=\sum_{n=0}^{\infty}\left(\frac{\nabla^2}{\alpha_M^2}\right)^n\frac{B}{2n+3}=J, \tag{66}$$

where J is the spectrally and specularly averaged monochromatic intensity,

$$J=\int_\nu\int_\Omega I_\nu d\Omega d\nu. \tag{67}$$

Next, in a manner similar the development of a viscous constitution from the elastic constitution (see, e.g., Prandtl [17]), adding identity

$$\left(\frac{1}{3}J-\Pi_{ij}\right)\delta_{ij}=0 \tag{68}$$

to Eq. (65), the Π_{ij}-tensor may be rearranged in terms of J-scalar,

$$\Pi_{ij}=\frac{1}{3}J\delta_{ij}+\sum_{n=0}^{\infty}\frac{2n\nabla^{2n-2}[\partial_i\partial_j-(1/3)\nabla^2\delta_{ij}]B}{\alpha_M^{2n}(2n+1)(2n+3)}. \tag{69}$$

The apparent similarity of Eq. (69) to the Stokesean viscous stress and the Maxwell electromagnetic stress should be noted. This similarity is to be expected in view of the assumed homogeneity for the elastic, viscous and electromagnetic continua (see, e.g., Stratton [18], and Prager [19]). The use of the first term of Eq. (69) in place of Eq. (65) is the well-known Eddington approximation. The local thermo-electro-magneto-mechanical entropy production resulting from the sum of thermo-electro-magneto-mechanical deformations becomes

$$s'''=\frac{1}{T}\left[\frac{1}{T}\left(k\frac{\partial T}{\partial x_i}+\frac{\eta}{\alpha_M}\frac{\partial\Pi_{ij}}{\partial x_i}\right)\frac{\partial T}{\partial x_i}+\tau_{ij}s_{ij}+\frac{\mathbf{J}\cdot\mathbf{J}}{\sigma}\right]. \tag{70}$$

The reader is referred to Arpacı [3,4,6] and Arpacı and Esmaeeli [20] for entropy production resulting from radiative deformation.

IV Conclusions

The present lecture is based on the original idea of suggesting a First Law in terms of entropy flux rather than the well known classical approach expressing the Second Law in terms of heat flux. Accordingly, heat flux is expressed by a product of temperature and entropy flux. A change in heat flux is identified as a combination of thermal displacement and thermal deformation. Only thermal deformation dissipates (irreversibly transforms) into internal energy and produces entropy. In terms of thermal deformation, the well-known thermodynamic irreversibility across a thermal discontinuity is replaced by actual irreversibility across a continuous thermal distribution. These considerations allow a transition from equilibrium concepts introduced in classical thermodynamics to actual concepts utilized in transport phenomena including heat transfer and gas dynamics.

An earlier version of this lecture was presented at the symposium on Thermal Science and Engineering honoring Chancellor Chang-Lin Tien, held on November 14, 1995 in Berkeley, California.

References

[1] Bird, R. B., Stewart, W. E., and Lightfoot, E. N., 1960, *Transport Phenomena*, Wiley, New York.
[2] Arpacı, V. S., 1966, *Conduction Heat Transfer*, Addison-Wesley, Massachusetts.
[3] Arpacı, V. S., 1986, "Radiative Entropy Production," AIAA J., **24**, pp. 1859–1860.
[4] Arpacı, V. S., 1987, "Radiative Entropy Production—Lost Heat into Entropy," Int. J. Heat Mass Transf., **30**, pp. 2115–2123.
[5] Arpacı, V. S., 1990, "Foundation of Entropy Production," *Advances in Thermodynamics*, S. Sieniutycz and P. Salomon, eds., Taylor and Francis, New York.
[6] Arpacı, V. S., 1991, "Radiative Entropy Production—Heat Loss into Entropy," *Advances in Heat Transfer*, **21**, J. P. Hartnett and T. F. Irvine, eds., Academic Press, New York.
[7] Bejan, A., 1982, *Entropy Generation through Heat and Fluid Flow*, Wiley, New York.
[8] Bejan, A., 1982, "Second Law Analysis in Heat Transfer and Thermal Design," *Advances in Heat Transfer*, **15**, J. P. Hartnett and T. F. Irvine, eds., Academic Press, New York, pp. 1–58.
[9] Bejan, A., 1988, *Advanced Engineering Thermodynamics*, Wiley-Interscience, New York.
[10] Bejan, A., 1996, "Entropy Generation Minimization: The New Thermodynamics of Finite-size Devices and Finite-time Processes," J. Appl. Phys., **79**, pp. 1191–1218.

[11] Fermi, E., 1956, *Thermodynamics*, Dover Publications Inc., New York.
[12] Planck, M., 1945, *Treatise on Thermodynamics*, Dover Publications Inc., New York.
[13] Shercliff, J. A., 1965, *A Textbook of Magnetohydrodynamics*, Pergamon Press, Oxford.
[14] Mitchner, M., and Kruger, C. H., 1973, *Partially Ionized Gases*, John Wiley & Sons, New York.
[15] Unno, W., and Spiegel, E. A., 1966, ''The Eddington Approximation in the Radiative Heat Equation,'' Publ. Astron. Soc. Jpn., **18**, pp. 85–95.
[16] Milne, E. A., 1930, ''Thermodynamics of Stars,'' *Handbuch der Astrophysik*, Springer-Verlag, Berlin, **3**, Chap. 2, pp. 65–255.
[17] Prandtl, L., and Tietjens, O. G., 1957, *Fundamentals of Hydro and Aeromechanics*, Dover Publications Inc., New York.
[18] Stratton, J. A., 1941, *Electromagnetic Theory*, McGraw-Hill, New York.
[19] Prager, W., 1961, *Introduction to Mechanics of Continua*, Ginn Press, Massachusetts, pp. 87–92.
[20] Arpacı, V. S., and Esmaeeli, A., 2000, ''Radiative Deformation,'' J. Appl. Phys., **87**, pp. 3093–3100.

Performance of Rectangular Fin in Wet Conditions: Visualization and Wet Fin Efficiency

Yur-Tsai Lin

Kuei-Chang Hsu

Department of Mechanical Engineering,
Yuan-Ze University,
Taoyuan, Taiwan

Yu-Juei Chang

Chi-Chuan Wang
Mem. ASME
e-mail: ccwang@itri.org.tw

Energy & Resources Laboratories,
Industrial Technology Research Institute,
Hsinchu, 310, Taiwan

An experimental study concerning the performance of a rectangular fin in both dry and wet condition was carried out. The visual observation of the dehumidifying phenomenon identified four regions, including the fully dry, very fine droplet, larger droplet, and film-like region. Experimental results showed that the effect of dry bulb temperature on the wet fin efficiency is very small. The dry fin efficiency is about 15–25 percent higher than that of the corresponding wet fin efficiency. For fully wet condition, the effect of relative humidity on the fully wet fin efficiency is also small. For partially wet surface, a considerable influence of the relative humidity on the fin efficiency is encountered. Test results for the fully wet fin efficiency agree well with some of the previous studies but disagree with some of the previous investigations. The main cause to this controversy may be attributed to the formulation of the relation between the humidity ratio and the fin temperature. The fully wet fin efficiency decrease slightly with increase of fin base temperature. However, the effect of fin base temperature on the dry fin efficiency is relatively small. [DOI: 10.1115/1.1391275]

Keywords: Dehumidification, Finned Surfaces, Heat Transfer

Introduction

Extended surfaces or fins are employed in heat exchangers for effectively improving the overall heat transfer performance. Extensive researches were related to this subject with single-phase heat transfer. However, there are many applications for extended surfaces involved with two-phase flow. For instance, in the case of cooling coils, when warm and humid air encounters a cold surface that is below its dew point temperature, condensation will take place and mass transfer occurs simultaneously with heat transfer. The performance of the extended surfaces is different from that of dry surfaces. One of the major differences for wet surfaces is the pronounced drop of fin efficiency. There are intensive numerical studies on the wet fin efficiency but only limited experimental information. Table 1 summarized the related investigations about the performance of extended fin surfaces under dehumidifying conditions [1–17].

However, as shown in Table 1, results of the relative humidity on the fully wet fin efficiency of extended surfaces is quite confusing. In the ARI 410-91 standard [1], the method shows that the fully wet fin efficiency is independent of inlet conditions (relative humidity). Notice that the method is based on the one-dimensional analysis by Ware and Hacha [18]. An analogous approach by Threlkeld [3] that incorporated with the influence of water film also revealed that the effect of relative humidity on the wet fin efficiency is also very small. Conversely, analysis by McQuiston [4], Hong and Webb [5], Elmahdy and Biggs [6], and Rosario and Rahman [14,15] shows a significant decrease of fully wet fin efficiency when the relative humidity is increased.

The previous studies were based on the one-dimensional approach. For detailed evaluation of the wet fin efficiency, Chen [9] and Liang et al. [17] proposed a two-dimensional model that took the complex fin geometry and the moist air properties over the fin into account. Both of these investigations reported that the fully wet fin efficiency is relatively insensitive to change of relative humidity. In addition, Liang et al. [17] had shown that the accuracy of the one-dimensional numerical model is comparable to that of the two-dimensional model. Besednjak and Poredoš [16] calculated the wet fin performance in a continuous fin-and-tube heat exchanger utilizing a three-dimensional approach. Their calculations also indicated that the fully wet fin efficiency is nearly constant at high condensate loading.

The previous studies were carried out via analytical and numerical approach. The only experimental work related to this subject was done by Coney et al. [7]. Coney et al. [7] reported performance of a blunt and elliptical fin in a very thick copper fin (20 mm thick). In their observation, they found that the copper fins promote dropwise condensation and no film condensation is observed. However, in practical implementation of the fin-and-tube heat exchangers in HVAC&R application, aluminum alloy is often employed. In view of the previous studies, though many analytical efforts had been devoted to the extended surfaces in wet conditions, it appears that considerable controversy still exits. Thus it would be very helpful to clarify this phenomenon via experimental study. It is the objective of the present study to make clear of this controversy.

Experimental Apparatus

Experiments were performed in an environmental chamber as shown in Fig. 1. The test apparatus is based on the air-enthalpy method proposed by ANSI/ASHRAE Standard 37 [19]. Cooling capacity was measured from the enthalpy difference of the air flowrate across the test sample. The air flow measuring apparatus is constructed from ASHRAE Standard 41.2 [20]. Dry and wet bulb temperature measurement devices of the airflow is constructed based on ASHRAE 41.1 Standard [21]. Experiments were performed in an environmental chamber. The environmental chamber can control the ambient conditions in the range of $10°C \leqslant T_{DB} \leqslant 50°C$ and $40\ \text{percent} \leqslant RH \leqslant 95\ \text{percent}$. Control resolution for the related dry bulb and wet bulb temperature is 0.1°C.

For the experimental investigations, a model of extended surface was designed and manufactured as depicted in Fig. 2. The aluminum alloy 601 is chosen as the base and fin material because of its relatively high thermal conductivity and rigidity. The fin is 100 mm deep, 100 mm wide, and 2 mm thick. The fins were

Contributed by the Heat Transfer Division for publication in the JOURNAL OF HEAT TRANSFER. Manuscript received by the Heat Transfer Division June 26, 2000; revision received April 2, 2001. Associate Editor: B. Chung.

Table 1 Experimental results for previous investigators

Investigators	Numerical or Experimental	Fin Shape	1-D or 2-D model	Boundary condition at fin tip	Examine partially wet condition	Effect of humidity on fully wet fin efficiency
ARI [1]	Standard	-		-	-	No effect
O'brien and Turner [2]	Numerical	Rectangular	1-D	Insulated	No	-
Threlkeld [3]	Numerical	Rectangular	1-D	Insulated	No	Very small
McQuiston [4]	Numerical	Rectangular	1-D	Insulated	No	Pronounced
Elmahdy and Biggs [5]	Numerical	Circular	1-D	Insulated	No	Pronounced
Coney et al. [6]	Numerical	Rectangular	1-D	Insulated	Yes	Very small
Coney et al. [7]	Experimental	Rectangular			-	Small
Coney et al. [8]	Numerical	Rectangular	1-D	Insulated	-	Pronounced
Chen [9]	Numerical	Rectangular	2-D	Insulated	Yes	Very small
Kazeminejad [10]	Numerical	Rectangular	1-D	Convective	-	-
Wu and Bong [11]	Numerical	Circular	1-D	Insulated	Yes	Very small
Hong and Webb [12]	Numerical	Circular	1-D	Insulated	No	Pronounced
Salah El-Din [13]	Numerical	Rectangular	1-D	Insulated Convective	Yes	-
Rosario and Rahman [14,15]	Numerical	Circular	1-D	Convective	Yes	Pronounced
Besednjak and Poredoš [16]	Numerical	Plate Fin-and-tube	3-D	Continuous fin	Yes	Small
Liang et al. [17]	Numerical	Circular	1-D and 2-D	Insulated	Yes	Negligible

mounted vertically on the aluminum alloy block as shown in Fig. 2. Care was taken to align the fin so that it was parallel to the air flow. The base block was carefully machined to have 155 U-grooves. The width and height of the groove is 2 mm. Noticed that a high thermal conductivity grease ($k=2.1$ W/m·K) was used to connect the fin and the base material to minimize the contact resistance. A mean gap distance of 0.05 mm is assumed between the attached fin and the base aluminum block. Actual fin base temperatures were then corrected from the measured temperatures. The fin spacing can be 3 or 8 mm. To measure the fin temperature in both directions of transverse and longitudinal to the airflow, a total of eighteen thermocouples were mounted on one of the fins that is located near the center position. Detailed locations of the thermocouples were shown in Fig. 2. These '*T*'-type thermocouples were pre-calibrated with a resolution of 0.1°C. To heat and cool the fin, water was circulated via four holes drilled beneath the fin base in the aluminum block. The water inlet temperature of the test section was controlled by low temperature thermostat. During the experiments, water was circulated with a sufficiently high velocity (>3 m/s) to maintain the fin base temperature at a constant level. For various operation frontal velocities, the thermostat temperature was adjusted to keep the variation of the fin base temperature between inlet and outlet to be less than 0.2°C. The test conditions are given as follows:

Inlet dry bulb temperature: 20~27°C
Inlet relative humidity: 40~90 percent
Water temperature at the inlet: 2–9°C
Base fin temperature: 3~13°C

Droplet formulation on the fin was recorded by a JVC digital video cam GR-DVM50 with a speed of 30 frames/s. Experimental uncertainties are tabulated in Table 2.

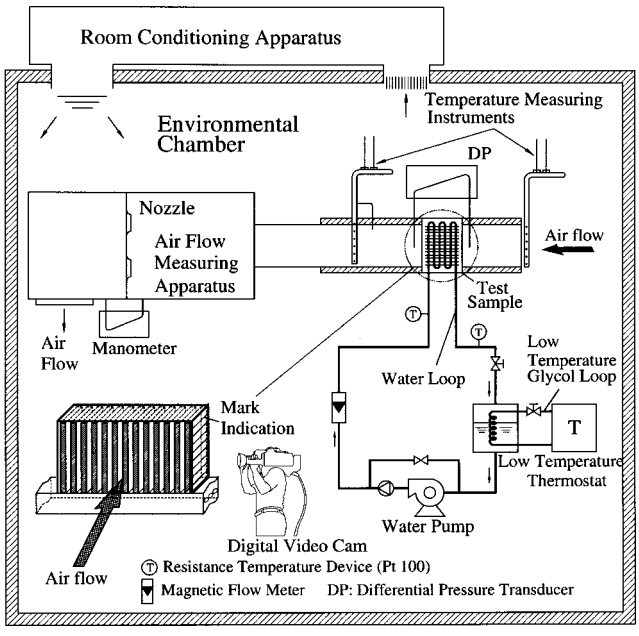

Fig. 1 Schematic of experimental setup

Results and Discussion

In the visualization study, photographs were taken for frontal velocities ranging from 0.3 m/s to 6 m/s. The corresponding fin base temperature and inlet dry bulb temperature were maintained at 9°C and 27°C with the inlet relative humidity ranging from 50 percent~90 percent. Selected photographs from the observations for $RH_{in}=50$, 70, and 90 percent are shown in Figs. 3(*a*), 3(*b*), and 3(*c*), respectively. The corresponding fin temperature variation in both axial and radial direction are also plotted in Figs. 4(*a*), 4(*b*), and 4(*c*). The dimensionless fin temperature Θ is defined as $(T_f-T_\infty)/(T_{fb}-T_\infty)$. The experiments were performed from high velocity to low velocity. This is because quicker steady-state can be achieved. Were experiments performed from low velocity to high velocity, it would take much more time to reach the final steady state. Notice that the final steady state is the same for both test situation.

In Fig. 3(*a*), at a high frontal velocity like 6 m/s or 4 m/s and an inlet relative humidity of 50 percent, formation of the droplet can be seen only at the vicinity of the fin base. One can clearly see the boundary separating the dry and wet portion. Note that the drop size at the boundary is very fine and the drop size increases as it approaches to the fin base. The height of the boundary increases as the frontal velocities are further decreased to 2.5 m/s or 1.5 m/s. The results may be further made clear from the corresponding temperature variation of Fig. 4(*a*). For a given frontal velocity,

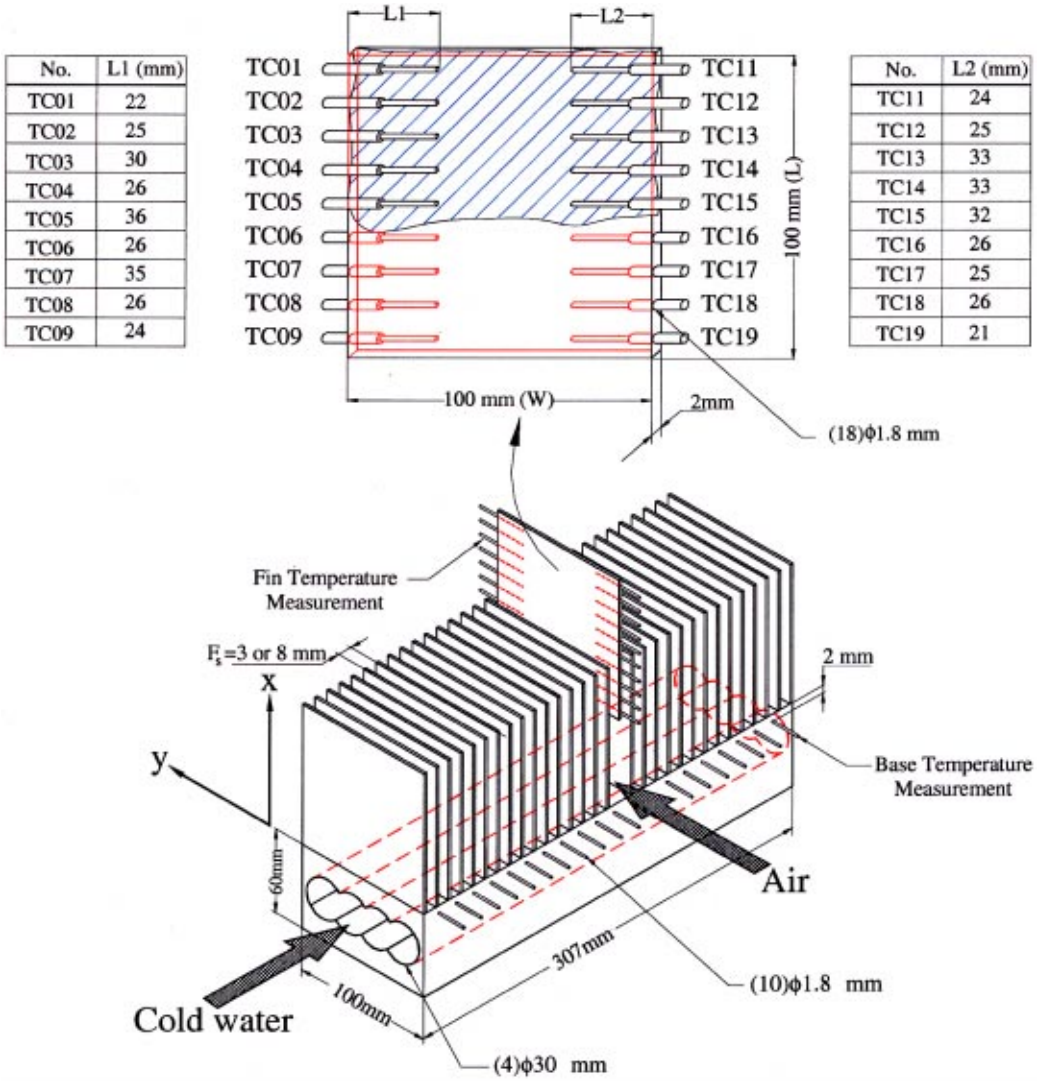

Fig. 2 Enlarged view of the test section

the dimensionless temperature Θ at the leading edge ($y/W=0.25$) is lower than those of the trailing edge ($y/W=0.75$). This is because higher heat transfer performance is seen in the leading edge. For $V_{fr}=0.3$ m/s, the corresponding inlet dew point temperature (evaluated as $\Theta_{\text{dew,in}}=(T_{\text{dew,in}}-T_\infty)/(T_{fb}-T_\infty)$) is lower than the dimensionless fin temperature. This implies the whole fin is in fully wet condition. However, for a frontal velocity of 1.5 m/s, the fin is in partially wet condition. A further increase of the relative humidity, as can be clearly seen from Figs. 3(*b*) and 3(*c*), the wet portion on the fin is increased. Notice that the boundary line is not horizontal, the dry portion near the leading edge is larger than that of trailing region.

The observation is quite different from those assumption made by the analytical analysis shown in Table 1. The analytical model of the "partially wet" fin always assumed a horizontally boundary line. The inclination of the boundary line increases with the decrease of velocity. Although the mean dew point temperature decreases along the airflow direction, by checking the visualization results of Fig. 3 and the relevant temperature variation along the fin from Fig. 4, the boundary line is located at the fin temperature that is close to the inlet dew point temperature. This is because the cross-flow arrangement of the present fin geometry. A further decrease of frontal velocities to 0.75 m/s and 0.3 m/s cause the boundary line to move up further. For $V_{fr}=0.3$ m/s, as seen from the fin temperature variation in Fig. 4(*a*), the entire fin is fully wet because all the fin temperature is below the inlet dew point temperature.

The results of $RH_{\text{in}}=70$ percent in Fig. 3(*b*) are analogous to those of $RH_{\text{in}}=50$ percent with the dry-wet boundary being moved further upward. Basically, the dehumidification phenomenon of a rectangular fin can be roughly classified into four region. For region (I) the fin temperature is above the inlet dew point temperature, the surface is fully dry. For region (II) that is near the dry-wet boundary, the drop size is very small (of the order of 0.1~0.5 mm). In region (II), the heat transfer is similar to dropwise condensation. Eventually, the very fine size of droplet may grow up in the down stream of airflow and join with the neighboring droplet to become larger droplets (region III). In this region, the larger droplet grew more quickly to a critical size,

Table 2 Summary of estimated uncertainties

Primary Measurements		Derived Quantities		
Parameter	Uncertainty	Parameter	Uncertainty $V_{fr}=0.3$ m/s	Uncertainty $V_{fr}=6$ m/s
$\dot{m}_{air}$	0.3-1%	Re_{Dh}	±1.0%	±0.57 %
T_a	0.1°C	$\dot{Q}_*$	±5.5%	±2.4%
RH_{in}	2 %	η	±5%	± 3.5%

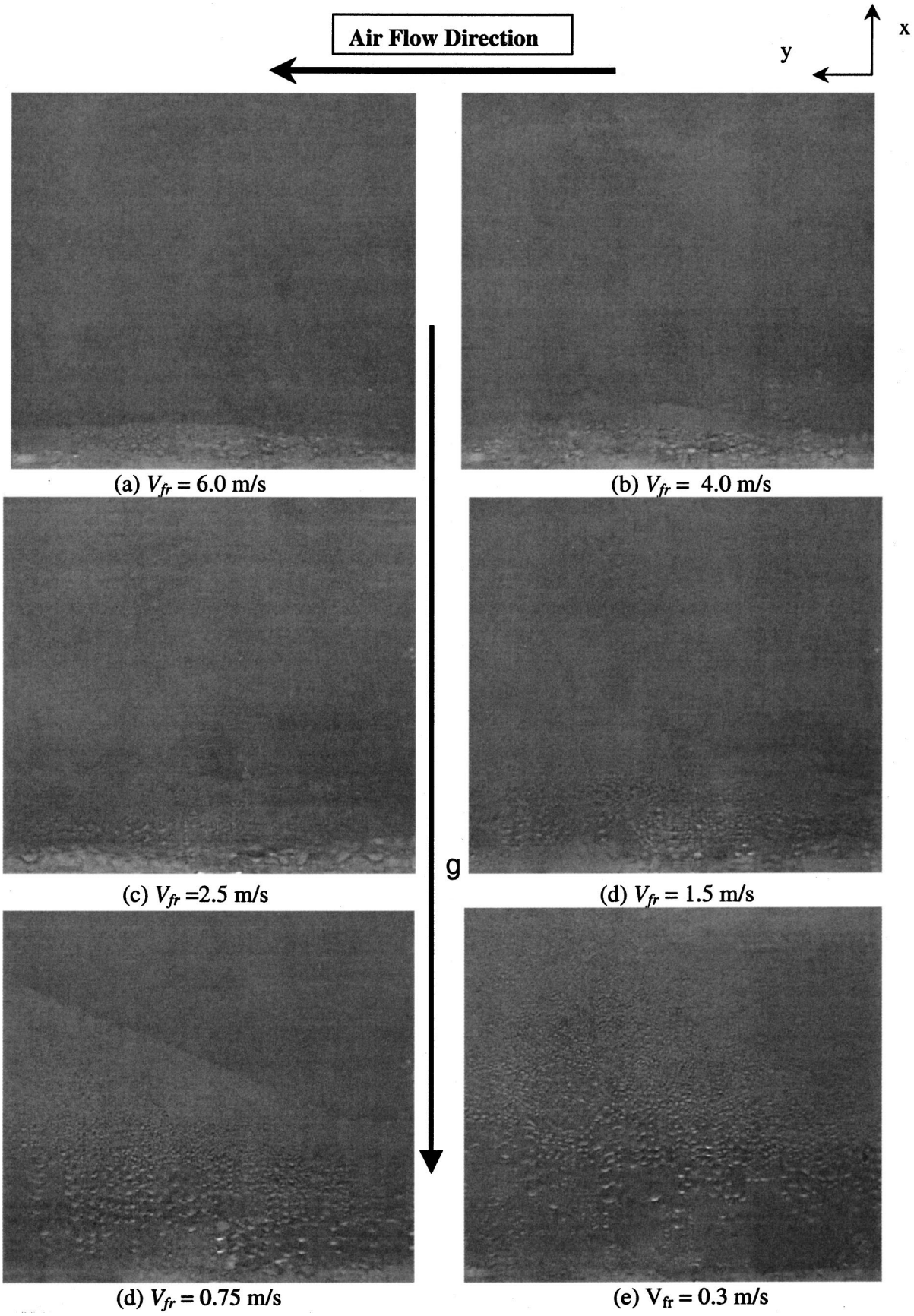

Fig. 3 (*a*) Droplet formation on a fin with RH_{in}=50 percent, $T_{DB,in}$=27°C, F_s=3 mm, T_{fb}=9°C; (*b*) droplet formation on a fin with RH_{in}=70 percent, $T_{DB,in}$=27°C, F_s=3 mm, T_{fb}=9°C; and (*c*) droplet formation on a fin with RH_{in}=90 percent, $T_{DB,in}$=27°C, F_s=3 mm, T_{fb}=9°C.

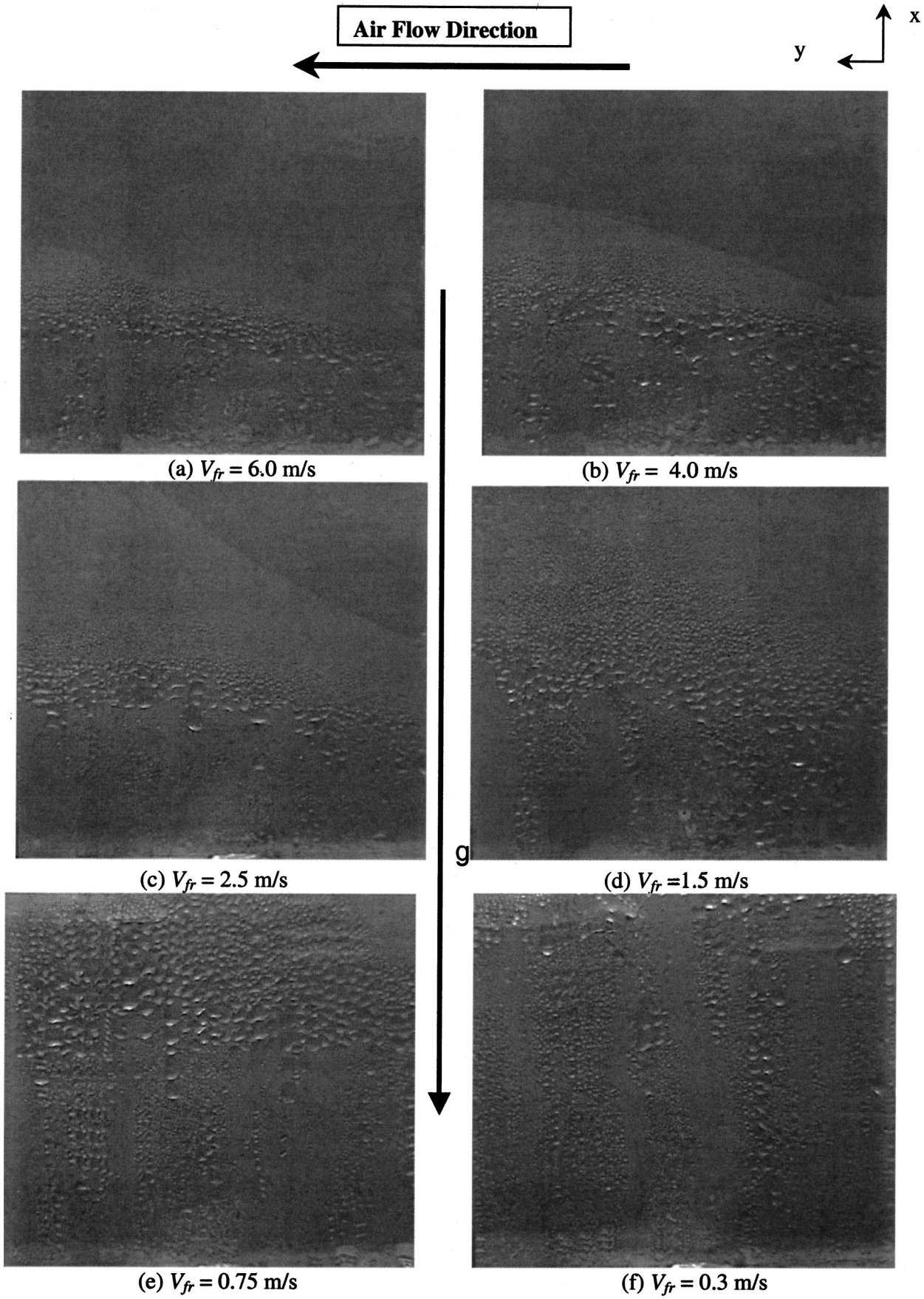

Fig. 3b (***Continued.***)

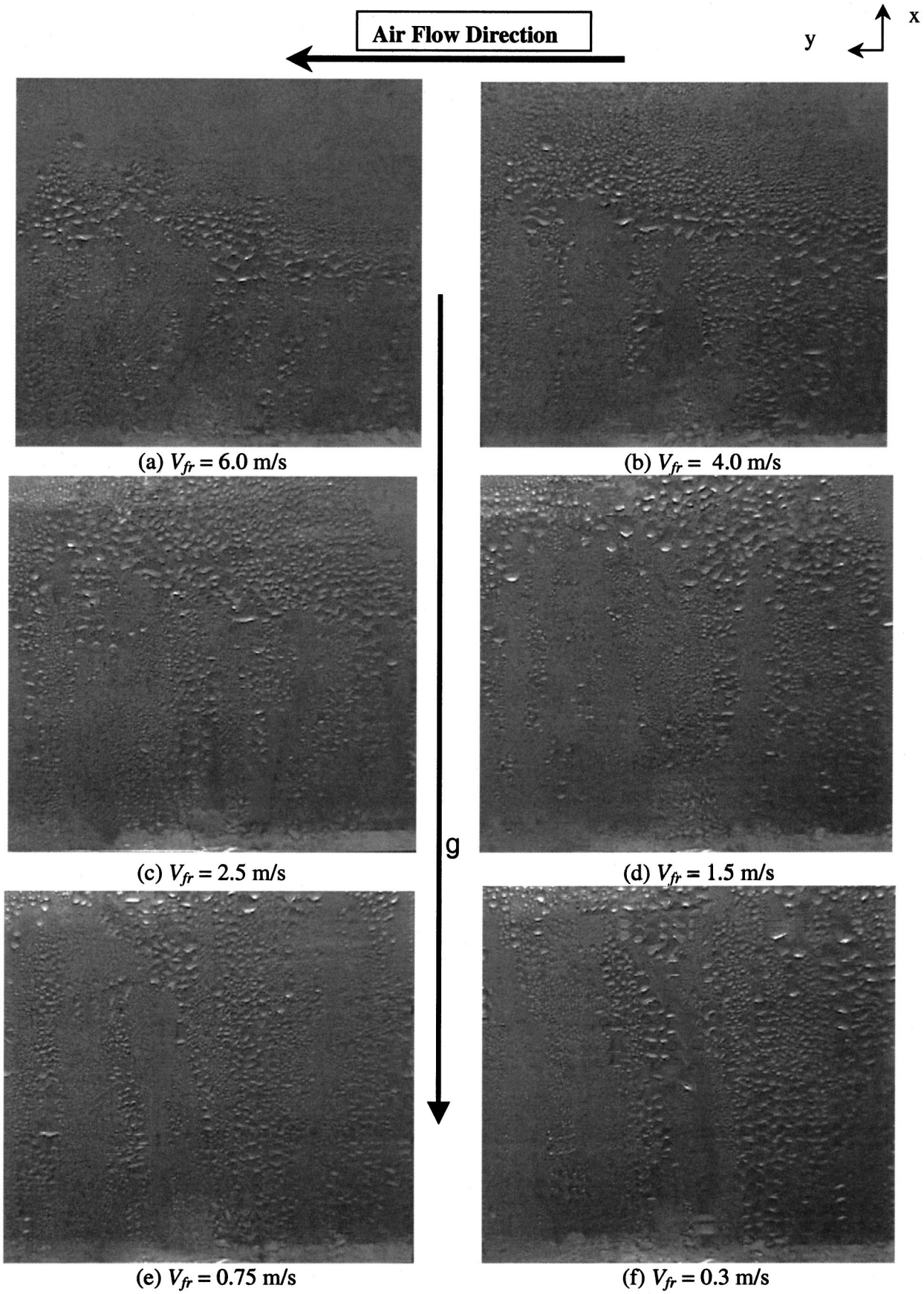

Fig. 3c (***Continued.***)

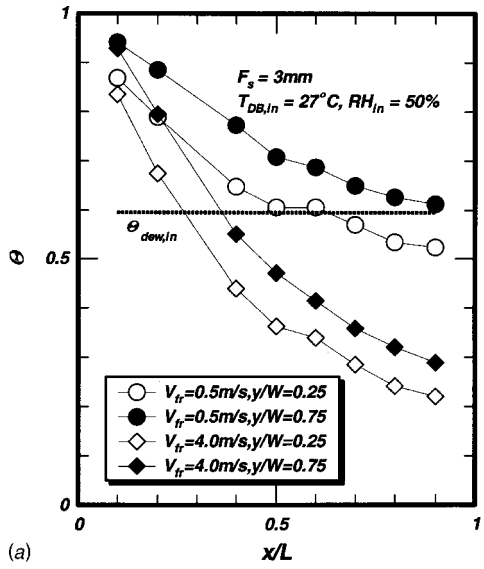

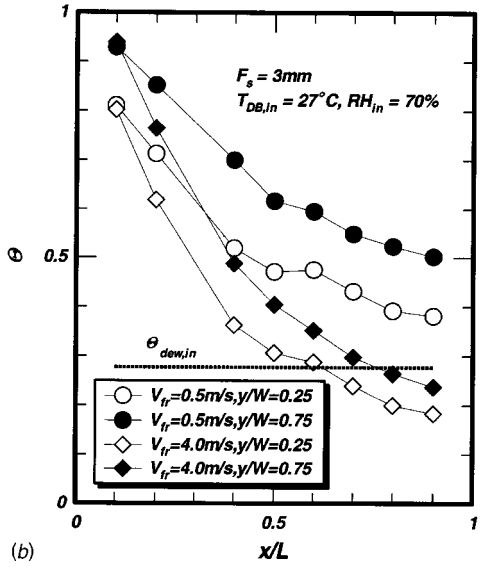

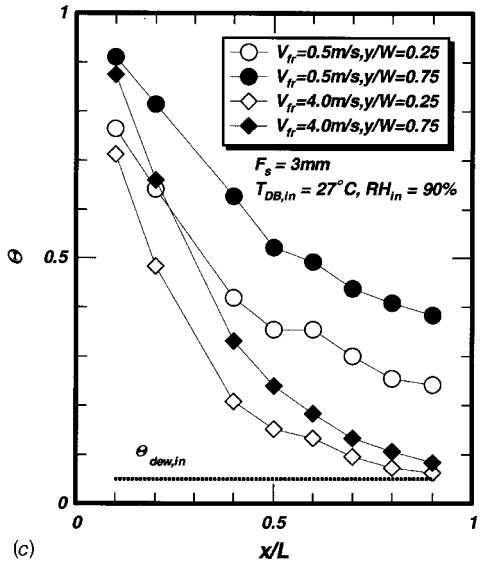

Fig. 4 (*a*) Variation of dimensionless temperature for $T_{DB,in}$=27°C, RH_{in}=50 percent; (*b*) variation of dimensionless temperature for $T_{DB,in}$=27°C, RH_{in}=70 percent; and (*c*) variation of dimensionless temperature for $T_{DB,in}$=27°C, RH_{in}=90 percent.

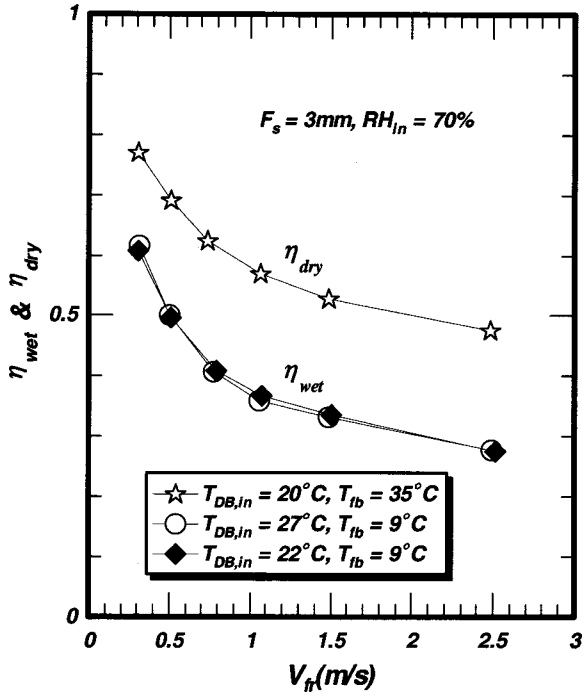

Fig. 5 Effect of the dry bulb temperature on the dry and wet fin efficiency

overcoming the force due to surface tension. They then rolled randomly down the fin due to gravity, dragging other droplets and drained the condensate close to the base of the fin. Notice that region (III) is quite unsteady when comparing to region (I) and (II). In region (IV) that is close to the base portion, a thin film was formed by the ''washed away'' droplet drained from region (III). Notice that a wave-like droplet may deposit on the film. It should be pointed out that region (I) will disappear when the surface temperature is below inlet dew point temperature and region (II) may also disappear when the air velocity is low and the inlet humidity is sufficiently high. As can be seen from Fig. 3(*c*), the region (II) is not seen for $V_{fr}<1.5$ m/s. The condensate drainage phenomenon is especially pronounced in the leading portion of the fin, one can see that the frequency of droplet falling off from region (II) is more rapid when comparing to the trailing edge of the fin. This phenomenon can be interpreted as follows. As is known, when the condensation takes place, the noncondensable air will form at the interface between the water condensate and the airflow, the mass transfer resistance will inhibit the heat transfer. In addition, the fall of local dew point temperature along the airflow direction will also contribute to reduce the heat transfer performance.

The loss of performance for a fin is characterized as the fin efficiency. This is defined as the ratio of actual heat transfer through a fin surface to the heat transfer of an ideal fin at the base fin temperature. The wet fin efficiency is calculated from the enthalpy fin efficiency, i.e.,

$$\eta_{\text{wet}}=\frac{i-i_{s,\text{fin}}}{i-i_{s,fb}} \tag{1}$$

Figure 5 shows the comparison of the dry fin efficiency and wet fin efficiency at $F_s=3$ mm and $RH_{\text{in}}=70$ percent. At low frontal velocities, the difference between dry and wet fin efficiency is smaller than that at higher velocities. For $V_{fr}=0.3$ m/s, the dry fin efficiency is about 15 percent higher than that of wet fin efficiency. The dry fin efficiency exceeds that of wet fin efficiency by approximately 20 percent at $V_{fr}=2.5$ m/s. The effect of dry bulb

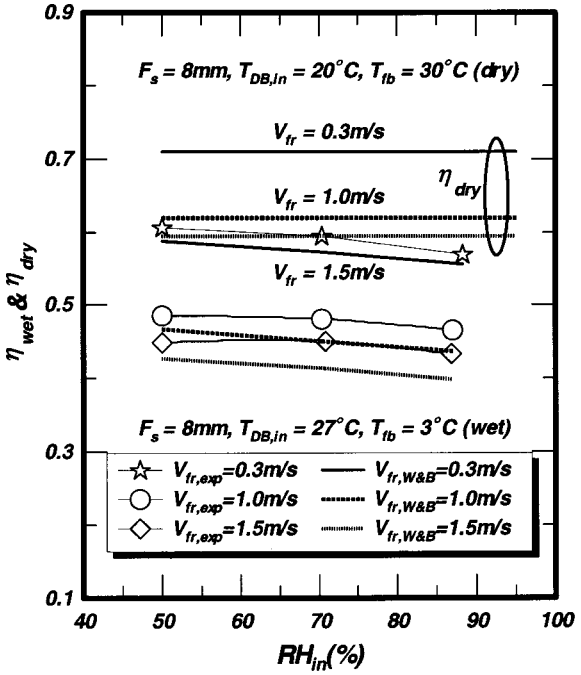

Fig. 6 Effect of relative humidity on the dry and fully wet fin efficiency

temperature on the wet fin efficiency is also shown in this figure. As expected, the effect of dry bulb temperature on the wet fin efficiency is rather small.

The effect of inlet relative humidity on the corresponding dry and wet fin efficiency is illustrated in Fig. 6. To avoid the presence of partially wet conditions along the fin for $RH_{\text{in}}=50$ percent, the fin base temperature shown in this experiment was reduced to 3°C, and only the fully wet fin efficiency is shown ($V_{fr} \leqslant 1.5$ m/s). One can see that the effect of relative humidity on the fully wet fin efficiency is small. However, as mentioned in Table 1, many researchers had investigated the effect of relative humidity on the wet fin efficiency, some of the researchers reported the effect of relative humidity on the wet fin efficiency is very small [3,6,7,9,11,17] but some of the researchers claimed a pronounced decrease of wet fin efficiency relative to the increase of relative humidity due to the presence of mass transfer [4,5,8,12,14,15]. Hence, it would be very helpful to identify the controversy between these studies.

Considering the analysis of a fully wet rectangular fin using the one-dimensional approach, the energy equation is usually derived as the following form:

$$\frac{d^2T_f}{dx^2}-\frac{1}{k_f t}[h_a(T_f-T_a)+i_{fg}K_m(\omega_f-\omega_a)]=0, \tag{2}$$

where t is the half-fin thickness, most of the investigators employed the Chilton-Colburn analogy (Chilton and Colburn, [22]):

$$\frac{h_a}{K_m C_p}=\text{Le}^{2/3} \text{ or } \frac{h_a}{K_m C_p}=1, \tag{3}$$

where Le is the Lewis number, thus Eq. (2) can be rewritten as

$$\frac{d^2\theta}{dx^2}-m_0^2\theta\left(1+\frac{i_{fg}}{C_p\text{Le}^{2/3}}(\omega_a-\omega_f)\right)=0, \tag{4}$$

where

$$\theta=T_a-T_f \tag{5}$$

$$m_0=\sqrt{\frac{h_a P}{k_f A_c}}. \tag{6}$$

To solve Eq (4), it is essential to relate $\omega_a-\omega_f$ and θ. The controversy in the investigators may be related to this approximation of the relation between the saturated humidity along the fin surface to the fin temperature. McQuiston [4] used the assumption that $(\omega_a-\omega_f)=C(T_a-T_f)$ in which C is a constant. Therefore, Eq. (4) can be solved relatively easily. Wu and Bong [11] argued that this assumption is physically inappropriate, this is because for fully wet condition at a fixed incoming air condition (T_a,ω_a) a constant C will allow only one possible value of the surface temperature T_f. Therefore, instead of the assumption of a constant C value, several investigations had proposed linear relationship ($\omega_f=a+bT_f$, Wu and Bong [11]) or quadratic relation ($\omega_f=a+bT_f+cT_f^2$, Coney et al. [6], Chen [9], and Liang et al. [17]) to approximate the relation between humidity and surface temperature. These approaches are more rationally based. Note that in fully wet region, the calculations by Coney et al. [6], Wu and Bong [11], Liang et al. [17], and Chen [9] indicated that the effect of the relative humidity is very small. However, the calculated results by McQuiston [4] showed a pronounced decrease to relative humidity. Although Coney et al. [6] showed the effect of relative humidity is very small on fully wet fin efficiency, however, their another study [8] revealed an opposite trend (a considerable drop of wet fin efficiency versus relative humidity). In order to explain the discrepancy, an examination of the Coney et al.'s work is carried out. It indicated that the Coney et al.'s work [8] is probably in error. Coney et al. [6] calculated the wet fin efficiency in terms of the following form:

$$\eta_{\text{wet}}=\int_0^1\left(\frac{R_b}{R}\right)\Theta_f d\xi, \tag{7}$$

where R is ratio of sensible to total heat transfer calculated at the fin temperature, and R_b is the ratio of sensible to total heat transfer calculated at the fin base temperature. Θ_f is the dimensionless fin temperature $(T_a-T_f)/(T_a-T_{fb})$ and ξ is the dimensionless distance from the fin base $(=x/L)$. By use of a different formulation, Coney et al. [8] defined the wet fin efficiency from the following process:

$$\eta_{\text{wet}}=\frac{Q_{fin}}{Q_{idf}}. \tag{8}$$

The ideal heat transfer rate from a wet fin of a strip of fin at x with a surface area is

$$Q_{idf}=2h_{ov}(T_a-T_{fb})Ldx, \tag{9}$$

where h_{ov} is the overall air heat transfer coefficient and is given by

$$h_{ov}=\left[1+\frac{i_{fg}C}{C_p}\right]h_a \tag{10}$$

$$C=\left[\frac{\omega_a-\omega_i}{T_a-T_i}\right]\cong\left[\frac{\omega_a-\omega_f}{T_a-T_f}\right]. \tag{11}$$

Coney et al. [8] use a second order polynomial that fits the psychrometric chart saturation line sufficiently well in the region of the fin temperature variation, i.e., $\omega_f=1.2075-0.9125\times10^{-2}T_f+0.1726\times10^{-4}T_f^2$. Apparently, the overall air heat transfer coefficient is related to the fin temperature variation along the fin, and the overall heat transfer coefficient h_{ov} and the sensible heat transfer coefficient h_a may not be assigning constant value at the same time. Examination of the results and formulation by Coney et al. [8] indicates that they might make a mistake by simultaneously assigning constant values to h_{ov} and h_a. As a consequence, the calculated results of [6] and [8] showed a completely different trend.

In addition to the rectangular fin, Hong and Webb [12] also showed that the wet fin efficiency decreases with increase of relative humidity in circular fin geometry. The results are not surprising because Hong and Webb [12] used the same assumption proposed by McQuiston (C is constant). It is interesting to note that Elmahdy and Biggs [5] use a linear relationship ($\omega_f = a + bT_f$) like Wu and Bong [11] but still reported a pronounced effect of relative humidity on the fully wet fin efficiency. Based on a complete mathematical proof, Kandlikar [23] re-examined the differential equation for the temperature distribution derived by Elmahdy and Biggs [5]. He showed that the fully wet fin efficiency should be independent of the relative humidity, and claimed an erroneous numerical solution of Elmahdy and Biggs [5]. Rosario and Rahman [14,15], however, showed that the wet fin efficiency is strongly influenced by the relative humidity. It is not clear about the formulation of the relationship between the humidity ratio and temperature in their study. Rosario and Rahman [15] argued their differences to those by Wu and Bong [11] is associated with the geometrical difference (rectangular fin versus circular fin). However, for circular fin, both the calculated results by one-dimensional and two-dimensional approach from Liang et al. [17] revealed that the fully wet fin efficiency is relatively independent of inlet relative humidity. In addition, a close examination of the fin temperature variation from their calculation [15] indicated that the fin may be in ''partially wet'' condition because part of the fin temperature was above the inlet dew point temperature. Their formulation is basically the same as Kazeminejad [10] who also presented the ''partially wet'' results in a rectangular fin. For a fin in partially wet condition, a detectable drop of the wet fin efficiency is expected (see Wu and Bong [11]).

For a detailed evaluation of the wet fin efficiency, Chen [9] and Liang et al. [17] had proposed a two-dimensional model that takes into account of the complex fin geometry and the moist air properties over the fin. Both studies reported that the fully wet fin efficiency is relatively insensitive to change of relative humidity. The experimental results by Coney et al. [7] in a thick wet fin also reveal that the fully wet fin efficiency is quite insensitive to change of relative humidity. In summary, based on the experimental evidence and the deductions from the aforementioned adiscussions, the present authors found that the fully wet fin efficiency should be insensitive to change of relative humidity. For comparison purpose, calculated results by Wu and Bong [11] were also plotted in Fig. 6. The results by Wu and Bong [11] also shows relatively small dependence of inlet relative humidity. The fin efficiency of the experimental data agree favorably with the predictive results by Wu and Bong [11].

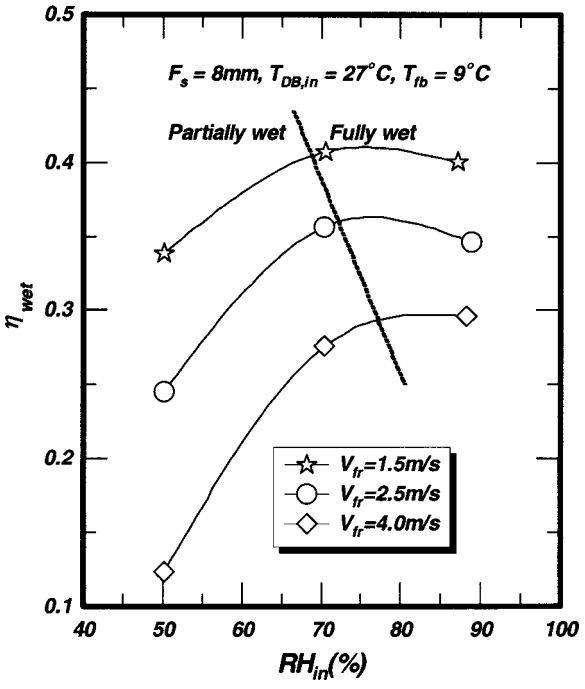

Fig. 7 Effect of inlet relative humidity on the partially wet surface

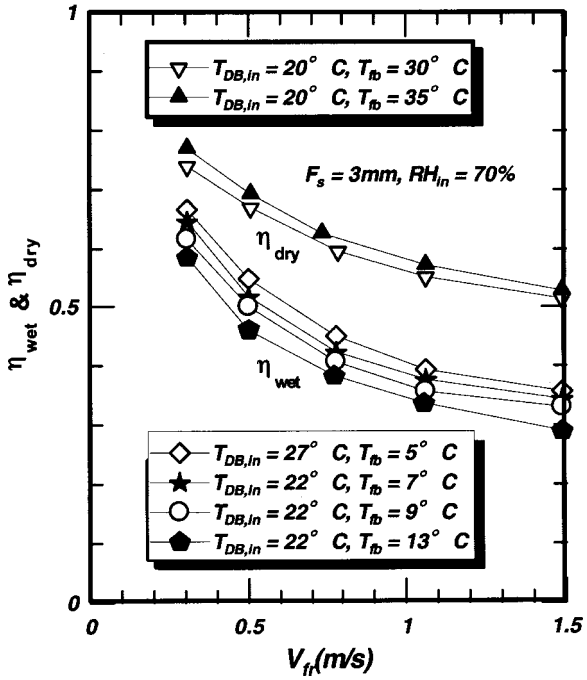

Fig. 8 Effect of fin base temperature on the fully wet efficiency

In some practical applications such as low relative humidity or high intake velocities, part of the fin surfaces may be dry. In this connection, fin efficiency may change significantly. Figure 7 shows the effect of inlet relative humidity on the fin efficiency of a partially wet surface. One can clearly see a sharp drop of fin efficiency in the partially wet region. The drop of fin efficiency is especially pronounced with increase of frontal velocities. The results are analogous to those previous findings. The effect of fin base temperature on the dry and wet fin efficiency is shown in Fig. 8. For a fully wet fin, the fin efficiency decrease slightly with increase of fin base temperature. Approximate 10 percent drop of wet fin efficiency is observed when the fin based temperature is increased from 5°C to 13 deg. The increase in fin base temperature may increase the value of the slope of saturated air humidity ratio, and hence increase the fin parameter m. As a consequence, it would reduce the fin efficiency. Also shown in Fig. 8, relative to the wet fin, the associated drop of dry fin efficiency is comparatively small.

Conclusions

An experimental study concerning the performance of a rectangular fin in both dry and wet condition was carried out. Based on the test results and observation, the following conclusions are made.

1 Visual observation of the dehumidification along the enlarged aluminum fin indicated the droplet formation can be roughly classified into four region. In region (I), the fin temperature is above the inlet dew point temperature, the surface is fully dry. In region (II) that is nearby the dry-wet boundary, the drop size is very small (of the order of 0.1~0.5 mm) and the heat transfer mode is similar to dropwise condensation. In region (III), the very fine size

of droplet may grow and join with the neighboring droplet to become larger droplet. In region (IV) that is close to the base portion, a thin film was formed.

2 The effect of dry bulb temperature on the wet fin efficiency is very small. Depending on the frontal velocities, the dry fin efficiencies are about 15~25 percent higher than the corresponding wet fin efficiency.

3 For fully wet condition, the effect of relative humidity on the fully wet fin efficiency is also small. The results agree well with some of the previous numerical calculations. However, some of the previous investigations show significant influence of inlet relative humidity on the fully wet efficiency. The main causes to the controversy between these calculated results from various investigators may be attributed to the formulation of the relation between the humidity ratio and the fin temperature, and mixed with "partially wet" fin efficiency. The fully wet fin efficiency decrease with increase of fin base temperature. However, the effect of fin base temperature on the dry fin efficiency is relatively small.

4 For a partially wet surface, a significant drop of fin efficiency is observed as the inlet relative humidity is decreased.

Acknowledgments

The authors are indebted to the Energy R&D foundation funding from the Energy Commission of the Ministry of Economic Affairs and National Science Committee (NSC 89-2212-E-155-007) of Taiwan for supporting this study.

Nomenclature

A_c = cross-section of fin
$A_{\min}$ = minimum free flow area
A_o = total surface area
C = parameter
C_p = moist air specific heat at constant pressure
D_h = hydraulic diameter$=4A_{\min}W/A_o$
F_s = fin spacing
h_a = sensible heat transfer coefficient for wet coils
h_{ov} = overall heat transfer coefficient
i = air enthalpy
i_{fg} = latent heat of water condensate
$i_{s,fb}$ = saturated air enthalpy evaluated at fin base temperature
K_m = overall mass transfer coefficient
k_f = thermal conductivity of fin
L = fin depth (see Fig. 1)
Le = Lewis number
m = fin parameter
m_0 = parameter defined in Eq. (6)
$\dot{m}_a$ = air mass flow rate
P = perimeter of the fin
Q_{fin} = actual heat transfer rate from the fin
Q_{idf} = maximum heat transfer rate from the fin
R = ratio of sensible to total heat transfer calculated at the fin temperature
R_b = ratio of sensible to total heat transfer calculated at the fin base temperature
Re_{Dh} = Reynolds number based on hydraulic diameter
RH = relative humidity
RH_{in} = inlet relative humidity of the intake air
t = half-fin thickness
T = temperature
T_{DB} = dry bulb temperature
$T_{DB,\mathrm{in}}$ = inlet dry bulb temperature of the intake air
$T_{\mathrm{dew,in}}$ = inlet dew point temperature
T_a = air ambient temperature
T_f = fin temperature
T_{fb} = fin base temperature
T_∞ = ambient temperature
V_{fr} = frontal velocity
W = width of the rectangular fin (see Fig. 1)
ω = humidity ratio
ω_a = air humidity ratio
ω_f = humidity ratio evaluated at fin temperature
ω_i = humidity ratio evaluated at the interface of condensate and air
x = distance from the fin base
y = distance from the leading edge of fin
η_{dry} = dry fin efficiency
η_{wet} = wet fin efficiency of a wet circular fin
η_f = fin efficiency
Θ = dimensionless fin temperature$(T_f-T_\infty)/(T_{fb}-T_\infty)$
$\Theta_{\mathrm{dew,in}}$ = $(T_{\mathrm{dew,in}}-T_\infty)/(T_{fb}-T_\infty)$
θ = T_f-T_a
ξ = dimensionless distance from the fin base $(=x/L)$

References

[1] ARI standard 410-91, 1991, "Forced-Circulation Air-Cooling and Air-Heating Coils," Air-Conditioning & Refrigeration Institute, Arlington.
[2] O'Brien, N. G., and Turner, R. L., 1963, "Fin Thermal Efficiency During Simultaneous Heat Mass Transfer," AIChE J., **11**, pp. 546–548.
[3] Threlkeld, J. L., 1970, *Thermal Environmental Engineering*, New-York: Prentice-Hall, Englewood Cliffs, NJ.
[4] McQuiston, F. C., 1975, "Fin Efficiency With Combined Heat and Mass Transfer," ASHRAE J., **81**, Part 1, pp. 350–355.
[5] Elmahdy, A. H., and Biggs, R. C., 1983, "Efficiency of Extended Surfaces With Simultaneous Heat Transfer and Mass Transfer," ASHRAE J., **89**, Part 1A, pp. 135–143.
[6] Coney, J. E. R., Kazeminejad, H., and Sheppard, C. G. W., 1989, "Dehumidification of Air on a Vertical Rectangular Fin: A Numerical Study," *Proc. Inst. Mech. Engrs*, J. of Mechanical Engng. Sci, **203**, pp. 165–175.
[7] Coney, J. E. R., Kazeminejad, H., and Sheppard, C. G. W., 1989, "Dehumidification of Turbulent Air Flow Over a Thick Fin: An Experimental Study," Proc. Inst. Mech. Engrs, J. of Mechanical Engng. Sci. **203**, pp. 177–188.
[8] Coney, J. E. R., Sheppard, C. G. W., and El-Shafei, E. A. M., 1989, "Fin Performance With Condensation From Humid Air: A Numerical Study," Int. J. Heat Fluid Flow, **10**, pp. 224–231.
[9] Chen, L. T., 1991, "Two-Dimensional Fin Efficiency With Combined Heat and Mass Transfer Between Water-Wetted Fin Surface and Moving Moist Airstream," Int. J. Heat Fluid Flow, **12**, pp. 71–76.
[10] Kazeminejad, H., 1995, "Analysis of One-Dimensional Fin Assembly Heat Transfer With Dehumidification," Int. J. Heat Mass Transf., **38**, pp. 455–462.
[11] Wu, G., and Bong, T. Y., 1994, "Overall Efficiency of a Straight Fin With Combined Heat and Mass Transfer," ASHRAE J., **100**, Part 1, pp. 367–374.
[12] Hong, T. K., and Webb, R. L., 1996, "Calculation of Fin Efficiency for Wet and Dry Fins," ISSN 1078-9669, **2**, No. 1, pp. 27–41.
[13] Salah El-Din, M. M., 1998, "Performance Analysis of Partially-Wet Fin Assembly," Appl. Therm. Eng., **18**, pp. 337–349.
[14] Rosario, L., and Rahman, M. M., 1998, "Overall Efficiency of a Radial Fin Assembly Under Dehumidifying Conditions," ASME J. Energy Resour. Technol., **120**, pp. 299–304.
[15] Rosario, L., and Rahman, M. M., 1999, "Analysis of Heat Transfer in a Partially Wet Radial Fin Assembly During Dehumidification," Int. J. Heat Mass Transf., **20**, pp. 642–648.
[16] Besednjak, A., and Poredoš, A., 1998, "Efficiency of Cooled Extended Surfaces," Int. J. Refrig., **21**, pp. 372–380.
[17] Liang, S. Y., Wong, T. N., and Nathan, G. K., 2000, "Comparison of One-Dimensional and Two-Dimensional Models for Wet-surface Fin efficiency of a Plate-Fin-Tube Heat Exchanger," Appl. Therm. Eng., **20**, pp. 941–962.
[18] Ware, C. D., and Hacha, T. H., 1960, "Heat Transfer From Humid Air to Fin and Tube Extended Surface Cooling Coils," ASME Paper 60-HT-17.
[19] ASHRAE Standard 33–78, 1978, "Method of Testing Forced Circulation Air Cooling and Air Heating Coils," American Society of Heating, Refrigerating and Air-Conditioning Engineers, Inc., Atlanta, GA.
[20] ASHRAE Standard 41.1-1986, 1986, "Standard Method for Temperature Measurement," American Society of Heating, Refrigerating and Air-Conditioning Engineers, Inc., Atlanta, GA.
[21] ASHRAE Standard 41.2-1987, 1987, "Standard Methods for Laboratory Air-Flow Measurement," American Society of Heating, Refrigerating and Air-Conditioning Engineers, Inc., Atlanta, GA.
[22] Chilton, T. H., and Colburn, A. P., 1934, "Mass Transfer Coefficients," Int. Eng. Chem., **26**, pp. 1183–1187.
[23] Kandlikar, S. G., 1990, "Thermal Design Theory for Compact Evaporators," in *Compact Heat Exchangers*, R. K. Kraus et al., eds., Hemisphere Publishing Corp., New York, pp. 245–286.

Numerical Study of Steady Forced Convection in a Grooved Annulus Using a Design of Experiments

Yannick Sommerer

Guy Lauriat
e-mail: lauriat@univ-mlv.fr

University of Marne-la-Vallée,
Cité Descartes, Bldg. Lavoisier,
Champs-sur-Marne,
F-77454 Marne-la-Vallée Cedex 2

Numerical simulations have been performed to study the flow and heat transfer characteristics in the annular space between an inner smooth-cylinder rotating at constant angular velocity and an outer stationary grooved one. A first series of calculations were conducted to determine the ranges of Taylor number and longitudinal aspect ratio for which a two-dimensional modeling can be considered as valid. To this end, a map showing the domain of validity of two dimensional computations is presented. The assumption of circumferential periodicity of the flow is then justified in the range of Taylor numbers investigated. A number of simulations were carried out to investigate the effects of the geometrical parameters describing the cross section of the grooved annulus for various Taylor numbers. To end, correlations describing the influences on the main parameters both on the friction factor and Nusselt numbers are derived by using a design of experiments. [DOI: 10.1115/1.1388299]

Keywords: Annular Flow, Computational, Forced Convection, Heat Transfer, Laminar, Rotating

1 Introduction

Grooved annuli are devices commonly used in electric rotating machinery since periodically embedded cavities made in the longitudinal direction of the rotor or stator are beneficial both for electromagnetic purpose and for removing heat generated within the device. The present numerical study deals with convective heat transfer across the gap between concentric cylinders in which no axial flow occurs. The outer cylinder is axially grooved while the rotating inner cylinder has a smooth surface. For this geometry, the assumption of two-dimensional (r, θ) flow is valid for an annulus of infinite length with the inner cylinder rotating at a velocity corresponding to subcritical Taylor number. The flow induced in the narrow annulus exhibits clear similarities with the circular Couette flow. However, the recirculations in the grooves render the flow two-dimensional, even at very low speed of rotation. When the Taylor number exceeds a critical value, Ta_c, the recirculating flows in the grooves are superimposed on the Taylor vortices so that the flow is much more complicated than for a smooth annulus.

Amongst the first studies devoted to grooved annuli, Gazley [1] considered several configurations through combinations of nine geometries of the rotor and seven for the stator. His experimental main results were on the investigation of the mean Nusselt number. Similar to a smooth annulus, the transition from Couette flow to Taylor flow causes a significant increase in the Nusselt number although the critical Reynolds number was found to be slightly modified by the presence of the grooves. The experiments showed that the Nusselt number is smaller before the transition than in the case of a smooth annulus whereas it is larger after the transition, whatever the geometry was. For subcritical flows, the value of the Nusselt number differs slightly according to the geometry considered. The onset of Taylor vortex flow was deeply investigated in the experimental study of Tachibana and Fukui [2] and it was observed that the value of Re_c can be higher, lower or close to the one obtained for smooth concentric cylinders of infinite length according to the fluid viscosity. Concerning the mean skin-friction coefficient, it was shown that $\overline{C_f}$ decreases linearly with Re^{-1} for low Reynolds numbers and exhibits a maximum above the first transition (Yamada [3]). For higher values of Re, it was shown that the geometry of the groove has almost no effect on the mean Nusselt number (Lee and Minkowycz [4]).

Numerical simulations were carried out by Murphy and Patankar [5] in a study devoted to the cooling of electrical machinery. They considered fins distributed on the inner cylinder and a parametrical study on the geometry of the grooves was conducted. The two-dimensional simulations were for low Reynolds numbers and the computational domain was restricted to one groove only by assuming circumferential periodicity of the flow. Symmetry of the flow about the spanwise midplane and circumferencial periodicity were also assumed by Hayase et al. [6]. Their simulations were for groove opening angles of 10 deg and 20 deg and for an angular periodicity of 30 deg so that twelve grooves constituted the complete annulus (the computational domain was thus restricted to 30 deg). Two and three-dimensional computations were performed and comparisons of the results showed a good agreement at low Reynolds numbers. Taylor vortices were obtained for Re greater than 185 and significant differences were found between the mean Nusselt numbers calculated by using two-dimensional or three-dimensional modeling. From the distributions of local Nusselt numbers at the grooved cylinder, they also demonstrated that the heat transfer rate presents a sharp peak at the part of the groove wall impacted by the fluid. The study of Ziouchi [7] on the influence of the geometry of the groove at low Reynolds numbers revealed that the heat transfer rate decreases when increasing the opening angle of the grooves. When the depth of the grooves is increased, the mean Nusselt number starts to decrease strongly and becomes then almost independent of the depth. For supercritical Reynolds numbers, an optimal opening angle for a maximum in heat transfer was shown to exist while the effect of the depth was found to be much less. Sommerer et al. [8] investigated numerically the influences of the radial clearance between rotor and stator, of the depth of the grooves, and of the curvature. They also found a linear dependence of $\overline{C_f}$ with Re^{-1} and exhaustive computations were conducted to correlate the dependency of $\overline{C_f}$ with the non-dimensional parameters describing the geometry. It should be mentioned here that all of the previous numerical studies were performed by assuming a circumferential periodicity of the flow. However, it is not yet clear that this assumption is valid.

Contributed by the Heat Transfer Division for publication in the JOURNAL OF HEAT TRANSFER. Manuscript received by the Heat Transfer Division May 23, 2000; revision received February 9, 2001. Associate Editor: M. Faghri.

For example, flow visualizations of Pecheux et al. [9] revealed unsteadiness in the flow and non-periodicity in the case of an annulus having a large aspect ratio ($A=128$) at Reynolds numbers just above the critical value for the onset of Taylor vortices. The present numerical study focuses attention on the convective heat-transfer characteristics in an annulus with a grooved outer cylinder and a smooth inner cylinder rotating at constant angular velocity. The rectangular grooves are periodically embedded in the outer cylinder. Both inner and outer cylinders are kept isothermal, the inner cylinder being hotter. The conservation equations and boundary conditions are presented in dimensionless form in section 2 together with the definitions of the skin-friction coefficient and Nusselt numbers used in the course of the analysis of the results. Section 3 contains a summary of the numerical method employed. Tests performed to verify the accuracy of the numerical procedure and grid independency of the results are shown also. Section 4 contains discussions of the computer simulations. The important points are as follows:

1 The ranges of Taylor number and longitudinal aspect ratio for which a two-dimensional modeling can be considered as valid are first determined through comparisons between two-dimensional and three-dimensional calculations. A map showing the domain of validity of two-dimensional computations is presented.
2 The assumption of circumferential periodicity of the flow is justified in the range of Taylor numbers investigated.
3 The influences on the friction factor and Nusselt number of the four geometrical parameters describing the cross section of the annulus is deeply investigated.
4 General correlations describing the influences on the main parameters both on the friction factor and Nusselt numbers are determined by using a design of experiment method (DOE).
5 The accuracy of the correlations obtained is examined.

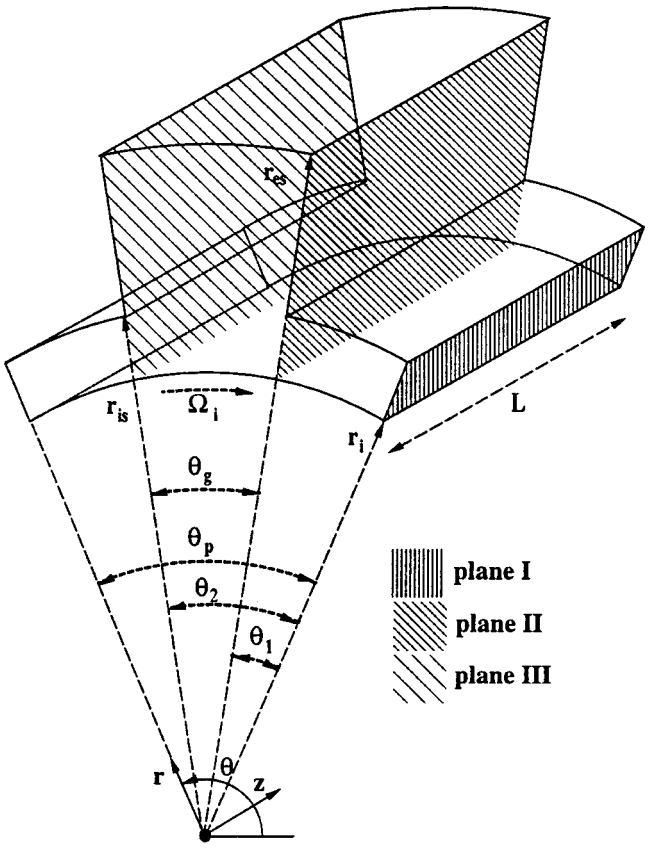

Fig. 1 Definition of the geometry

2 Problem Formulation

A sketch of the geometry investigated is shown in Fig. 1. The radii of the heated inner cylinder and of the cooled outer cylinders are r'_i and r'_{is}, respectively. The depth of a groove is characterized by the outer radius of the stator, r'_{es}, and the axial length of the annulus is L'. The inner cylinder rotates with a constant angular velocity Ω_i while the outer cylinder is stationary. The two cylinders are at different but uniform temperatures. Such a geometry can be defined by the following set of dimensionless parameters:

- ratio of the radius of the stator to the radius of the rotor: $R=r'_{is}/r'_i$
- radius ratio of the groove: $R_g=r'_{es}/r'_{is}$
- opening angle of the groove: θ_g
- angle of the groove pitch: θ_p
- axial aspect ratio $A=L'/e'$, where $e'=r'_{is}-r'_i$ is the gap width

The three-dimensional Navier-Stokes and energy equations for incompressible, Newtonian fluid flows are used in cylindrical coordinates (r',θ,z'). The flow is assumed to be laminar with constant properties. Buoyancy effects and viscous heating are neglected in the present study. The governing equations are put into dimensionless form by scaling velocity with $u'_i=\Omega_i r'_i$, pressure with $\rho u'^2_i$, axial coordinate with the gap width $e'=r'_{is}-r'_i$, and time with e'/u'_i. The dimensionless temperature difference is defined as $T=(T'-T'_o)/(T'_h-T'_c)$ with the reference temperature $T'_o=(T'_c+T'_h)/2$. The dimensionless radial coordinate is $r=(r'-r'_i)/e'$ so that $r=0$ at the rotating cylinder, $r=1$ at the inner surface of the grooved stationary cylinder, and $r=r_e$ at the base of the grooves with $r_e=(R_gR-1)/(R-1)$.

The continuity, momentum, and energy equations in dimensionless form are

$$\frac{\partial}{\partial r}(fu_r)+\eta\frac{\partial u_\theta}{\partial\theta}+\frac{\partial}{\partial z}(fu_z)=0 \tag{1}$$

$$\frac{\partial}{\partial r}(fu_ru_r)+\frac{\partial}{\partial\theta}(\eta u_\theta u_r)+\frac{\partial}{\partial z}(fu_zu_r)-\eta u_\theta^2 u_r = -f\frac{\partial P}{\partial r}+\frac{1}{\mathrm{Re}}\left(\frac{\partial}{\partial r}\left[f\frac{\partial u_r}{\partial r}\right]+\frac{\partial}{\partial\theta}\left[\frac{\eta^2}{f}\frac{\partial u_r}{\partial\theta}\right]+\frac{\partial}{\partial z}\left[f\frac{\partial u_r}{\partial z}\right]-\frac{2\eta^2}{f}\frac{\partial u_\theta}{\partial\theta}-\frac{\eta^2 u_r}{f}\right) \tag{2}$$

$$\frac{\partial}{\partial r}(fu_ru_\theta)+\frac{\partial}{\partial\theta}(\eta u_\theta u_\theta)+\frac{\partial}{\partial z}(fu_zu_\theta)+\eta u_ru_\theta = -\eta\frac{\partial P}{\partial\theta}+\frac{1}{\mathrm{Re}}\left(\frac{\partial}{\partial r}\left[f\frac{\partial u_\theta}{\partial r}\right]+\frac{\partial}{\partial\theta}\left[\frac{\eta^2}{f}\frac{\partial u_\theta}{\partial\theta}\right]+\frac{\partial}{\partial z}\left[f\frac{\partial u_\theta}{\partial z}\right]+\frac{2\eta^2}{f}\frac{\partial u_r}{\partial\theta}-\frac{\eta^2 u_\theta}{f}\right) \tag{3}$$

$$\frac{\partial}{\partial r}(fu_ru_z)+\frac{\partial}{\partial\theta}(\eta u_\theta u_z)+\frac{\partial}{\partial z}(fu_zu_z) = -f\frac{\partial P}{\partial z}+\frac{1}{\mathrm{Re}}\left(\frac{\partial}{\partial r}\left[f\frac{\partial u_z}{\partial r}\right]+\frac{\partial}{\partial\theta}\left[\frac{\eta^2}{f}\frac{\partial u_z}{\partial\theta}\right]+\frac{\partial}{\partial z}\left[f\frac{\partial u_z}{\partial z}\right]\right) \tag{4}$$

$$\frac{\partial}{\partial r}(fu_rT)+\frac{\partial}{\partial \theta}(\eta u_\theta T)+\frac{\partial}{\partial z}(fu_zT)$$
$$=\frac{1}{\mathrm{Re\,Pr}}\left(\frac{\partial}{\partial r}\left[f\frac{\partial T}{\partial r}\right]+\frac{\partial}{\partial \theta}\left[\frac{\eta^2}{f}\frac{\partial T}{\partial \theta}\right]+\frac{\partial}{\partial z}\left[f\frac{\partial T}{\partial z}\right]\right), \quad (5)$$

where $\eta=(R-1)$ is the curvature parameter and $f=(\eta r+1)$ a radial function.

The rotational velocity of the inner cylinder is characterized either by a rotating Reynolds number based on the hydraulic diameter of the annulus or by a Taylor number which are defined as

$$\mathrm{Re}=\frac{r_i'\Omega_i e'}{\nu}, \quad \mathrm{Ta}=\frac{R^2-1}{2}\mathrm{Re}^2. \quad (6)$$

The flow is assumed to be periodic in the peripheral direction with the angle of the groove pitch as the angular periodicity, and symmetric about the spanwise midplane of the annular gap. Therefore, the computational domain was restricted to one groove only, half in length with periodical boundary conditions imposed in the peripheral direction at $\theta=0$ and $\theta=\theta_p$, no-slip, impermeable and adiabatic conditions at $z=0$, and symmetric conditions at $z=A/2$. The dimensionless boundary conditions for the problem under consideration are thus written as follows:

$$r\text{-direction: } \begin{cases} r=0 \text{ and } 0<\theta<\theta_p: u_r=0,\ u_\theta=1,\ u_z=0,\ T=1 \\ r=1 \text{ and } 0<\theta<\theta_1 \text{ or } \theta_2<\theta<\theta_p: u_r=u_\theta=u_z=0,\ T=0 \\ r=r_e \text{ and } \theta_1<\theta<\theta_2: u_r=u_\theta=u_z=0,\ T=0 \end{cases}, \quad (7)$$

where $\theta_1=(\theta_p-\theta_g)/2$ and $\theta_2=(\theta_p+\theta_g)/2$.

$$\theta\text{-direction: } \begin{cases} \Phi(r,0,z)=\Phi(r,\theta_p,z) \\ \left.\dfrac{\partial\Phi}{\partial\theta}\right|_{\theta=0}=\left.\dfrac{\partial\Phi}{\partial\theta}\right|_{\theta=\theta_p} \end{cases}, \quad (8)$$

where Φ stands for the three velocity components, pressure, and temperature.

$$z\text{-direction: } \begin{cases} z=0: u_r=u_\theta=u_z=0,\ \dfrac{\partial T}{\partial z}=0 \\ z=A/2: \dfrac{\partial u_r}{\partial z}=\dfrac{\partial u_\theta}{\partial z}=0,\ u_z=0,\ \dfrac{\partial T}{\partial z}=0 \end{cases}. \quad (9)$$

Most of the numerical results shown in the following sections will be discussed in terms of friction factors and Nusselt numbers. Since a literature survey shows that various expressions of these quantities have been considered, it is better to make clear how they are defined in the present study.

The local shear stress at the inner wall is

$$\tau_{\omega i}=-\mu r_i'\frac{\partial}{\partial r'}\left(\frac{u_\theta'}{r'}\right)\bigg|_{r_1'}. \quad (10)$$

The torque G acting on the inner cylinder is

$$G=-\mu r_i'\int_0^{L'}\int_0^{2\pi} r'\frac{\partial}{\partial r'}\left(\frac{u_\theta'}{r'}\right)\bigg|_{r_i'} d\theta\, dz'. \quad (11)$$

From Eq. (10), a local friction coefficient can be introduced as

$$C_f(\theta,z)=\frac{\tau_{\omega i}}{\frac{1}{2}\rho(\Omega_i r_i')^2}, \quad (12)$$

which can be expressed in terms of the dimensionless variables as

$$C_f(\theta,z)=-\frac{2}{\mathrm{Re}}\frac{\partial}{\partial r}\left(\frac{u_\theta}{f}\right)\bigg|_0. \quad (13)$$

From the definition of G, an averaged friction coefficient is given by

$$\overline{C_f}=\frac{G}{\pi r_i' L'\rho(\Omega_i r_i')^2}=\frac{1}{2\pi A}\int_0^A\int_0^{2\pi} C_f(\theta,z)\,d\theta\,dz. \quad (14)$$

The heat transfer results are presented in terms of local and mean Nusselt numbers at the inner cylinder. In the absence of axial flow, the local Nusselt number based on the temperature difference between the rotor and the stator is the generally accepted parameter and is also being used in the present study. The local heat transfer rate at the inner cylinder is defined as

$$q_i'(\theta,z')=-k\frac{\partial T'}{\partial r'}\bigg|_{r_i'}=h_i(\theta,z')(T_h'-T_c'). \quad (15)$$

In order to reduce the dependence on the gap ratio, the Nusselt numbers considered in the course of the analysis of the numerical results are given in terms of the ratio of the convective heat flux at the inner cylinder to the conductive heat flux for a smooth annulus given by

$$q_{co,i}=\frac{T_h'-T_c'}{\frac{r_i'}{k}\ln(R)}. \quad (16)$$

Therefore,

$$\mathrm{Nu}(\theta,z)=\frac{h_i(\theta,z)r_i'}{k}\ln(R). \quad (17)$$

Or, equivalently, in terms of the dimensionless variables introduced above

$$\mathrm{Nu}(\theta,z)=-\frac{\ln(R)}{R-1}\frac{\partial T}{\partial r}\bigg|_0. \quad (18)$$

Calculations have been carried out for three-dimensional and two-dimensional (r, θ)-cases. The mean Nusselt numbers presented are defined as

$$\overline{\mathrm{Nu}_i}=\frac{r_i'\overline{h_i}}{k}\ln(R), \quad (19)$$

where $\overline{h_i}=1/A_i\int_0^{A_i}h_i(\theta,z)dA_i$.

A_i being the area of the inner cylinder of length L'. For the two-dimensional cases, the z-dependence of the heat transfer coefficient is omitted and $A_i=2\pi r_i'$.

3 Numerical Method

The equations governing the fluid motion were solved using a standard, staggered grid, finite-volume method with the SIMPLER algorithm for the pressure correction. For the convective terms, the QUICK scheme was used to interpolate from the

Table 1 Mean friction coefficient and mean Nusselt number for various two-dimensional grids at Ta=1,300

(r, θ)	(20, 22)	(40, 44)	(80, 88)	(160, 176)	(320, 352)
$\overline{C_f}$	0.01415	0.01373	0.01356	0.01350	0.01348
$\overline{Nu}$	0.9470	0.9403	0.9380	0.9376	0.9373

main grid points onto the control volume faces. The momentum and energy equations were cast in transient form, and the time-integration was performed by using an ADI scheme. All the computations discussed in the present paper were carried out on uniform grids. The teeth of the outer cylinder were considered as a part of the flow domain through the introduction of a Darcy's term in the momentum equation. A zero permeability was set into the teeth and an infinite permeability within the groove. Similarly, much higher thermal conductivity of the teeth than that of the fluid insured uniform temperature of the grooved cylinder. The convergence criteria for the solution was

$$\sum_X \frac{|X^i - X^{i-1}|_{\max}}{X_{\max}} < \varepsilon,$$

where superscript i denotes the iteration number, and X is a general symbol used for u_r, u_θ, P, and T. Since we considered forced convection flow with constant fluid properties, the temperature field was calculated after having obtained the velocity field. An independent convergence criterion for temperature was thus introduced in order to insure that the thermal steady-state régime was reached. In order to determine the appropriate value of the convergence criteria, the dependence of the mean friction coefficient and Nusselt number on ε was studied. The convergence to steady-state was shown to be independent of ε provided that $\varepsilon \leqslant 10^{-5}$ for the velocity components and pressure, and $\varepsilon \leqslant 10^{-6}$ for temperature.

3.1 Test Calculations. Grid refinement tests were performed both for two-dimensional and for three-dimensional computations in order to check the independence of solutions on the grid size. All the computations were carried out for the basic geometry of the cross-section ($R=1.0526$, $R_g=1.2$, $\theta_p=30$ deg, $\theta_g=10$ deg, $A=10$).

When assuming two-dimensionality of the flow field, the grid distribution was varied from 20×22 to 320×352 in the (r, θ)-plane. Table 1 gives a comparison of the mean friction coefficients and mean Nusselt numbers obtained with various grids. The results of the calculation with a 40×44 grid differ less than 1.5 percent on $\overline{C_f}$ and less than 1 percent on $\overline{\mathrm{Nu}}$ from the results obtained with the finest grid (320×352 points). The use of the QUICK discretization scheme for the convective terms explains the relative accuracy obtained on coarse grids. As a conclusion, the chosen grid structure was 160×176, optimizing the number of control volume while allowing to predict accurate results.

Grid tests for three-dimensional calculations were conducted for Ta=280 and $A=10$. On account of the computational time requirements, only two grids (r, θ, z) were considered: $20\times22\times20$ and $40\times44\times40$. The difference obtained are about 2.5 percent on $\overline{C_f}$ and $\overline{\mathrm{Nu}}$ (for a $20\times22\times20$ grid $\mathrm{Nu}=0.915$ and $\overline{C_f}=3.575\,10^{-2}$ while $\overline{\mathrm{Nu}}=0.892$ and $\overline{C_f}=3.654\,10^{-2}$ for a 40

Table 2 Mean friction coefficient and mean Nusselt number for various three-dimensional grids at Ta=2.370

(r, θ, z)	(20, 22, 10)	(20, 22, 20)	(20, 22, 30)	(20, 22, 40)
$10^2 \times \overline{C_f}$	1.880	2.120	2.168	2.178
$\overline{Nu}$	1.458	1.556	1.560	1.554

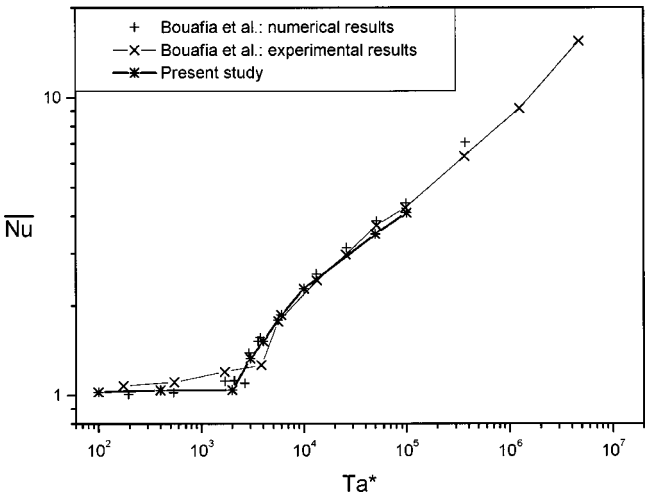

Fig. 2 Comparison of mean Nusselt number with experimental results and numerical predictions [10]

$\times44\times40$ grid). We also investigated the importance of grid size in the spanwise direction and the results obtained are reported in Table 2 for a supercritical Taylor number of Ta=2570. The differences in the friction coefficient and in the Nusselt number between the $20\times22\times20$ and $20\times22\times40$ grids are 2.8 percent and 0.2 percent, respectively. Owing to the large computational time required, most of the three-dimensional computations were carried out by using a $20\times22\times20$ grid for $A=10$.

Predictions of the mean Nusselt number as a function of a modified Taylor number, $\mathrm{Ta}^*=4(R+1)^2\mathrm{Ta}$, are compared with experimental and numerical data presented by Bouafia et al. [10] (1999) as shown in Fig. 2. Here the reference heat flux is the conductive flux for a grooved annulus, the value of which being numerically determined for a stationary inner cylinder ($\mathrm{Ta}^*=0$). For the geometry considered in [10] ($R=1.0357$, $R_g=1.1034$, $\theta_p=7.5$ deg, $\theta_g=3.28$ deg, $A=20$), the ratio of the conductive flux for a grooved annulus to the one for a smooth annulus (Eq. 16) is 0.897. The current results using a $22\times22\times40$ grid agree well with these data up to $\mathrm{Ta}^*=10^5$. The present computations were not carried on for higher Ta* because we believe that the steady-state solutions lose their reliability after this Ta*. The slightly higher experimental values of $\overline{\mathrm{Nu}}$ at low Taylor numbers are probably due to the influence of free convection as it has been verified experimentally (Gardiner and Sabersky [11]). The experimental data show indeed that the effect of the vortex motion on $\overline{\mathrm{Nu}}$ is postponed to a modified Taylor number of about 4000 compared to a value of about 2000 which is numerically predicted in the absence of free convection. However, it should be noted that the onset of Taylor vortices cannot be accurately predicted through a step increase in $\overline{\mathrm{Nu}}$ since their effect on the heat transfer rate is almost negligible when the vortex intensity is very small

4 Results and Discussion

4.1 Validity of Two-Dimensional Calculations. Since the purpose of the present work is to evaluate the heat transfer in a grooved annulus for steady state, two-dimensional flows, we determined firstly the ranges of Taylor number and longitudinal aspect ratio for which the two-dimensional assumption can be considered as valid. As it has been established experimentally and numerically, the flow becomes three-dimensional in a grooved annulus when the rotational velocity of the inner cylinder, or the Taylor number, exceeds a critical value which corresponds to the onset of Taylor cells since the base flow (i.e., as soon as the inner cylinder rotates) is two-dimensional. In addition, the two-

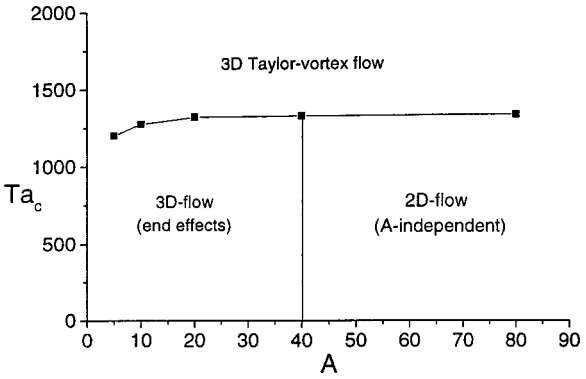

Fig. 3 Flow regimes and variations of Ta_c versus the axial aspect ratio

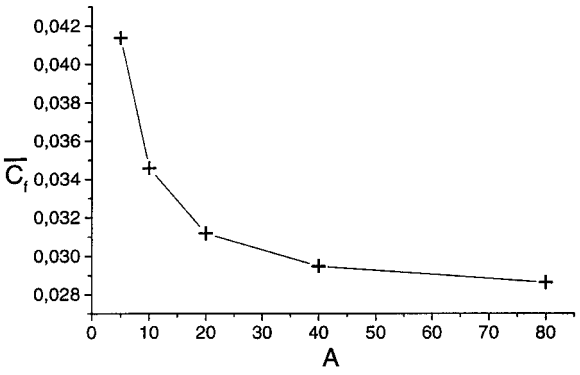

Fig. 5 Variation of the mean friction coefficient with the axial aspect ratio for $Ta=300$ (three-dimensional computations).

dimensional assumption is not valid when the axial aspect ratio is less than a certain value, even in the case of a smooth annulus, because the end effects characterized by Ekman cells propagate in the whole annulus. Due to the periodicity of the geometry, the calculations presented in previous studies (Murphy and Patankar [5], Hayase et al. [6], Ziouchi [7], Sommerer et al. [8], Bouafia et al. [10]) were made for one angular period only in order to save CPU-times. However, the experimental study of Pécheux et al. [9] does not show any angular periodicity in the flow in the case of a grooved annulus of large axial aspect ratio ($A=128$) for Ta just above the critical value. Therefore, this assumption is discussed in what follows through computations made for one, three or the totality of the grooves. The geometry considered in this section is for $R=1.0526$, $R_g=1.2$, $\theta_p=30$ deg, $\theta_g=10$ deg.

Critical Taylor Number. The value of the critical Taylor number for the onset of Taylor vortex flows, Ta_c, was determined as a function of the longitudinal aspect ratio. Figure 3 shows the limits of the three flows régimes obtained: three-dimensional flows due only to end effects, two-dimensional flows in the major part of the annulus provided that the aspect ratio is large enough ($A>40$), and three-dimensional multicellular flows whatever the aspect ratio is. When Ta is increased, cellular vortices appear in the vicinity of the plane $z=A/2$. For $Ta>Ta_c$ the vortex intensity suddenly increases which produces wavy isolines of the tangential velocity

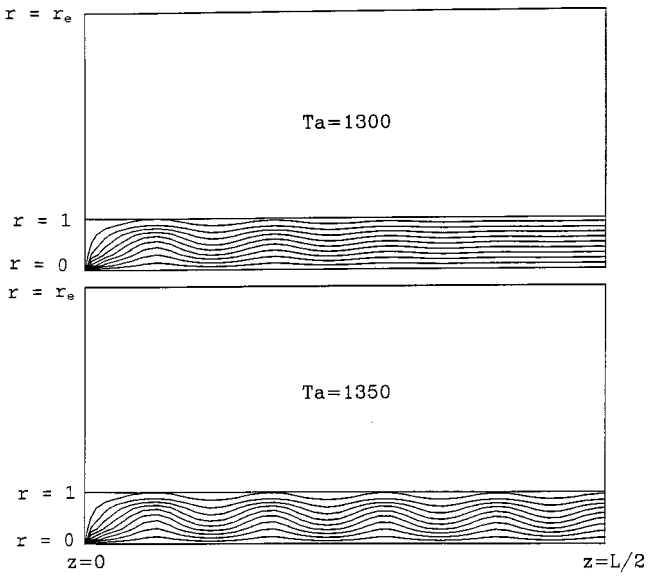

Fig. 4 Iso-u_θ[0(0.1)1] near the first transition in the plane *I* for $A=20$

(Alziary de Roquefort and Grillaud [12]). A sample of the plots of the iso-u_θ in the plane *I* (as marked in Fig. 1) is shown in Fig. 4 for $A=20$. The critical Taylor number for a smooth, infinite long annulus was theoretically found to be $Ta_c=1841$ [13]. Calculations carried out by introducing cyclic boundary conditions in the spanwise direction for $A=10$ (for example) and a smooth outer cylinder leads to a Ta_c-value in close agreement with the theoretical prediction ($1825<Ta_c<1850$). The experimental works on flow field characteristics in isothermal, grooved annuli are very few. To our best knowledge, the data on the critical Taylor number were deduced from heat transfer measurements. However, since free convection exerted an important influence on the results at low Taylor numbers due to the large difference between the rotor and the stator temperatures (up to 110°C in [10]) the data on Ta_c published in the archival literature cannot serve as a reference to check the reliability of the results from the present study. Numerical predictions of Ta_c are still quite difficult to perform because of the large time of computation required to obtain meaningful steady-state solutions (even by using supercomputers). Experimental studies conducted in smooth annuli have indeed revealed that the dimensional time for the occurrence of the Taylor vortices is about 15 rotating times [14]. This is probably why it was claimed in previous numerical studies conducted for the same radius ratio and stator geometry than in the present study and for $A=10$ that the value of the critical Reynolds number is $Re_c=185$ ($Ta_c=1847$) although any numerical simulation was carried out to check this assertion (Hayase et al. [6], Ziouchi [7], Bouafia et al. [10]). In the present study, we obtained $Ta_c\cong 1275(\pm 25)$ or $Re_c\cong 153.5(\pm 1.5)$ for $A=10$. Ta_c is reduced when decreasing the axial aspect ratio because the end cells of strong intensity sweep into the central part of the annulus for small *A*, and produce flow instabilities.

End Effects. In order to determine the axial aspect ratio above which a two-dimensional modeling can be considered as valid, three-dimensional computations were carried out for various aspect ratios ($A=5$, 10, 20, 40, and 80) at a low Taylor number ($Ta=300$). Figure 5 shows the variations of the mean friction coefficient as a function of the axial aspect ratio. The value of $\overline{C_f}$ for a two-dimensional model (annulus of infinite axial length) was found to be $\overline{C_f}=0.0277$. As it can be seen, $\overline{C_f}$ decreases when increasing the aspect ratio because the relative influence of the shear stress at the end walls is reduced. The rotating cells located at the end parts of the annulus (Ekman cells) increase the local value of the friction coefficient, $C_f(\theta,z)$, because the radial gradient of the tangential component of the velocity increase sharply. When integrating $C_f(\theta,z)$ on the surface of the inner cylinder, this increase in $C_f(\theta,z)$ have a significant influence on the mean coefficient if the aspect ratio is small. At this low Taylor number, the Eckman cells do not propagate within the central part of the annulus provided that the aspect ratio is large enough, say $A=20$.

Table 3 Mean Nusselt number and mean friction coefficient for various two-dimensional computations

	$\overline{Nu}$				$10^{+2}\times\overline{C_f}$			
Ta	300	500	800	1300	300	500	800	1300
θ_c=30°	0,9205	0,9283	0,9358	0,9438	2,8746	2,1885	1,7395	1,3526
θ_c=90°	0,9210	0,9288	0,9362	0,9441	2,8720	2,1860	1,7373	1,3507
θ_c=360°	0,9212	0,9290	0,9364	0,9431	2,8711	2,1850	1,7365	1,3449

The difference between $\overline{C_f}$ for $A=20$ and $A=80$ is less than 10 percent, and it is less than 3 percent between $A=40$ and $A=80$. Therefore, it can be considered that the three-dimensional structure of the flow has a negligible effect on $\overline{C_f}$ for $A>40$. The same conclusion can be drawn for other subcritical Taylor numbers because the present calculations lead to a correlation in the form of $\overline{C_f}=\alpha(A)\mathrm{Ta}^{-1/2}$, whatever the axial aspect ratio is. In addition, the influence of the axial length on the mean Nusselt number can be considered as negligible since the difference between the results for $A=5$ and $A=80$ is less than 1 percent. The adiabatic conditions applied at the end walls explain this result.

Circumferential Periodicity. We have already mentioned that the assumption of circumferential periodicity of the flow is a controversial point [9] for Ta just above Ta_c, although previous numerical works were based on this assumption because of the periodicity of the geometry. The results obtained by considering one, three or the twelve grooves are reported in Table 3 for Ta ranging from 300 to 1,300. It can be seen that the discrepancies between the values of $\overline{C_f}$ and $\overline{Nu}$ for the three angles of computation are less than 1 percent in the whole range of Ta considered.

Comparisons of the velocity and temperature fields have shown an excellent agreement between the profiles stem from simulations for 1, 3, or 12 grooves. The geometric periodicity of the flow is clearly displayed in Fig. 6 where the angular variations of $C_f(\theta)$ and of $\mathrm{Nu}(\theta)$ on the inner cylinder are reported for Ta $=1300$. It can be seen that the minimums of the friction coefficient and the maximums of the Nusselt number occur for θ-values close to the symmetry line of the grooves ($\theta\cong 15$ deg,[30 deg], 345 deg). The minimums of $\mathrm{Nu}(\theta)$ are located at the center of the narrow gap sections ($\theta\cong 0$ deg, [30 deg],360 deg), where the effect of the groove is the lowest. The maximums of $C_f(\theta)$ are at $\theta\cong 20$ deg,[30 deg],350 deg because the downward recirculating flows within the grooves have a significant effect on the tangential flow.

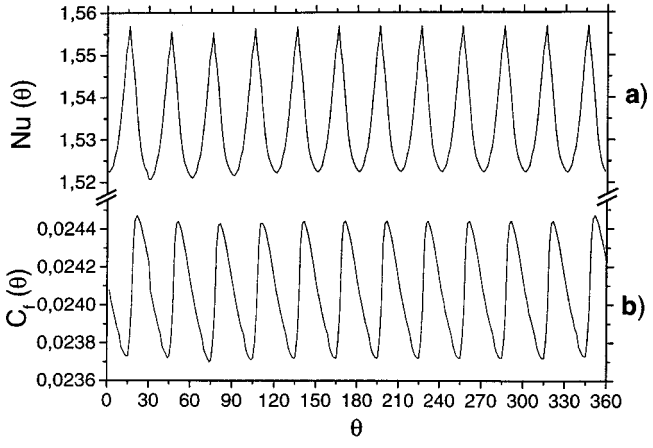

Fig. 6 Local Nusselt number and friction coefficient along the inner cylinder for *Ta*=1300

4.2 Influence of the Geometry. The purpose of this section is to investigate the effect of the geometry for various speeds of rotation. For two-dimensional flows, the geometrical parameters and their domains of variations considered are

- the radius ratio of the annulus: $R=r_{is}/r_i$: $1.007\leqslant R\leqslant 1.11$
- the radius ratio of the groove: $R_g=r_{es}/r_{is}$: $1.01\leqslant R_g\leqslant 1.4$
- the opening angle of the groove: θ_g: 2 deg$\leqslant\theta_g\leqslant$24 deg
- the groove pitch: θ_p: 14.4 deg$\leqslant\theta_p\leqslant$120 deg

The reference geometry (i.e., the geometry investigated in the works of Hayase et al. [6], Ziouchi [7], and Bouafia et al. [10]) was defined by the following values of these parameters: $R=1.0526$, $R_g=1.2$, $\theta_g=10$ deg, $\theta_p=30$ deg. When the influence of one parameter was studied, the three others kept the above values. The four parametric studies were conducted for seven values of the Taylor number (Ta$=$100, 200, 300, 500, 750, 1000, and 1250).

Samples of isotherms for $R=1.0526$ with Ta$=$1000 are shown in Fig. 7. The reference geometry is displayed in Fig. 7(*a*) whereas the other configurations are for the same radius ratio of the annulus so that the dimensional rotational speed of the inner cylinder is the same for all of the cases considered. When decreasing the radius ratio of the groove, the recirculating flow is damped and heat is transferred mainly by conduction into the cavity (Fig. 7(*b*)). On the other hand, increase of the opening angle of the groove enhances the flow in the groove and thus the average temperature of the recirculating fluid (Fig. 7(*c*)). However, such an increase does not compensate for the reduction in the heat transfer through the narrow part of the annulus gap, as it will be shown in what follows. Figure 7(*d*) shows that the isothermal pattern in the groove is very similar to the one predicted for the reference geometry. Since the opening angle of the groove has been reduced in proportion to the pitch angle, it is clear that the heat transfer across the annulus gap is increased.

Influence of the Radius Ratio. Computations were carried out for twelve values of *R*. From the variations of the mean friction coefficient versus Ta shown in Fig. 8(*a*) it is found that $\overline{C_f}$ varies linearly with $\mathrm{Ta}^{-1/2}$ for all the radius ratios considered. Like for a smooth annulus, increase in *R* yields an increase in $\overline{C_f}$. However, it should be mentioned that the rotation speed of the inner annulus decreases while the width of the annulus gap increases when increasing the radius ratio if Ta is kept constant. Therefore, the

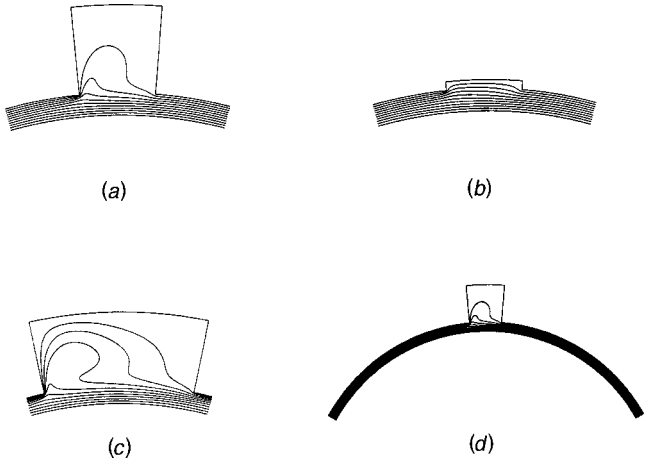

Fig. 7 Isothermal patterns [0(0.1)1] for various configurations of cross sections with *R*=1.0526 and at *Ta*=1000: (*a*) $R_g=1.20$, $\theta_p=30$ deg, $\theta_g=10$ deg (*b*) $R_g=1.02$, $\theta_p=30$ deg, $\theta_g=10$ deg (*c*) $R_g=1.20$, $\theta_p=30$ deg, $\theta_g=24$ deg; and (*d*) $R_g=1.20$, $\theta_p=120$ deg, $\theta_g=10$ deg

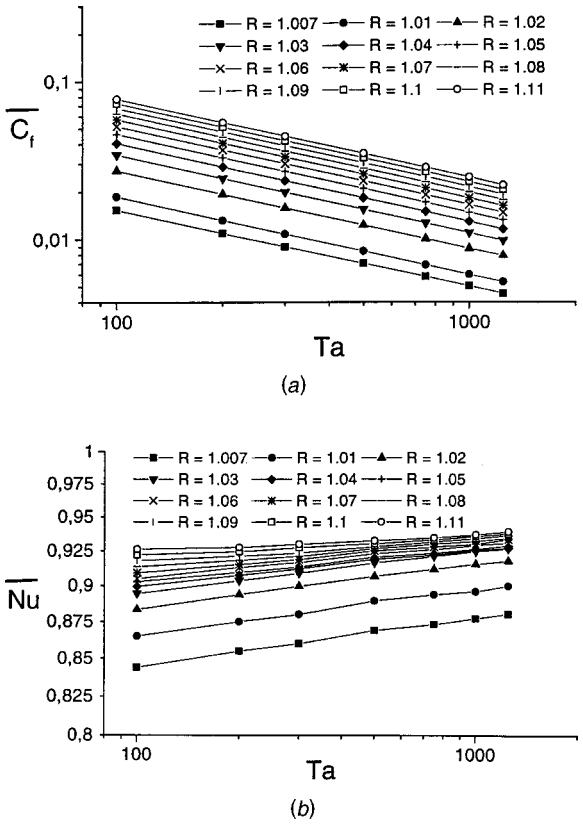

Fig. 8 Variations of $\overline{C_f}$ and $\overline{Nu}$ versus Ta for different radius ratios

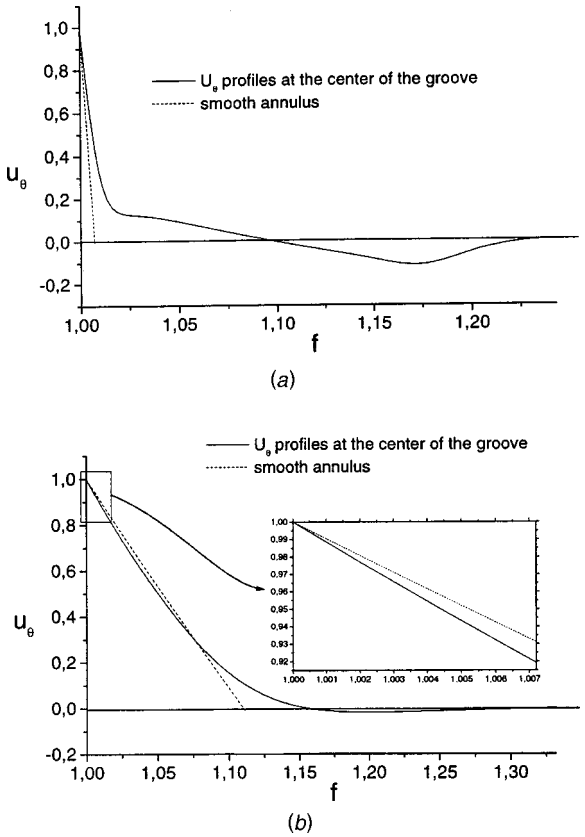

Fig. 9 Variation of the tangential velocity-component for $Ta = 100$ versus the curvature function: (*a*) $R = 1.007$; and (*b*) $R = 1.11$

torque acting on the inner cylinder decreases when R increases. For a smooth annulus, the theoretical expression of $\overline{C_f}$ is given by [3]:

$$\overline{C_f} = \frac{4R^2}{R+1}\mathrm{Re}^{-1} = \frac{4R^2}{R+1}\sqrt{\frac{R^2-1}{2}}\mathrm{Ta}^{-1/2}. \tag{20}$$

Equation (12) describes well the $\overline{C_f}$ calculated for the geometry of the groove investigated over most of the range of radius ratio considered here since the difference is about 9 percent for $R = 1.007$ ($\overline{C_{f\,\mathrm{smooth}}} = 1.694.10^{-2}$, $\overline{C_{f\,\mathrm{grooved}}} = 1.538.10^{-2}$) and 2.5 percent for $R = 1.11$ ($\overline{C_{f\,\mathrm{smooth}}} = 7.957.10^{-2}$; $\overline{C_{f\,\mathrm{grooved}}} = 7.752.10^{-2}$) at Ta$= 100$. Obviously, the effect of the groove on the friction coefficient is less at large gap width. The Couette velocity distribution in a smooth annulus and the numerical velocity profile at the center of the groove ($\theta = 15$ deg) axis are plotted against the curvature function $f(r)$ in Fig. 9 for $R = 1.007$ and $R = 1.11$. It can be seen that the discrepancy between the theoretical and the numerical variations of u_θ near the inner cylinder is much less for the largest radius ratio. From the 84 computations reported in Fig. 8(*a*), the following correlation has been obtained:

$$\overline{C_f} = (-5.72 + 5.87R)\mathrm{Ta}^{-1/2} \quad 1.007 \leqslant R \leqslant 1.11 \quad (R_g = 1.2,\ \theta_p = 30\ \mathrm{deg},\ \theta_g = 10\ \mathrm{deg}) \tag{21}$$

Figure 8(*b*) shows that the mean Nusselt number increases slightly with Ta, especially for the largest values of R for which the presence of the groove has a marginal effect on the flow structure close to the inner cylinder for Ta$<$Ta$_c$. It can also be observed that the radius ratio is not a very influential parameter on $\overline{\mathrm{Nu}}$ at large Taylor numbers when $R \geqslant 1.03$ since the differences in $\overline{\mathrm{Nu}}$ for $R = 1.03$ and for $R = 1.11$ are only 1.3 percent at Ta$= 1000$. For smaller radius ratios, the recirculating flow within the groove disturbs the temperature field up to the inner cylinder all the more since Ta is large. Therefore, the variations of $\overline{\mathrm{Nu}}$ as a function of Ta are different from the one observed in a smooth annulus. From the computations carried out for $R \geqslant 1.03$ reported in Fig. 8(*b*) the following correlation was derived:

$$\overline{\mathrm{Nu}} = (0.072 + 0.745R)\mathrm{Ta}^{(0.116 - 0.099R)} \tag{22}$$

Influence of the Radius Ratio of the Groove. The radius ratios of the groove investigated in this part are ranging from $R_g = 1.01$ to $R_g = 1.4$. The friction coefficient was found again to decrease linearly with $\mathrm{Ta}^{-1/2}$ for each value of R_g, whereas the radius ratio of the groove has a rather small effect on $\overline{C_f}$ owing to the one-third ratio of θ_g/θ_p. The variations of the mean Nusselt number as a function of the radius ratio of the groove are shown in Fig. 10 for various Ta. When the depth of the groove is very small, $R_g = 1.01$ for example, recirculating flows cannot develop and $\overline{\mathrm{Nu}}$ is almost independent of Ta, and close to unity since it can be assumed that the one-dimensional Couette flow is recovered. When increasing R_g up to 1.03, the heat transfer rate decreases independently of Ta because the flow remains basically one-dimensional while the exchange area at the cold surface increases. Figure 10 shows that there is a critical R_g at which recirculations can develop within the grooves. This critical value is a function of Ta, and is obviously higher for low Taylor numbers. For $R_g \geqslant 1.05$, the recirculations systematically produce a heat transfer enhancement when increasing the speed of rotation. However, the increase in $\overline{\mathrm{Nu}}$ is almost independent of the depth of the groove for $R_g \geqslant 1.10$. The explanation is that the increase of the heat exchange area at the cold surface almost compensates for the intensification of the recirculating flow in the groove, except for low Ta numbers at which slight decreases in $\overline{\mathrm{Nu}}$ are seen at the highest values of R_g.

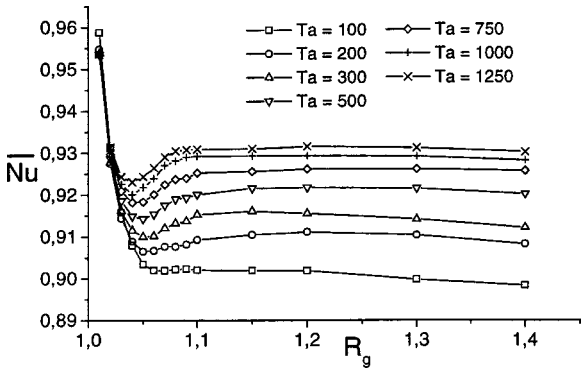

Fig. 10 Variations of the mean Nusselt number: (*a*) $\overline{Nu}$ versus Ta for various R_g; and (*b*) $\overline{Nu}$ versus R_g for various Ta

Influence of the Groove Pitch. The groove pitch was varied from $\theta_p = 14.4$ deg to $\theta_p = 120$ deg while the groove angle was kept to $\theta_g = 10$ deg. Therefore, the number of groove at the outer cylinder circumference was varied from 3 to 25. Figure 11(*a*) displays anew a linear decrease of $\overline{C_f}$ with $\mathrm{Ta}^{-1/2}$ for all of the groove pitches investigated. When the groove pitch is increased, the effect of the groove in the reduction of $\overline{C_f}$ becomes less important, and the theoretical value for a smooth annulus is asymptotically reached. For example, the difference between the numerical result for $\theta_p = 120$ deg and the theoretical prediction for a smooth annulus is of the order of 1 percent at Ta=1000 ($\overline{C_f}$ smooth$=5.02.10^{-2}$, $\overline{C_f}$ grooved$=4.96.10^{-2}$). On the other hand, a decrease in θ_p up to $\theta_p = 14.4$ deg (25 grooves) yields a 8.5 percent difference. From the variations of $\overline{C_f}$ with θ_p a correlation of the following form can be derived:

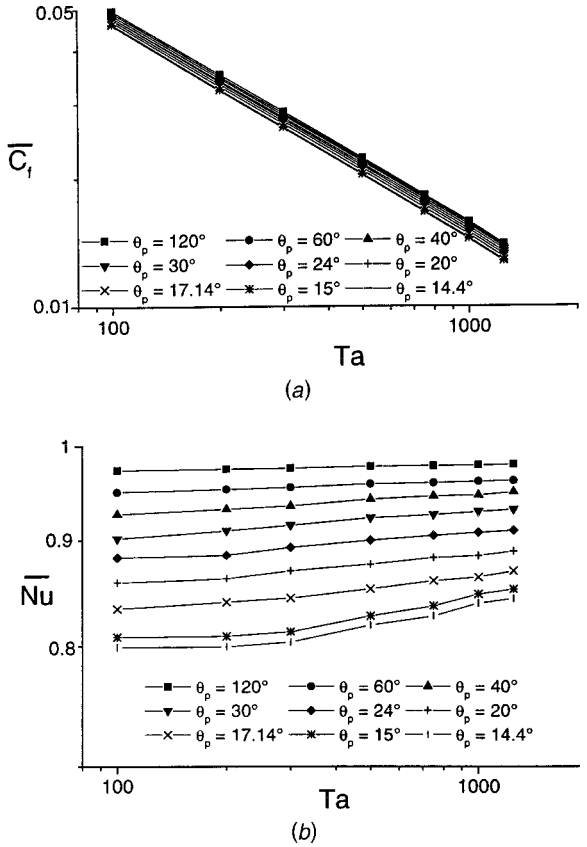

Fig. 11 Variations of $\overline{C_f}$ and $\overline{Nu}$ versus Ta for various θ_p

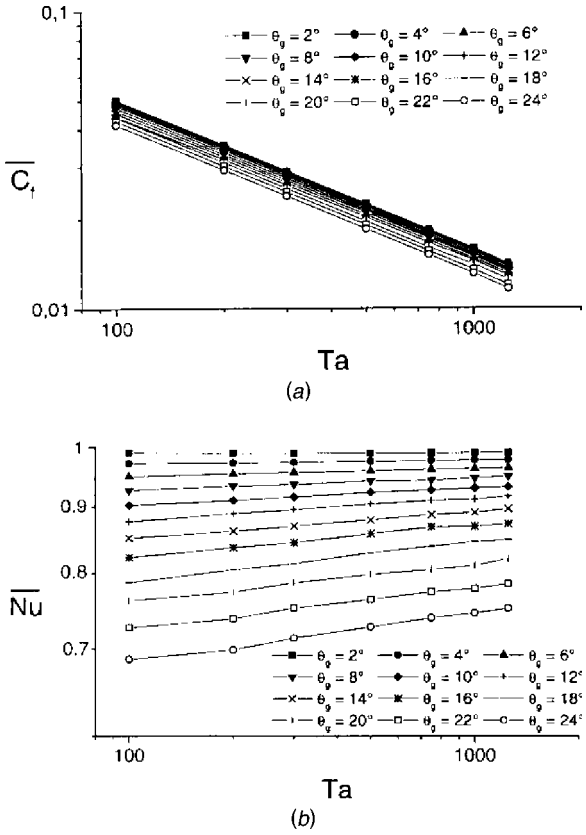

Fig. 12 Variations of $\overline{C_f}$ and $\overline{Nu}$ versus Ta for various θ_g

$$\overline{C_f} = (0.5 - 0.039e^{-0.073\theta_p - 1.052})\mathrm{Ta}^{-1/2}. \quad (23)$$

The $\overline{\mathrm{Nu}}$ variations with Ta shown in Fig. 11(*b*) being much less than with the groove pitch, except for a number of groove exceeding 20 ($\theta_p \leqslant 17.14$ deg), it can be assumed that the influence of Ta on $\overline{\mathrm{Nu}}$ is small. Therefore, a correlation as a function of θ_p only can be derived as

$$\overline{\mathrm{Nu}} = 0.973 - 0.131e^{(14.4 - \theta_p/14.618)} \quad (24)$$

Influence of the Opening Angle of the Groove. The computations carried out for various opening angles of the grooves show again a linear decrease of $\overline{C_f}$ with $\mathrm{Ta}^{-1/2}$ (Fig. 12(*a*)). When increasing θ_g, the friction coefficient is reduced since the average gap width is increased. The following correlation for $\overline{C_f}$ was derived:

$$\overline{C_f} = (0.518 - 3.86.10^{-3}\theta_g)\mathrm{Ta}^{-1/2}. \quad (25)$$

The mean Nusselt number also decreases when increasing the opening angle of the grooves while $\overline{\mathrm{Nu}}$ is almost independent of Ta (Fig. 12(*b*)). Therefore $\overline{\mathrm{Nu}}$ can be well correlated with θ_g as:

$$\overline{\mathrm{Nu}} = 1.02942 - 0.01088\theta_g. \quad (26)$$

4.3 Design of Experiments. The purpose of this section is to derive a general correlation to describe the influence of the main parameters both on the friction coefficient and on the mean Nusselt number. The statistical design of experiment (DOE) is well adapted to the present problem because the number of influent parameters renders difficult to derive such a correlation through the examination of the effect of one parameter while the others are kept constant.

According to the previous parametric study, we opted for a first-order polynomial because it was shown that the variations of the responses ($\overline{C_f}$ and $\overline{\mathrm{Nu}}$) are almost linear. However, the interactions

between the factors were accounted for. The number of parameters to investigate and the levels to run them have to be decided, knowing that the addition of a new parameter is possible if the model obtained is not satisfactory. These criteria lead us to use a centered complete factorial design, and the numerical experiments were conducted by changing all the parameters to their extreme values. When using a linear model, 2^k experiments are necessary for k parameters. In the present work, regressed variables were employed and the coefficients were obtained by using the Yates algorithm [15]. In order to reduce the number of computations, we eliminated the non influent parameters as observed in the parametric study.

Empirical Model for the Friction Coefficient. It has been shown that the friction coefficient is almost independent of the radius ratio of the groove. On the other hand, the variation of $\overline{C_f}$ with Ta is systematically proportional to $\mathrm{Ta}^{-1/2}$. Therefore, it is not necessary to carry out additional computations for modeling the effects of R_g and Ta. Thus, these two parameters were arbitrarily fixed to $R_g=1.4$ and $\mathrm{Ta}=100$, and only three parameters have to be considered. Eight numerical experiments were thus conducted for R, θ_g, and θ_p varying in the ranges $1.007<R<1.10$, $2\ \mathrm{deg}<\theta_g<17\ \mathrm{deg}$ and $18.9\ \mathrm{deg}<\theta_p<120\ \mathrm{deg}$. A linear model for R and θ_g is well suited but the variation of $\overline{C_f}$ with θ_p follows an exponential relationship. According to Eq. (23), a first parametrical transformation permits to properly depict such a behavior

$$\theta_p'=e^{-0.073\theta_p}. \tag{27}$$

Since normalized regressed variables should be used, the following parametrical transformations were introduced

$$R^*=21.5054R-22.656 \tag{28}$$

$$\theta_g^*=0.13\overline{3}\,\theta_g-1.26\overline{6} \tag{29}$$

$$\theta_p'^*=7.958\theta_p'-1=7.96e^{-0.073\theta_p}-1. \tag{30}$$

The results of the numerical simulations are reported in Table 4 together with the coefficients of the correlation. The model is as follows:

Table 4 DOE parameters for $\overline{C_f}$

R*	θ_g*	θ_p'*	$\overline{C_f}$ (10^{+2})	R	θ_g	θ_p	Coeff.
-1	-1	-1	1.691134	1.007	2°	120°	$a_0 = 4.594\ 10^{-2}$
+1	-1	-1	7.937598	1.1	2°	120°	$a_1 = 3.074\ 10^{-2}$
-1	+1	-1	1.610379	1.007	17°	120°	$a_2 = -2.064\ 10^{-3}$
+1	+1	-1	7.812051	1.1	17°	120°	$a_{12} = -5.023\ 10^{-4}$
-1	-1	+1	1.666835	1.007	2°	18.9°	$a_3 = -1.686\ 10^{-3}$
+1	-1	+1	7.918765	1.1	2°	18.9°	$a_{13} = -3.766\ 10^{-4}$
-1	+1	+1	1.110748	1.007	17°	18.9°	$a_{23} = -1.579\ 10^{-3}$
+1	+1	+1	7.005644	1.1	17°	18.9°	$a_{123} = -3.903\ 10^{-4}$

$$\overline{C_f}=a_0+a_1R^*+a_2\theta_g^*+a_3\theta_p'^*+a_{12}R^*\theta_g^*+a_{13}R^*\theta_p'^*+a_{23}\theta_g^*\theta_p'^*+a_{123}R^*\theta_g^*\theta_p'^*. \tag{31}$$

Comparisons of the coefficients show the preponderance of the radius ratio R in the variation of the friction coefficient since a_1 is one order of magnitude greater than the other coefficients. For example, in the case of the basic geometry considered in the present work ($R=1.0526$, $R_g=1.2$, $\theta_p=30$ deg, $\theta_g=10$ deg) and $\mathrm{Ta}=100$, the variation of $\overline{C_f}$ is about 18 percent when increasing R from $R=1.007$ to $R=1.10$. The variation of $\overline{C_f}$ is 3 percent only for $1.01\leqslant R_g\leqslant 1.4$; 7 percent for $14.4\ \mathrm{deg}\leqslant\theta_p\leqslant 120\ \mathrm{deg}$, and 17 percent for $2\ \mathrm{deg}\leqslant\theta_g\leqslant 24\ \mathrm{deg}$. Therefore, small variations in R produce large changes in $\overline{C_f}$. The influences of θ_p and θ_g are of the same order, and the double and triple interactions are very weak, except for θ_p and θ_g.

An inverse parametrical transformation and multiplication of the coefficients by $\mathrm{Ta}^{-1/2}$ yield the empirical model as

$$\overline{C_f}=[b_0+b_1R+b_2\theta_g+b_3e^{d_1\theta_p}+b_{12}R\,\theta_g+b_{13}Re^{d_1\theta_p}+b_{23}\theta_g e^{d_1\theta_p}+b_{123}R\,\theta_g e^{d_1\theta_p}]\mathrm{Ta}^{-1/2} \tag{32}$$

with

$b_0=-6.59989$ $\quad b_3=-0.1873777$ $\quad b_{23}=7.707863\ 10^{-2}$

$b_1=6.72302$ $\quad b_{12}=-3.196993\ 10^{-3}$ $\quad b_{123}=-8.906456\ 10^{-2}$

$b_2=2.682974\ 10^{-3}$ $\quad b_{13}=0.201516$ $\quad d_1=-0.0730392$

The domain of validity for the above correlation is:

$A\geqslant 40$ and $\mathrm{Ta}<\mathrm{Ta}_c$, (two-dimensional flows)

$1.007\leqslant R\leqslant 1.10$ $\quad 1.01\leqslant R_g\leqslant 1.4$.

$2\ \mathrm{deg}\leqslant\theta_g\leqslant 17\ \mathrm{deg}$ $\quad 18.9\ \mathrm{deg}\leqslant\theta_p\leqslant 120\ \mathrm{deg}$

Empirical Model for the Nusselt Number. According to the results of the parametric study, the groove pitch and the opening angle of the groove are the most important parameters since the changes in $\overline{\mathrm{Nu}}$ are about 3 percent in the range of variation of Ta, and small effects of R and R_g were observed if their ranges of variations are restricted to $1.05\leqslant R_g\leqslant 1.4$ and to $1.03\leqslant R\leqslant 1.11$. According to Eq. (24) the following parametrical transformation on θ_p is made first:

$$\theta_p'=e^{-0.054\theta_p}. \tag{33}$$

The regressed variables are obtained using the parametrical transformation (29) for θ_g and the following one for θ_p':

$$\theta_p'^*=7.958\theta_p'-1=7.96e^{-0.073\theta_p}-1 \tag{34}$$

With $R=1.0526$, $R_g=1.2$, and $\mathrm{Ta}=100$, only the four calculations reported in Table 5 were necessary to obtain the linear model. The correlation obtained for the regressed variables is as follows:

$$\overline{\mathrm{Nu}}=a_0+a_1\theta_p'^*+a_2\theta_g^*+a_{12}\theta_g^*\theta_p'^*. \tag{35}$$

Table 5 DOE parameters for $\overline{\mathrm{Nu}}$

θ_p'*	θ_g*	$\overline{Nu}$	θ_p	θ_g	Coeff.
-1	-1	0.997562	120°	2°	$a_0 = 0.92413$
+1	-1	0.991313	18.9°	2°	$a_1 = -0.05708$
-1	+1	0.964863	120°	17°	$a_2 = -0.07030$
+1	+1	0.742797	18.9°	17°	$a_{12} = -0.05395$

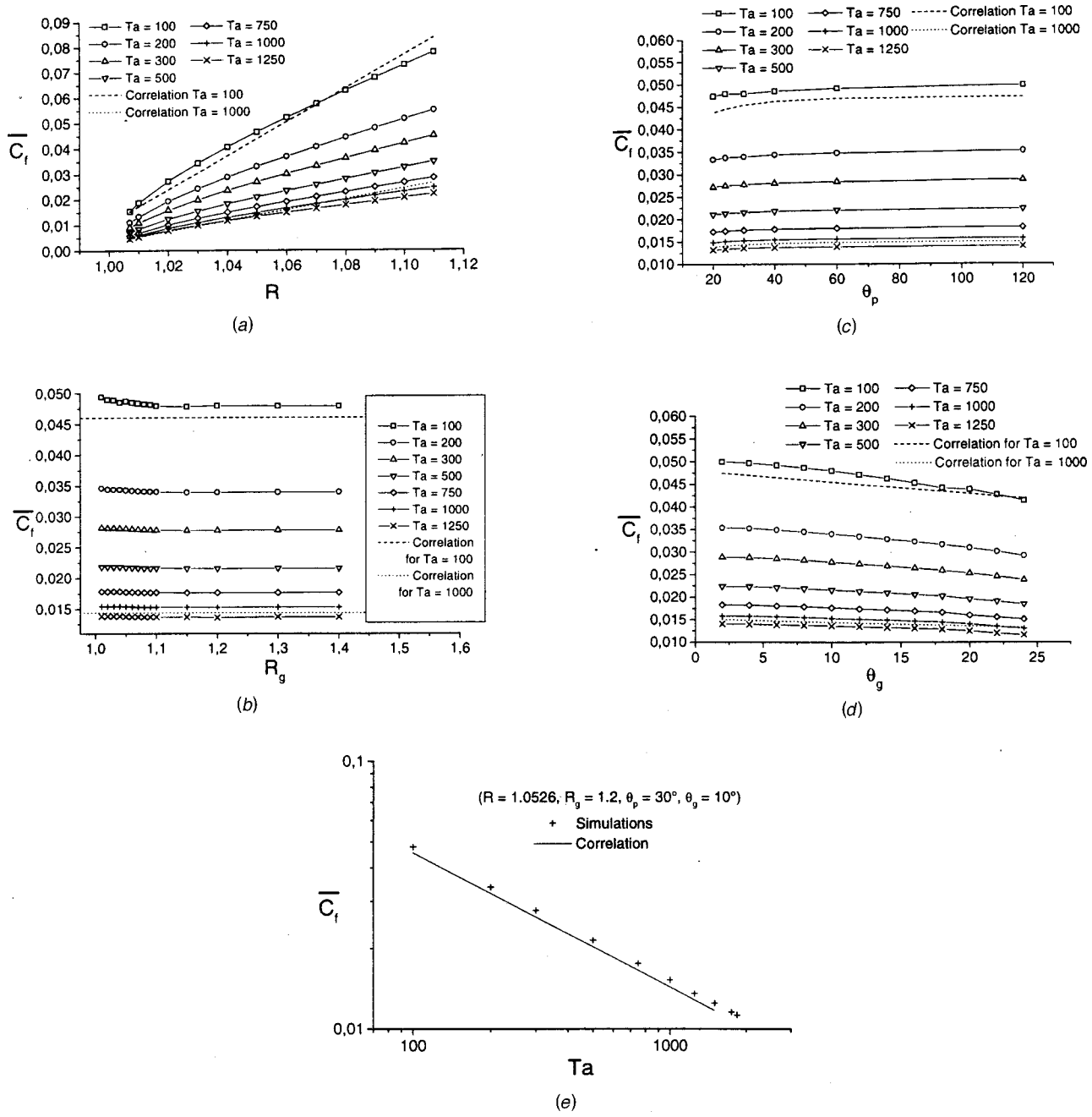

Fig. 13 Comparisons between calculations and correlation about the mean friction coefficient: (*a*) $\overline{C_f}$ versus *R*; (*b*) $\overline{C_f}$ versus R_g; (*c*) $\overline{C_f}$ versus θ_p; (*d*) $\overline{C_f}$ versus θ_g; and (*e*) $\overline{C_f}$ versus Ta.

The values of the coefficients show that all of the terms, including the interaction term, have a similar influence. The inverse parametrical transformation leads to the correlation

$$\overline{\mathrm{Nu}} = b_0 + b_1 e^{d_1\theta_p} + b_2\theta_g + b_{12}\theta_g e^{d_1\theta_p} \tag{36}$$

With

$b_0 = 1.00182$ $\quad b_2 = -6.260028\,10^{-2}$ $\quad d_1 = -0.0538433$
$b_1 = -2.117312\,10^{-3}$ $\quad b_{12} = -3.997931\,10^{-2}$

The domain of validity for correlation (36) is

$A \geqslant 40$ and $\mathrm{Ta} < \mathrm{Ta}_c$, (two-dimensional flows)

$1.03 \leqslant R \leqslant 1.10$ $\quad 1.05 \leqslant R_g \leqslant 1.4$. $\quad 2\ \mathrm{deg} \leqslant \theta_g \leqslant 17\ \mathrm{deg}$

$18.9\ \mathrm{deg} \leqslant \theta_p \leqslant 120\ \mathrm{deg}$.

Accuracy of the $\overline{C_f}$ and $\overline{\mathrm{Nu}}$ Correlations. The DOE method used to derive the correlations allows to reach a high level of accuracy for the coefficients. However, it is needed to check the accuracy of the responses, the adequacy of the mathematical model used and the levels to run the factors. To this end, the results given by correlations (32) and (36) were compared with the numerical results obtained through the parametric study.

Friction Coefficient. Figure 13 shows a good agreement be-

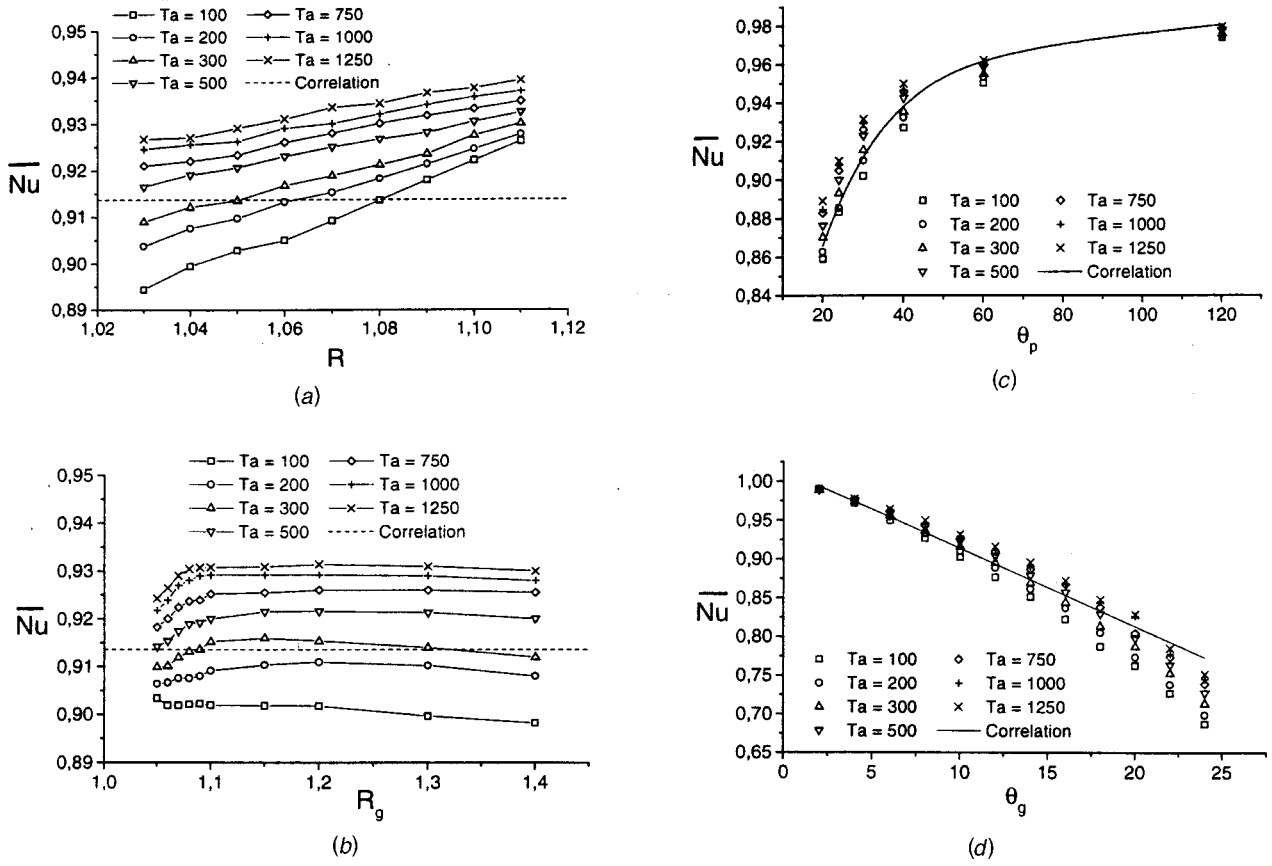

Fig. 14 Comparison between calculations and correlation about the mean Nusselt number: (*a*) $\overline{Nu}$ versus R; (*b*) $\overline{Nu}$ versus R_g; (*c*) $\overline{Nu}$ versus θ_p; (*d*) $\overline{Nu}$ versus θ_g

tween correlation (32) and the numerical simulations, whatever the value of a parameter is. It is relevant to notice that the variation of $\overline{C_f}$ with R, which is the dominant parameter, is nicely reproduced by Eq. (32). Also, the linear decrease of $\overline{C_f}$ with $\mathrm{Ta}^{-1/2}$ imposed in the correlation is appropriate as it is displayed in Fig. 13(*e*). Finally, the accuracy in the torque coefficient calculated with correlation (32) can be estimated to be about 6 percent.

Nusselt Number. The results for the Nusselt number are reported in Fig. 14 for all the geometrical parameters. Figures 14(*a*) and 14(*b*) are for the parameters R and R_g which were assumed to have a negligible influence when deriving correlation (36). The discrepancy is less than 3 percent for R and less than 2 percent for R_g so that the assumptions used can be considered as valid. Therefore, the dominant parameters are indeed the opening angle of the groove and the groove pitch, as it is shown in Figs. 14(*c*) and 14(*d*). The adequacy of the exponential variation of $\overline{Nu}$ with θ_p appears clearly since the maximum discrepancy is less than 3 percent. Concerning θ_g, the best domain of validity of the correlation is $2\ \mathrm{deg} < \theta_g < 17\ \mathrm{deg}$ but it is still working up to $\theta_g = 22.5\ \mathrm{deg}$ within a 10 percent accuracy. Finally, it can be concluded that overall accuracy of the correlation is about 3 percent.

5 Concluding Remarks

The three-dimensional computations discussed in the present paper permit to accurately establish the domain of validity of the two-dimensional assumptions for the flow in a grooved annulus of finite length. It has been shown that a two-dimensional modeling is valid provided that $\mathrm{Ta} < \mathrm{Ta}_c \cong 1350$, and $A \geqslant 40$. A special attention was paid to check the circumferential geometric periodicity of the flow. According to those limitations, two-dimensional computations may be carried out to physically understand the influence on the flow of each geometrical parameter and of the rotational speed. Investigations of the effects of the problem parameters on the friction coefficient and on the Nusselt number allowed us to chose a mathematical model for correlating $\overline{C_f}$ and $\overline{Nu}$ as a function of the geometrical and flow parameters. The use of a DOE method leads to a good accuracy and the values of $\overline{C_f}$ and $\overline{Nu}$ can be predicted with an accuracy of about 6 percent and 3 percent, respectively, for a large range of geometrical parameters and rotational velocity.

Acknowledgments

Grant #991030 and 200140 from the IDRIS-computer center (French National Institute for Advances in Scientific Computations) is gratefully acknowledged.

Nomenclature

A = axial aspect ratio of the annulus, $A = L'/e'$
A_i = area of inner cylinder
C_f = friction coefficient
e' = rotor-stator gap width, $e' = r'_{is} - r'_i$
f = radial function, $f = \eta r + 1$
G = torque acting on the inner cylinder
h = heat transfer coefficient
k = thermal conductivity
L' = length of the annulus
Nu = Nusselt number
P = pressure
q = heat flux density
q_{co} = conductive heat flux
R = radius ratio, $R = r'_{is}/r'_i$
R_g = radius ratio of the groove, $R_g = r'_{es}/r'_{is}$

Re = Reynolds number (Eq. 6)

r_i', r_{es}' = radius of inner and outer cylinder, respectively

r_{is}' = inner radius of outer cylinder

r_e = dimensionless inner radius of the outer cylinder, $r_e=(R_gR-1)/(R-1)$

T = temperature

Ta = Taylor number (Eq. 6)

T_h', T_c' = inner and outer cylinder temperature, respectively

T_0' = reference value of temperature, $T_0'=(T_c'+T_h')/2$

u_r, u_θ, u_z = radial, tangential, and axial velocity components, respectively

Greek Symbols

θ_p = angle of the groove pitch

θ_g, θ_1, θ_2 = angles determining the groove configuration (Fig. 1)

ν = kinematic viscosity of the fluid

μ = dynamic viscosity of the fluid

ρ = density of the fluid

η = curvature parameter, $\eta=R-1$

τ_ω = local shear stress

Ω_i = angular velocity of inner cylinder

Superscripts

$'$ = dimensional quantity

$\overline{\ }$ = mean quantity

Subscripts

i = inner cylinder

References

[1] Gazley, C., 1958, "Heat-Transfer Characteristics of the Rotational and Axial Flow Between Concentric Rotating Cylinders," Trans. ASME, **80**, pp. 79–90.

[2] Tachibana, F., and Fukui, S., 1964, "Convective Heat Transfer on the Rotational and Axial Flow Between Two Concentric Cylinders," Bull. JSME, **7**, pp. 385–391.

[3] Yamada, Y., 1962, "Torque Resistance of a Flow Between Rotating Coaxial Cylinders Having Axial Flow," Bulletin JSME, **5**, No. 5, pp. 634–642.

[4] Lee, Y. N., and Minkowycz, W. J., 1989, "Heat Transfer Characteristics of the Annulus of Two Coaxial Cylinders With One Cylinder Rotating," Int. J. Heat Mass Transf., **32**, pp. 711–722.

[5] Murphy, J. Y., and Patankar, S. V., 1983, "Numerical Study of Heat Transfer From a Rotating Cylinder With External Longitudinal Fins," Numer. Heat Transfer, **6**, No. 4, pp. 463–473.

[6] Hayase, T., Humphrey, J. A. C., and Greif, R., 1992, "Numerical Calculations of Convective Heat Transfer Between Rotating Coaxial Cylinders With Periodically Embedded Cavities," ASME J. Heat Transfer, **114**, pp. 589–596.

[7] Ziouchi, A., 1996, "Contribution à l'analyze et à la modélisation des échanges convectifs dans un entrefer de moteur électrique fermé", Ph.D. thesis, Université de Poitiers, France.

[8] Sommerer, Y., Lauriat, G., and Desrayaud, G., 1999, "Convection forcée dans l'entrefer rainuré d'un moteur électrique," *Proceedings of the SFT 99 Conference*, Elsevier, Paris, pp. 185–190.

[9] Pecheux, J., Bousgarbies, J. L., and Bellenoue, M., 1997, "Instabilité de Taylor entre un cylindre lisse tournant et un cylindre fixe encoché," C. R. Acad. Sci Paris, série II b, pp. 159–163.

[10] Bouafia, M., Ziouchi, A., Bertin, Y., and Saulnier, J. P., 1999, "Etude expérimentale et numérique des transferts de chaleur en espace annulaire sans débit axial et avec cylindre intérieur tournant," Int. J. Therm. Sci, **38**, pp. 547–559.

[11] Gardiner, S. R., and Sabersky, R. H., 1978, "Heat Transfer in an Annular Gap," Int. J. Heat Mass Transf., **21**, pp. 1459–1466.

[12] Alziary de Roquefort, T., and Grillaud, G., 1978, "Computation of Taylor Vortex Flow by a Transient Implicit Method," Comput. Fluids, **6**, pp. 259–269.

[13] Taylor, G. I., 1923, "Stability of a Viscous Liquid Contained Between Two Rotating Cylinders," Philos. Trans. R. Soc. London, Ser. A, **233**, pp. 289–343.

[14] Marcus, P. S., 1984, "Simulation of Taylor-Couette Flow: Part1—Numerical Methods and Comparison With Experiment," J. Fluid Mech., **146**, pp. 45–64.

[15] Yates, F., 1935, "Complex Experiments," J. R. Statist. Soc. Suppl., **2**, pp. 181.

Iztok Tiselj
Assistant Professor
Mem. ASME
"Jožef Stefan" Institute,
Jamova 39,
1000 Ljubljana, Slovenia
E-mail: iztok.tiselj@ijs.si

Robert Bergant
Graduate Student
"Jožef Stefan" Institute,
Jamova 39,
1000 Ljubljana, Slovenia

Borut Mavko
Professor
Mem. ASME
"Jožef Stefan" Institute,
Jamova 39,
1000 Ljubljana, Slovenia

Ivan Bajsić
Assistant Professor
Faculty of Mechanical Engineering,
University of Ljubljana,
1000 Ljubljana, Slovenia

Gad Hetsroni
Professor
Mem. ASME
Faculty of Mechanical Engineering,
Technion-Israel Institute of Technology,
32000 Haifa, Israel

DNS of Turbulent Heat Transfer in Channel Flow With Heat Conduction in the Solid Wall

The Direct Numerical Simulation (DNS) of the fully developed velocity and temperature fields in the two-dimensional turbulent channel flow coupled with the unsteady conduction in the heated walls was carried out. Simulations were performed at constant friction Reynolds number 150 and Prandtl numbers between 0.71 and 7 considering the fluid temperature as a passive scalar. The obtained statistical quantities like root-mean-square temperature fluctuations and turbulent heat fluxes were verified with existing DNS studies obtained with ideal thermal boundary conditions. Results of the present study were compared to the findings of Polyakov (1974), who made a similar study with linearization of the fluid equations in the viscous sublayer that allowed analytical approach and results of Kasagi et al. (1989), who performed similar calculation with deterministic near-wall turbulence model and numerical approach. The present DNS results pointed to the main weakness of the previous studies, which underestimated the values of the wall temperature fluctuations for the limiting cases of the ideal-isoflux boundary conditions. With the results of the present DNS it can be decided, which behavior has to be expected in a real fluid-solid system and which one of the limiting boundary conditions is valid for calculation, or whether more expensive conjugate heat transfer calculation is required.
[DOI: 10.1115/1.1389060]

Keywords: Channel Flow, Conjugate, Heat Transfer, Numerical Methods, Turbulence

Introduction

The Direct Numerical Simulation (DNS) became an important research tool of the turbulent heat transfer in the last decade [1]. Review of the turbulent heat transfer research in that time is given by Kasagi and Iida [2]. Particular attention was paid to the DNS of the fully developed turbulent channel flow, as it reveals the basic mechanisms of the convective heat transfer between the fluid and the solid wall. The first such DNSs were made by Kim and Moin [3] and Kasagi et al. [4] at moderate Reynolds numbers and Prandtl numbers of about one or less. Later, Kawamura et al. [5], Na and Hanratty [6] performed DNS of the turbulent channel at Prandtl numbers up to ten. Kawamura et al. [7] studied the influence of the Prandtl and Reynolds number and showed very weak influence of the Reynolds number on the turbulent heat transfer statistics (mean temperature, RMS-fluctuations, turbulent heat fluxes) in the near-wall region.

All the simulations mentioned above used isothermal boundary condition for the dimensionless temperature, which corresponds to the physical configuration where the fluid with negligible density, heat capacity and thermal conductivity is heated by a thick wall with high density, high heat capacity and high thermal conductivity (thermal activity ratio $K=\sqrt{\rho_f c_{pf} \lambda_f / \rho_w c_{pw} \lambda_w} \rightarrow 0$). Comparison of isoflux ($K=\infty$) and isothermal ($K=0$) boundary conditions has been given by Kong et al. [8], who performed DNS of the developing turbulent thermal boundary layer and observed the temperature fluctuations on the isoflux wall. Tiselj et al. [9] performed DNS of the turbulent flume flow with ideal isothermal and ideal isoflux thermal boundary condition and analyzed the differences between both types of boundary condition at $Pr=1$ and $Pr=5.4$.

In order to reveal the details of the heat transfer near the wall with a given thickness and material properties ($\rho_w, c_{pw}, \lambda_w$) a coupled problem of turbulent heat transfer and unsteady heat conduction in the solid wall has to be solved. Such conjugate heat transfer was studied by Polyakov [10], Khabakhpasheva [11], Sinai [12], Kasagi et al. [13], and Sommer et al. [14]. They showed analytically and experimentally, that the temperature fluctuations on the fluid-solid interface differ for different fluid-solid systems. The detailed study of conjugate heat transfer by Kasagi et al. [13] was performed with unsteady two-dimensional model of near-wall turbulence [15] and simultaneous solution of fluid energy equation and equation for solid heat conduction. Kasagi et al. [13] showed that in the experiments performed with air the wall temperature fluctuations are usually negligible. The experiments with water can be performed at almost isothermal boundary condition if a thick copper plate is used as a heater (Khabakhpasheva [11]) or at almost isoflux boundary condition, if the heated wall is very thin. Experiments with near-isoflux boundary condition were performed by Iritani et al. [16] and Hetsroni and Rozenblit, [17] and Mosyak et al. [18]. Probably the most accurate measurement of thewall temperature fluctuations at almost isoflux boundary condition was performed by Mosyak et al. [18] with water as a working fluid.

In the present work DNS was coupled with unsteady heat conduction in the wall. Simulations were performed at friction Reynolds number $Re_\tau=150$ and Prandtl numbers between 0.71 and 7. Results are compared with other DNS studies and with the Kasagi et al. [13] study of conjugate heat transfer. The main deficiencies of the simpler and cheaper methods used for conjugate heat trans-

Contributed by the Heat Transfer Division for publication in the JOURNAL OF HEAT TRANSFER. Manuscript received by the Heat Transfer Division September 9, 2000; revision received March 16, 2001. Associate Editor: D. Poulikakos.

fer calculations in the past [10,13] are discussed. Value of the wall temperature fluctuations for the ideal isoflux boundary condition is shown to be the crucial parameter for such simpler models, and the most accurate predictions of the wall temperature fluctuations under ideal isoflux boundary conditions are obtained by DNS.

Governing Equations

The flow in the channel is assumed to be fully developed. Both walls are assumed to have the same thickness, identical material properties, and the same constant volumetric heat source. The computational domain is shown in Fig. 1. The governing equations of the fluid, normalized with channel half width h, friction velocity u_τ, kinematic viscosity ν, and friction temperature $T_\tau = q_w/(u_\tau \rho / c_{pf})$ can be found in the papers of Kasagi et al. [4] or Kawamura et al. [5]:

$$\Delta \cdot \vec{u}^+ = 0, \tag{1}$$

$$\frac{\overline{\partial \vec{u}}^+}{\partial t} = -\nabla \cdot (\vec{u}^+ \vec{u}^+) + \frac{1}{\mathrm{Re}_\tau} \nabla^2 \vec{u}^+ - \nabla p + \vec{1}_x, \tag{2}$$

$$\frac{\partial \theta^+}{\partial t} = -\nabla \cdot (\vec{u}^+ \theta^+) + \frac{1}{\mathrm{Re}_\tau \cdot \mathrm{Pr}} \nabla^2 \theta^+ + \frac{u_x^+}{u_B^+}. \tag{3}$$

The terms $\vec{1}_x$ (unit vector in streamwise direction) and u_x^+/u_B^+ appear in the Eqs. (2) and (3) due to the splitting of the temperature and pressure gradients into mean and fluctuating part. Such splitting is required by the numerical scheme that is using periodic boundary conditions in the streamwise and the spanwise directions.

As can be seen from Eqs. (1)–(3) temperature is assumed to be a passive scalar. This assumption introduces two approximations: (1) neglected buoyancy and (2) neglected temperature dependence of the material properties—especially viscosity and heat conductivity. Therefore, results of the present study are very accurate only for the systems, where the temperature differences are not too large, while some caution is required for the systems, where the temperature differences are not negligible. The buoyancy can be for example neglected in the water flume experiment of Hetsroni and Rozenblit [17], while the viscosity and heat conductivity vary for approximately 10 percent in the range where the experiment was performed.

Dimensionless equation of heat conduction in the wall with internal heating is (see Kasagi et al. [13]):

$$\frac{\partial \theta^+}{\partial t} = \frac{1}{\mathrm{Re}_\tau \cdot \mathrm{Pr}} \nabla^{++2} \theta^+ - \frac{K}{d^{++}}, \tag{4}$$

where ∇^{++2} is the non-dimensional Laplace operator, and $-K/d^{++}$ dimensionless internal heat source.

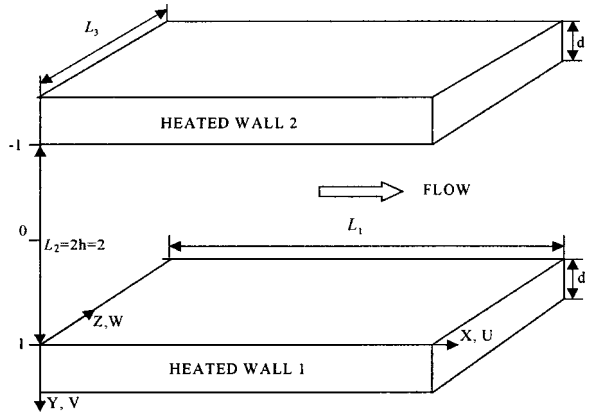

Fig. 1 Flow geometry

At the solid-fluid interface the boundary conditions for temperature and heat flux are

$$\theta_f^+ = \theta_w^+, \tag{5}$$

$$K \frac{\partial \theta_f^+}{\partial y^+} = \frac{\partial \theta_w^+}{\partial y^{++}}. \tag{6}$$

Mean dimensionless temperature at both fluid-solid interfaces is fixed to zero: $\langle \theta^+(y=\pm 1) \rangle_{x,z,t} = 0$, while the outer wall boundaries are assumed to be adiabatic.

Numerical Procedures

The fluid equations are solved with pseudo-spectral scheme using Fourier series in x and z directions and Chebyshev polynomials in wall-normal y direction. Second-order accurate time differencing (Crank-Nicholson scheme for diffusive terms and Adams-Bashfort scheme for other terms) is used with maximum CFL numbers approximately 0.4 and 0.2 for Pr=0.71 and Pr=7 respectively. Numerical procedure and the code of Gavrilakis et al. [19], modified by Lam and Banerjee [20] and Lam [21] are used to solve the continuity and momentum equations.

The two following major modifications of the code were performed for the present study:

1 Several energy equations with different boundary conditions (up to 40) are solved in parallel with a single velocity field solution. This approach reduces the CPU time but increases the required physical memory of the computer.

2 Heat conduction equations in both walls are solved with a mixture of spectral and finite difference method and coupled with the fluid energy equation. A natural approach is to retain the Fourier series in x and z directions (the same series are used in the fluid), while the remaining set of the first order partial differential equations in y direction

$$\frac{\partial \theta_{i,j}^+}{\partial t} = \frac{k_i^2 + k_j^2}{\mathrm{Re}_\tau \cdot \mathrm{Pr}} \theta_{i,j}^+ + \frac{1}{\mathrm{Re}_\tau \cdot \mathrm{Pr}} \frac{\partial^2 \theta_{i,j}^+}{\partial y^{++2}} - \frac{K}{d^{++}} \delta_{i,j} \tag{7}$$

is solved with the Crank-Nicholson finite difference scheme on an equidistant grid for each pair of wave numbers k_i, k_j. The tri-diagonal system of linear equations resulting from the Crank-Nicholson discretization has one more unknown variable then the number of the linear equations. This unknown variable is derivative $\partial \theta_{i,j}^+ / \partial y^{++}$ at the fluid-solid boundary. The same derivative $(\partial \theta_{i,j}^+ / \partial y^+)$ remains unspecified also on the fluid side and is determined from the boundary conditions Eqs. (5) and (6). Tri-diagonal system inside the wall is solved in three steps:

1 Despite the additional unknown variable on the fluid-solid boundary the tri-diagonal system can be transformed into the two-diagonal system. As a result of this transformation the following linear equation is obtained on the fluid side of the fluid-solid boundary:

$$a(\theta_{i,j}^+)_1^{n+1} + b\left(\frac{\partial \theta_{i,j}^+}{\partial y^+}\right)_1^{n+1} = c. \tag{8}$$

Values of coefficients a, b, c are known, outer subscript "1" denotes the boundary point and superscript "$n+1$" denotes unknown values at time step $n+1$.

2 Equation (8) is used as a mixed type boundary condition for the solution of the fluid energy equation, which is solved in the second step. The value of the derivative $\partial \theta_{i,j}^+ / \partial y^{++}$ at the fluid-solid boundary follows from the known fluid temperatures.

3 The wall temperatures are calculated in the third step from the remaining two-diagonal system and known value of derivative $\partial \theta_{i,j}^+ / \partial y^{++}$ at the fluid-solid boundary.

Eq. (7) was first solved separately to test the accuracy (grid refinement) and to estimate the time required to achieve statistically steady state distribution of the temperature fluctuations in-

side the solid wall. Different oscillatory boundary conditions ($\cos(k_x x + k_z z + \omega t)$) with different wave numbers and frequencies were imposed on one side of the heated wall at time zero, keeping the other side adiabatic. Propagation of the temperature fluctuations inside the wall was observed at different wall thickness and material properties. These calculations predicted faster convergence for higher wave numbers and thinner walls. Predicted convergence was similar to the convergence observed in DNS for thick walls, while the DNS convergence for thin walls turned out to be slower than the convergence predicted by the separate solutions of Eq. (7). Finally, the same time interval was used to achieve the development of the temperature fluctuations inside all type of walls. Appropriate number of grid points inside the wall in the wall-normal (y) direction was found to be between 2 points for the thinnest wall ($d^{++}=0.5$) and 40 grid points for the thickest walls ($d^{++}=20$, $d^{++}=50$.).

Calculations

(1) Non-Conjugate Heat Transfer Calculations at Pr =0.71. The first part of the present analysis was DNS with two temperature fields at the same Prandtl number but with different types of thermal boundary conditions: isoflux and isothermal, without wall heat conduction. For the air Prandtl number Pr $=0.71$ computation, the DNS computational domain was 5π and π (2356 and 471 in wall units) in the x and z directions, respectively. 128×64 Fourier modes and 97 Chebyshev polynomials were used in x, z, and y directions respectively (see Table 1 for the simulation parameters). The time increment was 0.12 ν/u_τ^2 and the averaging was performed over time interval 6000 ν/u_τ^2 after the fully developed flow was achieved. One criterion used to judge whether the velocity and thermal fields are fully developed was temporal behavior of the volume averaged bulk velocity and bulk temperatures ($\langle\overline{u}\rangle_{x,y,z}$, $\langle\theta\rangle_{x,y,z}$), that were acceptable when they did not show any global increase or decrease over a time interval of a few thousand ν/u_τ^2 time units. Another criteria for fully developed velocity and thermal fields were time and space averaged values of friction velocity and the frictions temperatures, which had to be within 0.5 percent of their expected values.

The applied resolution ($\Delta x^+=18.4$, $\Delta y^+=0.08-4.9$, $\Delta z^+=7.4$) is equal to the resolution applied by Kasagi et al. in 1992 [4] for a DNS with identical Reynolds and Prandtl numbers. The difference between the present DNS and DNS of Kasagi et al. [4] is two times shorter period in z direction in the present DNS (2π versus π), which is partially compensated with longer averaging period than in the calculation of Kasagi (6000 versus 2100 ν/u_τ^2). The results shown in the next section at Pr$=0.71$ are calculated as described above, although another calculation was performed on the finer grid $192\times145\times96$, time step 0.09 ν/u_τ^2 and averaging time 6000 ν/u_τ^2, which show that the agreement of the first-order statistics is within the estimated statistical uncertainty of 0.5 percent. Slightly higher (2 percent) statistical uncertainty was observed only for the value of the wall RMS temperature fluctuations in the isoflux boundary condition DNS shown in Fig. 3(a).

(2) Conjugate Heat Transfer Calculations at Pr=0.71. After the DNS with two ideal boundary conditions was finished, the conjugate heat transfer calculation was started. Since the temperature is a passive scalar and does not affect the velocity field, up to 40 temperature fields are calculated with a single velocity field. The first temperature field is a reference field calculated with ideal isoflux boundary condition and other 39 fields are calculated with walls of different thickness and with different thermal activity ratios. The initial fluid and wall temperatures for all 39 fields were taken from the ideal isoflux field, while zero temperature fields were assumed in the walls. The new fully developed temperature field in the fluid and in the wall for each of the 39 fields were typically developed after dimensionless time interval 50 to 500 ν/u_τ^2, which is significantly shorter than the time required to achieve fully developed flow after the modification of the Reynolds or Prandtl numbers. The time interval needed to achieve the statistically steady state turbulent fluctuations in the heated walls was observed from the value of the area averaged temperature RMS fluctuations on the fluid-solid interface.

After all thermal fields were fully developed the averaging was performed over time interval of 2400 ν/u_τ^2. Such time interval is roughly two times shorter than the averaging time interval of the typical DNS studies. However, as the temperature fluctuations of the fields with realistic walls were compared with the reference temperature field with ideal isoflux boundary condition ($R=\theta_{\text{RMS-BOUNDARY}}/\theta_{\text{RMS-ISOFLUX}}$), such averaging turned up to be sufficient to calculate the values of R with statistical uncertainty of approximately 1 percent. If in the observed time interval the temperature fluctuations at the wall are higher than the long time average value, then the same is true also for the reference field. The calculations have shown, that the temporal variations of the quotient $\langle R\rangle_{x,z}=\langle\theta_{\text{RMS-BOUNDARY}}\rangle_{x,z}/\langle\theta_{\text{RMS-ISOFLUX}}\rangle_{x,z}$ are much smaller than the temporal variations of the $\langle\theta_{\text{RMS-BOUNDARY}}\rangle_{x,z}$ or $\langle\theta_{\text{RMS-ISOFLUX}}\rangle_{x,z}$ values, and that even shorter time averaging periods of approximately 500 ν/u_τ^2 are sufficient.

(3) Non-Conjugate and Conjugate Heat Transfer Calculations at Pr=5, Pr=7. Second part of the analysis was DNS at water Prandtl numbers Pr$=5$ and Pr$=7$. As it is shown by Kasagi et al. [13] these Prandtl numbers are of much greater practical importance than Pr$=0.71$ of air, since the thermal activity ratio for the most of the water-solid systems is not negligibly small like in the case of air-solid systems. The thermal activity ratios for different water-solid systems range from 0.04 for copper to 0.22 for lead and 2.7 for Plexiglas.

The DNS computational domain at Pr$=5$ and Pr$=7$ is 5π and 1.25π (2356 and 589 in wall units) in the x and z directions, respectively. 160×80 Fourier modes and 161 Chebyshev polynomials were used in x, z, and y directions, respectively. The spatial resolution for Pr$=5$ and Pr$=7$ DNS is $\Delta x^+=14.7$, $\Delta y^+=0.029$

Table 1 Simulation parameters

Prandtl number	Pr=0.71	Pr=7
Grid (x, y, z)	128x97x65	160x161x80
Computational domain in code units and in wall units	5π x 2 x π 2356x300x471	5π x 2 x 1.25π 2356x300x589
Time step (ν/u_τ^2)	0.12	0.045
Averaging interval of non-conjugate heat transfer calculation (ν/u_τ^2)	6000	3600
Transient calculation for conjugate heat transfer calculation (ν/u_τ^2)	1200	940
Averaging interval of conjugate heat transfer calculation (ν/u_τ^2)	2400	560

-2.95, $\Delta z^+ = 7.4$ (Table 1). Theoretically, the grid spacing in all directions should be inversely proportional to the square root of Prandtl number [22]. This requirement was taken into account in the DNS studies of Kawamura et al. [5] and Tiselj et al. [9], however, as shown by Na and Hanratty [6] this requirement is probably too stringent. The grid refinement study of Na and Hanratty [6] at Pr=10 showed that finer grid is not required in streamwise and spanwise directions (x and z), but is necessary in the wall-normal direction y. Before the Pr=7 simulations were started, we confirmed the Na and Hanratty's [6] findings with DNS study at Pr=5.4. In the DNS of Tiselj et al. [9] the resolution at Pr=5.4 was two times finer in all three directions comparing to the Pr=1 simulation ($256\times129\times128$ at Pr=5.4 versus $128\times65\times64$ grid points at Pr=1 on the same computational domain). DNS at Pr=5.4 repeated on the grid refined only in y direction ($128\times129\times64$ grid points) did not produced significant changes to the first-order temperature statistics profiles: mean temperature, temperature RMS fluctuations and turbulent heat fluxes profiles of both calculations were within the statistical uncertainty of 1 percent. The wall RMS temperature fluctuations as the most sensitive parameter was 2 percent higher than in the DNS of Tiselj et al. [11] and the peak of the RMS temperature fluctuations was 1 percent higher.

It should be mentioned that despite very good agreement of the first order statistics, non-negligible differences were noticed in the streamwise and spanwise spectra of $256\times129\times128$ and $128\times129\times64$ simulations at Pr=5.4. These differences were not crucial for the current study since the most important parameter—RMS temperature fluctuations was predicted accurately, however they will require further study of the resolution requirements for DNS at high Prandtl numbers.

The DNS at Pr=5 and Pr=7 stated with two pairs of thermal fields for ideal isoflux and ideal isothermal boundary conditions. The time increment was $0.045\ \nu/u_\tau^2$ and the averaging was performed over time interval $3600\ \nu/u_\tau^2$ after the fully developed flow was achieved. After that, the conjugate heat transfer calculations were performed only for Pr=7 for $1500\ \nu/u_\tau^2$. Time averaging was performed over the last $560\ \nu/u_\tau^2$ time interval (see Table 1) and the statistical uncertainty of the ratio R was estimated to be 2–3 percent.

Results and Discussion

(1) Non-Conjugate Heat Transfer. The first part of the discussion is devoted to the ideal isoflux and ideal isothermal boundary conditions as the calculations with these two types of ideal boundary conditions set the limits for the conjugate heat transfer calculations. Beside that, the DNS with ideal isothermal boundary condition is used for the verification of the present calculation with the DNS results of Kasagi et al. [4] at Pr=0.71 and Kawamura et al. [5] at Pr=5.0. Figures 2–7 show that agreement with DNS of Kasagi et al. [4], which was performed at the same Reynolds number $\mathrm{Re}_\tau=150$ and Pr=0.71, is within the expected statistical error. Slightly larger differences are seen between the present DNS at Pr=5 and DNS of Kawamura et al. [5] at the same Prandtl number. Kawamura's DNS was performed with finite difference numerical scheme at slightly higher Reynolds number $\mathrm{Re}_\tau=180$ and beside the statistical error these might be additional reasons for the notable difference in the mean temperature profiles in Fig. 2(b).

One of the most important parameters—profile of RMS temperature fluctuations—is shown in Figs. 3(a)–3(b). Results shown in Fig. 3 are in agreement with results of Tiselj et al. [9], where similar calculations have been performed at $\mathrm{Re}_\tau=171$ and Pr=1 and Pr=5.4. Values of the $\vartheta_{\mathrm{RMS\text{-}BOUNDARY}}$ at the wall for isoflux boundary condition are 2.05, 7.0 and 8.8, for Prandtl numbers 0.71, 5, and 7, respectively. The statistical errors of the $\vartheta_{\mathrm{RMS\text{-}BOUNDARY}}$ values were estimated to approximately 1 percent for Pr=0.71 and 3 percent at Pr=5 and Pr=7. It is important to stress that the temporal oscillations of the $\langle \vartheta_{\mathrm{RMS\text{-}BOUNDARY}} \rangle_{x,z}$ values can be two to three times larger than the oscillations of the maximums of the $\langle \vartheta_{\mathrm{RMS}} \rangle_{x,z}$ profiles in Fig. 3. In other words: longer averaging time or larger computational domain are required for accurate predictions of the $\vartheta_{\mathrm{RMS\text{-}BOUNDARY}}$ values than for the similarly accurate values of other statistics.

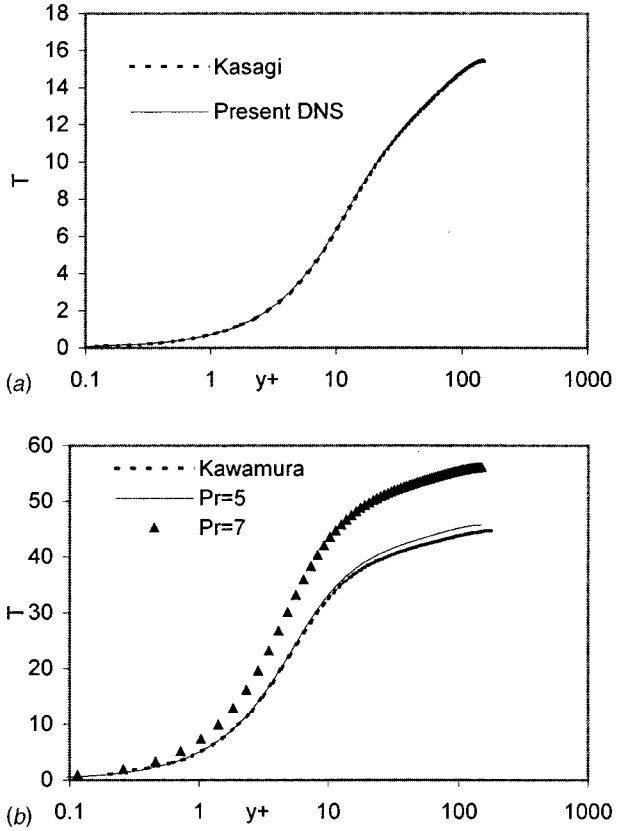

Fig. 2 Profiles of mean temperature: (*a*) Pr=0.71; (*b*) Pr=5, Pr=7.

Very similar $\vartheta_{\mathrm{RMS\text{-}BOUNDARY}}$ value (approx. 2.0) and ϑ_{RMS} profile were obtained by Kong et al. [8] in the study of the thermal boundary layer at $\mathrm{Re}_\tau=300$ and Pr=0.71. Comparison of the present study and study of Kong et al. shows that the ϑ_{RMS} profile does not change significantly for $\mathrm{Re}_\tau=150$ or $\mathrm{Re}_\tau=300$. Another study, which gave the $\vartheta_{\mathrm{RMS\text{-}BOUNDARY}}$ value and ϑ_{RMS} profile was performed by Kasagi et al. in 1989 [13]. This study predicted $\vartheta_{\mathrm{RMS\text{-}BOUNDARY}}$ values 1.8 and 5.8 for Pr=0.71 and Pr=7, respectively, however, the turbulence model (not DNS) was used to simulate the temperature fluctuations. Values of the $\vartheta_{\mathrm{RMS\text{-}BOUNDARY}}$ are very important also because they can be verified with the measurements. Probably the most accurate measurement was obtained by Mosyak et al. [18] in a horizontal turbulent channel heated from above. Very thin stainless steel foil was used as a heater and thermal images were taken from the top side of the foil with infrared camera. Boundary condition in this experiment was very close to the ideal isoflux. Value of the $\vartheta_{\mathrm{RMS\text{-}BOUNDARY}}$ measured by Mosyak et al. [18] at Pr=5.4 was 9.3 and is higher than the theoretical results predicted by Kasagi et al. [13] and the results of the present study.

Figures 4 and 5 show very similar behavior of streamwise and wall-normal turbulent heat fluxes for both types of the boundary conditions. Differences can only be seen in the near-wall layer of thickness $y^+\approx15$ for Pr=0.71 and $y^+\approx6-8$ for Pr=5–7. These near-wall layers represent also the influence range of the temperature boundary conditions. Influence of the thermal boundary conditions is negligible at the larger distances from the wall. The influence range of the temperature boundary condition is impor-

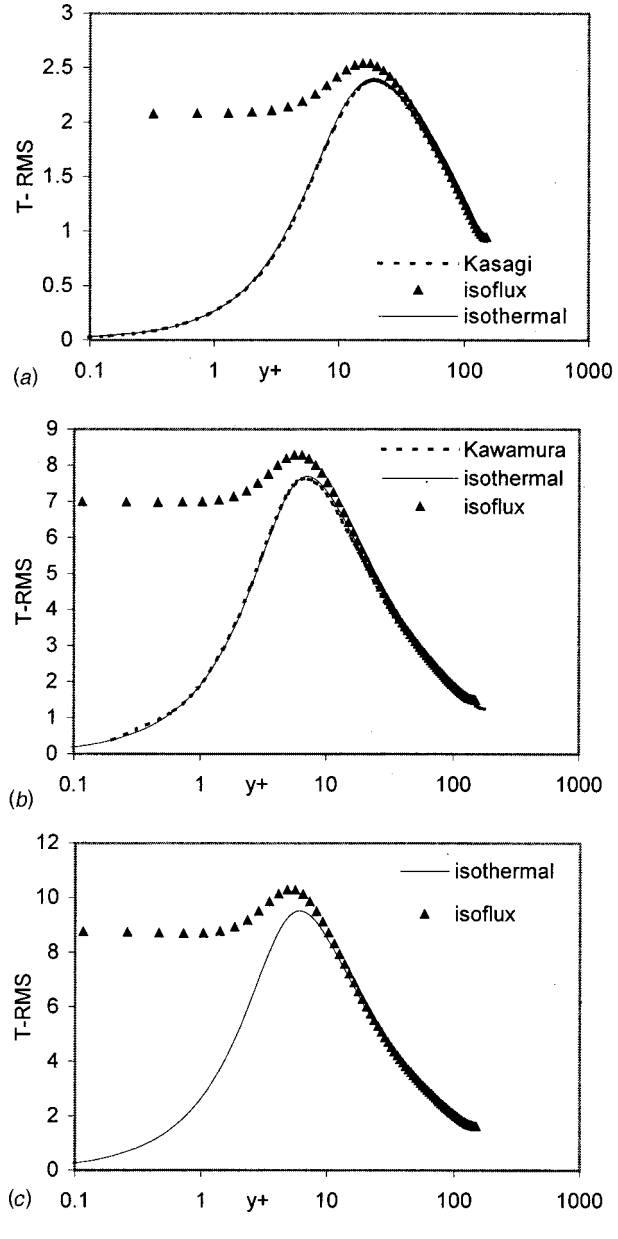

Fig. 3 Profiles of RMS temperature fluctuations: (*a*) Pr=0.71; (*b*) Pr=5; (*c*) Pr=7.

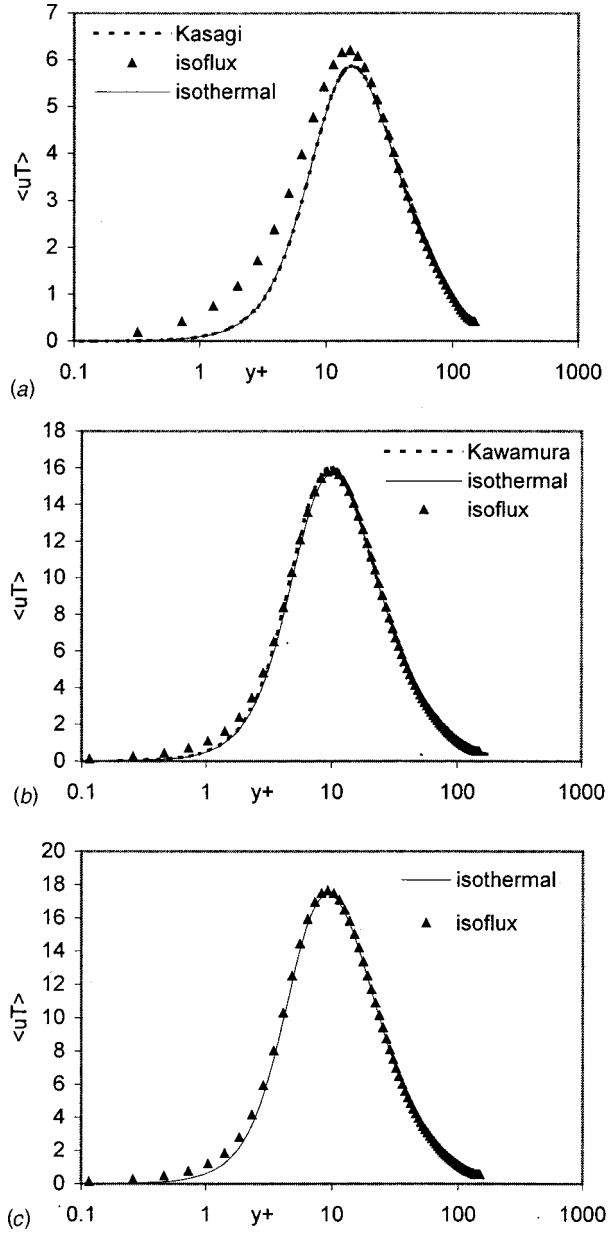

Fig. 4 Profiles of the turbulent axial heat flux: (*a*) Pr=0.71; (*b*) Pr=5; (*c*) Pr=7.

tant for the analytical approximation of the conjugate heat transfer that was performed by Polyakov [10]. He linearized the energy equation in the laminar sublayer $y^+<6$ and found analytical solutions for the conjugate heat transfer problem. Present results show that this approximation might be acceptable for Pr=5–7 but is not very accurate for Pr=0.71 calculations.

Figs. 6(*a*), 6(*b*) show the streamwise auto-correlation functions calculated near the wall. Both Figures show that the auto-correlation functions at isoflux boundary condition decay to zero at slower rate than the functions calculated with the isothermal boundary condition. Because the auto-correlation functions at isoflux boundary condition do not decay to zero in the computational domain used in the present work, a test DNS was performed also in two times longer computational domain at Pr=0.71. The differences between the present DNS and DNS in a longer domain did not show any differences larger that the statistical uncertainty. The results indicate that the periodicity length in the present work, which is long enough for the velocity field as an origin of the turbulence, is long enough also for the passive scalar fields, despite the behavior of the streamwise two-point correlation at isoflux boundary condition.

The spanwise auto-correlation functions of temperature are shown in Figs. 7(*a*) and 7(*b*). Minimums of functions in both Figures show, that the high temperature streaks do not coincide with the low speed streaks exactly. As seen from Figs. 7(*a*) and 7(*b*) the minimums are not necessarily at the distance $z^+=50$, where the minimum of streamwise velocity auto-correlation function appears. The temperature, which is merely a passive scalar, does not affect the turbulence and the coherent structures in the boundary layer. Thermal field is just a media, which reflects the structure of the flow and can be used as such to get an insight into the turbulence. However, the picture obtained through the temperature is slightly deformed picture of the real flow field. This ''deformation'' is seen in Figs. 7(*a*) and 7(*b*) that show the thermal field near the wall, which can exhibit thermal streak spacing that is larger (Pr=0.71 and isoflux BC) or smaller (Pr=7 and isother-

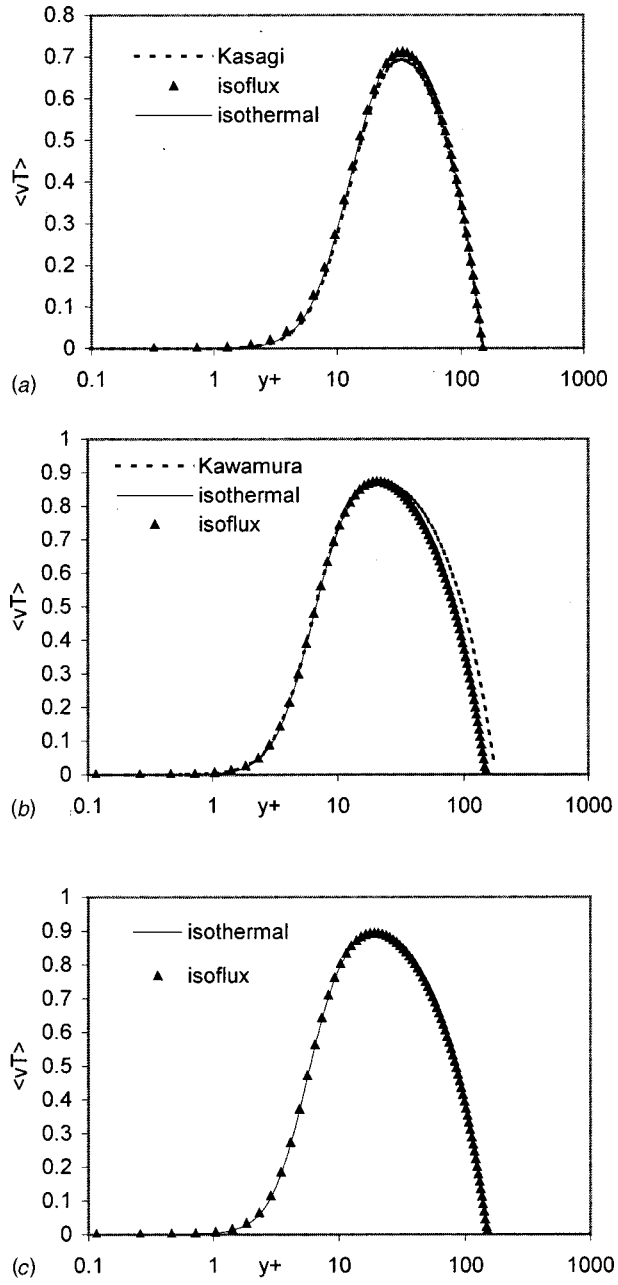

Fig. 5 Profiles of the turbulent wall-normal heat flux: (*a*) Pr =0.71; (*b*) Pr=5; (*c*) Pr=7.

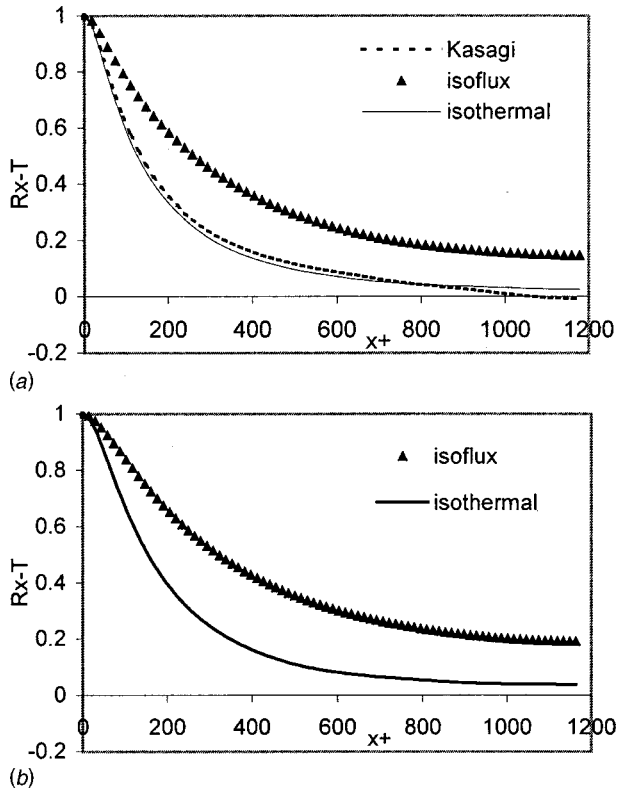

Fig. 6 Two-point streamwise correlation of temperature fluctuations: (*a*) Pr=0.71 at $y^+=6.5$ (Kasagi at $y^+=5.1$); (*b*) Pr=7 at $y^+=1.9$.

mal BC) than the corresponding low speed streak spacing (Tiselj et al. [9]). Further study of the relation between the temperature and velocity field in the near-wall layer is especially important for the experiments (for example Hetsroni, Rozenblit [17]), where the properties of the turbulent flow are studied through the images of the temperature field. The analytical approach similar to the approach of Polyakov [10] can be useful when the near-wall deformations are studied.

(2) Conjugate Heat Transfer. Second part of the results and discussion is devoted to the results of the conjugate heat transfer simulations. As pointed out by Kasagi et al. [13], the thermal activity ratio of air flow is very small for all practical wall materials. On the other side, the thermal activity ratios for the flow of water are large enough, that in the combination with the varying wall thickness, almost all kinds of boundary conditions can be achieved in experiments. Almost isothermal boundary condition was achieved in Khabakhpasheva [11] experiment by a thick copper plate ($K=0.04$), and almost isoflux boundary condition was achieved by Hetsroni and Rozenblit [17] and Mosyak et al. [18] with a thin constant foil ($K=0.12-0.18$, $d^{++}\leqslant 0.08$).

Figures 8(*a*) and 8(*b*) show the influence of the thermal activity ratio K on the ϑ_{RMS} fluctuations for Pr=7 and wall thickness $d^{++}=20$, which are very close to the results for the infinitely thick wall. Fluctuations in the fluid (Fig. 8(*a*)) are limited with the results calculated with the ideal isoflux and ideal isothermal boundary condition. Figure 8(*b*) shows decay of the fluctuations inside the wall. Results in Fig. 8(*a*) were obtained from the results averaged over 560 ν/u_τ^2 time interval with normalization:

$$\vartheta_{\mathrm{RMS}}(y^+)=\vartheta_{\mathrm{RMS}}(y^+)560\,\frac{\vartheta_{\mathrm{RMS\text{-}ISOFLUX}}(y^+)_{3600}}{\vartheta_{\mathrm{RMS\text{-}ISOFLUX}}(y^+)_{560}}$$

and results in Fig. 8(*b*) were normalized as

$$\vartheta_{\mathrm{RMS}}(y^{++})=\vartheta_{\mathrm{RMS}}(y^{++})560\,\frac{\vartheta_{\mathrm{RMS\text{-}ISOFLUX}}(y^{++}=0)_{3600}}{\vartheta_{\mathrm{RMS\text{-}ISOFULX}}(y^{++}=0)_{560}},$$

where subscripts ''560'' and ''3600'' stand for the quantities obtained with averaging over 560 and 3600 ν/u_τ^2 time units, respectively. Values of correction factors $\vartheta_{\mathrm{RMS\text{-}ISOFLUX}}(y^+)_{3600}/\vartheta_{\mathrm{RMS\text{-}ISOFLUX}}(y^+)_{560}$ are maximal at $y^+=0$ and are gradually decreasing with increasing distance from the wall. Maximal values in Figs. 8 at are: 1.03 ($K=0.1$, $K=100$), 1.05 ($K=5$) and 1.09 ($K=0.5$, $K=1$) (Three different calculations were performed at Pr=7 due to the computer memory limitations).

Figures 9(*a*) and 9(*b*) show the influence of the wall thickness at constant thermal activity ratio $K=1$. In that case the upper limit is set by the ideal isoflux BC profile and the lower limit is set by the infinitely thick wall ($d^{++}=20$ in Fig. 9(*a*)). Regarding the temperature fluctuations inside the wall shown in Fig. 9(*b*), it can

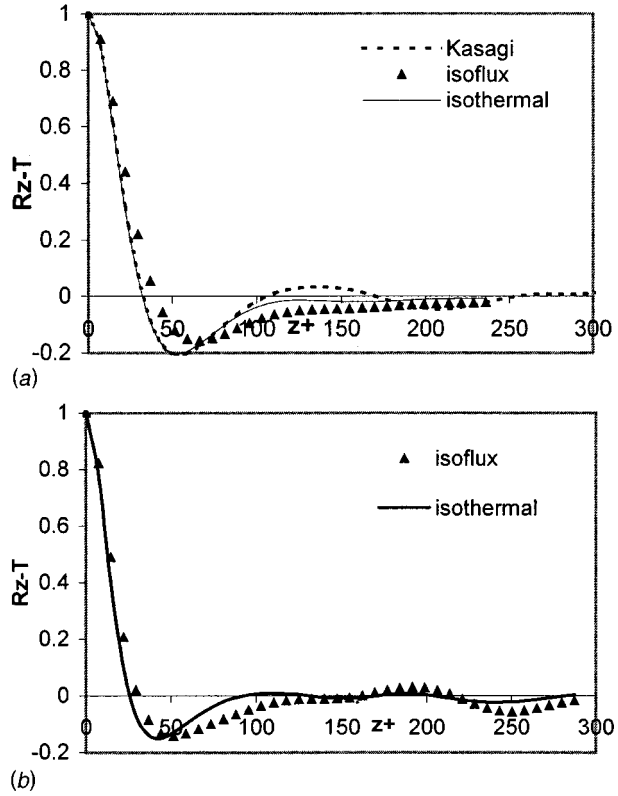

Fig. 7 Two-point spanwise correlation of temperature fluctuations: (*a*) Pr=0.71 at $y^+=6.5$ (Kasagi at $y^+=5.1$); (*b*) Pr=7 at $y^+=1.9$.

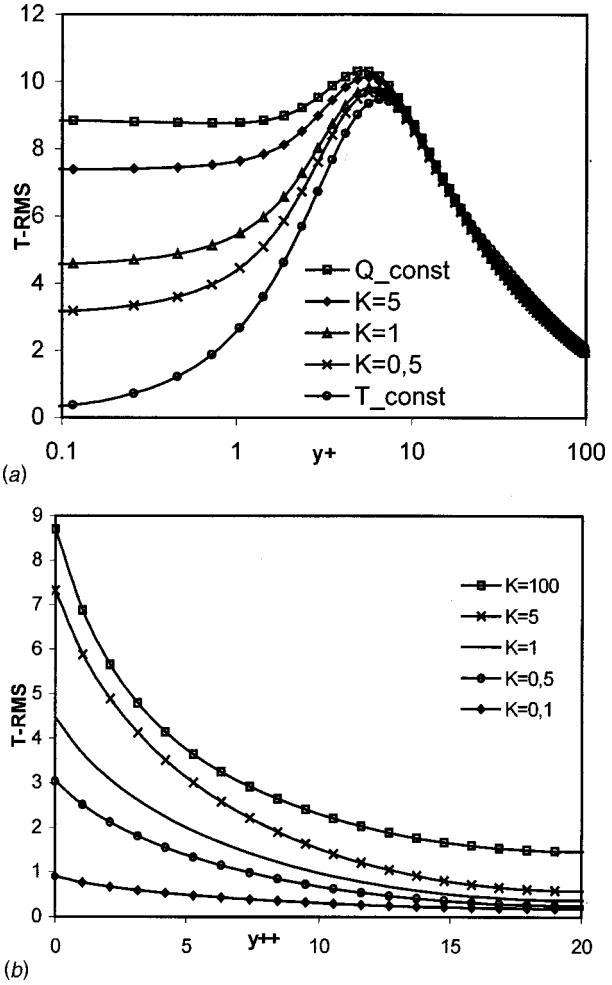

Fig. 8 Profiles of RMS temperature fluctuations at Pr=7 for different thermal activity ratios *K* and thick wall $d^{++}=20$: (*a*) fluctuations in the fluid; (*b*) fluctuations inside the wall.

be noted, that for the very thin wall ($d^{++}\leqslant 0.5$), the magnitude of the fluctuations on the isolated outer side of the wall remains practically the same as on the side exposed to the fluid. This is especially important for the experiments with very thin foil [17,18], where the temperature field was measured by the infrared camera on the outer side of heated foil. Correction factor applied for results in Fig. 8 was applied also for results in Fig. 9—maximal correction factor at $y^+=0$ for all results in Fig. 9 was 1.09.

Figures 10(*a*) and 10(*b*) show the main result of the conjugate heat transfer DNS. Ratio *R*, shown in Figs. 10, stands for the ϑ_{RMS} fluctuations on the fluid-solid interface normalized by the value of the ϑ_{RMS} fluctuations of the ideal isoflux wall. Points in which the DNS was performed are denoted with "+" and connected with solid lines. Dashed lines with "*x*" denotes the results of conjugate heat transfer calculations obtained by Kasagi et al. [13] with a turbulent model. The same thermal activity ratios were chosen in the present study as in the study of Kasagi et al. [13], while the thickness of the wall were slightly different. Fig. 10 shows that Kasagi et al. obtained very good approximations of the *R* ratio with their turbulence model. The main difference is faster decay of the *R* ratio predicted in [13] for both Prandtl numbers and for all thermal activity ratios. This is presumably due to the spectra of their turbulence model, which focused on the coherent structures but seemed to underestimate the contributions of the low frequency and long wave number oscillations. The decay of the realistic low frequency and long wave number oscillations is slower and is probably responsible for most of the differences in Figs. 10(*a*) and 10(*b*).

Two other DNS studies of conjugate heat transfer were performed for Pr=7:

1 The DNS with $K=0.18$ and $d^{++}=0.06$, which corresponds to the experiments of Hetsroni and Rozenblit [17] with a 50 μm thick constantan foil heated by AC current and cooled by water at Reynolds number Re=5100. The same DNS is also very close to the experiment of Mosyak et al. [18] with $K=0.12$ and $d^{++}=0.08$ where the measured value of the wall temperature fluctuations at Pr=5.5 was 9.3. The DNS predicted $R=0.930\pm0.005$ and practically the same fluctuations on the inner and outer side of the heated foil with the absolute value of the wall temperature fluctuations 8.2 at Pr=7, which corresponds to approximately 7.0 at Pr=5.5. This results is closer to the measured value than the result of Kasagi et al. [13] study.

2 The DNS with $K=0.04$ and $d^{++}=50$ which approximately corresponds to experiment of Khabakhpasheva [11] with thick copper plate cooled by water at Prandtl number between Pr=5 and Pr=7. The results of Khabakhpasheva are important because they were obtained at different Reynolds numbers between 11,500 and 61,000 and show very weak influence of the Reynolds number on the wall temperature fluctuations. Value of wall temperature RMS fluctuations measured by Khabakhpasheva was 0.3 ± 0.03. The DNS at Pr=7.0 predicted $R=0.047\pm0.005$, which means an absolute value of the dimensionless temperature fluctuations between 0.33 and 0.41 at Pr=5.0 and Pr=7.0, respectively ($R=0.047$ calculated at Pr=7 was used also for the Pr=5 estimate). Due to the limited accuracy of the $\vartheta_{\mathrm{RMS\text{-}WALL}}$ measurements of Khabakhpasheva, we cannot prove that the present DNS study gives more accurate results than the approach of Kasagi et al. [13].

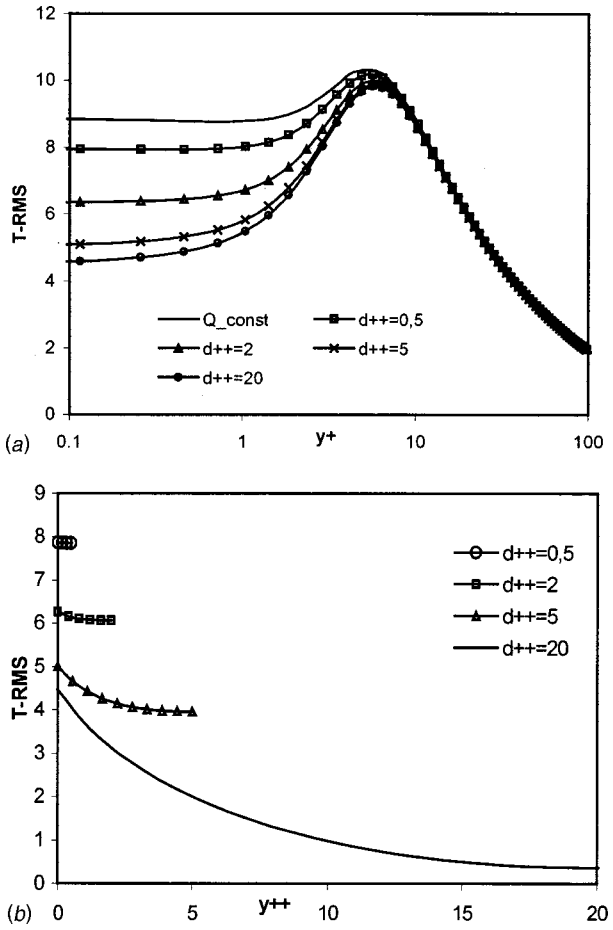

Fig. 9 Profiles of RMS temperature fluctuations at Pr=7 for thermal activity ratio $K=1$ and walls of different thickness d^{++}: (*a*) fluctuations in the fluid; (*b*) fluctuations inside the wall.

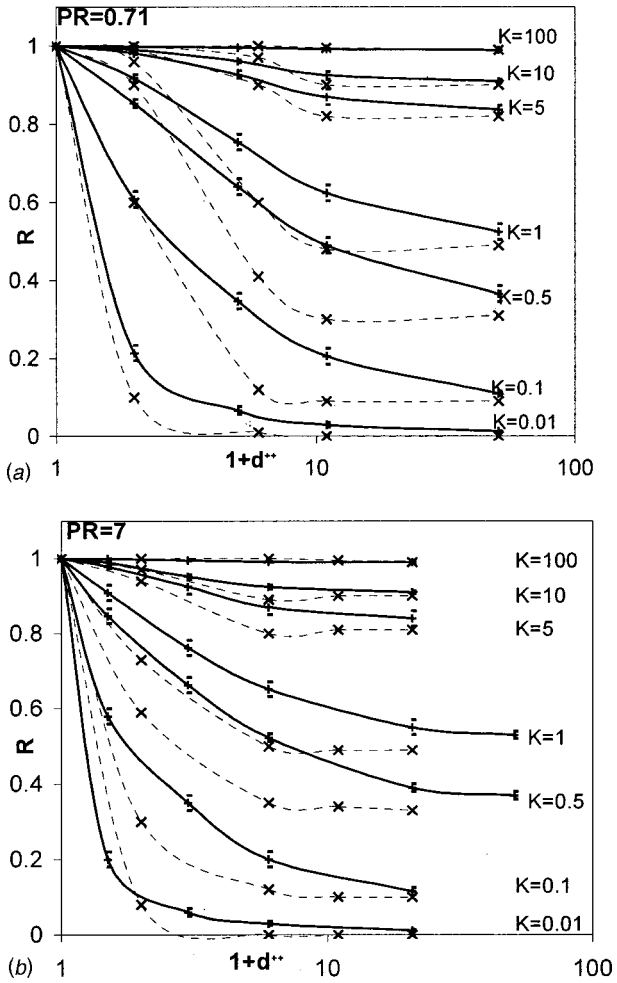

Fig. 10 Ratio of the RMS wall temperature fluctuations to that on the ideal isoflux wall: (*a*) Pr=0.71, (*b*) Pr=7. Solid lines with "+" and "−" for uncertainty denote the present DNS results, dotted lines with "*x*" are results of Kasagi et al. [2].

Conclusions

The turbulent heat transfer coupled with the unsteady conduction in the heated wall was analyzed with Direct Numerical Simulation of the fully developed velocity and temperature fields in the two-dimensional turbulent channel. Simulations were performed at constant friction Reynolds number $\mathrm{Re}_\tau=150$ and Prandtl numbers $\mathrm{Pr}=0.71$, 5, and 7, considering the fluid temperature as a passive scalar.

As results the statistical quantities of the thermal fields are given. It is shown that the influence of the thermal boundary condition is approximately 15 and 6 wall units for $\mathrm{Pr}=0.71$ and $\mathrm{Pr}=7$ respectively.

Results of the conjugate heat transfer study were compared to the findings of Kasagi et al. [13] that performed similar conjugate heat transfer using a deterministic near-wall turbulence model rather than DNS. The present DNS confirmed most of the Kasagi's conclusions. The main improvement of the present DNS study comparing to the results of Kasagi et al. [13] is prediction of the value of the wall temperature fluctuations calculated with ideal isoflux boundary condition. Higher values are predicted by the present DNS study, especially at Prandtl number $\mathrm{Pr}=7$. Differences are visible also in the conjugate heat transfer charts given in Fig. 10, which can be used to estimate the value of the temperature fluctuations on the fluid-solid interface of the realistic experimental devices.

Due to the large uncertainty of the available experimental results it is currently not possible to conclude that the DNS results are superior to the results obtained with less accurate models of Polyakov [10] and Kasagi et al. [13]. Thus, simpler mathematical models are recommended for the conjugate heat transfer calculations, while the role of the DNS is to be sought mainly in the tuning of the parameters in the simpler models. The most important such parameter is value of the wall temperature fluctuations calculated with ideal isoflux boundary condition.

Acknowledgments

The authors are grateful to the Ministry of Education, Science and Sport of the Republic of Slovenia Marand d.o.o.-SUN Microsystems Inc. Service Provider in Slovenia that enabled the use of their multi-processor SUN computers, and to Israeli High Performance Computing Unit-IUCC that obtained the resources on the SGI multi-processor computer.

Nomenclature

a, b, c = coefficients of linear equation
c_p = specific heat at constant pressure
d = wall thickness
h = channel half width
k = wave number
K = $\sqrt{\rho_f c_{pf} \lambda_f / \rho_w c_{pw} \lambda_w}$ thermal activity ratio
L_1, L_3 = streamwise and spanwise length of the computational domain

p = pressure
Pr = Prandtl number
q_w = wall-to-fluid heat flux
R = $\theta_{\text{RMS-BOUNDARY}}/\theta_{\text{RMS-ISOFLUX}}$ wall temperature RMS fluctuations normalized by the value of ideal-isoflux fluctuations
Re_τ = $2hu_B/\nu$ Friction Reynolds number
Rx = auto-correlation function in x direction
Rz = auto-correlation function in z direction
t = time
$\text{T}\tau$ = $q_w/(u_\tau \rho_f c_{pf})$ friction temperature
u, v, w = velocity components in x, y, and z directions
u_τ = $\sqrt{\tau_w/\rho}$ friction velocity
u_B = bulk mean velocity
x = streamwise direction
y = wall-normal direction
z = spanwise direction
α = $\lambda/(\rho c_p)$ thermal diffusivity
$\delta_{i,j}$ = $\begin{cases} 1, & \text{if } i=j=0 \\ 0, & \text{all other } i,j \text{ pairs} \end{cases}$
θ = $(T_w - T)/T_\tau$ dimensionless temperature difference
λ = thermal conductivity
ν = kinematic viscosity
ρ = density
$\vec{1}_x$ = unit vector in x direction (1,0,0)
$\langle\ \rangle_{x,z}$ = averaging in the directions denoted by the subscripts

Subscripts and Superscripts

$(\ )_w$ = solid wall
$(\ )_f$ = fluid
i, j = x and z direction wave number index
$(\ )^+$ = normalized by u_τ, T_τ, ν
$(\ )^{++}$ = $(\ )^+\sqrt{\alpha_f/\alpha_w}$-dimensionless length
RMS = root-mean-square fluctuations averaged over x, z, t
RMS-BOUNDARY = RMS fluctuations at the wall-fluid boundary averaged over x, z, t
RMS-ISOFLUX = RMS fluctuations at the ideal isoflux wall-fluid boundary averaged over x, z, t

References

[1] Moin, P., and Mahesh, K., 1999, "Direct Numerical Simulation: A Tool in Turbulence Research," Annu. Rev. Fluid Mech., **30**, pp. 539–578.
[2] Kasagi, N., and Iida, O., 1999, "Progress in Direct Numerical Simulation of Turbulent Heat Transfer," *Proceedings of the 5th ASME/JSME Joint Thermal Engineering Conference*, San Diego, CA.
[3] Kim, J., and Moin, P., 1989, "Transport of Passive Scalars in a Turbulent Channel Flow," in *Turbulent Shear Flows VI*, Springer-Verlag, Berlin, pp. 85.
[4] Kasagi, N., Tomita, Y., and Kuroda, A., 1992, "Direct Numerical Simulation of Passive Scalar Field in a Turbulent Channel Flow," J. Heat Transfer, **114**, pp. 598–606.
[5] Kawamura, H., Ohsaka, K., Abe, H., and Yamamoto, K., 1998, "DNS of Turbulent Heat Transfer in Channel Flow with low to medium-high Prandtl number fluid," Int. J. Heat Fluid, **19**, pp. 482–491.
[6] Na, Y., and Hanratty, T. J., 2000, "Limiting Behavior of Turbulent Scalar Transport Close to a Wall," Int. J. Heat Mass Transf., **43**, pp. 1749–1758.
[7] Kawamura, H., Abe, H., and Matsuo, Y., 1999, "DNS of Turbulent Heat Transfer in Channel Flow with Respect to Reynolds and Prandtl Number Effects," Int. J. Heat Fluid, **20**, pp. 196–207.
[8] Kong, H., Choi, H., and Lee, J. S., 2000, "Direct Numerical Simulation of Turbulent Thermal Boundary Layer," Phys. Fluids, **12**, No. 10, pp. 2555–2568.
[9] Tiselj, I., Pogrebnyak, E., Changfeng, Li., Mosyak, A., and Hetsroni, G., 2001, "Effect of Wall Boundary Condition on Scalar Transfer in a Fully Developed Turbulent Flume Flow," Phys. Fluids, **13**, No. 4, pp. 1028–1039.
[10] Polyakov, A. F., 1974, "Wall Effect of Temperature Fluctuations in the Viscous Sublayer," Teplofiz. Vys. Temp., **12**, pp. 328–337.
[11] Khabakhpasheva, Y. M., 1986, "Experimental Investigation of Turbulent Momentum and Heat Transfer in the Proximity of the Wall," *Heat Transfer 1986, Proceedings of The 8th International Heat Transfer Conference*, San Francisco, CA, USA.
[12] Sinai, Y. L., 1987, "A Wall Function for the Temperature Variance in Turbulent Flow Adjacent to a Diabatic Wall," J. Heat Transfer, **109**, pp. 861–865.
[13] Kasagi, N., Kuroda, A., and Hirata, M., 1989, "Numerical Investigation of Near-Wall Turbulent Heat Transfer Taking Into Account the Unsteady Heat Conduction in the Solid Wall," J. Heat Transfer, **111**, pp. 385–392.
[14] Sommer, T. P., So, R. M. C., and Zhang, H. S., 1994, "Heat Transfer Modeling and the Assumption of Zero Wall Temperature Fluctuations," J. Heat Transfer, **116**, pp. 855–863.
[15] Kasagi, N., Hirata, M., and Nishino, K., 1986, "Streamwise Pseudo-Vortical Structures and Associated Vorticity in the Near-Wall Region of a Wall-Bounded Shear Flow," Exp. Fluids, **4**, pp. 309–318.
[16] Iritani, Y., Kasagi, N., and Hizata, M., 1985, "Heat Transfer Mechanism and Associated Turbulence Structure in the Near-Wall Region of a Turbulent Boundary Layer," *Proceedings of the 4th Symposium on Turbulent Shear Flows*, Karlsruhe, Germany.
[17] Hetsroni, G., and Rozenblit, R., 1994, "Heat Transfer to a Liquid-Solid Mixture in a Flume," Int. J. Multiphase Flow, **20**, pp. 671–689.
[18] Mosyak, A., Pogrebnyak, E., and Hetsroni, G., 2001, "Effect of Constant Heat Flux Boundary Condition on Wall Temperature Fluctuations," ASME J. Heat Transfer , **123**, pp. 213–218.
[19] Gavrilakis S., Tsai, H. M., Voke, P. R., and Leslie, D. C., 1986, "Direct and Large Eddy Simulation of Turbulence," *Notes on Numerical Fluid Mechanics*, Vol. 15, U. Schumann, R. Friedrich, Vieweg, and D. B. R. Braunschweig, eds., pp. 105.
[20] Lam, K. L., and Banerjee, S., 1988, "Investigation of Turbulent Flow Bounded by a Wall and a Free Surface," *Fundamentals of Gas-Liquid Flows*, Sharma Michaelides, ed., **72**, ASME, Washington DC, pp. 29–38.
[21] Lam, K. L., 1989, "Numerical Investigation of Turbulent Flow Bounded by a Wall and a Free-Slip Surface," Ph.D. thesis, Univ. Calif. Santa Barbara.
[22] Tennekes, H., and Lumley, J. L., 1972, *A First Course in Turbulence*, MIT Press, Cambridge, MA.

Akira Murata
e-mail: murata@mmlab.mech.tuat.ac.jp
Associate Professor

Sadanari Mochizuki
Professor
Mem. ASME

Department of Mechanical Systems Engineering,
College of Engineering,
Tokyo University of Agriculture and Technology,
2-24-16 Nakacho, Koganei,
Tokyo 184-8588, Japan

Large Eddy Simulation of Turbulent Heat Transfer in an Orthogonally Rotating Square Duct With Angled Rib Turbulators

Heat transfer in a rotating rib-roughened duct was simulated with a Lagrangian dynamic subgrid-scale model. The angled 60 deg rib induced a pair of strong vortices in the stationary condition, and the heat transfer and the friction factor were larger than the 90 deg rib case. In the rotating condition, the high heat transfer areas at the midpoint between ribs and in front of the rib were observed only on the trailing wall. The friction factor and overall Nusselt number were decreased by the duct rotation for 60 deg rib case, although they were increased for 90 deg rib case. [DOI: 10.1115/1.1389463]

Keywords: Computational, Finite Difference, Heat Transfer, Turbines, Turbulence

1 Introduction

In the development of high performance gas turbines, effective blade cooling is essential because the higher efficiency of the turbine requires a higher inlet gas temperature. Generally, this blade cooling is performed by film cooling at the external surface of the turbine blade and also by internal forced-convection cooling which uses winding flow passages inside the turbine blade. The film cooling is an effective cooling method, but it lowers the fluid dynamic efficiency of the blade and the thermal efficiency of the thermodynamic cycle by ejecting air to the blade surface and consequently by lowering the gas temperature. Therefore, the further advancement of the internal cooling is needed. In internal forced-convection cooling, the real phenomena are very complicated due to external forces: the Coriolis force and the buoyancy force in the centrifugal acceleration field. In addition to these external forces, the effects induced by a 180 deg sharp turn and turbulence promoters (ribs) installed on the thermally severe opposing internal-surfaces result in phenomena that are far from understood [1].

As for the local heat transfer of a rib-roughened duct, several researchers investigated the spatial variation of the local heat transfer with various techniques: wall temperature measurement by using thermocouples [2–4], the naphthalene sublimation technique [5,6], and wall temperature measurement by using temperature-sensitive liquid crystal [7–9]. In these studies, the heat transfer variation induced by the flow separation and reattachment behind the rib was captured to a certain extent. However, it is difficult to perform experiments in a rotating condition which can identify the flow structure and its influence on the heat transfer. Thus, further progress in experimental studies has so far been prevented.

In previous numerical studies of rib-roughened ducts, the Reynolds-averaged Navier-Stokes equation with a turbulence model was solved for transverse [10] and angled [11,12] rib configurations. Launder et al. [13] pointed out that in order to quantitatively simulate the flow in a rotating system, the second moment closure, that is, the Reynolds stress equation model, is a minimum requirement considering a non-isotropic effect of the Coriolis force on turbulence. Although this approach using the Reynolds-averaged turbulence model could reproduce the heat transfer of blade cooling to a certain extent, even the Reynolds stress equation model has empirical constants and functions, and therefore the applicability of the model should carefully be examined. Recent advancement in computers enables us to numerically simulate the fluctuating components of the turbulent flow by using the large eddy simulation (LES) or the direct numerical simulation (DNS). Because LES and DNS directly resolve temporal variation of the fluctuating components, the results are more universal, in other words, more free from the empirical modeling than the Reynolds-averaged turbulence models. Although LES has empirical constants and functions, the modeling of the turbulence is confined to the subgrid-scale turbulence, and therefore the effect of the empirical modeling on the result is ideally less than that in the Reynolds stress equation model. So far, the turbulent flow in a stationary smooth duct with a square cross section was solved using DNS [14,15] and LES [16,17].

The authors' group has performed heat transfer measurements by using thermocouples in both stationary and rotating conditions [2–4]. Recently, numerical analyses were also performed by using a dynamic subgrid-scale model for a rotating smooth duct of which cross section was square [18] and rectangular [19], and the technique was further applied to a rotating transversely rib-roughened duct [20,21]. In our previous numerical results, the followings were examined and clarified: the effect of duct cross-sectional aspect ratio on the Coriolis induced secondary flow, the dissimilarity between velocity and temperature fields induced by the flow separation and reattachment around the ribs, and the very high heat transfer area located in front of the ribs which was caused by the unsteady movement of the separation bubbles there. However, because of the Cartesian coordinate limitation, only the transverse rib case was treated in the previous study, and therefore the effect of the secondary flow induced by angled ribs on the heat transfer has not been discussed yet.

This study examines the effect of the angled rib on the flow and heat transfer by performing the large eddy simulation of a fully developed turbulent flow and heat transfer in a rib-roughened square duct. The dynamic subgrid-scale model was adopted considering the highly three-dimensional flow structure of the rib-roughened duct. The effects of the flow separation and reattachment caused by the ribs, the secondary flow induced by the angled ribs, and the Coriolis force on the heat transfer are examined by making a comparison with the previous transverse rib case [21].

Contributed by the Heat Transfer Division for publication in the JOURNAL OF HEAT TRANSFER. Manuscript received by the Heat Transfer Division December 11, 1999; revision received March 22, 2001. Associate Editor: J.-C. Han.

2 Numerical Analysis

Figure 1 shows the computational domain and coordinate system used in this study. The duct had a square cross section with a side length of D which is the hydraulic diameter. The coordinate system was fixed to a rotating duct which had an angular velocity of ω. The streamwise (radially outward) direction was chosen in the z direction; the x and y directions were transverse and perpendicular directions to trailing and leading walls, respectively. Ribs were installed on the trailing and leading walls with the rib angle, γ. In this study, the buoyancy force was ignored, and the case of $\gamma=60$ deg was treated. By assuming the periodicity of the flow field with the streamwisely repeated ribs, streamwise one span was chosen for the computational domain. The cross section of the rib was square (side length, e, of $0.1D$), and streamwise pitch, P, was set equal to the hydraulic diameter, D. This rib arrangement gave the rib height-to-hydraulic diameter ratio, e/D, of 0.1 and the rib pitch-to-rib height ratio, P/e, of 10. This rib arrangement was chosen because it was within the previously reported optimal range [22,23]. The rib angle, 60 deg, was chosen as the angle which gave the maximum heat transfer in the study of Han et al. [24].

The present procedure of the numerical analysis is the extension of our previous procedure [18–21] to the generalized curvilinear coordinate system. After applying a filtering operation to the incompressible Navier-Stokes equation with a filter width equal to the grid spacing [16], the dimensionless governing equations scaled by a length scale, $\ell(=0.5D)$, and mean friction velocity, u_*, become a set of dimensionless governing equations with respect to grid resolvable components indicated by overbars as $(\overline{u},\overline{v},\overline{w})$ under the assumption of constant fluid properties. In order to simulate a fully developed situation, the pressure and temperature fields were decomposed into the steady and streamwisely linear component and the remaining component [25]. By this decomposition, the pressure and temperature fields became periodic in the streamwise direction. As shown in Eq. (1), F_i is an external force term including the Coriolis force. The buoyancy term was ignored in this study. The mean pressure gradient term (with a value of 2) was added to the external force term as follows:

$$F_i=\begin{pmatrix} 0 \\ 2\mathrm{Ro}_*\overline{w} \\ -2\mathrm{Ro}_*\overline{v}+2 \end{pmatrix}. \tag{1}$$

Because the mean pressure gradient which drove the flow in the streamwise direction was set to be constant in this study, the flow rate varied depending on the flow conditions (rib angle and rotation number); therefore, the flow rate was not known *a priori*, and the flow rate was calculated from the resultant computed flow field after the fully developed condition was attained.

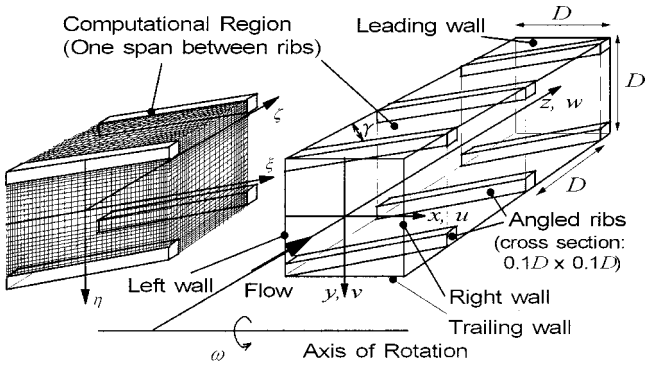

Fig. 1 Schematic of a rotating rib-roughened duct and a grid system fitted to angled ribs

The temperature was made dimensionless by using a bulk temperature, T_b, and a friction temperature, T_r, as $\theta=(T-T_b)/T_r$. Accordingly, the dimensionless energy equation was derived for the grid resolvable component, $\overline{\theta}$. In order to adopt the coordinate system fitted to the angled ribs, the governing equations in the Cartesian coordinates (x, y, z) were transformed into generalized curvilinear coordinates (ξ, η, ζ). Although a slanted grid system is enough for the present angled straight rib cases, the computer program can deal with the fully generalized curvilinear coordinate system considering future extension of the subject. The governing equations in the curvilinear coordinate system can be expressed as follows [26]

$$\frac{1}{J}\frac{\partial J\overline{U^j}}{\partial\xi^j}=0, \tag{2}$$

$$\frac{\partial\overline{u_i}}{\partial t}=-\overline{U^j}\frac{\partial\overline{u_i}}{\partial\xi^j}-\frac{\partial\xi^j}{\partial x_i}\frac{\partial\overline{p}}{\partial\xi^j}+\frac{1}{\mathrm{Re}_*}\frac{\partial\xi^j}{\partial x_\ell}\frac{\partial}{\partial\xi^j}\left(\frac{\partial\xi^k}{\partial x_\ell}\frac{\partial\overline{u_i}}{\partial\xi^k}\right)+\frac{\partial\xi^k}{\partial x_j}\frac{\partial\tau_{\mathrm{SGS}_{ij}}}{\partial\xi^k}+F_i, \tag{3}$$

$$\frac{\partial\overline{\theta}}{\partial t}=-\overline{U^j}\frac{\partial\overline{\theta}}{\partial\xi^j}-\frac{2\overline{w}}{\overline{w}_m}+\frac{1}{\mathrm{Re}_*\mathrm{Pr}}\frac{\partial\xi^j}{\partial x_\ell}\frac{\partial}{\partial\xi^j}\left(\frac{\partial\xi^k}{\partial x_\ell}\frac{\partial\overline{\theta}}{\partial\xi^k}\right)+\frac{\partial\xi^k}{\partial x_j}\frac{\partial\alpha_{\mathrm{SGS}_j}}{\partial\xi^k}, \tag{4}$$

where $\overline{U^j}$ is a contravariant component of velocity, and the following expressions are assumed: $J=\partial(x,y,z)/\partial(\xi,\eta,\zeta)$, $(x_1,x_2,x_3)=(x,y,z)$, and $(\xi^1,\xi^2,\xi^3)=(\xi,\eta,\zeta)$.

Subgrid-scale components of stress, $\tau_{\mathrm{SGS}_{ij}}$, and energy flux, α_{SGS_j}, are expressed as follows:

$$\tau_{\mathrm{SGS}_{ij}}=2\nu_{\mathrm{SGS}}\overline{S}_{ij}, \tag{5}$$

$$\alpha_{\mathrm{SGS}_j}=\frac{\nu_{\mathrm{SGS}}}{\mathrm{Pr}_{\mathrm{SGS}}}\frac{\partial\xi^k}{\partial x_j}\frac{\partial\overline{\theta}}{\partial\xi^k}, \tag{6}$$

where

$$\overline{S}_{ij}=\frac{1}{2}\left(\frac{\partial\xi^k}{\partial x_j}\frac{\partial\overline{u_i}}{\partial\xi^k}+\frac{\partial\xi^k}{\partial x_i}\frac{\partial\overline{u_j}}{\partial\xi^k}\right), \tag{7}$$

$$\nu_{\mathrm{SGS}}=C_S^2\overline{\Delta}^2\sqrt{2\overline{S}_{ij}\overline{S}_{ij}}, \tag{8}$$

$$\overline{\Delta}=(\Delta x\,\Delta y\,\Delta z)^{1/3}. \tag{9}$$

In our previous studies [18–21], the dynamic subgrid-scale model developed by Germano et al. [27] was used in order to calculate the value of C_S as a function of spatial location with the stable computational procedure of Lilly [28]; C_S was averaged taking advantage of the symmetric property in the transverse direction in addition to the time averaging in order to exclude negative values of C_S. However, the angled rib case of this study has no geometric symmetry in the rotating condition, and therefore we adopted the Lagrangian dynamic subgrid-scale model of Meneveau et al. [29] which averages the value of C_S along the pathline for a certain distance, and C_S was calculated from the following equations:

$$C_S^2=\frac{I_{LM}}{I_{MM}}, \tag{10}$$

where

$$\frac{\partial I_{LM}}{\partial t}+\vec{\mathbf{u}}\cdot\nabla I_{LM}=\frac{1}{t_{relax}}(L_{ij}M_{ij}-I_{LM}), \tag{11}$$

$$\frac{\partial I_{MM}}{\partial t}+\vec{\mathbf{u}}\cdot\nabla I_{MM}=\frac{1}{t_{relax}}(M_{ij}M_{ij}-I_{MM}), \tag{12}$$

$$t_{relax}=1.5\overline{\Delta}(I_{LM}I_{MM})^{-1/8}, \tag{13}$$

$$L_{ij} = \widehat{\overline{u_i u_j}} - \hat{\bar{u}}_i \hat{\bar{u}}_j , \tag{14}$$

$$M_{ij} = 2\overline{\Delta}^2 \left(\widehat{|\bar{S}|\bar{S}_{ij}} - \left(\frac{\hat{\Delta}}{\overline{\Delta}} \right)^2 |\hat{\bar{S}}|\hat{\bar{S}}_{ij} \right), \tag{15}$$

$$|\bar{S}| = \sqrt{2\bar{S}_{ij}\bar{S}_{ij}}. \tag{16}$$

When solving Eqs. (11) and (12), the left-hand side of the equations was approximated by using multilinear interpolation as performed by Meneveau et al. [29], and the computational load was reduced. The turbulent Prandtl number for the subgrid-scale component, Pr_{SGS}, was set to 0.5 [30]. The width of the test filter was double the grid spacing and the space filter was accurate to fourth order.

Discretization was performed by a finite difference method using the collocated grid system [26]. The spatial and temporal discretization schemes were similar to those of Gavrilakis [15]: the second order central differencing method and the Crank-Nicolson method for the viscous term and the second order differencing method satisfying the conservative property and the second order Adams-Bashforth method for the convective term. The external force term was also treated by the second order Adams-Bashforth method. The pressure field was treated following the MAC method [31], and the algebraic equation for each variable was solved by using the SOR method. The computational domain was one span between streamwise consecutive ribs (see Fig. 1) and its dimension was $2\times2\times2$ in x, y, z directions, respectively. This can be expressed by using an inner length scale, $\nu/u*$, as $700\times700\times700$.

The turbulent Reynolds number, $Re_*(=u_*\delta/\nu)$, was 350, and the rotation number, $Ro_*(=\omega\delta/u_*)$, was 0 and 1.0. The Reynolds number, Re_m, defined by the mean velocity and the hydraulic diameter was about 4110 and 3150 for 90 deg and 60 deg rib cases, respectively, for the stationary condition. In Table 1, the dimensionless numbers of Re_* and Ro_* defined by using the friction velocity are converted into Re_m and Ro_m defined by using the mean velocity. As explained above, the value of Re_m was calculated from the result of computation; Re_m was not known *a priori*. At the wall boundary, no-slip and constant heat flux conditions were imposed, although the rib side surfaces were set to be adiabatic. The adiabatic condition at the rib side surfaces was adopted to preserve the linear increase of the bulk temperature of the flow and also to consider the previous experiments in which the ribs were not heated. An additional computation with the constant heat flux condition at the rib side surfaces was also performed, and it was verified that even when the rib side surfaces were heated, the conclusions of this study were not changed. At the inlet and outlet boundaries, the periodic boundary condition [25] was imposed in order to obtain a fully developed flow. The validity of the one-span computational domain with the streamwise periodic boundary condition was examined by computing the streamwise one- and three-span cases with the same round-type ribs as used in Banhoff et al. [12] and Stephens et al. [11], and no major difference was observed between one and three-span results. The boundary conditions of the intermediate velocities and the pressure were set following the procedure of Kim and Moin [32] and Zang et al. [33].

Table 1 Dimensionless number range (Re_*,Ro_*) of this study and its conversion into the conventional form (Re_m,Ro_m); the data of the 90 deg rib are from Murata and Mochizuki [21].

γ	90deg		60deg	
Re_*	350			
Ro_*	0	1.0	0	1.0
Re_m	4106	3959	3148	3645
Ro_m	0	0.354	0	0.384

The grids in the physical domain were contracted to both the walls and the rib surfaces by using a tangent hyperbolic function (see Fig. 1). The grid number was $47\times47\times47$, and this grid configuration gave a grid spacing of $\Delta x^+ = 1.0-38$, $\Delta y^+ = 0.6-52$, and $\Delta z^+ = 4.0-28$. The effect of the grid spacing on the computed result was checked by increasing the grid number to $71\times71\times71$ ($\Delta x^+ = 0.7-25$, $\Delta y^+ = 0.4-34$, and $\Delta z^+ = 2.3-18$) for several cases, and no major difference was observed (the grid spacing effect will be shown later in Tables 2 and 3). The verification of the present computational procedure was also performed for the smooth straight duct as was performed in Murata and Mochizuki [18], and the agreement with the previous DNS results for the straight smooth square duct in stationary condition [14,15] was almost the same as that seen in Murata and Mochizuki [18]: the comparison was made in the mean velocity profile, the three components of the turbulence intensities, and the secondary flow intensity of the Prandtl's second kind. The time step interval was $\Delta t = 1.0\times10^{-4}$, which can be expressed as $\Delta t^+ = 0.035$ when made dimensionless by an inner time scale, ν/u_*^2. The computation of the rotating case was started using the result of the stationary case as an initial condition. The calculations were carried out to 120,000 steps to fully develop the flow. After the initial 120,000 steps were performed, additional 400,000 steps ($t=40$ or $t^+ = 14{,}000$) were performed for computing the statistical values. This 400,000-step computation needed about 76 CPU hours using an NEC SX4B. In this study, the second order scheme was used because of its lighter computational load in order to obtain statistically steady results by increasing the total time steps. The influence of the order of the scheme was discussed in detail in Murata and Mochizuki [21], and it was verified that the difference between the second and forth order of the scheme did not change the results. Further accuracy evaluation of the present numerical scheme was performed by performing additional computations with the same rib arrangement as the experiments of Chandra et al. [5]. The agreement between the numerical and experimental results was good, and it will be discussed in detail in Section 3.2.

3 Results and Discussion

3.1 Flow Behavior Induced by the Angled Ribs. Figure 2 shows the time-averaged velocity vectors of the 90 deg rib case in the y-z plane at two transverse locations. In the figure, left and right figures are for stationary ($Ro_*=0$) and rotating ($Ro_*=1$) conditions, respectively. Near the rib top surface at the entrance ($z=0$), the large inward-pointing velocity vectors are seen in the figure. This velocity vectors were also observed in the fine grid resolution case of $71\times71\times71$, and therefore it is not due to the numerical errors but reflecting the real phenomena caused by the strong flow passing beyond the rib. In the stationary case, the time-averaged vectors show the flow separation behind the ribs which is symmetric with respect to the horizontal plane of $y=0$. Due to the change of the transverse location, the velocity profile at around $y=0$ changes more drastically than that around the ribs. At the transverse center of the rotating case (Fig. 2(b) right), the higher intensity of the flow passing beyond the upper rib on the trailing wall is seen because the Coriolis induced secondary flow transports the fluid momentum from the leading side to the trailing side at the transverse center. On the contrary, near the side wall (Fig. 2(a) right) the flow directed from the trailing side to the leading side dominates, although the strong recirculating flow passing beyond the upper rib still exists.

Figure 3 shows the velocity vectors of the angled 60 deg rib case in the y-z plane at three transverse locations because there is no transverse symmetry in this angled rib case. In the stationary condition (left figures), the flow passing beyond the ribs reattaches intensively near the left wall (Fig. 3(a) left). On the other hand,

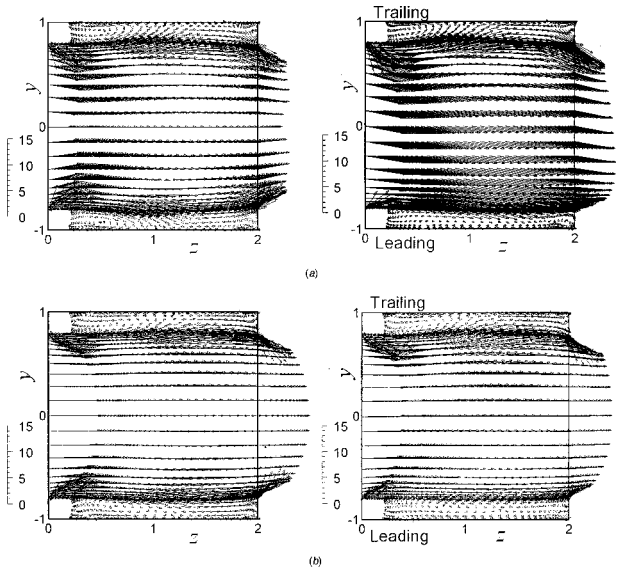

Fig. 2 Time-averaged velocity vectors in *y-z* plane at transverse two locations (90 deg rib; left and right figures are for $Ro_*=0$ and $Ro_*=1$, respectively. The scale in each figure indicates the vector magnitude): (*a*) near left wall ($x=-0.9$); and (*b*) at transverse center ($x=0$).

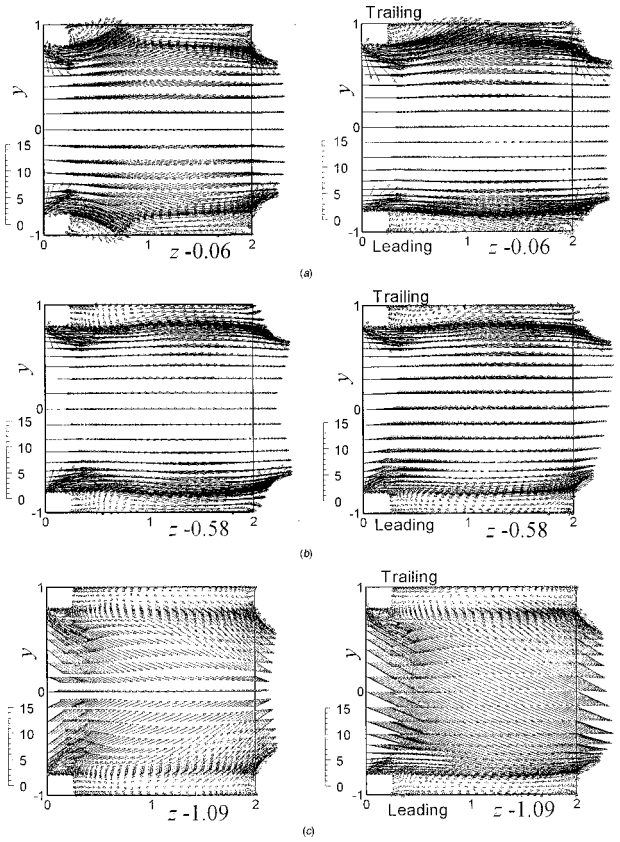

Fig. 3 Time-averaged velocity vectors in *y-z* plane at three different transverse locations (60 deg rib; legend is the same as that of Fig. 2): (*a*) near left wall ($x=-0.9$); (*b*) at transverse center ($x=0$); and (*c*) near right wall ($x=+0.9$).

near the right wall (Fig. 3(*c*) left), the dominant flow induced by the angled ribs is directed from the upper and lower walls to the vertical center ($y=0$). In the rotating case (right figures), the Coriolis induced secondary flow forces the velocity profile to be shifted to the trailing wall (pressure surface and upper wall in the figure) at the transverse center (Fig. 3(*b*) right). Near the right wall (Fig. 3(*c*) right), the flow directed from the trailing wall to the leading wall dominates. Near the left wall (Fig. 3(*a*) right), the size of the flow separation behind the leading-side rib becomes larger than that behind the trailing-side rib.

Figure 4 shows the time-averaged velocity vectors $(\overline{u},\overline{v})$ in the ξ-η plane which is parallel to the 60 deg ribs at the three different streamwise locations. In the figure, the value in the ξ-η plane is projected onto the *x-y* plane, and the streamwise locations are: (*a*) at rib location (rib streamwise center), (*b*) at the midpoint between the consecutive ribs, and (*c*) in front of the ribs (a half of rib width from the ribs). In the stationary case (left figures), the velocity component along the angled ribs directed from left to right in the figure is induced near the upper and lower ribs, and the flow in the opposite direction (from right to left in the figure) is seen as the return flow at the vertical center. As a consequence, a pair of vortices dominates the flow field. In the smooth and 90 deg rib-roughened duct cases, the Coriolis induced secondary flow transports the fluid from the leading wall side to the trailing wall side at the transverse center [18–21]. However, in the rotating condition of the angled rib case (right figures of Fig. 4), the Coriolis force effect and the angled-rib induced flow interfere, and this results in the inclined secondary flow directed from the lower right to the upper left in the central area of the duct. Due to this resultant secondary flow, near the trailing wall (upper wall in the figure) the flow from left to right is strong (Figs. 4(*b*), (*c*) right), and this flow goes down near the right wall (right-hand side wall in the figure). Near the leading wall (lower wall in the figure), the flow directed along the angled rib and the Coriolis induced flow collide with each other at around $x=0.2-0.5$. In the vicinity of the left wall (left-hand side wall in the figure), the flow directed from the upper wall to the lower wall can be seen. For the easier understanding of the flow and also for the future comparison of the present results with the other researchers' results, in Figs. 5 and 6, the time-averaged three velocity components on the nine lines of intersection between three *y-z* planes of Fig. 3 and three ξ-η planes of Fig. 4 are shown.

Figure 7 shows the time-averaged velocity vectors in the *x-z* plane which is parallel to and at a half of rib height from the rib-roughened wall. In the stationary 90 deg rib case of Fig. 7(*a*), the reattachment point is seen at about $z=1$ as the location where the velocity vectors become zero in their magnitude and change their direction from left to right. In the stationary 60 deg rib case of Fig. 7(*b*), the flow is directed from the left wall to the right wall, and no area where the magnitude of the velocity vector becomes zero is seen in the central area between the consecutive ribs. In the rotating case of 60 deg rib (Figs. 7(*c*), (*d*)), the flow field is similar to that of the stationary case, although the vector magnitude is larger on the trailing wall (pressure surface) than the leading wall (suction surface).

Figure 8 shows the isocontours of the time-averaged streamwise velocity, $\overline{w}$ (left figures), and temperature, $\overline{\theta}$ (right figures), in the ξ-η planes at the same streamwise locations as Fig. 4. Similar profiles between $\overline{w}$ and $\overline{\theta}$ are obtained in the plane at the rib location (Fig. 8(*a*)), but at midpoint between the ribs (Fig. 8(*b*)) the contour line density of $\overline{w}$ near the upper and lower walls becomes slightly higher than that of $\overline{\theta}$. In comparison with the 90 deg rib case of Murata and Mochizuki [21], the present 60 deg rib results show greater similarity between $\overline{w}$ and $\overline{\theta}$. In the central area of the right wall ($y=0$) in Fig. 8, the isocontour lines of $\overline{w}$ and $\overline{\theta}$ are projected to the duct center because of the secondary flow seen in Fig. 4. In the rotating case of Fig. 9, the contour lines of $\overline{w}$ and $\overline{\theta}$ become inclined due to the inclined secondary flow seen in Fig. 4. The similarity between $\overline{w}$ and $\overline{\theta}$ does not hold even in the plane at the rib location (Fig. 9(*a*)). The peak of $\overline{\theta}$ shifted to

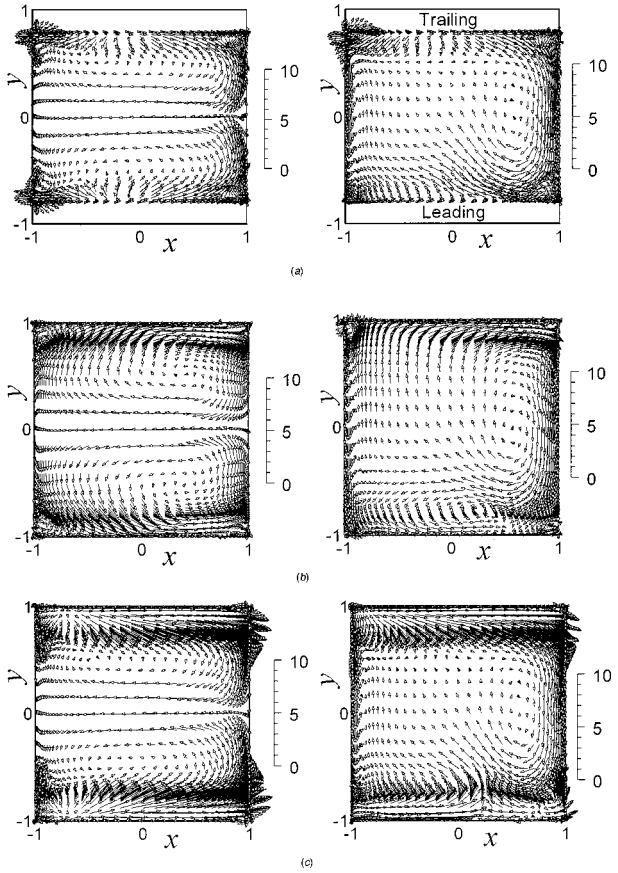

Fig. 4 Time-averaged velocity vectors ($\bar{u},\bar{v}$) in ξ-η plane at three different streamwise locations: (*a*) at rib location (at center in rib width); (*b*) at midpoint between ribs; (*c*) in front of ribs (a half of rib width from ribs). (60 deg rib; figures are projected onto *x*-*y* plane. The other legend is the same as that of Fig. 2)

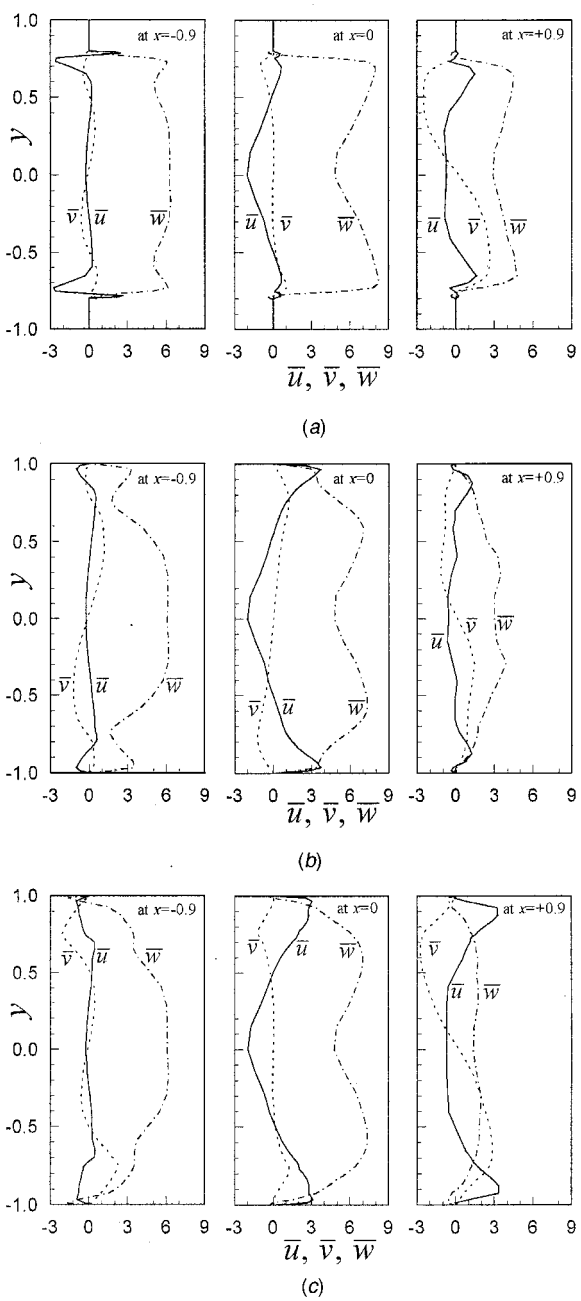

Fig. 5 Time-averaged velocity components on the nine lines of intersection between *y*-*z* and ξ-η planes ($Ro_* = 0$; left, middle, and right figures are for the transverse location of $x = -0.9$, 0, and $+0.9$, respectively): (*a*) at rib location (at center in rib width); (*b*) at midpoint between ribs; (*c*) in front of ribs (a half of rib width from ribs).

the trailing and right walls. In contrast to the $\bar{\theta}$ distribution, $\bar{w}$ (Fig. 9(*a*) left) has three peaks locating near the trailing-left, leading-left, and leading-right corners. The dissimilarity between $\bar{w}$ and $\bar{\theta}$ in the rotating case may be explained by the presence of the Coriolis force in the momentum equations with no corresponding counterparts in the energy equation.

3.2 Distribution of Streamwise Component of Wall Shear Stress and Nusselt Number. Figure 10 shows the streamwise component of the wall shear stress (Figs. 10(*a*) and (*c*)) and the local Nusselt number (Figs. 10(*b*) and (*d*)) on the four walls for the stationary case of 60 deg rib. Both instantaneous (Figs. 10(*a*) and (*b*)) and time-averaged (Figs. 10(*c*) and (*d*)) values are shown. For the rib area, the value at the rib top surface is shown. The Nusselt number is normalized using the following empirical correlation for a fully developed pipe flow [34]:

$$\mathrm{Nu}_\infty = 0.022\,\mathrm{Re}_m^{0.8}\,\mathrm{Pr}^{0.5}. \tag{17}$$

In the figures, out-of-range values are shown by white and black solid areas for very low and very high values, respectively. In Fig. 10(*c*), zero shear stress areas are also indicated by solid white. For easier understanding of the figures, the sign of the wall shear stress ((+), (−)) and the level of the Nusselt number (high, low) are added to the figures of the time-averaged results (Figs. 10(*c*) and (*d*)). It should be noted that the notches around the ribs are caused by the inadequate interpolation ability of the software used in drawing the figure, and the numerical results themselves do not oscillate. When the instantaneous values are compared in Figs. 10(*a*) and (*b*), the locations where the absolute value of wall shear stress becomes large and small are highly correlated to the locations of high and low local Nusselt numbers, respectively. The spots of large positive shear stress indicated by ellipses in Fig. 10(*a*) are considered to correspond to the sweep motion which transports cooler fluid from the main stream to the wall with high streamwise momentum. Therefore, the high heat transfer at the corresponding spots in Fig. 10(*b*) is reasonable. On the other hand, the spots of large negative shear stress indicated by circles in Fig. 10(*a*) are seen in front of the rib, and the spots also correspond to the high heat transfer in Fig. 10(*b*). This locally large negative shear stress is caused by the fluid which impinges on the wall in front of the rib after another impingement on the rib front

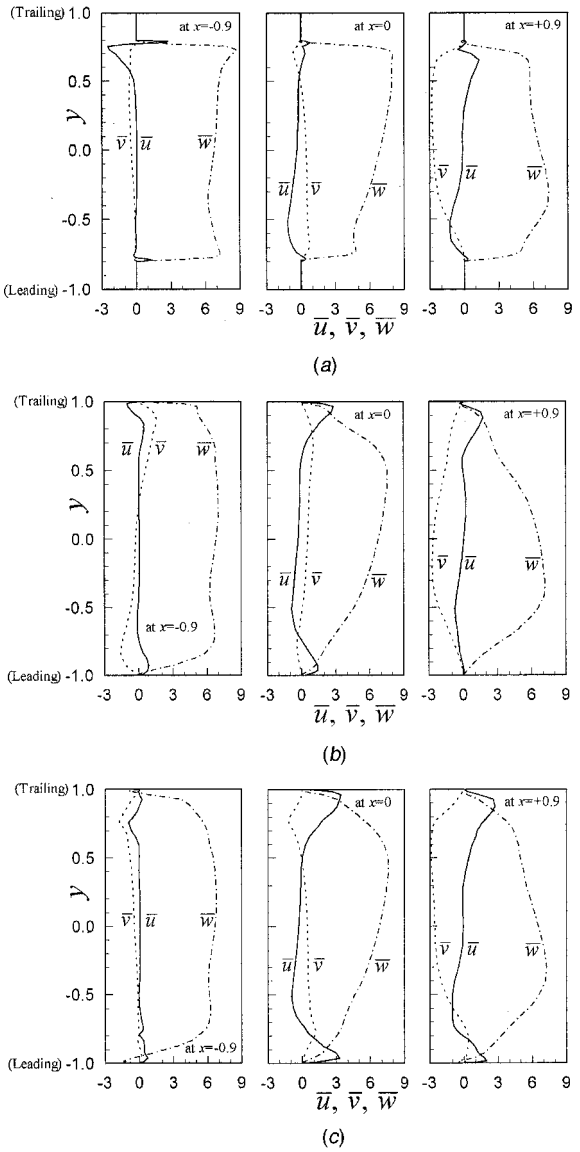

Fig. 6 Time-averaged velocity components on the nine lines of intersection between y-z and ξ-η planes ($Ro_* = 1$; left, middle, and right figures are for the transverse location of $x = -0.9$, 0, and $+0.9$, respectively): (*a*) at rib location (at center in rib width); (*b*) at midpoint between ribs; and (*c*) in front of ribs (a half of rib width from ribs).

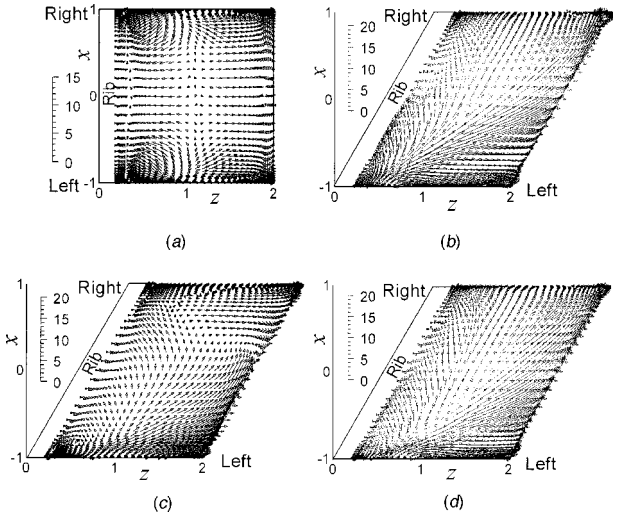

Fig. 7 Time-averaged velocity vectors in x-z plane at a half of rib height from rib-roughened wall: (*a*) 90 deg, $Ro_* = 0$; (*b*) 60 deg, $Ro_* = 0$; (*c*) 60 deg, $Ro_* = 1$, near leading wall; (*d*) 60 deg, $Ro_* = 1$, near trailing wall.

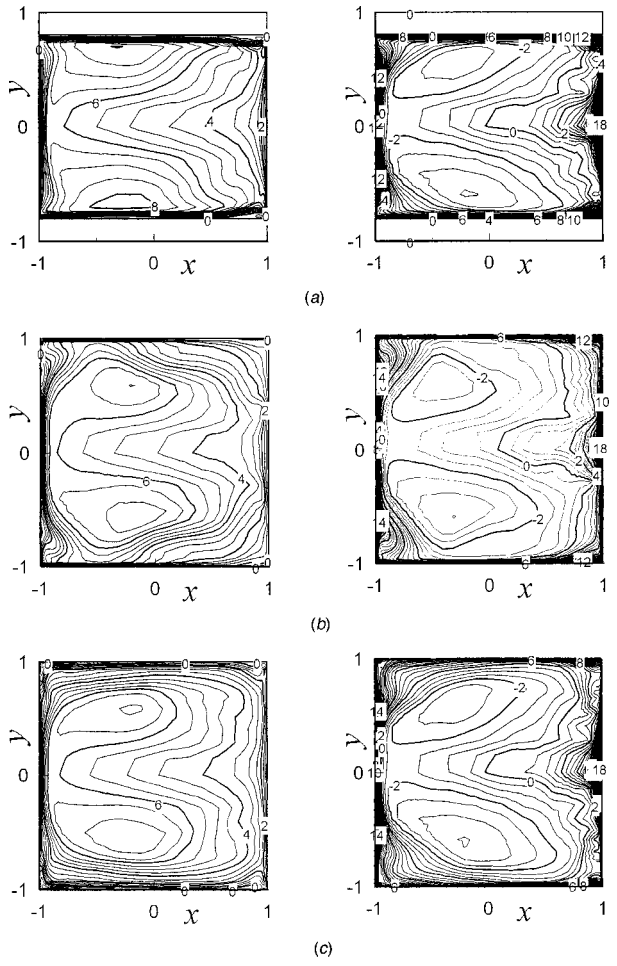

Fig. 8 Isocontours of time-averaged variables in ξ-η plane at three different streamwise locations (60 deg rib and $Ro_* = 0$; figures are projected onto x-y plane. Left and right figures are for streamwise velocity, $\overline{w}$, and temperature, $\overline{\theta}$, respectively): (*a*) at rib location (at center in rib width); (*b*) at midpoint between ribs; and (*c*) in front of ribs (a half of rib width from ribs).

surface. This mechanism is the same as the 90 deg rib case of Murata and Mochizuki [21]. In the time-averaged values of Figs. 10(*c*) and (*d*), the high Nusselt number area at the midpoint between the ribs corresponds to the positive large wall shear stress, and the area shifts to the left wall. In front of the ribs, the Nusselt number becomes very high, and this area is also slightly shifted to the left wall. These high Nusselt number areas were also experimentally observed [6–9]. It should be noted that the area in front of the rib seems only a separation bubble in the time-averaged flow field of Fig. 10(*c*), but the unsteady motion of the fluid with high momentum forms the very high Nusselt number area there. This high heat transfer area in front of the rib which is shifted to the left wall is also observed in the experimental results of Ekkad and Han [9]. The above-mentioned characteristics of the Nusselt number variation of the 60 deg rib are similar to those of 90 deg rib as shown in Fig. 11 except for the shift of the peaks to the left wall.

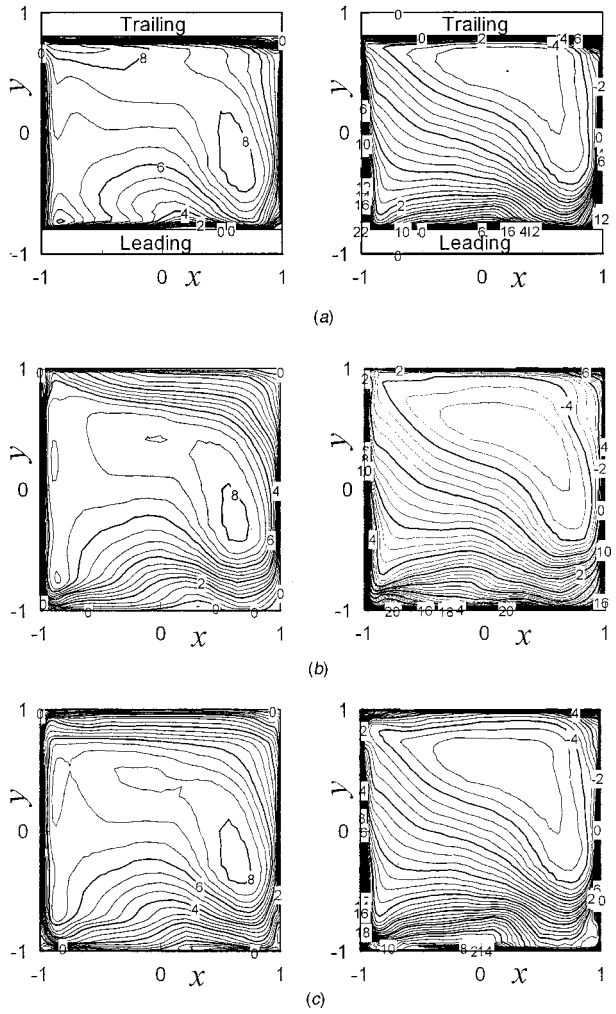

Fig. 9 Isocontours of time-averaged variables in ξ-η plane at three different streamwise locations (60 deg rib and $Ro_*=1$; figures are projected onto x-y plane. Left and right figures are for streamwise velocity, $\bar{w}$, and temperature, $\bar{\theta}$, respectively): (*a*) at rib location (at center in rib width); (*b*) at midpoint between ribs; and (*c*) in front of ribs (a half of rib width from ribs).

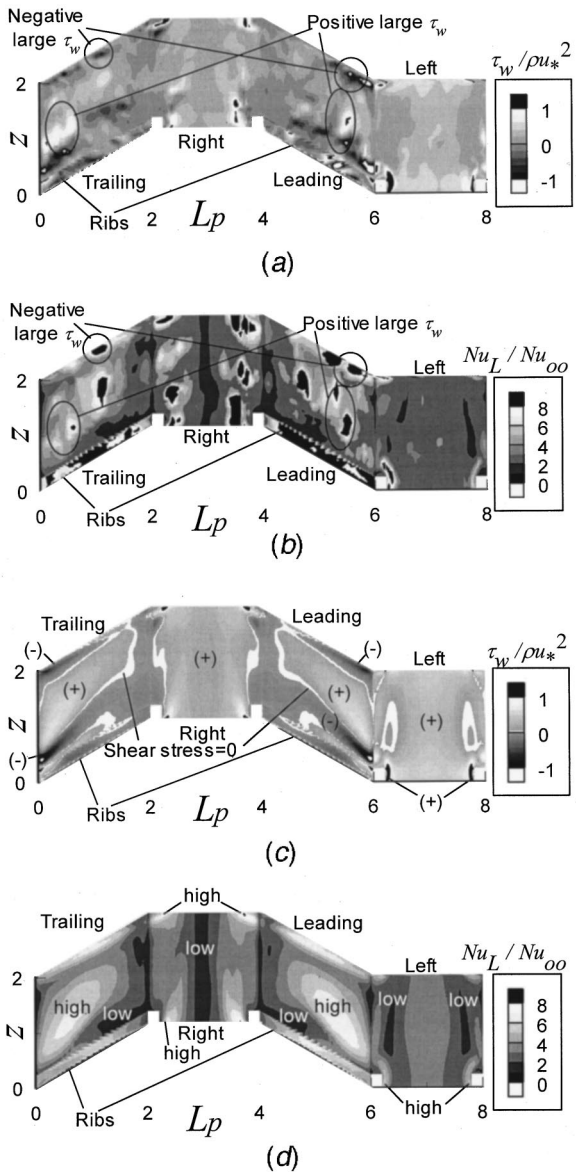

Fig. 10 Spatial variation of streamwise wall shear stress and Nusselt number on four walls (60 deg rib and $Ro_*=0$): (*a*) instantaneous wall shear stress; (*b*) instantaneous Nusselt number; (*c*) time-averaged wall shear stress; and (*d*) time-averaged Nusselt number.

For the rotating case of $Ro_*=1$, the time-averaged values of the wall shear stress and the Nusselt number are shown in Fig. 12. The wall shear stress (Fig. 12(*a*)) on the trailing wall (pressure surface) is similar to the stationary case of Fig. 10(*c*), although on the leading wall (suction surface) the absolute values become smaller and the profile becomes different from the stationary case. On the left wall, the value around the ribs on the trailing side becomes very high, and that on the leading side shows only a slight increase because of the weakened flow there. Due to the lower fluid temperature and the higher streamwise flow velocity on the trailing wall side as seen in Fig. 9, the Nusselt number of Fig. 12(*b*) gives higher and lower values on the trailing and leading walls, respectively. On the two side walls (right and left walls), the downwash of the Coriolis induced secondary flow goes from the tailing side to the leading side as seen in Fig. 4 (right), and therefore the Nusselt number increases from the leading side to the trailing side; this tendency is the same as the 90 deg rib case of Murata and Mochizuki [21].

Figure 13 shows the streamwise variation of the Nusselt number at the three transverse locations for 60 deg rib case. In the figure, thick and thin lines are for the values on the trailing and leading walls, respectively. The previous numerical results of the 90 deg rib [21] gave the quantitative agreement with the experimental results of Han et al. [35]. In Fig. 13(*a*), the experimental results of Chandra et al. [5] are also plotted for comparison; the experiments are for 60 deg rib, $Re_m=30{,}000$, $e/D=0.063$, $P/e=10$, and at transverse center ($x=0$). In order to quantitatively compare the numerical results with the experimental results, the additional computation with the same rib arrangement as that of Chandra et al. [5] was performed with larger grid number ($71\times71\times71$) and reduced averaging time steps (80,000 steps). The effect of the Reynolds number was also examined by increasing the Reynolds umber, Re_*, from 350 to 718 which corresponded to the increase of Re_m from 4349 to 8429. In Fig. 13(*a*), the agreement between the numerical (○, △) and experimental (□) results is good, and it becomes better by increasing the Reynolds number. In Table 2, the comparison between the numerical and experimental results is shown in the wall-averaged Nusselt number, Nu_w, normalized by using Nu_∞ (Eq. (17)). The effect of the grid number is small, and the agreement between the numerical and experimental results is good in both 90 deg and 60 deg rib cases.

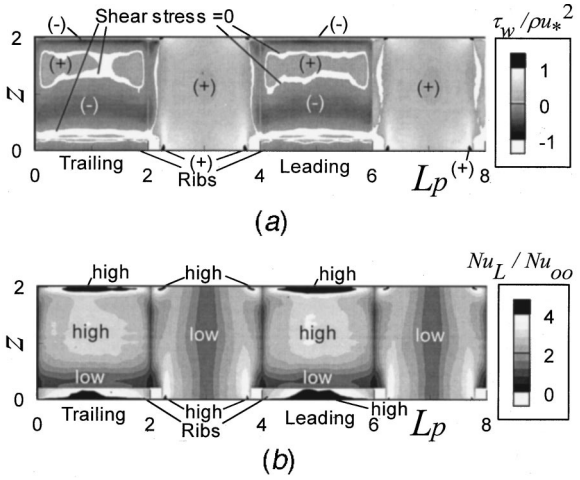

Fig. 11 Spatial variation of streamwise wall shear stress and Nusselt number on four walls (90 deg rib and $Ro_*=0$): (*a*) time-averaged wall shear stress; and (*b*) time-averaged Nusselt number.

In the stationary case of Fig. 13(*a*), the time-averaged Nusselt number becomes very high on the rib top surface. This very high Nusselt number was also observed in the higher grid resolution case of $71\times71\times71$, and therefore it is not due to the numerical errors but showing the high heat transfer at the rib front edge because of the thin boundary layer. The heat transfer behind the rib for a time becomes lower because of the flow separation and then takes a first local maximum near the reattachment point. The second local maximum is just in front of the rib. This profile is similar to that of the 90 deg rib case [21]. The difference due to the transverse location can be described as follows: from $x=-0.9$ to $x=0$ the heat transfer slightly increases, and then from $x=0$ to $x=+0.9$ the value decreases and the profile becomes flatter. In the previous experiments [4,5], this decrease of the heat transfer in the downstream region with respect to the secondary flow induced by the angled rib is also reported. In the rotating case of Fig. 13(*b*), on the trailing and leading walls, the heat

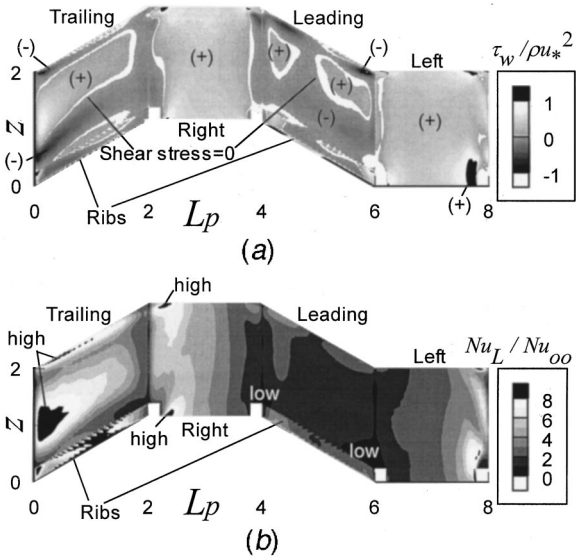

Fig. 12 Spatial variation of streamwise wall shear stress and Nusselt number on four walls (60 deg rib and $Ro_*=1$): (*a*) time-averaged wall shear stress; and (*b*) time-averaged Nusselt number.

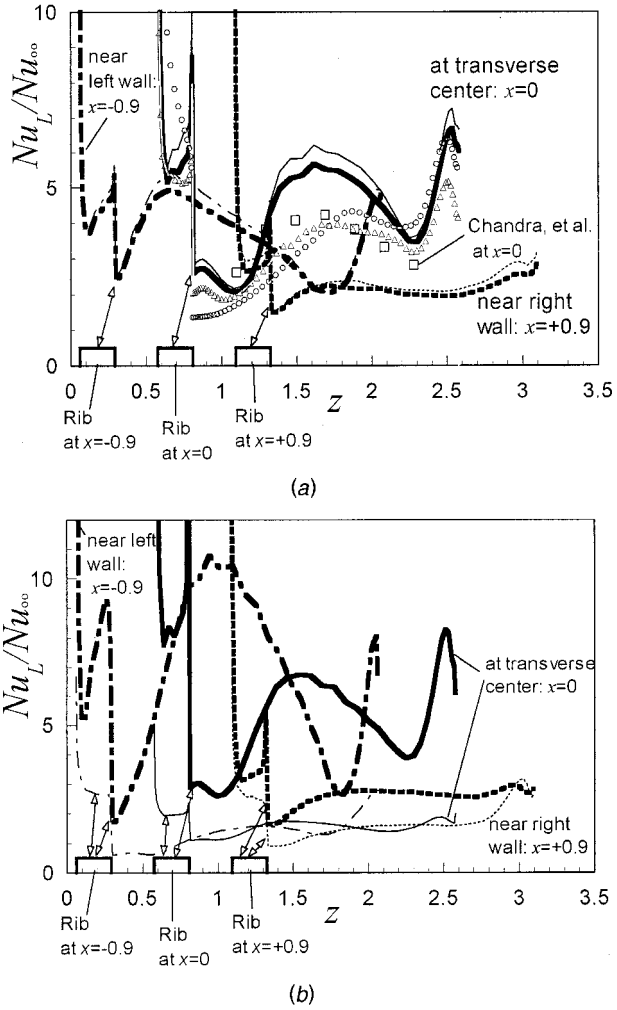

Fig. 13 Local Nusselt number profile at three different transverse locations on rib-roughened walls (60 deg rib); thick and thin lines are for trailing and leading walls, respectively, for $e/D=0.1$; □: experimental data of Chandra et al. [5] at $x=0$ for $Re_m=30{,}000$, $e/D=0.063$, and $P/e=10$; ○, △: numerical results for the same rib arrangement as Chandra et al. [5] for $Re_m=4349$ and 8429, respectively, with higher grid resolution of $71\times71\times71$: (*a*) $Ro_*=0$; and (*b*) $Ro_*=1$.

Table 2 Comparison between the numerical and experimental results in the wall-averaged Nusselt number, Nu_w/Nu_∞, for the stationary condition, $Ro_*=0$ ($P/e=10$; the values in parentheses are the results with higher grid resolution of $71\times71\times71$ and reduced sample size of 80,000 steps).

	e/D	Re_m	90deg rib		60deg rib		
			ribbed wall	side wall	ribbed wall	left wall	right wall
present results for $Re_*=350$	0.1	3148 (3252)	2.2	2.0	3.4 (3.4)	2.8 (2.6)	3.0 (2.9)
present results for $Re_*=350$	0.063	4398 (4349)	-	-	2.5 (2.6)	2.1 (2.2)	2.0 (2.0)
present results for $Re_*=718$	0.063	(8429)	-	-	(2.9)	(2.1)	(2.1)
Chandra et al. (1988)	0.063	30000	2.6	1.8	3.3	2.2	2.2
Rau et al.(1996)	0.1	30000	2.4	2.1	-	-	-

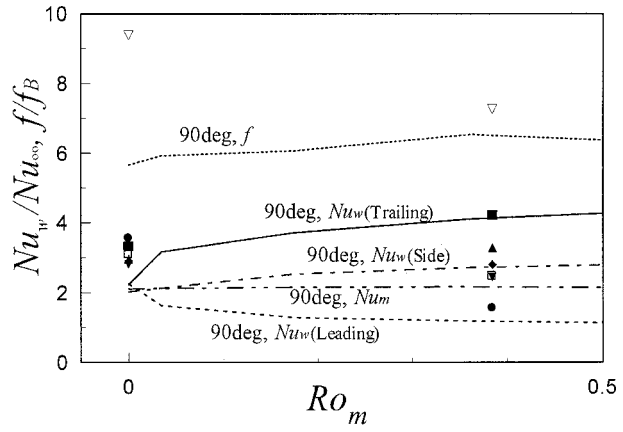

Fig. 14 Effect of rotation and angled ribs on wall-averaged Nusselt number, Nu_w, and friction factor, f (lines and symbols are for 90 deg and 60 deg rib cases, respectively; ■: trailing, ●: leading, ▼: left, ▲: right , □: Nu_m, △: f)

transfer increases and decreases, respectively; on the leading wall, the value becomes very low. As can be seen in comparing Fig. 10(*d*) with Fig. 12(*b*), on the trailing wall, the duct rotation shifts the high heat transfer area at the midpoint between the ribs to the left wall; therefore, in Fig. 13(*b*), the local maximum at the midpoint between the ribs monotonically decreases from $x=-0.9$ to $+0.9$.

Figure 14 shows the dependency of the friction factor, f, and the wall-averaged Nusselt number, Nu_w, on the rotation number, $Ro_m(=\omega D/U_m)$ defined by using the mean velocity and the hydraulic diameter. The Nusselt number and the friction factor are normalized by using Nu_∞ in Eq. (17) and f_B in the following Blasius equation:

$$f_B = 0.079\,\mathrm{Re}_m^{-0.25}. \tag{18}$$

In the figure, symbols are the present results of the 60 deg rib, and lines are from our previous studies [20,21] for the 90 deg rib for comparison. The duct-averaged values are also summarized in Table 3. The 60 deg rib results in the stationary condition show the higher values both in the Nusselt number and the friction factor as compared to the 90 deg rib case; especially the friction factor gives much higher values. The effect of rotation increases the friction factor of 90 deg rib but decreases that of 60 deg rib (-23 percent); the duct averaged Nusselt number also decreases (-20 percent). The change caused by the rotation was larger for the 60 deg rib case. In the 60 deg rib case, even in the stationary condition, a pair of strong vortices is formed by the angled rib effect (Fig. 4 (left)), and the introduction of the rotation forms one larger inclined vortex located at the upper right (Fig. 4 (right)); the larger vortex seems to be less effective in both friction and heat transfer enhancement than the pair of strong vortices of the stationary case. In the angled rib case, the flow fields near the right and left walls are not symmetric, although the Nusselt numbers on these walls almost coincide in the stationary condition. The effect of rotation causes the Nusselt number on the right wall to be higher than that on the left wall, because low temperature fluid comes closer to the right wall (Fig. 9 (right)), and therefore the heat transfer is enhanced on the large area of the right wall (Fig. 12(*b*)).

Table 3 Enhancement factors in f and Nu_m caused by rotation and rib angle (the values in parentheses are the results with higher grid resolution of 71×71×71 and reduced sample size of 80,000 steps).

	90deg rib		60deg rib	
	f/f_B	Nu_m/Nu_∞	f/f_B	Nu_m/Nu_∞
Ro_*=0	5.89	2.09	9.38 (8.86)	3.09 (3.01)
Ro_*=1	6.28	2.11	7.25 (7.21)	2.47 (2.53)
Change by rotation	+7%	+1%	-23% (-19%)	-20% (-16%)

Conclusions

In the angled 60 deg rib case, the correlation between the absolute value of the streamwise wall shear stress and the heat transfer was high, which was similar to the 90 deg rib case. Especially in front of the rib, the large negative value of the wall shear stress was highly correlated to the high heat transfer in the instantaneous field. This led to a very high value of the time-averaged heat transfer in front of the rib. In the 60 deg rib case, the similarity between the velocity and temperature fields held more as compared to the 90 deg rib case. In the stationary case of the 60 deg rib, the flow passing along the angled ribs induced the secondary flow, and both the heat transfer and the friction factor were increased as compared to the 90 deg rib case.

In the rotating case, the dissimilarity between the velocity and temperature fields was observed in the different number and location of the peaks. The duct-averaged Nusselt number and the friction factor were decreased by the rotation in the 60 deg rib case; it was opposite to the 90 deg rib case in which the rotation increased the values.

Nomenclature

C_S = Smagorinsky constant
D = side length of square duct (=hydraulic diameter), m
e = side length of ribs, m
f = friction coefficient ($=\Delta p/(2\rho U_m^2)$)
F_i = external force term
I_{LM}, I_{MM} = terms in Lagrangian dynamic subgrid-scale model
j = Colburn's j factor ($=\mathrm{Nu}_m/(\mathrm{Re}_m\mathrm{Pr}^{1/3})$)
J = Jacobian of coordinate transformation
ℓ = length scale ($=0.5D$), m
L_{ij} = term in Lagrangian dynamic subgrid-scale model
L_p = peripheral location
M_{ij} = term in Lagrangian dynamic subgrid-scale model
Nu = Nusselt number ($=hD/\lambda$)
Δp = pressure loss in streamwise length D, Pa
P = rib pitch ($=D$), m
Pr = Prandtl number (=0.71)
$\mathrm{Pr}_{\mathrm{SGS}}$ = Prandtl number of subgrid-scale model (=0.5)
$\dot{q}$ = wall heat flux, W/m^2
Re_m = Reynolds number ($=U_m D/\nu$)
Re_* = turbulent Reynolds number ($=u_*\ell/\nu$)
Ro_m = rotation number ($=\omega D/U_m$)
Ro_* = rotation number ($=\omega\ell/u_*$)
S_{ij} = rate-of-strain tensor
t = dimensionless time
T_r = friction temperature ($=\dot{q}/(\rho C_p u_*)$), K
u_* = mean friction velocity, m/s
U^j = dimensionless contravariant velocity
U_m = mean velocity, m/s
$\Delta x, \Delta y, \Delta z$ = grid spacing in x, y, z directions
α_{SGS_j} = subgrid-scale energy flux
$\bar{\Delta}$ = filter width of grid filter
λ = thermal conductivity, W/(mK)
ν_{SGS} = dimensionless subgrid-scale eddy viscosity

θ = dimensionless temperature ($=(T-T_b)/T_r$)
$\tau_{SGS_{ij}}$ = subgrid-scale stress tensor
τ_w = streamwise component of wall shear stress, Pa
ξ, η, ζ = curvilinear coordinates

Subscripts and Superscripts

B = Blasius
L = local value
m = duct average or based on mean velocity
∞ = fully developed
$*$ = friction velocity or defined by using u_*
$+$ = dimensionless value based on inner scales
$-$ = grid resolvable component (filtered value by using grid filter)
$\wedge$ = filtered value by using test filter

References

[1] Lakshminarayana, B., 1996, *Fluid Dynamics and Heat Transfer of Turbomachinery*, Chap. 7, John Wiley & Sons Inc., New York, pp. 597–721.
[2] Mochizuki, S., Beier, M., Murata, A., Okamura, T., and Hashidate, Y., 1996, "Detailed Measurement of Convective Heat Transfer in Rotating Two-Pass Rib-Roughened Coolant Channels," ASME Paper 96-TA-6.
[3] Mochizuki, S., Murata, A., and Fukunaga, M., 1997, "Effects of Rib Arrangements on Pressure drop and Heat Transfer in a Rib-Roughened Channel with a Sharp 180 deg Turn," ASME J. Turbomach., **119**, pp. 610–616.
[4] Murata, A., Mochizuki, S., and Takahashi, T., 1999, "Local Heat Transfer Measurements of an Orthogonally Rotating Square Duct with Angled Rib Turbulators," Int. J. Heat Mass Transf., **42**, pp. 3047–3056.
[5] Chandra, P. R., Han, J. C., and Lau, S. C., 1988, "Effect of Rib Angle on Local Heat/Mass Transfer Distribution in a Two-Pass Rib-Roughened Channel," ASME J. Heat Transfer, **110**, pp. 233–241.
[6] Hirota, M., Fujita, H., Yokosawa, H., Nakayama, T., and Tanaka, T., 1998, "Developing Heat/Mass Transfer in Low-Aspect-Ratio Rectangular Channels with Ribbed Walls," *Heat Transfer 1998, Proc. of 11th International Heat Transf. Conf.*, Taylor & Francis, **5**, pp. 363–368.
[7] Rau, G., Cakan, M., Moeller, D., and Arts, T., 1996, "The Effect of Periodic Ribs on the Local Aerodynamic and Heat Transfer Performance of a Straight Cooling Channel," ASME Paper 96-GT-541.
[8] Baughn, J. W., and Yan, X., 1992, "Local Heat Transfer Measurements in Square Ducts with Transverse Ribs," *Enhanced Heat Transfer ASME*, HTD-Vol. 202, pp. 1–7.
[9] Ekkad, S. V., and Han, J. C., 1997, "Detailed Heat Transfer Distributions in Two-Pass Square Channels With Rib Turbulators," Int. J. Heat Mass Transf., **40**, No. 11, pp. 2525–2537.
[10] Prakash, C., and Zerkle, R., 1995, "Prediction of Turbulent Flow and Heat Transfer in a Ribbed Rectangular Duct with and without Rotation," ASME J. Turbomach., **117**, pp. 255–264.
[11] Stephens, M. A., Shih, T. I.-P., and Civinskas, K. C., 1995, "Effects of Inclined Rounded Ribs on Flow and Heat Transfer in a Square Duct," AIAA Paper 95–2115.
[12] Banhoff, B., Tomm, U., and Johnson, B. V., 1996, "Heat Transfer Predictions for U-shaped Coolant Channels with Skewed Ribs and with Smooth Walls," ASME Paper 96-TA-7.
[13] Launder, B. E., Tselepidakis, D. P., and Younis, B. A., 1987, "A Second-Moment Closure Study of Rotating Channel Flow," J. Fluid Mech., **183**, pp. 63–75.
[14] Huser, A., and Biringen, S., 1993, "Direct Numerical Simulation of Turbulent Flow in a Square Duct," J. Fluid Mech., **257**, pp. 65–95.
[15] Gavrilakis, S., 1992, "Numerical Simulation of Low Reynolds Number Turbulent Flow Through a Straight Square Duct," J. Fluid Mech., **244**, pp. 101–129.
[16] Madabhushi, R. K., and Vanka, S. P., 1991, "Large Eddy Simulation of Turbulence-Driven Secondary Flow in a Square Duct," Phys. Fluids A, **3**, No. 11, pp. 2734–2745.
[17] Kajishima, T., Miyake, Y., and Nishimoto, T., 1991, "Large Eddy Simulation of Turbulent Flow in a Square Duct," Trans. Jpn. Soc. Mech. Eng., Ser. B, **57**, No. 540, pp. 2530–2537.
[18] Murata, A., and Mochizuki, S., 2000, "Large Eddy Simulation with a Dynamic Subgrid-Scale Model of Turbulent Heat Transfer in an Orthogonally Rotating Smooth Square Duct," Int. J. Transport Phenomena, **2**, pp. 27–41.
[19] Murata, A., and Mochizuki, S., 1999, "Effect of Cross-Sectional Aspect Ratio on Turbulent Heat Transfer in an Orthogonally Rotating Rectangular Smooth Duct," Int. J. Heat Mass Transf., **42**, pp. 3803–3814.
[20] Murata, A., and Mochizuki, S., 1998, "Large Eddy Simulation Applied to Internal Forced-Convection Cooling of Gas-Turbine Blades," *Heat Transfer 1998, Proc. of 11th International Heat Transf. Conf.*, Taylor & Francis, **6**, pp. 565–570.
[21] Murata, A., and Mochizuki, S., 1999, "Large Eddy Simulation with a Dynamic Subgrid-Scale Model of Turbulent Heat Transfer in an Orthogonally Rotating Rectangular Duct with Transverse Rib Turbulators," Int. J. Heat Mass Transf., **43**, pp. 1243–1259.
[22] Taslim, M. E., and Spring, S. D., 1994, "Effect of Turbulator Profile and Spacing on Heat Transfer and Friction in a Channel," J. Thermophys. Heat Transfer, **8**, No. 3, pp. 555–562.
[23] Korotky, G. J., and Taslim, M. E., 1996, "Rib Heat Transfer Coefficient Measurements, in a Rib-Roughened Square Passage," ASME Paper 96-GT-356.
[24] Han, J. C., Park, J. S., and Lei, C. K., 1985, "Heat Transfer Enhancement in Channels With Turbulence Promoters," ASME J. Eng. Gas Turbines Power, **107**, pp. 628–635.
[25] Patankar, S. V., Liu, C. H., and Sparrow, E. M., 1977, "Fully Developed Flow and Heat Transfer in Ducts Having Streamwise-Periodic Variations of Cross-Sectional Area," ASME J. Heat Transfer, **99**, pp. 180–186.
[26] Kajishima, T., Ohta, T., Okazaki, K., and Miyake, Y., 1998, "High-Order Finite-Difference Method for Incompressible Flows Using Collocated Grid System," Trans. Jpn. Soc. Mech. Eng., Ser. B, **41**, No. 4, pp. 830–839.
[27] Germano, M., Piomelli, U., Moin, P., and Cabot, W. H., 1991, "A Dynamic Subgrid-Scale Eddy Viscosity Model," Phys. Fluids A, **3**, No. 7, pp. 1760–1765.
[28] Lilly, D. K., 1992, "A Proposed Modification of the Germano Subgrid-Scale Closure Method," Phys. Fluids A, **4**, No. 3, pp. 633–635.
[29] Meneveau, C., Lund, T. S., and Cabot, W. H., 1996, "A Lagrangian Dynamic Subgrid-Scale Model of Turbulence," J. Fluid Mech., **319**, pp. 353–385.
[30] Moin, P., Squires, K., Cabot, W., and Lee, S., 1991, "A Dynamic Subgrid-Scale Model for Compressible Turbulence and Scalar Transport," Phys. Fluids A, **3**, No. 11, pp. 2746–2757.
[31] Harlow, F. H., and Welch, J. E., 1965, "Numerical Calculation of Time-Dependent Viscous Incompressible Flow of Fluid With Free Surface," Phys. Fluids, **8**, No. 12, pp. 2182–2189.
[32] Kim, J., and Moin, P., 1985, "Application of a Fractional-Step Method to Incompressible Navier-Stokes Equations," J. Comput. Phys., **59**, pp. 308–323.
[33] Zang, Y., Street, R. L., and Koseff, J. R., 1994, "A Non-Staggered Grid, Fractional Step Method for Time-Dependent Incompressible Navier-Stokes Equations in Curvilinear Coordinates," J. Comput. Phys., **114**, pp. 18–33.
[34] Kays, W. M., and Crawford, M. E., 1993, *Convective Heat and Mass Transfer*, 3rd ed., McGraw-Hill Inc., New York, p. 316.
[35] Han, J. C., Chandra, P. R., and Lau, S. C., 1988, "Local Heat/Mass Transfer Distribution Around Sharp 180 deg Turns in Two-Pass Smooth and Rib-Roughened Channels," ASME J. Heat Transfer, **110**, pp. 91–98.

Experimental and Numerical Study of Turbulent Heat Transfer in Twisted Square Ducts

Liang-Bi Wang[1]
Wen-Quan Tao
Qiu-Wang Wang
Ya-Ling He

School of Energy and Power Engineering,
Xi'an Jiaotong University,
Xi'an, Shaanxi 710049, PRC

This paper describes the experimental and numerical study of three mildly twisted square ducts (twisted uniform cross section square duct, twisted divergent square duct and twisted convergent square duct). Experiments are conducted for air with uniform heat flux condition. Measurements are also conducted for a straight untwisted square duct for comparison purpose. Numerical simulations are performed for three-dimensional and fully elliptic flow and heat transfer by using a body-fitted finite volume method and standard $k-\varepsilon$ turbulence model. Both experimental and numerical results show that the twisting brings about a special variation pattern of the spanwise distribution of the local heat transfer coefficient, while the divergent and convergent shapes lead to different axial local heat transfer distributions. Based on the test data, the thermal performance comparisons are made under three constraints (identical mass flow rate, identical pumping power and identical pressure drop) with straight untwisted square duct as a reference. Comparisons show that the twisted divergent duct can always enhance heat transfer, the twisted convergent duct always deteriorates heat transfer, and the twisted constant cross section duct is somewhat in between. [DOI: 10.1115/1.1389464]

Keywords: Channel Flow, Enhancement, Experimental, Heat Transfer, Numerical Methods

Introduction

The enhancement of single phase heat transfer inside a duct is often achieved by forming some swirling or secondary flows. This is because the swirling or secondary flow is usually accompanied with high turbulence intensity, which promotes the mixing of different parts of fluids, hence enhances the heat transfer. The swirling and secondary flow can be initiated by several ways, among which the insert of twisted tape or wire coil, the injecting or imparting a tangential flow, the use of integral tube with helical fins, spiral fluted duct and the twisted duct are often encountered. Most of these methods have been intensively studied. For example, the heat transfer and fluid flow behavior of the twisted tape have been studied and compared comprehensively by Manglik and Bergles [1,2]. Yampolsky [3] and Obot et al. [4] tested the fluid flow and heat transfer characteristics of the spirally fluted tubes. The imparting of a tangential flow was investigated by Gau and Chen [5]. Relatively speaking the study on the twisted duct is quite limited.

The purpose of this paper is to investigate the turbulent heat transfer and fluid flow in twisted uniform cross section, converging and diverging square ducts. As a technique for enhancing heat transfer, twisted duct has a unique feature in that it may induce swirling secondary flow and increase fluid contacted surface in some extent within a given axial length while still keeping smooth surfaces. Apart from the enhancement consideration, the present study was also motivated by the need in understanding the heat transfer mechanism of gas turbine blade cooling process. The cooling channel of a gas turbine is often modeled by a duct with a square cross section [6]. In the flow direction, the cooling passages may be twisted in a certain extent and its cross-section area varies along the flow direction. To study the effect of these factors on the heat transfer and fluid flow characters, we specially designed and manufactured a square duct with constant cross section twisted axially by 90 deg and a converging/diverging twisted square duct. Fig. 1 schematically shows the configurations studied in the present paper.

A search of literature only revealed a very limited works that are related to the present study. Todd [7] studied fluid flow in twisted tubes with elliptical cross-section. His intent was to understand and model flow behavior in flexible pipes. Masliyah and Nandakumar [8,9] numerically studied the fully developed steady laminar flow through twisted square ducts with a rotation coordinate system. Axial conduction in fluids was neglected to preserve the two-dimensional nature of the problem. Temperature along the periphery was assumed to be constant for each wall, but it might be different for four walls. It was observed that in the Reynolds number range between 1–1000 and a dimensionless twisted parameter of 2.5, swirling motion provides significant enhancement in overall heat transfer. Later, Xu and Fan [10,11] proposed the helical Cartesian coordinate system and derived viscous fluid flow equations for that coordinates. The twisted Couette flow was solved. In addition, they also pointed out the discrepancy in the viscous dissipation term adopted in the analysis by Masliyah and Nandakumar [8]. The flows and heat transfer studied in the aforementioned works were all laminar. Turbulent heat transfer results for twisted square duct are not found in the public literature available to the present authors.

In this study, both experimental and numerical approaches are adopted to investigate the fluid flow and heat transfer characteristics of air in the developing region for twisted square ducts with constant or varying cross section. The ratio of duct length over which the cross section rotates through 2π radians over the duct width is 42. This ratio will be called dimensionless twisted parameter hereafter. The effect of Reynolds number is conducted within the range of 10^4-10^5. No attempt was made to investigate the effect of the dimensionless twisted parameter. Since in the case of gas turbine blade cooling, the twist is quite mild and the dimensionless value adopted in this study may be regarded as a representative. To the authors' knowledge, this is seemingly the first work in the literature with respect to the turbulent flow in the

[1]Present address: Department of Mechanical Engineering, Lan Zhou Railway Institute, Lan Zhou, 730070, China

Contributed by the Heat Transfer Division for publication in the JOURNAL OF HEAT TRANSFER. Manuscript received by the Heat Transfer Division October 3, 2000; revision received March 23, 2001. Associate Editor: M. Faghri.

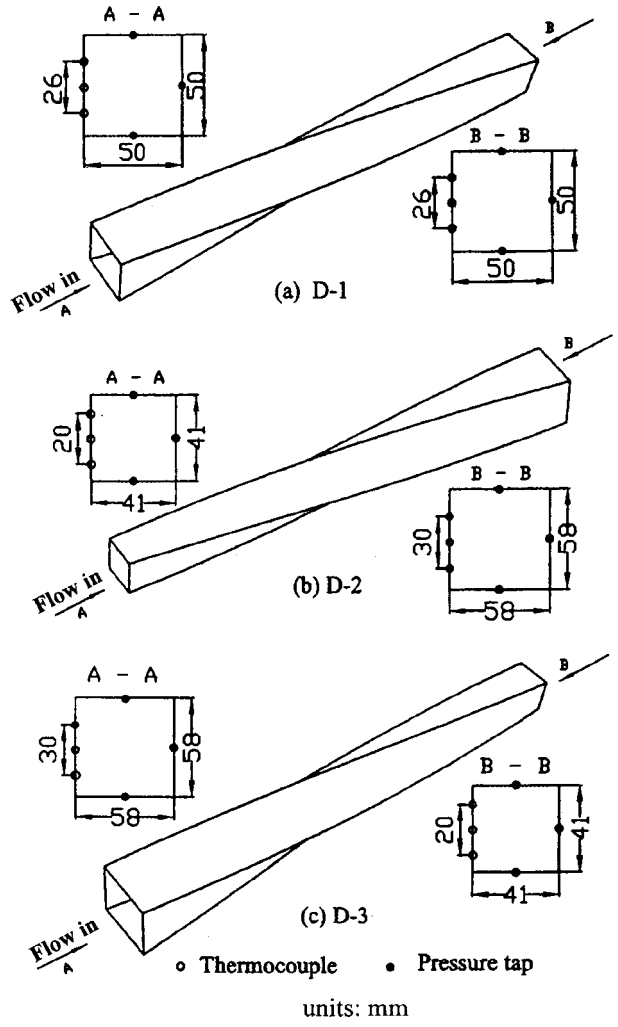

Fig. 1 Schematic diagram of test ducts: (*a*) twisted duct with constant cross section; (*b*) twisted divergent duct; and (*c*) twisted convergent duct

twisted duct. In the following, the experimental apparatus and data reduction method is first presented, followed by the numerical approach for dealing with such complicated configuration. The experimental and numerical results are then presented in a parallel way so that the comparisons between the two results can be conducted efficiently. Finally, conclusions are provided.

Experimental Investigation

Experimental Apparatus. A stereo picture of the test ducts is shown in Fig. 1. A schematic of the experimental setup is presented in Fig. 2. It is a suction system. A 3.5 kW blower was used to draw the air from the laboratory room to the test duct via

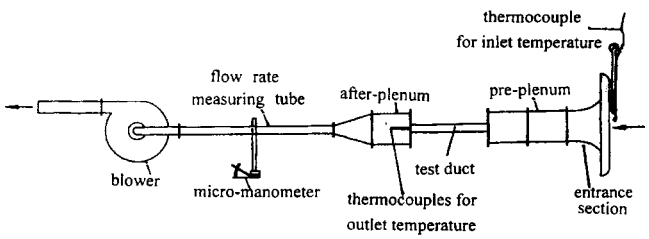

Fig. 2 Schematic diagram of test apparatus

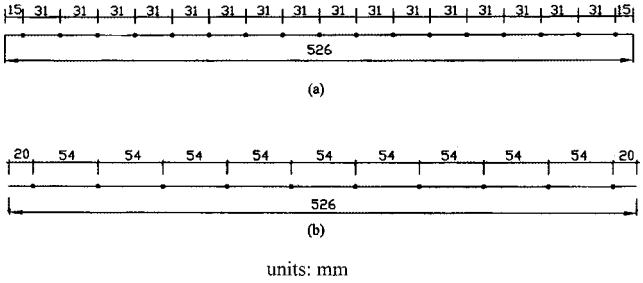

Fig. 3 Arrangement of thermocouples and pressure taps: (*a*) thermocouples; and (*b*) pressure taps

a convergent inlet and a pre-plenum, which is a square duct with $120\times120\,\mathrm{mm}^2$ and used to provide a sharp construction entrance condition. The test duct is connected to an after-plenum ($120\times120\,\mathrm{mm}^2$ square duct) and a transition duct whose cross-section gradually varies from square to circular. Connected to the transition duct is a tube with an inner diameter of 50 mm and a length of 1400 mm equipped with a multiport averaging Pitot tube [12] to measure flow rate.

The three test ducts are made of steel. Both the straight square duct and the twisted uniform cross section square duct have a cross section 50×50 mm. The twisted convergent/divergent duct has its largest cross-section of 58×58 mm and its smallest cross-section of 41×41 mm. The three test ducts are 526 mm long in axial direction and their two end-sections are twisted by 90 deg within this axial distance, leading to a dimensionless twisted parameter of 42. In the experiments, the convergent/divergent duct is used twice: one serves as a convergent duct and the other as a divergent duct.

The ducts are wrapped uniformly by resistance strip which is controlled by a variac transformer to provide a controllable electrical heating to the test duct. The ducts are insulated by plastic foam. Fifty one copper-constantan thermocouples are used to measure the axial wall temperature distribution of one wall of each test duct. Since the effect of the natural convection can be neglected, one wall can be regarded as a representative of the others. These thermocouples are arranged in three axial lines, with one being the center line of the wall. Their axial positions are shown in Fig. 3(*a*). For the three other walls without thermocouples, ten pressure taps along the centerline of the each wall are used for static pressure drop measurement. Axial pressure tap locations are given in Fig. 3(*b*). An incline manometer with a resolution of 1.36 Pa is used for pressure drop measurement in the test ducts. All the thermocouples signals are acquired with a data acquisition system and sent to a personal computer for data reduction. The temperatures of the entering fluid is measured by one thermocouple checked by a liquid thermometer with a resolution of 0.1°C, while the leaving fluid temperature is measured by five thermocouples distributed at a screen set up adjacent to outlet section of the test duct.

Data Reduction. The local heat transfer coefficient is calculated by the following equation:

$$h_x=(Q-Q_{\mathrm{loss}})/[A(T_{w,x}-T_{b,x})], \tag{1}$$

where Q is the total thermal energy supplied by the electrical heater, Q_{loss} is the heat loss to the environment, and A is the total inner surface area. The local wall temperature used in equation (1), $T_{w,x}$, is obtained from the output of the average thermocouple readings at each cross cross-section.

The local bulk temperature used in Eq. (1) is calculated by the following equation:

$$T_{b,x}=T_i+[(Q-Q_{\mathrm{loss}})A_x]/(A\dot{m}c_p), \tag{2}$$

where A_x is the partial surface area of the duct from the inlet to the axial position x, of which the determination method will be presented later. The heat loss to the environment is estimated by heat conduction through the plastic foam and the two end losses. And for the most cases studied the ratio of Q_{loss}/Q is less than 5 percent. This estimation is confirmed by the thermal energy balance between the fluid enthalpy increase and the total power input. In the data reduction Q_{loss} is determined from the measured outlet fluid temperature. The determination method of area A will be presented later. An estimation of the axial heat conduction along the duct wall shows that this part of heat transfer is always less than 1 percent of the total power input, hence the thermal boundary condition may be regarded as uniform heat flux

The local Nusselt number is defined by

$$\text{Nu}_x = h_x D_m / k. \tag{3}$$

The duct average Nusselt number is defined by

$$\text{Nu} = (Q - Q_{\text{loss}}) D_m / [k(T_w - T_b)], \tag{4}$$

where T_w is the center-line duct average wall temperature.

The characteristic length and the duct average fluid temperature are defined by

$$D_m = (D_{\text{in}} + D_{\text{out}})/2, \quad T_b = (T_{b,\text{in}} + T_{b,\text{out}})/2. \tag{5}$$

Attention is now turned to the definition of the duct friction factor. For the constant cross-section duct, the average friction factor is defined by

$$f = [(\Delta p / L) D_m)]/(\rho U_m^2/2), \tag{6}$$

where Δp is the pressure drop of the entire test duct.

As for the convergent or divergent duct, the definition of the friction factor should take the effect of the variation of the cross section into account [13]. The average friction factor for the duct is defined by

$$f = \frac{U_1^2}{U_m^2} \cdot \frac{D_m}{L} \lambda \left[1 - \left(\frac{A_{\text{in}}}{A_{\text{out}}} \right)^2 \right], \tag{7}$$

where λ is defined by

$$\lambda = 1 - C_p. \tag{8}$$

In Equation (8) C_p is the pressure recovery factor for the entire test duct. The local pressure recovery factor is defined by

$$C_{p,x} = \frac{p_{x+\Delta x/2} - p_{x-\Delta x/2}}{\rho U_{\text{in}}^2/2}, \tag{9}$$

where Δx is the distance between two neighboring pressure taps. This definition can be applied for C_p by replacing $p_{x+\Delta x/2}, p_{x-\Delta x/2}$ with $p_{\text{out}}, p_{\text{in}}$ respectively. The pressure drop data of the present investigation are obtained for the heated air.

The measurement accuracies of major parameters are estimated as follows: dynamic pressure drop -6 percent; electric power input -3 percent; cross-sectional or surface area -1~2 percent; thermophysical properties -2 percent; wall and fluid temperature -0.2°C. Using the uncertainty estimation method of Kline and McClintock [14] and Moffat [15], the maximum uncertainty in the average Nusselt number and average friction factor are estimated to be about 8 percent and 10 percent, respectively.

Numerical Investigation

The numerical simulations are performed by solving fully elliptic three-dimensional Navier-Stokes equations in body-fitted coordinate system. The flow and heat transfer are assumed to be incompressible, and in steady-state.

The compact forms of the time-averaged governing equations in the physical space are as follows:

Continuity Equations

$$\frac{\partial U_j}{\partial x_j} = 0 \tag{10}$$

Momentum Equation

$$\rho U_j \frac{\partial U_j}{\partial x_j} = -\frac{\partial p}{\partial x_i} + \frac{\partial}{\partial x_j}\left[\mu \left(\frac{\partial U_i}{\partial x_j} + \frac{\partial U_j}{\partial x_i} \right) - \rho \overline{u_i u_j} \right] \tag{11}$$

Energy Equation

$$\frac{\partial}{\partial x_j} \cdot (\rho U_j T) = \frac{\partial}{\partial x_j}\left(\frac{\mu}{\text{Pr}} \frac{\partial T}{\partial x_j} - \rho \overline{u_j \theta} \right) \tag{12}$$

In Eqs. (10)–(12) the doubled index represents summation, u_i, u_j are velocity fluctuations and θ is the temperature fluctuation.

The turbulent shear stress in equation (11) is determined by

$$-\rho \overline{u_i u_j} = \mu_t \left(\frac{\partial U_i}{\partial x_j} + \frac{\partial U_j}{\partial x_i} \right) - \frac{2}{3} \delta_{ij} \rho k, \tag{13}$$

where $\delta_{ij} = 1$ when $i = j$ and zero when $i \neq j$. The turbulent viscosity μ_t is determined by Prandtl-Kolmogorov equation

$$\mu_t = C_\mu \rho k^2 / \varepsilon. \tag{14}$$

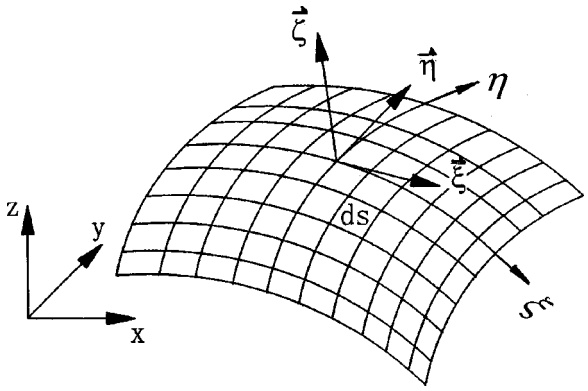

Fig. 4 Schematic diagram of surface area calculation

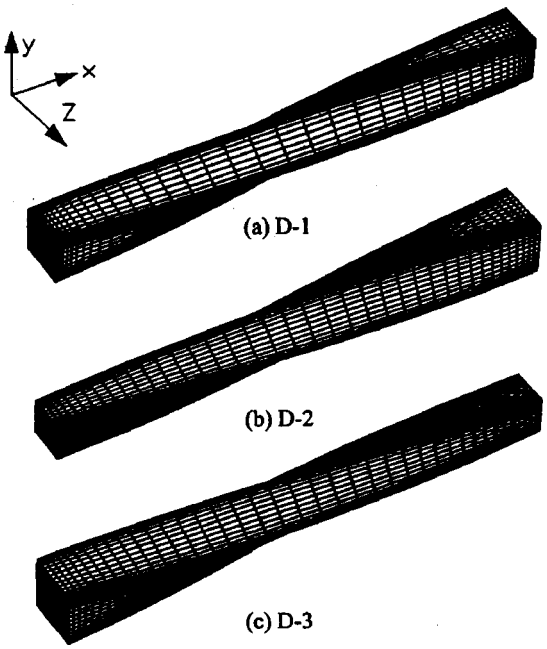

Fig. 5 Grid systems generated by multi-surface method

In the present calculation, the standard k-ε turbulent model is adopted [16] because of its simplicity in implementation and reasonable modelling accuracy. The governing equations for k and ε are as follows:

$$U_j\frac{\partial k}{\partial x_j}=\frac{1}{\rho}\frac{\partial}{\partial x_j}\left(\frac{\mu_t}{\sigma_t}\frac{\partial k}{\partial x_j}\right)+\frac{\mu_t}{\rho}\frac{\partial U_i}{\partial x_j}\left(\frac{\partial U_i}{\partial x_j}+\frac{\partial U_j}{\partial x_i}\right)-\varepsilon \quad (15)$$

$$U_j\frac{\partial \varepsilon}{\partial x_j}=\frac{1}{\rho}\frac{\partial}{\partial x_j}\left(\frac{\mu_t}{\sigma_\varepsilon}\frac{\partial \varepsilon}{\partial x_j}\right)+C_{\varepsilon 1}\frac{\varepsilon}{k}\frac{\mu_t}{\rho}\frac{\partial U_i}{\partial x_j}\left(\frac{\partial U_i}{\partial x_j}+\frac{\partial U_j}{\partial x_j}\right)-C_{\varepsilon 2}\frac{\varepsilon^2}{k} \quad (16)$$

The turbulent heat transfer term in Eq. (12), $\rho\overline{u_j\theta}$, is determined by the following equation:

$$\rho\overline{u_j\theta}=-\frac{\mu_t}{\sigma_\theta}\frac{\partial T}{\partial x_j}. \quad (17)$$

The constants in the above model take following values [17]:

$$C_\mu=0.09;\ \ C_{\varepsilon 1}=1.44;\ \ C_{\varepsilon 2}=1.92;$$

$$\sigma_\varepsilon=1.3;\ \ \sigma_k=1.0;\ \ \sigma_\theta=0.9.$$

The treatment of the boundary conditions is now addressed. The outlet boundary condition of the computational domain is treated by the local one-way method [18]. The inlet velocity is assumed to be constant (U_{in}=const, $V_{in}=0$, $W_{in}=0$) and the inlet kinetic energy of turbulence is calculated by $k=a_k 1/2U_{in}^2$, where $a_k=(0.5-1.5)$ percent. The inlet dissipation rate was taken as $\varepsilon_{in}=k_{in}^{2/3}/(0.05D)$. At the walls, the no-slip condition is used in conjunction with the wall functions method, which is implemented by the method provided in Tao [17]. For temperature equation the wall functions are used to determine the wall temperature from the computed near wall temperature fields, since the heat flux is prescribed at the wall. The difference between the wall temperature so determined and the local bulk temperature is then used to compute the local heat transfer coefficient.

The twisted duct in the physical space ($x-y-z$ coordinates) is transformed into a rectangular parallelpiped in the computational space ($\xi-\eta-\zeta$ coordinates) by using the multisurface algebraic method [19–21]. The schematic of the three grid systems generated by the multisurface method are shown in Fig. 5.

The governing equations shown above are then transformed into the computational space and discretized there by using the control-volume method [18]. In this procedure the computational domain is discretized by a series of control volumes, and the governing equations are then integrated over a control volume. During the integration the profile approximations are made in each coordinate direction for the dependent variables, leading to a system of algebraic equation that can be solved in an iterative manner. The velocity pressure-velocity coupling is handled by the SIMPLE algorithm [18]. The collocation grid arrangement is used in the present study. To ensure the coupling between velocity and pressure the momentum interpolation of Rhie and Chow [22] is adopted to determine the interface velocity. To make the numerical solution be independent of the under relaxation factor, the relaxation factor is resumed to one before the momentum interpolation is used to determine the interface velocity [23].

The heat transfer surface area A in Eq. (1) of the twisted duct is also computed using the transformed coordinates (Fig. 4):

$$A=\sum_{j=}^{n}\sum_{k=l}^{m}(ds)_{j,k} \quad (18)$$

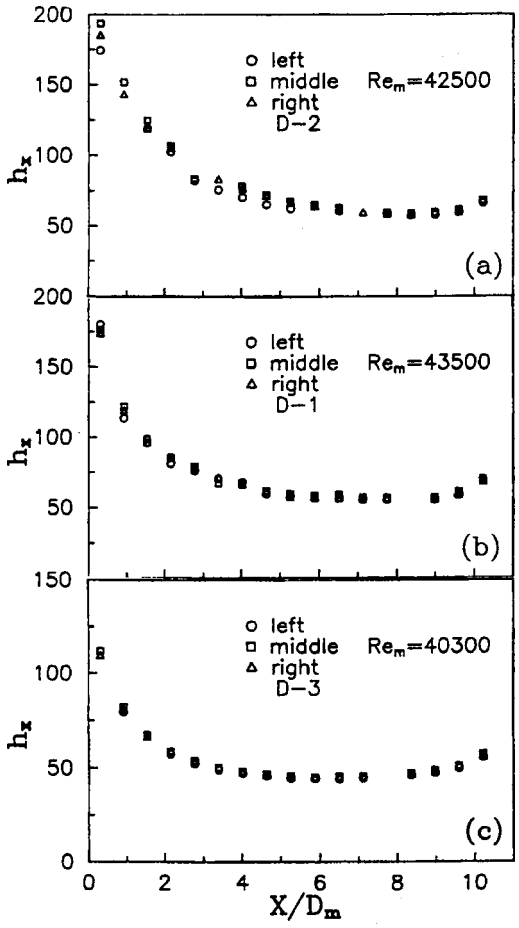

Fig. 6 Experimental local heat transfer coefficient

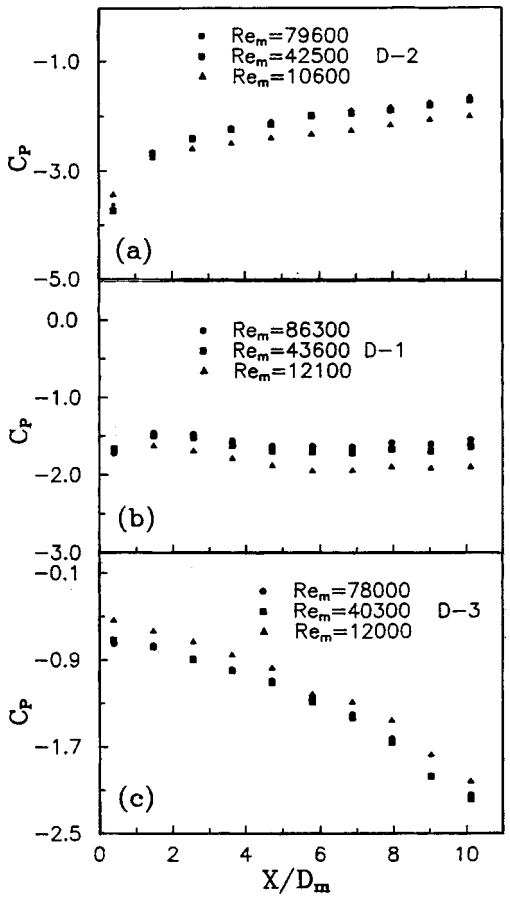

Fig. 7 Experimental local pressure recover factor

$$(ds)_{j,k} = |\vec{A}^{\xi=\text{const}}| = \sqrt{(y_\eta z_\zeta - y_\zeta z_\eta) + (x_\zeta z_\eta - x_\eta z_\zeta) + (x_\eta y_\zeta - x_\zeta y_\eta)}\, d\xi\, d\eta, \tag{19}$$

where $d\xi = d\eta = 1$, and n, m are number of control volumes in ξ, η directions, respectively. Similarly, the partial heat transfer surface area, A_x, can be calculated with an appropriate value of control volume in ξ direction.

Computations are conducted for three cases: one for the constant cross-section twisted duct, and the other two for divergent and convergent ducts, respectively. In the calculation, it is found that when the inlet k is in the range of 0.5 percent–1.5 percent of the inlet average kinetic energy of flow, there is no significant effect on the numerical results. A good agreement between numerical and experimental results is found when the values of y^+, z^+ are in the range of 11.5–40. Grid-independent studies are performed for the case of Re=100,000 of all the three ducts. Three grid sizes ($41\times16\times16$,$61\times16\times16$,$41\times21\times21$) are used. The difference in the duct average Nusselt number between the three results is about 1 percent, and the solutions presented in this paper were obtained using the finest grid of $41\times21\times21$.

Results and Discussion

In order to simplify the presentation, the following symbols are adopted for the three ducts and straight square duct: D-1—twisted uniform cross-section square duct; D-2—twisted divergent duct; D-3—twisted convergent duct; A-1—straight untwisted square duct.

Local Characteristics. The measured local heat transfer coefficient and pressure recovery factor of the three twisted test ducts are presented in Fig. 6 and Fig. 7. For the convenience of inspection and comparison, the three panels of each figure are arranged in the order of D2-D1-D3. From Fig. 6(*b*), it is found that for the uniform cross-section twisted duct h_x decreases as the x/D_m increases, when x/D_m is greater than 5, h_x reaches a constant value. As shown in Fig. 6(*a*), for the divergent twisted duct, h_x decreases as the x/D_m increases, but the decreasing rate is slower than that of the uniform cross-section twisted duct, and there seems no distinct sign to approach a constant value. For convergent duct, Fig. 6(*c*) shows that at the duct inlet h_x decreases

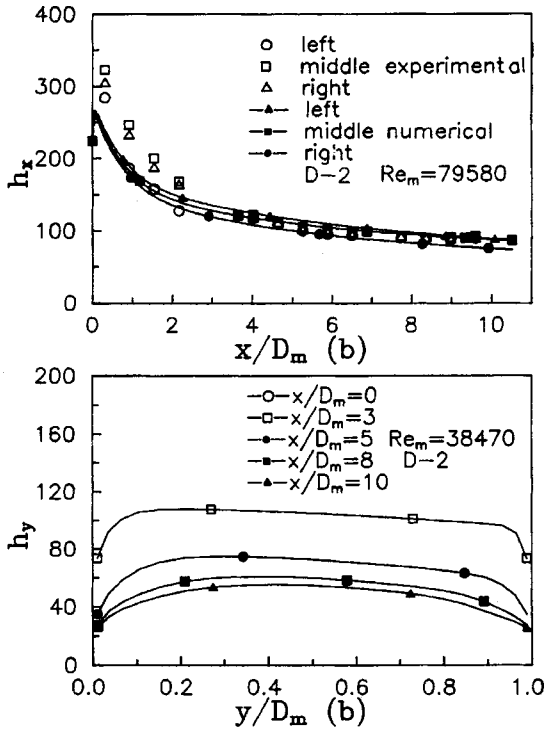

Fig. 9 Numerically predicted local heat transfer coefficient (*D*-2)

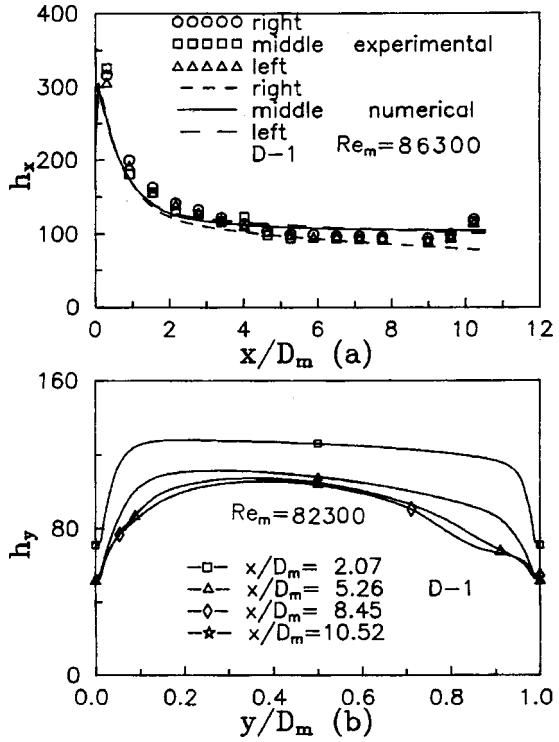

Fig. 8 Numerically predicted local heat transfer coefficient (*D*-1)

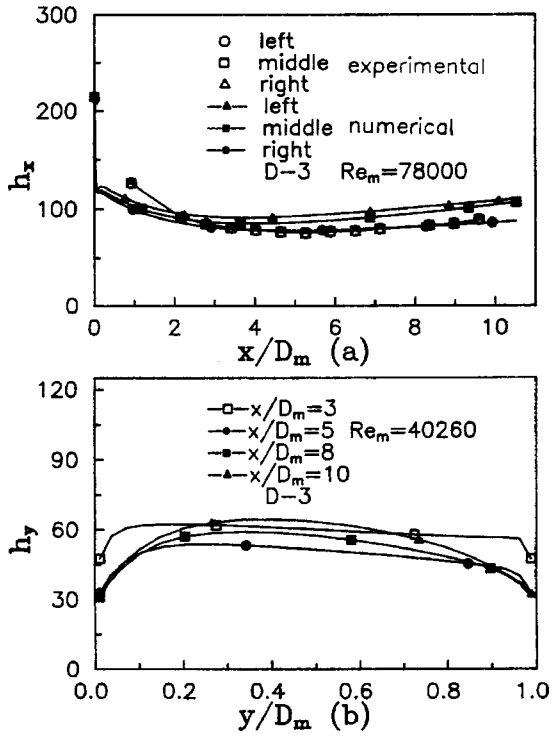

Fig. 10 Numerically predicted local heat transfer coefficient (*D*-3)

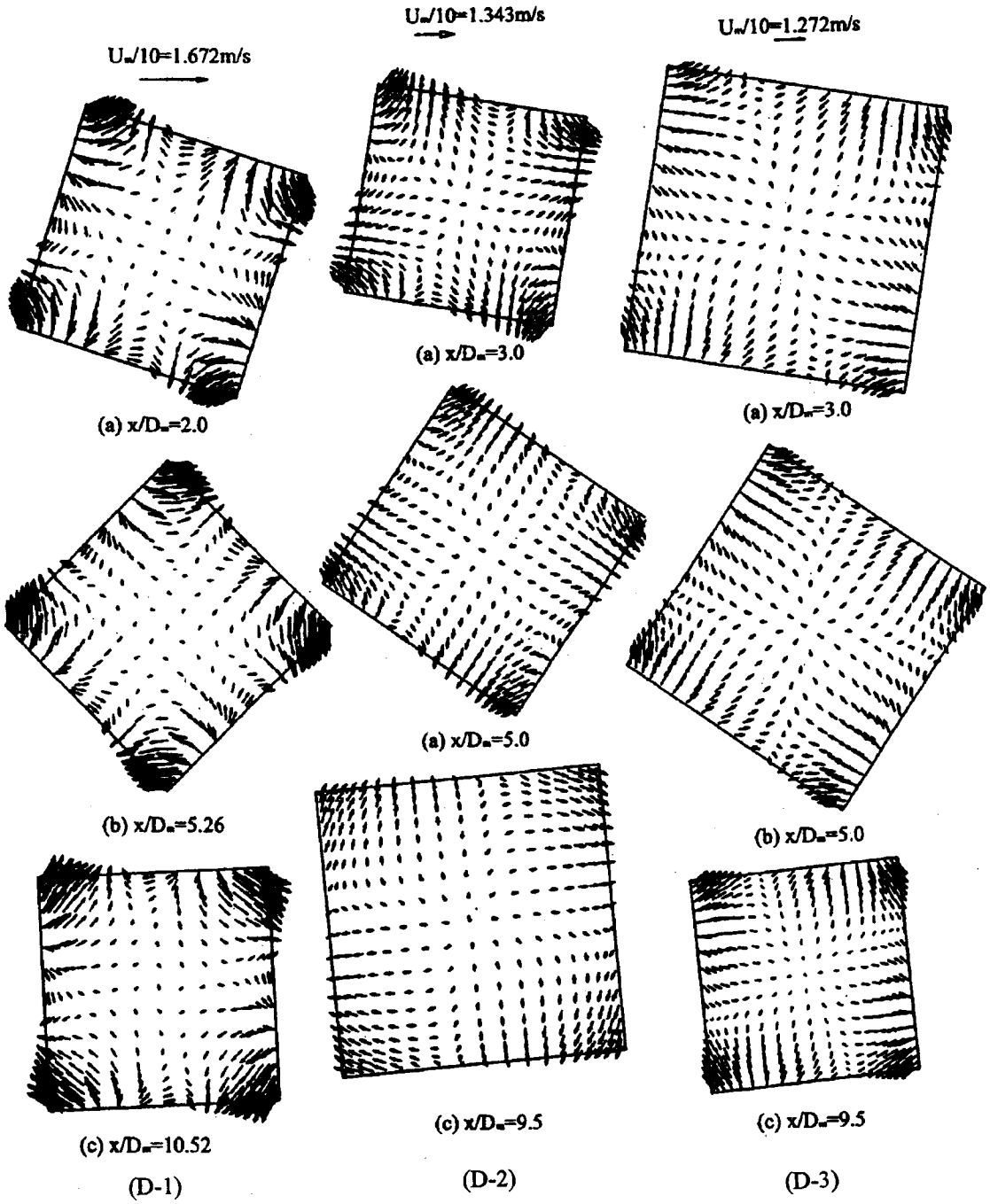

Fig. 11 Cross section velocity fields

with the increase in x/D_m, while when x/D_m increases to a certain value, h_x reaches its minimum and then it increases with x/D_m. A careful inspection of the figure finds that in the upstream region, the rate of h_x decrease in the convergent duct (D3) is faster than that of the other two ducts, while in the downstream region the increase of h_x in D3 is very mild. It seems that the acceleration effect of the convergent duct on heat transfer appear to be stronger over the entry region than that over the downstream region. Overall speaking, the acceleration effect of the convergent duct causes some reduction in the heat transfer rate. It should be noted that in the three figures, the heat transfer measurement data of the last and next to last stations all have a trend to increase. This is expected from the end heat loss, which makes the wall temperatures nearby decrease in some extent. The guide-heating method should have been adopted to alleviate such phenomenon. To be objective, the data of the last two stations are still retained in the pictures.

From Fig. 6 it can be seen that there is some minor difference between the local heat transfer coefficients at the three lines where thermocouples were imbedded. This difference can be recognized from the results of D-2. As shown in Fig. 6(*a*), h_x of the left line is a bit lower than that of the center and right line. The minor difference between the local heat transfer coefficients at the three lines is related to the twisted direction of the duct. Seeing along the flow direction, if the duct is twisted clockwise, the h_x at line in the right side of the centerline is a bit lower than that along left side line. Such variations trend can also be observed in Figs. 8, 9, 10.

From Fig. 7, it can be observed that the variation patterns of the

local pressure recovery factors for the three ducts are very different. For uniform cross-section twisted duct, the pressure drop is induced mainly by skin friction, hence the variation of C_p exhibits some characters of developing flow in duct with constant cross section (Fig. 7(*b*)). But for the divergent and convergent ducts, apart from the skin friction, the variation of the cross section contributes to the pressure drop significantly. In the divergent duct, the dynamic pressure of fluid is converted to the static pressure along the flow direction, while in the convergent duct, the static pressure is converted to the dynamic pressure of fluid. The going-upward and going-downward trends of C_p curves of D-2 (Fig. 7(*a*)) and D-3 (Fig. 7(*c*)), respectively, are mainly determined by different conversions between static and dynamic pressure.

Attention is now turned to the numerical results. The predicted local heat transfer coefficients for the three ducts are presented in Figs. 8–10. In each of the three figures, the top panels are the local heat transfer coefficients at the three lines. The experimental results are also shown there for comparison purpose. Generally speaking, the agreement between the numerical predictions and test data are satisfactory, with the most severe discrepancy occurs at the very beginning of the duct inlet. This discrepancy may be partly attributed to the uniform inlet velocity condition adopted in the numerical simulation. The bottom panels of Figs. 8, 9, 10 provide the spanwise distribution of the local heat transfer coefficients at the different axial cross section, where the difference between h_x along left, centerline, right side can be clearly observed. It should be noted that at the corners of ducts, the local heat transfer coefficient is significantly lower than that of the other part of the wall. If the walls of the corner region are excluded, the h_y decreases with increase in y/D_m because of the twist of ducts.

Secondary Flow at Cross Section. Figure 11 shows the cross section velocity fields at three cross sections of the three ducts. It can be seen that in the corner regions, there exist appreciable secondary flow. These secondary flows all exhibit the same pattern: departing from one wall, arriving at the other of the same corner and leaving a small region very close to the corner where the fluid flow is almost retarded. The spanwise variation trend of the local heat transfer coefficient may be attributed to such kind of secondary flow pattern. In the central part of any cross section, this secondary flow is very weak and can not be observed clearly. It is to be noted that at each cross section a global clockwise swirling flow can be observed, of which the secondary flows in the four corners constitute the major part. This is, of course, caused by the twisting of the duct even though the dimensionless twisted parameter is as large as 42. Obviously, when this parameter approaches infinite, the duct becomes a straight one. This twisting flow has some effect on the heat transfer, which will be shown in the later discussion on performance comparison.

Average Characteristics. The duct average Nusselt number based on the centerline measurement and friction factor of the three ducts obtained by experiments are presented in Fig. 12. The Dittus-Boelter equation is also presented for comparison. From Fig. 12(*a*) it can be clearly observed that among the three ducts, divergent duct (D-2) can enhance heat transfer, while the convergent duct (D-3) deteriorates the heat transfer in some extent. It is generally believed that this behavior of divergent and convergent ducts may be attributed to the relative thickness of thermal boundary layer over the velocity boundary layer. In the convergent duct, the axial acceleration reduces the thickness of the velocity boundary layer, hence the thermal boundary layer becomes relatively thicker. While in the divergent duct, the deceleration leads to a relatively thinner thermal boundary layer, which is in favor of enhancing convective heat transfer. Another possible explanation is related to the secondary flows. It may be observed from Fig. 11 that the secondary flow in the downstream part of the convergent duct is restrained in some extent compared to divergent duct, leading to some deterioration of heat transfer.

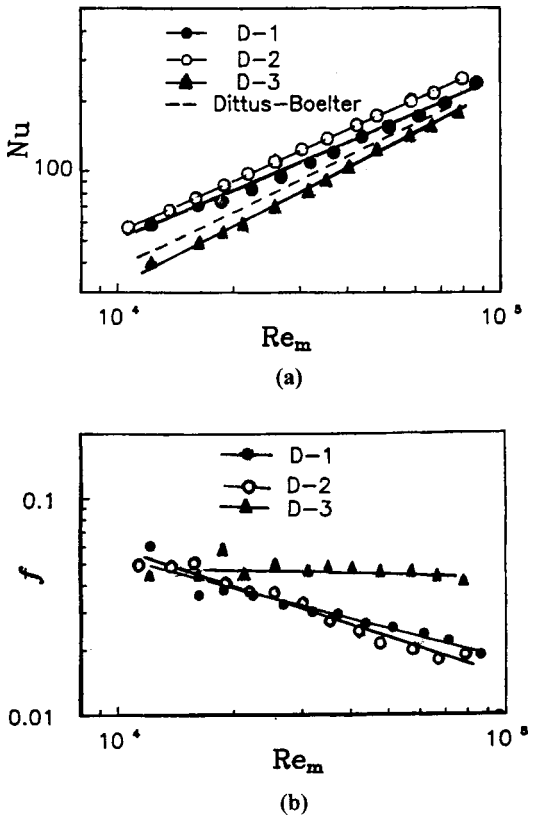

Fig. 12 Experimental results of average Nusselt number and friction factor

The friction factors of the three ducts are shown in Fig. 12(*b*). For the twisted uniform cross section duct and twisted divergent duct, the values of *f* decrease with the increase in Reynolds number, with the decrease of the divergent duct being a bit more significant. For the convergent duct, however, there seems no appreciable decrease of the friction factor with the Reynolds number. It's worth noting that in the definition of the friction factor, the static pressure variation caused by the non-uniformity of the cross sectional area has been excluded. The main reason account for these results may be attributed to the different effects of the acceleration and deceleration of flow on the skin friction. In the divergent duct, the flow velocity decreases along the flow direction, so the skin friction decreases accordingly. In the convergent duct, the flow velocity increases along the flow direction, so does the skin friction.

The predicted results of the duct average Nusselt number and the centerline average Nusselt number are shown in the Figs. 13(*a*), (*b*), (*c*), and the predicted friction factors are shown in the Figs. 13(*d*), (*e*), (*f*). The test data of centerline average Nusselt number and the friction factor are also provided for comparison. It can be seen that the numerical results of the centerline average Nusselt number agree with the experimental results quite satisfactory. And there also is a reasonably good agreement between the numerical and experimental friction factors. As expected, the duct average Nusselt number is less than the centerline average Nusselt number for all three ducts because of the corner effect.

Performance Comparison. Attention is now turned to the relative performance of the different twisted ducts with the straight untwisted square duct as a reference. The three widely used constraints are adopted: identical flow rate, identical pumping power, and identical pressure drop based on the constant property assumption and the same characteristic length, the formulations of the three constraints are given in the following:

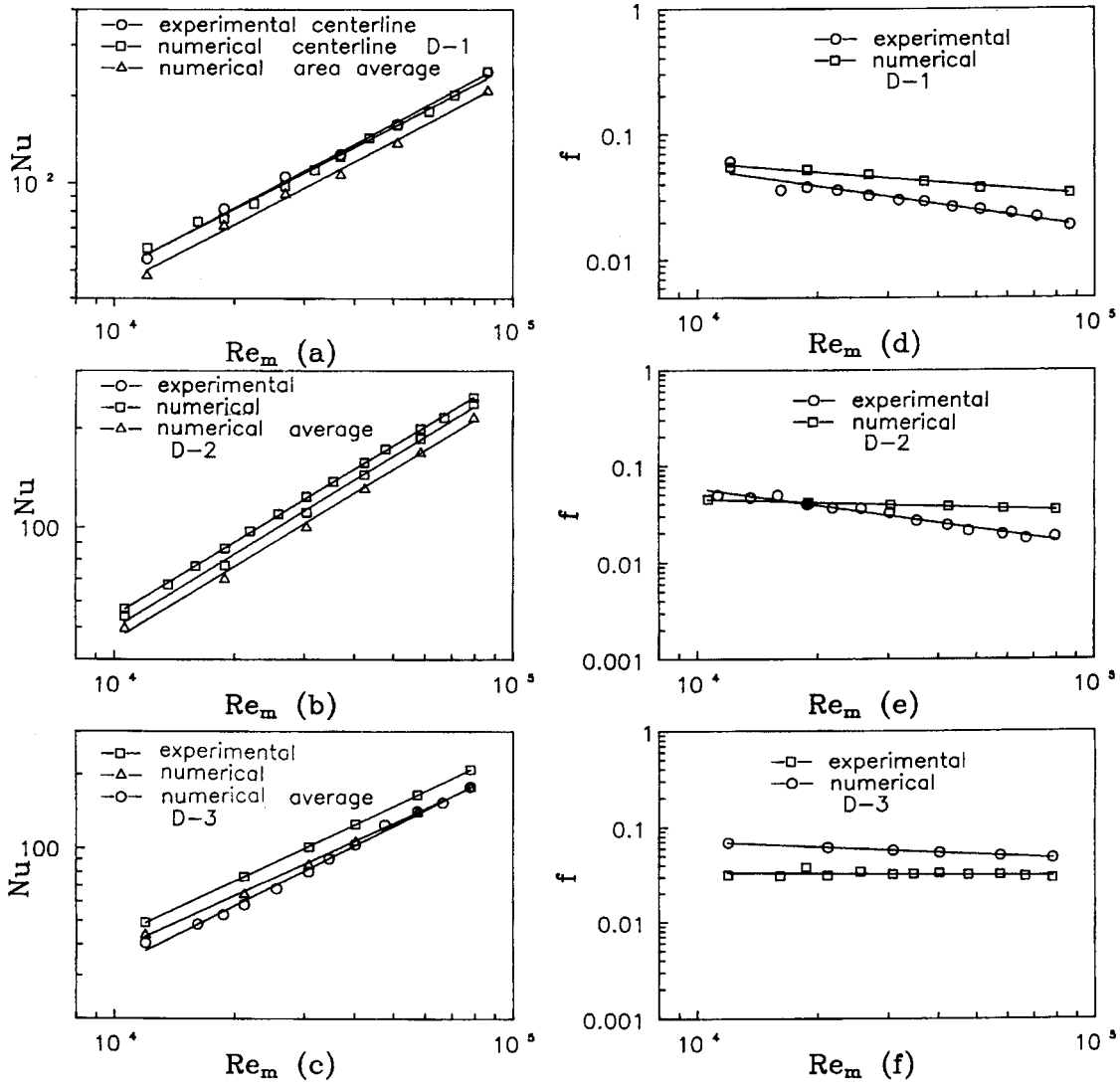

Fig. 13 Numerical results of average Nusselt number and friction factor

(a) Identical Mass Flow Rate

$$(\dot{m})^* = \dot{m}, \tag{20a}$$

where the superscript $*$ stands for the compared duct and the quantity without* for the referenced duct. From Eq. (20*a*) we can obtain following relationship between the Reynolds number of the duct compared and the reference duct:

$$\mathrm{Re}_m^* = \mathrm{Re}_m D_m^*/D_m\,. \tag{20b}$$

(b) Identical Pumping Power

$$\left(\frac{\dot{m}}{\rho}\Delta p\right)^* = \left(\frac{\dot{m}}{\rho}\Delta p\right). \tag{21a}$$

This leads to

$$\mathrm{Re}_m^* = \sqrt[3]{\frac{Af\,\mathrm{Re}_m^3}{(Af)^*}}. \tag{21b}$$

(c) Identical Pressure Drop

$$(fu^2)^* = fu^2. \tag{22a}$$

Then we have

$$\mathrm{Re}_m^* = \mathrm{Re}_m\sqrt{f/f^*}. \tag{22b}$$

Under the condition of same temperature difference between the fluid and the wall, the ratio of heat transfer between the compared duct and the reference duct may be formulated as follows:

$$\frac{Q^*}{Q} = \frac{[A\mathrm{Nu}(\mathrm{Re}_m)]^*}{A\mathrm{Nu}(\mathrm{Re}_m)}, \tag{23}$$

where $\mathrm{Nu}(\mathrm{Re}_m)$ represents the experimental correlation between Nusselt number and the Reynolds number, which are presented in Fig. 12.

The comparison results of the three twisted ducts to straight untwisted square duct (reference duct) are shown in Fig. 14. It can be seen from Fig. 14(*a*) that for $\mathrm{Re}_m = 2\times10^4$, the heat transfer enhancement is about 8 percent, 25 percent, −20 percent for the twisted square duct, twisted divergent duct and twisted convergent duct, respectively. Figure 14(*b*) shows that for the identical pumping power, at the same Reynolds number the heat transfer enhancement is about 0 percent, 15 percent, −25 percent for the above three twisted ducts, respectively. For the identical pressure drop, Fig. 14(*c*) shows that the heat transfer enhancement of the three ducts is about −5 percent, 5 percent, −27 percent, respectively. Totally speaking, the heat transfer in the divergent duct is always superior to the untwisted square duct, the heat transfer in the convergent duct is inferior to the untwisted square duct, while

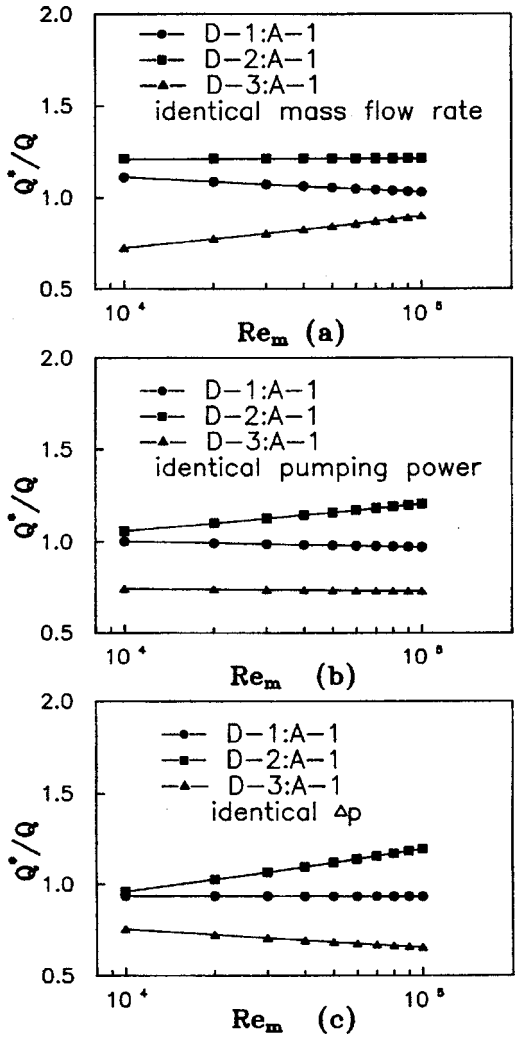

Fig. 14 Heat transfer performance comparison

the twisted square duct with constant cross section may be superior or inferior to the untwisted square duct depending on the comparison condition.

Conclusions

The work reported here is a systematic experimental and numerical study of three twisted square ducts with uniform cross section area, divergent and convergent shape. The dimensionless twisted parameter equals 42. Experiments are conducted for air with uniform heal flux condition. Measurements were also performed for an untwisted square duct with constant cross section for comparison. In the numerical study three-dimensional and fully elliptic turbulent flow and heat transfer are modelled by using the body-fitted finite volume method and the standard $k-\varepsilon$ model. The local heat transfer coefficient and pressure recovery factor distribution, the average Nusselt number and friction factor are presented. Generally speaking, the agreement between the numerically predicted and the experimental results is quite satisfactory, except for the local heat transfer character at the very beginning of the ducts where appreciable discrepancy exists partly because of the inlet condition might not be simulated appropriately. The heat transfer performance comparison is made between a straight untwisted square duct and the three twisted ducts based on the test data. The major findings may be summarized as follows:

1 Because of the decelerating and accelerating effects in the divergent and convergent ducts, the axial variation of the local heat transfer coefficients of the three twisted ducts are different: in the entrance region the decrease in local heat transfer coefficient of the constant cross section duct is faster than that of the divergent duct but slower than convergent; in the downstream region, the local heat transfer coefficient of the divergent dust exhibits an increasing trend, while for the other two ducts this trend is not be observed.

2 The twisting of duct causes an appreciable secondary flow in the corner regions at any cross section. While in the center part of a cross section this secondary flow is trivial. A global clockwise swirling flow is revealed by numerical simulation, of which the secondary flows in the corner region constitute the major part. The character of the spanwise distribution of the local heat transfer coefficients presented in Figs. 8(*b*), 9(*b*), and 10(*b*) may be attributed to this global swirling flow structure.

3 Thermal performance comparison under three constraints (identical mass flow rate, pumping power and pressure drop) with the straight duct as a reference reveals that the divergent twisted duct can always enhance heat transfer, the convergent duct always deteriorate heat transfer, while the twisted duct with uniform cross section may enhance or deteriorate heat transfer depending on the comparison condition: for the identical mass flow rate, it can enhance heat transfer, while for the identical pumping power and identical pressure drop it can not enhance, or even deteriorate heat transfer a bit. The physical mechanism which may be responsible for such character is discussed.

Acknowledgment

This work was supported by the National Key Laboratory of Air-Craft Engine at Beijing Aeronautical and Aerospace University and the National Key Project of Fundamental R & D of China (Grant No. G20000263030).

Nomenclature

A = area, m^2
A_x = partial surface area of the duct, m^2
c_p = heat capacity, J/kg·K
C_p = pressure recover factor
D = hydraulic diameter, m
f = friction factor
h = heat transfer coefficient, $W/m^2 K$
k = thermal conductivity, W/m·K; Kinetic energy of turbulence
L = axial length of duct, m
$\dot{m}$ = mass flow rate, kg/s
Nu = Nusselt number
p = pressure, Pa
Δp = pressure drop, Pa
Q = heat transfer rated, W
Q_{loss} = heat loss to the environment, W
Re_m = Reynolds number based on D_m
T = temperature, K
u_i, u_j = velocity fluctuation, m/s
U = cross section average axial velocity, m/s
x = streamwise direction, m
y, z = cross section coordinates, m
ρ = fluid density, kg/m^3
ε = dissipation rate
θ = temperature fluctuation, °C

Subscripts

b = bulk
in = inlet
m = mean
out = outlet
x = local
w = wall

References

[1] Manglik, R. M., and Bergles, A. E., 1993, ''Heat Transfer and Pressure Drop Correction for Twisted-Tape Inserts in Isothermal Tubes: Part I—Laminar Flow,'' ASME J. Heat Transfer, **115**, pp. 881–889.

[2] Manglik, R. M., and Bergles, A. E., 1993, ''Heat Transfer and Pressure Drop Correction for Twisted-Tape Inserts in Isothermal Tubes: Part II—Turbulent Flow,'' ASME J. Heat Transfer, **115**, pp. 890–896.

[3] Yampolsky, J. S., 1983, ''Spirally Fluted Tubing for Enhanced Heat Transfer,'' *Heat Exchangers—Theory and Practice*, J. Taborek, G. F. Hewitte, G., Afgan, eds. Hemisphere, Washington, D. C., pp. 945–952.

[4] Obot, N. T., Esen, E. B., Snell, K. H., Rabas, T. J., 1991, ''Pressure Drop and Heat Transfer for Spirally Fluted Tubes Including Validation of the Roles of Transition,'' in ASME HTD-**164**, T. J. Rabas, J. M. Chenoweth, eds., New York, pp. 85–92.

[5] Gau, C., and Chen, H. R., 1998, ''Enhancement of Heat Transfer With Swirling Flows Issued Into a Divergent Pipe,'' J. Thermophys. Heat Transfer, **12**, pp. 87–93.

[6] Han, J. C., Zhang, Y. M., Lee, C. P., 1991, ''Augmented Heat Transfer in Square Channels With Parallel, Crosses, and V-Shaped Angled Ribs,'' ASME J. Heat Transfer, **113**, pp. 590–596.

[7] Todd, L., 1977, ''Some Comments on Steady, Laminar Flow Through Twisted Pipes,'' J. Eng. Math., **11**, pp. 29–48.

[8] Masliyah, J. H., and Nandakumar, K., 1981, ''Steady Laminar Flow Through Twisted Pipes: Fluid Flow in Square Tubes,'' ASME J. Heat Transfer, **103**, pp. 785–790.

[9] Masliyah, J. H., and Nandakumar, K., 1981, ''Steady Laminar Flow Through Twisted Pipes: Heat Transfer in Square Tubes,'' ASME J. Heat Transfer, **103**, pp. 791–796.

[10] Xu, C. G., Fan, D. N., 1984, ''Discussion—Steady Laminar Flow Through Twisted Pipes: Fluid Flow in Square Tubes and Steady Laminar Flow Through Twisted Pipes: Heat Transfer in Square Tubes,'' ASME J. Heat Transfer, **106**, pp. 480–488.

[11] Xu, C. G., and Fan, D. N., 1986, ''Some Remarks on the Helical-Cartesian Coordinates System and Its Applications,'' ASME J. Heat Transfer, **108**, pp. 483–486.

[12] Miller, R. W., 1996, *Flow Measurement Engineering Handbook*, 3rd ed., McGraw-Hill, New York.

[13] Wang, L. B., 1996, ''Experimental and Numerical Study of Turbulent Fluid Flow and Heat Transfer in Sectionally Complex and Twisted Ducts,'' Ph.D. thesis, Xi'an Jiaotong University, Xi'an, China.

[14] Kline, S. J., and McClintock, F. A., 1953, ''Describing Uncertainties in Single-Sample Experiments,'' Mech. Eng. (Am. Soc. Mech. Eng.), **75**, pp. 3–8.

[15] Moffat, R. J., 1988, ''Describing the Uncertainties in Experimental Results,'' Exp. Therm. Fluid Sci., **1**, pp. 3–17.

[16] Launder, B. E., and Spalding, D. B., 1974, ''The Numerical Computation of Turbulent Flows,'' Comput. Methods in Applied Mechanics and Engineering, **3**, pp. 269–289.

[17] Tao, W. Q., 1988, *Numerical Heat Transfer*, Xi'an Jiaotong University Press, Xi'an, China.

[18] Patankar, S. V., 1980, *Numerical Heat Transfer and Fluid Flow*, Hemisphere Publishing Co., New York, pp. 95–96.

[19] Eiseman, P. R., 1979, ''A Multi-Surface Method of Coordinate Generation,'' J. Comput. Phys., **33**, pp. 118–150.

[20] Eiseman, P. R., 1982, ''Coordinate Generation With Precise Controls of Mesh Properties,'' J. Comput. Phys., **47**, pp. 330–351.

[21] Eiseman, P. R., 1982, ''High Level Continuity for Coordinate Generation With Precise Controls,'' J. Comput. Phys., **47**, pp. 352–374.

[22] Rhie, C. M., and Chow, W. L., 1983, ''Numerical Study of the Turbulent Flow Past an Airfoil With Trailing Edge Separation,'' AIAA J., **21**, pp. 1525–1532.

[23] Melaaen, M. C., 1992, ''Analysis of Fluid Flow in Constructed Tubes and Ducts Using Body-Fitted Non-Staggered Grids,'' Int. J. Numer. Methods Fluids, **15**, pp. 895–923.

Michael J. Barrett
Asst. Professor
Mem. ASME
Valparaiso University,
Mechanical Engineering Department,
Valparaiso, IN 46383
e-mail: Michael.Barrett@valpo.edu

D. Keith Hollingsworth
Assoc. Professor
Mem. ASME
University of Houston,
Department of Mechanical Engineering,
Houston, TX 77204
e-mail: Hollingsworth@uh.edu

On the Calculation of Length Scales for Turbulent Heat Transfer Correlation

Turbulence length scale calculation methods were critically reviewed for their usefulness in boundary layer heat transfer correlations. Using the variance of the streamwise velocity and the dissipation spectrum, a rigorous method for calculating an energy-based integral scale was introduced. A principal advantage of the new method is the capability to calculate length scales in a low-Reynolds-number turbulent boundary layer. The method was validated with data from grid-generated, free-shear-layer, and wall-bounded turbulence. Length scales were calculated in turbulent boundary layers with momentum thickness Reynolds numbers from 400 to 2100 and in flows with turbulent Reynolds numbers as low as 90. [DOI: 10.1115/1.1391277]

Keywords: Heat Transfer, Turbulence

Introduction

The study of the effects of elevated free-stream turbulence on boundary layer heat transfer requires that the turbulence in the free-stream and in the boundary layer be adequately characterized. When attempting to describe a turbulent flow, a minimal set of descriptors to characterize the turbulence must include a velocity and a length scale (or parameters that yield the equivalent dimensional information). In many cases these two scales alone are inadequate; however, any attempt that does not include at least these two scales is incomplete.

A review of the literature reveals a plenitude of length scale definitions. Restricting our survey to heat transfer in turbulent boundary layers, we still find more than ten different length scales in use. In some instances, the interpretation of two scales is similar but distinct calculation methods distinguish one scale from another. In this paper we critically examine five length scales commonly used in turbulent boundary layer heat transfer correlations. We then introduce a rigorous method for calculating an energy-based scale; advantages and disadvantages of the new calculation method are discussed. Experimental data is used to clarify the guidelines and performance traits for the new method. Based on the versatility of the new calculation method, the consistent behavior and physical significance of the resulting scale, and the detail to which the calculation is defined, the method is proposed as a standard for future correlative works.

Review of Existing Scale Definitions

The five scales chosen for review are all integral scales. In that sense, the scales are related to the largest eddies or the width of a shear flow [1]. The first three scales are closely related to the Eulerian integral scale, Λ_f, which, when Taylor's hypothesis holds, is given by Hinze [2] as

$$\Lambda_f = UT_{11}, \tag{1}$$

where U is the time-mean Eulerian velocity in the principal flow direction and T_{11} is the Eulerian integral time scale. The time scale, T_{11}, is found by integrating the Eulerian autocorrelation coefficient,

$$T_{11} = \int_0^\infty R_{11} dt. \tag{2}$$

This length scale, Λ_f, may be interpreted as a measure of the longest correlation distance between the velocities at two points in the flow field [2].

The first scale for review is frequently used in the gas turbine literature and is given by

$$\Lambda_I = U \int_0^\infty R_{11,\ \text{measured}}\ dt. \tag{3}$$

Young et al. [3], Van Fossen et al. [4], Camp and Shin [5], and Moss and Oldfield [6] are just a few of the authors that use this scale. (Additional studies are listed in Table 1.) Authors often terminate the correlation coefficient integration at the first zero crossing.

The next two scales are based on von Karman's turbulence spectrum [2],

$$UE_1\{f\}/(\Lambda_f u'^2) = 4[1 + (8\pi f \Lambda_f/3U)^2]^{-5/6}, \tag{4}$$

where f is frequency and $E_1\{f\}$ is the power spectral density of the streamwise fluctuating component, u'. The term $E_1\{f\}$ is also called the one-dimensional energy spectrum. The second scale, Λ_{II}, is calculated by curve fitting a measured energy spectrum to Eq. (4). Hollingsworth and Bourgogne [7] and Maniam and Hollingsworth [8] determine length scales by varying Λ_{II} until a best fit to a measured spectrum is found. The third scale, Λ_{III}, is found by extrapolating a measured spectrum to its zero frequency value and applying Eq. (4) at f equals zero,

$$\Lambda_{III} = UE_1\{0\}/4u'^2. \tag{5}$$

Authors that use this scale include Thole et al. [9] and Johnson and Johnston [10]. The Λ_{III} scale relies heavily on low frequency (low wave number) information.

The final two scales for review are termed "energy scales" because the definitions are related to the dissipation of turbulent kinetic energy, ϵ. In each case, there exists an underlying tie to the inviscid decay relation,

$$\epsilon \sim (u'^2)^{3/2}/L. \tag{6}$$

Each scale may be interpreted as an average length scale for the energy-containing eddies. The first of these two scales was given by Simonich and Bradshaw [11] as

Contributed by the Heat Transfer Division for publication in the JOURNAL OF HEAT TRANSFER. Manuscript received by the Heat Transfer Division January 26, 2000; revision received December 18, 2000. Associate Editor: R. L. Mahajan.

Table 1 Length scales used in example studies

Study	Λ_I	Λ_{II}	Λ_{III}	L_I	L_{II}
Simonich and Bradshaw [11]				•	
Blair [16]				•	
Hancock and Bradshaw [19]				•	
Castro [18]				•	
Hancock and Bradshaw [17]				•	
Johnson and Johnston [10]			•	•	
Ames and Moffat [12]	•				•
Sahm and Moffat [20]	•				•
Young, et al. [3]	•				
Thole, et al. [9]	•		•	•	
Hollingsworth and Bourgogne [7]		•			
Camp and Shin [5]	•				
Ames and Plesniak [21]	•				•
Thole and Bogard [22]	•		•	•	
Van Fossen, et al. [4]	•				
Thole and Bogard [23]	•		•	•	
Moss and Oldfield [6]	•				
Ames [24]	•				•
Bott and Bradshaw [25]				•	
Maniam and Hollingsworth [8]		•			

$$L_I = -(u'^2)^{3/2}/U \frac{d(u'^2)}{dx}. \quad (7)$$

The streamwise decay of u'^2 is directly related to the dissipation rate when, in a time-averaged sense, isotropic turbulence is uniformly advected downstream. Simonich and Bradshaw used Eq. (7) to calculate free-stream length scales downstream of a grid. Numerous authors (Table 1) have since used Eq. (7) to calculate free-stream length scales in decaying flows.

Our final scale for review was given by Ames and Moffat [12],

$$L_{II} = 1.5u'^3/\epsilon. \quad (8)$$

To estimate ϵ, Ames and Moffat fit the inertial subrange of a measured energy spectrum to the equation

$$E_1\{k_1\} = \frac{18}{55} A \epsilon^{2/3} k_1^{-5/3}. \quad (9)$$

Equation (9) results if the three-dimensional energy spectrum is modeled with a power-law relationship in the inertial subrange [2]. Ames and Moffat used a value of 1.62 for the constant A.

Summary of Merits and Deficiencies in Existing Scale Definitions

This summary is not an exhaustive discussion of the benefits or detriments of using the scales listed. This comparison highlights some general attributes of the conceptual and practical implications of using each scale. Attributes of the scales are summarized in Table 2. A merit common to these five scales is that they are all calculated using the streamwise fluctuating velocity, u': the fluctuating component most easily measured in many experiments.

A More Robust Energy Scale

An author may find a certain calculation method advantageous for experiment-specific reasons. However, to simplify the process of comparing results from different heat transfer investigations, a general consensus on a standardized calculation method would be useful. With a standardized method, in addition to any other length scales presented, authors could include the standardized scale values to reduce data comparison ambiguity.

When selecting a standard calculation method, we search for the following traits: versatility (ease of use in a number of different flows), historical concordance (results that are comparable with previously reported data), and clarity (process definition with enough detail to provide repeatability between investigators). With these criteria in mind, of the five scales reviewed, L_{II} holds the most promise as a standardized scale for the following reasons:

- the calculation requires information from only a single point in the flow field
- conceptually, the scale may be used in flows with mean velocity gradients if specific concerns related to Taylor's hypothesis are addressed
- the L_{II} scale is directly comparable with L_I which is widely used in the heat transfer literature

Table 2 Summary of merits and deficiencies of five length scale calculation methods

Scale	Merits	Deficiencies
Λ_I	Directly calculable from the autocorrelation curve. Does not rely on assumptions leading to a universal spectral curve. Directly relatable to dissipation of turbulent kinetic energy using isotropic assumptions and relationship between autocorrelation and spectrum.	Termination of integration can yield incorrect values; different flows can generate differently behaving and meaningful negative tails on the autocorrelation curve.
Λ_{II}	Simplicity of calculation. At large Reynolds numbers, results usually compare well with Λ_I values.	No rigorous/standardized "best fit" criteria; variation introduced between investigators. Up to +/-20% variation can still yield visually pleasing curve fits for moderate turbulence Reynolds numbers. Well-defined inertial subrange needed in measured spectrum to provide fitting capability over a wide range of wave numbers.
Λ_{III}	Simplicity of calculation.	Relies heavily on accurate extrapolation of low wave number portion of the measured spectrum. Low wave number range most sensitive to anisotropic effects. Also, because high sample rates are needed to obtain unaliased spectra and convergence of the low wave number range requires long sample times, large data file requirements accompany the proper use of this calculation method. (Of course, appropriate filtering techniques can reduce the file size requirements.)
L_I	Spectral information not required. Isotropic decay correlations may be used to verify downstream flow behavior. Easily related to dissipation of turbulent kinetic energy.	This scale cannot be used in any part of the flow where a production component is present (i.e., it cannot be used if a mean velocity gradient exists; this precludes its use within the boundary layer). It also cannot be calculated with information from only a single point in the flow field. Different techniques used to estimate the "measured" decay rate yield significantly different results.
L_{II}	Direct relationship to the dissipation of turbulent kinetic energy. Does not require information from multiple points in the flow field. Potential for use in flow field with mean velocity gradient. Equivalence with L_I for large Reynolds number flows in which L_I can be calculated.	No rigorous/standardized "best fit" criteria; variation introduced between investigators. Curve fit requires well-defined inertial subrange (large Re_t). While this scale may be useful in flows with a mean gradient, differences in local convection velocities that lead to spatial aliasing have not previously been addressed in the heat transfer literature.

In the remainder of this paper, we introduce and discuss a more robust energy scale calculation method that is based on L_{II}. The method is rigorously defined, lowers the turbulent Reynolds number at which the scale is calculable, and imposes limits that enable the scale to be confidently determined for flows with mean velocity gradients. While our scale is conceptually the same as L_{II}, to distinguish it from the other calculation methods, we call the scale L_e.

Background. From Tennekes and Lumley [1] we have, for isotropic turbulence,

$$\epsilon = \int_0^\infty D\{k_1\} dk_1, \tag{10}$$

where the dissipation spectrum is given by

$$D\{k_1\} = 2\nu k_1^2 E\{k_1\}. \tag{11}$$

Hinze [2] relates the three-dimensional energy spectrum to the one-dimensional spectrum,

$$E\{k_1\} = \frac{1}{2} k_1^2 \frac{d^2 E_1\{k_1\}}{dk_1^2} - \frac{1}{2} k_1 \frac{dE_1\{k_1\}}{dk_1} \tag{12}$$

so that we can generate the familiar result,

$$\epsilon = 15\nu \int_0^\infty k_1^2 E_1\{k_1\} dk_1. \tag{13}$$

Addressing time spectra measured in shear flows, Lumley [13] argues that, despite the mean shear, the trend toward isotropy in the dissipation range (the wave number range where most of the dissipation occurs) is very strong. We suspect that an isotropic estimate of ϵ obtained by integrating a measured dissipation spectrum may yield good results even in flows with mean velocity gradients. Lumley distinguishes between $E_1\{k_1\}$ and $E_1\{k_1\}_m$ (the subscript "m" refers to the measured spectra) because of "space" versus "time" spectra issues (issues that are related to the validity of Taylor's hypothesis and are presented later). Lumley gives a correction scheme for the high-wave-number region of the measured spectra in terms of the local fluctuating velocities,

$$E_1\{k_1\}_m = E_1\{k_1\} + \frac{Tu^2}{2}\left[\left(k_1^2 \frac{d^2 E_1\{k_1\}}{dk_1^2} - 2E_1\{k_1\}\right) - 2\left(k_1 \frac{dE_1\{k_1\}}{dk_1} + E\{k_1\}\right)\left(\frac{(v'^2 + w'^2)}{u'^2} - 2\right)\right]. \tag{14}$$

We substitute the solution to Eq. (12) [2],

$$E_1\{k_1\} = \int_{k_1}^\infty \frac{E\{k\}}{k}\left[1 - \left(\frac{k_1}{k}\right)^2\right] dk \tag{15}$$

into Eq. (14) and twice invoke Leibniz's rule to write

$$E_1\{k_1\}_m = \left(1 - Tu^2\left[1 + \left(\frac{v'}{u'}\right)^2 + \left(\frac{w'}{u'}\right)^2 - 2\right]\right) E_1\{k_1\} + Tu^2 E\{k_1\} + 2Tu^2\left[\left(\frac{v'}{u'}\right)^2 + \left(\frac{w'}{u'}\right)^2 - 2.5\right] k_1^2 \int_{k_1}^\infty \frac{E\{k\}}{k^3} dk. \tag{16}$$

Equation (16) assumes that the convect*ed* field is isotropic, but allows for anisotropy of the convect*ing* field. When the convecting field is also isotropic, Eq. (16) reduces to

$$E_1\{k_1\}_m = (1 - Tu^2) E_1\{k_1\} + Tu^2 E\{k_1\} - Tu^2 k_1^2 \int_{k_1}^\infty \frac{E\{k\}}{k^3} dk \tag{17}$$

illustrating that the measured one-dimensional spectrum is dependent on the local turbulence intensity as well as the form of the three-dimensional spectrum.

With Eqs. (10), (11), (12), and (17), Lumley shows that, for the isotropic convecting field, the resulting adjustment for a measured dissipation rate is given by

$$\epsilon = \epsilon_m / (1 + 5Tu^2). \tag{18}$$

Using Eq. (16) in the same manner, we find that the correction for the more general anisotropic case is

$$\epsilon = \epsilon_m (1 + Tu^2[1 + 2(v'/u')^2 + 2(w'/u')^2])^{-1}. \tag{19}$$

With a theoretical model of $E\{k_1\}$, Eqs. (15) and (16) allow us to predict the measured spectrum, $E_1\{k_1\}_m$, for a specified value of the local intensity. In this work the theoretical spectrum chosen was that of Panchev and Kesich as reported by Hinze [2] (p. 241).

Lumley [13] also gives criteria that can be used to determine when the spectral correction is valid; the energy distribution, mean velocity, and mean velocity gradient will determine the wave number range over which the correction may be applied. The pertinent relationships are given as

1 $k_1 \gg 2\pi (dU/dy)/U$ (to address convection velocity nonuniformity)
2 $E_1\{k_1\} \gg (2\pi^2/3)[(dU/dy)^2/U^2] d^2 E_1\{k_1\}/dk_1^2$ (considering spectral broadening)
3 $E_1\{k_1\} \ll\ll U^2/k_1$ (to verify a frozen convected pattern)
4 $E_1\{k_1\} \gg\gg 4\pi^2 (dU/dy)^2/k_1^3$ (negligible anisotropy due to mean shear)

Lumley recommends that the inequalities, $\gg$, be interpreted as a factor of three difference. However, using Reynolds stress spectra to support his position, he argues that the tendency toward isotropy is so strong in the high wave number range that weakening criterion four to simply exceeding equality will likely be satisfactory. We therefore adopt $E_1\{k_1\} \geqslant 4\pi^2 (dU/dy)^2/k_1^3$ as our fourth criterion.

Calculation Method. We now present the calculation method for L_e. The steps are as follows:

1 Measure the one-dimensional spectrum, $E_1\{k_1\}_m$.
2 Calculate ϵ_m using Eq. (13), $\epsilon_m = 15\nu \int_0^\infty k_1^2 E_1\{k_1\}_m dk_1$.
3 Apply Lumley's correction to get ϵ, $\epsilon = \epsilon_m/(1 + 5Tu^2)$ (isotropic case illustrated).
4 Check the agreement between the measured spectrum and the theoretical measured spectrum based on the corrected ϵ.
5 Check the validity of the correction for $k_1\eta > 0.05$ using Lumley's four criteria (η is the Kolmogorov length scale, $(\nu^3/\epsilon)^{1/4}$).
6 If the corrected ϵ is valid based on the checks in steps four and five, calculate L_e using the inviscid decay relation

$$L_e = \frac{3}{2}(u'^2)^{3/2}/\epsilon. \tag{20}$$

An Additional Consideration. There is an additional practical consideration that refines the calculation technique and fosters consistency between investigators. As the measured spectrum will have finite bandwidth, the upper and lower limits of the numerical integration in step two above must be values other than infinity and zero. In practice, for an adequately sampled velocity signal that has been low-pass filtered (i.e., the low wave number attenuation is due only to natural roll-off), substituting the lowest measured wave number for the lower limit is generally acceptable; the excluded portion of the spectrum contributes very little to the overall summation. The upper end of the measured spectrum, however, is highly dependent on sensor response (a function of wire size in hot-wire anemometry), filter cut-off frequency, and signal-to-noise ratio. For this reason it is recommended that the

integration be separated into two integrals. Starting at the lowest measured wave number, the first integral is terminated at a value of $0.2<k_1\eta<1.0$ where the actual and theoretical measured spectra agree to within 10 percent. Adequate sample-rate and sensor response characteristics will be required to meet this agreement constraint. The second integral then uses the theoretical measured spectra to carry the summation out to an upper limit of $k_1\eta=4$. The high-end roll-off of the dissipation spectrum makes integration beyond this value unnecessary.

Admittedly, this consideration increases the complexity of calculating ϵ by introducing an iterative component. However, based on the behavior observed during validation tests of the method, the improvement in sensitivity and consistency merits the added effort. From multiple-record samples of different stationary flows, experimental uncertainty in L_e was determined to be approximately 10 percent.

Advantages and Disadvantages of Using L_e. The new scale possesses the same advantages as L_{II} and overcomes the L_{II} disadvantages in Table 2. The integration method avoids "best fit" uncertainties and allows the calculation to be made at low Reynolds numbers. The low Reynolds number capability of L_e is a significant advantage. With the incorporation of Lumley's results, the scale can be calculated using the valid region of the spectrum despite the presence of a mean velocity gradient. This is a particularly attractive feature because it makes it possible to calculate the scale within a shear layer or boundary layer.

The primary disadvantage of L_e is the need to resolve a significant portion of the dissipation range. At large Reynolds numbers, this requires fast sample rates and very responsive sensors. Under these conditions the investigator may wish to use L_{II} instead. Fortunately, at high Reynolds numbers, there should be a well-defined inertial subrange and L_{II}, combined with Lumley's criteria, may yield useable results. However, by Lumley's criteria a large velocity gradient will invalidate the inertial subrange of the measured spectrum before the dissipation range; thus, the use of L_e may still be necessary.

Experimental Results. Figure 1 shows a measured energy spectrum to illustrate some of the previously addressed calculation issues presented in terms of the dimensional amplitude and nondimensional wave number. The spectrum shown meets all criteria for the range $0.04<k_1\eta<0.7$. The dissipation spectrum for the energy spectrum of Fig. 1 is presented in Fig. 2 to highlight the dissipation range. The high wave number range of dissipation spectra with attenuation due to filter response and elevation due to noise are shown in Fig. 3. In these cases the technique of splitting the integration to obtain ϵ is seen to yield good scaling in the range $0.05<k_1\eta<0.4$ for the attenuated signal and up to $k_1\eta=0.7$ for the noisy signal. This indicates that the integration was unaffected by the altered portion of the spectra and suitable ϵ values were obtained for these flows.

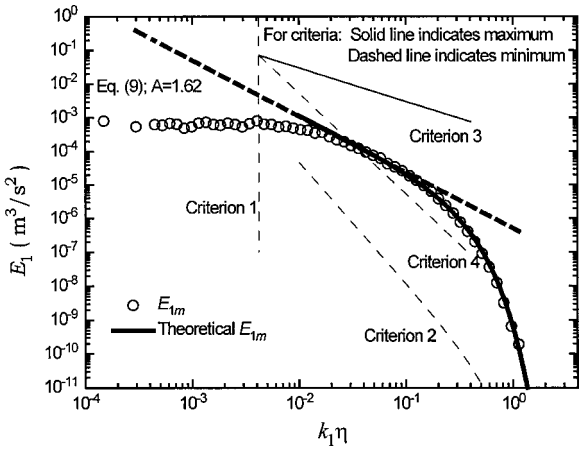

Fig. 1 Typical measured spectra with criteria and theory

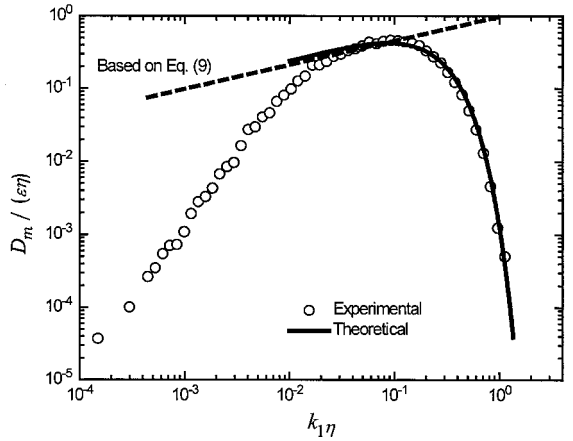

Fig. 2 Experimental and theoretical dissipation spectra

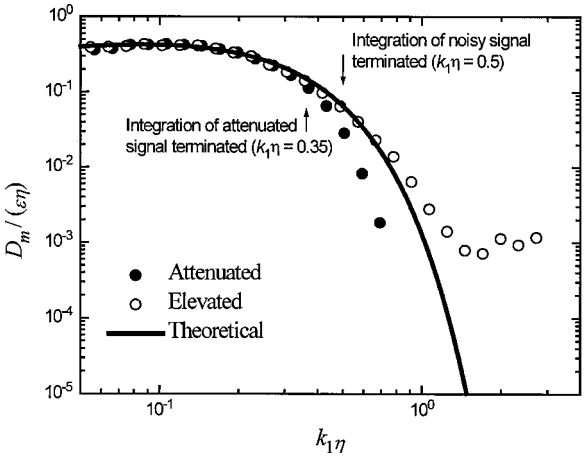

Fig. 3 High-end response characteristics

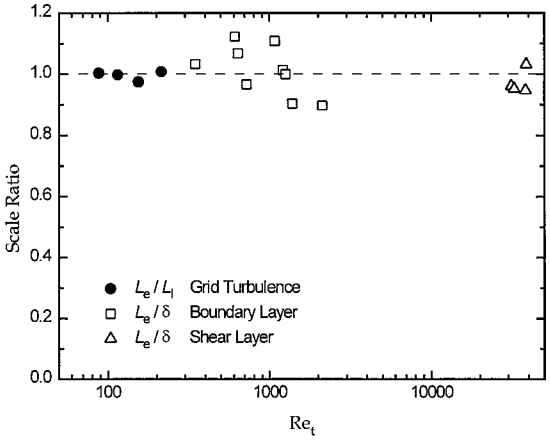

Fig. 4 Behavior of L_e in different types of flows

The L_e calculation method was tested in decaying grid-generated turbulence, near the center of a two-stream turbulent shear layer, and in the core of a turbulent boundary layer (without free-stream turbulence). Figure 4 shows the behavior of the calculation method for these three flows. The results show that the

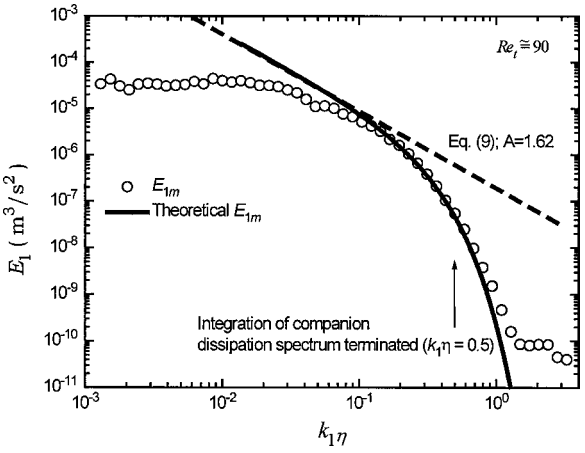

Fig. 5 Very low turbulent Reynolds number spectrum

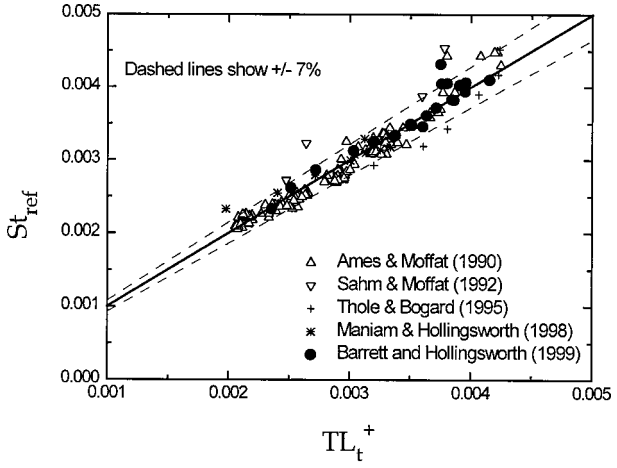

Fig. 7 Use of L_e in Stanton number correlation of Barrett and Hollingsworth [15]

ratio L_e/L_I downstream of a grid is unity as isotropic theory predicts. Examining the turbulent shear and boundary layers, the ratio L_e/δ, where δ is the vorticity thickness for the shear layer or the 99 percent thickness (based on free-stream velocity) for the boundary layer, is approximately one. This result reflects the accepted behavior of an integral scale as noted earlier. Figure 5 shows a very low turbulent Reynolds number spectrum ($Re_t \cong 90$) from the grid-generated turbulence case. The turbulent Reynolds number is given by $Re_t = [1.5(u')^2]^2/(\nu\epsilon)$. No inertial subrange is evident in Fig. 5, yet the L_e calculation matched the L_I calculation very well. Note that for this spectrum, L_{II} cannot be accurately determined.

The behavior of L_e across a turbulent boundary layer is shown in Fig. 6. The experimental values for $\nu\epsilon/u_\tau^4$ (using corrected, isotropic ϵ values) are compared with the DNS values calculated by Spalart [14]. The filled symbols denote points where all but the fourth of Lumley's criteria were satisfied; the open symbols represent points where the velocity gradient caused at least one of the other three criteria to be violated. In general, criterion four tends to be the most difficult to satisfy. But, as Lumley also noted, good results can be obtained assuming small-scale isotropy even when criterion four is not met. The point of departure from Spalart's curve is coincident with the violation of the remaining criteria and suggests that the criteria might be useful in dissipation calculations for other types of flows.

Finally, to explore the application of L_e in a heat transfer correlation, Fig. 7 presents results from Barrett and Hollingsworth [15] that indicate that the L_e scale is an appropriate choice to correlate a Stanton number based on a boundary-layer core reference temperature, $St_{ref} \equiv q_w/[\rho c_p(\overline{t_w} - \overline{t_{L_e^+}})U_\infty]$. The term $\overline{t_{L_e^+}}$ represents the mean temperature at a distance L_e from the wall. The parameter TL^+, developed in detail in the referenced work, is an involved expression that incorporates the L_e length scale described herein.

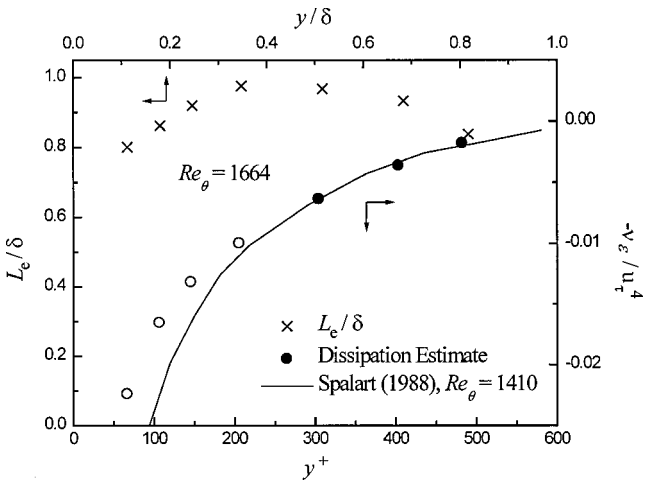

Fig. 6 Boundary layer scale and dissipation evaluation

Conclusions

To improve the comparability of heat transfer data between experimenters, a detailed method of calculating a turbulent length scale will be helpful. The authors recommend that L_e be adopted as a standard for the following reasons:

1 The method uses measurements from only a single-point in the flow field.
2 The method can be employed in flows with mean velocity gradients.
3 A well-defined inertial subrange is not required in the energy spectrum; the scale is calculable in low turbulent Reynolds number flows.
4 The scale is equivalent to L_I and L_{II} in flows in which the latter scales can be determined.
5 The scale can be calculated from the same information used to calculate Λ_I (a Fourier transform of the autocorrelation curve produces the energy spectrum); the added computation relative to Λ_I is minimal.
6 The method includes criteria to determine when the technique is invalid.
7 The calculation is more rigorous than "best fit" methods.

Acknowledgments

The authors would like to thank Dr. S. J. Kleis for the use of his wind tunnel facility and for his continuing interest and involvement. We also thank Dr. B. M. Maniam for providing the data for the two-stream mixing layer test case. These experiments have been supported by the Texas Higher Education Coordinating Board Advanced Technology Program through Grant # 003652-944, the UH Institute for Space Systems Operations, and the UH Energy Laboratory. Dr. Barrett received additional support from the NASA/Texas Space Grant Consortium and the SAE Doctoral Scholars Program.

Nomenclature

A = constant used in power-law fit of energy spectrum
D = dissipation spectrum

E = power spectral density of fluctuating velocity
L = experimentally determined length scale related to ϵ
R_{11} = Eulerian autocorrelation coefficient
Re_θ = momentum-thickness Reynolds number ($=U_\infty \theta/\nu$)
Re_t = turbulent Reynolds number ($=(1.5(u')^2)^2/(\nu\epsilon)$)
T_{11} = Eulerian integral time scale [defined in the text]
Tu = turbulence intensity ($=u'/U$)
U = time-mean Eulerian velocity in principal flow direction
c_p = specific heat
f = frequency
k = wave number
$\underline{q}$ = heat flux
t = mean temperature
u' = RMS fluctuating velocity in principal flow direction
u_τ = boundary layer friction velocity ($=\sqrt{\tau_w/\rho}$)
v', w' = RMS fluctuating velocities in non-principal flow directions
x = streamwise distance
y = distance from wall
y^+ = dimensionless distance from wall ($=yu_\tau/\nu$)
Λ = experimentally determined length scale related to Λ_f
Λ_f = Eulerian integral length scale (defined in the text)
δ = shear-layer vorticity thickness or boundary-layer thickness
ϵ = dissipation of turbulent kinetic energy
η = Kolmogorov length scale ($=(\nu^3/\epsilon)^{1/4}$)
θ = momentum thickness of the boundary layer
ν = kinematic viscosity
ρ = density
τ = shear stress

Subscripts

1 = x-component related
∞ = free-stream
$I-III$ = scale tracking reference
e = energy-based
m = measured
t = turbulent
w = value at the wall in a wall-bounded flow
θ = based on momentum thickness

References

[1] Tennekes, H., and Lumley, J. L., 1972, *A First Course in Turbulence*, MIT Press, Cambridge, MA.
[2] Hinze, J. O., 1975, *Turbulence*, McGraw-Hill, New York.
[3] Young, C. D., Han, J. C., Huang, Y., and Rivir, R. B., 1992, "Influence of Jet-grid Turbulence on Flat Plate Turbulent Boundary Layer Flow and Heat Transfer," ASME J. Heat Transfer, **114**, pp. 65–72.
[4] Van Fossen, G. J., Simoneau, R. J., and Ching, C. Y., 1995, "Influence of Turbulence Parameters, Reynolds Number, and Body Shape on Stagnation-region Heat Transfer," ASME J. Heat Transfer, **117**, pp. 597–603.
[5] Camp, T. R., and Shin, H.-W., 1995, "Turbulence Intensity and Length Scale Measurements in Multistage Compressors," ASME J. Turbomach., **117**, pp. 38–46.
[6] Moss, R. W., and Oldfield, M. L. G., 1996, "Effect of Free-Stream Turbulence on Flat-plate Heat Flux Signals: Spectra and Eddy Transport Velocities," ASME J. Turbomach., **118**, pp. 461–467.
[7] Hollingsworth, D. K., and Bourgogne, H.-A., 1995, "The Development of a Turbulent Boundary Layer in High Free-stream Turbulence Produced by a Two-stream Mixing Layer," Exp. Therm. Fluid Sci., **11**, pp. 210–222.
[8] Maniam, B. M., and Hollingsworth, D. K., 1998, "Experimental Investigation of Heat Transfer in a Three-Dimensional Boundary Layer Beneath a Mixing Layer," *Proceedings, 7th AIAA/ASME Joint Thermophysics and Heat Transfer Conference*, Paper 12-HT-3.1, Albuquerque, NM, June 15–18.
[9] Thole, K. A., Bogard, D. G., and Whan-Tong, J. L., 1994, "Generating High Freestream Turbulence Levels," Experiments in Fluids, **17**, pp. 375–380.
[10] Johnson, P. L., and Johnston, J. P., 1989, "The Effects of Grid-Generated Turbulence on Flat and Concave Turbulent Boundary Layers," Report No. MD-53, Department of Mechanical Engineering, Stanford University, Stanford, CA.
[11] Simonich, J. C., and Bradshaw, P., 1978, "Effect of Free-Stream Turbulence on Heat Transfer through a Turbulent Boundary Layer," ASME J. Heat Transfer, **100**, pp. 671–677.
[12] Ames, F. E., and Moffat, R. J., 1990, "Heat Transfer with High Intensity, Large Scale Turbulence: The Flat Plate Turbulent Boundary Layer and the Cylindrical Stagnation Point," Report No. HMT-44, Department of Mechanical Engineering, Stanford University, Stanford, CA.
[13] Lumley, J. L., 1965, "Interpretation of Time Spectra Measured in High-intensity Shear Flows," Phys. Fluids, **8**, pp. 1056–1062.
[14] Spalart, P. R., 1988, "Direct Simulation of a Turbulent Boundary Layer up to $R_\theta = 1410$," J. Fluid Mech., **187**, pp. 61–98.
[15] Barrett, M. J., and Hollingsworth, D. K., 1999, "On the Correlation of Heat Transfer in Turbulent Boundary Layers Subjected to Free-stream Turbulence," *Proceedings of the 33rd National Heat Transfer Conference*, ASME Paper HTD99-76; Albuquerque, NM, August 15–17.
[16] Blair, M. F., 1983, "Influence of Free-stream Turbulence on Turbulent Boundary Layer Heat Transfer and Mean Profile Development: Part II—Analysis of Results," ASME J. Heat Transfer, **105**, pp. 41–47.
[17] Hancock, P. E., and Bradshaw, P., 1989, "Turbulence Structure of a Boundary Layer Beneath a Turbulent Free Stream," J. Fluid Mech., **205**, pp. 45–76.
[18] Castro, I. P., 1984, "Effect of Free Stream Turbulence on Low Reynolds Number Boundary Layers," ASME J. Fluids Eng., **106**, pp. 298–306.
[19] Hancock, P. E., and Bradshaw, P., 1983, "The Effect of Free-stream Turbulence on Turbulent Boundary Layers," ASME J. Fluids Eng., **105**, pp. 284–289.
[20] Sahm, M. K., and Moffat, R. J., 1992, "Turbulent Boundary Layers with High Turbulence: Experimental Heat Transfer and Structure on Flat and Convex Walls," Report No. HMT-45, Department of Mechanical Engineering, Stanford University, Stanford, CA.
[21] Ames, F. E., and Plesniak, M. W., 1995, "The Influence of Large Scale, High Intensity Turbulence on Vane Aerodynamic Losses, Wake Growth, and the Exit Turbulence Parameters," *Proceedings, International Gas Turbine and Aeroengine Congress and Exposition*, ASME Paper 95-GT-290, Houston, TX, June 5–8.
[22] Thole, K. A., and Bogard, D. G., 1995, "Enhanced Heat Transfer and Shear Stress Due to High Free-Stream Turbulence," ASME J. Turbomach., **117**, pp. 418–424.
[23] Thole, K. A., and Bogard, D. G., 1996, "High Freestream Turbulence Effects on Turbulent Boundary Layers," ASME J. Fluids Eng., **118**, pp. 276–284.
[24] Ames, F. E., 1997, "The Influence of Large-Scale High-Intensity Turbulence on Vane Heat Transfer," ASME J. Turbomach., **119**, pp. 23–30.
[25] Bott, D. M., and Bradshaw, P., 1998, "Effect of High Free-Stream Turbulence on Boundary Layer Skin Friction and Heat Transfer," *Proceedings, 36th Aerospace Sciences Meeting & Exhibit*, Reno, NV, AIAA Paper 98-0531, January 12–15.

Inverse Boundary Design Combining Radiation and Convection Heat Transfer

Francis H. R. França

Ofodike A. Ezekoye

John R. Howell
e-mail: jhowell@mail.utexas.edu

Department of Mechanical Engineering,
The University of Texas at Austin,
Austin, TX 78712-1063

This work investigates inverse boundary design for radiation, convection and conduction combined-mode heat transfer. The problem consists of finding the heat flux distribution on a heater that satisfies both the temperature and the heat flux prescribed on a design surface of an enclosure formed by two finite parallel plates. A gray participating medium flows in laminar regime between the walls, which are gray, diffuse emitters and absorbers. All the thermal properties are uniform. This problem is described by an ill-conditioned system of non-linear equations. The solution is obtained by regularizing the system of equations by means of truncated singular value decomposition (TSVD).
[DOI: 10.1115/1.1388298]

Keywords: Channel Flow, Convection, Heat Transfer, Inverse, Radiation

Introduction

Many industrial processes require that two thermal conditions be imposed on some of the boundaries of the system. The designer attempts to find the conditions on the unconstrained elements of the system such that the two specifications are satisfied. For instance, it may be required that the temperature of a processing material be uniform, which in turn could be achieved only by means of a uniform heat flux distribution on the material. In conventional design, namely *forward design*, where the mathematical formulation relies on the knowledge of one and just one condition on each element of the system, the designer needs to guess one thermal condition on the unconstrained elements and, for the uniform temperature on the process material, check the corresponding heat flux. If it is not uniform, a new guess is made, and the calculations are rerun. This trial-and-error procedure, even if coupled with an optimization routine, can be cumbersome to deal with, and a great number of iterations may be necessary to achieve a satisfactory configuration. This can be especially undesirable if each calculation requires a large computational time.

Inverse design aims at finding the conditions in the unconstrained elements directly from the two specifications on the design surface, so it avoids the trial-and-error procedure of forward design. Inverse mathematical models allow some surfaces to have two prescribed boundary conditions, as well as some elements to have no prescribed condition at all. For problems that involve thermal radiation heat transfer, this type of formulation is described by a Fredholm integral equation of the first kind, known to result in an ill-posed problem, and can be solved only by means of regularization methods (Hansen [1]). The matrix of coefficients presents singular values that decay continuously and steeply, and conventional matrix solvers will probably fail to provide a useful solution. The system must be regularized.

The research undertaken on inverse design can be divided into two classes. The first includes the inverse boundary problem, in which the conditions on some of the boundaries are sought to satisfy the specifications on the design surfaces; the second includes the inverse heat source problem, where the heat source distribution in the unconstrained medium is to be found. Inverse boundary design for radiation dominated problems has been considered by Harutunian et al. [2], Oguma and Howell [3], Morales et al. [4], França and Goldstein [5], and Matsumura et al. [6]. Inverse heat source design in radiating systems was solved by Kudo et al. [7], and França et al. [8,9,10,11]. In most of those references, the radiative enclosure was represented by a two-dimensional rectangular geometry, formed by diffuse, gray surfaces, and containing either a non-participating or a gray participating medium. Most considered pure radiation heat transfer, and so the problem could be formulated by a system of linear equations. França et al. [11] considered the combined conduction and radiation heat transfer problem, which involves a system of non-linear equations.

This paper considers the inverse design of a two-dimensional enclosure, formed by two parallel surfaces. The objective is to find the conditions on the heater located on the upper wall that could satisfy the two specifications (temperature and the heat flux) on the design surface located on the bottom of the enclosure. A fully developed laminar flow of a participating medium exists between the plates. All physical properties are assumed constant, and the medium and wall are gray emitters and absorbers. The major contribution of this work is to extend previous solutions to the case where the heat transfer is governed by radiation, convection and conduction heat transfer modes. The zonal formulation is applied for the discretization of the radiative terms of the energy equation, while the diffusive and convective terms are treated by the control volume method.

As is the case in combined heat transfer problems, the discretization leads to a system of highly nonlinear equations. This system is also expected to be ill-conditioned, as an inverse analysis is involved. The set of equations is solved by first relating the known temperature and heat flux of the elements on the design surface directly to the unknown radiosity of the elements on the heater, and then finding the remaining heat transfer terms from the conditions found in the previous steps. This requires an iterative solution, where at each step an ill-conditioned system of linear equations on the radiosities of the heater elements is to be solved. However, the solution to the complete combined mode problem is found at the end of this iterative procedure, whereas an iterative solution is required within each trial-and-error iteration (i.e., an iterative loop within an iterative solution) necessary in a forward problem. The ill-conditioned nature of the system is treated by means of truncated singular value decomposition (TSVD).

Physical and Mathematical Formulation

Figure 1 shows a schematic view of the two-dimensional enclosure, formed by two parallel surfaces of length L, and separated by a distance of H. Steady state process is assumed. A gray par-

Contributed by the Heat Transfer Division for publication in the JOURNAL OF HEAT TRANSFER. Manuscript received by the Heat Transfer Division April 12, 2000; revision received February 20, 2001. Associate Editor: R. D. Skocypec.

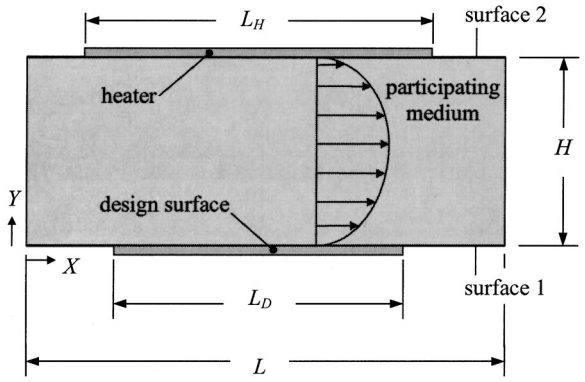

Fig. 1 Two-dimensional enclosure for inverse design

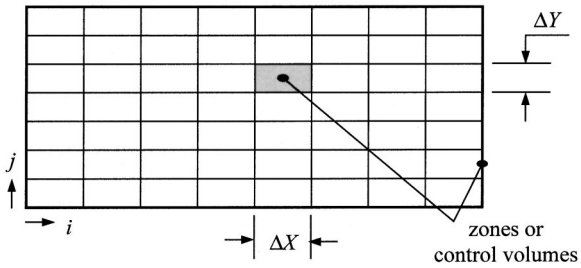

Fig. 2 Division of the enclosure into spatially coincident zones and control volumes

ticipating medium flows between the two plates, with a fully developed laminar velocity profile. The design surface and the heater are located in the center of surface 1, on the bottom, and surface 2, on the top. The lengths of the design and of the heater surfaces are L_D and L_H, respectively. All the physical properties are assumed to be constant. Surfaces 1 and 2 are diffuse, gray emitters and absorbers, and their emissivities are indicated by ε_1 and ε_2. The inlet and outlet of the enclosure are modeled as porous black surfaces at the same temperatures as the inlet and outlet bulk temperatures of the flowing medium. The elements on surface 1 and 2 that are not located on the design surface or on the heater are adiabatic. The inverse design consists of finding the total heat flux distribution on the heater that is able to provide the specified temperature and heat flux on the design surface. This configuration and set of conditions are representative of industrial drying and processing ovens, and the formulation presented here provides a useful design tool for such devices.

The mathematical formulation of the problem relies on energy conservation. Neglecting axial conduction, viscous dissipation and heat generation in the medium, the energy equation, in dimensionless form, is

$$\frac{1}{\mathrm{Pe}}\frac{\partial^2 t_g}{\partial y^2}-u\frac{\partial t_g}{\partial x}+\frac{\tau_H}{N_{cr}\mathrm{Pe}}\dot{Q}_r'''=0, \tag{1}$$

where the first and the second terms relate to the diffusion and convection of heat, respectively, and the third term accounts for the balance between the absorbed and the emitted thermal energy by the medium element.

For an element on one of the surfaces, 1 or 2, the energy balance is:

$$Q_{1t}=Q_{1r}+Q_{1c} \tag{2a}$$

$$Q_{2t}=Q_{2r}+Q_{2c} \tag{2b}$$

in which Q_t, Q_r, and Q_c stand for the total, radiative, and conductive dimensionless heat fluxes on the surface element.

To obtain the temperature distribution in the medium, and then to solve for the heat transfer between the heater and the design surface, it is necessary to relate the radiative terms of Eqs. (1) and (2) to the temperature distributions. This results in a system of integral-differential equations, which requires a numerical approach for most cases. Two distinct methods are combined for the solution of the problem: the integral terms of the radiative relations are treated by the zonal formulation (Siegel and Howell [12]); the control volume method (Patankar [13]) is used to deal with the diffusive and convection terms. Both methods are based on the subdivision of the continuous domain into finite size elements, as shown in Fig. 2. Although this is not a necessary requirement, the grids are spatially coincident in this work. To make the zonal method calculations less time consuming, the grid is uniform in the x and y directions, but ΔX and ΔY are not necessarily the same.

Using the upwind approximation for the discretization of the convective terms, and the second-order finite difference approximation for the diffusive terms, the conservation of energy for the medium element i, j becomes:

$$\frac{1}{\mathrm{Pe}}\frac{(2t_{g,i,j}-t_{g,i,j-1}-t_{g,i,j+1})}{(\Delta y)^2}-u_j\frac{(t_{g,i,j}-t_{g,i-1,j})}{\Delta x}+\frac{\tau_H}{N_{cr}\mathrm{Pe}}\dot{Q}_{r,i,j}'''=0. \tag{3}$$

In the zonal method, each element is assumed to have uniform emissive power and radiosity. Using this method for the discretization of the radiation term gives:

$$\dot{Q}_{r,i,j}'''=\frac{1}{4\Delta y}\Bigg(-4\tau_H\Delta y t_{g,i,j}^4+\sum_{k,l}\overline{G_{k,l}G_{i,j}}t_{g,k,l}^4+\sum_k\overline{S_{1k}G_{i,j}}Q_{1o,k}^4+\sum_k\overline{S_{2k}G_{i,j}}Q_{2o,k}^4+\overline{S_{e1}G_{i,j}}t_{e1}^4+\overline{S_{e2}G_{i,j}}t_{e2}^4\Bigg). \tag{4}$$

The first term on the right-hand side of Eq. (4) accounts for the thermal radiation emitted by the i, j medium element. The remaining terms account, respectively, for the absorption of thermal radiation originating from the other medium elements, from the wall elements on surfaces 1 and 2, and from the two ends of the enclosure, assumed to be black bodies at the medium bulk temperature. The terms $\overline{SG}$ and $\overline{GG}$ are the surface-to-medium and medium-to-medium direct-exchange areas per unit of depth. They depend only on the geometry and optical thickness τ_H, and are non-dimensionalized by ΔX.

For non-black walls, it is convenient to combine the emitted and the reflected radiation energy into one term, the radiosity. The dimensionless radiosity Q_o of an element located on surfaces 1 or 2 can be calculated by

$$Q_{1o,k}=Q_{1r,k}+\sum_j\overline{S_{2j}S_{1k}}Q_{2o,j}+\sum_{i,j}\overline{G_{i,j}S_{1k}}t_{g,i,j}^4+\overline{S_{e1}S_{1k}}t_{e1}^4+\overline{S_{e2}S_{1k}}t_{e2}^4 \tag{5a}$$

$$Q_{2o,k}=Q_{2r,k}+\sum_j\overline{S_{1j}S_{2k}}Q_{1o,j}+\sum_{i,j}\overline{G_{i,j}S_{2k}}t_{g,i,j}^4+\overline{S_{e1}S_{2k}}t_{e1}^4+\overline{S_{e2}S_{2k}}t_{e2}^4 \tag{5b}$$

The first term on the right-hand side is the dimensionless radiative heat flux on the element, which is a balance between the thermal radiation that leaves and arrives on it. The other terms account for the incidence of radiation from all the other surface

and medium elements, and from the ends of the enclosure. The radiosity can also be related to the temperature and radiative heat flux by

$$Q_{1o,k}=t_{1,k}^4-\frac{(1-\varepsilon_{1,k})}{\varepsilon_{1,k}}Q_{1r,k} \tag{6a}$$

$$Q_{2o,k}=t_{2,k}^4-\frac{(1-\varepsilon_{2,k})}{\varepsilon_{2,k}}Q_{2r,k} \tag{6b}$$

The dimensionless conductive heat flux from a wall element to an adjacent medium element is calculated by the second-order finite difference approximation

$$Q_{1c,k}=4N_{cr}\frac{8t_{1,k}+t_{g,k,j=2}-9t_{g,k,j=1}}{3\Delta x} \tag{7a}$$

$$Q_{2c,k}=4N_{cr}\frac{8t_{2,k}+t_{g,k,j=M-1}-9t_{g,k,j=M}}{3\Delta x}. \tag{7b}$$

The indices $j=1$ and M refers to the medium elements neighboring the bottom and upper wall, respectively.

Solution Procedure. Equations (3) to (7) contain all the relations necessary for the solution of the problem. They form a system of nonlinear equations, as the unknowns include both the dimensionless temperature t and the emissive power t^4 of the medium and wall elements. In forward problems, such systems have been often solved by using an iterative approach: some terms (for instance, the temperature) are chosen as the primary unknowns of the system, while others (for instance, the emissive power) are calculated from the conditions found in the previous iteration. The convergence of the solution depends on careful analysis of the physical system. The terms related to the dominant heat transfer process should be used as the primary unknowns, while the other terms are calculated from the conditions of the previous iteration. In inverse analyses, an even more careful analysis of the problem is necessary for the numerical scheme to converge, because of the inherent instability of ill-conditioned problems.

In the type of system considered in Fig. 1, the design surface is heated by the top surface by means of thermal radiation. The participating medium affects the heating process through thermal radiation and convection mechanisms, and convection is necessary to remove vapor released by drying on the design surface or as an auxiliary heat transfer mechanism. However, an effective design of such a system is the one that maximizes the effect of the heater (the controllable part of the system) on the design surface, so that the radiation exchange between the two surfaces is dominant in the process. This dominance should be reflected in the setting of the unknown and guessed terms. An optimum set of equations can be proposed that relates the two known conditions on the design surface directly to the unknown radiosity of the heater elements. All the other terms involved in the system (convective and diffusive) are calculated from the conditions found in the previous iteration. An attractive aspect of this procedure is that the ill-posed part of the problem (which arises from the fact that the design surface contains two imposed conditions, while the heater has no imposed boundary condition at all) is separated from the remainder of the problem.

In a similar sense, a well designed system should not have an optically thick participating medium (that is, $\tau=\kappa H\rightarrow\infty$) between the surfaces, because the effect of the heater on the design surface would be minimized by the presence of a highly absorbing medium. The inverse solution would probably not be able to find a proper solution for the heater, since any power input distribution to the heater would make a small difference on the design surface; the heating of the design surface could hardly be controlled by the heaters. Therefore, the inverse solution of interest should consider only low or moderate optical thickness, where the solution of the energy equation in the medium is based on the terms of diffusion and convection, while the radiative heat source is guessed at each iteration.

The known conditions of the problem are: the temperature and heat flux on the design surface elements, the heat flux on the adiabatic regions of surfaces 1 and 2 (that is, $Q_t=0$), and the inlet medium bulk temperature. The solution is achieved by the following iterative steps:

1 The medium temperature initially is assumed to be uniform and equal to the known inlet bulk temperature, $t_{g,i,j}=t_{e1}$. The conductive heat flux from the design element to the medium is assumed zero, $Q_{1c,k}=0$. The radiosity of the elements located in the adiabatic regions of surfaces 1 and 2 are guessed as t_{e1}^4.

2 The outlet medium bulk temperature is calculated from the medium temperature distribution at $x=L/H$.

3 The radiative heat flux and the radiosity on the elements of the design surface are calculated from Eqs. (2*a*) and (6*a*).

4 For every element on the design surface, Eq. (5*a*) can be rearranged to form the system of equations in terms of the unknown radiosities of the elements on the heater. The radiosity for the elements in the adiabatic region of surface 2 are included among the guessed terms as follows:

$$\sum_{j\text{-heater}}\overline{S_{2j}S_{1k}}Q_{2o,j}=Q_{1o,k}-Q_{1r,k}-\sum_{j\text{-adiabatic}}\overline{S_{2j}S_{1k}}Q_{2o,j}-\sum_{i,j}\overline{G_{i,j}S_{1k}}t_{g,i,j}^4-\overline{S_{e1}S_{1k}}t_{e1}^4-\overline{S_{e2}S_{1k}}t_{e2}^4. \tag{8}$$

5 Once the radiosity of each element on the heater surface is determined, the radiative heat flux and the temperature can be found, in this order, from Eqs. (5*b*) and (6*b*).

6 From the knowledge of the radiosity on each element of the wall, it is possible to calculate the medium radiation term from Eq. (4). Then, the energy balance equation, Eq. (3), can be solved to give the temperature distribution in the medium.

7 The conductive and the radiative heat transfer on the wall elements are calculated, in this order, by Eqs. (7) and (2).

8 With the new values for the medium temperature, conductive heat flux on the design surface, and radiosity of the elements in the adiabatic regions of surfaces 1 and 2, the calculations start again at step 2, and are repeated until convergence is achieved.

Regularization of the System of Equations

Step (4) of the above procedure involves the solution of a system of linear equations on the radiosities of the heater elements, which can be represented by

$$\mathbf{A}\cdot\mathbf{x}=\mathbf{b}(\mathbf{x}), \tag{9}$$

where the coefficient matrix **A** is formed by the surface-to-surface direct-exchange areas between the elements on the heater and the design surface, vector **x** represents the unknown radiosities of the heater elements, and vector **b** contains the terms guessed in the previous iteration, being dependent on **x**.

The system of Eq. (9) is the discretized form of a set of equations that includes Fredholm integral equations of the first kind, and so it is expected to present the characteristics of ill-posed problems. In general, the components of the exact solution vector **x** present steep oscillations between very large absolute numbers having alternating signs, and small perturbations cause a much amplified change in the solution. The solution of ill-posed problems does not aim at an exact solution, but rather to impose additional constraints to reduce the size (norm) of **x** to achieve a smooth solution. However, the greater the smoothness imposed on the solution, the greater will be the residual. This is the basic idea behind the regularization methods for the solution of ill-posed problems.

Among other regularization procedures, such as the conjugate gradient and Tikhonov methods, the truncated singular value decomposition (TSVD) is employed here. In singular value decomposition, the matrix **A** is decomposed into three matrices:

$$\mathbf{A}=\mathbf{U}\cdot\mathbf{W}\cdot\mathbf{V}^T. \tag{10}$$

U and **V** are orthogonal matrices, and **W** is a diagonal matrix formed by the singular values w_j, such that $w_1 \geqslant w_2 \geqslant \ldots \geqslant w_{N-1} \geqslant w_N \geqslant 0$. The solution vector **x** can be computed by

$$\mathbf{x}=\sum_{j=1}^{N}\left(\frac{\mathbf{b}\cdot\mathbf{u}_j}{w_j}\right)\mathbf{v}_j, \tag{11}$$

where N stands for the number of unknowns.

In ill-posed problems, the singular values w_j decay continuously to very small values with increasing j. As they are in the denominator of Eq. (11), the components of **x** can present very large absolute numbers. However, the smaller the singular value w_j is, the closer the corresponding vector $\mathbf{v}_j$ is to the null-space of **A**. In other words, the terms related to the smaller singular values can be eliminated from Eq. (11) without introducing a large error to the solution. This is the principle idea of the TSVD: only the terms related to the pth largest singular values are kept on Eq. (11), instead of all N terms. The TSVD regularized solution is given by

$$\mathbf{x}=\sum_{j=1}^{p}\left(\frac{\mathbf{b}\cdot\mathbf{u}_j}{w_j}\right)\mathbf{v}_j, \tag{12}$$

where the regularization parameter p is defined as the number of terms of the linear combination of Eq. (11) that are kept for the computation of **x**. The solution is the vector **x** with the smallest norm subject to minimum deviation in the residual $|\mathbf{A}\cdot\mathbf{x}-\mathbf{b}(\mathbf{x})|$.

Another aspect of the inverse solution concerns the number of unknowns and the number of equations. Equation (8) is set for all the elements on the design surface, while each element on the heater contains one unknown radiosity. Therefore, the number of equations equals the number of unknowns only when the numbers of elements on the design surface and heater are the same. This is not always the case. An important feature of the TSVD method is that it can be applied to the case where the numbers of unknowns and equations are not the same, as shown in the results section.

Verification of the Solution. Due to the need for regularization of the system on step (4), an exact solution is not expected. The following procedure is used for the verification of the solution. Once the heat flux on the heater is obtained, a forward problem is solved where the heat flux on surface 2 is known, and only the temperature on the design surface is imposed. The heat flux on each element k of the design surface is then calculated, and compared to the heat flux imposed by

$$\gamma_k=\left|\frac{Q_{\text{imposed},k}-Q_{\text{inverse},k}}{Q_{\text{imposed},k}}\right|, \tag{13}$$

where $Q_{\text{imposed},k}$ is the specified heat flux, and $Q_{\text{inverse},k}$ is the total heat flux resulting from the conditions on the heater that were obtained in the inverse solution. Once γ_k is calculated for each element, the maximum and arithmetic average errors $\gamma_{\max}$ and γ_{avg} can be readily found.

It is possible that a trial-and-error solution could provide a solution comparable with that from the inverse solution. Whether this is possible depends on many factors, such as the expertise of the analyst, the accuracy of an initial guess for the solution, and the comparison in time required for the standard forward solution compared with the time for an inverse solution. The latter factor is addressed in [14], where the speed of an inverse solution was compared with that of a forward solution on the same computer. The inverse solution required from 1.7 to 5 times the CPU time of a single forward solution. Thus, if a forward iterative solution takes between 1.7 and 5 iterations, the total times would be the same for either method. However, the number of iterations needed for a particular forward solution cannot be determined *a priori*.

Results and Discussion

For the system shown in Fig. 1, uniform temperature and heat flux are imposed on the design surface, equal to $t_1=1.0$, and $Q_{1t}=-16.0$ (the negative sign of Q_{1t} indicates that heat is transferred from the enclosure to the design surface). The elements on surfaces 1 and 2 that are not located on the design surface or on the heater are adiabatic; that is, $Q_t=0$. A participating medium enters the enclosure with a uniform temperature of $t_g=1.0$. The fully developed laminar flow has an average Reynolds number of Re=2000. The Prandtl number is Pr=0.69, and the Stark number is $N_{CR}=7.60\times10^{-4}$. The optical thickness of the enclosure is $\tau_H=\kappa H=0.2$. All the walls have the same emissivity: $\varepsilon_1=\varepsilon_2=0.8$. The dimensionless length of the enclosure and of the design surface are, respectively, $L/H=5.0$ and $L_D/H=3.0$. The proposed inverse design is applied to find the necessary heat flux distribution on the heater for different dimensionless lengths L_H/H and different regularization parameters p.

The grid is formed by 50 and 20 uniform size elements in the x and y direction, respectively. This results in $\Delta x=\Delta X/H=0.10$, $\Delta y=\Delta Y/H=0.05$, and $r=\Delta x/\Delta y=2$. The accuracy of this grid is verified later.

Because the dimensionless length of the design surface is 3.0, there are 30 design surface elements. As discussed previously, a total of 30 relations as Eq. (8) can be written. If the size of the heater is also set equal to $L_D/H=3.0$, the number of unknown radiosities on the heaters is also 30, making the number of unknowns and equations the same. The components of matrix **A** are the direct-exchange areas $\overline{S_{2j}S_{1k}}$ relating the elements in the design surfaces and heaters. Once the matrix **A** is formed, the singular value decomposition is performed to generate the singular values w_j, which are presented in Fig. 3 for $L_H/H=3.0$. As can be seen, the singular values decay continuously to a magnitude as small as 10^{-8}, a typical characteristic of ill-posed problems. The TSVD regularization is necessary to smooth the solution, as well as allow convergence of the iterative procedure. As verified in previous works (França et al. [8–11]), truncating all the terms related to singular values smaller that 10^{-3} usually leads to convergence and smooth solutions. Using this information, the first guess made to find the best regularization parameter was $p=10$, taken by checking the singular values of Fig. 3. Solving the problem for this p, it is found that some components of vector **x**

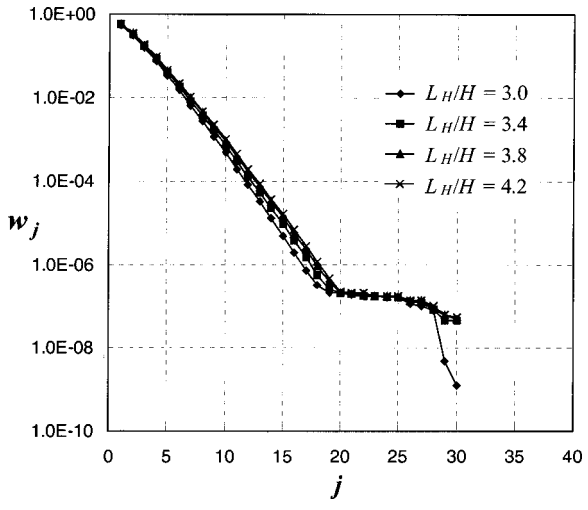

Fig. 3 Singular values of matrix A for different heater dimensionless lengths, L_H/H. $L/H=5.0$; $L_D/H=3.0$; $\tau_H=0.2$; $\varepsilon_1=\varepsilon_3=0.8$; Re=2,000; Pr=0.69; $N_{CR}=7.60\times10^{-4}$. Grid: 50×20.

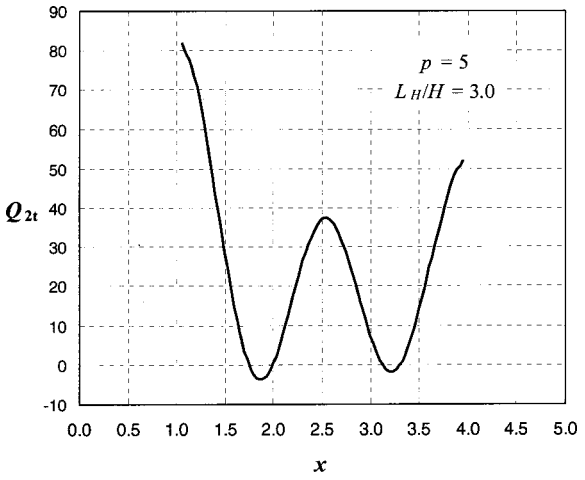

Fig. 4 Heat flux on the heater for $L_H/H=3.0$ with $p=5$. Design surface: $t_1=1.0$ and $Q_{1t}=-16.0$; $L/H=5.0$; $L_D/H=3.0$; $\tau_H=0.2$; $\varepsilon_1=\varepsilon_3=0.8$; Re=2,000; Pr=0.69; $N_{CR}=7.60\times10^{-4}$. Grid: 50×20.

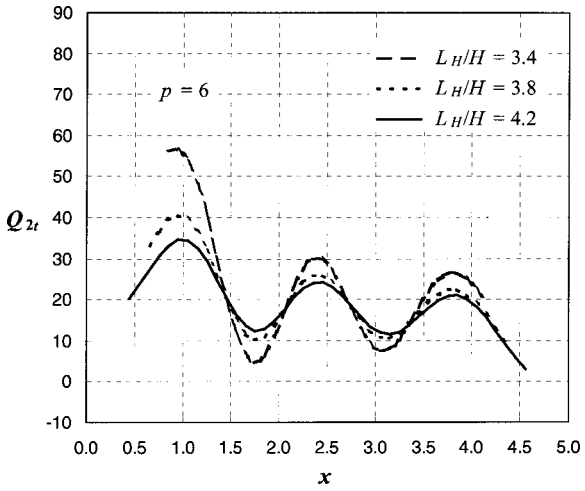

Fig. 5 Heat flux on the heater for different L_H/H with $p=6$. Design surface: $t_1=1.0$ and $Q_{1t}=-16.0$; $L/H=5.0$; $L_D/H=3.0$; $\tau_H=0.2$; $\varepsilon_1=\varepsilon_3=0.8$; Re=2,000; Pr=0.69; $N_{CR}=7.60\times10^{-4}$. Grid: 50×20.

converge to negative numbers, which is not physically acceptable, as they stand for the radiosity. Other solutions are attempted by decreasing p until the vector **x** contains only positive values. This occurs for $p=5$. The corresponding heat flux on surface 2 is presented in Fig. 4. The arithmetic average and maximum errors for this solution, as defined by Eq. (13), are rather high: $\gamma_{avg}=1.26$ percent and $\gamma_{max}=5.26$ percent. Another unsatisfactory aspect is the presence of a negative heat flux in some of the elements, which is not an interesting solution for a heater.

Figure 4 also indicates that, to keep the design surface at uniform heat flux and temperature, the heat flux should be the greatest for the elements close to the extremities of the heater. This can be an indication that if the heater is ''stretched'' towards the two ends of the enclosure, where a greater heat flux is needed, the peak heat flux can be reduced. (An alternative solution would be to shorten the size of the design surface.) The dimensionless size of the heater, L_H/H, can be set as 3.4, 3.8, and 4.2, instead of 3.0. The first implication of this concerns the change of the number of unknowns. Keeping the same grid resolution as before, the numbers of unknowns when L_H/H is 3.4, 3.8, and 4.2 are, respectively, 34, 38, and 42. The number of equations, related to the number of elements on the design surface, is still 30. This makes the number of unknowns greater than the number of equations, and the system is underdetermined. The singular values of matrix **A** for these three cases are presented and compared to the case where L_H/H is 3.0 in Fig. 3. There is no significant change in the singular value spectrum for the four cases presented. Only the 30 largest singular values are presented, as the remaining are zero for the system having more than 30 unknowns. The TSVD method can be applied in exactly the same way as before for such systems, by keeping the p largest singular values in Eq. (12). The elimination of the terms related to the zero singular values introduces no additional error to the solution. For the cases where L_H/H is 3.4, 3.8, and 4.2, it is possible to use p larger than 5 and still recover a solution having physical meaning. Figures 5 and 6 present the heat flux on surface 2 setting p equal to 6 and 7 for the different sizes of the heaters. The figures indicate that, for a given regularization parameter p, the greater is L_H/H, the smaller are the peaks of heat flux necessary on the heater, as it is distributed along a greater length. For a given L_H/H, increasing p from 6 to 7 adds one more oscillation to the heat flux.

Considering that the problem allows different solutions, as indicated on Figs. 4 through 6, it is of interest to establish a set of criteria for the choice of one or some of them. As already discussed, solutions that present negative heat flux on surface 2 are not interesting designs for a heater. This eliminates the solutions obtained for $L_H/H=3.0$ with $p=5$, and $L_H/H=3.4$ with $p=7$. Due to the need for regularization of the inverse problem, the maximum (γ_{max}) and average (γ_{avg}) errors must always be checked to validate or eliminate a given solution. For this particular problem, another aspect to be compared between the solutions is the efficiency η of the heating process; that is, the ratio between the total heat imposed on the design surface, and the necessary input of heat on the heater. Table 1 presents the maximum and the average errors for each solution of Figs. 5 and 6, as well as the efficiency of the heating process. Keeping constant the regularization parameter p, the average and the maximum errors of the inverse solution decrease as L_H/H is increased from 3.4 to 4.2. The efficiency of the heating process decreases only slightly as L_H/H increases from 3.4 to 4.2, because the increment in the size of the heater is balanced by the smoothing of the heat flux peaks. Considering that this small decrease in the efficiency is not a high price to pay for a smoother heat flux on the heater, the solutions for $L_H/H=4.2$ with $p=6$ and 7 can be chosen as the most interesting. If a minimum number of oscillations is preferred, then the

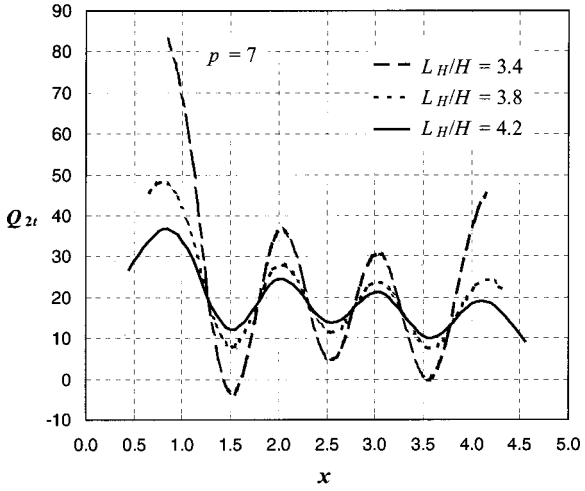

Fig. 6 Heat flux on the heater for different L_H/H with $p=7$. Design surface: $t_1=1.0$ and $Q_{1t}=-16.0$; $L/H=5.0$; $L_D/H=3.0$; $\tau_H=0.2$; $\varepsilon_1=\varepsilon_3=0.8$; Re=2,000; Pr=0.69; $N_{CR}=7.60\times10^{-4}$. Grid: 50×20.

Table 1 Average and maximum relative errors, and efficiency of the heating process for the inverse solutions of Figs. 5 and 6. Design surface: $t_1=1.0$ and $Q_{1t}=-16.0$; $L/H=5.0$; $L_D/H=3.0$; $\tau_H=0.2$; $\varepsilon_1=\varepsilon_3=0.8$; Re=2000; Pr=0.69; $N_{CR}=7.60\times10^{-4}$; Grid: 50×20.

L_H/H	p	γ_{max} (%)	γ_{avg} (%)	η (%)
3.4	6	2.182	0.703	60.9
3.8	6	1.319	0.467	60.0
4.2	6	0.925	0.364	59.2
3.4	7	0.773	0.208	60.1
3.8	7	0.335	0.107	59.1
4.2	7	0.152	0.059	58.2

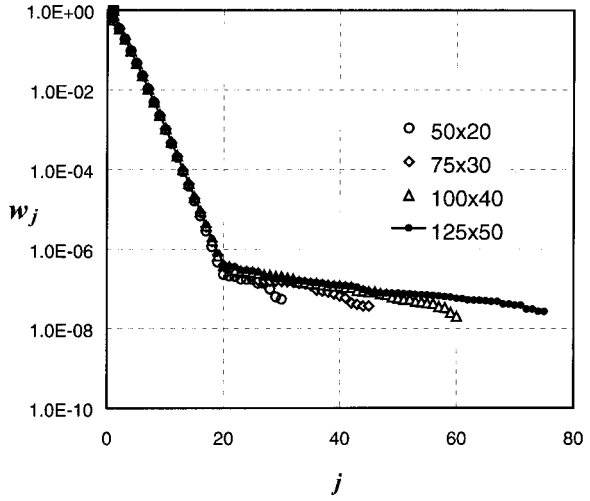

Fig. 7 Singular values of matrix A for different grid resolutions: 50×20, 75×30, 100×40, 125×50. $L/H=5.0$; $L_D/H=3.0$; $\tau_H=0.2$; $\varepsilon_1=\varepsilon_3=0.8$; Re=2,000; Pr=0.69; $N_{CR}=7.60\times10^{-4}$.

first of these two solutions is the best of the set. A typical computation required 1m 42s of CPU time (IBM PowerPC 604e-233 MHz), with no significant change as the considered parameters p and L_H were changed.

The validation of a numerical solution requires a grid independence study. It is of interest to learn how the change of resolution can affect the inverse solution, because for a given grid size the solution depends also on the regularization imposed on the system.

The grid is now divided into 30 and 75 uniform elements on the x and y directions, with $\Delta x=\Delta X/H=0.0667$, $\Delta y=\Delta Y/H=0.0333$, and $r=\Delta x/\Delta y=2$. For comparison with the previous grid, 20×50, the case $L_H/H=4.2$ is considered. For the 30×75 grid, the design surface and the heater are divided into 45 and 63 elements. The system of equations of step (4) will have consequently 45 equations and 63 unknowns on the radiosities of the heaters. Once matrix **A** is formed, it is regularized by the TSVD method. The singular values are presented in Fig. 7, which compares them to the singular values obtained for the previous 20×50 grid. As seen in the figure, the singular values for the two grids coincides at the higher values (lower j), which are the ones that are not truncated by the regularization. This is an indication that the same regularization parameter p can be used in both cases to generate a similar result. In fact, Fig. 8 shows that the heat fluxes on surface 2 for the two grids, both obtained by setting $p=6$, present a very good agreement.

Figures 7 and 8 also present the results for grid resolution of 100×40 and 125×50. The solutions match those obtained for the grid resolutions of 50×20 and 75×30, indicating that the proposed method is stable with respect to mesh refinement. Further

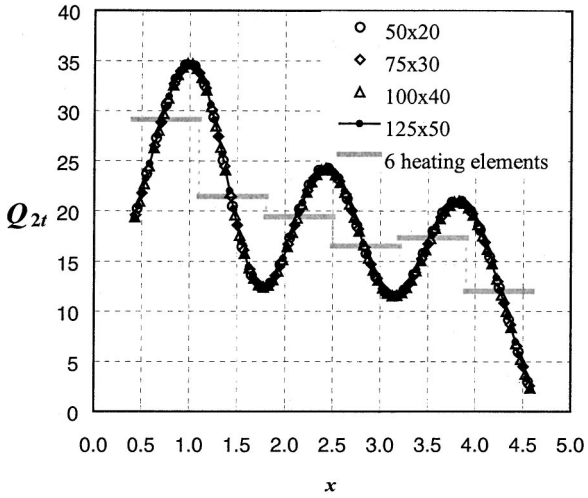

Fig. 8 Heat flux on the heater for four different grid resolutions: 50×20, 75×30, 100×40, and 125×50, and employing only 6 heating devices. Design surface: $t_1=1.0$ and $Q_{1t}=-16.0$; $L/H=5.0$; $L_D/H=3.0$; $\tau_H=0.2$; $\varepsilon_1=\varepsilon_3=0.8$; Re=2000; Pr=0.69; $N_{CR}=7.60\times10^{-4}$; $L_H/H=4.2$ with $p=6$.

refinement was barred by memory limitation. Although the present solution presents stability with respect to the grids tested (up to memory limitation), it has been reported [14] that inverse problems can face difficulties with mesh refinement, which may prevent an inverse solution from being found for very fine grids. The important point is that the error related to grid resolution is usually negligible in comparison to the level of precision that is required in inverse design (usually within about 1 percent).

A last aspect considered in this work concerns the implementation of the inverse solution. Considering again the solution for $L_H/H=4.2$ with $p=6$ as the most satisfactory, the designer must specify heating devices along the heater such that the distribution shown on Fig. 8 is attained. Within the constraint of the grid resolution of 50×20, a total of 42 heating elements should be installed. A practical design may be more interesting if a smaller number of heating elements were employed, even at the expense of accuracy. In Fig. 8, the heat flux distribution on the heater is

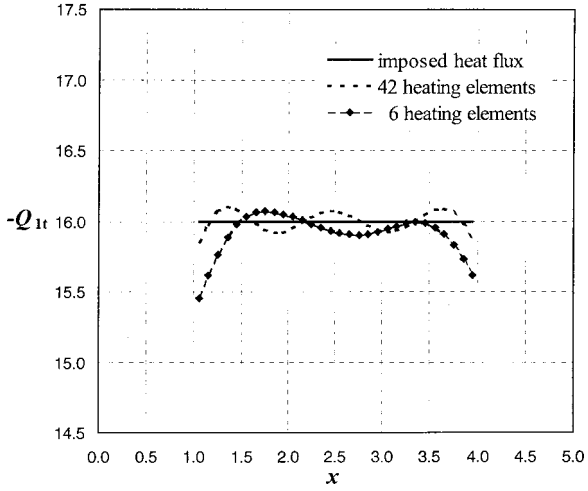

Fig. 9 Heat fluxes on the design surface: as imposed, and employing 42 and 6 heating elements. Design surface: $t_1=1.0$ and $Q_{1t}=-16.0$; $L/H=5.0$; $L_D/H=3.0$; $\tau_H=0.2.$; $\varepsilon_1=\varepsilon_3=0.8$; Re=2000; Pr=0.69; $N_{CR}=7.60\times10^{-4}$; $L_H/H=4.2$ with $p=6$; Grid: 50×20.

presented for six heating devices installed along the heater. The amount of energy to be provided by each heating device is determined by averaging the energy of the elements that form it, as found from the solution with the grid resolution of 42 elements. Such a solution leads to the heat flux on the design surface shown in Fig. 9, which compares it to the imposed heat flux, as well as the one obtained when all the 42 element devices are employed. The average and maximum errors of the solution having only the six uniformly heater elements are $\gamma_{avg}=0.676$ percent and $\gamma_{max}=3.401$ percent. The greater error is observed near the ends of the design surface, where the absolute value of the heat flux is smaller than the specified one. A better solution could be attempted by increasing the energy input of the heating elements close to the ends of the enclosure, or using heating devices with non-uniform sizes so that the oscillatory behavior of the inverse solution is better simulated.

Conclusions

This work considers the inverse boundary design where the power input on the heaters was determined to satisfy the specified temperature and heat flux distribution on the design surface. The mathematical formulation was described by a system of highly nonlinear equations describing combined radiation-convection heat transfer. The numerical discretization of the problem led to an ill-conditioned system of equations as expected in inverse design. This system cannot be solved by conventional matrix solvers, but requires regularization methods, such as truncated singular value decomposition (TSVD). The TSVD eliminates the linear combinations related to the smaller singular values of the system, keeping only the p largest ones. Regularization of the system introduces some error, but makes it possible to obtain practical and approximate solutions.

The proposed procedure was developed for the situation that is the most interesting for the design problem in Fig. 1: low to moderate channel optical thickness, so that the thermal radiation from the heater can properly control the conditions on the design surface. A system of equations was set to relate the two imposed conditions of the design surface directly to the unknown radiosity of the heater, calculating the other terms from the conditions found in the previous iterative step. Because the ill-conditioned part of the problem was isolated, it was necessary to apply regularization only to a reduced system of equations, whose matrix of coefficients did not vary at each iteration, allowing a single regularization.

The examples treated the case where both the prescribed temperature and heat flux on the design surface were uniform. In general, the required heat flux on the heater presented an oscillatory behavior, where the peaks were reduced by increasing the length of the heater. As seen in the examples, the required heat flux decreases along the channel, as the flowing medium increased in temperature and transferred more energy to the design surface by radiation and conduction. If there were no fluid flow (convection), the heat flux distribution would be symmetric with the channel length for the uniform conditions required on the design surface.

The necessary power to the heater was found for different lengths of the heater and regularization parameters p. As typical of inverse design, the problem presented a number of different solutions, which were compared to each other according to the practicality of the design, the error of the solution, and the thermal efficiency. The error of the inverse design decreased as the regularization parameter p was increased, but this added one more oscillation to the solution. Using different grid resolutions, it was possible to find the same solution by keeping the same regularization parameter p. The optimum regularization parameter p must be found for each inverse problem. The same is valid for most regulation methods, as required in finding the Tikhonov regularization parameter α, or the number of iterations for the conjugate gradient methods. Although a number of truncation parameters p must be tested, it should be observed that every single solution is a mathematical approximation for the problem, which can be selected if the imposed requirements (physical and practical constraints) are satisfied. Besides, as shown in the paper, there is usually a limited number of regularization parameters after which the solution becomes plagued by undesirable oscillations.

A last aspect investigated in the paper concerns the specification of a limited number of heaters, each one having finite size and uniform power input, instead of a continuous distribution. The power to each finite heater was calculated by simply averaging the heat flux on the elements contained in the heater. The average error of the solution was still below 1.0 percent, which can be considered satisfactory for many practical applications. It would be difficult to find a solution of similar accuracy using conventional trial-and-error methods.

Acknowledgments

The first author thanks CAPES (Brazil) for support under the grant BEX 2844/95-3. The authors also appreciate the support of the State of Texas Higher Education Coordinating Board under grant 003658-218 (ARP).

Nomenclature

$\mathbf{A}$ = matrix of coefficients
$\mathbf{b}$ = vector of independent terms
c_p = specific heat at constant pressure, J/kg·K
$\overline{GG}$ = dimensionless gas-to-gas direct exchange area
H = height of the enclosure, m
k = thermal conductivity, W/m·K
L = length of the enclosure, m
M = number of medium elements in y-direction
N = number of components of the vector of unknowns $\mathbf{x}$
N_{cr} = conduction-radiation parameter, $ka/4\sigma T_{ref}^3$
p = regularization parameter of the TSVD method
Pe = Peclet number, RePr
Pr = Prandtl number, $c_p\mu/k$
q = heat flux, W/m^2
Q = dimensionless heat flux, $q/\sigma T_{ref}^4$
Q_r''' = medium dimensionless radiative balance term
r = grid ratio, $\Delta x/\Delta y$
Re = average Reynolds number, $\rho U_m H/\mu$
$\overline{SS}$ = dimensionless surface-to-surface direct exchange area
$\overline{SG}$ = dimensionless surface-to-gas direct exchange area
T = temperature, K
t = dimensionless temperature, T/T_{ref}
w = singular values from SVD decomposition of $\mathbf{A}$
$\mathbf{W}$ = diagonal matrix from SVD decomposition of $\mathbf{A}$
x, y = dimensionless coordinates, X/H and Y/H
X, Y = dimensional coordinates, m
$\mathbf{x}$ = vector of unknowns
$\mathbf{v}_j$ = j^{th} column of matrix $\mathbf{V}$
u = elements of matrix $\mathbf{U}$; dimensionless velocity, U/U_m
U_m = medium bulk velocity, m/s
$\mathbf{U}, \mathbf{V}$ = orthogonal matrices from SVD decomposition of $\mathbf{A}$

Greek Symbols

ε = emissivity of surface
γ = error of the inverse solution
κ = medium absorption coefficient, m^{-1}
μ = medium viscosity, kg/m·s
ρ = medium density, kg/m^3
ξ = relative error of inverse solution
τ_H = optical thickness with the respect to the height, κH

Subscripts

c = conductive heat flux
D = design surface

g = medium
H = heater
i, j, k, l = indices
o = outgoing radiative heat flux (radiosity)
r = radiative heat flux
t = total heat flux

References

[1] Hansen, P. C., 1998, *Rank-Deficient and Discrete III-Posed Problems: Numerical Aspects of Linear Inversion*, SIAM, Philadelphia.

[2] Harutunian, V., Morales, J. C., and Howell, J. R., 1995, ''Radiation Exchange Within an Enclosure of Diffuse-Gray Surfaces: The Inverse Problem,'' *Proc. ASME/AIChE National Heat Transfer Conference*, Portland, OR.

[3] Oguma, M., and Howell, J. R., 1995, ''Solution of Two-Dimensional Blackbody Inverse Radiation Problems by Inverse Monte Carlo Method,'' *Proc. ASME/JSME Joint Thermal Engineering Conference*, Maui, Hawaii.

[4] Morales, J. C., Harutunian, V., Oguma, M., and Howell, J. R., 1996, ''Inverse Design of Radiating Enclosures With an Isothermal Participating Medium,'' *Radiative Transfer I: Proc. First Int. Symp. on Radiative Heat Transfer*, M. Pinar Mengüç, ed., Begell House, New York, pp. 579–593.

[5] França, F., and Goldstein, L., 1996, ''Application of the Zoning Method in Radiative Inverse Problems,'' *Proc. Brazilian Congress of Engineering and Thermal Sciences, ENCIT 96*, Florianópolis, Brazil, Vol. 3, pp. 1655–1660.

[6] Matsumura, M., Morales, J. C., and Howell, J. R., 1998, ''Optimal Design of Industrial Furnaces by Using Numerical Solution of the Inverse Radiation Problem,'' *Proc. of the 1998 Int. Gas Research Conf.*, San Diego, CA.

[7] Kudo, K., Kuroda, A., Eid, A., Saito, T., Oguma, M., 1996, ''Solution of the Inverse Radiative Heat Source Problems by the Singular Value Decomposition,'' *Radiative Transfer I: Proc. First Int. Symp. on Radiative Heat Transfer*, M. Pinar Menguç, ed., Begell House, New York, pp. 568–578.

[8] França, F., Morales, J. C., Oguma, M., and Howell, J., 1998, ''Inverse Radiation Heat Transfer Within Enclosures With Nonisothermal Participating Media,'' *Proc. of the 11th Int. Heat Transfer Conference*, Korea, **1**, pp. 433–438.

[9] França, F., Oguma, M., and Howell, J. R., 1998, ''Inverse Radiation Heat Transfer Within Enclosures With Non-Isothermal, Non-Gray Participating Media,'' *Proc. of the ASME 1998 International Mechanical Engineering Congress and Exposition*, Anaheim, CA, **5**, pp. 145–151.

[10] França, F., Ezekoye, O. A., and Howell, J. R., 1999, ''Inverse Determination of Heat Source Distribution in Radiative Systems With Participating Media,'' *Proc. of National Heat Transfer Conference*, Albuquerque, New Mexico.

[11] França, F., Ezekoye, O., and Howell, J., 1999, ''Inverse Heat Source Design Combining Radiation and Conduction Heat Transfer,'' *Proc. of the ASME 1999 International Mechanical Engineering Congress and Exposition*, Nashville, **1**, pp. 45–52.

[12] Siegel, R., and Howell, J. R., 1992, *Thermal Radiation Heat Transfer*, 3rd ed. Hemisphere Publishing Corporation, Washington.

[13] Patankar, S. V., 1980, *Numerical Heat Transfer and Fluid Flow*, Hemisphere Publishing Corporation, Bristol, PA.

[14] Morales Rebellon, Juan Carlos, 1998, *Radiation Exchange within Enclosures of Diffuse Gray Surfaces: The Inverse Problem*, Ph.D. dissertation, Department of Mechanical Engineering, The University of Texas, Austin, TX, May.

Analysis of Radiative Heat Transfer in Complex Two-Dimensional Enclosures With Obstacles Using the Modified Discrete Ordinates Method

M. Sakami[1]

A. El Kasmi

A. Charette
e-mail: acharett@uqac.uquebec.ca

Groupe de Recherche en Ingénierie des Procédés et Systèmes,
Université du Québec à Chicoutimi, 555, boulevard de l'université,
Chicoutimi, Québec, Canada, G7H 2B1

In this work, an extension of a modified discrete ordinates method recently proposed by other researchers is presented. It is intended to counter the ray effect inherent in this method. The media analyzed are absorbing, emitting and isotropically or anisotropically scattering and the enclosure geometry is arbitrary. Cases with obstructions are emphasized. The radiative intensity is broken into two parts: the wall-related intensity and the medium-related intensity. The former is treated separately by rigorous integration over the entire solid boundary. A new differencing scheme based on quadrangular grids is also proposed and used for the treatment of the medium-related intensity. Results confirm that the proposed method is a good general remedy for anomalies caused by the ray effect due to the geometry. [DOI: 10.1115/1.1375812]

Keywords: Gaseous, Heat Transfer, Participating Media, Radiation, Scattering

Introduction

Due to the difficulty in finding an exact analytical solution to the integro-differential radiative transfer equation (RTE) in general absorbing-emitting-scattering media, a diversity of numerical methods have been worked out over the last forty years. In this respect, the discrete ordinates method (DOM) stands as one of the most popular methods for the solution of the RTE [1–3]. It has received significant attention due to its good accuracy, its computational economy and its easy implementation. However, relatively few researchers have used the DOM in complex geometries. For this aspect, Cheong and Song [4] have developed a numerical scheme by interpolating the intensities and the volumetric source terms between nodes in irregular enclosures. In a related way, Raithby and Chui [5] and Chui et al. [6] proposed a finite volume method (FVM) applicable to arbitrary geometries. Chai et al. [7] also applied a similar FVM technique. Liu et al. [8] examined and compared the accuracy of the DOM and FVM procedures in general body-fitted coordinates.

Another practical problem which has received little attention, is the discrete ordinates modeling of radiative heat transfer in enclosures with obstacles. Sanchez and Smith [9] applied the DOM to two-dimensional rectangular enclosures with protrusions and obstructions containing a transparent medium. The same method was applied to radiative transfer in a three-dimensional furnace with complex geometry including cooling pipes [10]. Coehlo et al. [11] proposed a comparison between the discrete transfer method, the DOM and the finite volume method to handle enclosures with baffles and containing an emitting-absorbing medium.

Despite the fact that the DOM can be applied to different situations as mentioned above, this method still suffers from some shortcomings as the so-called ray effect [12]. The ray effect is due to the discretization of the angular distribution of the radiative intensity. Some remedies were proposed to tackle this phenomenon. An iterative procedure based on the stochastic generation of the sets of ordinates directions was used by Pasini and Castellano [13]. Ramankutty and Crosbie [14,15] adopted an idea originally proposed by Olfe [16] and Modest [17] and consisting in using a modified differential approximation based on breaking up the radiation intensity into two parts, i.e., the intensity due to the medium and the intensity due to the enclosure walls. The medium-related intensity was treated by the DOM (Olfe [16] and Modest [17] had used the spherical harmonics method). They applied the technique to two-dimensional and three-dimensional cartesian enclosures with non-uniform boundary conditions. Sakami and Charette [18] extended this modified discrete ordinates method (MDO) to the treatment of the ray effect in an absorbing, emitting and scattering medium enclosed in a cavity of irregular geometry. The MDO method was also used, with a new version of the DOM, by Wu and Liou [19] to analyze the radiative transfer in a cylindrical enclosure with Fresnel boundaries. Another shortcoming of the DOM, the false scattering, will be discussed in the Results section.

In this paper, the application of the MDO to complex geometry with obstruction is presented. A new quadrangular differencing scheme, based on a previous triangular differencing approach [20,21] is also introduced. Since in this work we deal with radiation in irregular geometry enclosures, the alternative angular discretization procedure proposed by Koch et al. [22], the Double Cyclic Triangles (DCT) quadrature, is used and its capacity to avoid directional biasing is tested. The standard and modified discrete ordinates (SDO and MDO, respectively) solutions are compared for different cases.

Modified Discrete Ordinates Method

An irregular enclosure the surfaces of which are perfectly diffuse opaque reflectors is considered. The cavity contains an absorbing, emitting and isotropically or anisotropically scattering medium, with or without obstructions.

The radiative transfer equation (RTE) in a given direction Ω is

[1]Current address: Department of Mechanical Engineering, Lamar University, P.O. Box 10028, Beaumont, Texas 77710: E-mail: msakami@yahoo.fr

Contributed by the Heat Transfer Division for publication in the JOURNAL OF HEAT TRANSFER. Manuscript received by the Heat Transfer Division December 10, 1999; revision received January 20, 2001. Associate Editor: J. P. Gore.

$$\frac{1}{\beta}\Omega\cdot\nabla I(s,\Omega)+I(s,\Omega)=(1-\omega)I_b(s)+\frac{\omega}{4\pi}\int_{4\pi}\Phi(\Omega',\Omega)I(s,\Omega')d\Omega'. \quad (1)$$

On each physical surface of the cavity, the associated boundary condition (here purely diffuse reflection) can be written as

$$I^{\text{leav}}(\Omega)=\varepsilon I_{b,w}+\frac{1-\varepsilon}{\pi}\int_{\mathbf{n_s}\cdot\Omega'>0}\mathbf{n_s}\cdot\Omega' I^{\text{inco}}d\Omega', \quad \mathbf{n_s}\cdot\Omega<0 \quad (2)$$

where $\mathbf{n_s}$ is the unit outward normal vector at the boundary and ε the emissivity of the wall.

In the discrete ordinates method, the RTE and the associated boundary condition are replaced with a set of equations for a finite number of M directions in the total 4π sr solid angle. The integral terms of Eqs. (1) and (2) are reformulated with the aid of an angular quadrature of order M. This discretization gives excellent results for a number of cases, but it suffers from a drawback, called the ray effect, under certain conditions, especially when the temperatures on the physical boundaries or in the medium are not uniform.

To tackle this shortcoming, Ramankutty and Crosbie [14] presented a modified DOM. This method consists in breaking up the intensity into two parts, as follows:

$$I(s,\Omega)=I^g(s,\Omega)+I^w(s,\Omega). \quad (3)$$

In this equation, $I^w(s,\Omega)$ is due only to the emission and reflection at the walls; it is obtained by considering the scenario where no emission and in-scattering occur in the medium. It represents the residual intensity at a given location after its attenuation by the absorbing and scattering medium. $I^g(s,\Omega)$ is the intensity at the same location due to the medium contribution by emission and in-scattering. The main feature of this modified DOM is that the computation of radiation emanating from the surfaces is treated separately. The attenuated wall-related intensity $I^w(s,\Omega)$ can be solved analytically and the corresponding in-scatter term as well as the heat flux distribution at the walls can be evaluated with good accuracy in a similar way as the zonal method.

Let I^w satisfy the equation obtained in the case where only attenuation by absorption and scattering occur. Then Eq. (1) reduces to

$$\frac{1}{\beta}\Omega\cdot\nabla I^w(s,\Omega)+I^w(s,\Omega)=0. \quad (4)$$

Integration leads to the following analytical solution

$$I^w(s,\Omega)=I^{w,\text{leav}}e^{-\beta s(x,y,\Omega)}, \quad (5)$$

where $s(x,y,\Omega)$ is the path length from the wall to a given point in the medium for the Ω direction and $I^{w,\text{leav}}$ is the upstream wall boundary condition for I^w, which is obtained from general Eq. (2). Substitution of Eqs. (3) and (4) into Eq. (1) gives

$$\frac{1}{\beta}\Omega\cdot\nabla I^g(s,\Omega)+I^g(s,\Omega)=(1-\omega)I_b(s)+\frac{\omega}{4\pi}\int_{4\pi}\Phi(\Omega',\Omega)\times[I^g(s,\Omega')+I^w(s,\Omega')]d\Omega'. \quad (6)$$

The boundary condition related to I^g is:

$$I^{g,\text{leav}}(\Omega)=\frac{1-\varepsilon}{\pi}\int_{\mathbf{n_s}\cdot\Omega'>0}\mathbf{n_s}\cdot\Omega' I^{g,\text{inco}}d\Omega', \quad \mathbf{n_s}\cdot\Omega<0, \quad (7)$$

which emphasizes that the walls are simply reflecting when the intensity of the medium is considered.

The Wall-Related Moments. Figure 1 illustrates a general case where the scattering medium receives radiation from boundaries of arbitrary shape. The in-scatter term due to the wall contribution can be extracted from Eq. (6) as:

$$J^w(s,\Omega)=\int_{4\pi}\Phi(\Omega',\Omega)I^w(s,\Omega')d\Omega'. \quad (8)$$

By introducing Eq. (5) into Eq. (8), and considering that $d\Omega'=dA'\cos\theta'/d^2$, one obtains

$$J^w(s,\Omega)=\int_{4\pi}\Phi(\Omega',\Omega)I^{w,\text{leav}}e^{-\beta s(x,y,\Omega')}\frac{\cos\theta' dA'}{d^2}, \quad (9)$$

where d is the distance from the wall (area dA') to the considered point $(x_s,y_s,0)$. It is given by

$$d=\sqrt{(x_s-x_t)^2+(y_s-y_t)^2+z_t^2}.$$

From Fig. 1, one can write for a two-dimensional geometry

$$J^w(s,\Omega)=\int_t\int_{-\infty}^{+\infty}\Phi(\Omega'(t,z),\Omega)I^{w,\text{leav}}\frac{e^{-\beta d}}{d^2}\cos\theta' dzdt. \quad (10)$$

$(x_s,y_s,0)$ are the spatial coordinates of point s lying in the plane of the paper, and (x_t,y_t,z_t) are those of a given point on the boundary. Note that the RHS of Eq. (10) is integrated over the complete boundary t independently of the complexity of this boundary.

Since in this work we deal with anisotropic scattering radiation in irregular geometry with non-uniform boundary conditions, a

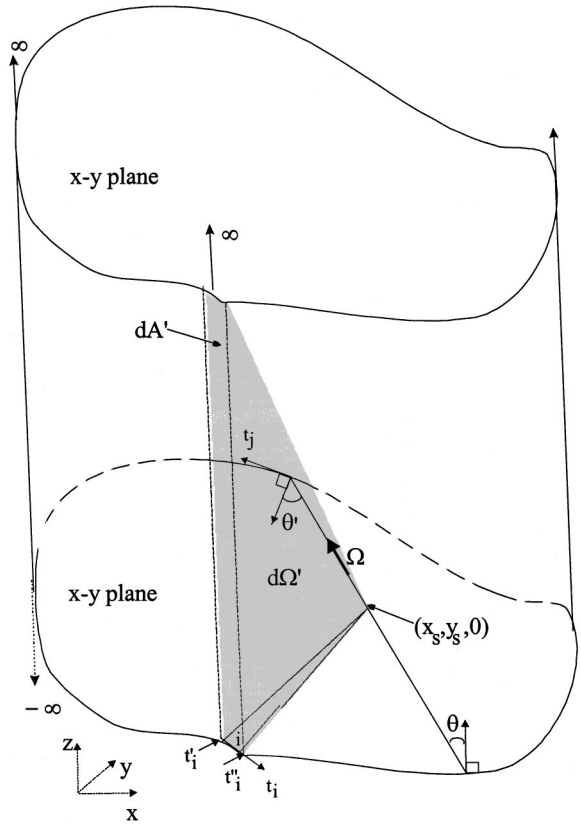

Fig. 1 Contribution of the infinite wall strip dA' to the in-scatter process within an arbitrary geometry. dA' and the point $(x_s,y_s,0)$ define the differential solid angle $d\Omega'$. Note that θ' has been displaced to the rear wall to avoid confusion on the figure, however, it should be seen as normal to dA'.

more general approach is to proceed as in the zonal method. It consists in breaking up the enclosure wall into N sub-surfaces of uniform intensity. Equation (10) then becomes

$$J^w(s,\Omega)=\sum_{j=1}^{N}\int_{t_j'}^{t_j''}\int_{-\infty}^{+\infty}\Phi(\Omega'(s,t_j,z_t),\Omega)I^{w,\text{leav}}\frac{e^{-\beta d}}{d^2}\times\cos\theta'\,dz_t dt_j$$
$$=\sum_{j=1}^{N}\int_{t_j'}^{t_j''}\int_{0}^{A}[\Phi(\Omega'(s,t_j,z_t),\Omega)+\Phi(\Omega'(s,t_j,-z_t),\Omega)]I^{w,\text{leav}}\frac{e^{-\beta d}}{d^2}\cos\theta'\,dz_t dt_j \tag{11}$$

with $\beta A\gg 1$. The transformation $|z_t|=[(x_s-x_t)^2+(y_s-y_t)^2]^{1/2}\sinh(u)$, proposed by Ramankutty and Crosbie [14], is used. $J^w(s,\Omega)$ is then evaluated numerically using the Gaussian quadrature. In presence of obstacles, cases where only a portion of the sub-surface j is seen by the local point s may occur. These cases are taken into account.

The Wall-Related Heat Flux. The wall-related heat flux can be evaluated at a subsurface i by

$$q^w=\sum_{j=1}^{N}\overline{s_i s_j}R_j-R_i, \tag{12}$$

where $\overline{s_i s_j}$ is a dimensinless interchange area evaluated per unit area of subsurface i and the radiosity R_i is given by

$$R_i=\varepsilon\pi I_b+(1-\varepsilon)\sum_{j=1}^{N}\overline{s_i s_j}R_j \tag{13}$$

$\overline{s_i s_j}$ can be obtained from:

$$\overline{s_i s_j}=\frac{1}{A_i}\int_{t_i'}^{t_i''}\int_{-\infty}^{+\infty}\int_{t_j'}^{t_j''}\int_{-\infty}^{+\infty}\frac{e^{-\beta d}}{d^2}\cos\theta\cos\theta'\,dz_j dt_j dz_i dt_i, \tag{14}$$

where A_i is the area of strip i and d_i is given by

$$d_i=\sqrt{(x_i-x_j)^2+(y_i-y_j)^2+(z_i-z_j)^2}.$$

For a two-dimensional case, we have

$$\overline{s_i s_j}=\frac{1}{l_i}\int_{t_i'}^{t_i''}\int_{t_j'}^{t_j''}\int_{-\infty}^{+\infty}\frac{e^{-\beta d}}{d^2}\cos\theta\cos\theta'\,dz_j dt_j dt_i. \tag{15}$$

Furthermore, for a small subsurface, one can assume that the double integral term associated with dz_j and dt_j is not dependent on the position within segment i. Since $l_i=t_i''-t_i'$, Eq. (15) then reduces to

$$\overline{s_i s_j}=\int_{t_j'}^{t_j''}\int_{-\infty}^{+\infty}\frac{e^{-\beta d}}{d^2}\cos\theta\cos\theta'\,dz_j dt_j. \tag{16}$$

The Medium-Related Moments. The in-scatter term due to the contribution of the medium is (from Eq. (6))

$$J^g(s,\Omega)=\int_{4\pi}\Phi(\Omega',\Omega)I^g(s,\Omega')d\Omega'. \tag{17}$$

The discrete ordinates form of this integral is

$$J_m^g=\sum_{m'=1}^{M}w_{m'}\Phi_{m'm}I_{m'}^g. \tag{18}$$

Integrating Eq. (6) over a quadrangular cell i, and applying the Gauss theorem, one obtains [20]:

$$\forall m\in\{1,.....,M\},$$

$$I_m^{g,i}-\frac{\omega}{4\pi}(J_m^{g,i}+J_m^{w,i})=(1-\omega)I_b^i-\frac{1}{\beta S^i}\sum_{k=1}^{4}(\Omega\cdot\mathbf{n}_k^i)l_k^i I_{k,m}^{g,i}, \tag{19}$$

where $J_m^{g,i}$ and $J_m^{w,i}$ are the source functions due to the medium (Eq. (18)) and the wall (Eq. (10)), respectively. S^i is the area of cell i. The last term is general: it can be applied to any type of cell.

Similarly, Eq. (7) becomes

$$I_m^{g,\text{leav}}=\frac{1-\varepsilon}{\pi}\sum_{\mathbf{n_s}\cdot\Omega_{m'}>0}w_{m'}\mathbf{n_s}\cdot\Omega_{m'}I_{m'}^{g,\text{inco}},\quad \mathbf{n_s}\cdot\Omega_m<0. \tag{20}$$

To close the system formed by Eqs. (19) and (20), relations between the central and lateral intensities are needed. These are obtained by using an appropriate differencing scheme. We have proposed previously an integrated exponential scheme (IES) used for unstructured triangular (two-dimensional) and tetrahedral grids (three-dimensional) [20,21]. In this work, an integrated exponential scheme (IES) for quadrangular grids is suggested. This closing procedure consists in solving rigorously the RTE monodimensionally in each direction of the angular quadrature. Integration leads to algebraic equations that replace the classical interpolation relations, as explained below.

The integration of the RTE over an optical path t in a given cell along direction m, where the intensity and the Planck function are assumed uniform, gives

$$I_m^{s_f}=I_m^{s_i}e^{-\beta t}+J_m^i(1-e^{-\beta t}), \tag{21}$$

where $t=s_f-s_i$, $I_m^{s_i}$ is the incoming intensity at a given point on the side of a cell, $I_m^{s_f}$ is the outgoing intensity of the ray after it travelled through the cell and the J_m^i is obtained from Eq. (18). Superscript g is omitted for simplification. The average intensities on the sides of the cells are obtained by considering an infinite number of parallel rays impinging on the cell walls. Figure 2 shows a quadrangular cell in which side 1 receives radiation from the three other sides. The subsides 1(a), 1(b), and 1(c) receive radiation from sides 2, 3, and 4, respectively. The average intensities on subsides 1(a) and 1(c) were determined in a previous work as [20]

$$I_{1a,m}^i=\frac{1}{l_{1a}}\int_{l_{1a}}I(x)dl_{1a}=I_{2,m}^i\chi_a+J_m^i(1-\chi_a) \tag{22}$$

and

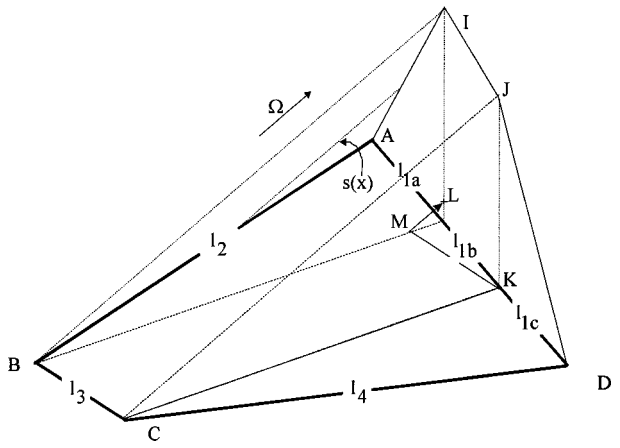

Fig. 2 Case where one side of a quadrilateral received radiation from the three other sides

$$I^i_{1c,m} = I^i_{4,m}\chi_c + J^i_m(1-\chi_c), \tag{23}$$

where $\chi_a = 1-e^{-\tau_a/\tau_a}$, $\chi_c = 1-e^{-\tau_c/\tau_c}$, and τ is the maximum optical thickness relative to the impact on the plane normal to ABCD and containing AD. Here $\tau_a = \beta\overline{BI}$ and $\tau_c = \beta\overline{CJ}$. In the same way, the average intensity on subside 1(b) can be given as

$$I^i_{1b,m} = I^i_{0,m}\chi_0 + J^i_m(1-\chi_0), \tag{24}$$

where $I^i_{0,m}$ is the mean intensity along the segment $[K,M]$, and $\chi_0 = 1-e^{-\tau_0/\tau_0}$ with $\tau_0 = \beta\overline{ML}$. Since the average intensity $I^i_{0,m}$ is related to that of segment 3 by

$$I^i_{0,m} = I^i_{3,m}e^{-\beta\overline{CJ}} + J^i_m(1-e^{-\beta\overline{CJ}})$$

one obtains

$$I^i_{1b,m} = I^i_{3,m}\chi_b + J^i_m(1-\chi_b) \tag{25}$$

and $\chi_b = e^{-\beta\overline{CJ}}(1-e^{-\tau_0/\tau_0})$.

Summing the three contributions yields the characteristic equation

$$I^i_{1,m} = \frac{l_{1a}}{l_1}[I^i_{2,m}\chi_a + J^i_m(1-\chi_a)] + \frac{l_{1b}}{l_1}[I^i_{3,m}\chi_b + J^i_m(1-\chi_b)] + \frac{1_{1c}}{l_1}[I^i_{4,m}\chi_c + J^i_m(1-\chi_c)]. \tag{26}$$

The other situations are taken care of by a similar procedure. The radiative heat flux at the boundary enclosure walls is given by

$$q = q^w + q^g. \tag{27}$$

The medium-related heat flux can be expressed as

$$q^g = \sum_{m=1}^{M} w_m \varphi^i_{k,m} I^g_m \tag{28}$$

with $\varphi^i_{k,m} = \Omega \cdot \mathbf{n}^i_k$.

Solution Procedure

The medium related moments are treated with the DOM. The enclosure is meshed with an arbitrary structured or unstructured arrangement of quadrilaterals. According to the procedure described by Sakami and Charette [20], the algorithm recognizes the orientation of the cells relative to each direction and applies the corresponding characteristic equations. The practice adopted in this study is to determine a sweeping path for each direction of the quadrature, prior to the radiation computation itself. This enables that at each cell, the appropriate local boundary conditions are available. The mean and lateral intensities due to the medium are then obtained via Eqs. (19) and (26).

For the contribution of the walls, the related moments are evaluated with Eqs. (11) and (12). The in-scatter term due to the wall contribution is then introduced into Eq. (19) to determine the medium-related intensities. For non-black walls, J^w and q^w are calculated in an iterative way. The double integrals in Eqs. (11) and (16) are evaluated by the Gaussian quadrature with five locations along the t_j direction and sixty locations along the z direction. A routine was introduced to determine the sub-surfaces (or the portion of them) being seen by a point in a given position s.

Results

First, a test was done to examine the accuracy of the proposed IES. It concerns a comparison with the scheme proposed by Cheong and Song [4] in their linear and cubic discrete ordinates interpolation methods (DOIM). The enclosure considered is an infinite quadrilateral cylinder containing a medium at uniform temperature. The enclosure is depicted in Fig. 3(a) where the dimensions are indicated. The walls are cold and black. The medium is absorbing-emitting and is assigned a temperature T_g. Under these conditions, the following analytical expression of the intensity at a given position holds:

$$I(s) = I_{bw}e^{-\kappa s} + I_b(s)(1-e^{-\kappa s}), \tag{29}$$

where the blackbody intensities I_{bw} and I_b are related to the temperature of the wall and the medium, respectively. The exact solution for the radiative heat flux at the walls can then be evaluated by analytical integration of Eq. (29) over the complete solid angle.

Figures 4(a) and 4(b) report the heat flux obtained at the bottom wall of the enclosure with 11×11 and 21×21 grids, respectively. The heat flux solutions are seen to be in good agreement with the exact solution and the DOM results obtained with the S_6 quadrature, even for the coarser grid.

As mentioned precedingly, the DOM, besides the ray effect, suffers also from another shortcoming: the so-called *false scattering or numerical scattering*, which occurs when the direction of radiation is oblique with respect to the grid lines. In some circumstances, results may seem good, whereas they are simply the consequence of counter—balancing errors coming from the ray effect and the false scattering. A simple test was carried out in order to assess the capability of the proposed IES to mitigate this numerical diffusion effect. A problem already examined by Chai et al. [12] was reworked for this purpose. This is illustrated in Figs. 5(a) and (b) where it is seen that a collimated pencil of radiation of unit intensity is incident on a transparent medium (non-emitting, non-absorbing, and non-scattering). In Fig. 5(a), the collimated radiation is propagating at an angle of 60 deg with respect to the x-axis. Results of the mean intensities are reported for classical step and diamond schemes (upper and lower figures, respectively) and for our IES (middle value). While nothing can be argued from the cells covered only partly by the collimated pencil, it is seen from the regions neighboring the pencil that the proposed scheme produces less false scattering (deviation from 1.0) than the step scheme and an amount of smearing comparable to that of the diamond scheme. One should note also that the set-to-zero intensities used in the diamond scheme (underlined values follow from this procedure) reduce the propagation of the false scattering, while no set-to-zero or overshoot clipping is needed in our proposed scheme. Figure 5(b) shows a case where the IES does not generate any false scattering. This is true for any diagonal direction (45 deg in this particular case since a square grid is used). The diamond scheme exhibits the same behavior, but only for the 45 deg direction; the accuracy of this scheme decreases for diagonal directions other than 45 deg.

Also, since in this method (MDO) the wall-related intensity $I^w(s,\Omega)$ and the corresponding in-scatter term $J^w(s,\Omega)$ are treated analytically, the false scattering due to the wall emission is reduced; $I^w(s,\Omega)$ and $J^w(s,\Omega)$ solutions are independent of the grid.

The enclosures considered hereafter in this work contain a purely scattering medium. Various cases are created by keeping one wall hot while the other walls are uniformly at a lower temperature. The following results are presented to prove the correctness of the MDO procedure. Comparison between the S_N [23] and the DCT quadratures [22] is also discussed. The directions and the weights of the DCT quadratures used in this paper are reported in Tables 1 and 2. Note also that the grids shown in Fig. 3 define only the general lay-out; finer grids are used in the calculations.

Square Enclosure With a Centered Obstruction. This case is illustrated in Fig. 3(b) showing the cavity together with the grid used. The medium is purely isotropically scattering and $\beta = 1\ \mathrm{m}^{-1}$. The walls are black. Wall 1 is assigned a temperature of 1000 K while all the other walls are at 500 K. Figure 6 displays the heat flux at rear wall 3 (behind the obstruction) as obtained with the SDO method for different orders of the S_N and DCT quadratures. Prediction obtained with the T_5 fine angular quadrature [3] is also reported for comparison (200 directions). It is seen from the figure that the DCT020-1246 (48 directions) and the DCT111-1246810

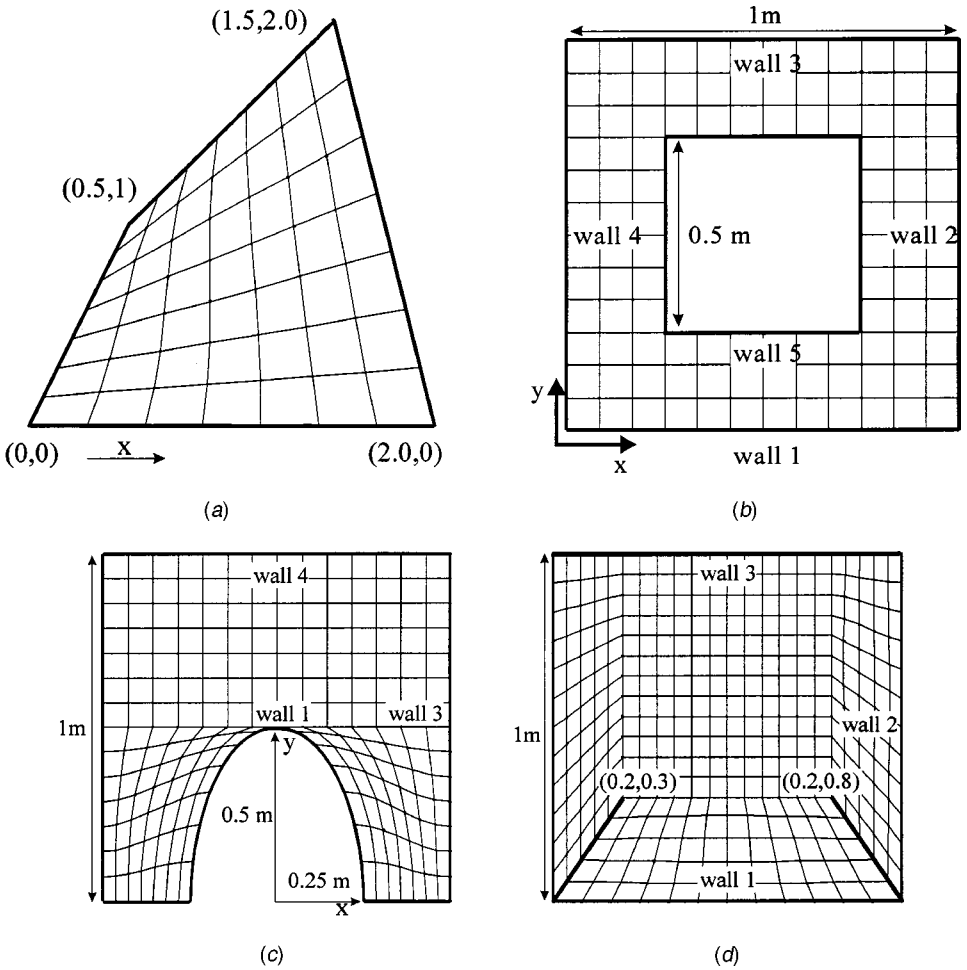

Fig. 3 (*a*) Irregular quadrilateral, (*b*) square obstacle, (*c*) elliptical protrusion, and (*d*) square enclosure with two oblique baffles (as obstacles with zero thickness)

(80 directions) predictions are closer to those obtained by T_5 (200 directions) than the S_6 and the S_8 predictions respectively, with correspondingly the same number of angular directions. The quality of this quadrature is highlighted here by its ability to represent adequately difficult situations. Figure 7 shows a comparison between the SDO and the MDO heat flux distributions at the same wall yielded by the S_8, DCT111 and T_5 quadratures. The MDO (T_5) method is taken as a reference since it was shown previously [18] that the results obtained are nearly identical to those of the Monte-Carlo method. The MDO method is seen to improve the results significantly only in the case of the S_8 quadrature. This again stresses the fact that the DCT111 is fundamentally better than the S_8 to mitigate the ray effects.

The heat flux distribution at wall 5 is presented in Fig. 8. When compared to the MDO T_5 results, the results obtained with the SDO method exhibit large discrepancies regardless of the quadrature used. On the other hand, all the MDO results confirm the efficiency of this method to reduce the ray effects. This is particularly true for the S_4 quadrature in which case a significant correction results from the application of the MDO method. The effect of the quadrature on the MDO results is marginal at this wall, but it can still be noticed that the DCT111 and the T_5 results are very close to each other. The effect of the emissivity at wall 5 is presented in Fig. 9. Walls 1, 2, 3, and 4 are assigned an emissivity of $\varepsilon_w = 0.9$ while $\varepsilon = \varepsilon_r$ at the other walls. The SDO method used in conjunction with the DCT111 quadrature yields similar anomalies for the two emissivities.

Square Enclosure With an Elliptical Protrusion. This enclosure is depicted in Fig. 3(*c*). The protrusion is assigned a temperature of $T_p = 1000$ K with $\varepsilon_p = 0.85$ while the other walls are at $T_w = 500$ K with $\varepsilon_w = 0.7$. Comparison between the SDO and the MDO methods is displayed in Fig. 10 for an isotropically scattering medium. The heat flux at cold wall 4 is presented. It can be seen that the MDO results obtained with the DCT111 quadrature produce a regular distribution, whereas the SDO results show anomalies due to the ray effects. Results for an anisotropically scattering medium are reported in Fig. 11 where the effect of the phase function is analyzed at wall 4. These phase functions are obtained by a Legendre polynomial expansion, the coefficients of which are reported by Kim and Lee [24]. F1 is highly forward scattering, B1 is backward scattering and ISO is isotropic scattering. As expected, the forward scattering phase function F1 produces the highest radiative flux, while the backward scattering phase function B1 yields lower radiative flux than the isotropic scattering phase function. Comparison between the SDO and the MDO solutions reveals discrepancies due to the ray effect which are similar for the three phase functions.

Square Enclosure with Two Oblique Baffles. In many practical cases, the thickness of obstructions is very small compared to the size of the furnace under study, and therefore a simplifying assumption of zero thickness is suggested to circumvent problems associated with the grid lay-out. Figure 3(*d*) simulates such a case where oblique baffles of zero thickness are inserted in an enclosure. The bottom wall is hot while the other walls and the baffles are kept cold (0 K). All the walls and the baffles are black.

Figure 12 shows the non-dimensional heat flux obtained at the

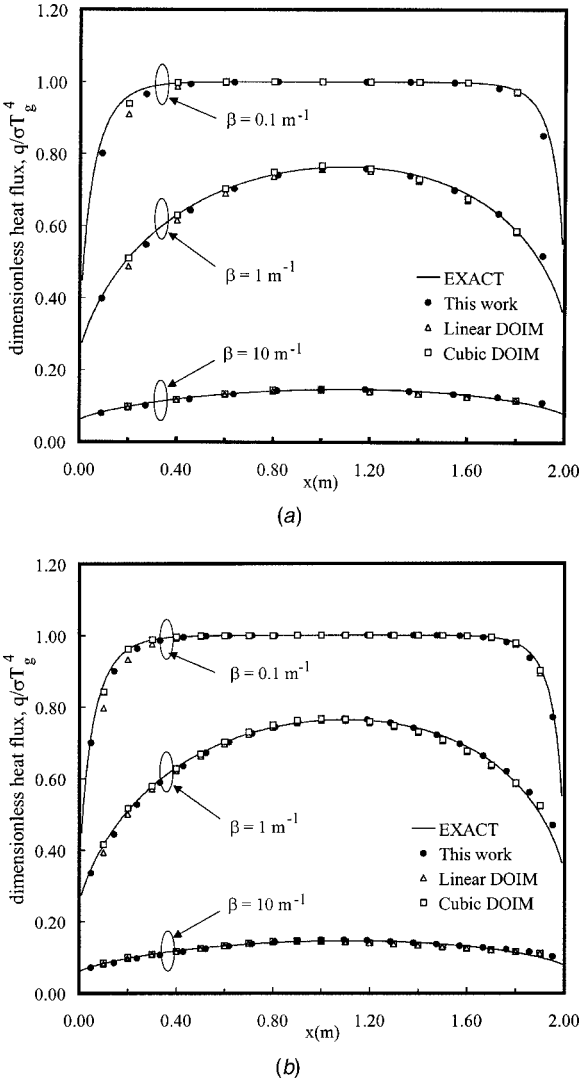

Fig. 4 (*a*) **Heat flux at the bottom wall (Fig. 3(*a*)) obtained by the S_6 quadrature, 11 × 11 grid, $\omega=0$; (*b*) heat flux at the bottom wall (Fig. 3(*a*)) obtained by the S_6 quadrature, 21 × 21 grid, $\omega=0$**

Table 1 Data of the DCT020-1246 quadrature

Direction ξ	Direction μ	Direction η	Point weight
0.13146076	0.13146076	0.98256609	0.168110131
0.25166076	0.68434890	0.68434890	0.355488645

top wall for different quadratures. Results obtained by both the SDO and MDO methods are presented. It is seen that, as in the previous examples, the MDO curves are close to each other with a small discrepancy for the S_4 quadrature (in this case the DCT111-1246810 may be taken as the reference since it was shown previously that this quadrature yields small discrepancies with respect to the T_5 quadrature). Once more, the ray effect is clearly demonstrated by the SDO curves which are seen to be very dependent on the quadrature used.

Finally, one word about the grids used. These can be obtained by various procedures, however, in the present work, the COSMOS code was used. It was also verified that the results are very marginally sensitive to the grid lay-out, i.e., the internal geometry of the grid for a given number of cells.

Computational Time. The CPU time required by the SDO and MDO methods on a Sun Ultra Sparc (CFP 12.9) workstation is given in Tables 3 and 4. Table 3 reports results for a purely isotropic scattering medium contained in a square cavity with and without an obstruction (see Fig. 3(*b*)). Obviously the MDO method is less computationally efficient than the SDO method: this is the price to pay for accurate results which are precluded when the SDO is used for the cases considered here. However, it is seen that the ratio of CPU times MDO/SDO decreases as the order of the angular quadrature increases. This is due to the fact that the computation time of the surface-related terms of the MDO method is independent of the quadrature order for an isotropic scattering case. On the contrary, for an anisotropic scattering case, the CPU time required by the in-scatter term due to the wall contribution ($J^w(s,\Omega)$) is dependent on the number of angular directions and the number of terms in the phase function. As shown in Table 4 (same physical case as in Table 3, except for the anisotropic scattering), the CPU time of the MDO method increases significantly with the number of these terms.

In practical problems, the grid may be required to be very fine in the medium. However, since the wall-related terms of the MDO method depend on the emission from the walls only, one could still use a coarse grid for the walls. The computational time could

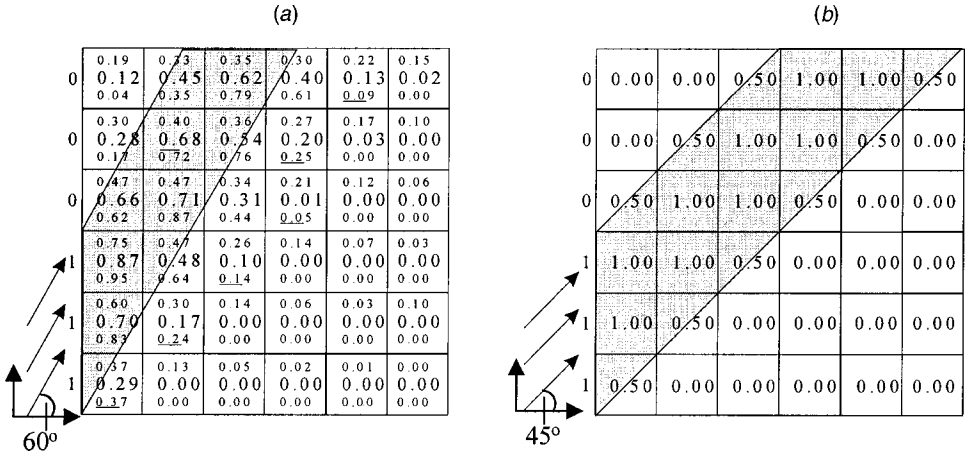

Fig. 5 False scattering test problem: (*a*) comparison between the diamond, step and the IES schemes for the 60 deg direction; and (*b*) IES scheme for the diagonal direction (45 deg). Step: upper value; IES: middle value; diamond: lower value.

Table 2 Data of the DCT111-1246810 quadrature

Direction ξ	Direction μ	Direction η	Point weight
0.19152567	0.49895503	0.84519925	0.1927139139
0.04640452	0.04640452	0.99784429	0.0714300262
0.57735027	0.57735027	0.57735027	0.2002241818

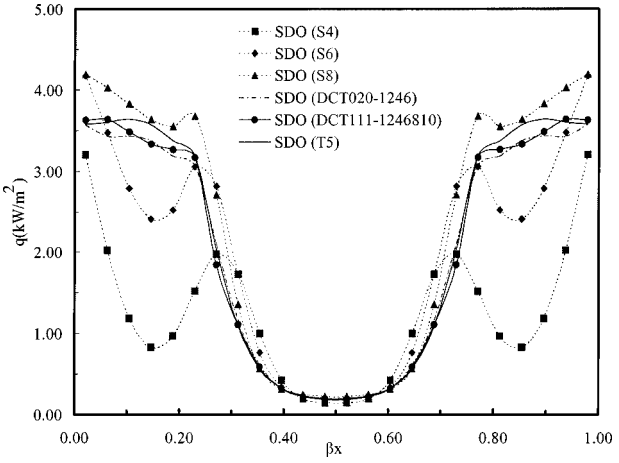

Fig. 6 Radiative heat flux at wall 3 (500 K, Fig. 3(*b*)) obtained by the SDO method for different quadratures, isotropic scattering case, average element size=0.04 m, $\omega=1$, $\beta=1$ m^{-1}

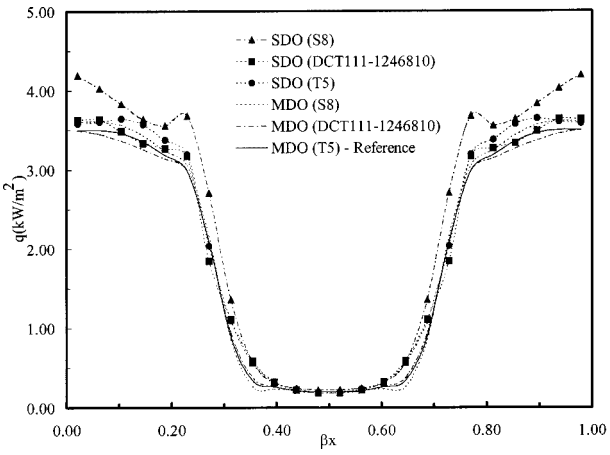

Fig. 7 Comparison of radiative heat flux at wall 3 (500 K, Fig. 3(*b*)) obtained by the SDO and MDO methods, isotropic scattering case, average element size=0.04 m, $\omega=1$, $\beta=1$ m^{-1}

thus be kept within reasonable limits. Another solution could consist in choosing a non-uniform grid for the medium, i.e., a coarser grid near the walls and a fine grid in the medium. This is possible since the IES accommodates to arbitrary grids.

Conclusion

In this work, the modified discrete ordinates method based on the superposition technique, i.e., addition of the contributions of the walls and the medium, is presented for a quadrangular grid lay-out. The method is extended to complex enclosures with irregular geometry and the presence of obstacles. It can also handle arbitrary intensity distribution at the walls and anisotropic scatter-

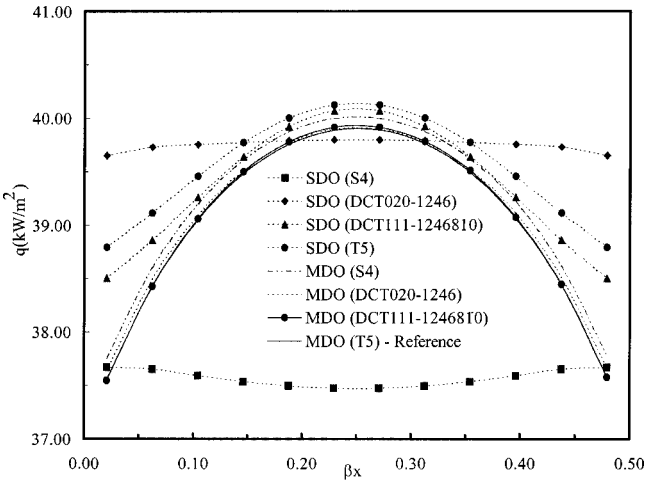

Fig. 8 Comparison of radiative heat flux at wall 5 (500 K, Fig. 3(*b*)) obtained by the SDO and the MDO methods, isotropic scattering case, average element size=0.40 m, $\omega=1$, $\beta=1$ m^{-1}

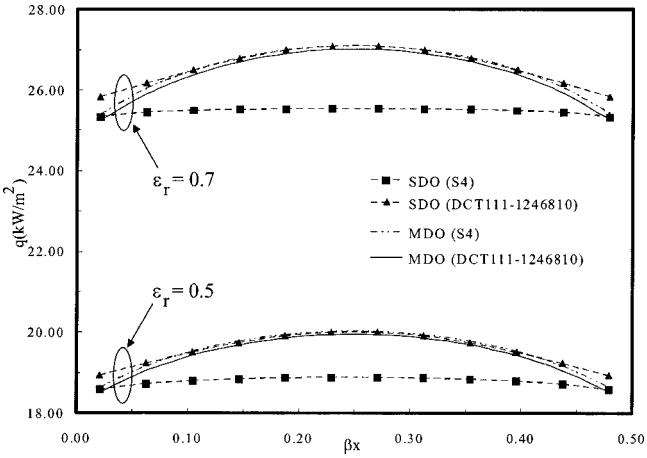

Fig. 9 Effect of the emissivity on the radiative heat flux at wall 5 (500 K, Fig. 3(*b*)) obtained by the SDO and the MDO methods, isotropic scattering case, average element size=0.40 m, $\omega=1$, $\beta=1$ m^{-1}

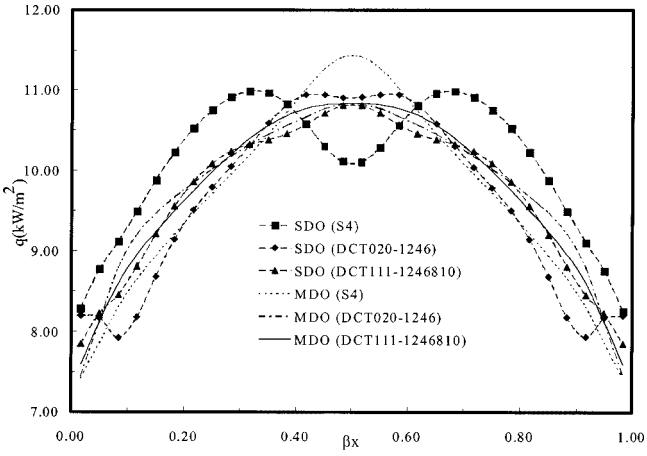

Fig. 10 Radiative heat flux at cold wall 4 (500 K, Fig. 3(*c*)) of the elliptical protrusion case, obtained by the SDO and the MDO methods, isotropic scattering case, average element size =0.033 m, $\omega=1$, $\beta=1$ m^{-1}

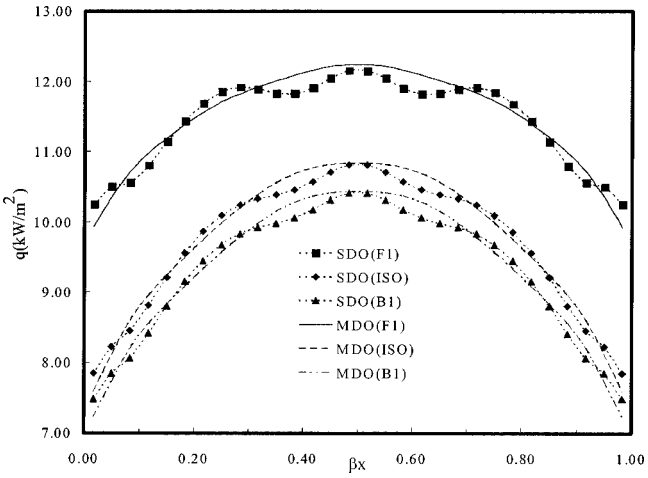

Fig. 11 Effect of the scattering phase functions on the radiative heat flux at wall 4 of the elliptical protrusion case obtained by the SDO and the MDO methods, average element size=0.033 m, ω=1, β=1 m^{-1}, DCT111-1246810 quadrature

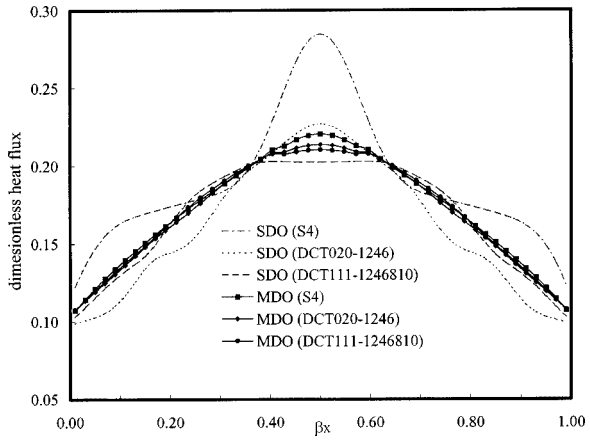

Fig. 12 Radiative heat flux at the top wall (cold, Fig. 3(*d*)) obtained by the SDO and MDO methods, average element size =0.04 m, ω=1, β=1 m^{-1}

Table 3 Computational time(s), 26 × 26 grid, ω=1, $\beta x=\beta y$ =1

Square without obstacle 26x26 (676 elements)	Quadrature	S_4	S_6	S_8
	SDO	1	2	4
	MDO	13	15	20
With obstacles (Fig. 3b) 26x26 (560 elements)	Quadrature	S_4	S_6	S_8
	SDO	0.5	1	4
	MDO	6	7	10

Table 4 Computational time(s), 26 × 26 grid, ω=1, $\beta x=\beta y$ =1, S_8 quadrature

Phase function	ISO	B2 (3 terms)	F2 (9 terms)
SDO	4	4	4
MDO	20	578	1120

ing. The integrated exponential scheme (IES) developed in this work facilitates the treatment of the complex enclosures. The results confirm the capability of the MDO method to minimize the anomalies due to the ray effect in various situations. It is also shown that the ray effect may be better suppressed by using the DCT quadrature.

Acknowledgments

Financial support for this work by the NSERC (National Sciences and Engineering Research Council) and by the FUQAC (Fondation de l'Université du Québec à Chicoutimi) is gratefully acknowledged.

Nomenclature

A_i = area of finite strip i [m^2]
I_b = Planck's function (black body intensity) [Wm^{-2} sr^{-1}]
$I(s,\Omega)$ = directional intensity for direction of propagation Ω at position s [Wm^{-2} sr^{-1}]
I^i_m = mean intensity of cell i for direction Ω_m [Wm^{-2} sr^{-1}]
I^i_{km} = lateral intensity of side k bounding cell i for direction Ω_m [Wm^{-2} sr^{-1}]
J = in-scatter term defined by Eq. (8) or Eq. (17)
l = length of a segment [m]
N = number of sub-surfaces on the enclosure wall
n^i_k = outward normal unit vector on side k bounding cell i
q = radiative flux on a surface element [Wm^{-2}]
R = radiosity [Wm^{-2}]
$\overline{s_i s_j}$ = dimensionless interchange area
t = surface coordinate; t_i is comprised between t_i' and t_i''
w_m = weight associated with discrete direction Ω_m
x,y,z = space coordinates

Greek Symbols

β = extinction coefficient [m^{-1}]
ε = surface emissivity
φ^i_{km} = stands for $\Omega_m \cdot \mathbf{n}^i_k$
$\Phi(\Omega',\Omega)$ = scattering phase function [sr^{-1}]
θ = angle between the direction of propagation Ω and the inward normal at the boundary
τ = maximum optical thickness
ω = scattering albedo
Ω = direction of propagation
Ω' = incoming direction of propagation
$d\Omega$ = differential solid angle

Superscripts

g = medium (gas)
w = wall
inco = incoming
leav = leaving

Subscripts

b = black body
m = a given direction of the angular quadrature
S = surface

References

[1] Fiveland, W. A., 1988, "Three-Dimensional Radiative Heat Transfer Solution by the Discrete-Ordinates Method," J. Thermophys. Heat Transfer, **2**, No. 4, pp. 309–316.
[2] Truelove, J., 1988, "Three-Dimensional Radiation in Absorbing-Emitting-Scattering Media Using the Discrete-Ordinates Approximation," J. Quant. Spectrosc. Radiat. Transf., **39**, No. 1, pp. 27–31.
[3] Thurgood, C. P.,1992, "A Critical Evaluation of the Discrete Ordinates Method Using HEART and Tn Quadrature," Ph.D. thesis, Queen's University, Kingston, Canada.
[4] Cheong, K. B., and Song, T. H., 1997, "An Alternative Discrete Ordinates Method With Interpolation and Source Differencing for Two-Dimensional Radiative Transfer Problems," Numer. Heat Transfer, Part B, **32**, pp. 107–125.
[5] Raithby, G. D., and Chui, E. H., 1990, "A Finite Volume Method for Predicting a Radiative Heat Transfer in Enclosures With Participating Media," ASME J. Heat Transfer, **112**, pp. 415–423.
[6] Chui, E. H., Raithby, G. D., and Hughes, P. M. J., 1992, "Prediction of Ra-

diative Transfer in Cylindrical Enclosures With the Finite Volume Method,'' J. Thermophys. Heat Transfer, **6**, pp. 605–611.
[7] Chai, J. C., Parthasarathy, G., Lee, H. S., and Patankar, S., 1995, ''Finite Volume Radiative Heat Transfer Procedure for Irregular Geometries,'' J. Thermophys. Heat Transfer, **9**, pp. 410–415.
[8] Liu, J., Shang, M., and Chen, Y. S., 1997, ''Prediction of Radiative Transfer in General Body-Fitted Coordinates,'' Numer. Heat Transfer, Part B, **31**, pp. 423–439.
[9] Sanchez, A., and Smith, T. F., 1992, ''Surface Radiation Exchange for Two-Dimensional Rectangular Enclosures Using the Discrete-Ordinates Method,'' ASME J. Heat Transfer, **114**, 465–472.
[10] Adams, B., and Smith, P. J., 1993, ''Three-Dimensional Discrete-Ordinates Modeling of Radiative Transfer in a Geometrically Complex Furnace,'' Combust. Sci. Technol., **88**, pp. 293–308.
[11] Coelho, P. J., Goncalves, J. M., Carvalho, M. J., and Trivic, D. N., 1998, ''Modeling of Radiative Heat Transfer in Enclosures With Obstacles,'' Int. J. Heat Mass Transf., **4/5**, pp. 745–756.
[12] Chai, J. C., Lee, H. S., and Patankar, S., 1993, ''Ray Effect and False Scattering in the Discrete Ordinates Method,'' Numer. Heat Transfer, Part B, **24**, pp. 373–389.
[13] Pasini, S., and Castellano, L., 1994, ''Numerical Experiments on the Application of the Diamond Scheme to Sets of Discrete Directions Obtained From a Random Numbers Generator, *Radiative Heat Transfer: Current Research*, ASME HTD-Vol. 276, pp. 99–104.
[14] Ramankutty, M. A., and Crosbie, A. L., 1997, ''Modified Discrete Ordinates Method of Radiative Transfer in Two-Dimensional Rectangular,'' J. Quant. Spectrosc. Radiat. Transf., **59**, No. 1, pp. 107–140.
[15] Ramankutty, M. A., Crosbie, A. L., and Crosbie, A. L., 1998, ''Modified Discrete Ordinates Solution of Radiative Transfer in Three-Dimensional Rectangular Enclosures,'' J. Quant. Spectrosc. Radiat. Transf., **60**, No. 1, pp. 103–134.
[16] Olfe, D. B., 1970, ''Radiative Equilibrium of a Gray Medium Bounded by Nonisothermal Walls,'' Prog. Astronaut. Aeronaut., **23**, pp. 295–317.
[17] Modest, M. M., 1989, ''The Modified Differential Approximation for Radiative Transfer in General Three Dimensional Media,'' J. Thermophys. Heat Transfer, **3**, No. 3, pp. 283–288.
[18] Sakami, M., and Charette, A., 2000, ''Application of a Modified Discrete Ordinates Method to Two-Dimensional Enclosures of Irregular Geometry,'' J. Quant. Spectrosc. Radiat. Transf., **64**, No. 3, pp. 275–298.
[19] Wu, C., and Liou, B., 1997, ''Discrete Ordinates Solutions for Radiative Transfer in a Cylindrical Enclosure with Fresnel Boundaries,'' Int. J. Heat Mass Transf., **40**, No. 10, pp. 2467–2475.
[20] Sakami, M., and Charette, A., 1998, ''A New Differencing Scheme for the Discrete Ordinates Method in Complex Geometry,'' Rev. Gen. Therm., **37**, pp. 440–449.
[21] Sakami, M., Charette, A., and Le Dez, V., 1998, ''Radiative Heat Transfer in Three-Dimensional Enclosures of Complex Geometry Using the Discrete Ordinates Method,'' J. Quant. Spectrosc. Radiat. Transf., **59**, No. 1/2, pp. 117–136.
[22] Koch, R., Krebs, W., Wittig, S., and Viskanta, R., 1995, ''Discrete Ordinates Quadratures Schemes for Multidimensional Radiative Transfer,'' J. Quant. Spectrosc. Radiat. Transf., **53**, No. 4, pp. 353–372.
[23] Fiveland, W. A., 1991, ''The Selection of Discrete Ordinates Quadrature Sets for Anisotropic Scattering,'' *Fundamentals of Radiation Heat Transfer*, ASME HTD-Vol. 160, pp. 89–96.
[24] Kim, T. K., and Lee, H. S., 1998, ''Effect of Anisotropic Scattering on Radiative Heat Transfer in Two-Dimensional Rectangular Enclosures,'' Int. J. Heat Mass Transf., **31**, No. 8, pp. 1711–1721.

Jet Impingement Boiling From a Circular Free-Surface Jet During Quenching: Part 1—Single-Phase Jet

David E. Hall
Michelin Americas Research Corporation,
515 Michelin Road,
Greenville, SC 29602

Frank P. Incropera
Notre Dame University,
South Bend, IN 46556
e-mail: fpi@nd.edu

Raymond Viskanta
School of Mechanical Engineering,
Purdue University,
West Lafayette, IN 47907

This paper reports results from an experimental study of boiling heat transfer during quenching of a cylindrical copper disk by a subcooled, circular, free-surface water jet. The disk was heated to approximately 650°C, and as quenching occurred, transient temperature measurements were taken at discrete locations near the surface and applied as boundary conditions in a conduction model to deduce transient heat flux distributions at the surface. Results are presented in the form of heat flux distributions and boiling curves for radial locations varying from the stagnation point to ten nozzle diameters for jet velocities between 2.0 and 4.0 m/s (11,300≤Re_d≤22,600). Data for nucleate boiling in the stagnation region and spatial distributions of maximum heat flux are presented and are in good agreement with correlations developed from steady-state experiments. Spatial distributions of minimum film boiling temperatures and heat fluxes are also reported and reveal a fundamental dependence on jet deflection and streamwise location. A companion paper (Hall et al., 2001) describes single-phase and boiling heat transfer measurements from a two-phase (water-air), free-surface, circular jet produced by injecting air bubbles into the jet upstream of the nozzle exit. [DOI: 10.1115/1.1389061]

Introduction

Metal processing industries widely employ liquid jet impingement cooling as a means of precisely controlling temperature histories during processing. In manufacturing operations such as hot-rolling, continuous casting, and forging, liquid jets are used to control cooling rates and consequently affect metallurgical phase transformations, solidification, and other temperature dependent processes [1]. However, due to the existence of different boiling regimes which depend on surface temperature and geometry as well as coolant flow conditions and subcooling, boiling from high temperature surfaces can be quite complex. Nucleate boiling up to the maximum or critical heat flux (CHF), transition boiling up to the rewetting temperature or Leidenfrost point, and film boiling can exist simultaneously at different streamwise locations on the target surfaces. Thus, a thorough understanding of jet impingement hydrodynamics and heat transfer is essential to predicting and optimizing material processing parameters.

Extensive studies of jet impingement boiling from rectangular (slot) jets in the V-regime, for which the maximum heat flux varies with velocity at or near atmospheric pressure [2], have been undertaken by several researchers. Vader et al. [3] examined boiling incipience in the impingement and parallel flow regions of a rectangular jet of water at moderate to high subcoolings. Temperature corresponding to the onset of nucleate boiling, T_{ONB}, were measured, and the effect of boiling incipience on transition to turbulence was noted. Partial and fully-developed nucleate boiling were studied by Wolf et al. [4], who determined that although streamwise location had a strong influence on partial boiling, it had no influence on fully-developed nucleate boiling. They also concluded that fully-developed nucleate boiling results are independent of jet velocity at all streamwise locations.

Using quenching experiments, Kumagai et al. [5] investigated boiling heat transfer on a 20 mm×150 mm surface initially at 400°C cooled by a free-surface planar water heat with subcoolings up to 50°C. They demonstrated a strong dependence of maximum heat flux on streamwise location and subcooling and obtained transition boiling data for different streamwise locations for a saturated jet. The term maximum heat flux is used in lieu of CHF to emphasize that, in data obtained from quenching studies, this condition does not represent a discontinuity in wall superheat with increasing surface heat flux; rather it is the maximum in the boiling curve demarcating transition and nucleate boiling. Filipovic et al. [6,7] experimentally investigated film boiling heat transfer during quenching with a subcooled wall jet. Their results in the film boiling regime downstream of the quench front agreed well with analytical Nusselt number correlations which they developed.

Few studies of circular impinging jets in the V-regime have examined boiling heat transfer in the radial flow region. Relations between surface heat flux and wall superheat, ΔT_{SAT}, for the nucleate boiling regime, which account for variations of thermophysical properties, have been proposed by several researchers [2], and most data suggest independence of fully developed nucleate boiling on jet velocity subcooling, nozzle diameter, and heater size. Maximum heat flux data have also been reported [2], and results have been correlated in terms of thermophysical properties, jet velocity and diameter, and heater size.

Several transient studies [6,7,8–10], have considered heat transfer at surface temperatures which exceed those corresponding to the maximum heat flux. In a quenching study of a planar, free-surface jet impinging vertically on a 2 mm thick stainless steel plate, Ishigai et al. [8] reported stagnation line boiling curves for a range of velocities (0.65≤V_n≤3.5 m/s) and subcoolings (5≤ΔT_{SUB}≤55°C). The minimum film boiling temperature and heat flux were demonstrated to be strong functions of subcooling. For a 6.2 mm wide 2.1 m/s jet, as ΔT_{SUB} increased from 5 to 15°C, T_{MIN}, identified as a local minimum in the boiling curve, increased from ~300°C to over 400°C. For ΔT_{SUB}=25 and 35°C, however, a shoulder region developed over which the heat flux remained nearly constant as T_s decreased. The author theorized that this corresponded to intermittent rewetting of the surface. At ΔT_{SUB}=55°C, however, no film boiling was observed, even

Contributed by the Heat Transfer Division for publication in the JOURNAL OF HEAT TRANSFER. Manuscript received by the Heat Transfer Division May 27, 1997; revision received March 22, 2001. Associate Editor: M. S. Sohal.

though the initial surface temperature was 1000°C. This suggests an interesting phenomenon: for highly subcooled jets, the minimum heat flux in the film boiling region occurs at temperatures beyond the condition at which water can remain liquid at atmospheric pressure. If the reported surface temperature are accurate, then this minimum cannot correspond to intermittent surface rewetting.

Using an apparatus similar to that of Ishigai et al. [8], Ochi et al. [9] deduced boiling heat transfer data from the stagnation point to a radial distance of 24 mm for a circular, free-surface jet with nozzle diameters of $5 \leqslant d \leqslant 20$ mm, velocities of $2.0 \leqslant V_n \leqslant 7.0$ m/s, and subcoolings of $5 \leqslant \Delta T_{SUB} \leqslant 80$°C. At the stagnation point, they observed that the minimum film boiling heat flux decreased with increasing nozzle diameter and increased with jet velocity and subcooling. In addition, stagnation point minimum film boiling temperatures decreased from over 800°C for $d=5$ mm and $V_n=5.0$ m/s to less than 400°C for $d=10$ mm and $V_n=2.0$ m/s for a subcooling of 15°C. Similarly, Filipovic et al. [11] measured values of T_{MIN} as high as 710°C from a subcooled wall jet and observed T_{MIN} to be a strong function of V_n, T_∞, and streamwise location. The observation of minimum film boiling temperatures well beyond the critical point indicates that for highly-subcooled jets, this temperature cannot correspond to surface rewetting.

The present study is concerned with local measurements of boiling from a free-surface, circular water jet in the stagnation and radial flow regions. Nucleate boiling data were obtained for the stagnation region, and radial distributions of the maximum heat flux were measured and compared with correlations developed from steady-state experiments. The effect of hydrodynamic conditions on rewetting temperatures and minimum film boiling heat fluxes is also described. Data in all regimes, with the exception of fully-developed nucleate boiling, demonstrate a dependence on jet velocity and streamwise location, and all data suggest independence of test cell initial temperature.

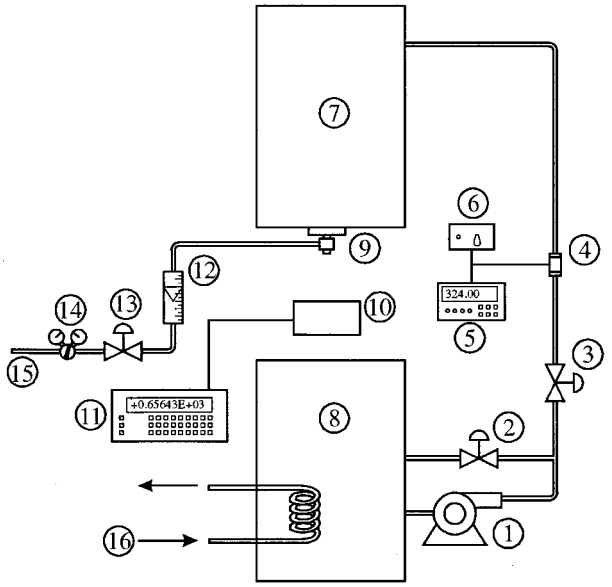

1	Centrifugal Pump	9	Nozzle
2	Bypass Valve	10	Test Cell
3	Control Valve	11	Data Acquisition
4	Flow Meter	12	Air Flow Meter
5	Frequency Counter	13	Air Control Valve
6	Voltage Supply	14	Pressure Regulator
7	Supply Tank	15	Compressed Air Cylinder
8	Reservoir	16	Coolant Water

Fig. 1 Experimental flow loop

Experimental Method and Apparatus

The flow loop used to supply the jet is depicted in Fig. 1. Deionized water from the reservoir was routed to the supply tank by a centrifugal pump, for which downstream control and bypass valves were adjusted to maintain the desired jet nozzle velocity, V_n. The flow rate was measured using an Omega ultra-low flow sensor. Once the supply head in the tank reached a steady value, the jet flow rate corresponded to the tank influx. The water temperature in the reservoir was maintained at 25°C by passing tap water through a coil in the tank. A convergent channel supplied a pipe-type nozzle of $d=5.1$ mm and 11 diameters in length. The nozzle assembly was bolted to the bottom of the supply tank, and immediately upstream of the nozzle entrance, a 51 mm thick section of aluminum honeycomb acted as a flow straightener to dampen circulation entering the nozzle from the supply tank. The nozzle utilized in this study was identical to the nozzle used to create the two-phase jet described in the companion paper [12] with the air injection turned off. Further details of the flow loop and nozzle design are induced in the companion paper.

Figure 2 depicts the test cell and stainless steel enclosure. The test cell was machined from a 25.4 mm thick oxygen-free copper disk, 112 mm in diameter, and a 2.5 mm relief, 12.7 mm deep, was machined around the perimeter to allow the retaining ring to secure the copper block in the carriage and to minimize water entering the carriage. Twelve thermocouple wells, 1.6 mm in diameter, were drilled at 45 deg angle from the bottom surface to a depth of 34.1 mm, which brought the hole tip to within 1.3 mm of the top surface. The hole tips were located at nine discrete radial locations spaced at 6.4 mm intervals from the centerline to a radial distance of 50.8 mm. Four thermocouples were placed at the 12.7 mm radial location spaced 90 deg apart. Measurements from these thermocouples verified that the jet was properly centered above the test cell during each experiment to insure axisymmetry. Type K thermocouples encased in an inconel sheath were fit into the holes. A small amount of MgO was inserted into the hole to insure good thermal contact between the thermocouple and copper. The test cell was nickel plated with a 13 μm layer to prevent oxidation at elevated temperatures. Prior to each experiment, the nickel surface was cleaned with metal polish, and surface profilometer measurements revealed little variation in the surface roughness after the first experiment. Before the first experiment, the average surface roughness, R_a, was measured to be 0.24 μm. After the first experiment, the surface roughness remained at a constant value of $R_a \approx 0.36$ μm.

The test cell was secured in a carriage fabricated from stainless steel, to which a stainless steel retaining ring was bolted to prevent test cell motion. Fiberfrax (Carborundum Co., Niagara Falls, NY, USA) pressed board ($k=0.123$ W/m-K at 538°C) was used to insulate the bottom of the test cell. Prior to each experiment, the test cell was aligned beneath the nozzle, and the entire assembly was heated for approximately two hours to 10°C above the desired initial temperature in an electric furnace. The assembly was subsequently removed from the furnace, and a one inch diameter peg joined to the bottom of the carriage was used to re-position the test cell directly beneath the jet, which was deflected until the quenching process was initiated.

Data were acquired using an HP 3852A data acquisition control unit with a high-speed thermocouple multiplexer read by an integrating voltmeter. The integration time was 0.1 power line cycles, which provided three significant digits of accuracy, and temperatures at nine radial locations were sampled at an interval of 0.25 s. Increasing the sampling rate above 4 Hz did not noticeably affect the results, so this frequency was used to maximize the voltmeter integration time to filter environmental noise. Data acquisition was started prior to the quench and terminated after boiling ceased on the test cell surface.

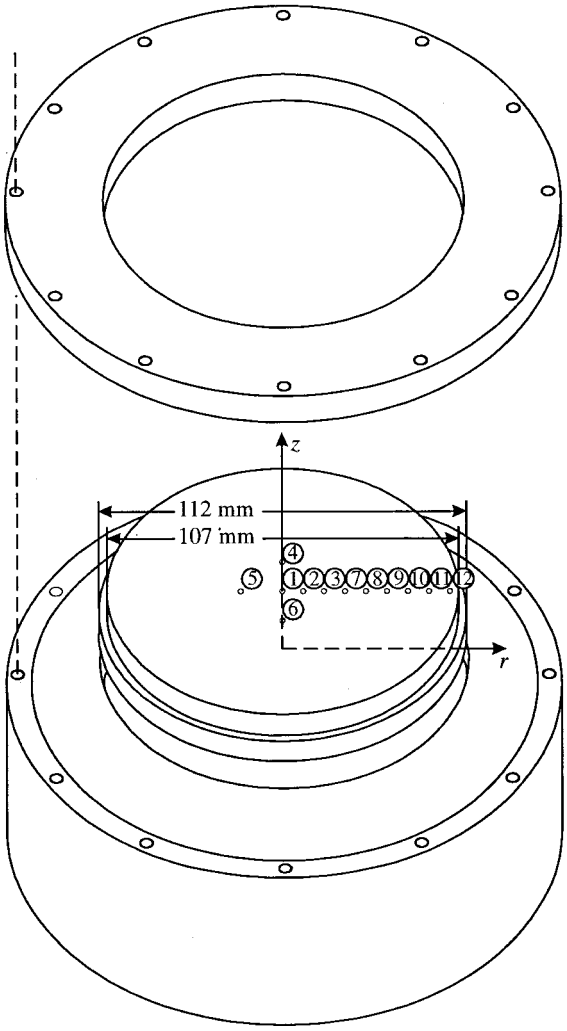

Fig. 2 Test cell assembly

The experimentally measured temperatures were interpolated using a two-step procedure. First, the temperatures at each radial location were interpolated in time using a third-order, least-squares b-spline approximation with fixed knots (IMSL routine BSLSQ; IMSL, Houston, TX, USA). Sixty b-splines were used to approximate the nearly 300 temperature readings. In the radial direction, the nine thermocouple temperatures were interpolated using an interpolation function suggested by El-Genk and Glebov [13]

$$T(r,t)=A_0(t)\cos\left[\pi\left(\frac{r}{R}\right)^{A_1(t)}\right]+A_2(t). \tag{4}$$

A nonlinear least-squares regression analysis was performed at each time step to determine the coefficients A_0, A_1, and A_2. The temperatures from the first ($r=0$ mm) and last ($r=50.8$ mm) thermocouples were weighted by a factor of 10 to insure that the distribution was properly bounded by the temperatures at the centerline and outer radius. Figure 3 compares the interpolated spatial temperature variations for 8 discrete times with the experimental measurements. The spatial interpolating function (Eq. (4)) has several important characteristics. First, the function is strictly increasing with radius. Second, for values of $A_1>0.5$ (which held for the data of this study for $t\gtrsim 5$ s), $\partial T/\partial r$ at the centerline is equal to zero, and $\partial T/\partial r$ at the outer radius is always equal to zero. This behavior preserves the symmetry and adiabatic boundary conditions at $r=0$ and $r=R$, respectively.

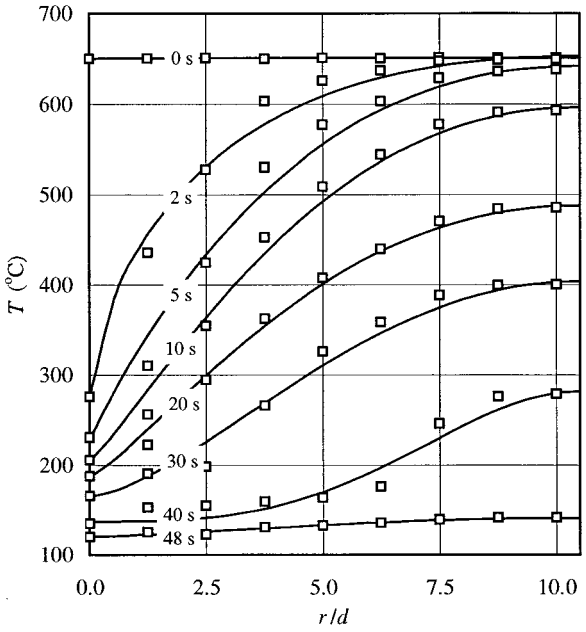

Fig. 3 Interpolated thermocouple temperature distributions ($T_i=650$°C, $V_n=3.0$ m/s, $\Delta T_{SUB}=75$°C)

A two-step procedure was implemented to deduce surface temperature and heat flux distributions. Because the thermocouples were 1.3 mm beneath the surface, temperatures and heat fluxes at the thermocouple depth had to be extrapolated to the surface using an inverse heat conduction technique. Since the nickel plating is only 13 μm thick, its presence was neglected. Heat fluxes at the thermocouple depth were deduced by using the control volume method [14] to solve the two-dimensional transient heat conduction equation,

$$\rho c_P\frac{\partial T}{\partial t}=\frac{1}{r}\frac{\partial}{\partial r}\left(kr\frac{\partial T}{\partial r}\right)+\frac{\partial}{\partial z}\left(k\frac{\partial T}{\partial z}\right) \tag{5}$$

subject to adiabatic boundaries at all but the instrumental surface ($z=L$) corresponding to location of the thermocouple junctions. Hence,

$$\left.\frac{\partial T}{\partial r}\right|_{r=R}=0,\quad \left.\frac{\partial T}{\partial z}\right|_{z=0}=0,\quad T(r,L,t)=T_{\text{experimental}}. \tag{6}$$

The control volume method applies an energy balance to discretized control volumes within the solution domain. Using the fully-implicit formulation, the resulting simultaneous equations were solved using a banded matrix routine. Mesh and time step optimization revealed that 66 control volumes in the r-direction, 38 control volumes in the z-direction, and a time step of 0.1 s were sufficient for convergence.

To extrapolate temperatures and heat fluxes from the thermocouple depth to the test surface, an exact series solution to the one-dimensional transient conduction equation was employed. Beck [15] presented the following solution in terms of the 0th through nth time derivatives of the temperature, $f(t)$, and axial temperature gradient, $g(t)$, at $\tilde{z}=0$ (the thermocouple depth)

$$T(\tilde{z},t)=\sum_{n=0}^{\infty}\frac{1}{(2n)!}\left(\frac{\tilde{z}^{2n}}{\alpha^n}\right)f^{(n)}(t)+\sum_{n=0}^{\infty}\frac{\tilde{z}}{(2n+1)!}\left(\frac{\tilde{z}^{2n}}{\alpha^n}\right)g^{(n)}(t). \tag{7}$$

From Fourier's law, the heat flux is, therefore,

$$q''(\tilde{z},t) = -\sum_{n=1}^{\infty} \frac{k}{(2n-1)!}\left(\frac{\tilde{z}^{2n-1}}{\alpha^n}\right) f^{(n)}(t)$$

$$-\sum_{n=0}^{\infty} \frac{k}{(2n)!}\left(\frac{\tilde{z}^{2n}}{\alpha^n}\right) g^{(n)}(t). \quad (8)$$

In Eqs. (7) and (8), the axial coordinate $\tilde{z}$ is measured from the thermocouple location ($z=L$), and $\tilde{z}=1.3$ mm corresponds to the test surface. Retention of the first five terms was found to be sufficient for convergence of each series. The first and second time derivatives of the surface temperature and axial heat flux were approximated using fourth-order, centered, finite-divided-difference formulas, and the third and fourth derivatives were estimated using second-order, centered, finite-divided-different formulas [16]. The applicability of extrapolating the surface temperatures was confirmed by applying the extrapolated surface temperatures to a two-dimensional transient conduction model of the full test section. The temperatures calculated at the thermocouple depth were nearly indistinguishable from the original interpolated temperatures.

The experiments conducted for this study were for a fixed nozzle diameter, $d=5.1$ mm, and a fixed nozzle-to-surface spacing of $H=100$ mm ($H/d=20$). The nozzle exit velocity was varied from 2.0 to 4.0 m/s, representing Reynolds numbers of 11,300 to 22,600 and consequently developing turbulent flow at the nozzle exit. The initial specimen temperature, T_i was held to within ± 3°C of 650°C, but tests for $T_i=500$°C and 800°C were performed for $V_n=3.0$ m/s to insure that results were independent of initial temperature. The water subcooling was fixed at 75°C.

Uncertainty Analysis

Results of an uncertainty analysis of the primary measurements (h, r, t, T, T_∞, V_n, and $\tilde{z}$) are presented in Table 1. The analysis follows that of Moffat [17] and Coleman Steele [18] for single-sample experiments and account for errors in measurement, calibration, and machining. All uncertainties were calculated for 95 percent confidence intervals. Although uncertainties in the thermocouple radial position and depth were small ($\delta r=\pm 0.65$ mm and $\delta\tilde{z}=\pm 0.25$ mm), the effect of these measurements on calculated heat fluxes and surface temperatures was significant. Propagation of these uncertainties into the calculated results are displayed in Table 2. Because the uncertainties varied significantly at different radial locations and times during the experiments, they were calculated separately for nucleate boiling in the stagnation region and for minimum and maximum heat flux conditions in the radial flow region at $r=19$ mm.

The sensitivity of computed results to the thermocouple depth, $\tilde{z}$, was calculated by differentiating Eqs. (7) and (8) with respect to $\tilde{z}$. Although $\delta\tilde{z}$ had little influence on the surface heat fluxes, its influence on the extrapolated surface temperature at $r=0$ mm was significant. This was the dominant factor contributing to the large uncertainty in ΔT_{SAT} during nucleate boiling. Sensitivities of the measured quantities to the uncertainty in radial position were determined by calculating radial gradients of the surface temperature and heat flux. The estimated contribution of positioning error to uncertainty in and q_s'' was particularly significant in the stagnation region. The sensitivity of results to measured thermocouple temperatures was calculated by numerically perturbing the data reduction procedure, as suggested by Moffat [17]. The influence of this uncertainty on the calculated results was relatively small. The uncertainty of T_s due to interpolation of the experimental temperatures was calculated from the precision index of the data. Because the temperatures from the centerline thermocouple are heavily weighted, the error in the stagnation region is small; the error due to interpolation in the radial flow region, however, is dominant. As shown in Fig. 3, however, Eq. (4) failed to match experimental temperatures as $r=13$ mm during the initial stages of the quench. During this time, A_1 was also <0.5, implying that $\partial T/\partial r$ at the centerline was nonzero. Due to these limitations, the calculated heat fluxes at the centerline for the first 5 s of data acquisition are not included in the results. The uncertainty of surface heat fluxes due to interpolation was estimated by comparing results calculated using Eq. (4) with results using a least squares regression spline. The precision index of the two results indicates that the error in q_s'' due to interpolation is the dominant uncertainty in both that stagnation and radial flow regions.

Table 1 Experimental uncertainties in measured quantities

Quantity	Relative or Total Uncertainty
h	$\delta h/h=-4.5\%$
r	$\delta r/R=\pm 1.3\%$
t	$\delta t=\pm 0.13$ s
T	$\delta T=\pm 2.1$°C ($r=0$ mm during nucleate boiling) $\delta T=\pm 2.5$°C ($r=19$ mm during maximum heat flux) $\delta T=\pm 2.1$°C ($r=19$ mm during rewetting)
T_∞	$\delta T_\infty=\pm 2.5$°C
V_n	$\delta V_n/V_n=\pm 2.5$ %
$\tilde{z}$	$\delta\tilde{z}/\tilde{z}=\pm 19.8$ %

Table 2 Uncertainties in calculated quantities

Quantity	Relative Uncertainty
q''_{NB}	$\delta q''_{NB}/q''_{NB}=\pm 32.4\%$
$\Delta T_{SAT,NB}$	$\delta\Delta T_{SAT,NB}/\Delta T_{SAT,NB}=\pm 20.5\%$
q''_{MAX}	$\delta q''_{MAX}/q''_{MAX}=\pm 17.0\%$
q''_{MIN}	$\delta q''_{MIN}/q''_{MIN}=\pm 19.5\%$
T_{MIN}	$\delta T_{MIN}/T_{MIN}=\pm 6.2\%$

Results and Discussion

Photographic Observations. A sequence of photographs of a quenching experiment is included in Fig. 4 for $V_n=3.0$ m/s. The sequence depicts events observed by Piggott et al. [19]. During early stages of the quench ($0\gtrsim t\gtrsim 30$ s), the stagnation region passes through transition and nucleate boiling. Initially, there is a brief period (~ 1 s) of no vapor production (film boiling), which is followed by vigorous vapor production (transition and nucleate boiling) after the stagnation region is wetted. As the stagnation region passes through nucleate boiling into single-phase convection ($t\approx 25$ s), a dark circular patch forms beneath the jet, and vapor production slows. Except for low amplitude oscillations, this patch remains stable at a nearly constant diameter for a period of approximately 10 s before the wetted region begins to grow. Immediately beyond this region, a narrow band of nucleate boiling exists.

At the outside edge of the nucleate boiling region, the liquid is deflected from the surface in a thin sheet which eventually breaks up due to surface tension. This deflection, noted by other researchers in both steady-state and transient experiments, is attributed to vigorous vapor production at the boiling front location, which corresponds to the maximum heat flux condition. As the liquid in the radial flow region passes over this vapor layer, the vapor momentum deflects the film from the surface. The angle formed between the liquid film and the plane of the surface increases and the velocity with which the jet is deflected decreases as the boiling front progresses outwards due to the decrease in liquid momentum. As the boiling front nears the outer edge of the test cell, the liquid collapses to form a continuous film boiling layer with the liquid flowing across a vapor blanket. In systems with higher heater-to-nozzle diameter ratios, this behavior is especially evident. In experiments from Hatta et al. [10], photographs reveal

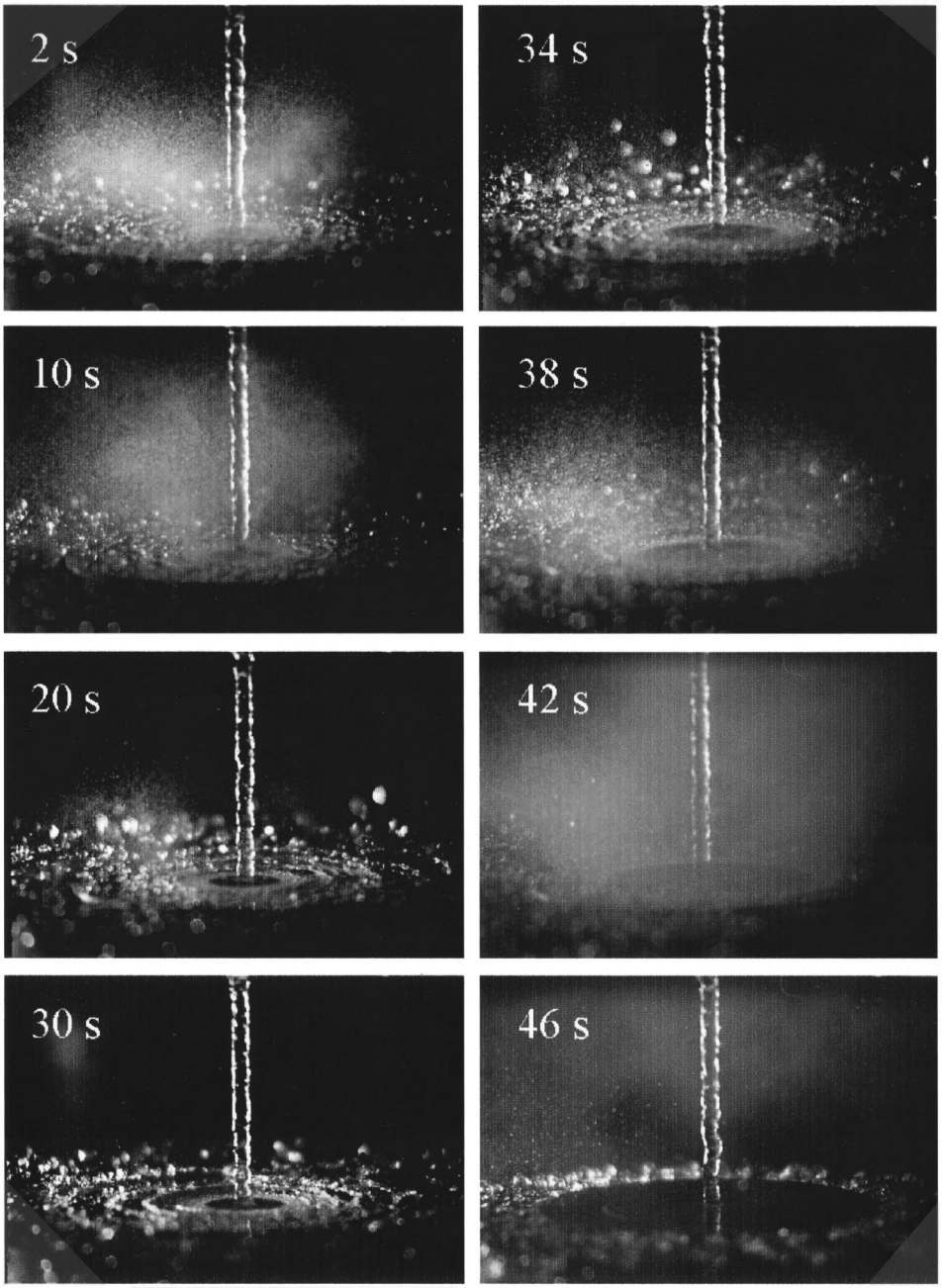

Fig. 4 Sequence of events associated with a quenching experiment (T_i=650°C, V_n=3.0 m/s, ΔT_{SUB}=75°C)

that at sufficient distances from the stagnation region, splashing decreases, and the liquid forms a continuous film boiling layer which persists until the local surface temperature drops below the minimum film boiling temperature.

A distinction between the deflection of impinging, free-surface jets from the target surface in steady-state and quenching experiments is that, in quenching experiments, the region of jet deflection is typically narrower. Steady-state experiments usually employ constant heat flux surfaces. Consequently, as maximum heat flux is reached, the entire surface dissipates q''_{MAX}. Boiling across the entire surface is extremely vigorous, and deflection occurs from a broad region. In contrast, surface heat flux distributions in quenching experiments are determined by heat transfer to the impinging jet and conjugate conduction within the test specimen. Consequently, the surface is neither isothermal nor isoflux. Since the surface heat flux upstream of the boiling front is less than q''_{MAX} and boiling is less vigorous, deflection is confined to a region immediately upstream of the boiling front. In steady-state experiments, Kumagai et al. [5] observed the same deflection phenomenon for saturated and subcooled jets, suggesting that it is independent of subcooling, although deflection was observed to be more violent for saturated jets.

Heat Flux Distributions and Boiling Curves. Heat flux distributions at times corresponding to the photographs of Fig. 4 are shown in Fig. 5. As the stagnation region passes through maximum heat flux into nucleate boiling, the stagnation point heat flux ($r=0$) exceeds 40 MW/m^2, and the heat flux decreases monotonically with radius. Once the boiling front begins to progress ($t \approx 34$ s), however, a local maximum in the heat flux distribution

moves radially outward. Actual differences between the maximum heat flux and heat fluxes in transition boiling (downstream) and nucleate boiling (upstream) are likely reduced by the interpolation procedure. Equation (4) does not preserve the steep temperature gradient in the boiling front region because it is a least-squares fit. An estimate of this error is included in the uncertainty analysis. The maximum heat flux is also observable in the boiling curves of Fig. 6.

Different boiling regimes are clearly demarcated in the boiling curves of Fig. 6. For radial locations greater than 10 mm, the heat flux quickly increases once the jet initially hits the surface. This increasing heat flux with decreasing surface temperature in the radial flow region is attributed to slow thermocouple response rather than a negative slope in the boiling curve. The heat flux then decreases to a local minimum and then increases to the maximum heat flux, as complete rewetting of the surface occurs. The surface then undergoes a brief period of nucleate boiling and finally single-phase convection. For the stagnation zone ($r<5$ mm), no local minimum is observed in the quench curves. In experiments with an initial test cell temperature of 800°C, early stages of quenching were characterized by a clearly-observable film boiling period and the stagnation point T_{MIN} was observed to be approximately 470°C. However, for $T_i=650$°C, a stable film boiling regime was not observed and is not manifested in the stagnation zone boiling curves. This is due to the relatively slow thermocouple response during this period of rapidly increasing heat flux.

The centerline boiling curve of Fig. 6 reveals surface reheating during the transition from nucleate boiling to single-phase convection. This temperature excursion was consistently reproducible and has been observed by other researchers in both steady-state and transient experiments. While steady-state experimental data for degassed water did display excursions in the study by Shibayama et al. [20], the addition of surfactants caused wall superheats to shift to the left after the onset of nucleate boiling. Nonn et al. [21] observed temperature excursions in jet impingement boiling data for subcooled FC-72 while measuring heat fluxes during both increasing and decreasing power. Ishigai et al. [8] observed excursions in transient experiments, but did not observe them in steady-state experiments employing the same apparatus. While data from the literature suggest that the addition of surfactants, the direction of heating, and differences between transient and steady-state conditions may all affect temperature excursions during boiling incipience or cessation, conclusions concerning its physical origins have not yet been drawn.

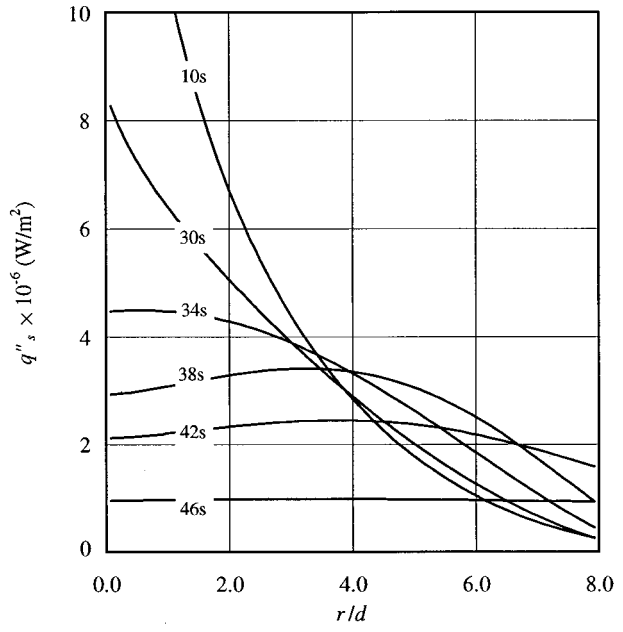

Fig. 5 Heat flux distributions demonstrating boiling front progression ($T_i=650$°C, $V_n=3.0$ m/s, $\Delta T_{SUB}=75$°C)

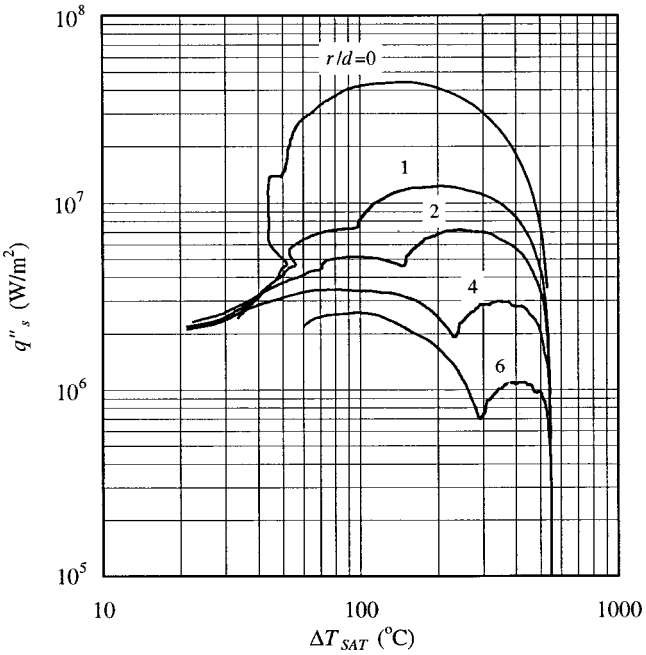

Fig. 6 Boiling curves ($T_i=650$°C, $V_n=3.0$ m/s, $\Delta T_{SUB}=75$°C)

Nucleate Boiling. Because the boiling front progressed so rapidly, reliable nucleate boiling data could only be deduced for the stagnation region, within which nucleate boiling existed for approximately 20 s. The nucleate boiling data for $V_n=2.0$, 3.0, and 4.0 m/s are presented in Fig. 7, and were correlated using the relation

$$q''_{NB}=C\Delta T^n_{\mathrm{SAT}}. \tag{9}$$

Although the data demonstrate a dependence on jet velocity, most studies of nucleate boiling from saturated, free-surface jets suggest independence of jet velocity [2]. Other studies [20,22,23], however, have demonstrated an increase in wall superheat with increasing jet velocity. No explanation of the shift of the boiling curve, however, has been suggested.

The data of Shibayama et al. [20] for saturated jets of water and water/surfactant mixtures suggest that increasing jet velocity increases the wall superheat required to maintain the same heat flux. Unfortunately, their results are complicated by the influence of other parameters, such as surfactant additives and nozzle diameter. In jet impingement experiments using water and R-113, Katsuta and Kurose [22] found increasing wall superheat with velocity for water, but not for R-113. In transient studies of near-saturated water jets, Ma et al. [23] deduced that increasing jet velocity shifted the entire boiling curve, including nucleate, transition, and film boiling, to higher surface excess temperatures.

Maximum Heat Flux. Figure 8 displays the variation of maximum heat flux with radius for nozzle exit velocities of $V_n=2.0$, 3.0, and 4.0 m/s. A sharp reduction in q''_{MAX} clearly demarcates the impingement zone and the radial flow region. Although there is an increase in T_{SAT} corresponding to an increase of the local pressure in the impingement zone, it only varies from approximately 0.5 to 2.1°C for $2.0\leqslant V_n\leqslant 4.0$ m/s. Moreover, the variation of pressure and T_{SAT} is continuous. Hence, it is not likely responsible for the large change in the maximum heat flux. A more likely explanation rests with the change from a radially

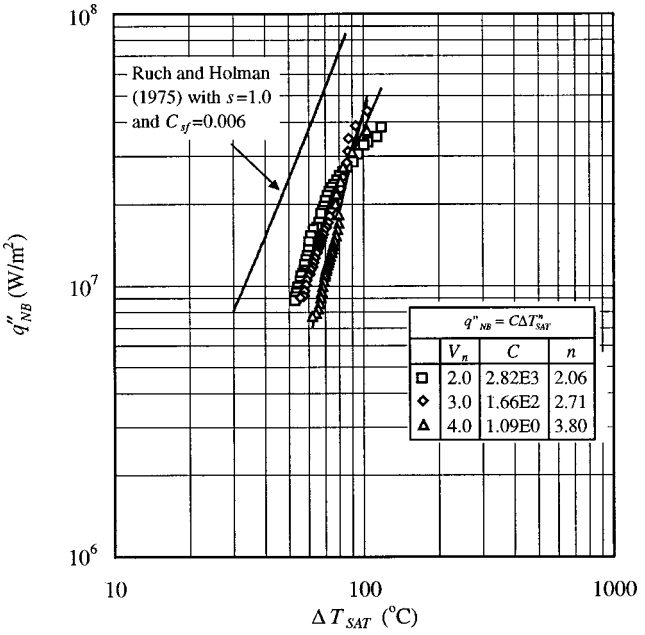

Fig. 7 Stagnation point nucleate boiling curves (T_i=650°C, V_n=3.0 m/s, ΔT_{SUB}=75°C)

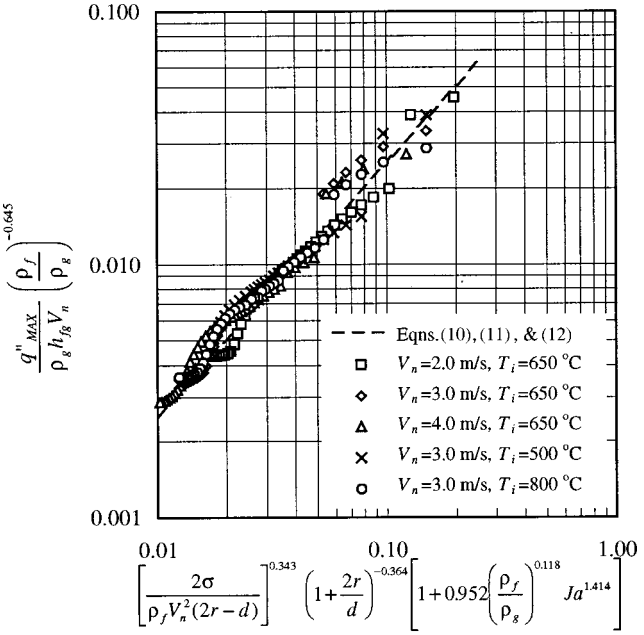

Fig. 9 Correlated variation of maximum heat flux with velocity and position in the radial flow region (ΔT_{SUB}=75°C)

accelerating flow to a decelerating flow at a radial location of approximately one jet diameter. In addition to reducing shear forces on the vapor bubbles outside the hydrodynamic boundary layer, this change yields a significant increase in thermal and hydrodynamic boundary layer thickness which reduce the maximum heat flux.

As noted by Wolf et al. [2], in the V-regime (low pressure regime in which maximum heat flux is velocity dependent), q''_{MAX} in the radial flow region depends on jet velocity and heater size, among other parameters. In steady-state jet impingement boiling experiments, the maximum heat flux occurs at the downstream location furthest from the stagnation point, and data for q''_{MAX} are typically correlated in terms of the largest heater dimension. One widely accepted correlation developed by Monde [24] is of the form

$$\frac{q''_{MAX}}{\rho_g h_{fg} V_n} = 0.221\left(\frac{\rho_f}{\rho_g}\right)^{0.645}\left[\frac{2\sigma}{\rho_f V_n^2(2r-d)}\right]^{-.343}\left(1+\frac{2r}{d}\right)^{-0.364} \tag{10}$$

with similar correlations having been proposed by other investigators [25–29]. The heater dimension in Eq. (10) has been replaced by twice the radial location, $2r$, since for transient experiments, the location of maximum heat flux moves outward as the test piece cools. This relation pertains to a saturated jet, and Monde et al. [30] recommended application of the following correction for a subcooled jet

$$\Phi = \frac{q''_{\mathrm{MAX,SUB}}}{q''_{\mathrm{MAX,SAT}}} = 1 + \varepsilon_{\mathrm{SUB}}\,. \tag{11}$$

However, the subcooling parameter suggested by Monde et al. [30] overpredicts maximum heat flux data for high subcoolings (their data only included subcoolings up to 30°C), and the parameter suggested by Nonn et al. [21] provides a better approximation to the data

$$\varepsilon_{\mathrm{SUB}} = 0.952\left(\frac{\rho_f}{\rho_g}\right)^{0.118}\mathrm{Ja}^{1.414}. \tag{12}$$

The experimental data for q''_{MAX} from this study are compared with Eqs. (10), (11), and (12) in Fig. 9 for ΔT_{SUB}=75°C, and there is good agreement between the data and the steady-state correlations in the radial flow region. However, near the stagnation zone ($r/d \gtrsim 2$), the data significantly exceed predictions based on Eqs. (10), (11), and (12). The curvature of the data is attributed to characteristics of the spatial interpolating function, rather than to departures from the functional form of Eq. (10).

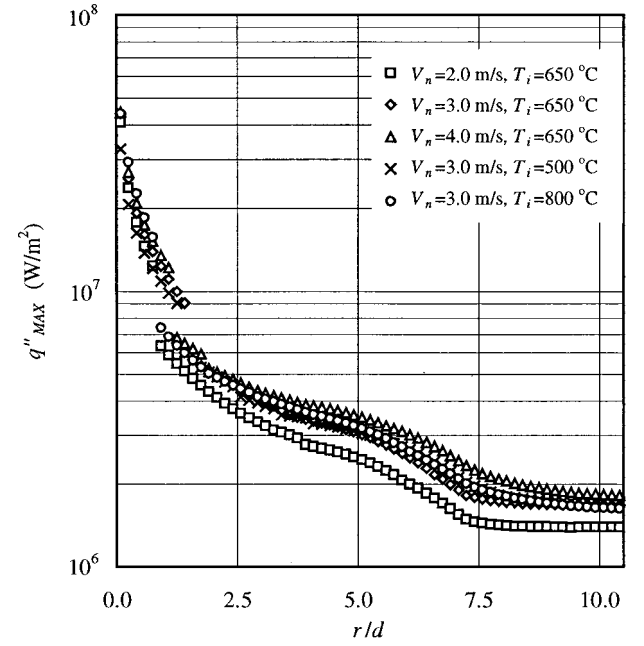

Fig. 8 Variation of maximum heat flux with velcoity and position (ΔT_{SUB}=75°C)

Minimum Film Boiling Heat Fluxes and Temperatures. The boiling curves of Fig. 6 may be used to infer the minimum film boiling heat flux, q''_{MIN}, and the corresponding minimum film boiling temperature, T_{MIN}. The location of q''_{MIN} corresponds to a

minimum in the heat flux at temperatures beyond the maximum heat flux point. This condition is typically reached just prior to intermittent liquid-solid contact as the vapor film begins to collapse. The corresponding temperature, T_{MIN}, is often referred to as the rewetting temperature and is equal to the Leidenfrost temperature for saturated liquids on isothermal surface [31]. Numerous studies of jet impingement boiling, however, have reported T_{MIN} well in excess of the critical temperature [8,9,11]. Therefore, it is likely that for highly subcooled jets, this minimum corresponds to a hydrodynamic phenomenon not observed for saturated jets or for pool boiling and does not represent partial rewetting of the surface. A possibility is that the minimum film boiling condition for subcooled jets corresponds to a relative maximum in the vapor blanket thickness. As the surface temperature decreases, this thickness may decrease as well until surface temperatures are low enough to sustain direct liquid-solid contact. The time at which the minimum film boiling temperature is reached may be inferred from measured temperature histories and corresponds to a point of minimum curvature (which is proportional to $\partial^2 T/\partial t^2$) prior to the maximum in curvature corresponding to the maximum heat flux, often referred to as the ''shoulder'' of the quench curve.

The local of minima in the boiling curves corresponding to q''_{MIN} versus $T_{MIN}-T_{SAT}$ is plotted in Fig. 10. The value of q''_{MIN} decreases monotonically with increasing radius and increases with increasing velocity. Although the literature revealed no pre-existing data for the distribution of q''_{MIN} in the radial flow region associated with free-surface circular jet impingement, transition boiling data from the study of planar jets by Kumagai et al. [5] demonstrate that transition boiling heat fluxes decreases with downstream location from the stagnation point. This decrease is attributed to both the decrease of momentum of the flowing film and the increase in local water temperature due to sensible heat addition.

Although the minimum film boiling temperature, T_{MIN}, increases with radius, this behavior is seemingly inconsistent with the decrease in free stream momentum and increase in local coolant temperature which occurs with increasing radius. Moreover, temperature histories and boiling curves from transient experiments performed by Kumagai et al. [5] and Filipovic et al. [6,7] for planar jets, and Ochi et al. [9] and Hatta et al. [10] for circular jets indicate conflicting trends for T_{MIN}. Significant differences in the experiments relate to hydrodynamic conditions in the parallel or radial flow region. Both Kumagai et al. [5] and Ochi et al. [9] reported deflection of the jet from the surface at the boiling front. Temperature histories from both studies reveal that T_{MIN} (identified as the point of maximum curvature in the temperature histories) increases with increasing streamwise location. In contrast, the jets observed in studies by Filipovic et al. [6] (for wall jets) and Hatta et al. [10] showed no such deflection. Instead, a continuous liquid film flowed across the vapor blanket in the film boiling region. Temperature histories from these studies demonstrated a decrease in T_{MIN} with increasing streamwise location.

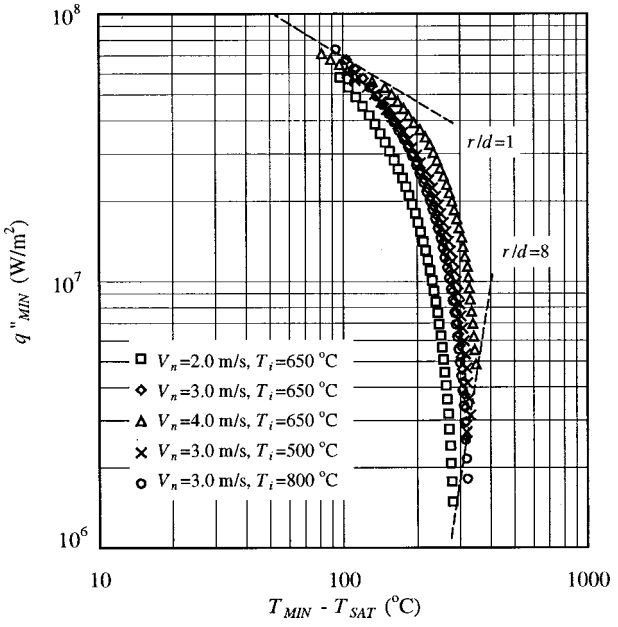

Fig. 10 Minimum film boiling heat flux as a function of T_{MIN} (ΔT_{SUB}=75°C)

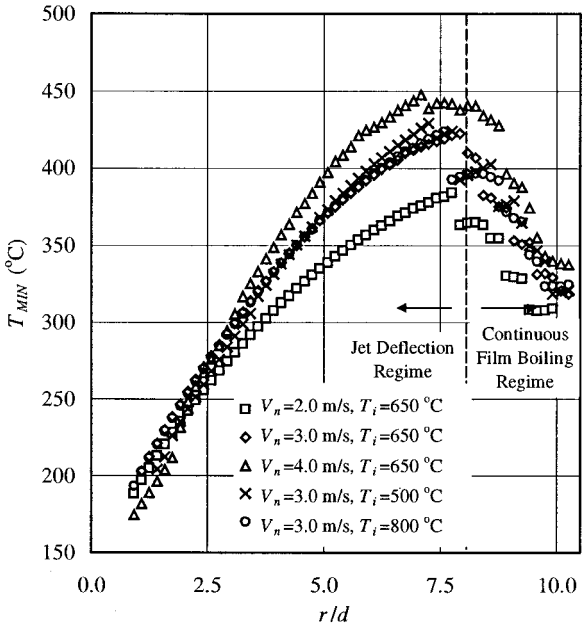

Fig. 11 Radial distribution of T_{MIN} (ΔT_{SUB}=75°C)

Heat transfer immediately downstream of the quench front appears to be inhibited by deflection of the jet from the surface. As the quench front progresses and the momentum of the liquid approaching the quench front decreases, the velocity of the deflected liquid decreases, and film boiling heat transfer is enhanced (T_{MIN} increases). At a sufficient distance downstream of the stagnation point, the liquid will no longer be deflected from the surface and will flow across a vapor blanket in a film boiling region that extends over the remaining unwetted portion of the test surface. This flowing film is more likely to penetrate the vapor layer. The minimum film boiling temperature will then decrease with increasing radius due to the increase in liquid temperature and further decrease in momentum. This behavior is demonstrated by the plot of T_{MIN} as a function of radial location in Fig. 11. Beyond $r/d=8$, a continuous film boiling layer exists. Unfortunately, the test cell dimensions were not large enough to capture much of this region.

To insure that experimental results were independent of the test cell initial temperature, T_i, experiments were repeated for $V_n=3.0$ m/s and $T_i=500$°C and 800°C. The results for q''_{MAX}, q''_{MIN}, and T_{MIN} are included in Figs. 8–11. The results are clearly independent of initial temperature, and also demonstrate the excellent repeatability of the data.

Conclusions

The quenching measurements of this study encompass three distinct boiling regimes: (1) nucleate boiling in the impingement zone, (2) the upper limit of nucleate boiling, maximum heat flux, for the entire surface, and (3) transition boiling characterized by the minimum film boiling heat fluxes and temperatures for the

radial flow region. A key distinction between these results and those of previous studies is the emphasis on variations with streamwise location. While such variations have been studied extensively for both planar and circular jets in single-phase convection and planar jets in boiling, they have not been emphasized in previous circular jet impingement boiling studies.

Nucleate boiling in the impingement zone was correlated with wall superheat, and although a dependence on jet velocity was demonstrated, it was within the range of experimental uncertainty. Radial distributions of the maximum heat flux correlated extremely well with relations developed by other researchers from steady-state experiments for the radial flow region. Minimum film boiling heat flux was shown to decrease with radial location, and the minimum film boiling temperature demonstrated a strong dependence on the hydrodynamics of the liquid film.

This study also demonstrated the efficacy of using transient (quenching) experiments to obtain spatial distributions of boiling data for a wide range of surface temperatures. Moreover, this technique may be the only feasible approach for collecting distributed jet impingement boiling data at elevated temperatures since instabilities associated with the negative slope of the boiling curve in the transition boiling regime limit the use of traditional steady-state techniques. However, a significant limitations of the technique is its large experimental uncertainties.

Acknowledgments

The authors are grateful for support of this research by the National Science Foundation under Grant CTS-9307232.

Nomenclature

A_0, A_1, A_2 = coefficients for interpolant
c_p = specific heat at constant pressure
d = nozzle diameter
$f(t)$ = surface temperature history
$g(t)$ = axial thermocouple-depth temperature graident $(\partial T/\partial z|_{z=L})$ history
G = mass flux
h = tank head
h_{fg} = latent heat of vaporization
H = nozzle-plate spacing
Ja = Jakob number$=c_p \Delta T_{\mathrm{SUB}}/h_{fg}$
k = thermal conductivity
L = test cell thickness minus thermocouple depth
q''_s = surface heat flux
q''_{MAX} = maximum heat flux
q''_{MIN} = minimum film boiling heat flux
q''_{NB} = fully-developed nucleate boiling heat flux
r = radial coordinate
R = test cell radius
R_a = average surface roughness
Re_d = Reynolds number$=V_n d/v$
t = time
T_s = surface temperature
T_i = test cell initial temperature
T_{MIN} = minimum film boiling temperature
T_{ONB} = temperature corresponding to onset of nucleate boiling
T_{SAT} = saturation temperature
T_∞ = fluid temperature at nozzle exit
ΔT_{SAT} = excess temperature (wall superheat) $= T_s - T_{SAT}$
ΔT_{SUB} = subcooling $= T_{SAT} - T_\infty$
V_n = jet velocity at nozzle exit
z = axial coordinate measured from the bottom of the test specimen
$\tilde{z}$ = axial coordinate measured from the thermocouple depth
α = thermal diffusivity $= k/\rho c_p$
δ = uncertainty
ε_{SUB} = subcooling parameter
ν = kinematic viscosity
ρ = density
σ = surface tension
Φ = correction factor for q''_{MAX}

Subscripts

f = liquid
g = vapor
ISO = thermal surface
s = solid

Superscripts

(i) = i^{th} derivative

References

[1] Viskanta, R., and Incropera, F. P., 1992, "Quenching with Liquid Jet Impingement," Heat and Mass Transfer in Materials Processing, Hemisphere, I. Tanasawa and N. Lior, eds., New York, pp. 455–476.
[2] Wolf, D. H., Incropera, F. P., and Viskanta, R., 1993, "Jet Impingement Boiling," Advances in Heat Transfer, J. P. Hartnett, T. F. Irvine, and Y. I. Cho, eds., Academic Press, Inc., Boston, **23**, pp. 1–132.
[3] Vader, D. T., Incropera, F. P., and Viskanta, R., 1992, "Convective Nucleate Boiling on a Heated Surface Cooled by an Impinging, Planar Jet of Water," ASME J. Heat Transfer, **114**, pp. 152–160.
[4] Wolf, D. H., Incropera, F. P., and Viskanta, R., 1996, "Local Jet Impingement Boiling Heat Transfer," Int. J. Heat Mass Transf., **39**, pp. 1395–1406.
[5] Kumagai, S., Suzuki, S., Sano, Y., and Kawazoe, M., 1995, "Transient Cooling on a Hot Metal Slab by an Impinging Jet with Boiling Heat Transfer," L. S. Fletcher and T. Aiahara, eds., *Proceedings, ASME/JSME Thermal Engineering Joint Conference*, Vol. 2, ASME, New York, pp. 347–352.
[6] Filipovic, J., Incropera, F. P., and Viskanta, R., 1995, "Quenching Phenomena Associated with a Water Wall Jet: I. Transient Hydrodynamic and Thermal Conditions," Experimental Heat Transfer, **8**, pp. 97–117.
[7] Filipovic, J., Incropera, F. P., and Viskanta, R., 1995, "Quenching Phenomena Associated with a Water Wall Jet: II. Comparison of Experimental and Theoretical Results for the Film Boiling Region," Exp. Heat Transfer, **8**, pp. 119–130.
[8] Ishigai, S., Nakanishi, S., and Ochi, T., 1978, "Boiling Heat Transfer for a Plane Water Jet Impinging on a Hot Surface," *Proceedings, 6th International Heat Transfer Conference*, Vol. 1, Hemisphere, Washington, pp. 445–450.
[9] Ochi, T., Nakanishi, S., Kaji, M., and Ishigai, S., 1983, "Cooling of a Hot Plate with an Impinging Circular Water Jet," *Proceedings, Multi-Phase Flow and Heat Transfer III*, T. N. Veziroglu and A. E. Bergles, eds., Elsevier, Amsterdam, pp. 671–681.
[10] Hatta, N., Kokado, J.-I., and Hanasaki, K., 1983, "Numerical Analysis of Cooling Characteristics for Water Bar," Trans. Iron Steel Inst. Jpn., **23**, pp. 555–564.
[11] Filipovic, J., Incropera, F. P., and Viskanta, R., 1995, "Rewetting Temperatures and Velocity in a Quenching Experiment," Exp. Heat Transfer, **8**, pp. 257–270.
[12] Hall, D. E., Incropera, F. P., and Viskanta, R., 2001, "Jet Impingement Boiling From a Circular Free-Surface Jet During Quenching: II—Two-Phase Jet," ASME J. Heat Transfer, **123**, pp. 911–917.
[13] El-Genk, M. S., and Glebov, A., 1995, "Numerical Solution of Transient Heat Conduction in a Cylindrical Section During Quenching," Numer. Heat Transfer, Part A, **28**, pp. 547–574.
[14] Patankar, S. V., 1980, *Numerical Heat Transfer and Fluid Flow*, Hemisphere, New York.
[15] Beck, J. V., Blackwell, B., and St. Clair, C. R., 1985, *Inverse Heat Conduction*, John Wiley & Sons, New York.
[16] Chapra, S. C., and Canale, R. P., 1988, *Numerical Methods for Engineers*, 2nd ed., McGraw-Hill, New York.
[17] Moffat, R. J., 1988, "Describing the Uncertainties in Experimental Results," Exp. Therm. Fluid Sci., **1**, pp. 3–17.
[18] Coleman, H. W., and Steele, W. G., 1989, *Experimental and Uncertainty Analysis for Engineers*, John Wiley & Sons, New York.
[19] Piggott, B. D. G., White, E. P., and Duffey, R. B., 1976, "Wetting Delay Due to Film and Transition Boiling on Hot Surfaces," Nucl. Eng. Des., **36**, pp. 169–181.
[20] Shibayama, S., Katsuta, M., Suzuki, K., Kurose, T., and Hatano, Y., 1979, "A Study on Boiling Heat Transfer in a Thin Liquid Film (Part 1: In the Case of Pure Water and an Aqueous Solution of a Surface Active-Agent as the Working Liquid)," Heat Transfer—Jpn. Res., **8**, pp. 12–40.
[21] Nonn, T., Dagan, Z., and Jiji, L. M., 1988, "Boiling Jet Impingement Cooling of Simulated Microelectronic Heat Sources," ASME Paper No. 88-WA/EEP-3.
[22] Katsuta, M., and Kurose, T., 1981, "A Study on Boiling Heat Transfer in Thin Liquid Film (2nd Report, the Critical Heat Flux of Nucleate Boiling)," Transactions of JSME, **47B**, pp. 1849–1860.
[23] Ma. C.-F., Yu, J., Lei, D. H., Gan, Y. P., Auracher, H., and Tsou, F. K., 1989,

''Jet Impingement Transient Boiling Heat Transfer on Hot Surfaces,'' *Proceedings, Multiphase Flow and Heat Transfer Second International Symposium*, Vol. 1, X.-J. Chen, T. N. Veziroglu and C. L. Tien, eds., Hemisphere, New York, pp. 349–357.
[24] Monde, M., 1985, ''Critical Heat Flux in Saturated Forced Convective Boiling on a Heated Disk with an Impinging Jet,'' Wäerme- und Stroffüebertrag, **19**, pp. 205–209.
[25] Sharan, A., and Lienhard, J. H., 1985, ''On Predicting Burnout in the Jet-Disk Configuration,'' ASME J. Heat Transfer, **107**, pp. 398–401.
[26] Cho, C. S. K., and Wu. K., 1988, ''Comparison of Burnout Characteristics in Jet Impingement Cooling and Spray Cooling,'' *Proceedings, 1988 National Heat Transfer Conference*, Vol. 1, H. R. Jacobs, ed., ASME, New York, pp. 561–567.
[27] Katto, Y., and Yokoya, S., 1988, ''Critical Heat Flux on a Disk Heater Cooled by a Circular Jet of Saturated Liquid Impinging at the Center,'' Int. J. Heat Mass Transf., **31**, pp. 219–227.
[28] Kandula, M., 1990, ''Mechanisms and Predictions of Burnout in Flow Boiling Over Heated Surfaces with an Impinging Jet,'' Int. J. Heat Mass Transf., **33**, pp. 1795–1803.
[29] Skema, R. K., and Slanciauskas, A. A., 1990, ''Critical Heat Fluxes as Jet-Cooled Flat Surfaces,'' *Heat Transfer in Electronic and Microelectronic Equipment*, A. E. Bergles, ed., Hemisphere, New York, pp. 621–626.
[30] Monde, M., 1980, ''Burnout Heat Flux in Saturated Forced Convection Boiling with an Impinging Jet,'' Heat Transfer–Jpn. Res., **9**, pp. 31–41.
[31] Carbajo, J. J., 1985, ''A Study on the Rewetting Temperature,'' Nucl. Eng. Des., **84**, pp. 21–52.

Jet Impingement Boiling From a Circular Free-Surface Jet During Quenching: Part 2—Two-Phase Jet

David E. Hall
Michelin Americas Research Corporation,
515 Michelin Road,
Greenville, SC 29602

Frank P. Incropera
Notre Dame University,
South Bend, IN 46556
e-mail: fpi@nd.edu

Raymond Viskanta
School of Mechanical Engineering,
Purdue University,
West Lafayette, IN 47907

A proposed technique for controlling jet impingement boiling heat transfer involves injection of gas into the liquid jet. This paper reports results from an experimental study of boiling heat transfer during quenching of a cylindrical copper specimen, initially at a uniform temperature exceeding the temperature corresponding to maximum heat flux, by a two-phase (water-air), circular, free-surface jet. The second phase is introduced as small bubbles into the jet upstream of the nozzle exit. Data are presented for single-phase convective heat transfer at the stagnation point, as well as in the form of boiling curves, maximum heat fluxes, and minimum film boiling temperatures at locations extending from the stagnation point to a radius of ten nozzle diameters. For void fractions ranging from 0.0 to 0.4 and liquid-only velocities between 2.0 and 4.0 m/s $(11{,}300 \leqslant \mathrm{Re}_{d,fo} \leqslant 22{,}600)$*, several significant effects are associated with introduction of the gas bubbles into the jet. As well as enhancing single-phase convective heat transfer by up to a factor of 2.1 in the stagnation region, addition of the bubbles increases the wall superheat in nucleate boiling and eliminates the temperature excursion associated with cessation of boiling. The maximum heat flux is unaffected by changes in the void fraction, while minimum film boiling temperatures increase and film boiling heat transfer decreases with increasing void fraction. A companion paper (Hall et al., 2001) details corresponding results from the single-phase jet.* [DOI: 10.1115/1.1389062]

Introduction

Jet impingement boiling is frequently employed to cool metals during primary processing operations such as hot rolling, continuous casting, and forging. In many such operations, precise control of heat removal rates is essential to achieving desired operating conditions and/or properties of the final product [1]. For example, during startup in continuous casting operations, heat transfer rates must be reduced to minimize deformation of the billet end, but maintained large enough to form a strong shell capable of carrying large tensile loads [2]. Following startup, heat transfer rates are increased to facilitate greater casting speeds. As a means of controlling heat removal rates to free-surface jets of water that issue from the mold and impinge on the ingot surface, it has been proposed that air bubbles be introduced into the jets [3]. The presumption is that the amount of air injection can be varied to reduce heat transfer during startup of the casting operation, thereby minimizing deformation, and to increase heat transfer thereafter, thus increasing casting speeds.

Several researchers have observed heat transfer augmentation resulting from the addition of a gas (or vapor) phase to an impinging liquid jet. Serizawa et al. [4] investigated single-phase convection heat transfer from an axisymmetric, two-phase, confined jet. Using both contoured parabolic and parallel confining nozzle plates, a two-phase mixture of air bubbles and water was directed to a heated surface. Turbulence measurements, which were made to characterize the two-phase flow, indicated increasing turbulence intensity in the radial flow region with increasing gas flow rate, as well as an increase in the turbulent kinetic energy at higher frequencies (above approximately 20 Hz). Void fraction measurements were conducted for radial locations greater than $r = 40$ mm, and plots of the drift flux parameters revealed little slip between the two phases. Heat transfer measurements demonstrated a nearly three-fold increase in local Nusselt numbers at the stagnation point, and results for convection in the radial flow region ($r > 50$ mm) were correlated by the equation

$$\mathrm{Nu}_{d,tp} = \mathrm{Nu}_{d,fo} + \frac{\alpha d}{\delta_m}, \tag{1}$$

where δ_m is the minimum liquid film thickness separating a moving bubble from the heated surface (estimated to be 60 μm). Equation (1) implies proportionality between the local Nusselt number and the void fraction in the radial flow region. Heat transfer measurements were also made for a free-surface jet, and enhancements due to two-phase flow were not as pronounced as those for the confined jets.

Chang et al. [5] experimentally investigated single-phase convection and boiling heat transfer to single and multiple confined two-phase jets. The two-phase flow was produced by flashing nearly saturated R-113 through a throttle valve immediately upstream of the test section to produce qualities up to 0.31 for single jets and 0.23 for multiple jets. Assuming that the specific enthalpy of the mixture remained constant during the expansion, the quality was predicted by measuring the downstream pressure or temperature. Relative to a single-phase jet ($x = 0$), convection heat transfer for the single jet configuration was enhanced by a factor of 1.4 for a mixture quality of 0.11 and for radial locations up to 10 jet diameters. Enhancement was attributed to the increase in the mixture mean velocity. Enhancement of the stagnation point Nusselt number due to the two-phase flow was correlated using the Martinelli turbulent, two-phase flow parameter, χ_{tt}, which was developed to correlate two-phase flow pressure gradients [6]:

$$\frac{\mathrm{Nu}_{d,tp}}{\mathrm{Nu}_{d,sp}} = 1.0 + 1.187\chi_{tt}^{-0.438}. \tag{2}$$

Contributed by the Heat Transfer Division for publication in the JOURNAL OF HEAT TRANSFER. Manuscript received by the Heat Transfer Division May 27, 1997; revision received March 22, 2001. Associate Editor: M. S. Sohal.

In the fully-developed nucleate boiling regime, the boiling curve shifted towards higher wall superheats with increasing flow quality, while the slope of the boiling curve remained unchanged.

Most recently, Zumbrunnen and Balasubramanian [7] measured single-phase convection heat transfer augmentation due to air bubbles injected into a free-surface planar jet by capillary tubes inserted through the nozzle and extending to the nozzle exit. Over the range of liquid-only Reynolds numbers of $3700 < \mathrm{Re}_{d,fo} < 21{,}000$ and void fractions between $0 < \alpha < 0.86$, heat transfer was increased by as much as a factor of 2.2 at the stagnation point and 1.6 at downstream locations extending to five jet widths. Results were correlated to within ± 25 percent using the form of the relation developed by Chang et al. [5]:

$$\frac{\mathrm{Nu}_{w,tp}}{\mathrm{Nu}_{w,fo}} = 1 + 4.4331 \chi_n^{-0.7385}. \tag{3}$$

The foregoing studies have addressed heat transfer enhancement for two-phase jets in single-phase convection, and, to a limited extent, nucleate boiling, but no studies appear to have been performed under conditions for which surface temperatures were larger than those corresponding to maximum heat flux. In contrast, this study is concerned with heat transfer from a test surface, initially at 650 °C, to an impinging two-phase, free-surface jet of water and air. Results are presented for single-phase convection, nucleate boiling, maximum heat flux, and surface rewetting for a constant jet diameter of $a = 5.1$ mm, liquid-only jet velocities between $2.0 \leqslant V_{fo} \leqslant 4.0$ ($11{,}300 \leqslant \mathrm{Re}_{d,fo} \leqslant 22{,}600$), void fractions between $0.0 \leqslant \alpha \leqslant 0.4$, a constant subcooling of $\Delta T_{SUB} = 75°\mathrm{C}$, and a constant nozzle-to-plate spacing of $H/d = 20$.

Experimental Method and Apparatus

The flow loop used to supply water and air to the two-phase jet is described by the companion paper [8]. Air is supplied to the nozzle from a compressed air cylinder through two pressure regulators and a flow meter. As depicted in Fig. 1, a convergent section supplies a pipe-type nozzle 5.1 mm in diameter and 11 diameters long. Five diameters upstream of the nozzle exit, four 1.0 mm diameter orifices were drilled in the nozzle wall at 90 deg. intervals and oriented normal to the nozzle centerline. Air from the gas cylinder was supplied to the orifices through a plenum epoxied to the nozzle. The entire assembly was bolted to the bottom of the water supply tank, and the two-phase jet was directed normal to the instrumented copper test cell with a fixed nozzle-to-plate spacing of 20 nozzle diameters.

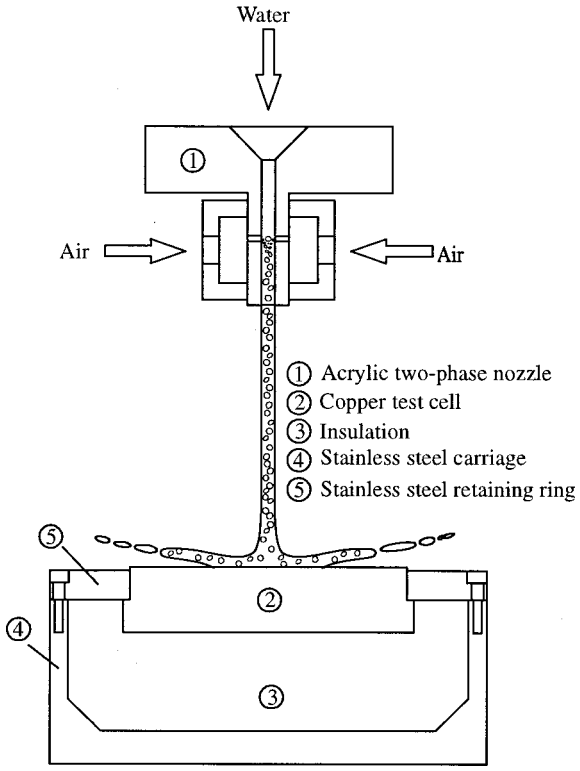

Fig. 1 Schematic of two-phase nozzle and boiling on the test surface

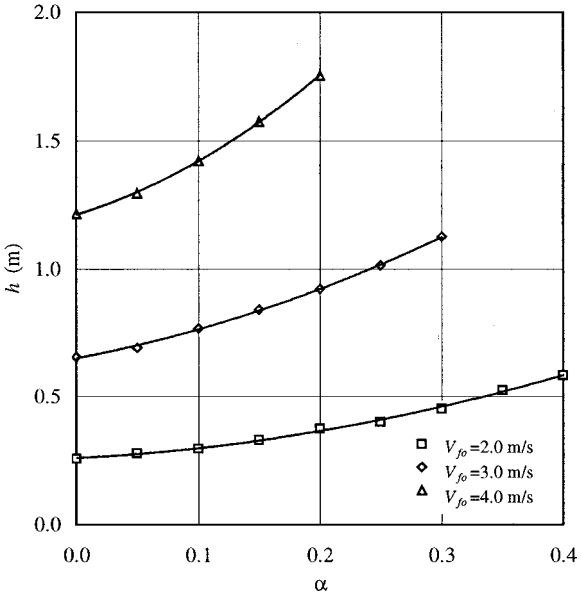

Fig. 2 Dependence of static head on void fraction for selected liquid-only velocities

Assuming homogeneous two-phase flow (no slip between the gas and liquid phases), the jet void fraction is calculated as

$$\alpha = \frac{Q_g}{Q_g + Q_f}, \tag{4}$$

where Q_g and Q_f are the volumetric flow rates of air and water, respectively. An approximate analysis indicated that the bubbles accelerate to their terminal velocity relative to the liquid phase well before the nozzle exit, but that the buoyancy force opposing the drag force on individual bubbles precludes equilibrium of the bubble and liquid velocities. The terminal bubble velocity within the jet was estimated to be within 12 percent of the liquid velocity for all experimental conditions considered in this study. The assumption of homogeneous two-phase flow was made to describe the experimental parameters of the study and quantify trends among the data, and for practical purposes, this assumption is reasonable. The liquid-only velocity (also referred to as the superficial liquid velocity), V_{fo}, is then defined as $V_{fo} = Q_f / A_n$, where A_n is the cross-sectional area of the nozzle exit. The two-phase, or mixture, velocity is defined as $V_{tp} = V_{fo} + Q_g / A_n$. Injection of gas bubbles into the water jet increases the head required to maintain a fixed value of V_{fo}, since the pressure drop across the nozzle increases due to acceleration of the water/air mixture and the increased friction losses associated with the two-phase bubbly flow downstream of the air orifices. The static head in the supply tank required to maintain a constant value of V_{fo} increases approximately in proportion to the square of the void fraction, and for liquid-only velocities of 2.0, 3.0, and 4.0 m/s, measurements of the static head as a function of the void fraction are depicted in Fig. 2.

Details of the instrumented copper test piece, data reduction procedure, and uncertainty analysis are described in the companion paper. In addition to uncertainties described in Tables 1 and 2

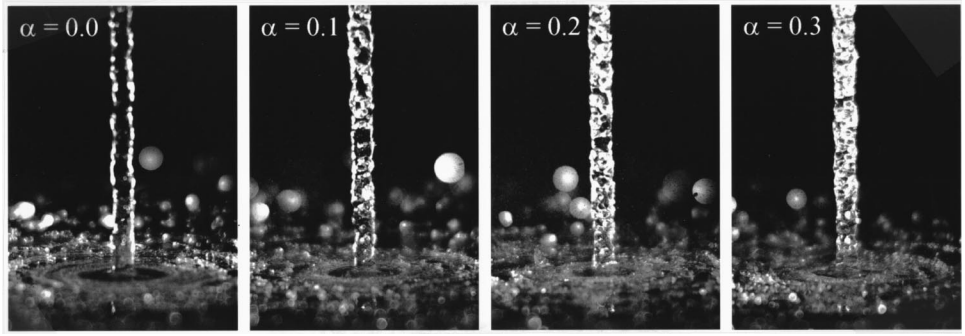

Fig. 3 Jet impingement following initiation of quench (t=2 s) for for=0.0, 0.1, 0.2, and 0.3 (T_i=650°C, V_{fo}=3.0 m/s, ΔT_{SUB}=75°C)

of the companion paper, the maximum uncertainty in the void fraction measurements was ±16.4 percent for $V_{fo}=2.0$ m/s and $\alpha=0.1$, but was below ±11.1 percent for all other experimental conditions.

Results and Discussion

Two-Phase Flow Characterization. Photographs of jets taken shortly after the initial vapor production had slowed, but before progression of the boiling front, are displayed in Fig. 3 for $V_{fo}=3$ m/s and void fractions of 0.0, 0.1, 0.2, and 0.3. At void fractions above 0.5, the jet begins to break-up, but remains continuous, though wavy, below this value. Bubbles remain entrained within the jet and, except for some coalescence between neighboring bubbles, remain intact until impact on the surface. The photographs were used to characterize the bubbles generated by the nozzle. By electronically enhancing the images, measurements of bubble sizes were possible. One-hundred measurements of characteristic bubble diameters were taken from photographs for $V_{fo}=3.0$ m/s and void fractions of 0.1, 0.2, and 0.3, where the characteristic bubble diameter, b, was calculated as the average of the vertical and horizontal bubble dimensions. The resulting bubble size distribution is depicted in Fig. 4. The distribution is nearly Gaussian, with mean diameters of 1.59, 1.73, and 1.87 mm and standard deviations of 0.26, 0.30, and 0.30 mm for jet void fractions of 0.1, 0.2, and 0.3, respectively. From the mean bubble diameter and air flow rate, the frequencies of bubble generation for void fractions of 0.1, 0.2, and 0.3 are 3210, 5610, and 7610 Hz, respectively.

Boiling Curves. Figure 5 depicts boiling curves for five radial positions, $r/d=0$, 2, 4, 6, and 8, and void fractions of 0, 0.1, 0.2, and 0.3 for $V_{fo}=3.0$ m/s. For an initial temperature of 650°C, thermocouple response was too slow to capture the minimum film boiling point in the stagnation zone. In experiments with an initial test cell temperature of 800°C, early stages of quenching were characterized by a clearly-defined period of film boiling and the stagnation point minimum film boiling temperature was observed to be approximately 470°C. Transition boiling in the stagnation zone is manifested by vigorous vapor production, and the wetted zone appears as a dark circular patch in the photographs of Fig. 3. As ΔT_{SAT} at the stagnation point ($r/d=0$) decreased from $T_i - T_{SAT}$, the stagnation zone passed through transition boiling, as characterized by the negative slope of the boiling curve. In this region, the boiling curves for the four void fractions are indistinguishable, and only after boiling had progressed through the maximum heat flux into the fully-developed nucleate boiling regime did the effect of air injection become discernible. The $r/d=0$ boiling curves of Fig. 5 are expanded in Fig. 6 for $\Delta T_{SAT} \leq 100$°C. The heat flux decreased from a peak value above 40 MW/m^2 (maximum heat flux) to a linear region (on log-log scales) corresponding to fully-developed nucleate boiling. In the nucleate boiling regime, air injection shifted the boiling curves towards higher wall superheat, but that effect diminished with increasing void fraction. Below a wall superheat of $\Delta T_{SAT}=40$°C, heat transfer occurred by single-phase forced convection, which was significantly enhanced by the air injection.

The minimum film boiling point in the radial flow region is apparent in the boiling curves of Fig. 5. After the jet struck the surface, the calculated heat fluxes increased over a period of ~3 s from the initial condition ($q''_s \approx 0$) to values corresponding to film boiling. In this interval, results are strongly influenced by the inability of the thermocouples to respond to the rapidly changing surface heat flux immediately following initiation of the quench. Due to deflection of the jet from the surface at the boiling front location, heat transfer from surface locations for which $r/d \geq 2$ occurs by radiation and single-phase convection (to the ambient air) until the minimum film boiling temperature is reached. Although not observable in the stagnation point boiling curves of Fig. 5, the duration of the initially vigorous vapor production increased with increasing void fraction. This result is attributed to the decrease in heat fluxes in the radial flow region with increasing void fraction, which resulted in slower cooling of the test specimen. As shown in Fig. 5 and the enlargement of the $r/d=4$ boiling curves in Fig. 7, surface heat fluxes beyond the minimum film boiling point decreased by nearly a factor of 2 with

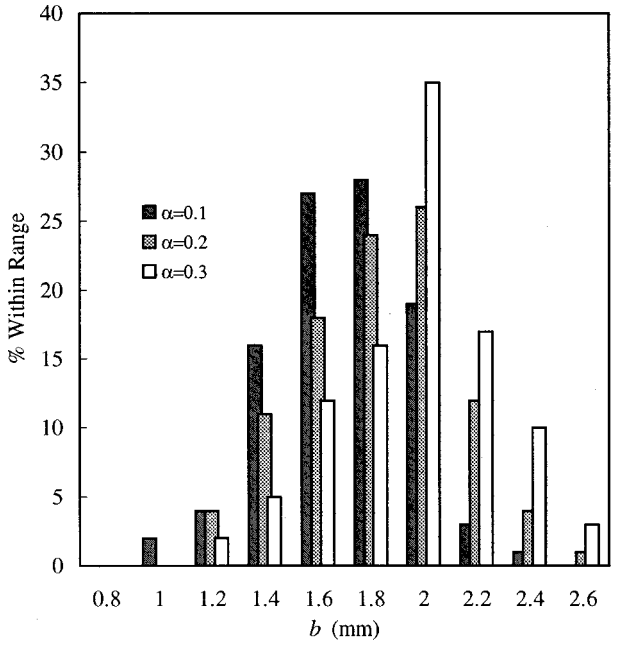

Fig. 4 Bubble size distribution for various void fractions (V_{fo} =3.0, s. $Re_{d,fp}$=17,000)

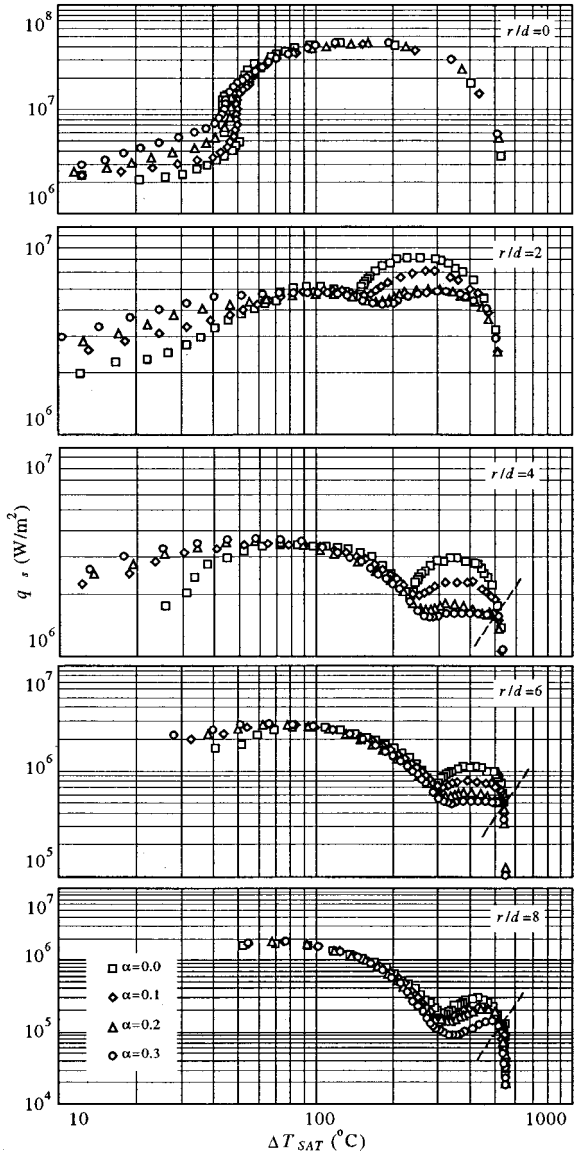

Fig. 5 Effect of void fraction on the boiling curves for $r=0$, 10, 20, 30, and 40 mm ($T_i=650°C$, $V_{fo}=3.0$ m/s, $\Delta T_{SUB}=75°C$)

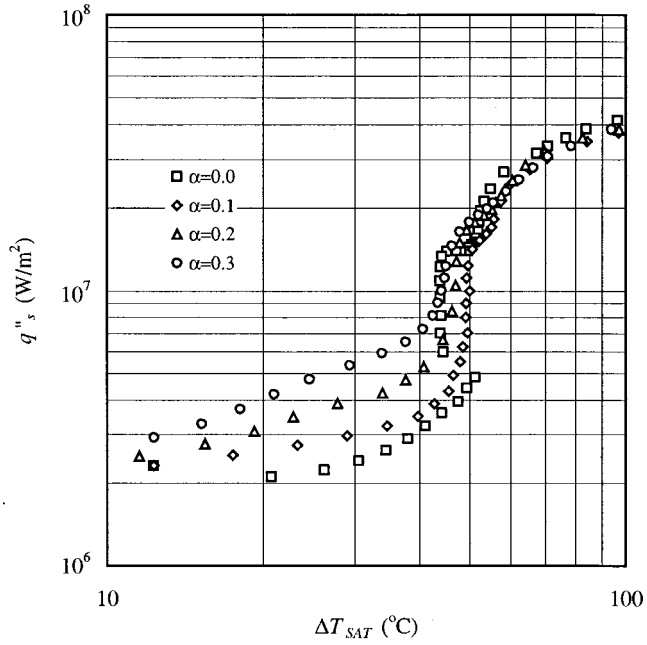

Fig. 6 Effect of void fraction on the stagnation point boiling curve ($T_i=650°C$, $V_{fo}=3.0$ m/s, $\Delta T_{SUB}=75°C$)

increasing α from 0 to 0.3. This decrease in surface heat fluxes downstream of the boiling front might be attributable to a change in jet deflection parameters with increasing void fraction. At surface temperatures below T_{MIN}, the surface heat flux increases until the maximum heat flux is reached, and there is no distinction among the boiling curves for the different void fraction jets.

Rewetting Temperatures. The temperature corresponding to the minimum film boiling heat flux, or rewetting temperature, T_{MIN}, in the radial flow region was determined from the boiling curves of Figs. 5 and 7. The minimum film boiling heat flux decreased and shifted towards higher temperatures with increasing void fraction. The variations of T_{MIN} with radius for $V_{fo}=3.0$ m/s and void fractions between 0.0 and 0.3 are plotted in Fig. 8. As described in the companion paper (for $\alpha=0.0$), the minimum film boiling point in the radial flow region occurs in either a jet deflection regime or a continuous film boiling regime. At radial locations within the jet deflection regime (observed in this study to be less than approximately eight jet diameters), T_{MIN} increased with increasing radius. This trend is attributed to separation of the jet from the surface in the vicinity of the boiling front due to the vigorous vapor production at the boiling front. The velocity decreased and the angle (measured with respect to the plane of the surface) of the deflected film increased as the boiling front progresses outward. As the jet was deflected less vigorously from the surface, liquid supply to the boiling front region increased, and film boiling heat transfer was enhanced. In contrast, beyond eight jet diameters, the liquid film was no longer deflected from the surface, and T_{MIN} decreased with increasing radius. This trend was due to the decrease in free-stream momentum and increase in free-stream temperature that occurred with increasing radial location. In the jet deflection regime, the temperature at

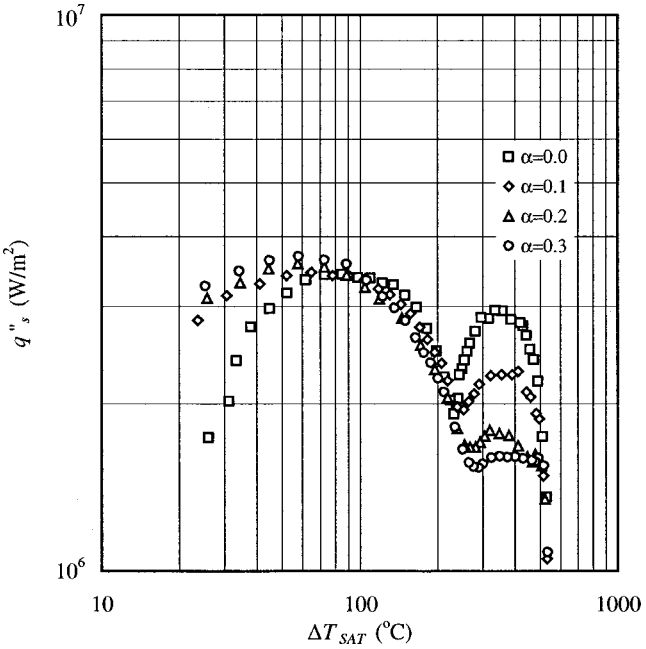

Fig. 7 Effect of void fraction on the boiling curve for $r=20$ mm ($T_i=650°C$, $V_{fo}=3.0$ m/s, $\Delta T_{SUB}=75°C$)

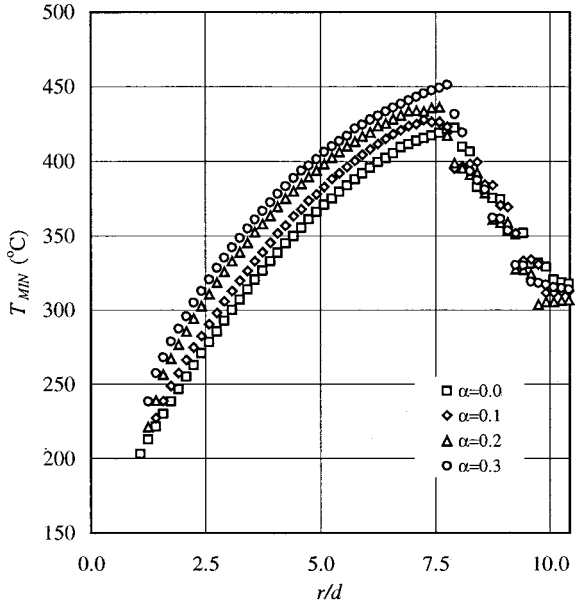

Fig. 8 Minimum film boiling temperature distribution (T_i = 650°C, V_{fo} = 3.0 m/s, ΔT_{SUB} = 75°C)

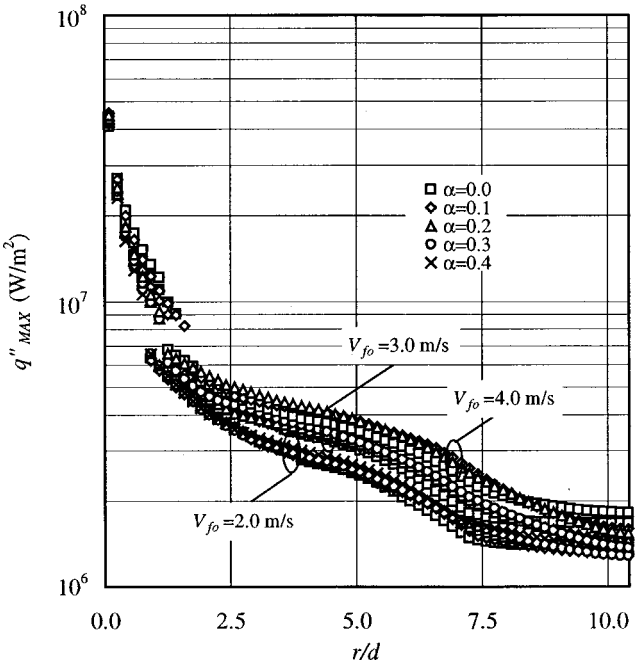

Fig. 9 Variation of maximum heat flux with position, ∝, and V_{fo} (T_i = 650°C, ΔT_{SUB} = 75°C)

which the minimum point was observed increased monotonically with increasing void fraction. This behavior was attributed to an increase in the mixture velocity, V_{tp}, with increasing α. For fixed α, T_{MIN} also increased with increasing V_{fo}. In the continuous film boiling regime, however, no definitive effect of void fraction was discerned, suggesting that the minimum film boiling point in this regime depended primarily on the rate at which liquid was supplied to the surface, and hence on V_{fo}, rather than V_{tp}. Both of these conclusions were supported by rewetting data for $\alpha = 0$, which were characterized by increasing T_{MIN} with increasing jet velocity in both the jet deflection and continuous film boiling regimes.

Maximum Heat Flux. The maximum in the stagnation point boiling curves and the secondary maximum (occurring at lower wall superheats) in the boiling curves of the radial flow region ($r/d \approx 2$) represent the maximum heat flux associated with continuous wetting of the surface, and the data are plotted as a function of radial location in Fig. 9. As noted in the companion paper, the discontinuous decrease in q''_{MAX} at a radial location of $r/d \approx 1$ was attributed to transition from a radially accelerating flow in the impingement zone to a radially decelerating flow in the radial flow region and the corresponding increase in boundary layer thickness. For the same liquid-only velocity, the maximum heat flux was virtually independent of void fraction. This result suggests that q''_{MAX} depended primarily on V_{fo} rather than V_{tp}. As such, the correlating equations cited in the companion paper to predict q''_{MAX} in the radial flow region of single-phase jets can be used to predict q''_{MAX} for the two-phase jets by utilizing V_{fo} in the place of V_n.

Nucleate Boiling. Due to the large radial temperature gradients near the boiling front, nucleate boiling only occurred in a narrow band of the radial flow region. Moreover, because the front progressed rapidly during the transient quenching process, nucleate boiling was not discernible in the boiling curves for $r/d > 0$. However, nucleate boiling data were obtained for the stagnation point, and two important features are evident in Fig. 6. First, the centerline boiling curve for the single-phase jet ($\alpha = 0$) exhibits a temperature excursion near the cessation of nucleate boiling. As nucleate boiling on the surface ceased, the surface temperature momentarily increased before decreasing. Bar-Cohen and Simon [9] reviewed temperature excursion data for incipient pool and flow boiling of dielectric liquids. They suggested that, as highly wetting fluids come in contact with a surface, they may completely flood surface cavities, thereby precluding entrapment of vapor embryos. As such, bubble nucleation must first occur homogeneously in the bulk fluid, rather than at the surface, requiring greater superheat than heterogeneous bubble nucleation at the surface. While their observations were for highly-wetting fluids and increasing surface temperature, conditions which differ from those of this study, a similar explanation may apply. That is, in boiling of water with a decreasing surface temperature, cavities may be prematurely flooded, causing an increase in ΔT_{SAT}. However, as evidenced by the data of Fig. 6, results for jets with air injection consistently revealed no such excursions, suggesting that air bubbles suppress the temperature excursion near cessation of boiling in the stagnation zone. If the temperature excursion during boiling cessation is related to flooding of cavities on the surface, the air bubbles may seed cavities near the incipience point, thereby eliminating the excursion.

A second feature of the centerline boiling curves is that, for $\alpha = 0.1$, nucleate boiling occurs at significantly higher surface temperatures than for $\alpha = 0.0$ (the boiling curve is shifted to the right). As the void fraction is increased, however, the boiling curve is progressively shifted to the left, until for $\alpha = 0.3$, the data are coincident with results for $\alpha = 0$. This trend also characterized the $V_{fo} = 2.0$ and 4.0 m/s data, and similar trends were observed by Chang et al. [5]. Hence, although a suitable explanation is currently lacking, heat transfer is clearly suppressed for low levels of air injection ($\alpha = 0.1$), but increases with increasing α.

Single-Phase Convection Heat Transfer. Due to rapid progression of the boiling front and the fact that experiments were halted immediately after the boiling front had progressed to the outer edge of the test surface, the radial flow region was only briefly exposed to single-phase convection, and single-phase heat transfer measurements were limited to the stagnation zone. The stagnation point boiling curves in Fig. 6 indicate increasing single-phase convection heat transfer with increasing void fraction, and enhancement by approximately a factor of 2.1 is achieved for $\alpha = 0.3$. Nusselt numbers were calculated as a func-

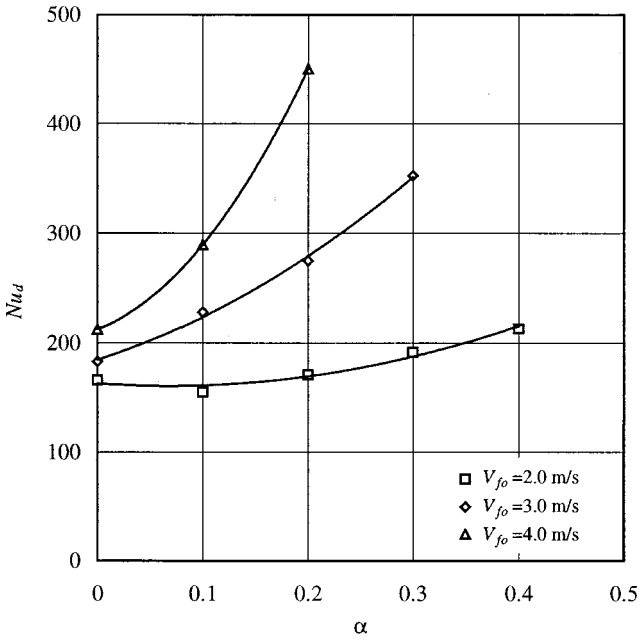

Fig. 10 Variation of single-phase heat transfer Nusselt numbers with V_{fo} and ∝

tion of jet velocity and void fraction, and the results are depicted in Fig. 10. For $V_{fo}=2.0$ m/s, the Nusselt number decreases from 166 for $\alpha=0$ to 155 for $\alpha=0.1$, before increasing to 213 for $\alpha=0.4$. Nusselt numbers for $V_{fo}=3.0$ and 4.0 m/s increase monotonically from 183 to 353 and from 213 to 451, respectively. The increase in Nusselt number with increasing void fraction is primarily attributed to the increase in V_{tp}. Nusselt numbers for the single-phase jet ($\alpha=0.0$) agree very well with experimental results of several studies summarized by Webb and Ma [10].

The enhancements observed in this study significantly exceed those observed by Zumbrunnen and Balasubramanian [7] for air bubbles injected into a planar water jet. For a void fraction of 0.32 and Reynolds number of 17,600, they observed enhancement at the stagnation line by a factor of 1.3, whereas the enhancement in this study for $\alpha=0.3$ and $\mathrm{Re}_{d,fo}=17{,}000$ ($V_{fo}=3.0$ m/s) was 2.1 at the stagnation point. This discrepancy is attributed to the different methods by which air bubbles are injected into the jet. In the present study, air bubbles are injected upstream of the nozzle exit, and the liquid must therefore accelerate to accommodate the increased volume flow rate. In the nozzle of Zumbrunnen and Balasubramanian [7], air is injected at the nozzle exit, and the jet free surface may expand to accommodate the air bubbles. While the nozzle design employed in this study produces increased enhancements over the design of Zumbrunnen and Balasubramanian [7], this benefit may be offset by the substantially higher pumping requirements.

Conclusions

An experimental study was performed to determine the effect of air bubbles on heat transfer associated with jet impingement boiling for impinging two-phase (water-air), free-surface circular jets. The specific effect of the second phase was found to depend on the boiling regime. In single-phase convection, injection of air bubbles enhanced heat transfer by more than a factor of two, and the effect was attributed to the increase in the mixture velocity with increasing void fraction. Air bubbles had the effect of shifting nucleate boiling data to higher wall superheats, although the effect was most pronounced for $\alpha=0.1$. A temperature excursion associated with the cessation of boiling for $\alpha=0$ was suppressed by the addition of air bubbles, while the maximum heat flux was unaffected by addition of the air. Conditions associated with film boiling and surface heat fluxes downstream of the boiling front strongly depended on void fraction, with increasing α acting to reduce heat transfer downstream of the boiling front (including q''_{MIN}) and to increase T_{MIN}.

The extent to which bubble injection can be used as a control parameter in quenching processes depends upon the local surface temperature and the associated heat transfer mechanism. For example, injection may be used to reduce the surface heat flux at temperatures in excess of that corresponding to the minimum film boiling point and to decrease the temperature associated with the cessation of nucleate boiling. Bubble injection also increases heat transfer for forced convection in the absence of boiling, but has no effect on the value of the maximum heat flux. However, enhancements due to injection of the air bubbles come at the expense of increased pumping power required to maintain the same liquid flow rate. Alternate methods of bubble injection, such as capillary tubes extended into the jet to the nozzle exit [7], which require little or no additional power to maintain the liquid supply, could be employed under conditions for which pumping requirements are of concern.

Acknowledgments

The authors are grateful for support of this research the National Science Foundation under Grant CTS-9307232.

Nomenclature

A_n = nozzle cross-sectional area$=\pi d^2/4$
b = characteristic bubble diameter
d = nozzle diameter
h = single-phase heat transfer coefficient; tank static head
H = nozzle-plate spacing
k = thermal conductivity
Nu_d = Nusselt Number$=hd/k_f$
q''_{MAX} = maximum heat flux
q''_{MIN} = minimum film boiling heat flux
q''_s = surface heat flux
Q = volumetric flow rate
r = radial coordinate
$\mathrm{Re}_{d,fo}$ = liquid-only Reynolds number$=V_{fo}d/\upsilon_f$
t = time from start of quench
T_i = initial test cell temperature
T_{MIN} = minimum film boiling temperature
T_s = surface temperature
T_{SAT} = liquid saturation temperature
T_∞ = liquid temperature
ΔT_{SAT} = excess temperature (wall superheat) $=T_s-T_{SAT}$
ΔT_{SUB} = subcooling$=T_{SAT}-T_\infty$
V_{fo} = liquid-only velocity$=Q_f/A_n$
V_{tp} = mixture or two-phase velocity$=(Q_g+Q_f)/A_n$
x = homogeneous two-phase flow quality$=(1+\rho_f/\rho_g 1-\alpha/\alpha)^{-1}$
α = void fraction
δ_m = mean thickness of residual film
μ = dynamic viscosity
υ = kinematic viscosity
ρ = density
χ_{tt} = Martinelli's turbulent two-phase flow parameter$=(\mu_f/\mu_g)^{0.1}(1-x/x)^{0.9}(\rho_f/\rho_g)^{0.5}$

Subscripts

f = liquid phase (water)
g = gas phase (air)
sp = single-phase flow
tp = two-phase flow

References

[1] Viskanta, R. and Incropera, F. P., 1992, ''Quenching with Liquid Jet Impingement,'' I. Tanasawa and N. Lior, eds., *Heat and Mass Transfer in Materials Processing*, Hemisphere, New York, pp. 455–476.

[2] Wagstaff, R. B. and Bowles, K. D., 1995, ''Practical Low Head Casting (LHC) Mold for Aluminum Ingot Casting,'' J. Evans, ed., *Proceedings, TMS Light Metals Committee*, The Minerals, Metals & Materials Society, Warrendale, PA, pp. 1071–1075.

[3] Fischer, H., Wagstaff, F. E., and Ekenes, J. M., 1989, ''Airslip and Turbo Development for Aluminum Sheet Ingot,'' *Proceedings, Ingot and Continuous Casting Process Technology Seminar for Flat Rolled Products*, The Aluminum Association, pp. 417–426.

[4] Serizawa, A., Takahashi, O., Kawara, Z., Komeyama, T., and Michiyoshi, I., 1990, ''Heat Transfer Augmentation by Two-Phase Bubbly Flow Impinging Jet with a Confining Wall,'' G. Hetsroni, et al., eds., *Proceedings, 9th International Heat Transfer Conference*, Hemisphere, New York, Vol., 4, pp. 93–98.

[5] Chang, C. T., Kojasoy, G., Landis, F., and Downing, S., 1995, ''Confined Single- and Multiple-Jet Impingement Heat Transfer—II. Turbulent Two-Phase Flow,'' *International journal of Heat and Mass transfer*, Vol. 38, pp. 843–851.

[6] Lockhart, R. W., and Martinelli, R. C., 1949, ''Proposed Correlation of Data for Isothermal Two-Phase, Two-Component Flow in Pipes,'' *Chemical Engineering Progress*, Vol. 45, pp. 39–48.

[7] Zumbrunnen, D. A. and Balasubramanian, M., 1995, ''Convective Heat Transfer Enhancement Due to Gas Injection Into an Impinging Liquid Jet,'' *ASME Journal of Heat Transfer*. Vol. 117, pp. 1011–1017.

[8] Hall, D. E., Incropera, F. P., and Viskanta, R., 2001, ''Jet Impingement Boiling From a Circular Free-Surface Jet During Quenching: 1—Single-Phase Jet,'' ASME J. Heat Transfer, **123**, pp. 901–910.

[9] Bar-Cohen, A. and Simon, T. W., 1988, ''Wall Superheat Excursions in the Boiling Incipience of Dielectric Fluids,'' *Heat Transfer Engineering*, Vol. 9, pp. 19–31.

[10] Webb, B. W. and Ma, C.-F., 1995, ''Single-Phase Liquid Jet Impingement Heat Transfer,'' J. P. Hartnett and T. F. Irvine, eds., *Advances in Heat Transfer*, Academic Press, New York, Vol. 26, pp. 105–217.

Flow Boiling Heat Transfer From Plain and Microporous Coated Surfaces in Subcooled FC-72

K. N. Rainey

G. Li

The University of Texas at Arlington,
Department of Mechanical and Aerospace Engineering,
PO Box 19023,
Arlington, TX 76019-0023

S. M. You

Seoul National University,
School of Mechanical & Aerospace Engineering,
San 56-1, Shinrim-Dong, Kwanak-Gu,
Seoul 151-742, KOREA

The present research is an experimental study of subcooled flow boiling behavior using flat, microporous-enhanced square heater surfaces in pure FC-72. Two 1-cm^2 copper surfaces, one highly polished (plain) and one microporous coated, were flush-mounted into a 12.7 mm square, horizontal flow channel. Testing was performed for fluid velocities ranging from 0.5 to 4 m/s (Reynolds numbers from 18,700 to 174,500) and pure subcooling levels from 4 to 20 K. Results showed both surfaces' nucleate flow boiling curves collapsed to one line showing insensitivity to fluid velocity and subcooling. The log-log slope of the microporous surface nucleate boiling curves was lower than the plain surface due to the conductive thermal resistance of the microporous coating layer. Both, increased fluid velocity and subcooling, increase the CHF values for both surfaces, however, the already enhanced boiling characteristics of the microporous coating appear dominant and require higher fluid velocities to provide additional enhancement of CHF to the microporous surface. [DOI: 10.1115/1.1389465]

Keywords: Boiling, Enhancement, Flow, Forced Convection, Heat Transfer

Introduction

Recent advances in the electronics industry are producing microelectronic chip designs that dissipate more heat than can be properly removed by conventional (single-phase) cooling schemes. Both direct and indirect liquid cooling schemes, involving boiling heat transfer, are currently being researched as a practical solution to the high heat flux requirements predicted for future electronics. In particular, subcooled flow boiling is receiving much attention, however, there are still many issues, which must be resolved before it can be successfully implemented.

It has been known for a long time that fully developed water nucleate flow boiling heat transfer performance in pipes is seemingly unaffected by either fluid velocity or subcooling (McAdams [1]). With regard to insensitivity to fluid velocity, Engelberg-Forster and Greif [2] explained that in both, forced convection and boiling heat transfer, the heat is first transferred to a thin layer of fluid adjacent to the surface. The heat is then transferred to the bulk liquid through diffusion by eddies in forced convection and/or through a bubble pumping or ''vapor-liquid exchange'' mechanism in boiling (commonly referred to as microconvection). This boiling microconvection mechanism was thought to be much more efficient due to the high departure frequency of bubbles and thus dominate the heat transfer over the eddy diffusion mechanism of forced convection.

With regard to insensitivity of nucleate flow boiling to fluid subcooling, Engelberg-Forster and Greif [2] believed that this behavior was due to the counterbalancing effects of subcooling on the maximum bubble size and the bubble departure frequency. Increased subcooling decreases the departing bubbles' size through condensation, which then decreases the amount of heated fluid it removes in its wake (decreased microconvection). From the results of Ellion [3], Engelberg-Forster and Greif also believed that the increased subcooling increases the bubble departure frequency, which helped to compensate for the decreased microconvection and thus show insensitivity to fluid subcooling. However, Yin et al. [4] observed that increased subcooling reduces both, the bubble departure diameter and frequency for subcooled flow boiling of R-134a in an annular duct. Alternatively, Gunther [5] observed that departing bubbles would slide along the entire length of the heated wall before departing at high subcooling of water in a rectangular duct. Later, Bibeau and Salcudean [6] and Klausner et al. [7] observed similar sliding behavior in water and R-113, respectively. These more recent observations of bubble behavior in subcooled flow boiling suggest that increased bubble sliding, not increased bubble departure frequency, may be responsible for the compensation of decreased microconvection heat transfer as put forth by Engelberg-Forster and Greif.

More recently, Willingham and Mudawar [8] observed insensitivity of the entire nucleate boiling curve to both fluid velocity and subcooling in flow channels with small (10 mm$\times$10 mm), discrete heat sources in FC-72 for a velocity and subcooling range of 0.013 to 0.400 m/s and 3 to 36 K, respectively. Heindel et al. [9], and later Tso et al. [10], found similar results at high heat fluxes where fully developed nucleate boiling existed, however, they found a significant effect of both fluid velocity and subcooling at low heat fluxes due to partial boiling conditions. In contrast, Kirk et al. [11], using a larger (19 mm$\times$38 mm) thin film surface in R-113, found that increased fluid velocity increased heat transfer performance over the entire nucleate boiling curve for a velocity range of 0.04 to 0.325 m/s at 11.1 K subcooling. Samant and Simon [12] also found a significant effect of fluid velocity on the nucleate boiling curve of their thin film heater in FC-72, but at relatively high fluid velocities (4.1 to 9.3 m/s) and subcooling ($\approx$55 K).

The effects of fluid velocity and subcooling on the critical heat flux (CHF) of small, discrete surfaces have also been previously studied. Kutateladze and Burakov [13] studied the effects of fluid velocity and subcooling on CHF for a vertical plate flow boiling in Dowtherm A (26.5 percent diphenyl and 73.5 percent diphenyl oxide). They observed that for a given velocity, CHF increases linearly with increasing subcooling and for a given subcooling, the CHF increases with increasing velocity for a velocity range of 1.2 to 5 m/s and a subcooling range of about 20 to 110 K. Using a very small (0.25 mm$\times$2.0 mm) thin film heater in FC-72, Samant and Simon [12] also found that CHF increased with increasing velocity for a velocity range of 2 to 17 m/s. In addition, Kutateladze and Burakov observed that the subcooling effect was more pronounced at higher velocities. Using a small rectangular

Contributed by the Heat Transfer Division for publication in the JOURNAL OF HEAT TRANSFER. Manuscript received by the Heat Transfer Division October 16, 2000; revision received March 23, 2001. Associate Editor: F. B. Cheung.

surface (12.7 mm×12.7 mm) in FC-72, Mudawar and Maddox [14] observed an increase in CHF with both increased velocity and subcooling and identified two distinct CHF regimes for low and high velocities. The transition from low to high velocity was characterized by an increase in the rate of CHF enhancement with velocity. This trend has also been observed by McGillis et al. [15], Willingham and Mudawar [8], and Tso et al. [10].

From pool boiling research it has been found that the microporous coating provides significant enhancement throughout the nucleate boiling curve (Chang and You [16,17]), however, its enhancement ability under flow boiling has not yet been determined. Therefore, the objective of the present research is to study the effects of fluid velocity and subcooling on the heat transfer performance from a microporous enhanced surface. The heat transfer performance from a highly polished plain surface is used as a reference. More specifically, two 1-cm^2 (10 mm×10 mm) flat copper test surfaces (plain and microporous) simulating small microelectronic devices were flush-mounted in the bottom of a 12.7 mm×12.7 mm square, horizontal flow channel. To study the effect of fluid velocity, three different velocities (0.5, 2, and 4 m/s) were tested in addition to reference pool boiling tests for each test surface. Fluid subcooling levels of 4, 10, and 20 K were also tested. All testing was performed in pure FC-72 at atmospheric pressure.

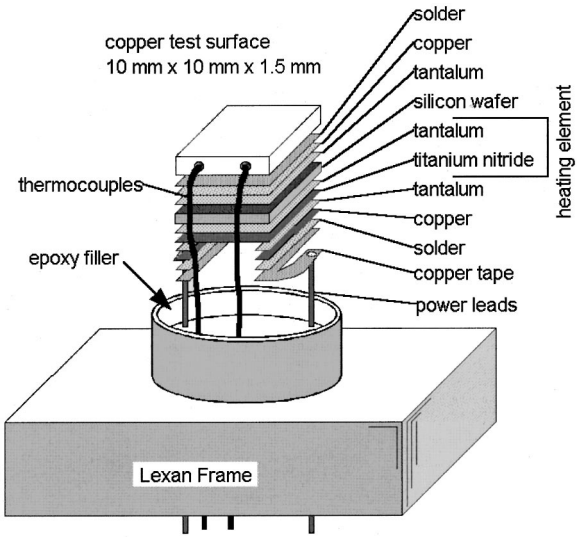

Fig. 2 Flow boiling test heater assembly

Experimental Apparatus and Procedure

Test Facility. A schematic of the closed-loop flow boiling test facility used for the present study is shown in Fig. 1. The degassing tank allows for the removal of non-condensables during the degassing process and serves as a fluid reservoir and pressure regulator during testing. The condenser above the degassing tank is used to prevent loss of test fluid during the degassing process. The degassing bottles are used to visually ensure that all non-condensables have been removed. From the degassing tank, the fluid passes through a heat exchanger and then a fixed speed centrifugal pump. The heat exchanger is used to cool the fluid and prevent cavitation in the pump during the degassing process. Since the pump operates at a fixed speed, a bypass loop is used to control the flow rate. After passing through the pump and filter, the fluid then passes through either a low or high flow rate range turbine flowmeter. The fluid then passes through a pre-heater prior to the test section for test section inlet temperature control. The heat exchanger after the test section is used only during testing to cool the fluid prior to entering the pump to prevent cavitation (replaces the function of the heat exchanger located after the degassing tank, which is used during degassing). During the degassing process, valve 4 is closed while valves 5 and 6 are open

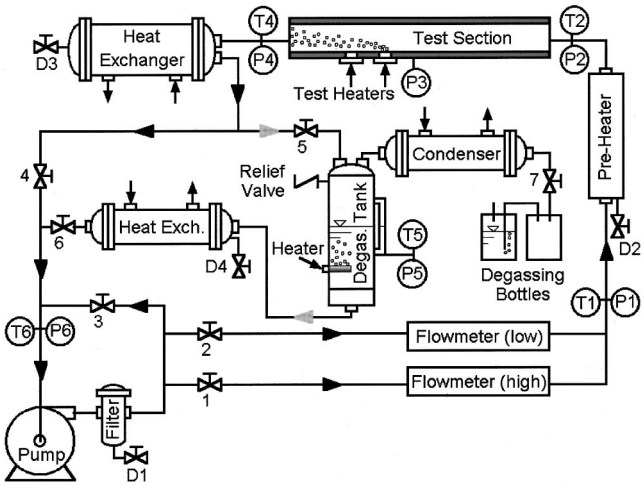

Fig. 1 Flow boiling test loop schematic

(forcing all of the fluid to pass through the degassing tank), however, during testing, valve 4 is opened and valve 6 is closed (which bypasses the degassing tank and allows it to be used as a reservoir and pressure regulator since valve 5 is left open). Pressure transducers and thermocouples are located at the pre-heater inlet, test section inlet, heater location and exit, degassing tank, and pump inlet as indicated in Fig. 1.

The test section in Fig. 1 is constructed of Lexan, which allows for test heater visualization from both the side and top. The flow channel has a 12.7 mm×12.7 mm square cross section and is 552 mm long. Although only one heater is tested at a time, the test section allows for the installation of two test heaters. The test heaters are located 400 and 464 mm (31.5 and 36.5 hydraulic diameters) from the test section inlet and are in the horizontal, upward facing orientation. The fluid flow at the test heaters is estimated to be fully developed turbulent flow for the present flow rate range. The test heaters are secured in the test section with clamps and are sealed using o-rings. To ensure proper inlet pressure control, a pressure transducer was installed 47 mm upstream of the first heater.

Test heater power is provided by a computer controllable DC power supply. A shunt resistor connected in series with the test heater and power supply, rated at 100 mV and 20 A, was used to determine the current in the electric circuit. The measured voltage drop across the test heater (along with the current measurement) was used to calculate power applied to the test heater. A computer controlled data acquisition system is used for test heater control as well as all temperature, pressure, voltage, and flowmeter measurements.

Test Heater. The test heater design is shown in Fig. 2. The heating element consists of thin tantalum and titanium nitride films. The heating element was sputtered onto a 0.5 mm thick oxidized silicon wafer along with copper for solder connections. The total heating element electrical resistance was about 25 Ω. The heating element side of the wafer was soldered to copper tape for the power lead connections while the other side of the wafer was soldered to the copper test surface. The test surfaces were cut from 1.5 mm thick solid copper plate with dimensions of 10 mm ×10 mm. The test surfaces contain two thermocouple wells centered in the base surface and spaced 5 mm apart and 5 mm deep. The test surface/heating element assembly was glued into a cylindrical Lexan frame using epoxy. The same epoxy was used to fill the space around the test surface. The top of the test surface was flush with the frame sidewalls. Copper wire power leads, which

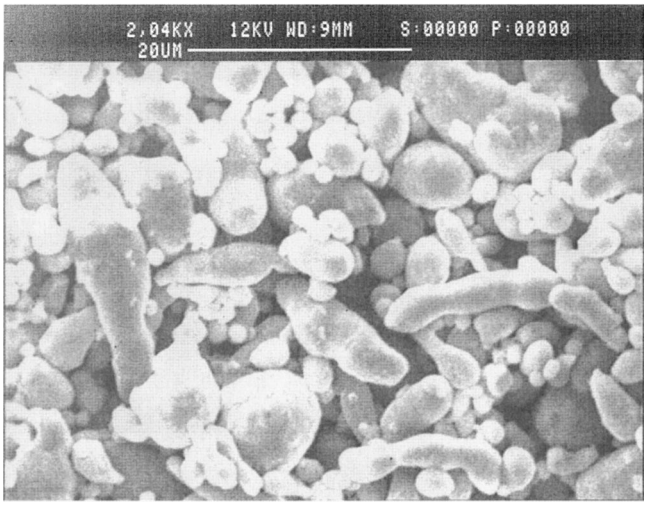

Fig. 3 SEM image of ABM microporous coating (top view)

were fed through holes in the bottom of the frame, were soldered to the copper tape. The thermocouple wires were also fed through holes in the frame bottom.

The surface condition of the plain test surface was highly polished (mirror finish). The plain copper test surface was polished using Brasso metal polish and a finger. After polishing, a small amount of epoxy was applied around the perimeter of the heater surface to prevent undesired edge nucleation sites. The plain surface was cleaned with acetone prior to testing.

For the microporous coated heater, the coating used is the ABM coating (shown in Fig. 3) introduced by Chang and You [17]. The microporous coating technique was previously developed by O'Connor and You [18], further refined by Chang and You [16,17], and patented by You and O'Connor [19]. The coating is a surface treatment technique used to increase vapor/gas entrapment volume and active nucleation site density by forming a porous structure of about 0.1–1 μm size cavities that is approximately 50 μm thick. The ABM coating was named from the initial letters of its three components: 1–20 μm Aluminum particles/Devcon Brushable Ceramic epoxy/Methyl-Ethyl-Keytone (M.E.K.). The mixture of the three components was drip-coated over the test surface using a paintbrush. After the carrier (M.E.K.) evaporated, the resulting coated layer consisted of microporous structures of aluminum particles and epoxy. The microporous coating provides no significant increase of the heat transfer surface area. Detailed descriptions of the coating are provided by O'Connor and You [18] and Chang and You [16,17].

Test Procedure. In order to obtain accurate flow boiling test data, a sound degassing and test procedure must be developed. Some of the common pitfalls in flow boiling research from discrete heat sources are (1) allowing premature edge nucleation to skew the nucleate boiling curve and prevent the collection of accurate incipience data, (2) not properly degassing the test fluid, which can significantly alter the nucleate boiling curve (Collier [20]), and (3) not maintaining constant pressure at the test section inlet (maintaining constant test section outlet pressure causes significant scatter in the test data due to changing inlet pressure from the two-phase pressure drop). The authors believe that all of these potential problems have been successfully addressed with the present test section/heater design and test procedure.

Prior to testing, the FC-72 test fluid was degassed. First, valves 5 and 6 are opened while valve 4 is closed to force all of the fluid to pass through the degassing tank (Fig. 1). The flow rate in the loop is then set to about 14 liters/min by adjusting valve 3. After the pump, the pre-heater heats the fluid to near saturation (saturation conditions are not allowed in the pre-heater to prevent dryout, which can cause FC-72 decomposition). The pressure drop through the line, test section, and heat exchanger (not in use during degassing) produces saturated fluid conditions at the degassing tank inlet. The fluid inside the degassing tank is maintained at saturation with a cartridge heater. To prevent cavitation, the heat exchanger at the degassing tank exit is used to slightly cool the fluid before entering the pump. The condenser above the degassing tank is used to prevent loss of test fluid during degassing. The top of the condenser was attached to two degassing bottles (one is empty while the other is filled with water and open to ambient). This degassing bottle arrangement allows for: viewing the escaping air bubbles, maintaining atmospheric pressure in the degassing tank, and preventing introduction of water into the test loop if the loop pressure drops below atmospheric pressure. The test fluid is considered completely degassed when no more air bubbles are observed to exit the condenser. After reaching saturation conditions in the degassing tank, the FC-72 test fluid is completely degassed in approximately 2 hours.

Once degassing is complete, the test loop is closed off from atmospheric pressure by closing valve 7 (Fig. 1). The degassing tank is then bypassed by closing valve 6 and opening valve 4. Valve 5 is left open to allow the degassing tank to be used as a fluid reservoir and pressure regulator. The pressure at the test section inlet is controlled by adjusting the cartridge heater power and condenser cooling power. During testing, the heat exchanger at the test section outlet is used to cool the fluid prior to entering the pump to prevent cavitation while the pre-heater is used to set the test section inlet temperature. Once the fluid velocity, pressure, and temperature reached steady-state conditions, testing was initiated.

The test heater heat flux was controlled by voltage input. After each voltage change (heat-flux increment), a 15-second delay was imposed before initiating data acquisition. After the delay, the computer repeatedly collected and averaged 125 base surface temperature measurements over 15 seconds until the temperature difference between two consecutive averaged temperature measurements for all thermocouples was less than 0.2 K. The test section at this point was assumed to be at steady state. After reaching steady state, heater surface and bulk fluid temperatures were measured and the heat flux was calculated. For heat flux values greater than $\approx$80 percent of CHF, instantaneous surface temperature was monitored for 45 s after each increment to prevent heater burnout. Each instantaneous surface temperature measurement was compared with the previous increment's average surface temperature. If a temperature difference larger than 20 K was detected, CHF was assumed and the power shut off. The CHF value was computed as the steady-state heat-flux value just prior to power supply shutdown plus half of the increment.

Experimental Uncertainty. Single-sample uncertainties for this study were estimated using the method of Kline and McClintock [21]. Fluid velocity uncertainty was estimated as 5.4 percent at 0.5 m/s and 2.1 percent at 2 and 4 m/s. Uncertainty in pressure measurements was estimated as 2.0 percent. Heat flux measurement uncertainty was estimated based upon the values of Rainey and You [22], whose test heater was of similar design to the present one. Although Rainey and You tested in pool boiling, the only difference between their setup and the present one is that in the present study the heat transfer coefficients are generally higher and the test heater substrate conduction loss is lower. Therefore, basing the present uncertainties on Rainey and You's values is considered conservative. The heat flux uncertainty (taking into account uncertainties in voltage, current, and area) for the present test heater is estimated as 6.0 percent at both 20 and 60 W/cm^2. In addition, temperature measurement uncertainty (both loop and test heater) was estimated considering thermocouple calibration error, temperature correction for the embedded thermocouples, and thermocouple resolution error. The uncertainty for temperature measurement was $\pm$0.4 K.

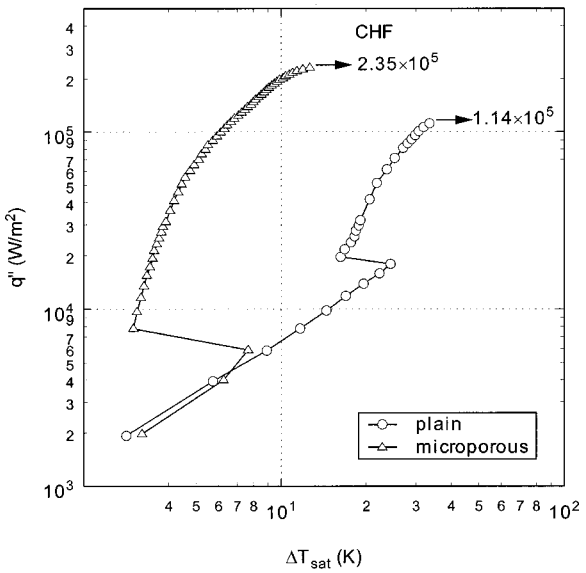

Fig. 4 Reference pool boiling curves

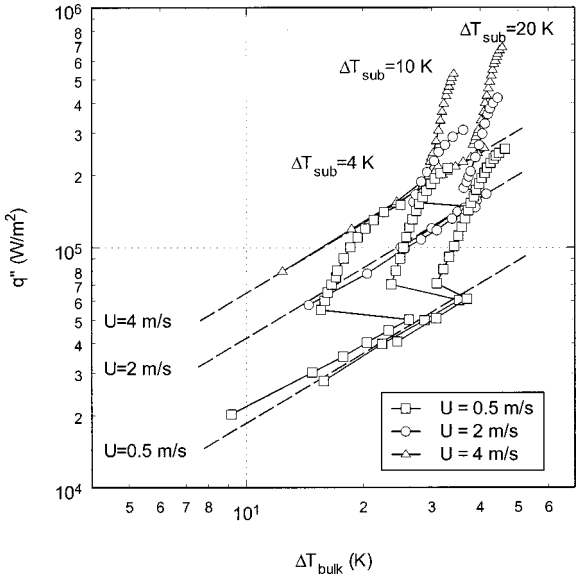

Fig. 5 Flow boiling curves of plain surface

Results and Discussion

The present study is to understand the effects of fluid velocity and subcooling on nucleate boiling and CHF for both plain and microporous coated flat surfaces. The test surfaces are 1-cm^2 (10 mm$\times$10 mm) copper blocks flush mounted in the bottom of a rectangular, horizontally positioned flow channel. The heating surfaces, one highly polished and one microporous coated, are positioned in the horizontal, upward facing orientation and are intended to simulate a small microelectronic device. The fluid velocity and subcooling are varied from 0.5 to 2 m/s (Reynolds numbers from 18,700 to 174,500) and 4 to 20 K, respectively. The 2 m/s and 4 m/s cases at 4 K subcooling were not included in the reported results due to excessive inlet flow instability related to cavitations. All testing is performed in pure FC-72 at atmospheric pressure.

Pool Boiling Tests of Reference Surfaces. In order to qualify the present test heater surfaces, pool boiling curves in saturated FC-72 at atmospheric pressure were generated. Figure 4 illustrates the plain and microporous coated surfaces' pool boiling test results. For reference, the pool boiling tests were conducted in the same facility and with the same procedures used by Rainey and You [22]. The single-phase natural convection data of the present heaters exhibited comparable heat transfer coefficients showing negligible surface microstructure effects. Incipient superheat values ranged from 19 to 24 K for the plain surface and 4 to 8 K for the microporous coated surface showing the superior nucleation characteristics of the microporous coating. Throughout the nucleate boiling regime, the microporous coated surface consistently augmented heat transfer coefficients by more than 300 percent when compared to those of the plain surface. This enhancement is the result of the dramatically increased active nucleation site density caused by the surface microstructures provided by the microporous coating (O'Connor and You [18]). The CHF values for the plain surface ranged between 11.3 to 13.0 W/cm^2 while the microporous coated surface showed consistently enhanced CHF values of 23.5 W/cm^2. In addition, these results are comparable to those reported by Chang and You [23] for their plain and microporous coated 1-cm^2 surfaces of similar construction.

Plain Surface Flow Boiling Results. The flow boiling curves of the plain surface are shown in Fig. 5 plotted versus ΔT_{bulk}. The single-phase, forced convection data clearly shows the effects of fluid velocity as indicated by the dashed trend lines. Boiling generally spread over the entire surface of the heater at incipience, however, there appeared to be a higher concentration of active nucleation sites near the downstream edge indicating a slightly higher wall temperature. This active nucleation site density pattern appeared to be prevalent throughout the boiling curve. The incipient superheats for the plain surface boiling curves in Fig. 5 are listed in Table 1. In addition, there appears to be no discernable trend in incipient superheat with respect to either fluid velocity or subcooling showing only the typical large scatter of a highly-wetting fluid. This apparent insensitivity of incipience to inlet subcooling and velocity is consistent with the R-113 tube flow boiling results of Hino and Ueda [24] and the R-12 and R-114 tube flow boiling results of Celata et al. [25]. However, both Samant and Simon [12] and Heindel et al. [9] observed that incipience was affected by inlet subcooling and velocity for small heaters in FC-72 flow boiling. For a given fluid subcooling, the nucleate boiling data in Fig. 5 appear to follow one line. This insensitivity of the nucleate boiling heat transfer coefficient to fluid velocity shows that the nucleate boiling heat transfer mechanism completely dominates the heat transfer process for the range of fluid conditions tested.

By plotting the boiling curve data versus ΔT_{bulk} in Fig. 5, the effect of fluid subcooling on nucleate boiling heat transfer appears to be directly related to subcooling level. The data of Willingham and Mudawar [8] and Gersey and Mudawar [26] show a similar effect. There is also an interesting trend concerning the characteristic bend in the boiling curve near CHF. As the fluid velocity increases, the bend appears to diminish considerably. This may be due to increased disruption of the larger, secondary vapor layer above the surface causing instability in the vapor removal mechanism near CHF.

Table 1 Flow boiling incipient superheats, K

U	ΔT_{sub}=20 K		ΔT_{sub}=10 K		ΔT_{sub}=4 K	
	plain	micro.	plain	micro.	plain	micro.
m/s	Run 1/2	Run 1/2	Run 1/2	Run 1/2	Run 1/2	Run 1/2
0.5	17.1/25.8	9.4/8.4	26.9/25.2	2.9/10.1	17.4/23.1	11.7/5.3
2	24.5/21.3	13.1/14.9	24.6/28.6	6.4/9.3	-	-
4	20.2/21.1	10.0/10.4	20.5/21.1	5.9/7.8	-	-

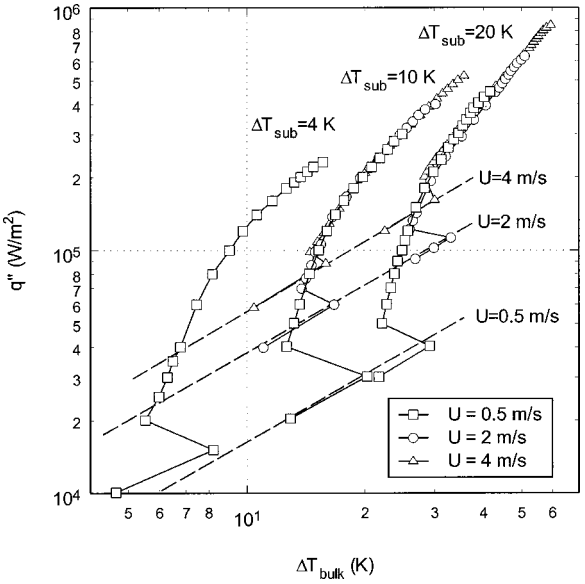

Fig. 6 Flow boiling curves of microporous surface

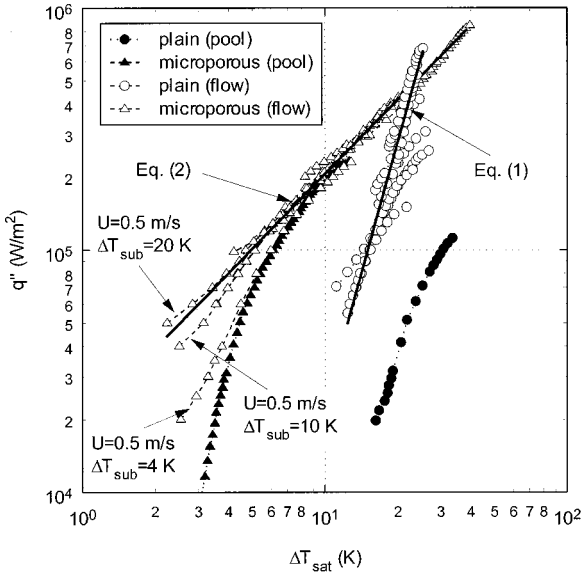

Fig. 7 Correlation of nucleate boiling curves

Detailed visual observations were made of the nucleate boiling behavior for the 2 m/s, 10 K subcooling case. After incipience, the nucleate boiling was characterized by very small bubbles departing and flowing parallel to the heater surface. Increasing the heat flux appeared to cause the departing bubbles to merge, forming a ''blanket'' of thin streams that would merge with other streams. As the heat flux approached CHF, the vapor removal was very chaotic with large, wavy vapor streams. A high-speed video camera was used to observe the CHF phenomena. For about one second prior to CHF, it appeared that large portions of the surface (up to 75 percent) would alternately be covered with vapor and then rewetted until, suddenly, the entire surface was covered with vapor. Although video was taken at 600 frames/sec, the final blanketing of the surface by the vapor was too fast to determine the initial origin on the surface of the dryout.

Microporous Surface Flow Boiling Results. The flow boiling curves of the microporous surface are shown in Fig. 6 plotted versus ΔT_{bulk}. The single-phase, forced convection data (indicated by the dashed trend lines) of the microporous surface are slightly worse than that of the plain surface data shown in Fig. 5 for all flow velocities tested, which appears to contradict the single-phase natural convection data shown in Fig. 4. Since O'Connor and You [18] estimated the effective thermal conductivity of the microporous coating layer to be very low (0.95 W/m·K), the degradation in the single-phase forced convection of the microporous surface is most likely due to the added conductive thermal resistance of the coating. This degradation effect was probably not observed in the single-phase natural convection data shown in Fig. 4 because the additional temperature drop from conduction through the coating was estimated to be within the experimental uncertainty for those low heat flux levels (much lower than those for forced convection). Similar to the plain surface, boiling spread over the entire surface of the heater at incipience, however, there was a much greater number of active nucleation sites than the plain surface and they appeared to be more evenly distributed. The bubbles departing the surface formed a relatively smooth layer of small discrete bubbles above the heater surface. The incipient superheats for the microporous boiling curves in Fig. 6 are listed in Table 1. From the table it can be seen that the microporous surface maintains its superior nucleation characteristics when moving from pool to flow boiling. At the lower fluid velocities and subcoolings, the nucleate boiling heat transfer coefficients of the microporous surface are still much better than those of the plain surface, however, at higher velocities and subcoolings, the reduction in slope of the microporous boiling curves causes the enhancement to disappear. The reason for this degradation in microporous surface performance is explained later. As with the plain surface, the microporous nucleate boiling data in Fig. 6 appear to follow one line for a given fluid subcooling showing the same insensitivity of the nucleate boiling heat transfer coefficient to fluid velocity. It is also interesting to note that there is virtually no bending in the microporous boiling curves near CHF as seen in the lower velocity plain surface data in Fig. 5.

Visual observations of the 2 m/s, 10 K subcooling case showed a slightly different boiling behavior for the microporous surface compared to the plain surface. As previously mentioned, the departing bubbles from the microporous surface formed a relatively smooth bubble layer above the heater surface after incipience. However, as the heat flux increased, the bubble layer remained smooth and stable unlike the plain surface, changing only in its thickness. About one second prior to CHF (using the high-speed video camera), the amount of vapor exiting the surface began to pulse rapidly. Once CHF was reached, the pulsing stopped indicating complete dryout of the heater surface.

Correlation of Flow Boiling Data. Figure 7 shows all of the plain and microporous boiling curves plotted versus ΔT_{sat}. The single-phase forced convection data have been removed for clarity. The most striking feature of this graph is how both surfaces' nucleate boiling curves collapse to one line showing insensitivity of the nucleate boiling heat transfer to both fluid velocity and subcooling. The plain surface data are well correlated with the following equation:

$$q'' = 5.39 \cdot \Delta T_{\text{sat}}^{3.63}. \tag{1}$$

Equation (1) was found by fitting all of the nucleate boiling data excluding the bending portions prior to CHF. The log-log slope of 3.63 from Eq. (1) is similar to that observed by Willingham and Mudawar [8] (slope $\approx$3.7) and Gersey and Mudawar [26] (slope $\approx$3.5). Both of these references used 10 mm$\times$10 mm flat copper heaters in FC-72 at atmospheric pressure.

As can be seen in Fig. 7, the plain surface saturated pool boiling curve has a slope similar to the plain surface subcooled flow boiling curves but is shifted significantly to the right. This suggests that the boiling heat transfer performance is significantly affected by either fluid velocity or subcooling or both somewhere in the

low velocity range between 0 to 0.5 m/s. Using a highly polished thin gold film heater in R-113, Kirk et al. [11] found that increasing fluid velocity from 0.041 to 0.325 m/s significantly shifted the entire nucleate boiling curve to the left by about 5 K. Further, Willingham and Mudawar [8] observed a negligible effect of fluid subcooling (3 to 36 K) on the flow boiling heat transfer from a vapor-blasted copper surface at a fluid velocity of 0.50 m/s in FC-72. In contrast, both Heindel et al. [9] and Tso et al. [10] found a significant effect of both subcooling and velocity at low heat fluxes due to partial boiling conditions. Since the partial boiling conditions described by Heindel et al. and Tso et al. were not observed in the present study, the observations of Kirk et al. and Willingham and Mudawar seem to suggest that the transition from pool boiling to subcooled flow boiling seen in the present plain surface data is primarily due to fluid velocity effects, however, more testing in this velocity range is needed before any conclusions can be made.

The microporous surface flow boiling data in Fig. 7 are well correlated by the following equation:

$$q'' = 1.94 \times 10^4 \cdot \Delta T_{\text{sat}}^{1.02}. \quad (2)$$

The microporous surface boiling curves also show a transition in heat transfer performance from pool boiling to flow boiling. From Fig. 7, it appears that the transition of the microporous surfaces is caused by fluid subcooling alone and is only significant in the lower heat flux region of the boiling curves. The microporous coating provides nucleate boiling enhancement by increasing the number of active nucleation sites at low heat fluxes (O'Connor and You [18]). It is hypothesized that the increased number of bubbles generated by the coating causes increased blockage to the fluid rewetting the surface. Increased fluid subcooling would reduce the bubble sizes through condensation and thus decrease the amount of blockage seen by the fluid allowing for more forced convection heat transfer. As the heat flux (and velocity) is increased, the effect of subcooling on the nucleate boiling heat transfer disappears.

Compared to the plain surface data, the microporous surface data in Fig. 7 have a much lower slope. In fact, above a heat flux of about 50 W/cm^2, the microporous coating actually provides worse heat transfer performance than the plain surface. It is postulated that this is caused by the apparent conductive thermal resistance of the microporous coating layer in the nucleate boiling situation (coating plus fluid within cavities) previously mentioned. To help explain this, the average surface heat transfer coefficients of all the boiling curves from Fig. 7 are plotted versus ΔT_{sat} in Fig. 8. The heat transfer coefficients calculated from Eqs. (1) and (2) are also plotted in Fig. 8. Very simply, the total thermal resistance for the plain heater is dependent only on the thermal resistance of flow boiling (latent heat and convection heat transfer), $R_{\text{tot}} = R_{\text{boil}}$, while the total thermal resistance for the microporous heater is dependent on the thermal resistance of flow boiling plus the thermal resistance of conduction for the thin microporous coating layer, $R_{\text{tot}} = R_{\text{boil}} + R_{\text{cond}}$. Since R_{cond} may be constant, this places a lower limit on R_{tot} for the microporous surface as R_{boil} becomes smaller at higher fluid velocities and subcoolings. Referring to Fig. 8, the nearly constant h-value ($\approx 2 \times 10^4$ W/m^2·K) for the microporous surface means that $R_{\text{boil}} \ll R_{\text{cond}}$. From this realization, the effective thermal conductivity of the present (ABM) microporous coating layer can be estimated from $R_{\text{tot}} \approx R_{\text{cond}}$ as 1 W/m·K (coating thickness = 50 μm), which compares well with the values of 1.08 W/m·K estimated by O'Connor et al. [27] for their DOM microporous coating and 0.95 W/m·K estimated by O'Connor and You [18] for their silver flake microporous coating. It should also be noted that both O'Connor et al. and O'Connor and You compared pool boiling data of different coating thickness to determine their thermal conductivities, which is different from the present method. It is also interesting to observe that the maximum heat transfer coefficient seen in pool boiling on the microporous surface is also the maximum for subcooled flow boiling. The previously discussed transitions from pool to flow boiling for both surfaces can also be seen in Fig. 8.

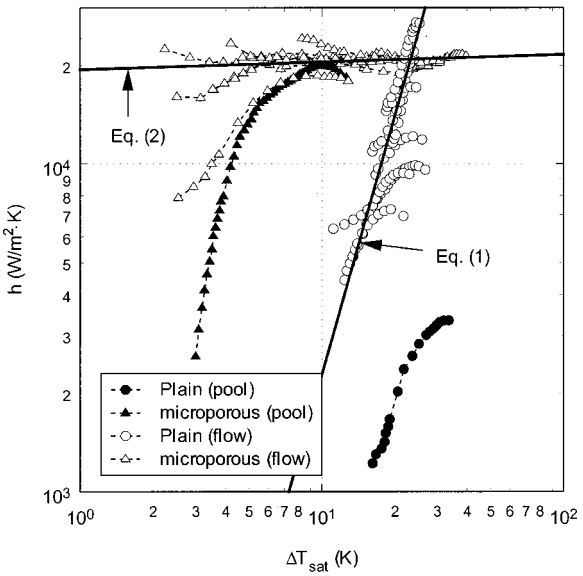

Fig. 8 Average nucleate boiling heat transfer coefficients

Critical Heat Flux Behavior. The fluid velocity and subcooling effects on CHF for the plain and microporous surfaces are presented in Fig. 9 and Table 2. Both surfaces in Fig. 9 show significant enhancement of CHF with both increased fluid velocity and subcooling. The positive effect of fluid subcooling on CHF has already been noted by many researchers (Mudawar and Maddox [14] and Tso et al. [10]) and is due to a reduction, by condensation, in vapor covering the heater surface, which decreases the resistance to the liquid rewetting the surface and delays CHF. With respect to fluid velocity, the plain surface data show a change in slope near 2 m/s similar to that observed by Mudawar and Maddox [14]. Using Haramura and Katto's [28] macrolayer dryout model, Mudawar and Maddox explained that the low velocity CHF was caused by dryout of the liquid sublayer beneath a large continuous vapor blanket near the downstream edge of the

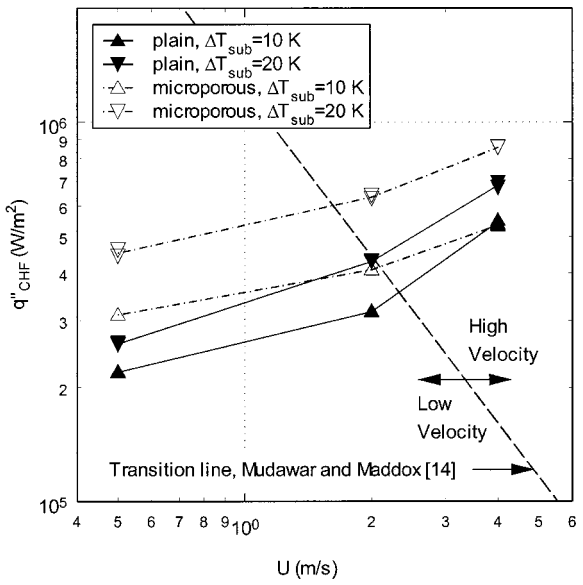

Fig. 9 Effect of velocity and subcooling on CHF

Table 2 Flow boiling CHF values, W/cm^2

U	ΔT_{sub}=20 K		ΔT_{sub}=10 K		ΔT_{sub}=4 K	
	plain	micro.	plain	micro.	plain	micro.
m/s	Run 1/2	Run 1/2	Run 1/2	Run 1/2	Run 1/2	Run 1/2
0.5	26.2/25.9	46.0/44.3	22.0/21.9	31.1/31.1	15.5/15.5	24.0/23.6
2	42.8/43.0	64.0/62.8	31.6/31.8	40.8/40.8	-	-
4	67.1/69.0	85.8/85.6	55.1/53.9	53.4/53.5	-	-

heater. In the high velocity CHF regime, they observed that the thin vapor layer covering the surface was broken into continuous vapor blankets much smaller than the heater surface. This most likely decreases the resistance to the fluid rewetting the liquid sublayer, providing an additional enhancement to CHF and subsequent increase in slope as seen in Fig. 9. The dashed line in Fig. 9 represents the transition line proposed by Mudawar and Maddox to separate low and high velocity behavior. The microporous surface CHF values show this behavior as well, but to a lesser degree.

The lower slope of the microporous data compared to the plain surface data in Fig. 9 shows reduction in CHF enhancement as velocity increases similar to the reduction in nucleate boiling enhancement of the microporous surface previously discussed. Figure 10 shows the ratio of the microporous surface CHF data to the plain surface CHF data versus fluid velocity at $\Delta T_{sub}=10$ and 20 K. From Fig. 10 it can be seen that the microporous coating's effectiveness of enhancing CHF decreases linearly with increasing fluid velocity. In addition, from Fig. 10, it can be seen that increased subcooling causes a proportional increase in CHF, but the rate of reduction in CHF enhancement of the microporous coating with velocity appears to be the same.

Comparing the saturated pool boiling CHF values of the plain and microporous surfaces in Fig. 4 to their corresponding CHF values for the 0.5 m/s, 4 K subcooled flow boiling case in Table 2 reveals an interesting observation. The plain surface CHF increased by 36 percent when moving from saturated pool boiling to 0.5 m/s, 4 K subcooled flow boiling while the microporous surface CHF remained virtually unchanged. This suggests that the microporous coating already provides a more dominant nucleate boiling heat transfer mechanism, which requires higher fluid velocities than the plain surface to provide further enhancement of CHF.

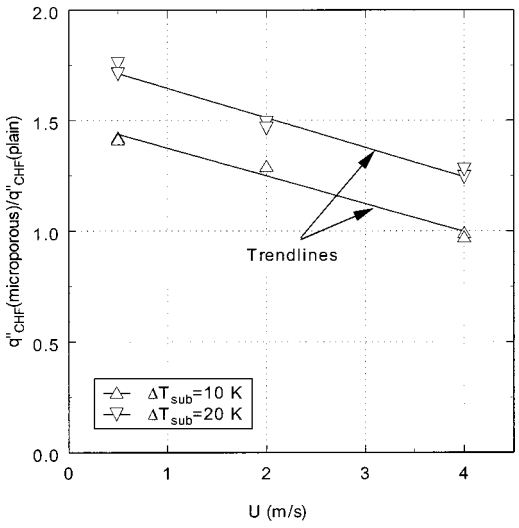

Fig. 10 Effect of velocity and subcooling on microporous coating effectiveness

Conclusions

To understand the effects of fluid velocity and subcooling on nucleate boiling and CHF from a microporous enhanced surface, two 1-cm^2 (10 mm×10 mm) copper test surfaces were flush-mounted in the bottom of a rectangular, horizontally positioned flow channel. The heating surfaces, one highly polished and one microporous coated, are intended to simulate small microelectronic devices. The fluid velocity and subcooling were varied from 0.5 to 2 m/s and 4 to 20 K, respectively. All testing was performed in pure FC-72 at atmospheric pressure.

1 Both plain and microporous surfaces showed insensitivity to fluid velocity and subcooling level within the subcooled flow boiling ranges tested, which is in agreement with the prevailing trend seen in the literature. The plain and microporous nucleate flow boiling curves collapsed to one line and were well correlated by Eqs. (1) and (2).

2 The plain surface nucleate boiling heat transfer performance was significantly affected by fluid velocity and/or subcooling between 0 and 0.5 m/s and 0 to 4 K. The microporous surface was significantly affected by fluid subcooling at low heat flux levels for the lowest velocity tested (0.5 m/s); however, the behavior disappears with increased velocity and/or heat flux.

3 The log-log slope of the nucleate flow boiling curve for the microporous surface was much lower than for the plain surface and actually provided worse heat transfer performance than the plain surface above a heat flux of about 50 W/cm^2. This degradation in heat transfer performance of the microporous surface was caused by the limiting effect of the thermal resistance of conduction for the microporous coating layer. Using the heat transfer coefficient data, the effective thermal conductivity of the microporous coating in nucleate flow boiling was estimated as 1 W/m·K, which compares well with previously published estimations using pool boiling data.

4 The CHF values of the plain surface, increased with increasing fluid velocity and subcooling. The log-log slope of CHF versus fluid velocity significantly increased at about 2 m/s, which supports the earlier observations of Mudawar and Maddox [14] regarding low and high velocity CHF regimes. The microporous surface showed similar behavior, although to a lesser degree.

5 Due to the already enhanced nucleate boiling characteristics of the microporous coating, higher fluid velocities than for the plain surface are required to provide additional enhancement of nucleate boiling heat transfer. In addition, the enhancement of CHF provided by the microporous coating over the plain surface increases with increased fluid subcooling, however, compared to the plain surface, the enhancement effectiveness of the coating decreases linearly with increased velocity.

Acknowledgments

This study was supported by the Texas Higher Education Coordinating Board: Advanced Research/Technology Program grant number 003656-014. The authors extend their thanks to the 3M Industrial Chemical Products Division for the donation of FC-72 test liquid.

Nomenclature

h = average heat transfer coefficient, [W/m^2·K]
q'' = heat flux, [W/m^2]
R = thermal resistance, [K/W]
T = temparature, [K]
U = fluid velocity, [m/s]

Greek Symbols

ΔT_{bulk} = wall superheat, $T_w - T_{bulk}$, [K]
ΔT_{sat} = wall superheat, $T_w - T_{sat}$, [K]
ΔT_{sub} = inlet subcooling, $T_{sat} - T_{bulk}$, [K]

Subscripts

boil = flow boiling
bulk = bulk fluid entering test section
CHF = critical heat flux
cond = conduction
sat = saturated
tot = total
w = heater wall

References

[1] McAdams, W. H., 1954, *Heat Transmission*, McGraw-Hill, New York.
[2] Engelberg-Forster, K., and Greif, R., 1959, ''Heat Transfer to a Boiling Liquid—Mechanism and Correlations,'' ASME Journal of Heat Transfer , **81**, No. 1, pp. 43–53.
[3] Ellion, M. E., 1954, ''A Study of the Mechanism of Boiling Heat Transfer,'' Memo No. 20–88, Jet Propulsion Laboratory, California Institute of Technology, p. 72.
[4] Yin, C. P., Yan, Y. Y., Lin, T. F., and Yang, B. C., 2000, ''Subcooled Flow Boiling Heat Transfer of R-134a and Bubble Characteristics in a Horizontal Annular Duct,'' Int. J. Heat Mass Transf., **43**, No. 11, pp. 1885–1896.
[5] Gunther, F. C., 1951, ''Photographic Study of Surface-Boiling Heat Transfer to Water with Forced Convection,'' ASME Journal of Heat Transfer , **73**, No. 2, pp. 115–123.
[6] Bibeau, E. L., and Salcudean, M., 1994, ''A Study of Bubble Ebullition in Forced-Convective Subcooled Nucleate Boiling at Low Pressure,'' Int. J. Heat Mass Transf., **37**, No. 15. pp. 2245–2259.
[7] Klausner, J. F., Mei, R., Bernhard, D. M., and Zeng, L. Z., 1993, ''Vapor Bubble Departure in Forced Convection Boiling,'' Int. J. Heat Mass Transf., **36**, No. 3, pp. 651–662.
[8] Willingham, T. C., and Mudawar, I., 1992, ''Channel Height Effects on Forced-Convection Boiling and Critical Heat Flux From a Linear Array of Discrete Heat Sources,'' Int. J. Heat Mass Transf., **35**, No. 8, pp. 1865–1880.
[9] Heindel, T. J., Ramadhyani, S., and Incropera, F. P., 1992, ''Liquid Immersion Cooling of a Longitudinal Array of Discrete Heat Sources in Protruding Substrates: II-Forced Convection Boiling,'' ASME J. Electron. Packag., **114**, No. 1, pp. 63–70.
[10] Tso, C. P., Tou, K. W., and Xu, G. P., 2000, ''Flow Boiling Critical Heat Flux of FC-72 From Flush-Mounted and Protruded Simulated Chips in a Vertical Rectangular Channel,'' Int. J. Multiphase Flow, **26**, No. 3, pp. 351–365.
[11] Kirk, K. M., Merte, Jr., H., and Keller, R., 1995, ''Low-Velocity Subcooled Nucleate Flow Boiling at Various Orientations,'' ASME Journal of Heat Transfer , **117**, No. 2, pp. 380–386.
[12] Samant, K. R., and Simon, T. W., 1989, ''Heat Transfer From a Small Heated Region to R-113 and FC-72,'' ASME Journal of Heat Transfer, **111**, No. 4, pp. 1053–1059.
[13] Kutateladze, S. S., and Burakov, B. A., 1969, ''The Critical Heat Flux for Natural Convection and Forced Flow of Boiling and Subcooled Dowtherm,'' *Problems of Heat Transfer and Hydraulics of Two-Phase Media*, Pergamon, Oxford, pp. 63–70.
[14] Mudawar, I., and Maddox, D. E., 1989, ''Critical Heat Flux in Subcooled Flow Boiling of Fluorocarbon Liquid on a Simulated Electronic Chip in a Vertical Rectangular Channel,'' Int. J. Heat Mass Transf., **32**, No. 2, pp. 379–394.
[15] McGillis, W. R., Carey, V. P., and Strom, B. D., 1991, ''Geometry Effects on Critical Heat Flux for Subcooled Convection Boiling from an Array of Heated Elements,'' ASME Journal of Heat Transfer , **113**, No. 2, pp. 463–471.
[16] Chang, J. Y., and You, S. M., 1997, ''Boiling Heat Transfer Phenomena From Micro-Porous and Porous Surfaces in Saturated FC-72,'' Int. J. Heat Mass Transf., **40**, No. 18, pp. 4437–4447.
[17] Chang, J. Y., and You, S. M., 1997, ''Enhanced Boiling Heat Transfer From Micro-Porous Surfaces: Effects of a Coating Composition and Method,'' Int. J. Heat Mass Transf., **40**, No. 18, pp. 4449–4460.
[18] O'Connor, J. P., and You, S. M., 1995, ''A Painting Technique to Enhance Pool Boiling Heat Transfer in FC-72,'' ASME Journal of Heat Transfer , **117**, No. 2, pp. 387–393.
[19] You, S. M., and O'Connor, J. P., 1998, ''Boiling Enhancement Paint,'' U.S. Patent #5814392.
[20] Collier, J. G., 1981, *Convective Boiling and Condensation*, 2nd ed, McGraw-Hill, New York.
[21] Kline, S. J., and McClintock, F. A., 1953, ''Describing Uncertainties in Single-Sample Experiments,'' Mech. Eng. (Am. Soc. Mech. Eng.), **75**, No. 1, pp. 3–8.
[22] Rainey, K. N., and You, S. M., 2000, ''Pool Boiling Heat Transfer From Plain and Microporous, Square Pin Finned Surfaces in Saturated FC-72,'' ASME Journal of Heat Transfer , **122**, No. 3, pp. 509–516.
[23] Chang, J. Y., and You, S. M., 1996, ''Heater Orientation Effects on Pool Boiling of Micro-Porous-Enhanced Surfaces in Saturated FC-72,'' ASME Journal of Heat Transfer , **118**, No. 4, pp. 937–943.
[24] Hino, R., and Ueda, T., 1985, ''Studies on Heat Transfer and Flow Boiling Characteristics in Subcooled Flow Boiling-Part 1. Boiling Characteristics,'' Int. J. Multiphase Flow, **11**, No. 3, pp. 269–281.
[25] Celata, G. P., Cumo, M., and Setaro, T., 1992, ''Hysteresis Phenomena in Subcooled Flow Boiling of Well-Wetting Fluids,'' Exp. Heat Transfer, **5**, No. 4, pp. 253–275.
[26] Gersey, C. O., and Mudawar, I., 1992, ''Effects of Orientation on Critical Heat Flux From Chip Arrays during Flow Boiling,'' ASME J. Electron. Packag., **114**, No. 3, pp. 290–299.
[27] O'Connor, J. P., You, S. M., and Price, D. C., 1995, ''A Dielectric Surface Coating Technique To Enhance Boiling Heat Transfer From High Power Microelectronics,'' IEEE Trans. Compon., Packag. Manuf. Technol., Part A, **18**, pp. 656–663.
[28] Haramura, Y., and Katto, Y., 1983, ''A New Hydrodynamic Model of Critical Heat Flux, Applicable Widely to Both Pool and Forced Convection Boiling an Submerged Bodies in Saturated Liquids,'' Int. J. Heat Mass Transf., **26**, No. 3, pp. 389–399.

Condensate Retention Effects on the Performance of Plain-Fin-and-Tube Heat Exchangers: Retention Data and Modeling

C. Korte

A. M. Jacobi
e-mail: a-jacobi@uiuc.edu

Department of Mechanical and Industrial Engineering,
University of Illinois at Urbana-Champaign,
1206 West Green Street,
Urbana, IL 61801

A study of condensate retention is presented for plain-fin-and-tube heat exchangers typical to those used in air-cooling applications. An experiment in which the retained mass of air-side condensate was measured under dynamic conditions is described, and the results are analyzed using conventional thermal-hydraulic measurements of j and f. With the coupling between condensate retention and thermal performance established, a new model for predicting the mass of retained condensate is described and compared to the steady-state retention data. The model is successful in predicting retained condensate under relatively restricted conditions. The promise of this new approach, and possible refinements that will add engineering value are discussed. [DOI: 10.1115/1.1391276]

Keywords: Condensation, Convection, Dehumidification, Heat Transfer, Heat Exchangers

Introduction

In many air-cooling applications, a heat exchanger is operated below the dewpoint of the moist air it cools, and water condenses onto the air-side surface. Once condensate forms on the heat transfer surface, it accumulates until gravitational, capillary, or flow forces remove it. Retained condensate can adversely affect heat transfer and energy efficiency because it restricts the air flow and occupies heat-transfer area. Furthermore, retained condensate affects human comfort because it can blow off the heat exchanger with the conditioned air creating an unwanted fog, and if it remains on the surface it provides a medium for biological activity that might cause odors or other problems. Therefore, it is important to understand how condensate is retained on the heat-transfer surface and how it affects the heat transfer and pressure-drop performance of the heat exchanger.

Combined latent and sensible heat transfer in air-cooling applications has attracted the interest of many researchers; however, the effects of condensate retention on heat transfer and pressure drop are not clearly understood. While it is generally accepted that retained condensate causes an increase in the air-side pressure drop, the extent of the increase appears to depend on the geometry and surface condition as well as air flow rate—there may be cases where retained condensate results in a reduced pressure drop. Condensation has been shown to have a significant effect on sensible heat transfer, but the direction and magnitude of this effect depend on the particular heat exchanger geometry and operating conditions.

Although many researchers have noted the impact of condensate retention on heat exchanger performance and operation, few studies have focused on characterizing the retained condensate itself. The effects of surface wettability, geometry, and operating condition on the amount, location, and shape of retained water droplets are not understood. Furthermore, there is no general model to predict the amount of water retained on a heat exchanger in these applications. Understanding the nature of the retained condensate is key to understanding its impact. The overall objective of this work is to explore retention effects and to describe a new approach to model condensate retention in air-cooling applications. The presentation will begin with a review of the literature and statement of the research goals, the experimental and modeling methods will be discussed, and model predictions will be compared to new experimental data. Finally, weaknesses in the model will be discussed and recommendations will be proposed for further work.

Review of the Literature

Performance of Plain-Fin Heat Exchangers. Bettanini [1] conducted experiments on simultaneous heat and mass transfer to a vertical surface. He observed an increase in sensible heat transfer under wet conditions for both the filmwise and dropwise condensation of water from a flowing moist air stream, with a greater increase for dropwise condensation. A direct relationship was observed between surface roughness and an increase in heat transfer. Higher mass transfer rates resulted in larger enhancements in sensible performance. Bettanini concluded the enhancements were due to combined effects of surface roughness and mass transfer.

An enhancement in heat transfer and an increased pressure drop were reported by Guillory and McQuiston [2] for a parallel-plate heat exchanger operating under wet conditions. These effects were attributed to an increase in surface roughness associated with retained condensate. In later work, McQuiston [3] found the friction factor to be approximately 25 percent higher under condensing conditions. Visual studies revealed dropwise condensation on the test specimen, and a downward-flowing air stream did not appear to affect the droplets for Reynolds numbers between 600 and 4000 based on hydraulic diameter. At low Reynolds numbers, McQuiston claimed there was a significant time required for steady-state droplet formation[1]. Tree and Helmer [4] conducted studies with a very simple parallel-plate heat exchanger. An increase in pressure drop and sensible heat transfer was measured under wet conditions in the transitional and fully turbulent flow regimes.

Contributed by the Heat Transfer Division for publication in the JOURNAL OF HEAT TRANSFER. Manuscript received by the Heat Transfer Division January 3, 2000; revision received April 2, 2001. Associate Editor: B. Chung.

[1]The *steady-state* condition in droplet formation or condensate retention prevails when the total mass of water on the heat exchanger surface is unchanging with time. The rate of condensation equals the rate of condensate shedding at this *steady-state retention* condition. We will use *dynamic retention* to mean the mass of condensate on the heat exchanger as a function of time, which often asymptotically approaches the steady-state retention.

McQuiston [5,6] studied plain-fin heat exchangers with four tube rows in a staggered-tube configuration. The heat exchangers were identical, except for fin spacing, which took values of 1.8, 2.1, 2.5, 3.2, and 6.4 mm. Three different surface conditions were tested for each heat exchanger: dry, wet with filmwise condensation, and wet with dropwise condensation. The dropwise mode was obtained by cleaning the heat exchangers with perchloroethylene and the filmwise mode by boiling in household dishwashing detergent and water. The mode of condensation was reported to be stable throughout the experiments. McQuiston claimed the surface type, and its condition, affected the transport processes. McQuiston also stated that the mode of retained condensate has an important effect on performance. Measured heat transfer rates were typically higher for dropwise than for filmwise condensation. The effect of condensate on the friction factor was more pronounced at low Reynolds numbers. Although not discussed by McQuiston, this effect may have been caused by increased condensate retention at low flow rates. As the air-side Reynolds number increased, more condensate might be removed by the flow forces leading to a lower steady-state value of retained condensate.

Eckels and Rabas [7] studied plain-fin-and-tube heat exchangers with a fin spacing from approximately 2.0 to 3.2 mm. An enhanced sensible heat transfer was observed under wet conditions. An increase in pressure drop was observed under wet conditions; however, this effect diminished at high Reynolds numbers, with trends similar to those observed by McQuiston [5,6]. Using arguments similar to those of Bettanini, the results of Eckels and Rabas were explained as being caused by boundary-layer suction associated with condensation. However, Kandlikar [8] later challenged this explanation and convincingly showed that for typical operating conditions the augmentation due to this effect would be less than 0.5 percent of the dry case.

In a more recent paper, Wang et al. [9] report heat transfer and pressure drop for nine plain-fin-and-tube heat exchangers under wet conditions. They studied the effects of fin spacing, the number of tube rows, and inlet air condition. Their findings indicate that the sensible j factor and wet-surface f factor do not depend on inlet air humidity. Under wet conditions, the friction factor increased markedly over the dry-surface result. At low Reynolds numbers, the sensible j factor decreased, and a small enhancement was observed at high Reynolds numbers (greater than about 2000). Finally, with respect to wet, plain-fin heat exchanger performance, other recent experimental work has been reported [10], and work on calculating the efficiency of wet fins has been reported [11–14].

Other Fin Geometries. In addition to the plain-fin studies discussed above, several other configurations have been studied. The effect of condensation on the heat exchanger performance of complex fins remains unclear. Mirth and Ramadhyani [15,16] studied wavy-fin heat exchangers and developed design correlations for wet heat exchanger performance. They found the effects of condensation on sensible heat transfer performance to be inconclusive; in other words, comparing wet to dry heat transfer coefficients, the wet-surface values were sometimes higher and sometimes lower than the corresponding dry-surface values with no clear trends.

Hu et al. [17] used simulated droplets on the fin surface and naphthalene sublimation experiments to characterize effects of retained condensate on heat transfer on circular fins. They observed an increase in sensible heat transfer of up to 30 percent over the smooth-surface result. Small horseshoe vortices associated with the simulated droplets significantly influenced local sublimation rates. The basis for the size and location of the simulated droplets was not described in detail or justified. Recently, further work on wet circular fins has been reported by Jang et al. [18]; they found the sensible j factor to increase 20 percent and f to increase 15 percent over the dry-surface values.

Fu et al. [19] studied louver-fin-and-tube heat exchangers under wet conditions. The sensible heat transfer was reported to decrease as the inlet air relative humidity increased. The friction factor decreased as the inlet air relative humidity increased. The heat transfer coefficients decreased and the friction factor increased as the fin spacing decreased. At Reynolds numbers high enough to blow condensate off the heat exchanger—at air-side Reynolds numbers between 1000 and 3000 based on collar diameter—the heat transfer and pressure drop became less sensitive to fin spacing. Wang and Chang [20] recently reported similar results.

Hong [21] studied the effects of hydrophilic surface coatings on wavy, lanced, and louver fins. Under wet-surface conditions, the heat transfer coefficient decreased, and the coating had little effect. However, the coating significantly decreased the ratio of wet-to-dry-surface pressure drop. Unfortunately, contact-angle measurements indicated that after the first 1000 wet-dry cycles, the coated and uncoated surfaces had approximately the same wetting characteristics. The contact angle data reported by Hong were obtained using a sessile-drop method with a consistent procedure; unfortunately, advancing and receding contact angles were not reported[2].

Modeling Retained Condensate. With respect to modeling condensate retention in air-cooling applications, very little work has been reported. Loosely related work has been reported for modeling condensate film drainage during the condensation of a pure vapor without vapor shear (see [22–24]), but there is little hope of generalizing these models for the air-cooling applications of interest. Jacobi and Goldschmidt [25] considered an air-cooling application and presented a simple model of condensate retained as ''bridges'' between adjacent fins. The model was qualitatively successful in explaining the crossover between a degradation and enhancement in sensible heat transfer coefficient observed in their data and the data of others.

Closure and Objectives. In general, plain-fin sensible heat transfer is reduced under wet conditions at low Re but is increased at high Re. The wet-surface behavior of interrupted fins is different, and for louvered fins the j factor decreases under wet conditions over a wide Re range. These findings can be explained considering the effects of retained condensate. On plain fins at low Re, retained condensate bridges the inter-fin gap, occupies heat transfer area and fouls the surface. For a high Re or large fin spacing, retained condensate does not bridge the inter-fin gap but is retained as droplets that increase heat transfer. In the louver-fin geometry, condensate blocks the inter-louver gap, spoiling the flow-directing ability of the louvers and reducing heat transfer. Clearly, the mode, quantity, and location of retained condensate affect heat transfer and pressure drop. Understanding the nature of the retained condensate is key to understanding its impact. Unfortunately, little work has been undertaken to quantify the nature of retained condensate. Modeling efforts are scant and insufficient for the applications of interest. There are no reports in the open literature quantifying retained condensate in air-cooling applications.

The specific objectives of this study are to quantify the condensate retained on plain-fin-and-tube heat exchangers, to develop and validate a general condensate retention model, and to provide heat-transfer and pressure-drop performance data. These objectives are pursued through experiments that include dynamic and steady-state measurements of retained condensate. The retention experiments appear to be the first of their kind and provide new insights into the dynamics of water retention. The effects of Re, fin spacing, and surface condition are studied. Observed droplet size distributions and a balance between gravity, surface tension, and flow forces form the basis of the retention model. Air-side heat transfer and pressure drop data are interpreted using conventional methods and are compared to data from the literature.

[2]Note that advancing and receding contact angle data quantify the qualitative description of *wettability*. More *wettable* surfaces, or those with *increased wettability*, have smaller contact angles.

Methods

Experimental Apparatus and Instrumentation. The closed-loop wind tunnel used in these experiments is shown in Fig. 1. The airflow was conditioned with resistance heaters (3 kW) and a computer-controlled steam injection system providing up to about 0.2 kg/min. The air flow was drawn from the inlet plenum, through honeycomb flow straighteners, screens, and a 9:1 area contraction into the test section at rates up to about 9 m^3/min. The design of the wind tunnel is detailed elsewhere [26].

The test section shown in Fig. 2 allows flow and thermal measurements upstream and downstream of the heat exchanger and visual access to the specimen; furthermore, it provides the ability to measure the mass of condensate retained on the heat exchanger during an experiment. Using a constant-temperature anemometer, 21 measurements of air velocity were obtained on an equally spaced grid (measured to within ± 1 percent at each point) at the heat exchanger face. The air temperature at the heat exchanger inlet was measured using a six-junction, equally spaced thermocouple grid (± 0.3°C), and a twelve-junction grid was used at the heat exchanger outlet (± 0.5°C). Each thermocouple was calibrated against a NIST-traceable mercury-in-glass thermometer. The dewpoint upstream and downstream of the exchanger was measured using conventional chilled-mirror hygrometers, with air drawn from the tunnel, through a sampling tube, and returned to the tunnel. The uncertainty in dewpoint was estimated to be less than ± 0.2°C. Pressure drop across the heat exchanger was measured with static pressure taps connected to an electronic manometer (± 0.02 mm wc). It should be noted that the flow-area changed by about 5 percent at most at the exchanger entrance or exit, and entrance and exit losses are expected to be negligible.

As shown in Fig. 2, the test section consisted of an inner frame mounted to an outer shell using high-precision linear bearings. The inner frame included a second flow contraction (4:1), designed using techniques developed by Morel [27]. The inner frame supported the heat exchanger, and the assembly was suspended on load cells using a cable, pulley and counterweight system. Load cell precision was negligible in comparison to other uncertainties in dynamic condensate retention (discussed later). During an experiment, the test section was well insulated, but the insulation was removable to provide visual access. At the end of an experiment, the specimen could be quickly removed with a special tray to catch condensate. The tray was constructed so that it could be slid into place under the heat exchanger at the end of a test and withdrawn with the heat exchanger, catching any condensate that shook free during heat exchanger removal; thus, all retained condensate was captured for weighing. Retained condensate could be weighed using an electronic balance (± 0.1 g) at the conclusion of an experiment.

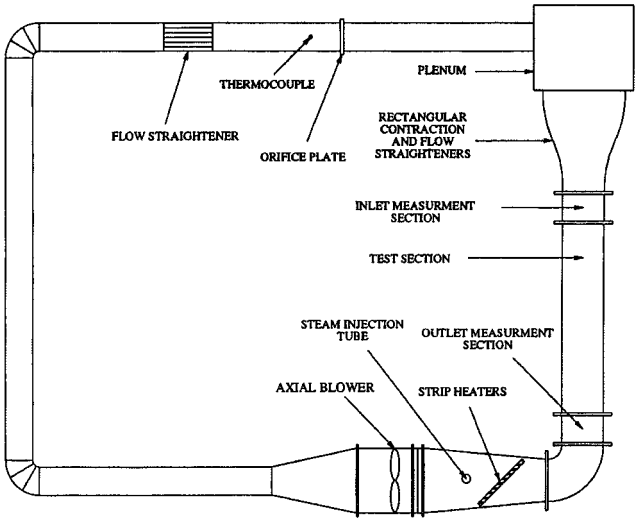

Fig. 1 Wind tunnel for condensate retention experiments. The flow is clockwise, moving from the axial blower to the flow straightener, orifice plate, inlet plenum, flow conditioning, and test section. Downstream of the test section, the temperature and humidity are set using the strip heaters and stream injection.

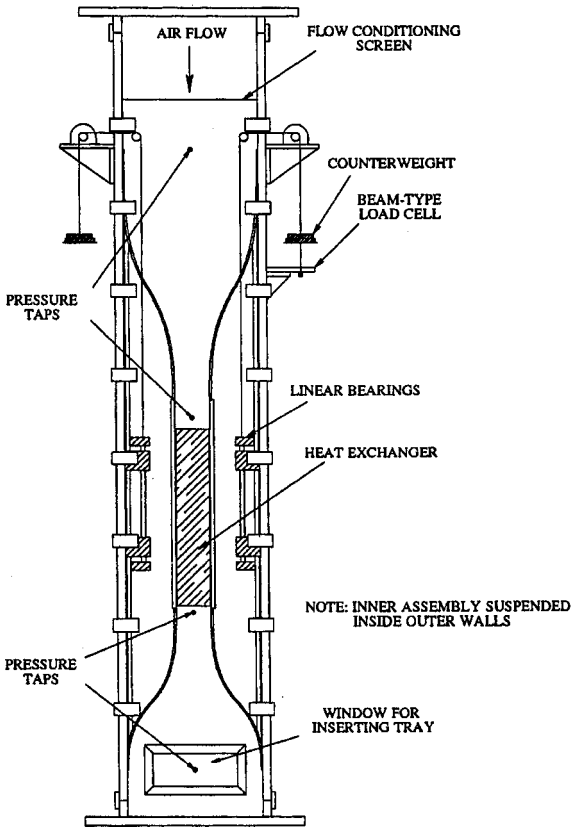

Fig. 2 Heat exchanger test section. This design allows the real-time (dynamic) measurement of retained condensate, along with conventional thermal hydraulic measurements. At the end of a test, the heat exchanger could be quickly withdrawn for steady-state retention data after a tray was inserted at the location shown in the schematic.

During an experiment, the heat exchanger was supplied with a single-phase mixture of ethylene glycol and water as a coolant. The coolant temperature was controlled by a chiller system and circulated at tube-side flow rates up to about 0.15 kg/s. Coolant-side temperatures were measured using type-T thermocouples (± 0.5°C). The thermocouples were installed in well-insulated sections of pipe, approximately 2 m upstream and downstream of the heat exchanger—this design provided good thermal mixing. The test heat exchanger was connected to the chiller supply and return pipes using flexible tubing that was insulated with about 10 mm of foam. An oscillating-piston flow meter was used to measure the coolant flow rate (± 0.5 percent). The coolant properties and chiller-loop design are discussed in detail elsewhere [26].

Conventional contact-angle goniometry was used to obtain measurements of the advancing and receding contact angles, θ_A and θ_R respectively. This approach provides a more complete description than a simple sessile-drop measurement. As noted by Chappuis [28], the contact angle obtained by placing a sessile drop on a surface will represent an equilibrium between θ_A and θ_R and may range over several dozen degrees for engineering surfaces. Therefore, we used methods discussed by Johnson and Dettre [29] to measure θ_A and θ_R. In particular, we fed and

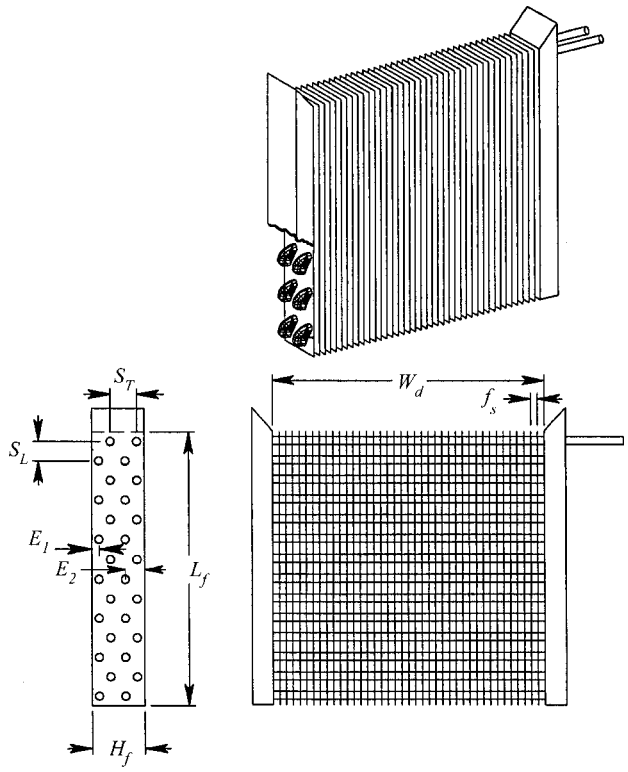

Fig. 3 Schematic showing the design of the test plain-fin-and-tube heat exchangers; dimensions are provided in Table 1

drained droplets while viewing them through the microscopic objective, and we viewed drops on tilted surfaces. For all the contact angle measurements reported, ultrapure, milliQ water was used.

Experimental Procedure, Scope, and Data Interpretation A geometric description of the heat exchangers is provided in Fig. 3, with dimensional information provided in Table 1. Each heat exchanger was constructed using collared fins and mechanically expanded tubes to provide intimate thermal contact and eliminate fin-to-tube contact resistance. The plain-fin-and-tube heat exchangers for which data are now presented were identical, except that one had $f_s = 3.18$ mm, and the other had $f_s = 6.35$ mm. Heat

Table 1 Heat exchanger dimensions

No. tube rows	14	14
W_d (mm)	264.0	264.0
H_f (mm)	50.8	50.8
L_f (mm)	269.0	269.0
E_1 (mm)	7.15	7.15
E_2 (mm)	18.25	18.25
f_s (mm)	6.35	3.18
S_t (mm)	25.4	25.4
S_l (mm)	19.25	19.25
δ (mm)	0.17	0.17
D (mm)	7.94	7.94

transfer, pressure drop, and dynamic retention data were recorded during an experiment. The final (steady-state) mass of retained condensate was measured by removing the heat exchanger from the test section at the end of an experiment, placing it on the balance, weighing it, drying it, and weighing it again. During some experiments, the foam on the return bends was removed to allow visual access to the fins (see Fig. 3). The experimental program spanned air-side face velocities from about 1 to 10 m/s, and inlet coolant temperatures ranged from -1 to 12°C. The inlet air temperature was held between about 30 and 34°C, and the inlet dewpoint was held at approximately 24°C for wet-surface experiments. An experiment was initiated by bringing the airflow to the desired velocity, temperature, and dewpoint, then suddenly starting the coolant flow. At steady state, all conditions remained constant within their experimental uncertainty. However, for a brief period at the beginning of a transient test (a few minutes), the inlet dewpoint sometimes deviated from its set point by as much as 8°C, and the inlet dry-bulb temperature varied by as much as 1°C from its set point. After this short period, the dewpoint and dry-bulb temperatures were maintained within the experimental uncertainty throughout the rest of the test (typically more than one hour).

The overall experimental program from which this paper is drawn [26] included nine plain-fin-and-tube heat exchangers. Unfortunately, only limited data are available for the other seven heat exchangers. Namely, steady-state retention data at a few operating conditions, and air-side pressure drop were recorded for the other specimens. The experimental and data reduction are somewhat more complicated for these other test articles. Therefore, only data for two heat exchangers over a wide range of conditions will be presented.

Experiments designated as ''dry'' were conducted by setting the inlet coolant temperature above the dewpoint to avoid condensation. The experimental conditions for the ''wet'' runs were determined so that the entire heat-transfer surface was below the dewpoint. That is, the calculated fin temperatures from the sector method were everywhere below the local, mixing-cup dew-point temperature, determined by accounting for upstream condensation for the measured experimental conditions (see [26]). Because the apparatus allowed visual inspection of the heat exchanger during testing, we were able to confirm that the entire surface was fully wet (i.e., showed condensation in some mode) during the wet-surface experiments. This approach avoided wet-dry partitioning in the data reduction. Furthermore, visual inspection during experiments confirmed the expectation that there was no condensation on the adiabatic wind tunnel walls.

When dynamic condensate retention data were obtained, the average load-cell output and other experimental conditions were recorded at 45 second intervals throughout the experiment. Measurements of the unsteady differential pressure across the heat exchanger and frame assembly were recorded, and these data were used to subtract the drag-force contribution from the load-cell data. In this way, a transient measurement of retained condensate mass was deduced—the time dependent mass of water on the air-side surface. It should be noted that the force applied to the heat exchanger by the flexible tubes during an experiment was found to be negligible in dry runs (i.e., conducting an experiment above the dew point would result in no measured effect from the flexible tubes when tube-side flow rates changed). A conventional error-propagation analysis was used to estimate the uncertainty in transient retention data. Due mainly to pressure-drop uncertainty, the estimated errors in dynamic measurements of condensate mass were as high as ± 15 percent of the retained mass. At the end of an experiment, the weight measurement confirmed the load cell data to within this uncertainty. A detailed description of this procedure and the uncertainty analysis is provided elsewhere [26].

The measured temperature and flow-rate were used to determine the steady-state heat transfer coefficient in a method described in detail by Korte and Jacobi [26]. In a fashion similar to

Mirth and Ramadhyani [15], the heat exchanger was discretized on a tube-by-tube basis. However, in the current work the area partitioning between tubes was established using iteratively calculated adiabats in the fin. The enthalpy potential method for simultaneous heat and mass transfer [30,31] was adopted for interpreting the total and sensible heat transfer rates. The dry and wet-surface fin efficiencies were determined using the sector method, with thirty-two sectors per tube. This approach for calculating fin efficiency was compared to the ARI method [31] and found to differ by less than 5 percent for all the conditions now reported; however, we believe the sector method is more accurate than the ''equivalent circular area'' recommended for plain fins in the ARI standard. The coolant-side transfer coefficient was calculated using Gnielinski's [32] correlation, which is valid for the coolant-side Reynolds numbers of this study. Conduction resistance through the tube wall was calculated assuming steady, one-dimensional conduction, and the fin-tube contact resistance was neglected because collared fins were used. With the coolant-side and conduction resistance known, the heat transfer rate and enthalpy driving potential were used in an iterative approach to find the air-side convection coefficient.

Wet surface partitioning, that is the determination of which portions of the fin were wet and which were dry, was conducted by comparing the local fin temperatures to the local dew point (the dew point changes as the air flow passes through the heat exchanger). However, for all the data now presented, the heat exchanger was either completely dry or completely wet, implying that under wet conditions the fin temperature at the exit face of the heat exchanger was below the exiting dew point.

The air-to-coolant energy balance was directly affected by the coolant-side temperature uncertainty, and for a few data at high coolant flow rates the energy error exceeded 10 percent; nevertheless, all energy balances were within the estimated uncertainties. Because of the high coolant energy uncertainty at high flow rates, each data set was analyzed prior to data reduction. If the coolant-side uncertainty exceeded the air-side uncertainty, then air-side data were used in the data reduction. Otherwise, the air-side and coolant-side heat transfer rates were averaged for purposes of data reduction.

Once the convection coefficient was determined, the following standard relations were used to represent the data (Kays and London [33]):

$$j = \frac{\mathrm{Nu}_D}{\mathrm{Re}_D \mathrm{Pr}^{1/3}}, \tag{1}$$

and

$$f = \frac{2\Delta p \rho_a}{G_{\max}^2}\left(\frac{A_{\min}}{A_T}\right) - (1+\sigma^2)\left(\frac{\rho_{a,1}}{\rho_{a,2}} - 1\right)\left(\frac{A_{\min}}{A_T}\right)\left(\frac{\rho_a}{\rho_{a,1}}\right), \tag{2}$$

with

$$\mathrm{Re}_D = \frac{G_{\max} D}{\mu_a}, \quad \mathrm{Nu} = \frac{hD}{k_a} \quad \text{and} \quad \rho_a = \frac{\rho_{a,1} + \rho_{a,2}}{2}. \tag{3}$$

Modeling Condensate Retention. In order to develop a model of the condensate mass retained on the heat exchanger surface, we begin by considering only the droplets retained on the fins—later we will discuss how this approach could be modified to include inter-fin bridges and other condensate elements. The current approach is based on an assumption that the fins are too far apart for bridging to occur. Under this assumption,

$$M = \rho_w \int_{A_T} \int_d n(\xi) \forall(\xi) d\xi dA. \tag{4}$$

In Eq. (4), M is the total mass of retained condensate on the heat exchanger, ρ_w is the mass density of water, $\forall(\xi)$ is the volume of a droplet with diameter ξ, and $n(\xi)$ is the number of droplets with diameter ξ per unit area and per droplet diameter. The integration

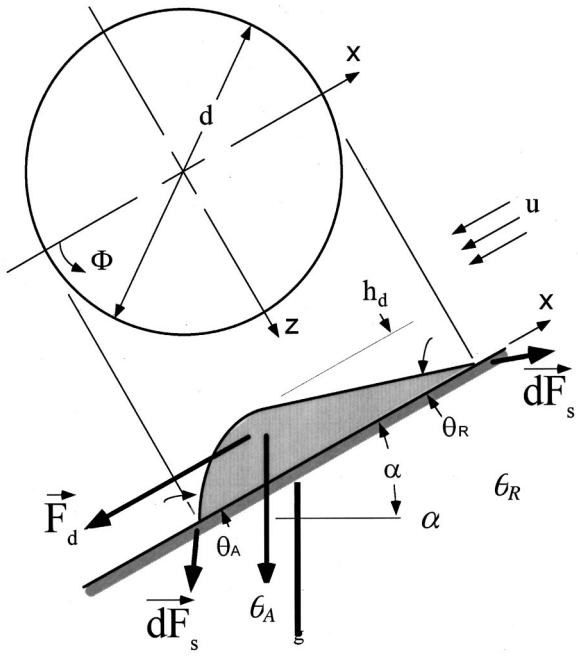

Fig. 4 A schematic of a droplet on an inclined surface; the gravitational force, F_g, and drag force due to the air flow, F_d, are acting to remove the droplet, and the net surface tension force, F_s, acts to retain it

is performed for all drop sizes over the entire surface area of the heat exchanger (A_T). The model is now pursued by developing expressions for $n(\xi)$ and $\forall(\xi)$, and in the current version of the model we will not distinguish between the tube and fin in developing these functions.

Consider the droplet shown in Fig. 4, where gravitational, flow, and surface tension forces are indicated, along with a coordinate system. Approximating the droplet as a truncated sphere with an average contact angle given by $\overline{\theta} = (\theta_A + \theta_R)/2$, its volume can be found using a volume integral and expressed as follows (see [26]):

$$\forall(d) = \frac{\pi d^3}{24}\left(\frac{2 - 3\cos\overline{\theta} + \cos^3\overline{\theta}}{\sin^3\overline{\theta}}\right) \tag{5}$$

Graham [34] conducted detailed photographic studies of the condensation of water on copper surfaces. In order to account for differing physical mechanisms important at small and large scales, he divided the distribution into two regimes and modeled them with power-law fits to the data. We adopted the same approach for our fins, using

$$\Delta N(d) = B_1 d^{-1.73} \quad \text{for } 10\ \mu\mathrm{m} \leq d \leq 0.2 d_{\max}, \tag{6a}$$

and

$$\Delta N(d) = B_2 d^{-2.8} \quad \text{for } 0.2 d_{\max} < d \leq d_{\max}. \tag{6b}$$

In Eq. (6), $\Delta N(d)$ is the number of droplets of diameter $d \pm 0.2d$ (μm) per cm^2, and $d_{\max}$ is the largest droplet diameter on the surface. We used the exponents determined by Graham but regard B_1 and B_2 as constants to be determined for our surfaces. Their values were calculated using digital analysis of the photograph shown in Fig. 5; this image was recorded for a typical specimen under typical conditions. Based on Graham's microscopy, we assumed 82 percent of the area was occupied by droplets larger than 10 μm. On the basis of our digital image analysis, droplets larger than $0.2 d_{\max}$ occupied 36 percent of the area. Using these area fractions, the image analysis, and Eq. (6), the con-

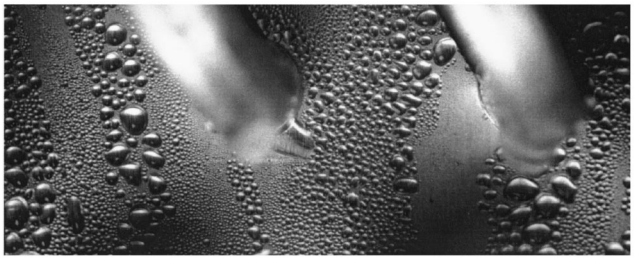

Fig. 5 This photograph shows a typical droplet distribution on the plain-fin heat exchanger. This image was recorded at steady state on a new surface, near the top of the exchanger (between the first and second tube rows). This image was used to quantify the area coverage by droplets larger than 0.2 d_{max}, which in turn was used to find the constants B_1 and B_2, in Eq. (5).

stants were found to be[3] $B_1=2.042(10^6)\ \mu m^{1.73}/cm^2$ and $B_2=4.467(10^9)\ \mu m^{2.8}/cm^2$. Equation (6) can be cast into the form required for Eq. (4) by noting

$$n(d)=\left.\frac{\Delta N}{\Delta d}\right|_d, \tag{7}$$

and, with $\Delta d=0.4d$, Eq. (6) becomes

$$n(d)=5.104(10^6)d^{-2.73} \quad \text{for } 10\ \mu m\leqslant d\leqslant 0.2d_{max}, \tag{8a}$$

and

$$n(d)=1.117(10^{10})d^{-3.8} \quad \text{for } 0.2d_{max}<d\leqslant d_{max}. \tag{8b}$$

Closure of the model has now been reduced to finding d_{max}. One approach would be to determine the largest droplet size on a surface from digital image analysis. Unfortunately, while image analysis might describe the distribution of droplets smaller than d_{max} without much loss of generality, using image analysis to determine d_{max} would severely restrict generality: the maximum droplet size, d_{max}, must certainly depend on θ_A, θ_R and the flow conditions. In order to account for these effects in a more general fashion, we calculate the maximum droplet size by performing a force balance on the droplet shown in Fig. 4; thus,

$$F_{g,x}+F_{d,x}+F_{s,x}=0. \tag{9}$$

The x-component of the gravitational force is simply

$$F_{g,x}=-\rho_w g\forall(d)\sin\alpha. \tag{10}$$

In this version of the model, we considered only vertical surfaces (α=90 deg). Because the surface integration of Eq. (4) included the area of the tubes, the model treats condensate on the tubes as though it were on the fins (no distinction in surface orientation is considered). We have developed the model in a general sense, with α as a variable, to allow for refinements such as separately accounting for fin and tube areas, and for modeling inclined heat exchangers; however, in this paper we have not implemented such refinements. For heat exchangers such as these, where the tube area is small in comparison to the fin area, the first-order approach of treating tube surface area like fin area is justified.

The flow forces are calculated using the results of Al-Hayes and Winterton [35] for drag on bubbles on a submerged surface. During their experiments the contact angles varied from 22 to 90 deg, and they found $C_d=1.22$ for $Re_d=\rho_a u d/\mu_a$ from 20 to 400. For our experimental conditions with droplets, $50<Re_d<970$, but we used $C_d=1.22$ for all cases—this extrapolation is justifiable since the flow regime is not expected to change over this Re_d range. Should new experiments or computations provide updated drag coefficients for droplets on surfaces, that information could be easily adopted in an improved model. Following Al-Hayes and Winterton, the drag force on the droplet was then calculated using

$$F_{d,x}=-C_d\rho_a u^2 A_p/2, \tag{11a}$$

where A_p is the projected area, u is the local boundary-layer velocity at the droplet half-height, $h_d/2$, and

$$A_p=d^2(\bar{\theta}-\cos\bar{\theta}\sin\bar{\theta})/(4\sin^2\bar{\theta}) \tag{11b}$$

and

$$h_d=d(1-\cos\bar{\theta})/(2\sin\bar{\theta}). \tag{11c}$$

In a fashion consistent with Al-Hayes and Winterton, u was calculated using a laminar (Blasius) boundary-layer profile evaluated at a normal distance of $h_d/2$ and a streamwise location midway through the heat exchanger ($L_f/2$). In undertaking this calculation, flow development effects within the exchanger and edge effects due to the wind tunnel walls were neglected. The free stream velocity was simply taken as equal to the maximum velocity in the heat exchanger (velocity at A_{min}), and the boundary layer profile was taken as that of a flat-plate flow.

Finally, the surface tension force was determined by assuming a linear variation[4] in θ, from θ_A to θ_R, and integrating around the contact line

$$F_{s,x}=\gamma d\int_0^{\pi}\cos(\pi-\Phi)\cos(\theta_A+(\theta_R-\theta_A)\Phi/\pi)d\Phi. \tag{12a}$$

The result is [26]

$$F_{s,x}=\frac{\gamma\pi d}{2}\left(\frac{\sin\theta_R-\sin(\theta_A-\pi)}{\theta_R-\theta_A+\pi}+\frac{\sin\theta_R-\sin(\theta_A+\pi)}{\theta_R-\theta_A-\pi}\right). \tag{12b}$$

Using Eqs. (10)–(12) with (5), the force balance of Eq. (9) allows estimation of the maximum droplet size retained on the surface with the following equation:

$$\Xi_2 d_{max}^2+\Xi_1 u^2 d_{max}+\Xi_0=0 \tag{13a}$$

where

$$\Xi_2=-\frac{\rho_w g\pi\sin\alpha}{24}\left(\frac{2-3\cos\bar{\theta}+\cos^3\bar{\theta}}{\sin^3\bar{\theta}}\right). \tag{13b}$$

$$\Xi_1=-\frac{\rho_a C_d(\bar{\theta}-\cos\bar{\theta}\sin\bar{\theta})}{8\sin^2\bar{\theta}}, \tag{13c}$$

and

$$\Xi_0=\frac{\gamma\pi}{2}\left(\frac{\sin\theta_R-\sin(\theta_A-\pi)}{\theta_R-\theta_A+\pi}+\frac{\sin\theta_R-\sin(\theta_A+\pi)}{\theta_R-\theta_A-\pi}\right). \tag{13d}$$

In Eq. (13), Ξ_0, Ξ_1, and Ξ_2 are constants for a particular surface. The velocity, u, is evaluated from the Blasius profile as discussed above; it is a function of d_{max}. Equation (13) was solved using a Newton-Raphson method. It is useful to note that the case with no air flow can be solved in closed form. The solution to this degenerate case was compared to the literature and found to agree closely with estimates of the maximum size of a two-dimensional droplet; i.e., a ''speed bump'' (see [26]).

The model is thus complete and can be implemented with the above analysis. First, using measured contact-angle data and the prescribed operating conditions, d_{max} is calculated with Eq. (13). The droplet drag coefficient is set to $C_d=1.22$, and the velocity u is found by evaluating a boundary-layer velocity profile half way

[3]These values are of the same order as found by Graham and others for similar systems, as summarized by Graham [34].

[4]This linearization serves as an approximation in this first-order model. Refinements to the linear variation of θ can be implemented as new data become available; see Brown et al. [36] and Milinazzo and Shinbrot [37] for related work.

through the heat exchanger at a distance $h_d/2$ from the fin (given in Eq. 11). Using the calculated value for $d_{\max}$, the droplet distribution functions are established: we propose Eq. (8) for untreated aluminum fin stock, but new distributions could be obtained from photography of any surface. Finally, with the droplet volume function as given in Eq. (5), the total mass of retained condensate is calculated using

$$M = \rho_w A_T \int_{\xi=10\ \mu\text{m}}^{0.2d_{\max}} n(\xi)\forall(\xi)d\xi + \rho_w A_T \int_{\xi=0.2d_{\max}}^{d_{\max}} n(\xi)\forall(\xi)d\xi. \tag{14}$$

Results and Discussion

Conventional j and f data will be presented first, followed by dynamic and steady-state condensate retention results. Finally, a comparison will be drawn between the measured retention data and predictions from the new model. Through an error-propagation analysis, Korte and Jacobi [26] found the 2-σ uncertainty in interpreted data to be less than 8 percent for Re_D. It was 21.5 percent in f at low Re_D and 6 percent in f at high Re_D. The 2-σ uncertainty in j was 10 percent at low Re_D and 17 percent at high Re_D. The 2-σ uncertainty in retention mass, M, was estimated to be 15 percent under dynamic conditions and about 3 percent at steady state. The uncertainty in measuring M dynamically was due to difficulties in subtracting flow drag from weight.

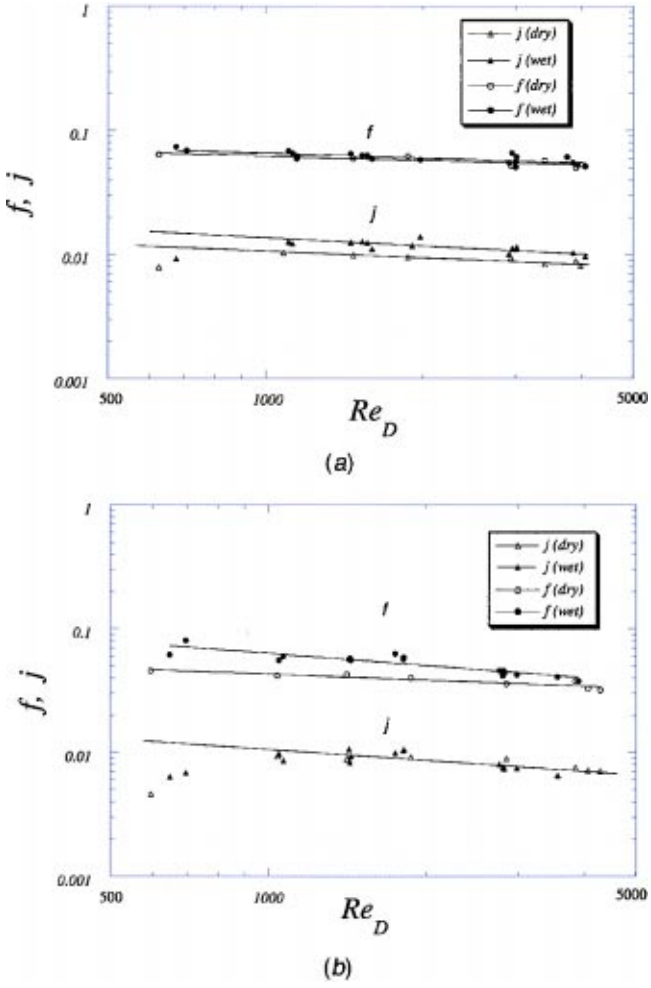

Fig. 6 Conventional sensible Colburn j factor and Darcy f factor as a function of Reynolds number based on collar diameter, Re_D, for the two test specimens under dry and wet-surface conditions, with (*a*) $f_s = 6.35$ mm, and (*b*) $f_s = 3.18$ mm

At steady state (using the balance), the uncertainty was due to small fluctuations associated with the discrete nature of shedding.

Air-Side Thermal Behavior. Air-side heat transfer and pressure-drop results for wet and dry conditions, in the form of sensible j and f versus Re_D, are presented in Fig. 6. The figure suggests that j increases by roughly 20 percent under wet-surface conditions for $f_s = 6.35$ mm but not for $f_s = 3.18$ mm. These results are similar to those of McQuiston [5] who observed an increased j when the fin pitch was large ($f_s > 3.18$ mm) and a decrease if the fin pitch was small. Jacobi and Goldschmidt [25] suggested McQuiston's observation was caused by increased retention at small f_s, and the ensuing increased ''fouling'' effect. However, new retention data presented later in this section will prove that M/A_T for $f_s = 3.18$ mm is lower than for $f_s = 6.35$ mm. Therefore, the simple ''fouling'' explanation is untenable. Further complicating the situation, the f factor for $f_s = 6.35$ mm is almost unaffected by condensation, but f for $f_s = 3.18$ mm is higher under wet conditions. Although the trends in the results are clear, it should be noted that the differences between dry and wet j and f are almost within the experimental uncertainty.

Wang et al. [9] proposed correlations for plain-fin wet heat exchangers with up to 6 rows. For the current 14-row exchangers, their Nu predictions are 300 percent to 500 percent too high, and their f predictions are about 200 percent too high (for $f_s = 3.18$ mm, the closest to their geometry). The comparison is made only for completeness, with the recognition that our geometry differs from theirs, and it is not surprising that their correlations do not predict our data. The discrepancy in j is clearly due to tube-row effects. If one uses their 6-row predictions, the Nu-predictions are 10 percent to 20 percent higher than the current data (almost within the uncertainty), but the f factor is still over predicted by about 200 percent. Unfortunately, we found no correlation in the literature for the current geometry with 14 tube rows and, thus, we cannot provide a direct comparison of our limited heat transfer and pressure-drop data to existing results.

Dynamic Condensate Retention Data. The heat exchangers were initially dry, and during the experiments condensate accumulated on the air-side surface, as shown in Figs. 7 and 8. The mass of retained condensate, M, asymptotically approached a maximum for these heat exchangers. Early in the test, condensate was deposited and retained on the surface, but as the droplets grew through condensation and coalescence, gravitational and flow forces eventually overcame surface-tension retaining forces. At this point, ''shedding'' was initiated and condensate began to drain from the heat exchanger. Finally, a steady condition was achieved when the rate of deposition was balanced by shedding, without oscillations in retained condensate. The importance of these results resides in the general trends and characteristics of transient retention. The time required to achieve steady state, τ_{ss}, is heat-transfer-rate dependent—it takes less time to reach τ_{ss} for a higher condensation flux because $d_{\max}$ can be established faster. Therefore, τ_{ss} must depend on temperature and relative humidity, and the results in Figs. 7 and 8 are only representative in that sense. The figures also suggest that as the velocity increased, τ_{ss} decreased. This behavior is manifested because an increase in air velocity causes a reduced $d_{\max}$, allowing the steady-state droplet-size distribution to be attained earlier. In view of the start-up excursion in dewpoint discussed earlier, data from the first 150 or so seconds were not used to draw conclusions. To our knowledge, these dynamic retention data represent the first of their kind presented in the literature.

Steady-State Condensate Retention. The final value of M depends on the gravitational, flow, and surface-tension forces acting on elements (droplets) of condensate on the heat-transfer surface. These forces are not rate dependent unless the boundary-layer suction of condensation affects frictional forces on the droplets. Kandlikar's [8] analysis clearly shows the suction effect

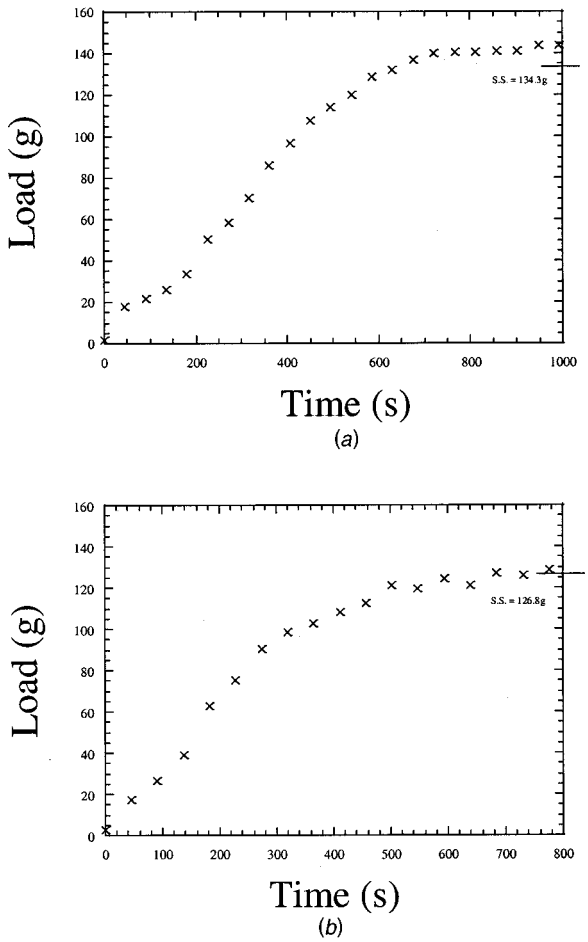

Fig. 7 The mass of retained condensate on the f_s=6.35 mm plain-fin-and-tube heat exchanger, as a function of time. These data were obtained for the approach conditions given in the text, at a maximum velocity of (*a*) V_{max}=2.2 m/s, and (*b*) V_{max} =3.9 m/s. The retained mass at the end of the test, as measured by withdrawing and weighing the heat exchanger, is noted by the tic on the right-hand border of the plot.

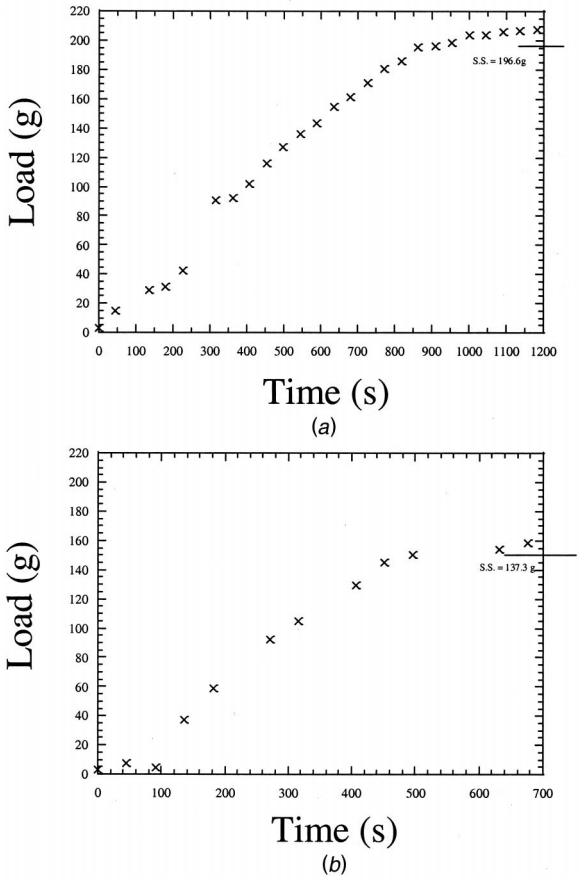

Fig. 8 The mass of retained condensate on the f_s=3.18 mm plain-fin-and-tube heat exchanger, as a function of time. These data were obtained for the approach conditions given in the text, at a maximum velocity of (*a*) V_{max}=2.1 m/s, and (*b*) V_{max} =5.6 m/s. The retained mass at the end of the test, as measured by withdrawing and weighing the heat exchanger, is noted by the tic on the right-hand border of the plot.

to be negligible under the current conditions. Therefore, we expect M at steady-state will not depend on temperature or relative humidity, except through their indirect effect on thermophysical properties (e.g., surface tension), or through modifications to the droplet-size distribution functions (such effects will be discussed later).

The steady-state condensate retention results depend on fin spacing, air flow rate, and surface wettability. Steady-state retention results are shown in Fig. 9. Interestingly, while the total retained mass of condensate is larger for the exchanger with smaller fin spacing, f_s, the retention per unit heat transfer area was smaller for a smaller f_s. This finding seems to contradict the idea that heat transfer is reduced through a simple fouling effect of the retained condensate at small f_s. Certainly, more condensate is retained when the fin spacing is small, but the retention per unit area is smaller as f_s decreases. Therefore, the physics of wet-exchanger thermal performance must be more complex than the simple ''fouling'' idea. It is clear that droplets enhance heat transfer through their modification to the surface and thus the flow [17]. We hypothesize that while droplets increase heat transfer, inter-fin condensate bridging has a deleterious impact on heat transfer and pressure drop. Large condensate bridges occupy heat transfer area and create relatively large wake regions where the heat transfer is low. The pressure drop associated with the formation of these large wakes is significantly higher than that associated with droplets. This explanation unifies the results presented in Figs. 6 and 9. When the fin spacing is small, condensate is more likely to bridge the inter-fin gap; therefore, condensate is more likely to adversely affect heat transfer at a small fin spacing, even if there is less condensate per unit area retained under those conditions.

As to the physical mechanism responsible for a decrease in condensate retained per unit of heat transfer area when the fin spacing decreases, we offer a conjectural explanation related to the condensate removal mechanisms. Earlier in this paper, we suggested a simplified view that condensate is retained by surface tension forces and removed by gravitational and flow forces for the current geometry. These mechanisms probably dominate the retention behavior when f_s is large; however, condensate can be also removed when it is swept from the surface by condensate running along the heat exchanger surface. When the fin spacing is decreased, condensate running along a fin might sweep a droplet from a neighboring fin. Thus, as the fin spacing decreases, complex inter-fin interactions between retained condensate might become important. We believe these inter-fin interactions are responsible for the finding that M/A_T decreased with fin spacing. We do not believe this finding will carry to arbitrarily small f_s.

The results shown in Fig. 9 clearly show that less condensate is retained as the air-side Reynolds number increases. This finding is intuitive, because the flow forces acting to remove condensate

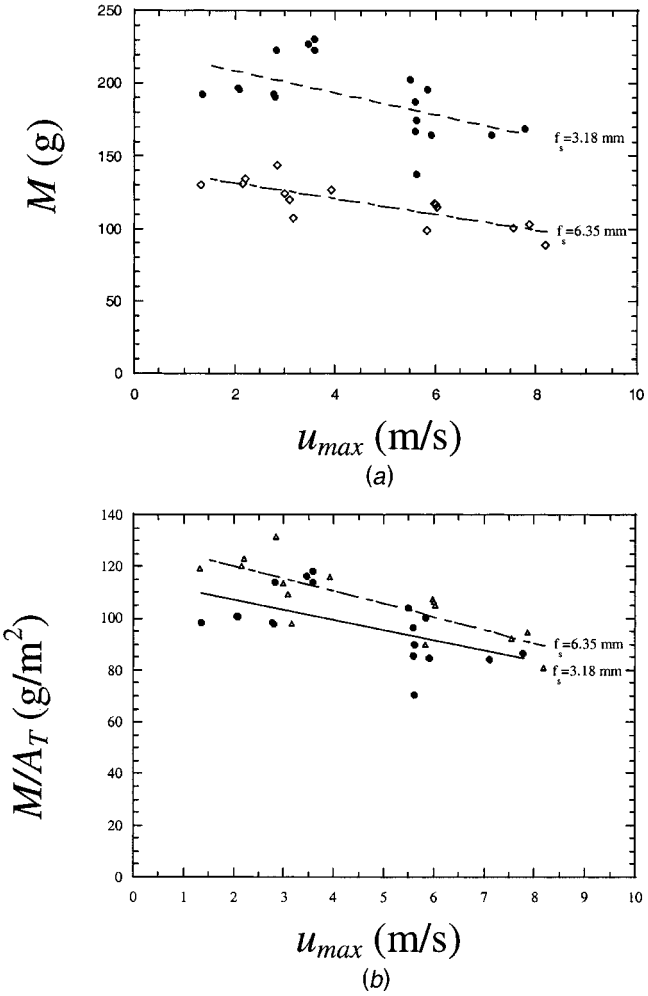

Fig. 9 The steady-state retention behavior as determined from a weight measurement at the end of an experiment as a function of the maximum velocity (*a*) total retained mass of condensate on the heat exchangers, and (*b*) retained mass per unit of heat-transfer surface area

increase with the square of the velocity. Thus, as the velocity increases, $d_{\max}$ decreases, leading to an overall decrease in M (and M/A_T) for a particular heat exchanger. Some of the limited data obtained for other heat exchangers [26] suggests this trend can change with geometry and surface condition.

The scatter in Fig. 9 is larger than the experimental uncertainty. The main contributor to this scatter is the unavoidable change in wettability that occurred during heat-exchanger exposure to the condensing environment. Early in the testing, contact angles on the aluminum fin stack were relatively high, as given in Table 2. These high contact angles were due to oil and other organic compounds on the metal. During the course of the experiments, some of these contaminants were removed and the contact angles were reduced. These changes in contact angle occurred over a period of about 100 hours of exposure in the wind tunnel, and the contact

Fig. 10 This photograph shows a typical droplet distribution on the plain-fin heat exchanger after more than 100 hours exposure to condensing condition. This image was recorded under the same conditions and at the same location as that shown in Fig. 5.

angles after exposure are also provided in Table 2. These findings are in close agreement with similar results on contact angle changes reported by Hong [21]. The nature of the retained condensate was altered by these changes, and a photograph of the wet fin after more than 100 hours of exposure is given in Fig. 10—a comparison to Fig. 5 makes the changes clear.

Comparison to the Model. For known contact angles, air velocity, and surface tension, Eq. (13) was solved for the maximum droplet size. The result was used with the droplet distributions presented in Eq. (8), and the droplet volume presented in Eq. (5), to complete the integration of Eq. (14). The resulting predictions of retained condensate are compared to the measured data in Fig. 11 for $f_s = 6.35$ mm. In the figure, predictions are provided for $\theta = 73$ deg and for $\theta = 58$ deg; these contact angles represent the measured conditions at the beginning and the end of the testing program (as presented in Table 2). The figure shows good agreement between the model and the experimental results. At low air velocities, the prediction is within the scatter of the data, but at the highest velocity the prediction is about 20 percent higher than the measurement. The model not only predicts the correct magnitude of the retained condensate, it predicts the correct trend with air velocity, and the scatter in the data is roughly equivalent to the predicted changes with wettability. It should be emphasized that although changes in surface condition are likely to affect droplet-size frequencies of Eq. (8), the distribution functions were never changed. Once, the constants B_1 and B_2 were determined, they were not adjusted. The changes in predicted retention are due to changes in contact angle, and its effect on droplet volume and $d_{\max}$. Although this approach certainly does not capture the complex physics of the droplet size distributions, it appears to provide reasonable predictions.

The model is not successful in predicting retention data for $f_s = 3.18$ mm, where inter-fin effects may become important—the model neglects such interactions. Although the current model suffers from a limitation in this respect, its formulation provides guidance as to the severity of this limitation. Namely, the neglect of inter-fin interactions implies that $f_s > 2h_d$. The height of the droplet can be estimated by calculating the $d_{\max}$ as outlined above, and an explicit evaluation of the applicability of the model is possible. For the current situation with $f_s = 3.18$ mm, $f_s/(2h_d) \sim 1$, and the model is expected to break down. Although a smaller f_s suggests that flow development effects may be playing a role,

Table 2 Contact angle data for test fins

surface	θ_A (deg)	$\sigma_{\theta A}$ (deg)	θ_R (deg)	$\sigma_{\theta R}$ (deg)
fin stock, new	92.3	1.3	53.0	5.0
fin stock, after 100+ exposure	81.9	10.8	35.1	7.0

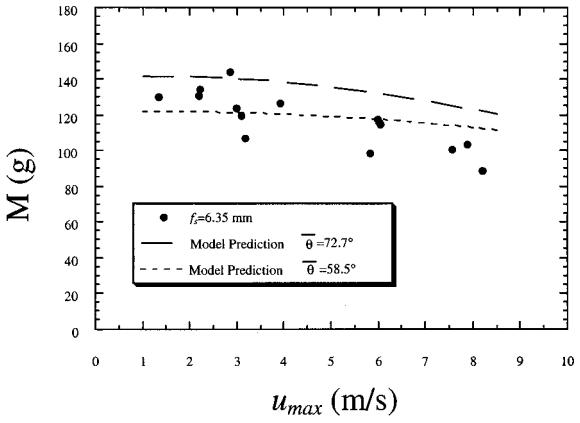

Fig. 11 Measured and predicted condensate retention on the plain-fin-and-tube heat exchanger with f_s=6.35 mm. Predictions for two mean contact angles are given. The $\theta_M=(\theta_1+\theta_R)/2=72.7$ deg case represents the "new" surface condition for this heat exchangers, and the $\theta_M=58.5$ deg case represents the surface condition after more than 100 hours exposure to condensing conditions.

we believe the growth of boundary layers on the fins and wind tunnel walls (edge effects) has a small impact on the model results: the entering velocity profile is nearly flat, and the velocity used to calculate flow drag on a droplet is determined by using a fictitious Blasius profile at the middle of the flow passage. This approach—consistent with [35]—represents a compromise, because near the entrance the boundary layer is thinner and the droplets see a higher velocity; whereas, the exiting profile is more parabolic-like and the droplets see a lower velocity. For the purpose of this first-order model, our approach is justified by the apparent insensitivity of the results to velocity (Fig. 9). However, because the data appear to be more sensitive to velocity than the model, we believe refinements to the drag model may help improve overall veracity of its retention predictions.

This model relies on a number of simplifications in calculating droplet size and distribution. We approximated droplets as spherical caps (with a fixed contact angle) to calculate their volume; however, we assumed a linear variation of contact angle on a circular contact line to calculate surface tension retaining force. Although it may seem somewhat inconsistent, this approach is justified to avoid complete calculations of each droplet shape; such calculations are very complex and the added computational burden would detract from the utility of this model (see recent work [38]). In view of the calculations by Brown et al. [36] and Milinazzo and Shinbrot [37], the assumed linear contact angle variation is reasonable as a first-order approximation. In addition to the geometrical simplifications of droplet shape, the version of the model presented here does not account for liquid bridges on the surface at all—all the water is assumed to be in the form of droplets. The geometrical simplifications and droplet distribution functions used in this model ultimately result in a model that predicts the magnitude and trends of retention data within engineering accuracy, with no artificial empirical adjustment. While those predictions represent a success, the ultimate extension and refinement of the model may require careful reconsideration of the geometrical and size-distribution simplifications used in this first-order model.

Summary and Conclusions

The condensate retained on plain-fin-and-tube heat exchangers for air-cooling applications was studied, and a general condensate retention model was developed and compared to experimental results. The retention experiments appear to be the first of their kind and provide insights into the dynamics of retention. The effects of Re, fin spacing, and surface condition have been reported, and conventional methods have been used to provide air-side heat transfer and pressure drop data.

The new model was successful in predicting the magnitude and trends of condensate retention for plain-fin-and-tube heat exchangers with fin spacing much larger than the height of retained droplets. The main shortcoming of the current model is in this restriction, and its use of droplet size distribution data from one location on a fin. Such an approach does not recognize the effects of condensate sweeping on large fins and the potential effect of heat flux on droplet-size distributions. The model also neglects complex flow development and edge effects in the heat exchanger. Nevertheless, the modeling approach has clear promise. Future research into this modeling approach should address these problems. Furthermore, extensions of this plain-fin model to the complex, interrupted-fin geometry often used in air-cooling is desired, and future work should address that geometrical complexity. Korte and Jacobi [26] have proposed modifications to account for inter-fin coupling, and work in this direction is continuing. Yin and Jacobi [39] and Kim and Jacobi [40] have proposed modifications to include surface-interruption effects, which may allow modeling of slit-fin or louvered-fin heat exchangers.

Another important extension to this approach is to consider heat exchangers with a horizontal airflow, rather than the down-flow configuration studied in this work. A vertical airflow is often used in refrigeration systems, and this model can be applied to defrost scenarios in such applications. However, in air-conditioning systems it is more common to use a horizontal air-flow configuration, and adapting the model to that situation is straightforward. We have experiments underway to measure retention with a horizontal airflow.

In this research, a clear link between retained condensate and thermal performance is established, and—for the first time—an attempt to establish a link between the quantity and nature of the retained condensate to its thermal effect has been provided with a model of retention. Ultimately, wet-fin thermal performance modeling should recognize and account for the coupling between condensate retention and thermal behavior. An approach that uses a "wet-surface multiplier" on conventional j and f factors as a function of retained condensate, surface condition and geometry, would provide a valuable engineering tool for treating this complex problem.

Nomenclature

A = area
B_1, B_2 = empirically determined constants in droplet-size distribution (see Eq. 6)
C_d = drag coefficient for droplet on a surface (see Eq. 11)
D = outside tube (collar) diameter
d = diameter of water droplet (see Fig. 4)
E_1, E_2 = tube position relative to fin edge (see Fig. 3)
F = force on a liquid droplet (see Eq. 9)
f = Fanning friction factor (see Eq. 2)
f_s = fin spacing (see Fig. 3)
$G_{\max}$ = mass velocity, $\rho_a u_{\max}$
H_f = fin height (see Fig. 3)
g = gravitational acceleration
h = heat transfer coefficient
h_d = projected height of droplet (see Fig. 4)
j = Colburn j factor, $\mathrm{Nu}/(\mathrm{Re}\,\mathrm{Pr}^{1/3})$
k = thermal conductivity
L_f = fin length (see Fig. 3)
M = mass of retained condensate (liquid water) on the heat-transfer surface
Nu_D = Nusselt number based on tube diameter, hD/k_a
n = number density of droplets (number per unit area, per diameter; see Eq. 8)
Pr = Prandtl number

Re_D = Reynolds number based on tube diameter, $G_{\max}D/\mu_a$
S_l = longitudinal tube spacing (see Fig. 3)
S_t = transverse tube spacing (see Fig. 3)
u = air velocity
$u_{\max}$ = air velocity measured at the minimum free-flow area in heat exchanger
$\forall(d)$ = volume of liquid in truncated-spherical droplet (see Eq. 5)
W_d = width of heat exchanger, see Fig. 3

Greek Symbols

α = inclination angle of surface with respect to horizontal
δ = fin thickness
Δp = air-side pressure drop across heat exchanger
$\Delta N(d)$ = number of droplets of size $d \pm 0.2d$ in μm, per unit area in cm^2 (see Eq. 6)
θ = contact angle at fin-droplet confluence
Φ = azimuth, droplet on surface (see Fig. 4)
γ = surface tension
ρ = mass density
σ = free-to-frontal area ratio, $A_{\min}/A_{fr}$
Ξ_0, Ξ_1, Ξ_2 = constants in maximum-drop diameter model (see Eq. 13)

Subscripts

1, 2 = at the inlet or exit face of the heat exchanger, respectively
A = advancing
a = of the air
d = drag due to fluid flow or denoting a property of the droplet
fr = frontal (at inlet cross-section of heat exchanger)
g = gravitational
max = maximum
p = projected into a plane perpendicular to the flow
R = receding
s = surface tension
T = total for heat transfer
w = of water (as condensate)
x = in the x-direction, per Fig. 4

an overbar indicates an averaged quantity

References

[1] Bettanini, E., 1970, "Simultaneous Heat and Mass Transfer on a Vertical Surface," International Institute of Refrigeration Bulletin, **70**, pp. 309–317.
[2] Guillory, J. L., and McQuiston, F. C., 1973, "An Experimental Investigation of Air Dehumidification in a Parallel Plate Heat Exchanger," ASHRAE Trans., **79**, pp. 146–151.
[3] McQuiston, F. C., 1976, "Heat, Mass, and Momentum Transfer in a Parallel Plate Dehumidifying Exchanger," ASHRAE Trans., **84**, pp. 266–293.
[4] Tree, D., and Helmer, W., 1976, "Flow in a Parallel Plate Heat Exchanger," ASHRAE Trans., **82**, pp. 289–299.
[5] McQuiston, F. C., 1978, "Heat, Mass, and Momentum Transfer Data for Five Plate-Fin-Tube Heat Transfer Surfaces," ASHRAE Trans., **84**, pp. 266–293.
[6] McQuiston, F. C., 1978, "Correlation of Heat, Mass, and Momentum Transport Coefficients for Plate-Fin-Tube Heat Transfer Surfaces with Staggered Tubes," ASHRAE Trans., **84**, pp. 294–308.
[7] Eckels, P. W., and Rabas, T. J., 1987, "Dehumidification: On the Correlation of Wet and Dry Transport Processes in Plate Finned-Tube Heat Exchangers," ASME J. Heat Transfer, **109**, pp. 575–582.
[8] Kandlikar, S. G., 1990, "Thermal Design Theory for Compact Evaporators," in *Compact Heat Exchangers*, Kraus et al., eds., Hemisphere Publishing Corp., New York, NY, pp. 245–286.
[9] Wang, C. C., Hsieh, Y. C., and Lin, Y. T., 1997, "Performance of Plate Finned Tube Heat Exchangers Under Dehumidifying Conditions," ASME J. Heat Transfer, **119**, pp. 109–117.
[10] Chuah, Y. K., Hung, C. C., and Tseng, P. C., 1998, "Experiments on Dehumidification Performance of a Finned Tube Heat Exchanger," International Journal of HVAC&R Research, **4**, pp. 167–178.
[11] Hong, T. K., and Webb, R. L., 1996, "Calculation of Fin Efficiency for Wet and Dry Fins," International Journal of HVAC&R Research, **2**, pp. 27–41.
[12] El-Din, M. M. S., 1998, "Performance Analysis of Partially Wet Fin Assembly," Appl. Therm. Eng., **18**, pp. 337–349.
[13] Rosario, L., and Rahman, M. M., 1998, "Overall Efficiency of Radial Fin Assembly Under Dehumidifying Conditions," ASME J. Energy Resour. Technol., **120**, pp. 299–304.
[14] Vardhan, A., and Dhar, P. L., 1998, "A New Procedure for Performance Prediction of Air Conditioning Coils," Int. J. Refrig., **21**, pp. 77–83.
[15] Mirth, D. R., and Ramadhyani, S., 1993, "Prediction of Cooling-Coil Performance under Condensing Conditions," Int. J. Heat Fluid Flow, **14**, pp. 391–400.
[16] Mirth, D. R., and Ramadhyani, S., 1994, "Correlations for Predicting the Air-Side Nusselt Numbers and Friction Factors in Chilled-Water Cooling Coils," Exp. Heat Transfer, **7**, pp. 143–162.
[17] Hu, X., Zhang, L., and Jacobi, A. M., 1994, "Surface Irregularity Effects of Droplets and Retained Condensate on Local Heat Transfer to Finned Tubes in Cross-Flow," ASHRAE Trans., **100**, pp. 375–381.
[18] Jang, J. Y., Lai, J. T., Liu, L. C., 1998, "The Thermal-Hydraulic Characteristics of Staggered Circular Finned-Tube Heat Exchangers Under Dry and Dehumidifying Conditions," Int. J. Heat Mass Transf., **41**, pp. 3321–3337.
[19] Fu, W. L., Wang, C. C., and Chang, C. T., 1995, "Effect of Anti-Corrosion Coating on the Thermal Characteristics of a Louvered Finned Tube Heat Exchanger Under Dehumidifying Condition," *Advances in Enhanced Heat/Mass Transfer and Energy Efficiency*, ASME HTD-Vol. 320/PID-Vol. 1, pp. 75–81.
[20] Wang, C. C., and Chang, C. T., 1998, "Heat and Mass Transfer for Plate Fin-and-Tube Heat Exchangers, With and Without Hydrophilic Coating," Int. J. Heat Mass Transf., **41**, pp. 3109–3120.
[21] Hong, K., 1996, "Fundamental Characteristics of Dehumidifying Heat Exchangers With and Without Wetting Coatings," Ph.D. thesis, Pennsylvania State University, PA.
[22] Rudy, T. M., and Webb, R. L., 1981, "Condensate Retention on Horizontal Integral-Fin Tubing," in *ASME Advances in Enhanced Heat Transfer*, Vol. HTD-18, pp. 35–41.
[23] Rudy, T. M., and Webb, R. L., 1985, "An Analytical Model to Predict Condensate Retention on Horizontal Integral-Fin Tubes," ASME J. Heat Transfer, **107**, pp. 361–368.
[24] Webb, R. L., Rudy, T. M., and Kedzierski, M. A., 1985, "Prediction of the Condensation Coefficient on Horizontal Integral-Fin Tubes," ASME J. Heat Transfer, **107**, pp. 369–376.
[25] Jacobi, A. M., and Goldschmidt, V. W., 1990, "Low Reynolds Number Heat and Mass Transfer Measurements of an Overall Counterflow, Baffled, Finned-Tube, Condensing Heat Exchanger," Int. J. Heat Mass Transf., **33**, pp. 755–765.
[26] Korte, C. M., and Jacobi, A. M., 1997, "Condensate Retention and Shedding Effects on Air-Side Heat Exchanger Performance," TR-132, ACRC, University of Illinois, Urbana.
[27] Morel, T., 1975, "Comprehensive Design of Axisymmetric Wind Tunnel Contractions," ASME J. Fluids Eng., **97**, pp. 225–233.
[28] Chappuis, J., 1982, "Contact Angles," in *Multiphase Science and Technology*, Hewitt et al., eds., **1**, Hemisphere Publishing Corporation, Washington, D.C., pp. 387–505.
[29] Johnson, R. E., Jr., and Dettre, R. H., 1969, "Wettability and Contact Angles," in *Surface and Colloid Science*, E. Matijevic, ed., **2**, Wiley-Interscience, New York, NY, pp. 85–153.
[30] Ware, D. D., and Hacha, T. H., 1960, "Heat Transfer from Humid Air to Fin and Tube Extended Surface Cooling Coils," ASME Paper No. 60-HT-17.
[31] ARI, 1981, "Standard for Forced-Circulation Air-Cooling and Air-Heating Coils," ARI-410.
[32] Gnielinski, V., 1976, "New Equations for Heat and Mass Transfer in Turbulent Pipe and Channel Flow," Int. Chem. Eng., **16**, pp. 359–368.
[33] Kays, W. M., and London, A. L., 1984, *Compact Heat Exchangers*, 3rd ed., McGraw-Hill, New York.
[34] Graham, C., 1969, "The Limiting Heat Transfer Mechanisms of Dropwise Condensation," Ph.D. thesis, Massachusetts Institute of Technology, MA.
[35] Al-Hayes, R. A. M., and Winterton, R. H. S., 1981, "Bubble Diameter on Detachment in Flowing Liquids," Int. J. Heat Mass Transf., **24**, pp. 223–230.
[36] Dimitrakopoulos, P., 1996, "Computational Studies of Droplet Displacement in Stokes Flow," Ph.D. thesis, University of Illinois, Urbana, IL.
[37] Brown, R. A., Orr, Jr., F. M., and Scriven, L. E., 1980, "Static drop on an inclined plate: Analysis by the Finite Element Method," J. Colloid Interface Sci., **73**, pp. 76–87.
[38] Milinazzo, F., and Shinbrot, M., 1988, "A Numerical Study of a Drop on a Vertical Wall," J. Colloid Interface Sci., **121**, pp. 254–264.
[39] Yin, J., and Jacobi, A. M., 1999, "Condensate Retention Effects on the Air-Side Heat Transfer Performance of Plain and Wavy-Louvered Heat Exchangers," TR-158, ACRC, University of Illinois, Urbana.
[40] Kim, G., and Jacobi, A. M., 1999, "Condensate Accumulation Effects on the Air-Side Performance of Slit-Fin Surfaces," CR-26, ACRC, University of Illinois, Urbana.

Melting of a Solid Sphere Under Forced and Mixed Convection: Flow Characteristics

Y. L. Hao[1]

Y.-X. Tao[1]

Department of Mechanical Engineering,
Tennessee State University,
Nashville, TN 37209-1561

An experimental investigation on flow around a melting ice sphere in horizontally flowing water is conducted. The flow field is measured quantitatively using the particle image velocimetry (PIV) technique. The distributions of velocity, streamline, and z-component of rotation vector around the ice sphere are obtained for different upstream velocities and temperatures. General flow characteristics around the melting ice sphere and effects of velocity and temperature are analyzed. The visualization of melting of a dyed ice sphere is also conducted to investigate the motion of the melt, its mixing with mainstream, and the separation of the boundary layer. Comparisons with the flow around a non-melting ball are made to investigate the effect of melting on the flow boundary layer. The original experimental results are published to serve as benchmark data for numerical model development. [DOI: 10.1115/1.1389466]

Keywords: Boundary Layer, Heat Transfer, Melting, Visualization

Introduction

Melting of solid particles has been studied extensively as it relates to many engineering and environmental applications, such as material processing, space applications, water resource and energy conversion and conservation. When solid objects are immersed in a fluid with a temperature higher than the melting temperature of the solid, they melt and produce molten material that then mixes with the surrounding fluid. The solid particles experience not only size variation from their initial size but also changes of their shape. This becomes more pronounced when the melting occurs in a forced, convective flow. Due to the influence of phase-change, the characteristics of momentum exchange and heat transfer between two phases are remarkably different from those between two phases with no phase change. The difference lies mainly in non-thermal-equilibrium mixing of melt with supply fluid flow. The understanding of the flow characteristics around the solid particle in the melting process, therefore, is very important to develop a better dynamic model to predict the melting rate in a process typical to engineering applications. These include the melting of solid silicon for production of almost all silicon crystals for microelectronics applications, the thawing of frozen foods, the melting of hail in meteorology and icebergs in glaciology and oceanography, and the melting of solid particles under various gravity levels in space applications.

The previous studies of melting of solid particle in fluid mainly focused on either the melting process of a sphere in a pool of liquid (Tkachev [1], Schenk and Schenkels [2], Vanier and Tien [3], Anselmo [4,5], Mukherjee et al. [6], Mcleod et al. [7]) or the heat transfer characteristics between fluid and solid particle in a flowing liquid (Eskandari [8], Eskandari et al. [9], Aziz et al. [10], Hao and Tao [11–13]). So far experimental investigations of flow around a melting solid particle are limited to the qualitative visual observations (Schenk and Schenkels [2], Vanier and Tien [3], Mukherjee et al. [6], Mcleod et al. [7]). An accurate and complete description of the phase interactions between fluid and melting solid particles is not available at this time.

In reality, when melting of a particle or particles occurs in a non-thermally equilibrium flow, the particle's movements (translation and rotation) further complicates the interaction between particles and fluid. In this study we focus on the relative translation interaction between a melting particle and a parallel flow with the effect of mixed convection induced by the discharged melt. For this purpose, we design an experimental configuration such that an ice ball is constrained on a fixed base subject to a convective melting process in horizontally flowing water. The quantitative and qualitative visual measurements are conducted using the Particle Image Velocimetry (PIV) technique and color visual trace method, in order to provide information of flow characteristics for further theoretical modeling and numerical simulation. This paper also serves as a base and preliminary study for further study on the subject of heat transfer and phase interaction in liquid-solid, two-phase flow with the phase change.

Experimental Setup and Procedure

The experimental setup is shown in Fig. 1. The test section is an open channel and held horizontally. A MARCH TE-7R-MD pump moves water from the reservoir and discharges it to the head tank, from which the water flows into the channel. Water flows downstream in the channel past the sphere, which is mounted near the middle of the channel, and is then routed back to the reservoir. The discharge line has a gate valve and a John C. Ernst Co S100 flow meter to measure and control the flow rate of water. Water temperature is controlled by a refrigerated circulator with a measured fluctuation of 0.1°C during a typical experiment.

The length, width, and height of the test section are 500 mm, 152 mm, and 216 mm, respectively, as shown in Fig. 2. A uniform velocity at the inlet of the test section is attained by the use of a flow straightener made of Duocel aluminum foam. An overflow plate is placed at the downstream location to control the water level. The water level can also be controlled using the gate placed at the exit location, providing a certain degree of flexibility. A water height of 130 mm can be achieved in the present study. The test section and head tank are made of Plexiglas so that experiments could be visualized and videotaped. Twelve thermocouples are mounted at the inlet, test section, and outlet to measure the water temperature at different locations along the flow direction. A pair of thermocouples is placed in the center of the ice sphere to measure its central temperature during the melting process. A computer data acquisition system is used to record readings from the thermocouples during a test.

[1]Present address: Department of Mechanical/Chemical Engineering, Florida International University, Miami, Florida 33174.

Contributed by the Heat Transfer Division for publication in the JOURNAL OF HEAT TRANSFER. Manuscript received by the Heat Transfer Division August 21, 2000; revision received March 28, 2001. Associate Editor: C. Beckermann.

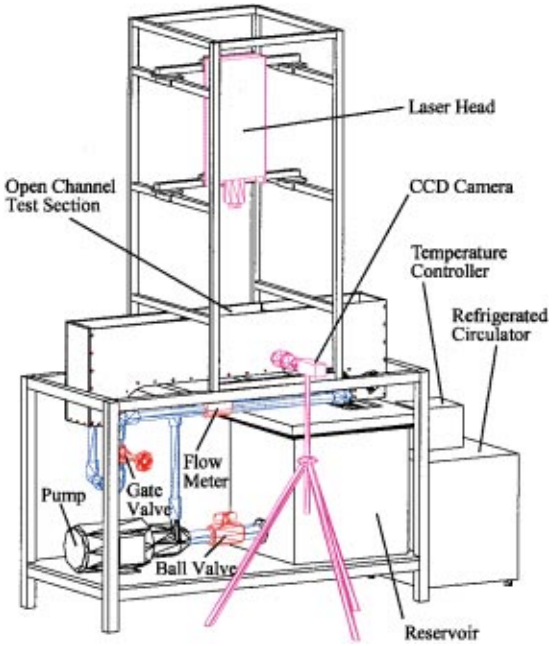

Fig. 1 Schematic of the test apparatus

In the present study, the water flow field around a melting ice sphere is measured quantitatively using a TSI cross-correlation PIV system. The flow field is taken in alignment with the vertical axial plane of the ice sphere parallel to the main flow direction. The PIV system contains dual mini Nd:YAG lasers, LaserPulse computer controlled synchronizer, PIVCAM 4–30 cross/auto correlation CCD camera, and PC computer with high-speed camera interface and TSI's INSIGHT PIV software, as shown in Fig. 2. The dual mini Nd:YAG lasers provide light pulses with energy of 12 mJ/pulse at a wavelength of 532 nm. The collimated laser beam is transmitted through three cylindrical lenses of -12.7, -25.4 and -50 mm focal length to diverge the beam into a sheet. A spherical lens of 500 mm focal length is used to control the thickness of the lightsheet. The laser head is placed vertically above the test section at a distance of 500 mm from the center of ice sphere. The laser light sheets illuminate the plane of interest within the flowing fluid. The fluid is seeded with tracer particles, which are hollow glass beads of 8–12 micron meters in diameter and 1050–1150 kg/m^3 in density. The illuminated field is aligned with the center plane of the ice sphere parallel to the main flow direction. The CCD camera takes the images of the tracer particles with the resolution of 768×484 pixels and frame rate of 30 frames/s. A typical image is shown in Fig. 3.

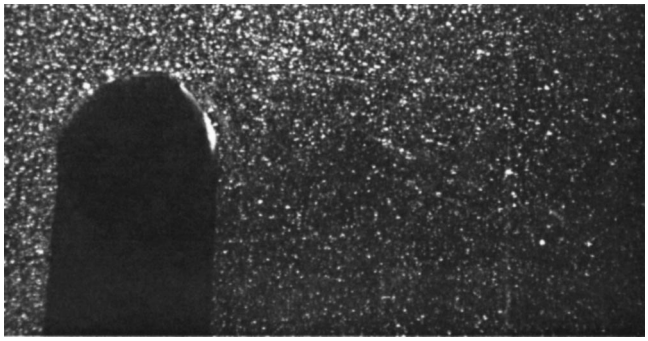

Fig. 3 Typical instantaneous image of the measured flow field at $t^*=0.3$: $V_w=0.05$ m/s, $T_w=4°C$, $d_0=36$ mm, $T_{i,0}=-15°C$, $t_{total}=760$ s.

The PIV system measures velocity by determining particle displacement over time using a double-pulsed laser technique. Two-frame cross-correlation method is employed in the present study. The synchronizer controls the dual lasers through the computer triggers and fires two laser pulse sequences at a given separation time and a given frequency during the measurement. The laser light sheets illuminate the plane of interest within the flowing fluid, which is seeded with tracer particles. In the meantime, the synchronizer triggers the CCD camera to take two image frames of particles in the measured region of the plane with one laser pulse on each frame. Frame 1 contains the image from the first laser pulse, and frame 2 has the image from the second laser pulse. The time between frame 1 and frame 2 is the same as that between laser pulse 1 and laser pulse 2. The flow velocity is found by measuring the distance the particle has traveled from frame 1

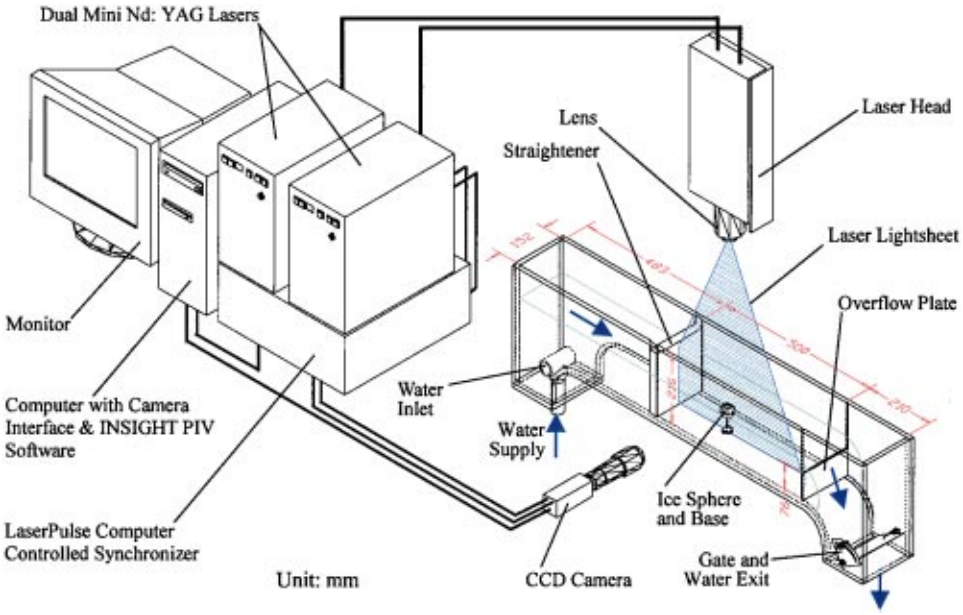

Fig. 2 Test section and PIV system setup

to frame 2. The digital data of both image frames is transferred directly into the computer's RAM by the camera's high-speed interface. TSI's INSIGHT PIV software generates the entire velocity profile in the measured flow field, based on the particle displacement from two image frames. Complete separation of the two images allows velocity to be measured without directional ambiguity. The 2-frame cross-correlation can measure zero displacements and reversing flows without image shifting, and has specific advantages for the complex flow including uniform main flow, low velocity flow in boundary layer, and reverse flow in the wake as occurring in the present study. After the x and y-components of velocity, u and v, are obtained, the z-component of rotation vector, ω_z, can be calculated by $(\partial v/\partial x - \partial u/\partial y)/2$.

The limitation of using 2-frame cross-correlation is evident in the effective image captures rate, or framing rate. The particle must move less than one-fourth of the interrogation spot in the time between the first and second laser pulses. The flow investigated in the present study is of low velocity with the typical mainstream velocity ranging from 0.01 to 0.1 m/s. Therefore we choose 30 ms for the time between laser pulses and 30 Hz for the frame rate. The distances that the particles move between the first and second laser pulses are 1.5, 7.4, and 14.8 pixels in x-direction and 1.3, 6.3, and 12.6 pixels in y-direction for the velocity of 0.01, 0.05, and 0.1 m/s, respectively. They are less than one-fourth of the interrogation spot, which is 32 pixels for 0.01 and 0.05 m/s and 64 pixels for 0.1 m/s. Based on Adrian's method [14], the maximum uncertainty in the velocity measurements is estimated as ± 0.40 percent in x-direction and ± 0.41 percent in y-direction within the range of this study.

The maximum random error in the x and y-coordinates is ± 0.29 percent, according to the calibration of the PIV system. Based on the method of Kline and McClintock [15], the maximum uncertainty in the z-component of rotation vector, ω_z, is ± 0.70 percent.

Another source of error is the ability of tracer particles to follow the fluid flow. The particle's Stokes number gives an estimate of the particle's response to changes in the fluid motion. It can be calculated as the ratio of the particle's relaxation time to the characteristic flow time, $St = \tau_p / \tau_f$. The details on the error analysis method and equations can be found in Refs. [14,16]. In the present study, the particle's relaxation time is 7.66×10^{-6} s. The characteristic flow time is 3.6, 0.72, and 0.36 s for the main flow velocity of 0.01, 0.05, and 0.1 m/s, respectively. The Stokes number is then 2.13×10^{-6}, 1.06×10^{-5}, and 2.13×10^{-5} accordingly. It can be concluded that the timescale for the particle to respond to fluid motion change is much smaller than the fluid motion timescale (less than 2.13×10^{-3} percent). Therefore, the particles closely follow the changes in fluid motion.

The visual observations are also conducted in the present study using a digital video camcorder recording the image of melting process of dyed ice sphere, in order to investigate qualitatively the characteristics of motion of melt, boundary layer separation, and mixture of melt with mainstream.

The ice spheres are made by freezing tap water dyed with food coloring for visual observations, or tap water dyed with food coloring and containing tracer particles for PIV measurements. If the ice sphere made from clear tap water is used in the PIV measurement, the ice sphere illuminated by the laser produces a very bright area on the captured images. The strong optical noise signals cause the software to fail to process the images and to give the correct velocity information near the ice sphere. The tracer particles are added to the ice in order to generate tracer particles in the wake and obtain good velocity information resulting from the melt fluid. A thin plastic straw is sandwiched in the sphere to allow the sphere be fixed on a base made of stainless steel. In this study, the diameter of the ice sphere is 36 mm and the diameter of the thin plastic straw is 2 mm. The depth of the straw's insertion into the sphere is about 18 mm. A pair of thermocouples is placed at the center of the ice sphere through the plastic straw.

During a typical test, a steady open channel flow at the desired flow rate and temperature is established by pumping water through the refrigerated circulator and the adjusted opening of the gate valve. The digital video camcorder and computer data acquisition system are initialized to record video images and temperatures. The ice sphere, fixed on the base by the thin plastic straw, is then placed into the flowing water, and the test is begun. A circle is drawn on the bottom of the test section to ensure that the ice sphere with the base can be placed at the predetermined center location relative to the laser sheet. The maximum allowable error in the positioning the laser light sheet on the centerline through the sphere is less than ± 0.5 mm. The PIV system is activated to record a set of images of measured flow field for every given time interval, and the digital image files are saved on the hard disk drive. When the remaining ice breaks away from the plastic straw and drifts downstream, the test is ended. A set of images in sequence with specified time intervals during the melting process is obtained for each case. Intervals of 10, 15, 20, or 30s are used in the different cases. After the test is finished, the information of flow field around ice particle at each measured time can be obtained by using the INSIGHT software [17,18].

For visualization observation, only the digital video camcorder and the computer data acquisition system are used to record the video images and the temperatures.

To test the repeatability of the experiments, a number of tests are conducted under identical conditions. The qualitative results agree reasonably well, and no detectable differences in main quantitative results are found.

Results and Discussion

Upon immersion into flowing water with a temperature higher than the phase change temperature (0°C), the ice sphere begins to melt. The water temperature close to the ice decreases due to heat transfer between the water and ice. Low temperature melt detaches from the ice sphere's downstream side and mixes with the water. Density differences in water around the ice sphere, caused by the temperature difference, strongly influence the flow pattern of downstream water. For many results presented below, the water temperature of 4°C is chosen to reduce the effect of density difference because that the water density reaches its maximum value (10000.00 kg/m^3) at 3.98°C and the difference of density in the range of 0–4°C is very small (999.87 kg/m^3 at 0°C). For other results, a high water temperature (30°C) is chosen for studying the influence of natural convection.

Flow Field Around a Convectively Melting Ice Sphere. The flow field of water at first is disturbed immediately after the ice sphere attached to the base is suddenly placed in the water flow. The stable water flow gradually resumes. The initial transient period lasts about 6 to 15 s under the conditions of the present work. Figure 4 shows the results just after the initial transient period under the condition of $V_w = 0.05$ m/s, $T_w = 4$°C, $T_{i,0} = -15$°C, $d_0 = 36$ mm, and $Re_0 = 1077$ (based on the initial diameter, d_0). The time ($t = 0$) begins when the ice sphere is placed in the water flow. In the figures, x stands for the horizontal coordinate, and y is in the vertical direction from the bottom wall. The flow direction of water is horizontal from left to right. It should be noted that the laser light sheet cannot illuminate the shadow area under the ice sphere, as shown in Fig. 3, so that flow field in the shadow area cannot be measured by the PIV system. Again, all the images are taken with the laser sheet aiming at the center plane of the sphere that is parallel to the main flow direction (x-direction).

The velocity vector distribution in Fig. 4(a) clearly shows the direction and magnitude of the water velocity in the axial plane around the ice sphere. The streamline, obtained based on the velocity vector field, shown in Fig. 4(b), illustrates the nature of the velocity vector field and the visual profile of the water flow in the field. The distribution of ω_z is shown in Fig. 4(c). The distributions of the velocity components in the x-direction (mainstream direction) and y-direction are shown in Fig. 4(d) and (e), respectively.

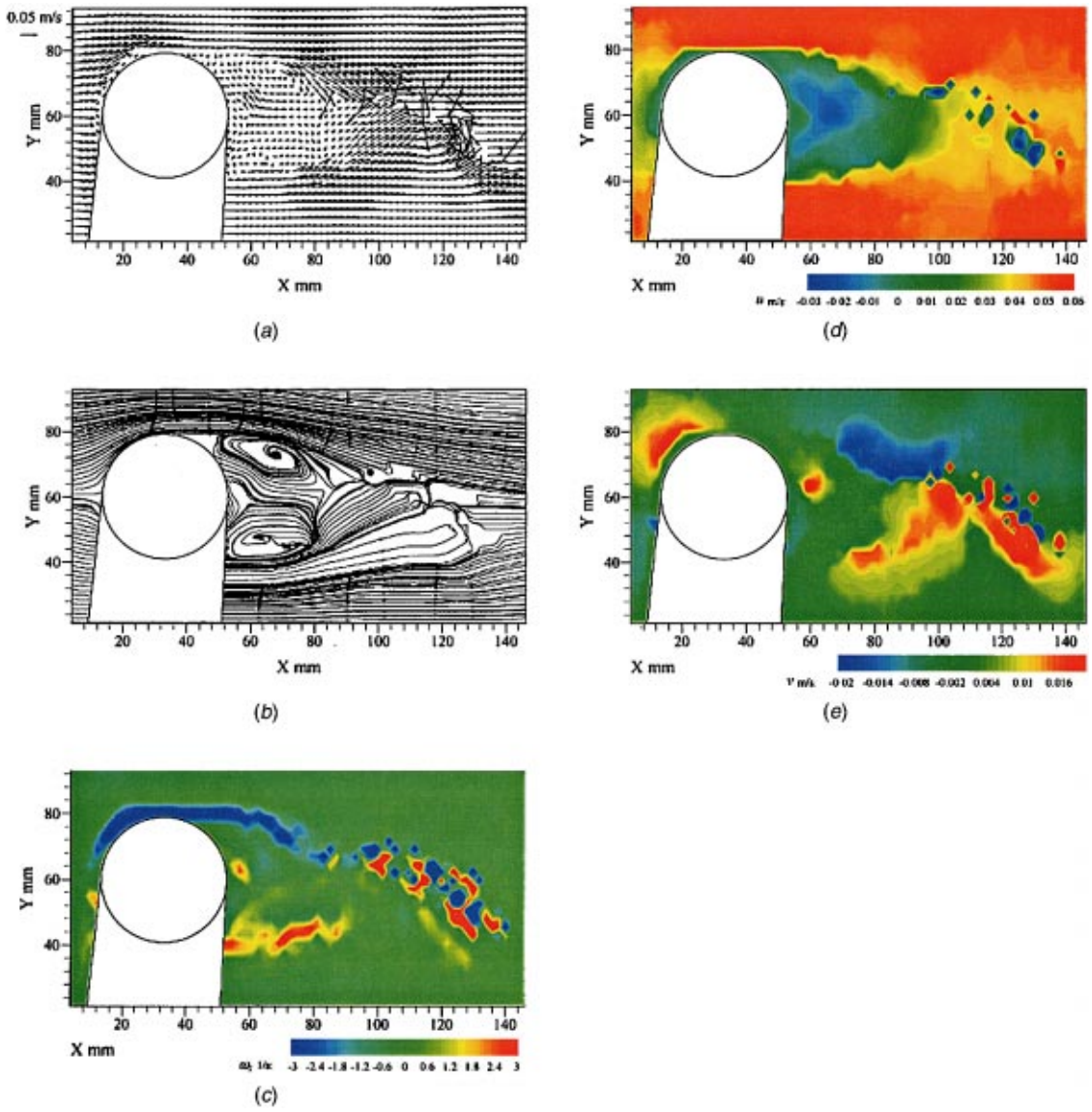

Fig. 4 Flow field results in the axial plane: $t^*=0.0079$, $V_w=0.05$ m/s, $T_w=4°C$, $d_0=36$ mm, $T_{i,0}=-15°C$, $Re_0=1077$, $Gr_0=883$, $Gr_0/Re_0^2=7.6\times10^{-4}$, $t_{total}=760$ s: (*a*) velocity vector distribution; (*b*) streamline; (*c*) *z*-component of rotation vector; (*d*) velocity component in *x*-direction; and (*e*) velocity component in *y*-direction.

The results shown in Fig. 4 indicate that upstream, steady, uniform water flow changes direction in front of the ice sphere, bypasses it and produces a wake behind it. Viscosity causes the velocity to decrease in the *x*-direction and to increase in the *y*-direction close to the surface of sphere. A boundary layer can be seen over the upper surface of the melting sphere, as shown in Fig. 4(*d*) and (*e*). The influence of viscosity extends into the wake, where the velocity on the edge of the wake is smaller than in the mainstream, and negative velocity appears in the wake (Fig. 4(*d*)). Two opposite circulating cells are formed in the wake, as evidenced in Fig. 4(*a*) and (*b*). The flow from upper and lower sides meet together behind the circulating cells, causing a strong disturbance of flow and mixing of melt with mainstream flow there. The viscous effect and mixing result in a rotational flow, and the value of ω_z reaches the relatively large magnitude near the surface of sphere and at the edge of wake. This phenomenon can be seen in Fig. 4(*c*). The distribution of ω_z also indicates the approximate range of the boundary layer. The liquid's velocity gradually decreases in the *x*-direction and increases in the *y*-direction while it flows towards the sphere. A region of lower velocity is formed surround the stagnation point, as shown in Fig. 4(*d*), in which the value of ω_z approaches zero. The magnitude of ω_z (negative above the sphere and positive under the sphere) gradually increases with the angular coordinate, θ, of the sphere (the angle equal to zero at the stagnation point) while the boundary forms over the surface. The distribution of ω_z indicates that there are large velocity gradients and significant shear stresses in the boundary layer and at the edge of wake, especially behind about $\theta=\pm20$ deg. The boundary finally separates at about $\theta=116$ deg. At the separation point, the boundary layer's thickness reaches a maximum that equals nearly half of the sphere radius. The circulation in the wake enhances the heat transfer between water and ice surface, causing a higher local melting rate at the rear surface than at the area near the separation point. The shape at the rear becomes flat (Hao and Tao [13]).

The dimensionless time, defined as the ratio of time to total melting time, $t^*=t/t_{total}$, is used to present temporal results in the

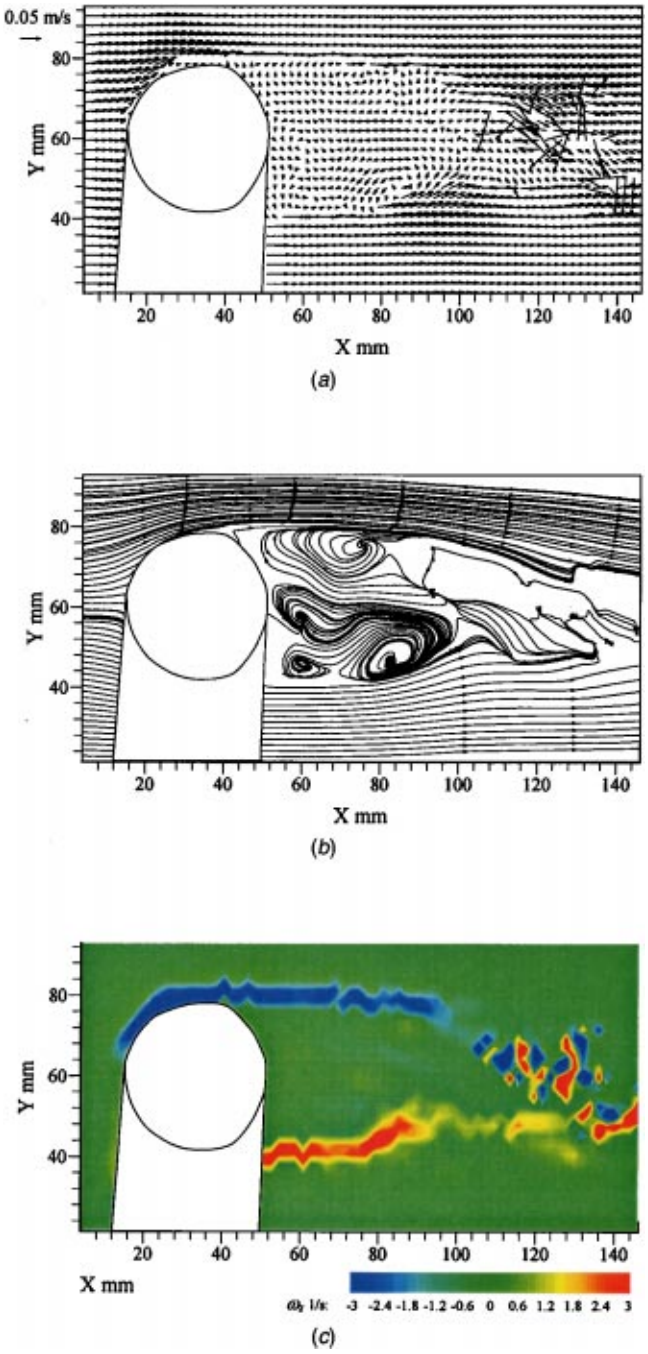

Fig. 5 Flow field results in the axial plane: $t^*=0.3$, $V_w=0.05$ m/s, $T_w=4°C$, $d_0=36$ mm, $T_{i,0}=-15°C$, $Re_0=1077$, $Gr_0=883$, $Gr_0/Re_0^2=7.6\times10^{-4}$, $t_{total}=760$ s: (*a*) velocity vector distribution; (*b*) streamline; and (*c*) *z*-component of rotation vector.

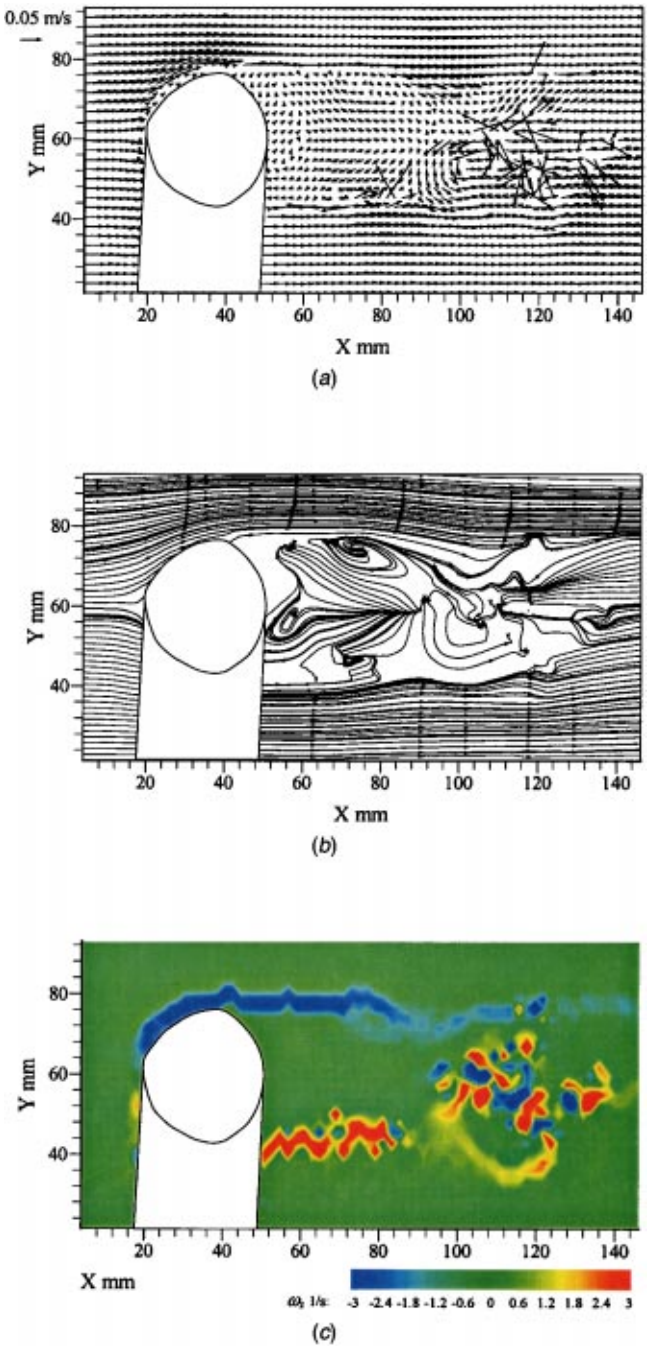

Fig. 6 Flow field results in the axial plane: $t^*=0.6$, $V_w=0.05$ m/s, $T_w=4°C$, $d_0=36$ mm, $T_{i,0}=-15°C$, $Re_0=1077$, $Gr_0=883$, $Gr_0/Re_0^2=7.6\times10^{-4}$, $t_{total}=760$ s: (*a*) velocity vector distribution; (*b*) streamline; and (*c*) *z*-component of rotation vector.

present study. This consideration is based on the fact that the total time period from the start to the time when the remaining ice breaks away from the plastic straw is different under different test conditions. The actual total time of the test is also listed in the description of results to give the real time value of actual tests for the quantitative comparison. Figure 4 shows the result at the time ($t^*=0.0079$) just after the flow field settles down from the disturbance caused by placing the ice sphere with the basis in the water flow. Figures 5, 6 and 7 show the velocity vector distributions, streamlines, and ω_z distributions in the axial plane at different times, $t^*=0.3$, 0.6, and 0.9, respectively. The other test conditions are the same as that in Fig. 4. The flow characteristic around the ice is changing while the ice sphere is melting. The shape of ice gradually changes into a scallop shape because the differences in flow pattern at different local positions causes a difference in heat transfer between water and ice surface and melting rate. In turn, the flow pattern around the ice gradually changes, along with changes in the curvature of the surface near the front of ice and the maximum radius in the cross direction of water flow. For the time period less than $t^*=0.3$, the flow pattern remains basically the same as we compare Fig. 5 with Fig. 4. The main difference is that the separation point appears at the position of

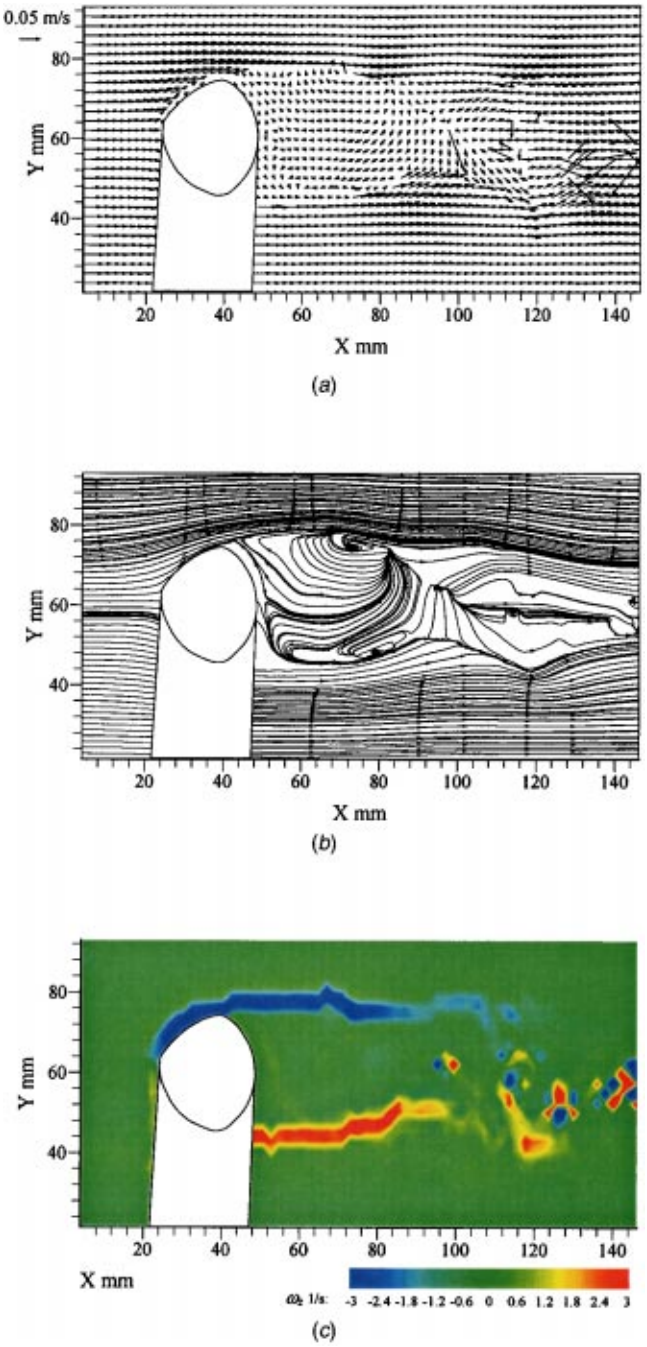

Fig. 7 Flow field results in the axial plane: $t^*=0.9$, $V_w=0.05$ m/s, $T_w=4°C$, $d_0=36$ mm, $T_{i,0}=-15°C$, $Re_0=1077$, $Gr_0=883$, $Gr_0/Re_0^2=7.6\times10^{-4}$, $t_{total}=760$ s: (*a*) velocity vector distribution; (*b*) streamline; and (*c*) *z*-component of rotation vector.

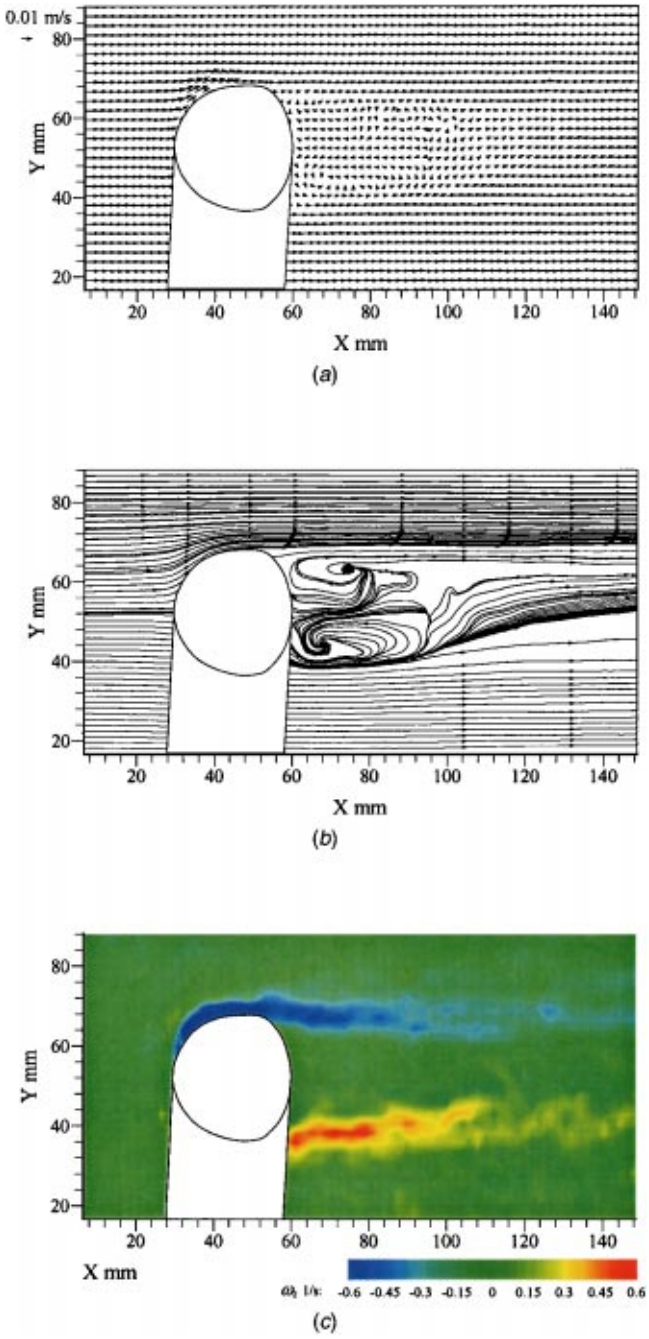

Fig. 8 Flow field results in the axial plane: $t^*=0.5$, $V_w=0.01$ m/s, $T_w=4°C$, $d_0=36$ mm, $T_{i,0}=-20°C$, $Re_0=215$, $Gr_0=883$, $Gr_0/Re_0^2=0.019$, $t_{total}=1614$ s: (*a*) velocity vector distribution; (*b*) streamline; and (*c*) *z*-component of rotation vector.

maximum radius in the traverse direction of water flow, and the region of wake also increases. The surface contour behind the location of the maximum radius experiences a sudden change, caused by higher melting rate over the rear surface. As a result the boundary layer cannot continue to develop, and flow separation occurs. These differences are shown more clearly in the example processes in Fig. 6 and Fig. 7.

The sequence of measured results in the convective melting process of ice sphere in Fig. 4 to Fig. 7 indicates that the circulation of cells in the wake is not steady. The circulating cells follow a pattern of continuous generation, growth and breakup.

Effect of Mainstream Velocity. Figures 8, 9, and 10 show the velocity vector distributions, streamlines, and ω_z distributions of three cases at $t^*=0.5$. The three tests are all conducted under the condition of $T_w=4°C$, $T_{i,0}=-20°C$, and $d_0=36$ mm. Water velocities are at 0.01, 0.05, and 0.1 m/s ($Re_0=215$, 1077 and 2154), respectively. The results indicate that the effect of mainstream velocity is most significant compared to other variables such as mainstream temperature. The influence of the presence of the ice sphere on the mainstream flow field is within a relatively small region at the low mainstream velocity of 0.01 m/s, as shown in Fig. 8. There are two slow and opposite circulation cells near

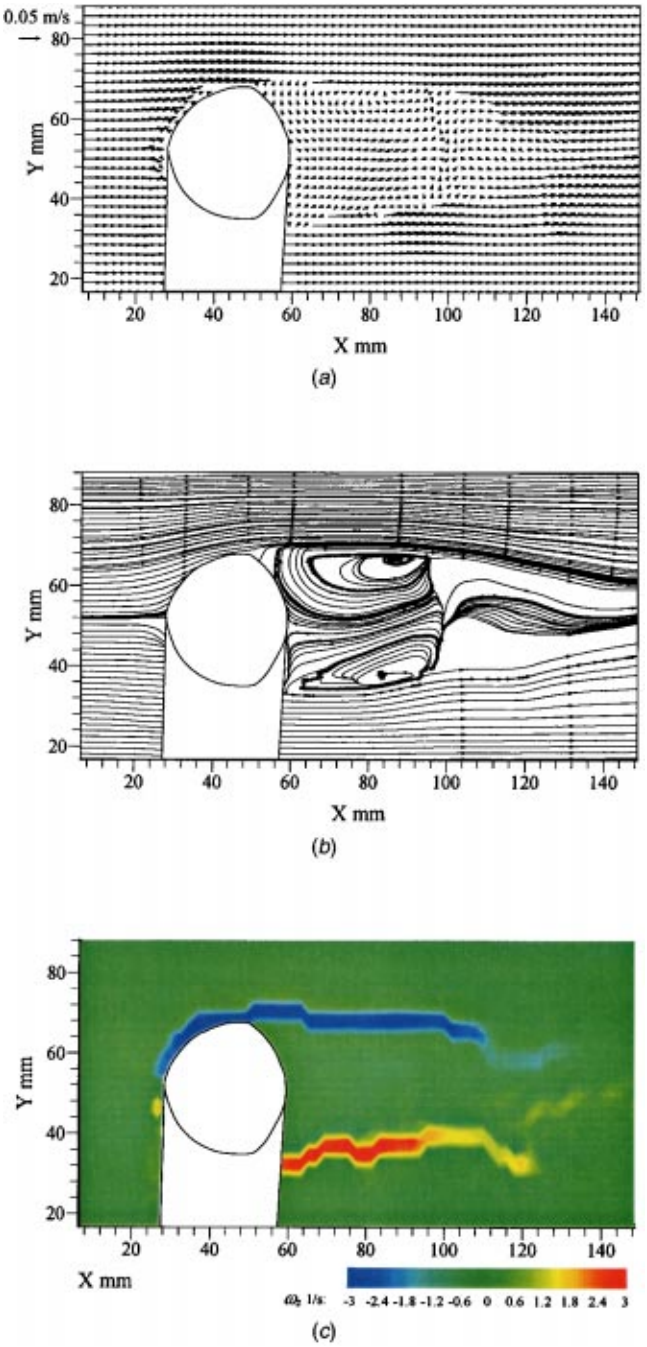

Fig. 9 Flow field results in the axial plane: $t^*=0.5$, $V_w=0.05$ m/s, $T_w=4°C$, $d_0=36$ mm, $T_{i,0}=-20°C$, $Re_0=1077$, $Gr_0=883$, $Gr_0/Re_0^2=7.6\times10^{-4}$, $t_{total}=1009$ s: (*a*) velocity vector distribution; (*b*) streamline; and (*c*) *z*-component of rotation vector.

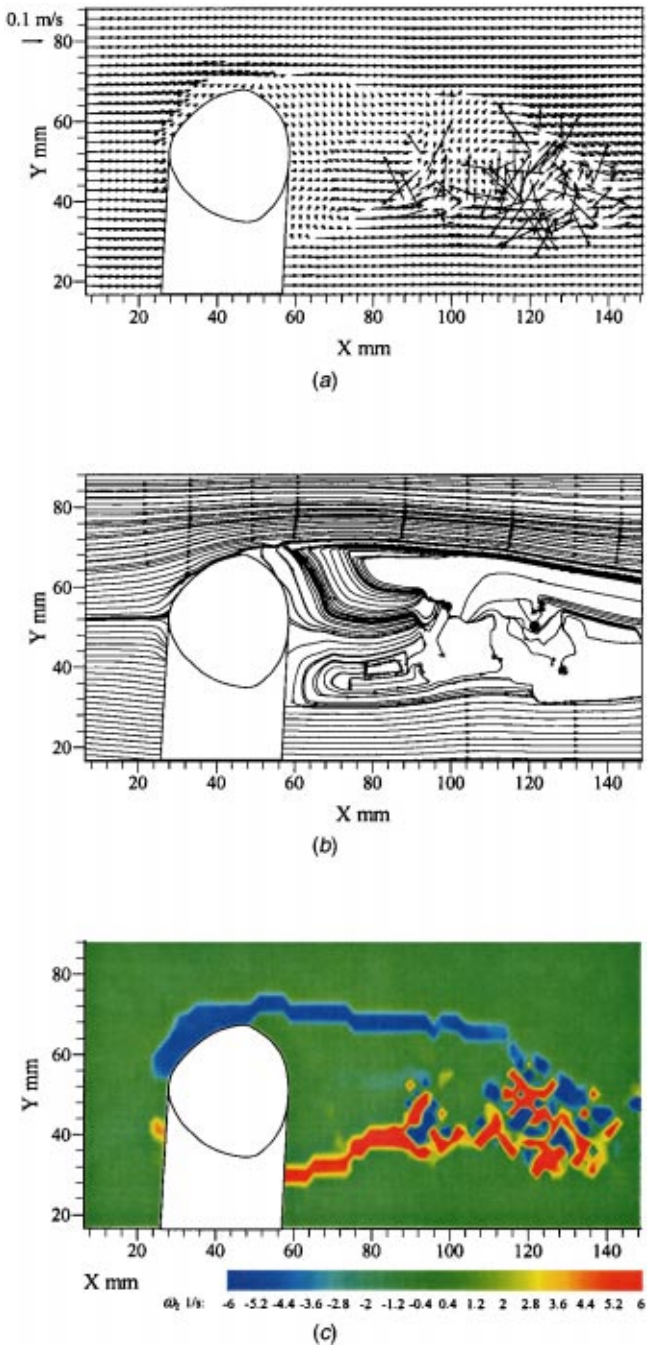

Fig. 10 Flow field results in the axial plane: $t^*=0.5$, $V_w=0.10$ m/s, $T_w=4°C$, $d_0=36$ mm, $T_{i,0}=-20°C$, $Re_0=2154$, $Gr_0=883$, $Gr_0/Re_0^2=1.9\times10^{-4}$, $t_{total}=689$ s: (*a*) velocity vector distribution; (*b*) streamline; and (*c*) *z*-component of rotation vector.

the ice in the wake. There is nearly no disturbance in the wake region behind the circulation region. In the case with velocity of 0.05 m/s, the disturbance to the mainstream flow, caused by the presence of the ice sphere, reaches the entire measured field, as shown in Fig. 9. There are two opposite, relatively strong circulating cells near the ice in the wake. There are no major disturbances in the wake region behind the circulation region. For the relatively high velocity of 0.1 m/s, as shown in Fig. 10, there are strong disturbances in the wake, in addition to the strong disturbance to the mainstream flow. The circulating cells are being quickly generated, growing and breaking up in the wake. The presence of two opposite, circulating cells in the wake is nearly unobservable. It is obvious that there are strong disturbances and mixing of melt with mainstream behind the circulation region in this case.

Effect of Mainstream Temperature. Figures 11 and 12 show the results of two cases at $t^*=0.5$. Both tests are conducted at $T_w=30°C$, $T_{l,0}=-20°C$, and $d_0=36$ mm. The water velocities are 0.01 and 0.05 m/s ($Re_0=316$ and 1579), respectively. The two tests under relatively high water temperature are conducted to investigate the effect of free convection on the flow around the ice

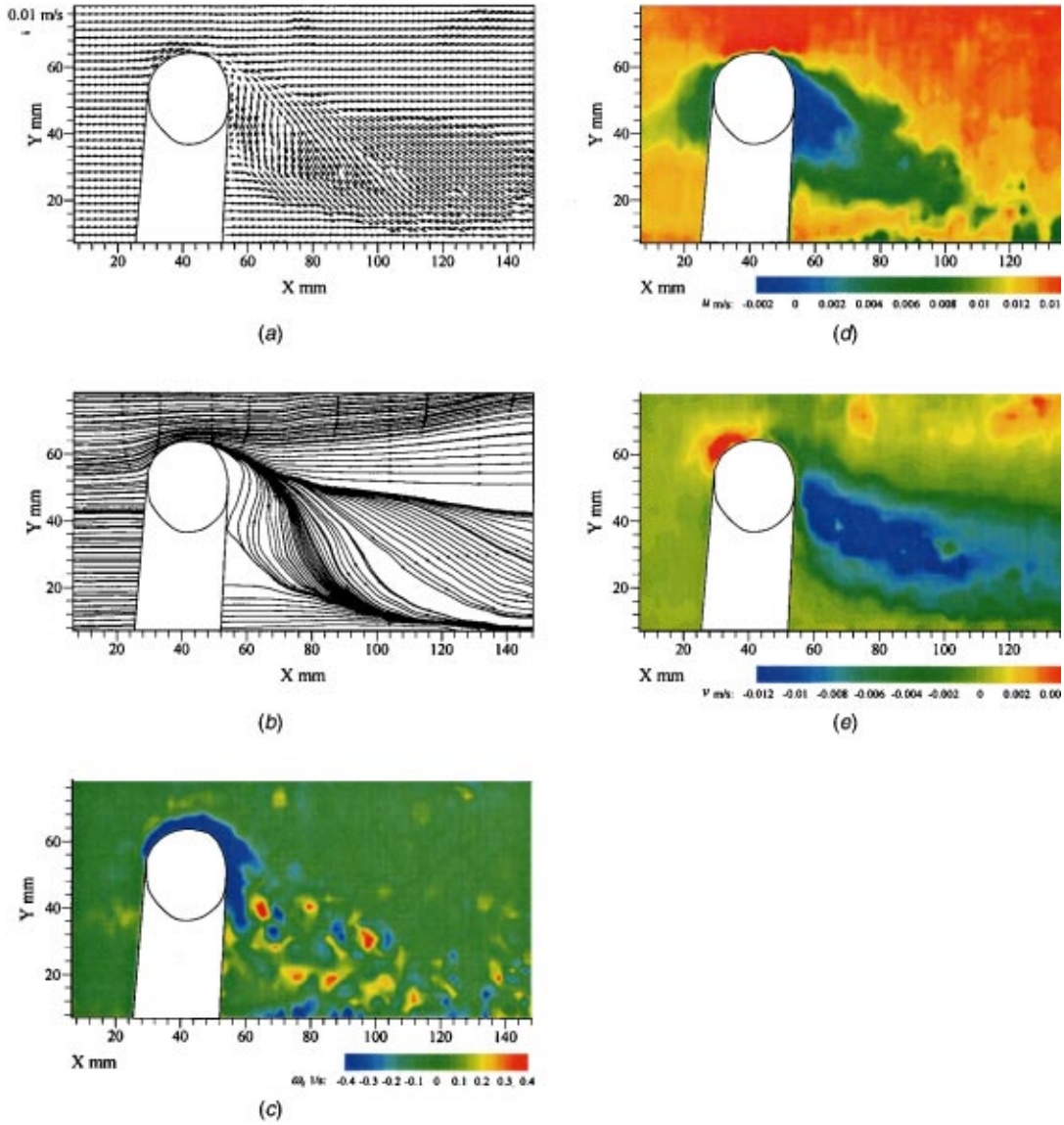

Fig. 11 Flow field results in the axial plane at a high water temperature: $V_w=0.01$ m/s, $T_w=30°C$, $d_0=36$ mm, $T_{i,0}=-20°C$, $Re_0=316$, $Gr_0=6.8\times10^6$, $Gr_0/Re_0^2=68.1$, $t^*=0.5$, $t_{total}=229$ s: (*a*) velocity vector distribution; (*b*) streamline; (*c*) *z*-component of rotation vector; (*d*) velocity component in *x*-direction; and (*e*) velocity component in *y*-direction.

sphere. The Grashof number based on the initial diameter is 6.8×10^6 and the corresponding (Gr/Re^2) for two cases are 68.1 and 2.73, respectively.

Figure 11 shows that free convection has an important effect on wake flow in the case of 0.01 m/s. The liquid in the thermal boundary layer is cold because of heat transfer to the ice. The cooled water and melt from the ice have a higher density than that of mainstream. The density difference causes the strong downward flow in the region behind the ice sphere and the downward extension of the wake. This phenomenon is a result of combined advection of discharging melt and mixed convection of mainstream fluid due to a temperature gradient. It can be seen that circulating cells cannot be generated, and the upper separation point moves towards the rear of ice sphere. The downward velocity component (opposite *y*-direction) in the wake reaches, and even exceeds, the mainstream velocity of 0.01 m/s, as shown in Fig. 11(*e*). This flow feature causes heat transfer and melting of the ice sphere, and its shape changes to be much different from that under conditions with dominant forced convection, such as in the cases shown in Fig. 4 to Fig. 10, where the initial Grashof number is 883, and the initial (Gr/Re^2) are 0.019, 7.6×10^{-4} and 1.9×10^{-4} for the mainstream velocity of 0.01, 0.05, and 0.1 m/s, respectively.

Figure 12 shows the flow pattern around the convectively melting ice sphere under the typical combined (or mixed) effects of free and forced convection. The downward flow in the wake is not very strong in comparison with the mainstream flow. The downward velocity component (opposite *y*-direction) in the wake is smaller than the mainstream velocity of 0.05 m/s, shown in Fig. 12(*e*). Again no circulating cell appears in the wake, and the upper separation point moves towards the rear of ice sphere. The downward extension of the wake is much smaller than that under the condition of 0.01 m/s in Fig. 11.

Motion of the Melt. Visualization tests of convective melting of the dyed ice sphere are conducted to observe the motion of melt and its mixing patterns with the mainstream. The typical results at $t^*=0.3$ are shown in Fig. 13 and Fig. 14.

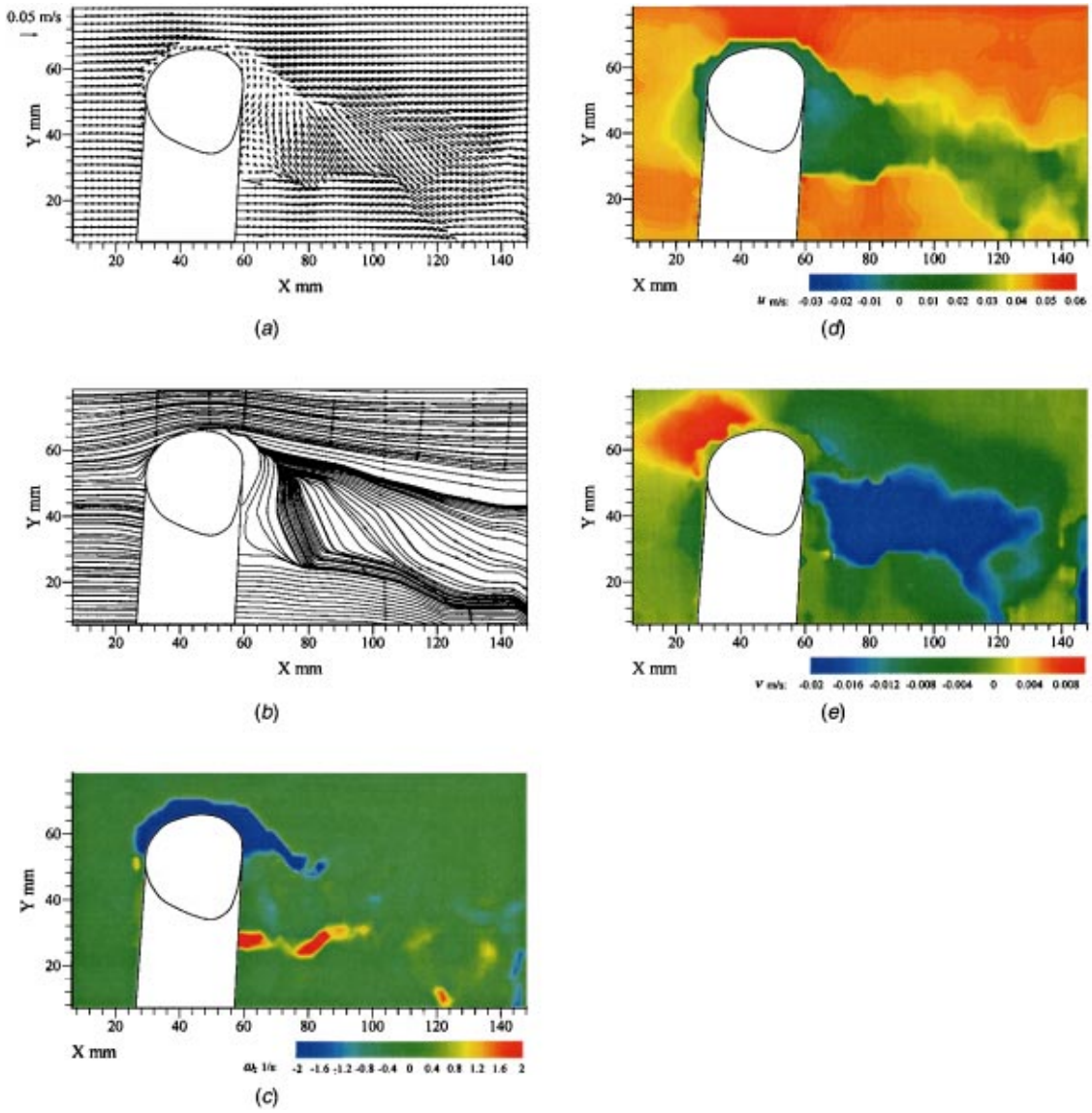

Fig. 12 Flow field results in the axial plane at a high water temperature: $V_w=0.05$ m/s, $T_w=30°C$, $d_0=36$ mm, $T_{i,0}=-20°C$, $Re_0=1579$, $Gr_0=6.8\times10^6$, $Gr_0/Re_0^2=2.73$, $t^*=0.5$, $t_{total}=133$ s: (*a*) velocity vector distribution; (*b*) streamline; (*c*) *z*-component of rotation vector; (*d*) velocity component in *x*-direction; and (*e*) velocity component in *y*-direction.

The three cases in Fig. 13 are all tested with $T_w=4°C$, $T_{i,0}=-20°C$, and $d_0=36$ mm. The initial Grashof number of three cases is 883. They are at a mainstream velocity of 0.01, 0.05, and 0.1 m/s ($Re_0=215$, 1077 and 2154), and an initial (Gr/Re^2) of 0.019, 7.6×10^{-4} and 1.9×10^{-4}, respectively. The dye yields a very clear image of flow pattern of the melt as the sphere melts. For these cases, the effect of free convection on the flow around the ice sphere is hardly noticeable and can be neglected, as shown in Fig. 13. The melt forms a thin layer over the upstream surface of ice. The melt layer flows downstream as a thin boundary sheet and then detaches from the sphere's downstream side at the separation point to go into the wake and mix with the mainstream. The effect of mainstream velocity is clearly illustrated in these images. The flow of melt at the low velocity of 0.01 m/s is quite steady except in the region near the rear of ice sphere, as shown in Fig. 13(*a*), where slow random motion is observed. The mixing process of melt with mainstream occurs slowly and within a long region behind the ice. The disturbance and mixing in the wake goes stronger as the velocity increases, as shown in Figs. 13(*b*) and (*c*). The mixing region in the wake becomes shorter, indicating that the mixing process strengthens and finishes quickly. The boundary separation occurs earlier with increasing velocity. Figure 15 shows the variation of separation points with time in the melting processes for different mainstream velocities. As mentioned above, water reaches its highest density (1000.00 kg/m^3) at 3.98°C. The temperature of the melt increases from 0°C to the mainstream temperature of 4°C while the melt is forming, detaching from ice, and mixing with mainstream. The slight difference in temperature between the melting fluid and mainstream flow causes a slight asymmetry between flows above and under ice. This also explains why the upper and lower separation points are not absolutely symmetrical. The absolute angle of the lower separation point is slightly greater than that of the upper separation point, as shown in Fig. 15.

The three cases in Fig. 14 are all for a high upstream temperature with $T_w=30°C$, $T_{i,0}=-20°C$, and $d_0=36$ mm. The initial Grashof number of the three cases is 6.8×10^6. They are at the water velocity of 0.01, 0.05, and 0.1 m/s ($Re_0=316$, 1579 and 3158). Therefore, the initial (Gr/Re^2) is higher at 68.1, 2.73 and

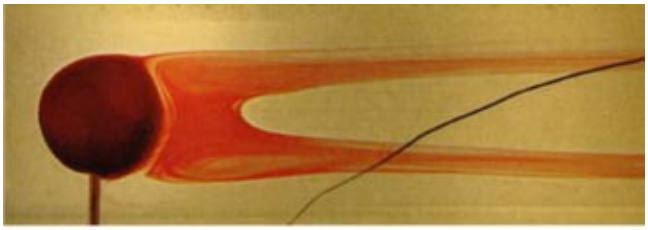

(a)

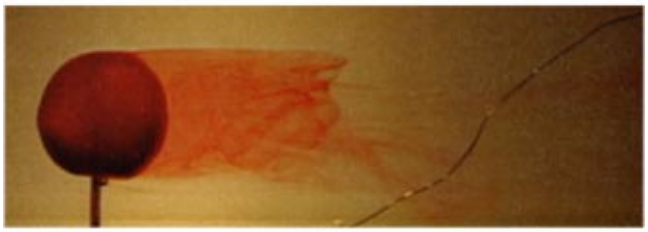

(b)

(c)

Fig. 13 Video images of melting dyed ice sphere at different water velocities: $T_w = 4°C$, $d_0 = 36$ mm, $T_{i,0} = -20°C$, $Gr_0 = 883$, $t^* = 0.3$: (*a*) $V_w = 0.01$ m/s, $Re_0 = 215$, $Gr_0/Re_0^2 = 0.019$, $t_{total} = 1542$ s; (*b*) $V_w = 0.05$ m/s, $Re_0 = 1077$, $Gr_0/Re_0^2 = 7.6 \times 10^{-4}$, $t_{total} = 816$ s; and (*c*) $V_w = 0.10$ m/s, $Re_0 = 2154$, $Gr_0/Re_0^2 = 1.9 \times 10^{-4}$, $t_{total} = 567$ s

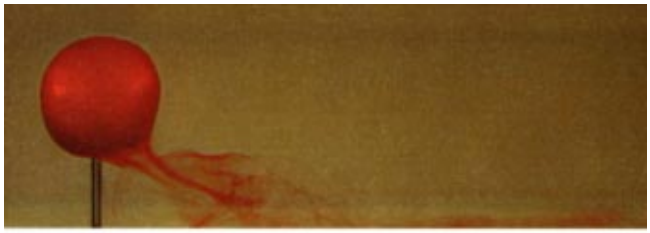

(a)

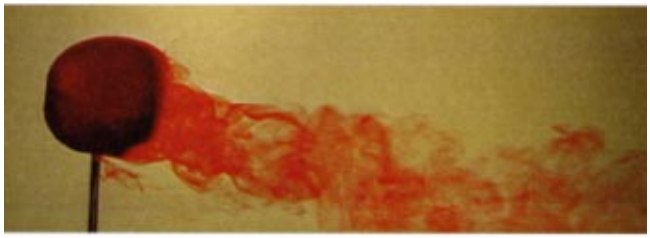

(b)

(c)

Fig. 14 Video images of melting, dyed ice sphere at different water velocities and a high water temperature: $T_w = 30°C$, $d_0 = 36$ mm, $T_{i,0} = -20°C$, $Gr_0 = 6.8 \times 10^6$, $t^* = 0.3$: (*a*) $V_w = 0.01$ m/s, $Re_0 = 316$, $Gr_0/Re_0^2 = 68.1$, $t_{total} = 209$ s; (*b*) $V_w = 0.05$ m/s, $Re_0 = 1579$, $Gr_0/Re_0^2 = 2.73$, $t_{total} = 141$ s; and (*c*) $V_w = 0.10$ m/s, $Re_0 = 3158$, $Gr_0/Re_0^2 = 0.682$, $t_{total} = 82$ s

0.682, respectively. The effect of free convection on the flow of melt is clearly displayed in Fig. 14(*a*), which shows that the strong downward flow at the mainstream velocity of 0.01 m/s causes the boundary layer to extend to the rear surface of ice sphere. Figures 14(*b*) and (*c*) show that the effect of free convection on the melt flow gradually decreases while the mainstream velocity increases. The resultant upper and lower separation points are very asymmetrical, as shown in Fig. 16.

Effect of Melting on the Flow Boundary Layer. The comparison tests are conducted to investigate the effect of melting process on the flow boundary layer over a sphere using an ice sphere and a plastic sphere under the same control conditions. The typical results are shown in Fig. 17 with melting and Fig. 18 without melting. Flow across a solid sphere starts to change the direction near the stagnation point much earlier than the flow with melting, as indicated in Fig. 17(*a*) and Fig. 18(*a*). The gradual change in flow direction near and within the boundary layer causes the normal velocity gradient to increase until reaching a uniform value before separation, as shown in Fig. 17(*b*) and Fig. 18(*b*). The boundary layer forms after flow turns around the stagnation (at about $\theta = 20$ deg with melting and $\theta = 25$ deg without melting). The velocity gradient increases further, causing a large negative value of ω_z to occur in the boundary layer, as shown in Fig. 17(*c*) and Fig. 18(*c*). The thickness of the boundary layer without melting is relatively uniform before the separation. In the melting case, the melt from ice discharges into the boundary layer, causing thickening of the boundary layer, especially in the range of $\theta = 40$ deg to 70 deg. This results in a relatively high melting rate in that region [13]. The melt from ice can form and stabilize the boundary layer pushing the separation point downstream. The separation point can be seen at about $\theta = 116$ deg in the case with melting (Fig. 17) and at about $\theta = 103$ deg in the case without melting (Fig. 18). The same test is repeated several times, and the same results are obtained within the experimental accuracy in the

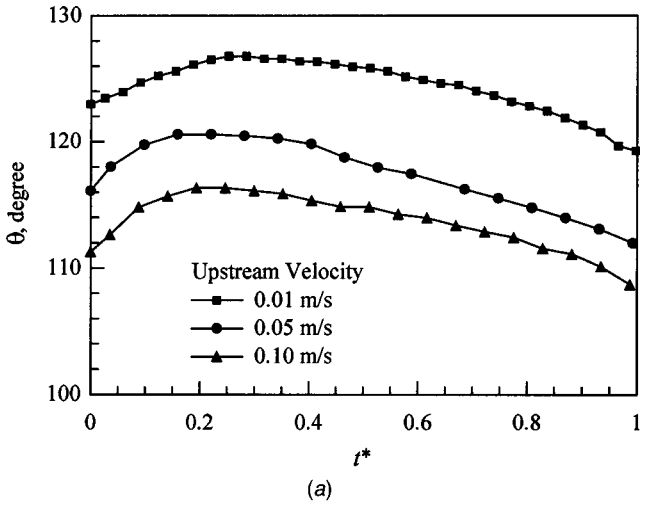

Fig. 15 Variation of flow separation locations with time at different upstream velocities in melting processes: $T_w=4°C$, $d_0=36$ mm, $T_{i,0}=-20°C$, $Gr_0=883$: (*a*) upper separation points; and (*b*) lower separation points.

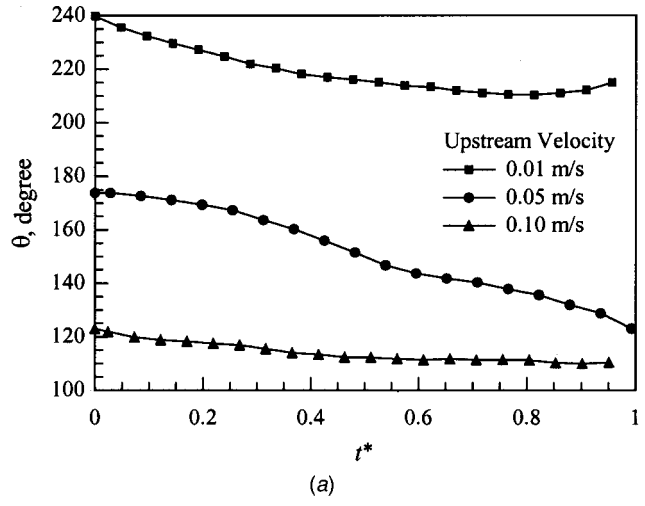

Fig. 16 Variation of flow separation locations with time at different upstream velocities in melting processes: $T_w=30°C$, $d_0=36$ mm, $T_{i,0}=-20°C$, $Gr_0=6.8\times10^6$: (*a*) upper separation points; and (*b*) lower separation points.

present study. To interpret this comparison, the following hypothesis is proposed. The melting, occurring at the bottom of the boundary layer, tends to mobilize the original solid surface, which effectively reduces the viscous effect, or reduces the vertical momentum exchange within the boundary layer as compared with a similar case without melting. This would cause a delay in flow separation. Melting also causes the solid surface to recede, resulting in thickening of the flow boundary layer before the separation point. It should be noted that in the above quantitative discussion about the comparison between melting and non-melting spheres, the ice sphere is at a controlled initial temperature of $-15°C$. The trend and hypothesis should remain the same even though the value of separation point may be different if the initial ice temperature is different. As a quantitative benchmark result, Fig. 19 illustrates numerical values of velocity components in x and y-directions along different x lines for a typical case.

Conclusions

Water flow around a melting ice sphere subject to forced or mixed convection is quantified with the aid of a PIV system. The characterization of the entire flow field around the ice sphere is achieved by both flow measurement and visualization of melting of a dyed ice sphere. The motion of the melt and the mixing of the melt with mainstream are analyzed qualitatively. Based on the experimental results, the following conclusions can be drawn:

1 Within the scope of the present study, the flow pattern around a melting ice sphere during the early melting period is typically rotational, qualitatively similar to the flow around a non-melting, isothermal solid with the formation and separation of flow boundary layer. The main difference lies on the interaction of melt discharge with mainstream flow. The melt advection and induced thermal diffusion alter the boundary layer and adjacent flow field quantitatively, especially during the later stage of melting.

2 The circulation in the wake enhances heat transfer between water and ice surface at the rear position of sphere. Therefore, the local melting rate increases, causing the shape at the rear to become flat. In turn, the flow pattern around the ice particle is also changed as a result of change in the curvature of the surface over the front of ice and the maximum radius in the traverse direction of mainstream flow. The separation of the flow boundary layer occurs at the position where the maximum radius of the melting particle aligns in the traverse direction of mainstream flow.

3 When the mainstream velocity increases, the influence of the

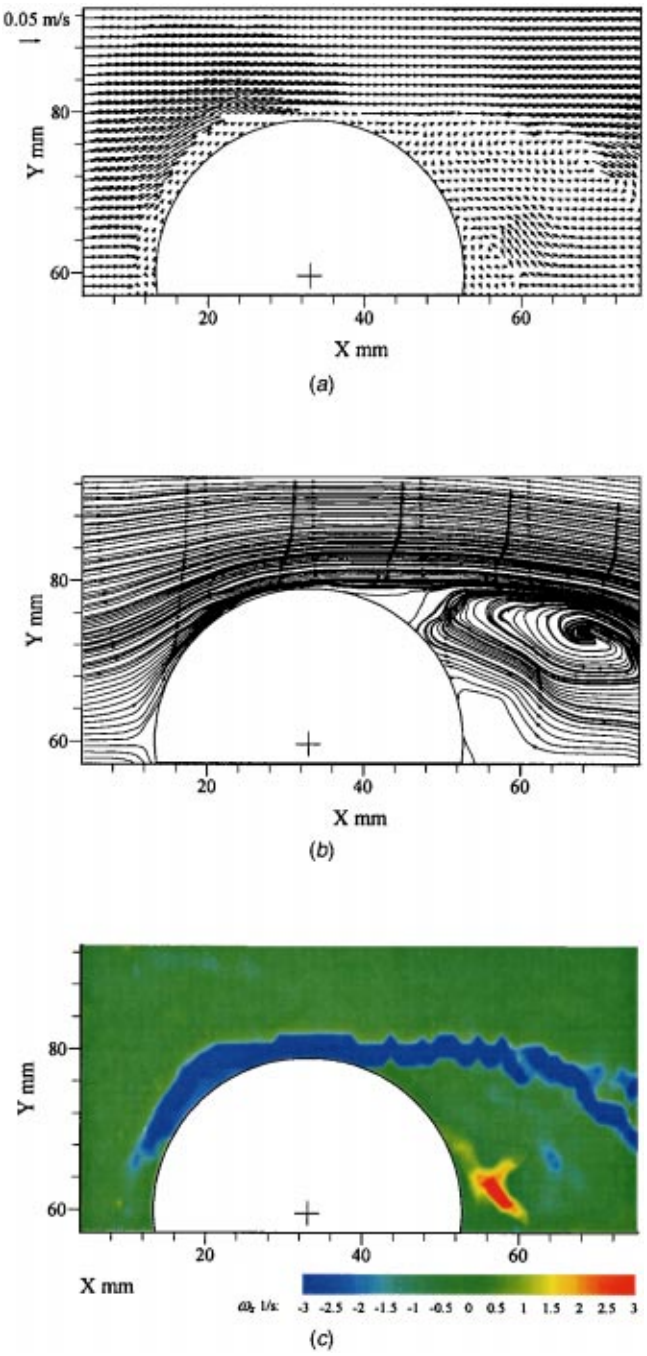

Fig. 17 Flow field around a melting ice sphere in the axial plane: $t^*=0.0079$, $V_w=0.05$ m/s, $T_w=4°C$, $d_0=36$ mm, $T_{i,0}=-15°C$, $Re_0=1077$, $Gr_0=883$, $Gr_0/Re_0^2=7.6\times10^{-4}$, $t_{total}=760$ s: (*a*) velocity vector distribution; (*b*) streamline; and (*c*) *z*-component of rotation vector.

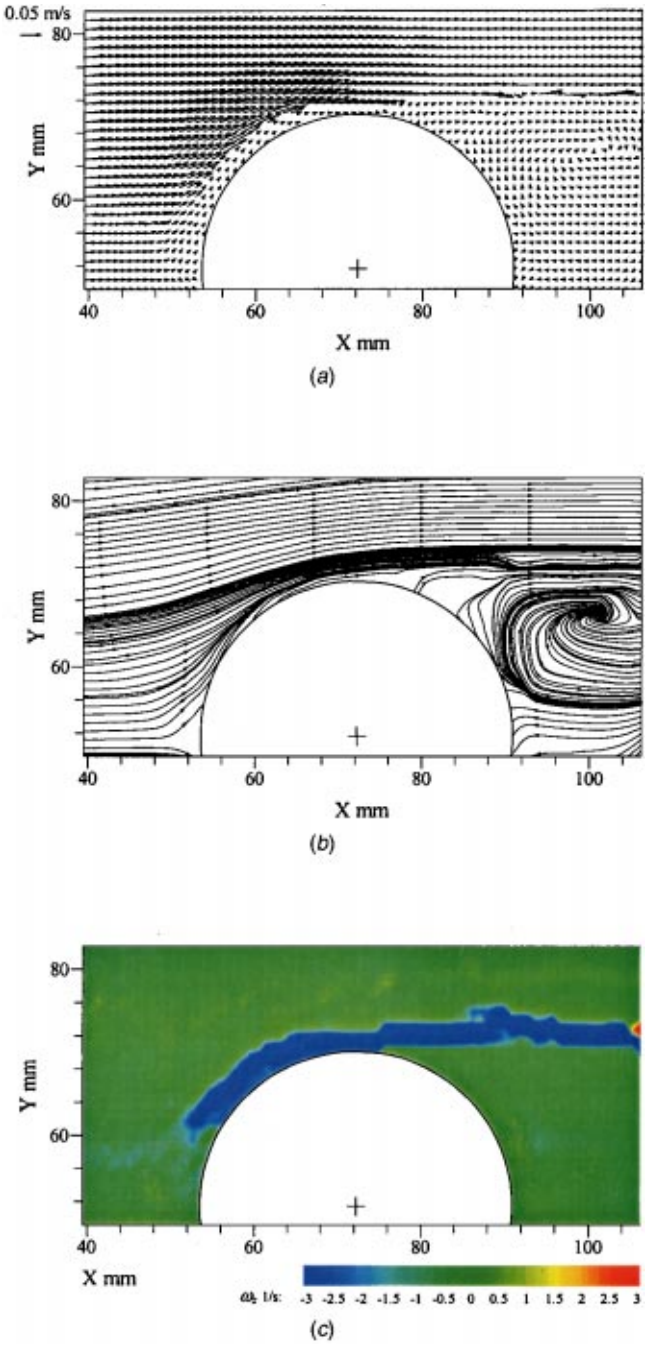

Fig. 18 Flow field around a plastic sphere in the axial plane: $V_w=0.05$ m/s, $T_w=4°C$, $d_0=36$ mm, $T_i=4°C$, $Re_0=1149$, $Gr_0=0$, $Gr_0/Re_0^2=0$: (*a*) velocity vector distribution; (*b*) streamline; and (*c*) *z*-component of rotation vector.

ice sphere's presence on the mainstream becomes stronger. The resulting location of the boundary layer separation point moves upstream under the present experimental conditions. The circulation behind the ice becomes faster and the circulation region becomes bigger with the increase in the mainstream velocity. The disturbance behind the circulation region and mixing of melt with the mainstream in the wake are enhanced. The mixing region in the wake becomes shorter.

4 The effect of free convection on the flow pattern around the ice sphere increases as the parameter (Gr/Re^2) increases. For the range of experiments conducted, the free convection cannot be considered negligible when $Gr/Re^2>0.682$. The stronger free convection is, the more rear surface of ice sphere the melting layer covers, and the more downward the resulting wake moves. The free convection decreases the strength of flow circulation in the wake.

5 The flow across a non-melting solid sphere starts changing the direction near the stagnation point much earlier than the flow interacting with a melting sphere. The thickness of the boundary layer around a non-melting sphere is relatively uniform before the separation. The melt from the ice can thicken and stabilize the

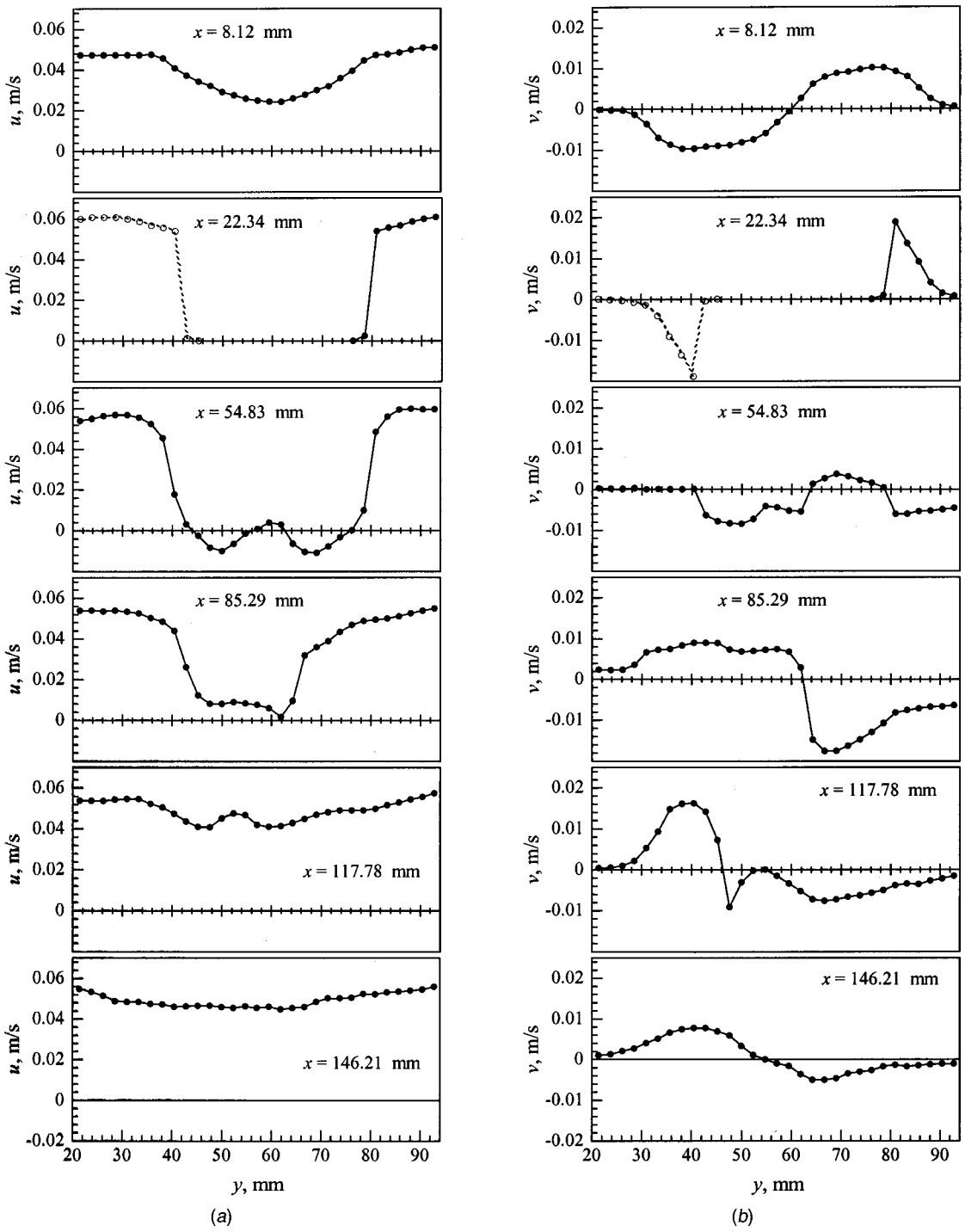

Fig. 19 Velocity components in x and y-direction along different x lines around a melting sphere: $t^* = 0.0079$, $V_w = 0.05$ m/s, $T_w = 4°C$, $d_0 = 36$ mm, $T_{i,0} = -15°C$, $Re_0 = 1077$, $Gr_0 = 883$, $Gr_0/Re_0^2 = 7.6 \times 10^{-4}$, $t_{total} = 760$ s. (Broken lines indicate a projected result below the ice sphere where no PIV data are available.): (*a*) velocity component in x-direction; and (*b*) velocity component in y-direction.

boundary layer, and can also delay its separation from the ice surface as compared to the case of an isothermal, non-melting sphere.

Acknowledgments

Support from NASA (Grant No. NAG3-1797) and NSF (Grant No. HR-97206268) is greatly appreciated.

Nomenclature

d = diameter, m
Gr = Grashof number
Re = Reynolds number
St = Stokes number
T_i = temperature of ice, °C
T_w = upstream temperature of water, °C

t = time, s
t_{total} = total time, s
t^* = dimensionless time, t/t_{total}
u = velocity in x-direction, m/s
v = velocity in y-direction, m/s
V_w = upstream velocity of water, m/s
x, y = Cartesian coordinates, m

Greek

θ = angular coordinate relative to stagnation point, degree
τ_f = characteristic time of fluid, s
τ_p = relaxation time of particle, s
ω_z = z-component of rotation vector, 1/s

Subscripts

0 = initial

References

[1] Tkachev, A. G., 1953, ''Heat hExchange in Melting and Freezing of Ice,'' in *Problem of Heat Transfer During Change of Phase: A Collection of Articles*, AEC-TR-3405, translated from Russian, State Power Press, pp. 169–178.

[2] Schenk, J., and Schenkels, F. M., 1968, ''Thermal Free Convection from an Ice Sphere in Water,'' Appl. Sci. Res., pp. 465–476.

[3] Vanier, C. R., and Tien, C., 1970, ''Free Convection Melting of Ice Spheres,'' AIChE J., **16**, pp. 76–82.

[4] Anselmo, A., Prasad, V., and Koziol, J., 1991, ''Melting of a Sphere when Dropped in a Pool of Melt with Applications to Partially-Immersed Silicon Pellets,'' *Heat Transfer in Metals and Containerless Processing and Manufacturing*, ASME HTD, **162**, pp. 75–82.

[5] Anselmo, A., Prasad, V., Koziol, J., and Gupta, K. P., 1993, ''Numerical and Experimental Study of a Solid-pellet Feed Continuous Czochralski Growth Process for Silicon Single Crystals,'' J. Cryst. Growth, **131**, pp. 247–264.

[6] Mukherjee, M. K., Shih, J., and Prasad, V., 1994, ''A Visualization Study of Melting of an Ice Sphere in a Pool of Water,'' ASME 94-WA/HT-14.

[7] McLeod, P., Riley, D. S., and Sparks, R. S. J., 1996, ''Melting of a Sphere in Hot Fluid,'' J. Fluid Mech., **327**, pp. 393–409.

[8] Eskandari, V., 1981, ''Forced Convection Heat Transfer from Ice Spheres in Flowing Water,'' Master's thesis, University of Toledo, Toledo, OH.

[9] Eskandari, V., Jakubowski, G. S., and Keith, T. G., 1982, ''Heat Transfer from Spherical Ice in Flowing Water,'' ASME 82-HT-58.

[10] Aziz, S. A., Janna, W. S., and Jakubowski G. S., 1995, ''Forced Convection Heat Transfer From an Isothermal Melting Ice Sphere Submerged in Flowing Water,'' *Proc. ASME Heat Transfer Division*, **1** ASME, New York, pp. 213–217.

[11] Hao, Y. L., and Tao, Y. X., 1999, ''Convective Melting of a Solid Particle in a Fluid,'' *Proc. 3rd ASME/JSME Joint Fluids Engineering Conference*, P. A. Pfund et al., eds., ASME, New York.

[12] Hao, Y. L., and Tao, Y. X., 1999, ''Heat Transfer Characteristics in Convective Melting of a Solid Particle in a Fluid,'' *Proc. ASME Heat Transfer Division*, **2** L. C. Witte, ed., ASME, New York, pp. 207–212.

[13] Hao, Y. L., and Tao, Y. X., 2000, ''Local Melting and Heat Transfer Characteristics in Convective Melting of a Solid Particle in a Fluid,'' *Proc. 2000 National Heat Transfer Conference*, S. C. Yao et al., eds., ASME, New York.

[14] Adrian, R. J., 1986, ''Multi-Point Optical Measurements of Simultaneous Vectors in Unsteady Flow—A Review,'' Int. J. Heat Fluid Flow, **7**, pp. 127–145.

[15] Kline, S. L., and McClintock, F. A., 1953, ''Describing Uncertainties in Single-Sample Experiments,'' Mech. Eng. (Am. Soc. Mech. Eng.), **75**, pp. 3–8.

[16] Hassan, Y. A., Schmidl, W., and Ortiz-Villafuerte, J., 1998, ''Investigation of Three-Dimensional Two-Phase Flow Structure in a Bubbly Pipe Flow,'' Meas. Sci. Technol., **9**, pp. 1–18.

[17] TSI, 1999, *Instruction Manual of INSIGHT™ 2 & INSIGHT™ Stereo Particle Image Velocimetry Software (Version 2)*, TSI Incorporated, St. Paul; MN.

[18] TSI, 1999, *Reference Manual of the PIV System*, TSI Incorporated, St. Paul, MN.

Numerical Study on the Influence of Radiative Properties in Porous Media Combustion

Isabel Malico
E-mail: isabel@navier.ist.utl.pt
Instituto Superior Técnico,
Mechanical Engineering Department,
Av. Rovisco Pais, 1049-001 Lisboa, Portugal

José Carlos F. Pereira
E-mail: jose@pomar.ist.utl.pt
Mem. ASME
Instituto Superior Técnico,
Mechanical Engineering Department,
Av. Rovisco Pais, 1049-001 Lisboa, Portugal

The importance of radiation and of radiative properties (extinction coefficient, scattering albedo and scattering phase function) in inert porous media combustion was numerically assessed. The two-dimensional mass, momentum, solid and gas energy, and species conservation equations were solved. Emission, absorption and scattering by the porous media were taken into consideration and the S_6 approximation was used to solve the radiative transfer equation. The temperature profiles are very sensitive to a perturbation in the radiative coefficients, particularly when the scattering albedo is increased. When compared to the isotropic scattering assumption, using zero, large diffuse spheres', linear-anisotropic and modified Henyey–Greenstein phase functions leads to an average temperature difference no bigger than 7 percent. When radiation is neglected, the predicted temperature profile is not in agreement with the available experimental values.
[DOI: 10.1115/1.1389059]

Keywords: Heat Transfer; Porous Media; Properties; Radiation; Scattering

Introduction

Porous burners are characterized by high efficiencies, high power densities, large dynamic ranges and low NO_x and CO emissions, e.g., [1,2]. Their porous matrixes can be made of several materials: packed beds of spheres, reticulated porous ceramics, metallic fibres, etc. However, reticulated porous ceramics have a set of characteristics, which makes them particularly well suited for application to this kind of burners. These materials have several advantages over other forms of porous materials: good thermal resistance, high surface area per unit volume and high porosity, which leads to a smaller pressure drop.

Numerical design tools including combustion and heat transfer models, and thermal properties of the reticulated porous ceramics are needed for a rapid development of this technology. In this context, the knowledge of the radiative properties (extinction coefficient, scattering albedo and scattering phase function) of reticulated porous ceramics is required. The numerical prediction of these properties is very difficult because of the complex reticulated structure of the medium, which is itself poorly characterized. Fundamental treatments of radiative interactions on a microscopic scale through modeling of radiation absorption and reflection from the struts and strut interception nodes of the solid portion of the reticulated structure has not yet been attempted [1].

Despite some works dedicated to the measurement of the radiative properties having been reported, e.g., [3,4], the knowledge of the radiative properties of reticulated porous ceramics is limited and a good database is needed for the development and use of mathematical models [4]. As a consequence, several models involving the solution of the radiative transfer equation in high-temperature ceramic foams used assumed radiative properties and/or performed parametric studies. Common assumptions are considering isotropic scattering, e.g., [5–8], or no scattering at all, e.g., [9,10].

Yoshizawa et al. [9] stressed the relevance of the porous medium absorption coefficient and total optical thickness in calculating the thermal structures (temperature profiles, radiant energy density, etc.) and the position of the flame within the porous medium for the one-layer porous burner studied. They showed that an increase in the absorption coefficient resulted in a thickening of the reaction zone and in a decrease in the maximum temperature and burning velocity. They also showed that the burning velocity and maximum temperature for a thicker medium were larger than for a thinner medium. In his study, Baek [11] stated that, as the absorption coefficient decreases, the maximum temperature increases and the reaction front gets thinner and is displaced upstream. Sathe et al. [5] verified that the radiative characteristics of the porous matrix had a considerable effect on flame speed and stability. They showed that decreasing the scattering albedo caused the temperatures in the preheat and reaction zones to increase and that the peak temperature and flame speed had a maximum for a given optical thickness, i.e., they decreased as the optical thickness was either decreased or increased. Hsu et al.'s predictions [10] showed that the absorption coefficient had a significant effect on the flame characteristics. For the one layer porous burner studied, increasing the absorption coefficient, decreased the thickness of the preheating zone, which resulted in a decrease in the peak flame temperature. Fu [12] verified that the temperatures and the radiation efficiency of the porous radiant burner studied had a small sensitivity to the extinction coefficient, single scattering albedo and forward scattering fraction of the porous solid, if the flame was stabilized in the flame support layer and the opacity of this layer was sufficiently large. Lim [7] concluded that the scattering albedo was the most affecting factor on flame structure. He showed that increasing the scattering albedo in the post-flame region of a two-layer porous burner resulted in an increase of the gas and solid temperatures at the post-flame zone. However, increasing the scattering albedo at the pre-heating zone resulted in a decrease in the peak and post-flame temperatures. Malico and Pereira [13] studied a porous burner similar to the one studied in this work. They showed that the absorption coefficient affected the most the centerline temperature distribution: increasing the absorption coefficient resulted in a decrease in the post-flame temperatures; but increasing the scattering coefficient had no significant changes in the temperature profile.

In previous work, a two-dimensional code to treat premixed combustion in inert porous media was developed. A finite difference/control volume approach was used to solve the mass, momentum, energy and species conservation equations. Thermal non-equilibrium between the gas and the solid phases was taken into account by using separate energy equations for these two

Contributed by the Heat Transfer Division for publication in the JOURNAL OF HEAT TRANSFER. Manuscript received by the Heat Transfer Division October 7, 1999; revision received March 8, 2001. Associate Editor: J. P. Gore.

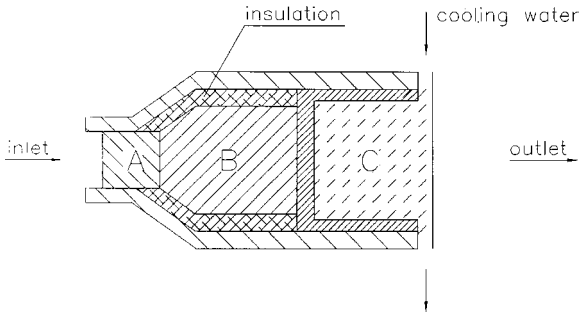

Fig. 1 Sketch of the porous burner with integrated heat exchanger prototype modeled in this study

phases coupled through a convective heat transfer term. The combustion reaction was modeled both with a single step reaction [8] and with a skeletal mechanism [14]. The porous media was assumed to emit, absorb and isotropically scatter radiation and the axissymmetric dicrete ordinates method was applied to solve the radiative transfer equation. Centerline temperatures were compared with measurements for two different porous burner prototypes proving that the algorithm is a valid tool for engineering design [9,13,14]. CO and NO measurements were compared with experimental values in [14].

The main objective of this work is to infer the importance of radiation and radiative properties for a porous burner prototype developed at LSTM—Erlangen [2]. A sensitivity study to the extinction coefficient and scattering albedo was performed with the objective of finding out to what extent do they influence the numerical results. For the purpose, the extinction coefficient was perturbed by ± 50 percent and the scattering albedo by about ± 30 percent. The influence of the phase function was also assessed by investigating several phase functions: zero, unity, large diffuse spheres', linear-anisotropic and modified Henyey-Greenstein phase functions. The results obtained were compared in terms of differences in the temperature profiles, radiative flux per control volume, flame front location and peak temperature. The case where radiation is neglected was also studied and the results compared with the experimental values of Ernd [15].

Porous Burner Prototype

The 10 kW porous burner prototype considered in this study was developed and tested at LSTM—Erlangen [2] (see Fig. 1). Premixed methane enters the burner through the preheating zone (region A), then combustion occurs in the combustion zone (region B) and afterwards the hot combustion products flow through a heat exchanger zone (region C) and heat the cold water that flows inside the heat exchanger. The preheating and heat exchanger zones are filled with 5 and 3 mm alumina spheres and the combustion region with a 10 ppi SiC ceramic foam. The maximum internal diameter of this burner is 74 mm, the minimum 40 mm and the total length of the porous matrixes is 260 mm (region A has 35 mm, region B 105 mm and region C 120 mm). The burner walls are water cooled, but the combustion region is insulated from the cold walls by a 3 mm ceramic insulation, in order to prevent the CO formation due to a low wall temperature [2]. The heat exchanger is a water-cooled fined structure and was not integrated in region B to avoid high CO formation resulting from the contact of the reaction radicals with the cold surface of the heat exchanger [16].

Mathematical Formulation

Two-dimensional, steady, laminar, axisymmetric and Newtonian flow in inert and noncatalytic porous media was assumed.

Continuity Equation.

$$\nabla \cdot (\rho \mathbf{v}) = 0 \tag{1}$$

***z*-Momentum Equation.**

$$\nabla \cdot (\rho u \mathbf{v}) = -\frac{\partial p}{\partial z} + \nabla \cdot (\mu \nabla u) - \frac{\Delta p}{\Delta L} \tag{2}$$

***r*-Momentum Equation.**

$$\nabla (\rho v \mathbf{v}) = -\frac{\partial p}{\partial r} + \nabla \cdot (\mu \Delta v) - \frac{\Delta p}{\Delta L} \tag{3}$$

Gas Phase Energy Equation.

$$\nabla \cdot (\rho \mathbf{v} h) = \nabla \cdot \left(\frac{\varepsilon k_f}{c_p} \nabla h \right) + H(T_s - T_f) + \Delta H_c S_{fu} \tag{4}$$

Solid Phase Energy Equation.

$$0 = \nabla \cdot ((1-\varepsilon) k_s \nabla T_s) + H(T_f - T_s) - \nabla . \mathbf{q} \tag{5}$$

Fuel Conservation Equation.

$$\nabla \cdot (\rho \mathbf{v} Y_{fu}) = \nabla \cdot (\rho D_{AB} \nabla Y_{fu}) - S_{fu} \tag{6}$$

Oxygen Conservation Equation.

$$\nabla \cdot (\rho \mathbf{v} Y_{ox}) = \nabla \cdot (\rho D_{AB} \nabla Y_{ox}) - s_{ox} S_{fu} \tag{7}$$

The Ergun model [17] modified by Macdonald et al. [18] was used to account for the pressure loss due to the porous matrix, $\Delta p / \Delta L$.

$$\frac{\Delta p}{\Delta L} = 180 \frac{(1-\varepsilon)^2}{\varepsilon^3} \frac{\mu u_i}{d_p^2} + 1.8 \frac{1-\varepsilon}{\varepsilon^3} \frac{\rho |\mathbf{v}| u_i}{d_p} \tag{8}$$

Since locally, the solid and gas temperature may be different, separate energy equations for the solid and the gas phases were used. These two equations were coupled through a convective heat transfer term that accounts for the convective heat transfer between the two phases. The correlations adopted in this study for this coefficient were taken from [19] for the packed beds of spheres and from [20] for the SiC foam. In [14]. The authors analyzed the sensitiveness of the results to this parameter. A ± 50 percent perturbation in this coefficient yielded a 4 percent difference in the maximum temperature.

The combustion reaction was described by the irreversible one-step reaction:

$$CH_4 + 2\Psi(O_2 + 3.76N_2) \rightarrow CO_2 + 2H_2O + 2(\Psi - 1)O_2 + 7.52\Psi N_2 .$$

The location of the flame was not assigned *a priori*, being a result of the calculations. The rate of fuel consumption, S_{fu}, was determined by a one-step Arrehnius rate equation [21].

$$S_{fu} = A \rho^2 Y_{fu} Y_{ox} \exp[-E/RT], \tag{9}$$

where the pre-exponential factor, A, and the activation energy, *E*, were taken from [22] and are $1 \times 10^{10}\ \mathrm{m^3\ kg^{-1}\ s^{-1}}$ and $1.4 \times 10^8\ \mathrm{J\ kmol^{-1}}$, respectively.

Radiation. Gas radiation was not considered since the solid has a high emissivity when compared to the gas. Emission, absorption and scattering by the porous media were considered. To determine the radiative heat flux, the solid and fluid phases were treated as a single continuum homogeneous phase and the radiative transfer equation, Eq. (10), was solved. This equation can be derived by making an energy balance on the radiative energy traveling in a given direction within an infinitesimal control volume. (e.g., [23] present the fundamental mathematical development of the radiative transfer equation for a homogeneous medium).

Table 1 Base values used for the radiative properties

Porous Medium	Absorption coefficient, κ	Scattering coefficient, σ_s	Phase function, Φ
Packed Bed of Spheres	$a\pi R^2 N$	$\rho\pi R^2 N$	$\frac{8}{3\pi}(\sin\theta-\theta\cos\theta)$
SiC foam	28	66	1

$$\frac{dI_\eta}{ds}=\hat{\mathbf{s}}\cdot\nabla I_\eta=\kappa I_{b\eta}-\beta_\eta I_\eta+\frac{\sigma_{s\eta}}{4\pi}\int_{4\pi} I_\eta(\hat{\mathbf{s}})\Phi_\eta(\hat{\mathbf{s}}_i,\hat{\mathbf{s}})d\Omega_i \tag{10}$$

The first term accounts for the change of intensity, I, in a given direction, $\hat{\mathbf{s}}$, and is equal to the summation of the contributions from emission (first term on the right hand side), absorption and scattering away from the direction $\hat{\mathbf{s}}$ (second term on the right hand side), and scattering into the direction $\hat{\mathbf{s}}$ (third term on the right hand side). κ_η is the linear absorption coefficient, $\sigma_{s\eta}$ the scattering coefficients, $\beta_\eta=\kappa_\eta+\sigma_{s\eta}$ the extinction coefficient and Φ_η the scattering phase function. The scattering albedo is defined as the ratio between the scattering and extinction coefficients. Each porous medium section is assumed to be gray and homogeneous. After solving the radiative transfer equation and obtaining the radiative intensity, the source term of the solid energy conservation equation is obtained by Eq. (11).

$$\nabla\cdot\mathbf{q}=\kappa\left(4\pi I_b-\int_{4\pi} I d\Omega\right) \tag{11}$$

The base values for the radiative properties, presented in Table 1, were taken from [4] for the SiC foam and calculated considering large independent diffusely reflecting spheres for the packed beds of spheres [23]. Note that the properties of [4] were determined from reflectance and transmittance measurements on test specimens using inverse analysis techniques and assuming isotropic scattering. Therefore, these properties should only be used while assuming isotropic scattering. Mital et al. [4] determined these properties in the 1300–1400 K range and chose the two-flux approximation to solve the inverse radiation problem. Since these results are used with other solution method, the S_6 approximation, additional uncertainty in the radiative properties is present. This stresses the need for the sensitivity analysis performed in this study.

In the sensitivity study of porous media combustion to the scattering and absorption coefficients performed in this study, the scattering phase function was kept constant (as listed in Table 1) and these coefficients perturbed by ± 50 percent and around ± 30 percent, respectively. When the influence of the SiC phase function was studied, the scattering and absorption coefficients were kept constant and several phase functions were investigated: $\Phi=0$ (no scattering), $\Phi=1$ (isotropic scattering), the phase function for large diffuse spheres, Eq. (12), the linear-anisotropic phase function, Eq. (13), and the modified Henyey-Greenstein phase function, Eq. (14).

$$\Phi(\theta)=\frac{8}{3\pi}(\sin\theta-\theta\cos\theta) \tag{12}$$

$$\Phi(\theta)=1+g\cos\theta, \tag{13}$$

where g is a dimensionless asymmetry factor and $-1\leqslant g\leqslant+1$. For the case of isotropic scattering the asymmetry factor is equal to zero. If the medium scatters more radiation into the forward directions g is positive, if, on the contrary, it scatters more radiation into the backscattering direction g is negative. The results obtained in this study considered $g=1$.

The modified Henyey-Greenstein phase function [24] is given by Eq. (14).

$$\Phi_{hg}(\lambda,\theta)=f_{is,\lambda}+(1-f_{is,\lambda})\frac{1-g_{hg,\lambda}^2}{(1+g_{hg,\lambda}^2-2g_{hg,\lambda}\cos\theta)^{1.5}}, \tag{14}$$

where $-1\leqslant g_{hg,\lambda}\leqslant+1$. A variety of forward, isotropic and backscattering combinations can be modeled by adjusting the parameters $f_{is,\lambda}$ and $g_{hg,\lambda}$. Hendricks and Howell [3] used an inverse analysis technique (with the S_6 approximation) to recover the spectral radiative coefficients and phase function parameters for 10 ppi oxide-bonded silicon carbide (OB SiC). Since the radiative coefficients and modified Henyey–Greenstein phase function parameters exhibited only small spectral variations for 10 ppi OB SiC, an average value over the wavelengths was considered in this study. Therefore, the absorption coefficient was set equal to 150 m^{-1}, the scattering coefficient to 460 m^{-1}, f_{is} to 0, and g_{hg} to 0.7. The phase functions used in this study can be seen in Fig. 2.

The radiative coefficients and the scattering phase function should be compatible and retrieved simultaneously from an inverse analysis. That is the case for the radiative coefficients of the unity and the modified Henyey-Greenstein phase functions used in this study. However, for the zero, linear-anisotropic and large diffuse spheres' phase function, radiative data obtained simultaneously is not available. In these cases, the phase functions were tested using the base values of the extinction coefficient and scattering albedo (except for the no-scattering case where the extinction is only due to absorption). Despite the additional error imposed, it is the authors' belief that it is worthwhile comparing the results obtained with the several phase functions.

Problem Formulation and Boundary Conditions

The following boundary conditions were used:

At the Inlet.

$$u=u_{in};\ \ v=0;\ \ T_f=T_{f,in};Y_{fu}=Y_{fu,in};Y_{ox}=Y_{ox,in};(1-\varepsilon)k_s\frac{\partial T_s}{\partial z}=-\varepsilon_r\sigma(T_s^4-T_0^4);\ \ I=\frac{\sigma T_s^4}{\pi}, \tag{15}$$

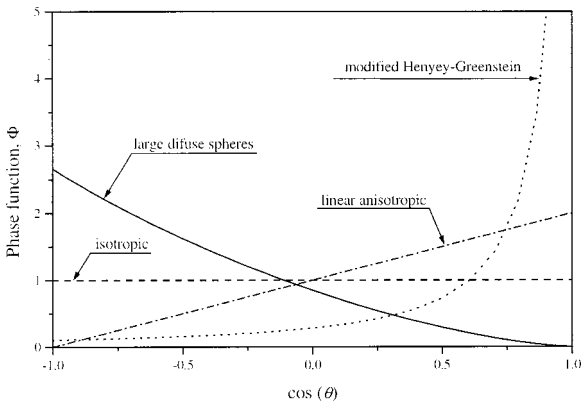

Fig. 2 Phase functions analyzed in this study

Table 2 Maximum difference in the temperature and in the radiative flux obtained with the perturbed and base radiative properties for a 2 kW power and a 1.5 excess air coefficient

Case	1	2	3	4	5	6	7	8
β	+50%	-50%	0	0	+50%	+50%	-50%	-50%
ω	0	0	+30%	-30%	+30%	-30%	+30%	-30%
Temperature	5.2%	9.4%	56.7%	10.9%	57.9%	16.5%	39.6%	3.1%
Flux	50.2%	201.8%	330.7%	46.5%	272.4%	71.2%	51.4%	101.0%

where T_0, the temperature of the surroundings, is set equal to 300 K to simulate a cold environment and ε_r is assumed equal to the absorptivity and considered 1. The emittance from the whole porous layer was considered because the solid energy equation and the radiative transfer equation are strongly linked through the outlet solid iterative temperature values.

At the Outlet.

$$\frac{\partial u}{\partial z}=\frac{\partial v}{\partial z}=\frac{\partial T_f}{\partial z}=\frac{\partial Y_{fu}}{\partial z}=\frac{\partial Y_{ox}}{\partial z}=0;(1-\varepsilon)k_s\frac{\partial T_s}{\partial z}$$

$$=-\varepsilon_r\sigma(T_s^4-T_0^4);\quad I=\frac{\sigma T_s^4}{\pi} \tag{16}$$

At the axis, symmetry conditions were imposed

$$\frac{\partial u}{\partial r}=v=\frac{\partial T_s}{\partial r}=\frac{\partial T_f}{\partial r}=\frac{\partial Y_{fu}}{\partial r}=\frac{\partial Y_{ox}}{\partial r}=0 \tag{17}$$

At the heat exchanger surface and burner walls, no-slip and impenetrability conditions were imposed on the momentum equations. These surfaces were considered opaque, diffusely emitting and reflecting; therefore, the boundary conditions for the radiative transfer equation are expressed as

$$I=\varepsilon_w I_w+\frac{\rho_w}{\pi}\int_{\mathbf{n}\cdot\mathbf{s}<0} I|\mathbf{n}\cdot\mathbf{s}|d\Omega. \tag{18}$$

The burner wall in the combustion region is considered to be adiabatic but, in the other zones, the walls are water-cooled. The heat flux to the cooled surfaces is given by

$$q=-\left(k_s\frac{\partial T_s}{\partial n}+k_f\frac{\partial T_f}{\partial n}\right)=\frac{T-T_c}{R_t}. \tag{19}$$

Numerical Method

The finite difference/control volume approach [25] in an axisymmetric cylindrical geometry was used as the numerical method to solve the set of governing equations presented in the mathematical formulation section. The radiative transfer model used is the discrete ordinates method (S_6 approximation with the step scheme). In this method, the radiative transfer equation is solved for a set of n different directions $\hat{\mathbf{s}}_i$, $i=1,2,\ldots,n$.

Each direction is associated with a solid angle where the radiative intensity is assumed constant. The number of directions considered depend on the approximation used (For the S_6 approximation, 48 directions are considered). After the integrals over direction being replaced by numerical quadratures, the radiative transfer equation becomes

$$\hat{s}_i\cdot\nabla I(\mathbf{r},\hat{\mathbf{s}}_i)=\kappa(\mathbf{r})I_b(\mathbf{r})-\beta(\mathbf{r})I(\mathbf{r},\hat{\mathbf{s}}_i)$$

$$+\frac{\sigma_s(\mathbf{r})}{4\pi}\sum_{j=1}^{n} w_j I(\mathbf{r},\hat{\mathbf{s}}_i)\Phi(\mathbf{r},\hat{\mathbf{s}}_i,\hat{\mathbf{s}}_j)\quad i=1,2,\ldots n. \tag{20}$$

Since the radiative calculations are time consuming, the radiative heat flux is not updated on every iteration, but only every 5 iterations (When compared to the case where the radiative heat transfer is neglected, solving the radiative transfer equation every iteration increases the running time 19 times).

The number of grid nodes used were 132×20 and the solution was considered to have been reached when the sum of the normalized residuals was lower than 1 percent, which typically was achieved in around 10,000 iterations.

The model presented in this paper for the calculation of combustion and heat transfer in porous media burners was validated through a comparison of the centerline temperatures obtained numerically and experimentally [8]. The results have demonstrated that the algorithm is a valid tool for engineering design.

Results and Discussion

The sensitivity analysis presented in this section was performed for the case of a 2 kW power and a 1.5 excess air ratio. In the next sub-section, the influence of the radiative coefficients is assessed. The extinction coefficient was perturbed ±50 percent and the scattering albedo around ±30 percent. The results obtained were compared in terms of temperature and radiative flux per control volume differences, flame front location and peak temperature. After this sensitivity study, in the scattering phase function subsection, five different phase functions (zero, unity, large diffuse spheres', linear-anisotropic and Henyey-Greenstein phase functions) were compared. At the end of this section, temperature predictions where radiation was and was not considered were compared with the experimental values of [15].

If multi-step kinetics were considered, the temperature predictions would improve [26]. However, the computational time required to obtain two-dimensional predictions using multistep kinetics is much higher than the one required to obtain predictions with a 1-step reaction and a sensitivity study like the one presented in this work, would have been prohibitive. The authors preferred to concentrate on the sensitivity study itself rather than on the accuracy of the temperature profiles because the predicted temperature field is close enough to the experimental values to be able to draw conclusions about the influence of the radiative properties.

Extinction Coefficient and Scattering Albedo. The extinction coefficient was perturbed by ±50 percent and the scattering albedo by about ±30 percent. While performing this sensitivity study, the scattering phase functions were kept constant and equal to the ones listed in Table 1. The radiative properties of all the porous layers were perturbed simultaneously. When, for example, the extinction coefficient of region A was increased by 50 percent, the extinction coefficients of layers B and C were also increased by 50 percent.

The differences in the temperatures and in the radiative fluxes at each control volume between the base and perturbed calculations were determined. In Table 2, the maximum values of these differences are shown. The very high perturbation in the radiative flux is less noticeable in term of temperature difference, although the latter cannot be neglected. For example, in case 3, when the scattering albedo is perturbed by around 30 percent, the maximum difference between the radiative flux reaches 330.7 percent, while the maximum temperature difference is 56.7 percent.

The maximum temperature and radiative flux differences is not sufficient to characterize the perturbation in the temperature and radiative flux fields. For this reason, in Table 3, the average differences in the control volume temperature and in the radiative flux between the base and perturbed calculations are presented. Increasing the scattering albedo (cases 3, 5, and 7) is responsible

Table 3 Average difference in the temperature and in the radiative flux obtained with the perturbed and base radiative properties for a 2 kW power and a 1.5 excess air coefficient

Case	1	2	3	4	5	6	7	8
Temperature	2.2%	4.7%	14.3%	5.1%	11.6%	7.2%	18.4%	1.3%
Flux	8.9%	23.3%	55.5%	16.4%	42.2%	23.0%	82.3%	8.3%

for the highest perturbations in the temperature profiles. When the scattering albedo is increased by around 30 percent, the packed beds of spheres become a purely scattering medium and the SiC foam a nearly purely scattering medium (the absorption coefficient is almost zero). In this case, the radiative heat transfer from the flame front to the up and downstream regions decreases, thus leading to an increase in the post-flame temperatures. The post-flame region is, precisely, the zone where the biggest differences in the temperature profiles occur (In the other regions, the differences are much smaller).

In Figure 3, the predicted centerline gas temperature profile obtained with the base radiative coefficients is compared to the one obtained with the extinction coefficient and scattering albedo increased by 50 and around 30 percent, respectively (case 5). It can be seen that the major temperature differences are located in the flame and post-flame regions. The maximum centerline temperature differences occur in the vicinity of the heat exchanger (the heat exchanger is located for $z \geqslant 146$ mm) and are of around 9 percent. In Figure 4, also for case 5, the predicted gas temperature profile at $r = 33$ mm, obtained with the base coefficients is compared to the one obtained with the perturbed extinction coefficient and scattering albedo. The maximum temperature differences in the post-flame region before the heat exchanger is around 10 percent (similar to the centerline results), however the highest temperature differences occur after the heat exchanger and may reach 30 percent. This tendency is verified in the other cases studied.

As far as the peak flame temperature is concerned, the maximum difference occurred in case 3. When the scattering albedo is increased by around 30 percent, the peak flame temperature increases 4.4 percent. As already mentioned, using large scattering albedos results in a smaller absorption of the radiative heat transfer, and therefore in a smaller preheating of the premixed gas at the inlet. As a consequence, the peak temperature increases. Yoshizawa et al. [9], Hsu et al. [10], and Back [11] also verified that decreasing the absorption coefficient led to an increase in the peak flame temperature. When the scattering albedo was decreased, the vertical temperature gradient at the flame front location decreased.

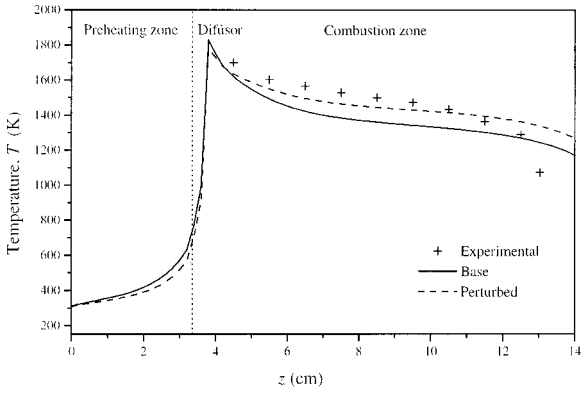

Fig. 3 Experimental and predicted centerline gas temperature profiles for a 2 kW power and a 1.5 excess air coefficient. Base—Predictions obtained with the base values of the radiative coefficients listed in Table 1; Perturbed—Predictions obtained with the extinction coefficient and the scattering albedo increased by 50 percent and 30 percent, respectively

Increasing the extinction coefficient corresponds to increasing both the absorption and scattering coefficients and to decreasing the mean penetration length of the radiation, which results in a higher axial post-flame temperature gradient. The energy feedback towards the upstream direction increases and consequently the temperature peak decreases.

For all the calculations the flame front location was the same. The authors believe that the flame location remained fixed for a variety of solutions due to the stability of the flame front promoted by the interface of the two porous media with different porosities, near where the flame is located. For example, [10] refers this fact.

Scattering Phase Function, Φ. The effects of the SiC scattering phase function were also investigated and several phase functions were studied. The base results were considered the ones obtained with the isotropic scattering phase function. The maximum differences in the temperature and in the radiative flux obtained with the perturbed and base phase functions are presented in Table 4, and in Table 5 the average differences are listed. As expected, the more the phase function is similar to the isotropic phase function, the smaller the temperature and radiative flux differences are. For the large diffuse spheres' and linear-anisotropic phase functions (cases 10 and 11, respectively), these differences are negligible (lower than 2.0 percent). When no scattering is considered, the temperature differences reach 4.0 percent and when the modified Henyey-Greenstein phase function is used the average temperature difference is 7.0 percent. For all the cases, except the latter, the flame front location is the same. However,

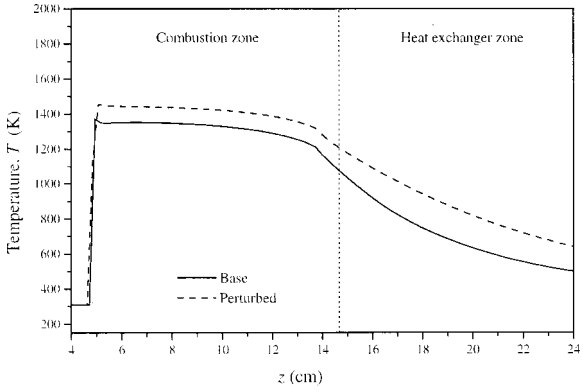

Fig. 4 Predicted gas temperature profiles at $r = 33$ mm for a 2 kW power and a 1.5 excess air coefficient. Base—Predictions obtained with the base values of the radiative coefficients listed in Table 1; Perturbed—Predictions obtained with the extinction coefficient and the scattering albedo increased by 50 percent and 30 percent, respectively

Table 4 Maximum difference in the temperature and in the radiative flux obtained with the perturbed and base scattering phase functions for a 2 kW power and a 1.5 excess air coefficient

Case	9	10	11	12
Scattering phase function	0	Eq. (12)	Eq. (13)	Eq. (14)
Temperature	4.0%	1.5%	0.9%	65.7%
Flux	16.2%	6.6%	4.5%	56.0%

Table 5 Average difference in the temperature and in the radiative flux obtained with the perturbed and base scattering phase functions for a 2 kW power and a 1.5 excess air coefficient

Case	9	10	11	12
Scattering phase function	0	Eq. (11)	Eq. (12)	Eq. (13)
Temperature	2.2%	0.9%	0.05%	7.0%
Flux	8.5%	3.9%	2.3%	21.5%

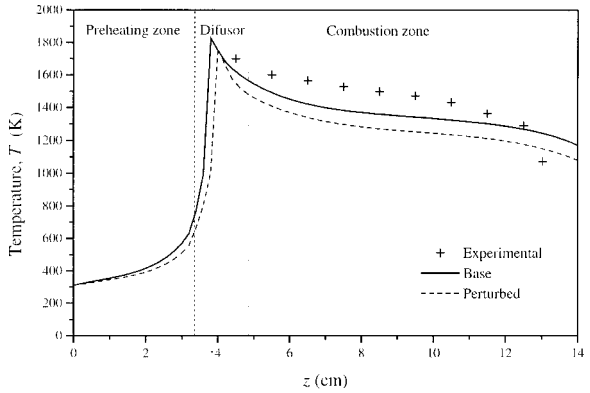

Fig. 5 Experimental and predicted centerline gas temperature profiles for a 2 kW power and a 1.5 excess air coefficient. Base—Predictions obtained assuming isotropic scattering; Perturbed—Predictions obtained using the modified Henyey-Greenstein phase function.

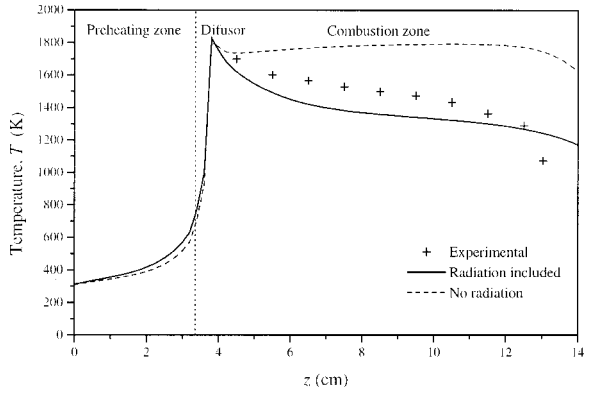

Fig. 6 Experimental and predicted centerline gas temperature profiles for a 2 kW power and a 1.5 excess air coefficient. The predictions were obtained both considering and neglecting radiation

when the modified Henyey-Greenstein phase function is used the flame front moves downstream as can be observed in Fig. 5. The fact of the flame front being shifted is responsible for the very high maximum differences in the control volume temperatures and radiative flux. The differences in the post-flame temperatures are smaller than 8.0 percent.

When the phase function for large diffuse spheres is considered, the post-flame temperatures are higher than the ones for the isotropic scattering case. For the contrary, when the linear-anisotropic (with $g=1$) and modified Henyey-Greenstein ($f_{is}=0$ and $g_{hg}=0.7$) phase function are considered, the post-flame temperatures are lower than for the base results. This is related with the back and forward-scattering components of these phase functions (see Fig. 2).

No Radiation. The base temperature predictions were compared with the temperatures calculated neglecting radiation. The maximum temperature difference occurred in the post-flame region and reached 67 percent. The importance of radiation in the temperature profiles can be seen in Fig. 6, where the centerline temperatures obtained considering radiation are compared with the predictions obtained neglecting it. The predictions differ considerably, the ones obtained with radiation are much closer to the experimental data of Ernd [15]. This supports the claim that, for this particular case of porous burners, radiative heat transfer should be considered and that, by neglecting it, the numerical predictions may be very different from the reality.

Conclusions

Numerical predictions of flow, heat transfer and combustion in porous burners were reported. The discrete ordinates method (S_6 approximation) was used for the treatment of radiative heat transfer, and the media was considered emitting, absorbing and scattering. A sensitivity study was performed to determine the importance of radiation and radiative properties for the case of a porous burner prototype developed by LSTM—Erlangen. With this objective in mind, the extinction coefficient was perturbed by ± 50 percent and the scattering albedo by about ± 30 percent. The influence of the phase function was also assessed by investigating several phase functions: zero, unity, large diffuse spheres', linear-anisotropic and modified Henyey–Greenstein phase functions. The results obtained were compared in terms of temperature and radiative flux per control volume differences, flame front location and peak temperature.

Perturbing the extinction coefficient and the scattering albedo greatly affects the temperature profile in the post-flame region. The higher perturbations in the temperature profiles occur when the scattering albedo is increased.

For the phase functions studied, only the modified Henyey-Greenstein phase function predictions present significant differences when compared to the isotropic scattering case.

The temperature profiles differ considerably for the cases where radiation is and is not considered, proving that the radiative heat transfer should not be neglected and a radiation model incorporated in the modeling of porous media burners.

Acknowledgments

The first author would like to acknowledge the grant conceded by *Fundação para a Ciência e a Tecnologia* (Reference No. PRAXIS XXI/BD/5885/95). The authors would like to express their deepest appreciation to Prof. P. J. Coelho for his valuable collaboration in the radiative model and to Prof. F. Durst and Dr.-Ing. D. Trimis for their collaboration and interest in this work.

Nomenclature

a = surface area per unit volume [m^{-1}]
A = pre-exponential factor [$m^3\,kg^{-1}\,s^{-1}$]
c_p = specific heat of the fluid [$J\,kg^{-1}\,K^{-1}$]
d_p = particle diameter [m]
D_{AB} = binary diffusion coefficient [$m^2\,s^{-1}$]
E = activation energy [$J\,k\,mol^{-1}$]
f_{is} = fraction of incident energy isotropically scattered [$-$]
g = asymmetry factor of the linear-anisotropic phase function [$-$]
g_{hg} = spectral Henyey-Greenstein asymmetry factor [$-$]
h = enthalpy [$J\,kg^{-1}$]
h_c = heat transfer coefficient [$W\,m^{-2}\,K^{-1}$]
H = volumetric heat transfer coefficient, ah_c, [$W\,m^{-3}\,K^{-1}$]
I = radiant intensity [$W\,m^{-2}\,sr^{-1}$]
k = thermal conductivity [$W\,m^{-1}\,K^{-1}$]
n = outward normal to the heat exchanger surface [$-$]
N = number of particles per unit volume [m^{-3}]

p = pressure [$\mathrm{N\,m^{-2}}$]
$\mathbf{q}$ = radiant heat flux [$\mathrm{W\,m^{-2}}$]
q' = heat flux to the cooled walls [$\mathrm{W\,m^{-2}}$]
$\mathbf{r}$ = position vector [m]
r = radial coordinate [m]
R = universal gas constant [8314 $\mathrm{J\,kmol^{-1}\,K^{-1}}$]
R_t = total thermal resistance [$\mathrm{m^2\,K\,W^{-1}}$]
s = radiative geometric path length [m]
$\hat{\mathbf{s}}$ = unit vector into a give direction [−]
S_{fu} = rate of fuel consumption [$\mathrm{kg\,m^{-3}\,s^{-1}}$]
s_{ox} = ratio of stoichiometric combustion [$\mathrm{kg_{ox}/kg_{fu}}$]
T = temperature [K]
u = axial velocity [$\mathrm{m\,s^{-1}}$]
v = radial velocity [$\mathrm{m\,s^{-1}}$]
$\mathbf{v}$ = velocity vector [$\mathrm{m\,s^{-1}}$]
w_i = quadrature weights associated with the direction $\hat{\mathbf{s}}_i$ [−]
Y_i = mass fraction of species i [−]
z = axial coordinate [m]

Greek Symbols

α = absorptivity [−]
β = extinction coefficient [$\mathrm{m^{-1}}$]
ΔH_c = heat of combustion [$\mathrm{J\,kg^{-1}}$]
$\Delta p/\Delta L$ = pressure loss along ΔL due to the porous matrix [$\mathrm{N\,m^{-3}}$]
ε = porosity [−]
ε_r = porous matrix surface emissivity [−]
κ = absorption coefficient [$\mathrm{m^{-1}}$]
μ = viscosity [$\mathrm{kg\,m^{-1}\,s^{-1}}$]
θ = angle between incident and scattering directions [rad]
ρ = density [$\mathrm{kg\,m^{-3}}$] or reflectivity [−]
σ = Stephan-Boltzmann constant [$5.670\times10^{-8}\,\mathrm{W\,m^{-2}\,K^4}$]
σ_s = scattering coefficient [$\mathrm{m^{-1}}$]
ω = scattering albedo [−]
Ω = solid angle [sr]
Ψ = air equivalent ratio [−]

Subscripts

b = blackbody
c = coolant
f = fluid
fu = fuel
in = inlet
ox = oxygen
s = solid
η = at a given wavenumber

References

[1] Howell, J. R., Hall, M. J., and Ellzey, J. L., 1996, "Combustion of Hydrocarbon Fuels Within Porous Inert Media," Prog. Energy Combust. Sci., **22**, pp. 121–145.
[2] Durst, F., and Trimis, D., 1997, "Combustion by Free Flames Versus Combustion Reactors," *Proceedings, IV International Conference on Technologies and Combustion for a Clean Environment*, Vol. 11, pp. IL 7.
[3] Hendricks, T. J., and Howell, J. R., 1996, "Absorption/scattering Coefficients and Scattering Phase Functions in Reticulated Porous Ceramics," ASME J. Heat Transfer, **118**, pp. 79–87.
[4] Mital, R., Gore, J. P., and Viskanta, R., 1996, "Measurements of Radiative Properties of Cellular Ceramics at High Temperatures," J. Thermophys. Heat Transfer, **10**, pp. 33–38.
[5] Sathe, S. B., Peck, R. E., and Tong, T. W., 1990, "Flame Stabilization and Multimode Heat Transfer in Inert Porous Media: A Numerical Study," Combust. Sci. Technol., **70**, pp. 93–109.
[6] Drift, A., van der Beckers, G. J. J., Smit, K., and Beesteheerde, J., 1994, "An Experimental and Numerical Study of Porous Radiant Burners," *Proceedings, Eurotherm Seminar no. 37*, pp. 275–285.
[7] Lim. I.-G., 1997, "Effect of Solid Properties on CO and NO Emission in Premixed Combustion Within Porous Ceramic Burner," *Proceedings, IV International Conference on Technologies and Combustion for a Clean Environment*, Vol. II, p. 28.
[8] Malico, I., and Pereira, J. C. F., 1999, "Numerical Predictions of Porous Burners with Integrated Heat Exchanger for Household Applications," Journal of Porous Media, **2**, pp. 153–162.
[9] Yoshizawa, Y., Sasaki, K., and Echigo, R., 1988, "Analytical Study of the Structure of Radiation Controlled Flame," Int. J. Heat Mass Transf., **31**, pp. 311–319.
[10] Hsu, P.-F., Howell, J. R., and Matthews, R. D., 1993, "A Numerical Investigation of Premixed Combustion Within Porous Inert Media," ASME J. of Heat Transfer, **115**, pp. 744–750.
[11] Baek, S. W., 1989, "The Premixed Flame in a Radiatively Active Porous Medium," Combust. Sci. Technol., **64**, pp. 277–287.
[12] Fu. X., 1997, "Modelling of a Submerged Flame Porous/radiant Heater," Ph.D. thesis, Purdue University, West Lafayette, IN.
[13] Malico. I., and Pereira, J. C. F., 1997, "Numerical Predictions of Two-dimensional Radiative Heat Transfer in Porous Burners," *Proceedings, IV International Conference on Technologies and Combustion for a Clean Environment*, Vol. II, pp. 27.24.
[14] Malico, I., Zhou, X.-Y., and Pereira, J. C. F., 2000, "Two-dimensional Numerical Study of Combustion and Pollutants Formation in Porous Burners," Combust. Sci. Technol., **152**, pp. 57–59.
[15] Ernd, K., 1994, "Optimierung der Betriebsparameter von Porösen Brennräumen durch Experimentelle Parametrische Untersuchung der Einflußgrößen," Diplomarbeit, Lehrstuhl für Strömungsmechanik, Erlangen.
[16] Trimis, D., and Durst, F., 1996, "Compact Low Emission Combustion Reactors with Integrated Heat Exchangers Using Porous Medium Combustion," *Proceedings, First European Conference on Small Burner Technology and Heating Equipment*, Vol. I.
[17] Ergun, S., 1952, "Fluid Flow through Packed Columns," Chem. Eng. Prog., **48**, pp. 89–94.
[18] Macdonald, I. F., El-Sayed, M. S., Mow, K., and Dullien, F. A. L., 1979, "Flow through Porous Media—Ergun Equation Revisited," Ind. Eng. Chem. Fundam., **18**, pp. 199–208.
[19] Wakao, N., and Kaguei, S., 1982, *Heat and Mass Transfer in Packed Beds*, Gordon and Breach Science Publishers, London.
[20] Younis, L. B., and Viskanta, R., 1993, "Experimental Determination of the Volumetric Heat Transfer Coefficient Between Stream of air and Ceramic Foam," Int. J. Heat Mass Transf., **36**, pp. 1425–1434.
[21] Kuo, K. K., 1986, *Principles of Combustion*, John Wiley and Sons, New York.
[22] Mohamad, A. A., Ramadhyani, S., and Viskanta, R., 1994, "Modelling of Combustion and Heat Transfer in a Packed Bed with Embedded Coolant Tubes," Int. J. Heat Mass Transf., **37**, pp. 1181–1191.
[23] Siegel, R., and Howell, J. R., 1992, *Thermal Radiation Heat Transfer*, Taylor & Francis, Washington, DC.
[24] Prahl, S. A., 1988, "Light Transport in Tissue," Ph.D. dissertation, University of Texas at Austin.
[25] Patankar, S. V., 1980, *Numerical Heat Transfer and Fluid Flow*, Hemisphere Publishing Corporation, New York.
[26] Hsu, P.-F., and Matthews, R. D., 1993, "The Necessity of Using Detailed Kinetics in Models for Premixed Combustion within Porous Media," Combust. Flame, **93**, pp. 457–466.

A New Two-Phase Flow Map and Transition Boundary Accounting for Surface Tension Effects in Horizontal Miniature and Micro Tubes

Ahmadali Tabatabai

Amir Faghri

Department of Mechanical Engineering,
University of Connecticut,
Storrs, CT 06269-3139

A new flow map is proposed to emphasize the importance of surface tension in two-phase flow in horizontal miniature and micro tubes. A transition boundary based on a force balance including shear, buoyancy and surface tension forces is also proposed. The flow map is compared against a number of existing experimental data sets totaling 1589 data points. Comparison of the proposed map and model with previous models shows substantial improvement and accuracy in determining surface tension dominated regimes. Furthermore, the proposed flow map shows how each regime transition boundary is affected by surface tension. [DOI: 10.1115/1.1374440]

Keywords: Flow, Heat Transfer, Microscale, Surface Tension, Two-Phase

Introduction

To better predict pressure and heat transfer coefficients in heat pipes, it is desirable to develop a flow map for predicting the flow regimes for two-phase flow systems in horizontal miniature and micro tubes. While existing flow maps are effective for predicting flow in larger diameters, they generally are ineffective for miniature and micro-size tubes. This is an area of growing importance due to the increasing interest in miniaturization technologies. An example is the development of smaller and faster electronic devices, an area which can utilize heat pipes extensively to discard large quantities of heat very fast [1].

In general, film or interface instability can be used as a criterion for flow transitions. Ostrach and Koestel [2] provide a review of criteria and phenomena associated with film instabilities. While the growth rate of instability was considered a main criterion, surface tension was not considered to have much effect in their study. Rabas and Minard [3] suggest two forms of flow instabilities occurring inside horizontal tubes with complete condensation. The two forms are distinguished by a transition Froude number. It is suggested that the first instability results from the low vapor flow rate associated with a stratified exit condition and vapor flowing into the tube exit causing condensate chugging or water hammer instability. The second instability results from a high vapor flow rate, leading to inadequate distribution of the vapor and the tube becoming full at the tube exit, in turn causing large subcooled condensate temperature variations.

Instability can also occur in small diameter tubes, due mainly to capillary blocking where the liquid film bridges across the tube to form a plug. In an integro-differential approach by Teng et al. [4], capillary blocking was investigated in a thermosyphon condenser tube with an axisymmetric, viscous annular condensate film with a vapor core. It was found that at low relative vapor velocities, surface tension is responsible for film instability in capillary tubes. At high relative vapor velocities, on the other hand, hydrodynamic force is responsible for the instability. Additionally, liquid bridges are maintained by buoyant motion of the vapor bubbles.

Contributed by the Heat Transfer Division for publication in the JOURNAL OF HEAT TRANSFER. Manuscript received by the Heat Transfer Division July 12, 2000; revision received January 22, 2001. Associate Editor: G. P. Peterson.

Figure 1 shows patterns of flow particularly relevant to a capillary tube, that is, annular, slug, plug, and bubble. For two-phase flow, initially an annular layer forms on the inside of the tube. As vapor or gas velocity increases, it causes ripples to form on the liquid surface, leading to formation of collars. The collar can also result from condensation of the vapor on the liquid film in the tube. Eventually, the collars grow to form a bridge. The relative size of the gap formed as a result of bridging establishes slug, plug and bubble regimes. In a large tube, because of high gravitational pull on the liquid film, the bridge does not form. The recognition of, and accuracy in reporting various flow regimes and their respective operating conditions, is a major consideration in developing a flow map. Some investigators have reported more intermittent (slug and plug) regimes than others. For example, Dobson et al. [5] report annular, wavy, wavy annular and mist annular for condensation of refrigerants while Soliman [6] has identified annular, semiannular, semiannular-wavy, spray annular, annular wavy and spray for condensation of refrigerants. In general, there is bound to be some subjectivity in regime reporting reflecting accuracy of measurement, visualization and regime identification techniques. This fact becomes even more critical in tubes of smaller diameter where flow regimes may be more difficult to observe.

Table 1 lists chronologically some features from pertinent literature [5–29] relating to two-phase flow in a tube, including working fluids and tube diameter. A number of existing flow maps [7,13,18,19] are based on visual separation of a large number of experimental data into various regimes. This approach does not

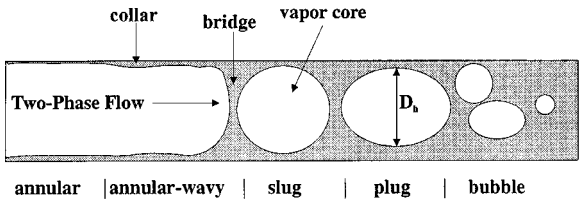

Fig. 1 Flow patterns of two-phase condensation flow in capillary horizontal tubes

Table 1 Summary of relevant existing investigations for two-phase flow in horizontal tubes

Investigator	Working Fluids	D_i, mm	Features/observations
Baker, 1954 [7]	a. air/water b. oil/water	25.4, 50.8, 101.6	a. most experimental data at 1 atm, 20°C b. flow map of modified $G_{g,s}$ vs $G_{l,s}$ based on experimental data c. correction factors allowing for deviation from 1 atm, 20°C d. inadequate for small tubes
Chato, 1962 [8]	R-113	14.5	a. horizontal and inclined tubes b. momentum-energy integral method for determining condensation along inside walls and bottom of tube
Suo and Griffith, 1963 [9]	air/water	1 – 1.5	a. gravitational/surface tension ratio significant in capillary tubes b. focus on slug flow
Griffith and Lee, 1964 [10]	a. air/water b. air/glycerine	1	transition from annular to slug at constant liquid volume fraction
Soliman and Azer, 1971 [11]	R-12	12.7	a. four flow maps proposed b. nine flow regimes identified: spray, annular, semiannular, wavy, slug, plug, annular-wavy, semiannular-wavy, spray-annular c. original experimental data
Traviss and Rohsenow, 1973 [12]	R-12	8	a. flow map of liquid phase Re versus Martinelli parameter, X b. Froude number of 45 between annular/semiannular
Soliman, 1974 [6]	a. R-12 b. R-134a	4.76, 8.15, 12.3	a. four flow maps proposed b. nine flow regimes identified: spray, annular, semiannular, wavy, slug, plug, annular-wavy, semiannular-wavy, spray-annular c. original experimental data
Mandhane *et al.*, 1974 [13]	a. air/water b. air/oil c. water/oil	12.7 – 165.1	a. map based on 5935 experimental data points b. correction factor for scaling axis c. inadequate for small tubes
Taitel and Dukler, 1976 [14]	general two-phase flow	---	a. flow map based on physical concepts of momentum and energy balances b. flow map of dimensionless parameters versus Martinelli parameter c. regime transition criteria based on force balances. Surface tension not considered. d. five major zones: annular/dispersed, dispersed bubble, stratified wavy, stratified smooth, intermittent
Jaster and Kosky, 1976 [15]	steam	12.5	a. original experimental data b. single criteria for annular/stratified transition
Weisman *et al.*, 1979 [16]	a. air/water b. air/oil c. R-11	12 – 50	ratio of volumetric flow rates of gas and liquid to establish flow regimes
Palen *et al.*, 1979 [17]	a. water b. n-pentane	22	a. condensation due to two forces: shear-controlled flow and gravity controlled flow b. a single dimensionless gas velocity term to distinguish between annular, mist annular and wave, slug, stratified

provide accurate predictions incases deviating from the average data set. Furthermore, the majority of the experimental data used in these maps are for large-diameter tubes and therefore the maps are inadequate for small-diameter tubes.

In a more accurate flow map proposed by Taitel and Dukler [14], a momentum balance was performed on each phase of a two-phase flow in a tube. Additionally, using the Kelvin-Helmholtz theory, a stability criterion for wave propagation was developed. The waves lead to formation of slug or wavy regimes. Several criteria relate the velocity of the gas or liquid phase to the height of the liquid in the tube. When plotted against the Martinelli parameter, *X*,

Table 1 Continued

Investigator	Working Fluids	D_i, mm	Features/observations
Breber *et al.*, 1980 [18]	a. R-12 b. R-113 c. R-11 d. steam e. n-pentane	4.8 – 50.8	a. flow map of dimensionless gas velocity versus Martinelli parameter, X, based on experimental data b. four major zones on flow map: annular/mist annular, wavy/stratified, slug/plug, bubble c. proposed criteria to establish flow type: 1. shear forces/gravity forces 2. vapor volume/liquid volume d. inadequate for small tubes
Tandon *et al.*, 1980 [19]	a. R-12 b. R-113	4.8 – 15.9	a. flow map of dimensionless gas velocity J_g^* versus $(1-\alpha)/\alpha$ based on experimental data b. Six major zones on flow map: spray, slug annular/semiannular, wavy, plug, transition c. Inadequate for small tubes
Soliman, 1982 [20]	a. R-12, b. R-134a c. R-113 d. steam	4.8 – 15.9	Froude number of 7 for wavy/annular transition
Barnea *et al.*, 1983 [21]	air/water	4 – 12.3	a. original experimental data b. regime transition accounting for surface tension between stratified/slug regime
Soliman, 1983; [22] Soliman, 1986 [23]	a. R-12 b. R-113 c. steam	4.8-13.4	Weber number of 25 for mist/annular transition
Rahman *et al.*, [24] 1985; Fathi, 1980 [25]	steam	13.4, 25.3	original experimental data
Damianides and Westwater, 1988 [26]	air/water	1 – 5	a. description of original experimental data b. no stratified regime for 1 mm tube c. creeping action along tube surface for 2 mm tube suggesting surface tension forces
Galbiatti and Andreini, 1992 [27]	air/water	4 – 12.3	a. surface tension term added to Kelvin-Helmholtz stability equation for annular/stratified transition. b. surface tension/shear transition at about 3 mm
Palen *et al.*, 1993 [28]	---	---	a. review of correlations in tube condensation b. recognizing limitations of existing correlations in spite of considerable progress c. no reference to surface tension forces in small tubes
Dobson *et al.*, 1994b [29]	a. R-12 b. R-134a	4.57	a. original experimental data b. observed flow regimes: wavy, wavy/annular, annular, mist annular
Dobson and Chato, 1998 [5]	a. R-12 b. R-134a c. R-22 d. R-32/R-125	3.14, 7.04	a. original experimental data b. observed flow regimes: stratified, wavy, wavy/annular, annular/annular mist, slug

$$X = \left| \frac{\left(\frac{dP}{dz}\right)_{l,s}}{\left(\frac{dP}{dz}\right)_{g,s}} \right|^{0.5} \tag{1}$$

$$-\left(\frac{dP}{dz}\right)_{g,s} = \frac{2 f_g G_g^2}{D \rho_g} \tag{2}$$

$$-\left(\frac{dP}{dz}\right)_{l,s} = \frac{2 f_l G_l^2}{D \rho_l}. \tag{3}$$

these criteria establish the boundaries separating flow regimes of the Taitel and Dukler [14] flow map. The single-phase pressure drops in X are related to their respective standard formulas according to

The map of Taitel and Dukler [14], however, does not take surface tension effects into consideration resulting in considerable error for tubes of smaller diameters. Barnea et al. [21], in an investigation of air/water flow in horizontal tubes ranging from 4

mm to 12 mm in diameter, suggested that the surface tension effect is pronounced only in the stratified-slug transition region. It was proposed that surface tension forces act to push or raise the liquid to the top of the tube at some point along the tube, thereby reducing the liquid level in the vicinity of the rise, and leading to the formation of a slug. For this to occur, the surface tension forces must overcome gravitational forces. Barnea et al. [21] proposed the following transition criterion as a ratio of surface tension to gravitational forces, taking the geometry of the tube into account:

$$h_g \leqslant \frac{\pi}{4}\sqrt{\frac{\sigma}{\rho g\left(1-\frac{\pi}{4}\right)}} \tag{4}$$

as the condition for transition between annular and intermittent flow regimes. For smaller size tubes, Barnea et al. [21] suggested that Eq. (4) is always satisfied and the transition occurs for $h_g \leqslant \pi D/4$.

Galbiati and Andreini [27] suggested surface tension effects to be significant only in the annular-stratified regime. A surface tension term was added to the Kelvin-Helmholtz equation to establish the criterion for annular-stratified transition. In reality, in sufficiently small-diameter tubes and under the right operating conditions, a stratified regime may not even exist long enough to be observed. This can be noted in the experimental data of Damianides and Westwater [26].

Griffith and Lee [10] proposed the use of three dimensionless groups to determine the stability of a liquid annulus. These were liquid volume fraction, dimensionless diameter, and a group ratio of viscous to surface tension forces. Griffith and Lee suggested that the most unstable wavelength (suggested to be equivalent to 5.5 diameters) was not affected by viscous forces, but rather by surface tension forces. Their analysis was based on flow of water or glycerine in a 1 mm ID tube. The liquid volume fraction for transition from annular to slug regime was determined to be

$$m = \frac{(\pi r^2)2r - \frac{4}{3}\pi r^3}{\pi r^2(5.5)(2r)} = 0.06. \tag{5}$$

The numerator in Eq. (5) is the total liquid volume per slug in the tube and the denominator is the total volume of the slug at the most unstable wavelength of 5.5.

Proposed Flow Map

A new flow map is proposed in this work to determine the relative effect of surface tension forces compared to shear forces. The proposed map also determines surface tension effects on the various regime boundaries. Since the effect of surface tension forces compared to that of shear forces is the desired goal, one of the map axes is assigned ratio of pressure drop due to surface tension forces and that due to shear forces. The other axis should represent the liquid and gas flow rate inside the tube. A ratio of superficial gas to superficial liquid velocities would meet this requirement. This results in a map with dimensionless parameters for each axis. The purpose of the map is also to provide a distinct region for each flow regime. In developing the proposed flow map, the flow parameters are determined according to

$$G_g = \rho_g V_{g,s} \tag{6}$$

$$G_l = \rho_l V_{l,s} \tag{7}$$

$$SV_{\text{ratio}} = \frac{V_{g,s}}{V_{l,s}}. \tag{8}$$

The pressure loss factors considered in this study result from shear and capillary effects. For the shear friction force of each phase, the pressure drop is determined by Eqs. (2) and (3). The maximum pressure change due to capillary or surface tension forces, $\Delta P_{\text{capillary}}$, is determined by the Young-Laplace equation using [1]

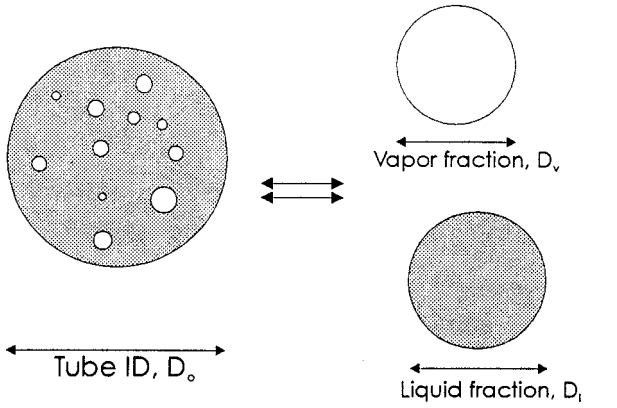

Fig. 2 Equivalent liquid and gas fraction in two-phase flow in a horizontal tube

$$\Delta P_{\text{capillary}} = \frac{2\sigma}{r_{\text{eff}}}, \tag{9}$$

where r_{eff} is the effective pore radius. It is proposed that radius r_{eff} would be represented by the hydraulic diameter of the tube as an approximation to account for two-phase flow inside the tube. This approximation becomes more accurate for tubes of small diameter since the vapor core compared to the liquid layer on the inside tube wall is small and a meniscus forms more readily in the tube. As tube diameter is reduced, size of bubbles present in the tube approach the size of the tube diameter. In such a situation, for the bubbles to form, the liquid volume required to wet the tube wall must be very small. Furthermore, as the tube diameter size is reduced, shape of slug and plug regimes approach that of a bubble. As tube diameter is increased, the vapor core and pore diameter size become too large and therefore r_{eff} is not an accurate representation of the effective diameter in Eq. (9). However, the effect of Eq. (9) is insignificant for larger diameter tubes and therefore the added error for r_{eff} is not important in larger diameter tubes. The effective radius is given by

$$r_{\text{eff}} = \frac{D_h}{2} = \frac{2*\text{cross sectional area of flow}}{\text{wetted perimeter}}. \tag{10}$$

The wetted perimeter of the tube is determined using the void fraction in the tube. The equivalence of the two-phase flow treated as separated flows is described by Carey [30] and is illustrated in Fig. 2. It can be deduced that

$$\alpha = \frac{D_g^2}{D_o^2} = \frac{r_g^2}{r_o^2} \tag{11}$$

The void fraction in the flow, α, is the ratio of vapor volume to total volume. The choice of a correlation for the void fraction is extremely important as substantial changes can result in choosing one correlation over another. In this work, the following correlations were tested to determine the best results: Homogeneous [30], Zivi [31], Wallis [32] separate-cylinder model, Baroczy [33], Thom [34], Lockhart and Martinelli [35], Smith [36], and the Wedekind et al. [37] system mean void fraction model. Carey [30] provides a summary of the first six correlations. While the other correlations provided varying degrees of accuracy against experimental results, the correlations by Lockhart and Martinelli [35] as well as Smith [36] provided the best comparisons. Ultimately, in this study α was determined from the correlation by Smith [36] which was suggested to be applicable to all flow conditions including flow rates and patterns, pressure, and void frac-

tion. Smith's [36] empirical correlation was developed based on a large number of experimental data from various investigators and is given by

$$\alpha = \left\{ 1 + \left(\frac{\rho_g}{\rho_l}\right)\left(\frac{1-x}{x}\right) \times \left[0.4 + 0.6 \sqrt{\frac{\left(\frac{\rho_l}{\rho_g}\right) + 0.4\left(\frac{1-x}{x}\right)}{1 + 0.4\left(\frac{1-x}{x}\right)}} \right] \right\}^{-1}. \quad (12)$$

The quality, x, is defined as

$$x = \frac{G_g}{G_g + G_l}. \quad (13)$$

For the vapor core, using a cross-sectional area of $\pi D_g^2/4$ and a wetted-perimeter of πD_g and rearranging Eq. (11) and substituting in Eq. (10), the effective radius is

$$r_{\text{eff}} = 2^* \left(\frac{\frac{\pi D_g^2}{4}}{\pi D_g} \right) = \frac{D_o \alpha^{0.5}}{2}. \quad (14)$$

Using Eqs. (9) and (14), the pressure drop due to surface tension in two-phase flow in a tube is approximated by

$$\left(\frac{dP}{dz}\right)_{\text{surface tension}} \approx \frac{\Delta P_{\text{capillary}}}{\Delta z} \approx -\frac{2\sigma / r_{\text{eff}}}{r_{\text{eff}}} = -\frac{2\sigma}{\left(\frac{D_o \alpha^{0.5}}{2}\right)^2} = -\frac{8\sigma}{D_o^2 \alpha}. \quad (15)$$

It should be noted that Δz for the axial pressure drop due to surface tension forces is approximated by r_{eff}. Using r_{eff} for Δz represents the immediate vicinity of the regime for which $\Delta P_{\text{capillary}}$ is determined. As tube diameter is reduced, Eq. (15) becomes more significant and the approximation of $(dP/dz)_{\text{surface tension}} \approx \Delta P_{\text{capillary}}/\Delta z$ becomes more accurate. The last term on the right hand side of Eq. (15) indicates that as tube diameter is reduced or as the surface tension of the working fluid is increased, the pressure drop due to capillary effects increases. Additionally, as α decreases, the pressure drop due to surface tension force is increased. The last term in Eq. (15) indicates the absolute magnitude of the pressure drop due to surface tension. For practical considerations, the proposed flow map allows determination of the flow regime for a set of operating conditions. Furthermore, once operating temperature or pressure is known at two points along a tube, it can be determined whether condensation or vaporization is occurring in going from the first point to the second point.

The pressure drop due to shear is the sum of shear pressure drop terms for both liquid and gas phases. The following ratio of pressure drop due to surface tension and shear force serves as one of the axes for the proposed flow map.

$$\Delta P_{\text{ratio}} = \frac{\left(\frac{dP}{dz}\right)_{\text{surface tension}}}{\left(\frac{dP}{dz}\right)_{\text{shear}}} = \frac{\left(\frac{dP}{dz}\right)_{\text{surface tension}}}{\left(\frac{dP}{dz}\right)_{l,s} + \left(\frac{dP}{dz}\right)_{g,s}}. \quad (16)$$

The gas and liquid mass fluxes are implicit in the terms in the denominator as noted from Eqs. (2) and (3). Plotting the ratio of superficial velocities (Eq. (8)) versus the ratio of pressure drop terms (Eq. (16)) results in a flow map delineating the flow regimes corresponding to flow in a particular tube size. While this map is developed for horizontal tubes, it should be noted that as tube size is sufficiently reduced and surface tension sufficiently increased, surface tension forces become more significant than gravitational forces. In such a situation, the angle of tube will be less significant and therefore results of this work can be extended to tubes beyond the horizontal plane.

Transition Boundary Due to Surface Tension/Shear

A new transition boundary accounting for regimes dominated by surface tension effects is proposed. The surface tension-dominated regime refers to plug, slug and bubbly flow, particularly in tubes of small diameter. The shear-dominated regime refers to annular, mist, stratified and wavy. The surface tension/shear transition boundary refers to the boundary separating the surface tension-dominated regimes and shear-dominated regimes.

As shown in Fig. 3, the criterion for the proposed transition boundary results from a force balance accounting for shear, buoyancy and surface tension forces acting on the two-phase flow. This transition is represented by curve A in the flow maps. As suggested by Taitel and Dukler [14], at high flow rates, the shear force will: (*a*) cause ripples to form on the liquid surface, and (*b*) overcome the buoyant effects of the gas region leading to the formation of bubble or slug regimes. The surface tension forces must be strong enough to overcome both shear and buoyant forces to form a liquid bridge. *Per unit length of the flow regime,* each of the force terms can be used to develop a criterion to separate the surface tension dominated regimes and shear dominated regimes. Using and rearranging Eq. (11) to obtain D_l in terms of α, the surface tension force per unit length of the flow regime is given by

$$\frac{F_{\text{surface tension}}}{L} = \frac{2\sigma p_l}{p_t} = \frac{2\sigma \pi D_l}{\pi D_o} = 2\sigma(1-\alpha)^{0.5}. \quad (17)$$

The term (p_l/p_t) in Eq. (17), a dimensionless ratio of liquid regime perimeter to total perimeter, is introduced to determine the effective surface tension force over the wetted perimeter by accounting for the fraction of the tube circumference wetted by the liquid surface tension. The value of 2σ is a result of the surface tension force wetting the tube surface for both the receding and leading fronts of the bubble [21]. Equation (17) suggests that as the void fraction decreases, surface tension effects increase. For flow in conduits, the shear force per unit length of the flow regime over a given wetted surface as accounted for by α, including radial velocity fluctuations [14,38] is given by

$$\frac{F_{\text{shear}}}{L} = (\pi D_o \alpha)(f_l)\left(\frac{\rho_l u_l^2}{4}\right). \quad (18)$$

The liquid friction factor, f_l, is related to the liquid phase Reynolds number which is a function of liquid fraction. The buoyancy force per unit length of the flow regime is given by

$$\frac{F_{\text{buoyancy}}}{L} = g(\rho_l - \rho_g)\alpha A = g(\rho_l - \rho_g)A_g. \quad (19)$$

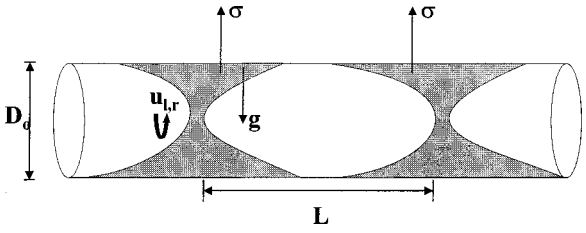

Fig. 3 Schematic of force balance elements for a given unit length of flow

Per unit length of the flow regime, the surface tension forces are dominant when

$$|F_{\text{surface tension}}| > |F_{\text{shear}}| + F_{\text{buoyancy}}. \tag{20}$$

For the liquid bridge to form and remain in place, that is not separate to the top or bottom, surface tension force in the positive or negative *y*-direction (hence the absolute value) must overcome buoyancy force due to gravity in the *y*-direction and radial shear force (due to radial velocity fluctuations) in the negative or positive *y*-direction (hence, the absolute value). Equation (20) uses as a criterion the minimum force due to surface tension required to overcome the maximum force due to buoyancy and radial velocity to maintain the liquid bridge.

Inserting Eqs. (17), (18), and (19) into Eq. (20) and rearranging results in

$$u_l < B = \left(\frac{2\sigma(1-\alpha)^{0.5} - g(\rho_l - \rho_g)A_g}{\left(\frac{\pi D_o \alpha \rho_l f_l}{4}\right)} \right)^{0.5}. \tag{21}$$

The superficial velocity terms $V_{g,s}$ and $V_{l,s}$ are respectively related to the axial velocity terms u_g and u_l according to

$$u_g = \frac{V_{g,s}}{\alpha}; \quad u_l = \frac{V_{l,s}}{(1-\alpha)}. \tag{22}$$

In dimensionless form, Eq. (21) takes the form

$$\frac{V_{g,s}}{V_{l,s}} > \frac{V_{g,s}}{(1-\alpha)B}. \tag{23}$$

Transition From Annular to Slug or Bubble

Taitel and Dukler [14] proposed a transition boundary between intermittent (slug and plug) and dispersed bubble regimes for horizontal tubes based on the assumption that annular or slug regimes develop depending on the equilibrium liquid level of the stratified regime. Taitel and Dukler suggest that if the dimensionless liquid level (h_l/D_o) is above 0.5, then intermittent flow will develop and if the level is less than 0.5, annular flow will develop. This resulted in a line corresponding to $X = 1.6$, separating annular and intermittent regimes.

The problem with using the equilibrium level of the stratified regime as the reference point is that in miniature or micro size tubes and under certain conditions, stratified flow may not even exist. For smaller diameter tubes, another point of reference must be used for the transition from annular to intermittent regime. In this study, the transition boundary between intermittent and annular flow is that proposed by Griffith and Lee [10] (Eq. (5)). This transition was based on instability in an annulus occurring at a wavelength of 5.5 diameters and leading to formation of a collar and eventual formation of a bridge and slug. Although Griffith and Lee focused on the transition from annular to slug, a transition from annular to dispersed bubble regimes in a small-diameter tube can also be observed using the same criteria. This is because a smaller tube facilitates easier formation of a meniscus using a much smaller liquid film thickness along the inside wall of the tube.

The proposed transition boundary between the annular and slug or bubble as represented by *B* in the Figs. 4–8, compared to the experimental data used in this study, is effective for tube sizes larger than approximately 4 mm. The annular regime falls above this transition and slug and/or bubble fall below this transition. The liquid volume fraction corresponding to this transition boundary in the proposed flow map is determined according to

$$m = \frac{V_{l,s}}{V_{l,s} + V_{g,s}} = 0.06. \tag{24}$$

Any combination of $V_{l,s}$ and $V_{g,s}$ resulting in a value of 0.06 for *m* corresponding to Eq. (5), satisfies the criterion for this boundary.

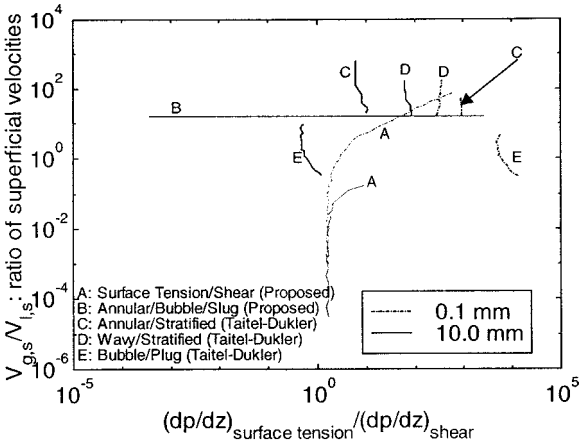

Fig. 5 Effect of tube diameter on transition boundaries for the proposed flow map for two-phase condensation horizontal flow of R-12 at T_{sat}=83.4°C

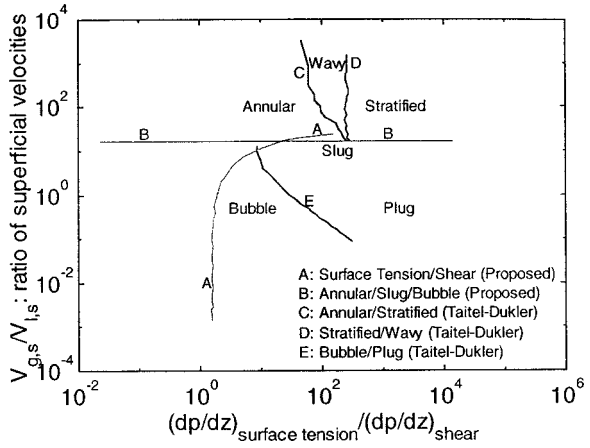

Fig. 4 Proposed generalized flow map with transition boundaries

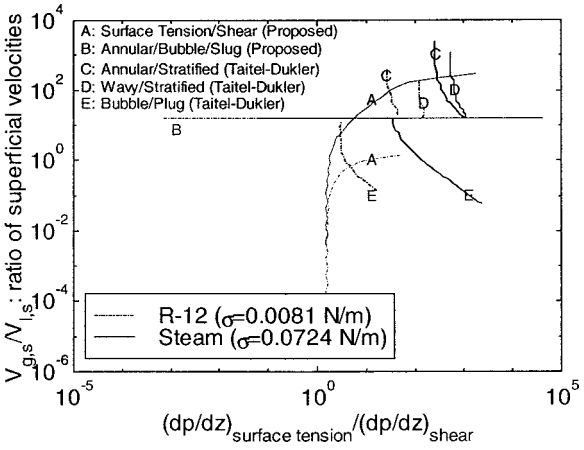

Fig. 6 Effect of working fluid (steam at 110°C and R12 at 83.4°C) surface tension on transition boundaries for the proposed flow map for flow in 4 mm horizontal tube

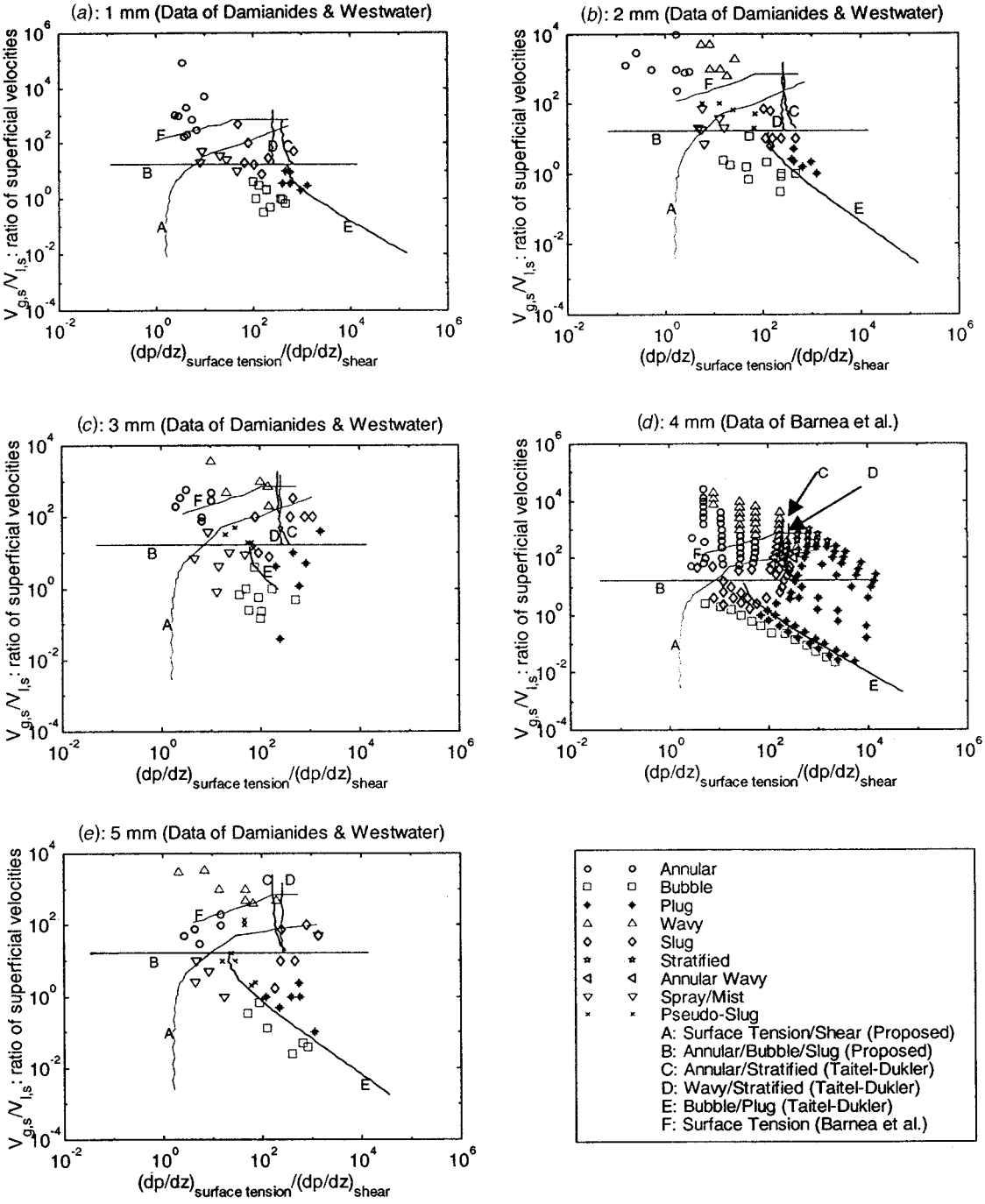

Fig. 7 Comparison of proposed flow map and transition boundaries for two-phase flow in horizontal tubes with experimental data for air (20°C)/water (15°C): (*a*) 1 mm; (*b*) 2 mm; (*c*) 3 mm; (*d*) 4 mm (air and water at 25°C); (*e*) 5 mm.

Transition Boundaries for Other Regimes

Other boundaries used in this study are those proposed by Taitel and Dukler [14], specifically for transitions between: (*a*) stratified and intermittent or annular-dispersed liquid (transition *C* in flow maps), (*b*) stratified smooth and stratified wavy (transition *D* in flow maps), and (*c*) intermittent and dispersed bubble (transition *E* in flow maps). Taitel and Dukler [14] use intermittent to describe slug and plug regimes. The proposed surface tension/shear transition boundary in conjunction with the above boundaries allows determination of the flow regimes particularly in miniature and micro size tubes. It should be noted that transition *D* as defined by Taitel and Dukler is not a function of line size. The variation in transition *D* occurs as a result of friction factor affecting the shear pressure drop as used on the flow map abcissa. Transitions *C* and *E* are a function of line size and are more significantly affected by line size as noted in the flow maps.

Existing Experimental Data

The experimental data used for comparison in this study include 1589 data points from several sets of existing two-phase flow data. The data include two-phase flow for pure component condensation runs with water, R-12, R-113, R-22, and R-134a as working fluids. No existing experimental data reporting flow regimes in tubes smaller than 4.8 mm were available for pure com-

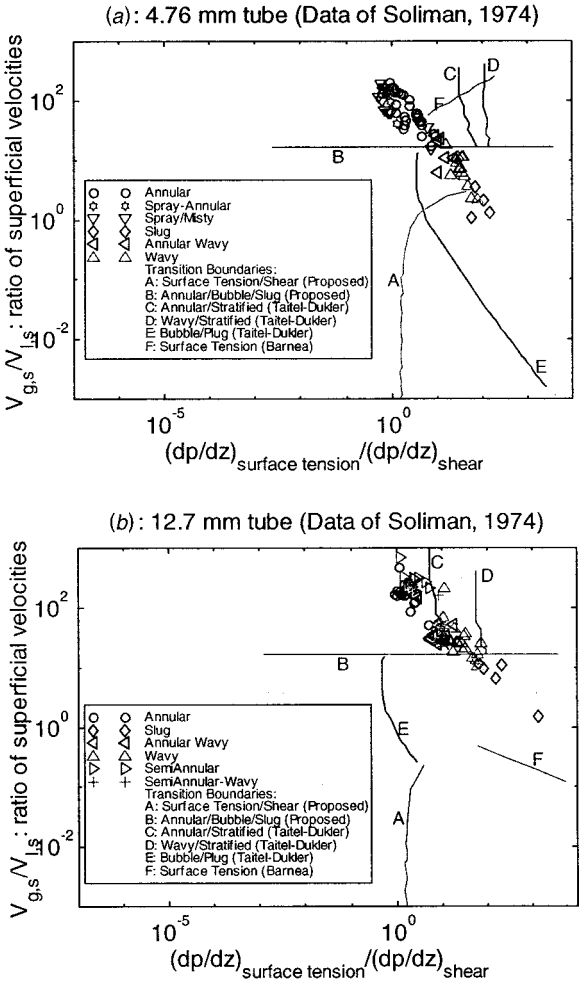

Fig. 8 Comparison of proposed flow map and transition boundaries for two-phase condensation flow in horizontal tubes with experimental data for R-113: (*a*) 4.76 mm (T_{sat}=143.9°C); and (*b*) 12.7 mm (T_{sat}=139.1°C).

ponents. To confirm the proposed model against tube sizes of approximately 1 mm ID, existing air/water data were also used for comparison. Table 2 shows a summary of the data sets and average properties of the flow components and corresponding diameters considered in this investigation. The experimental data range in diameter from 15.88 mm down to 4.8 mm for condensation runs and from 12.3 mm down to 1 mm for air/water runs.

General Features of Proposed Flow Map

The general features of the proposed flow map are shown in Fig. 4. Five transition boundaries are used to differentiate between the various regimes. The proposed surface tension/shear transition boundary highlights regimes dominated by surface tension. The regimes below and to the right of the surface tension/shear transition boundary are affected more by surface tension forces, whereas the regimes above and to the left of this boundary are affected more by shear forces. As tube size is reduced or surface tension of the working fluid is increased, this boundary extends up and to the left. The effect of tube diameter on the flow map transition boundaries is shown in Fig. 5 while the effect of working fluid surface tension is shown in Fig. 6.

One of the general features of the proposed map is that as surface tension forces become more dominant, the bubble/plug and stratified/annular transition boundaries shift to the right and start to diminish with decreasing tube diameter reflecting the diminished role of the regimes they represent in two-phase flow. This effect is shown in Fig. 5. As the diameter size is reduced from 10.0 mm to 0.1 mm, all transition boundaries shift to the right except for the surface tension/shear transition boundary which shifts upward, indicating the increase in surface tension-dominated regimes. The same effect can be observed in Fig. 6 where steam with a surface tension of 0.0724 N/m compared with R-12 with a surface tension of 0.0081 N/m causes the transition boundaries to shift to the right except for the surface tension-dominated boundary which shifts upward.

Of particular importance in the shifting of the transition boundaries is that between bubble and plug regimes. As diameter size is sufficiently reduced or surface tension is sufficiently increased, the bubble/plug transition boundary moves to the right and eventually crosses and passes to the right of the stratified/wavy transition at a vertical threshold. Once this occurs, stratified and wavy regimes become insignificant. Also around this point, the surface

Table 2 Average values of properties of working fluids corresponding to each data set considered in this work

Investigators	D_i, mm	Working Fluid	ρ_g Kg/m^3	ρ_l Kg/m^3	$\mu_g x10^5$, Kg/m.sec	$\mu_l x10^4$, Kg/m.sec	σ N/m	T_{sat} °C
Barnea *et al.*, 1983 [21]	4.0	Air/Water	1.2	1000.0	1.80	9.00	0.072	25.0
Barnea *et al.*, 1983 [21]	8.2	Air/Water	1.2	1000.0	1.80	9.00	0.072	25.0
Barnea *et al.*, 1983 [21]	12.3	Air/Water	1.2	1000.0	1.80	9.00	0.072	25.0
Soliman, 1974 [6]	4.8	R-12	42.6	1295.0	1.30	2.10	0.0081	83.4
Soliman, 1974 [6]	15.9	R-12	47.5	1269.5	1.30	2.10	0.0075	91.7
Soliman, 1974 [6]	4.8	R-113	11.5	1489.9	1.10	4.50	0.0149	143.9
Soliman, 1974 [6]	12.7	R-113	10.8	1492.5	1.10	4.50	0.0151	139.1
Soliman, 1974 [6]	15.9	R-113	11.7	1487.8	1.10	4.50	0.0148	144.9
Traviss *et al.*, 1973 [12]	8.0	R-12	41.5	1298.9	1.30	2.20	0.0082	81.7
Fathi, 1980 [25]	13.4	Steam	0.8	952.0	1.20	2.50	0.0724	110.0
Dobson *et al.*, 1994b [29]	4.6	R-134a	43.5	1165.3	1.30	1.90	0.0069	35.0
Dobson *et al.*, 1994b [29]	4.6	R-12	48.9	1272.0	1.30	2.00	0.0073	35.0
Dobson *et al.*, 1998 [5]	7.0	R-22	56.8	1154.0	1.40	1.90	0.0065	35.0
Dobson *et al.*, 1998 [5]	7.0	R-134a	43.5	1165.3	1.30	1.90	0.0069	35.0
Damiandes *et al.*, 1988 [26]	1.0	Air/Water	6.0	997.5	1.75	10.90	0.074	Air(20.0), Water(15.0)
Damiandes *et al.*, 1988 [26]	2.0	Air/Water	6.0	997.5	1.75	10.90	0.074	Air(20.0), Water(15.0)
Damiandes *et al.*, 1988 [26]	3.0	Air/Water	6.0	997.5	1.75	10.90	0.074	Air(20.0), Water(15.0)
Damiandes *et al.*, 1988 [26]	4.0	Air/Water	6.0	997.5	1.75	10.90	0.074	Air(20.0), Water(15.0)
Damiandes *et al.*, 1988 [26]	5.0	Air/Water	6.0	997.5	1.75	10.90	0.074	Air(20.0), Water(15.0)

tension/shear transition boundary separates the annular regime to the top and plug, slug and dispersed bubble to the bottom. This effect can be observed in Fig. 7(*a*). It should also be noted that as tube diameter is reduced, bubble regime approaches plug regime as reflected in Fig. 5 where transition *E* separating bubble and plug regimes is diminished with decreasing tube diameter. This is because the bubble size becomes significant relative to the tube size resulting in a regime with a thin liquid wall and a large vapor core.

Since the proposed map accounts for the effect of surface tension, changes in transition boundaries due to the surface tension or tube diameter for various regimes can readily be observed. This is a major advantage of the proposed flow map, particularly for smaller tube sizes.

Flow Map Comparison and Verification

Figures 7–10 compare the proposed flow map and transition boundaries with selected sets of experimental data as well as flow maps previously proposed by other investigators. As shown in Figs. 7 and 8, regimes dominated by surface tension force are on the lower right quadrant of the map. These include the plug, slug and dispersed bubble regimes. As tube diameter size is reduced, the surface tension/shear transition boundary extends upward. Furthermore, for smaller diameter tubes, the proposed surface tension/shear transition boundary separates with excellent accuracy surface tension dominated regimes (plug, slug, dispersed bubble) from shear-dominated regimes (stratified, wavy, annular).

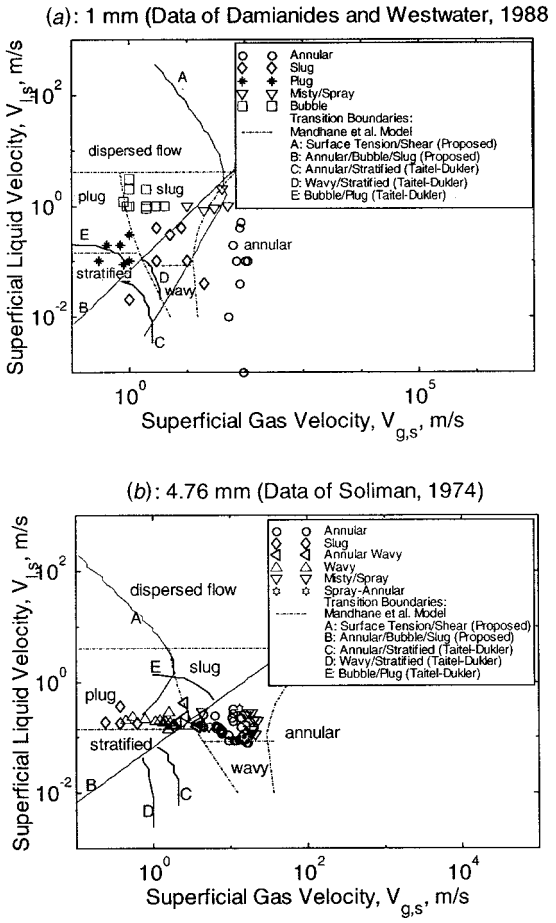

Fig. 9 Comparison of proposed transition boundaries in horizontal tubes with flow map and regimes of Mandhane et al. [10] (Mandhane et al. regimes spelled in small letters): (*a*) air (20°C)/water (15°C) in 1 mm; and (*b*) R113 (143.9°C) in 4.76 mm.

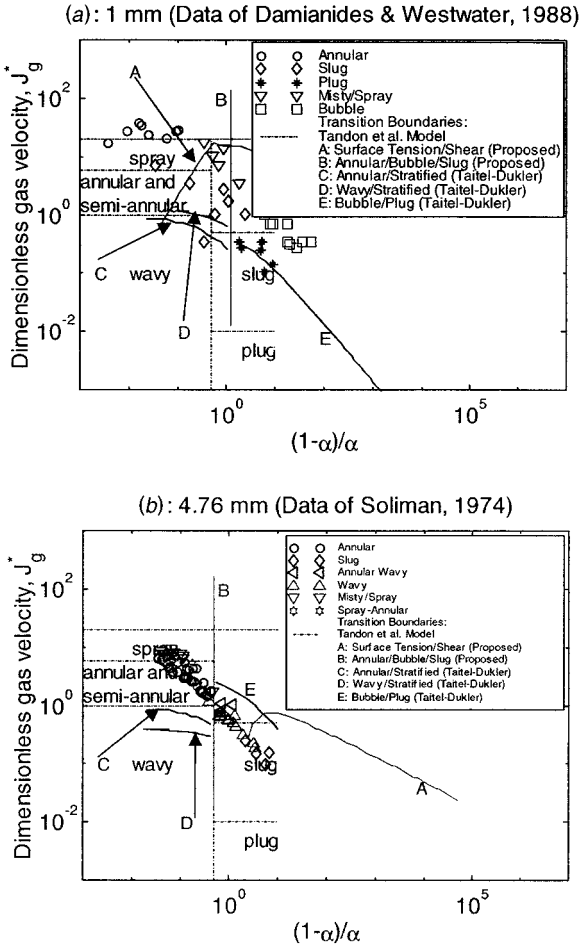

Fig. 10 Comparison of proposed transition boundaries in horizontal tubes with flow map and regimes of Tandon et al. [8] (Tandon et al. regimes spelled in small letters): (*a*) air (20°C)/water (15°C) in 1 mm; and (*b*) R113 (143.9°C) in 4.76 mm.

The Taitel and Dukler [14] model, while appropriate for larger diameter tubes, does not account for surface tension forces in its analysis. For smaller tube sizes where surface forces are significant, the Taitel and Dukler [14] model does not provide a good prediction. In fact, as shown in Fig. 7(*a*); the proposed transition for annular/stratified is not even applicable since it was reported that no stratified regime existed. The use of the proposed transition boundaries with those of Taitel and Dukler [14] provide a substantial improvement in prediction of regimes in smaller tube sizes. As shown in Fig. 7(*a–e*), the model for surface tension-dominated transition boundary proposed in this work provides a good agreement with that of Barnea et al. [21] for air/water. For R113 shown in Fig. 8(*a–b*), however, the Barnea et al. model is far less accurate. Furthermore, Barnea et al. [21] suggest that surface tension forces affect only the stratified slug transition, whereas the present proposed model shows that surface tension force is also responsible for transition from annular to slug, plug and dispersed bubble regimes, particularly in smaller tube sizes.

For a given working fluid in a small diameter tube, as the liquid wets the inside walls of the tube, the meniscus forms more readily. Smaller quantities of liquid will be needed for surface tension force to dominate the flow regime. Accordingly, for the shear force to dominate, the gas to liquid ratio must be relatively substantially higher. In such a situation, the liquid will be present as mist and it neither exists in sufficient quantity to wet the surface nor has sufficient time to spread and wet the inside of the tube. Therefore it will not lead to meniscus formation. In general,

surface tension forces are dominant at a relatively low ratio of $V_{g,s}/V_{l,s}$ while shear forces are dominant at a relatively high ratio of $V_{g,s}/V_{l,s}$. As tube diameter is reduced, surface tension forces become dominant even at a higher ratio of $V_{g,s}/V_{l,s}$.

Figures 9(*a–b*) compare the map proposed in this work with the model of Mandhane et al. [13]. The Mandhane et al. [13] map, being based on a large pool of experimental data for larger tube sizes, provides a scaling factor to correct the transition boundaries for different working fluids. The Mandhane et al. model is only approximately accurate for most applications and is marginally accurate for smaller tube sizes and most refrigerants. It can be noted in Fig. 9(*a*) that for air/water in a 1 mm tube, the Mandhane et al. model provides a somewhat reasonable prediction. As shown in Fig. 9(*b*), for R113 in a 4.76 mm tube, the Mandhane et al. model predictions are far less accurate.

A comparison of the proposed model with models of Breber et al. [18] and Tandon et al. [19] was also performed. Since similar results were obtained for both Breber et al. and Tandon et al., for brevity a comparison of the proposed model is shown only with the Tandon et al. model in Fig. 10(*a–b*). Tandon et al. [19] identify general zones based on their visual observations of a large data pool for relatively larger diameter tubes. Breber et al. [18] and Tandon et al. [19], similar to Mandhane et al. [13], do not account for surface tension observed in smaller diameter tubes. Although reasonable predictions are shown for larger tube sizes of around 4.76 mm and larger, their proposed models deviate substantially for systems different from the data pool considered in their models. This can be seen in Fig. 10(*a*) where the slug and plug regimes are completely misidentified by Tandon et al. for air/water flow in a 1 mm tube. The proposed model in this work, on the other hand, provides a better prediction for the transition between shear-dominated and surface tension-dominated regimes, that is between annular and plug, slug and bubble.

Conclusions

This work proposes a new flow map for two-phase flow in horizontal tubes by plotting Eq. (8) versus Eq. (16). The flow map as generically featured in Fig. 4 is particularly advantageous for small diameter tubes where surface tension forces are more dominant than shear forces. The model also shows the effects of surface tension on all regime transition boundaries.

Equation (21) proposes the criteria for a new surface tension/shear transition boundary based on a force balance accounting for surface tension, shear and buoyancy forces. The proposed boundary separates surface tension-dominated regimes that is, slug, plug and bubble from shear-dominated regimes of misty, annular, wavy and stratified. This boundary is particularly effective in small diameter tubes of less than about 4 mm.

It is also suggested that a transition boundary previously proposed by Griffith and Lee [10] for only annular to slug regimes, is also applicable for annular to dispersed bubble regimes, particularly for smaller tubes. The proposed model is compared with existing experimental data and models. For smaller tubes, the proposed model provides substantial improvement in regime identification.

Acknowledgments

Funding for this work was provided by NSF Grant CTS 9706706 and NASA Grant NAG3-1870.

Nomenclature

A = area of flow, m^2
B = as defined by Eq. 21
D = diameter, m (unless unit specified otherwise)
f = friction factor, for $Re<2100$, $f=16/Re$; for $Re\geqslant 2100$, $f=0.079/Re^{0.25}$
F = force, N
g = gravity, m/sec^2
G = mass flux, $kg/m^2.sec$
h = height of liquid or gas, m, Eq. (4)
J = dimensionless gas velocity, Fig. 10
L = length of flow regime, m, Eqs. (17), (18), and (19)
m = as defined by Eqs. (5) and (24)
p = perimeter, m
P = pressure, N/m^2
r = tube radius, m
SV = ratio of gas to liquid superficial velocities as defined by Eq. (8)
u = axial velocity of fluid, m/sec
V = superficial velocity, m/sec
x = quality, Eq. (13)
X = dimensionless Martinelli parameter, Eq. (1)
z = distance along the two-phase flow tube, m
α = void fraction
ρ = density, kg/m^3
σ = surface tension, N/m

Subscripts

eff = effective
g = gas
h = hydraulic
i = inside
l = liquid
o = original
r = radial
s = superficial
shear = effect due to shear
capillary = effect due to surface tension
t = total

References

[1] Faghri, A., 1995, *Heat Pipe Science and Technology*, Taylor & Francis, Washington.
[2] Ostrach, S., and Koestel, A., 1965, "Film Instabilities in Two-Phase Flows," AIChE J., **11**, No. 2, pp. 294–303.
[3] Rabas, T. J., and Minard, P. G., 1987, "Two Types of Flow Instabilities Occurring Inside Horizontal Tubes With Complete Condensation," Heat Transfer Eng., **8**, No. 1, pp. 40–49.
[4] Teng, H., Cheng, P., and Zhao, T. S., 1999, "Instability of Condensate Film And Capillary Blocking In Small-Diameter-Thermosyphon Condensers," Int. J. Heat Mass Transf., **42**, pp. 3071–3083.
[5] Dobson, M. K., and Chato, J. C., 1998, "Condensation in Smooth Horizontal Tubes," ASME J. Heat Transfer, **120**, pp. 193–213.
[6] Soliman, H. M., 1974, "*Analytical and Experimental Studies of Flow Patterns During Condensation Inside Horizontal Tubes*," Ph.D. dissertation, Kansas State Univ.
[7] Baker, O., 1954, *Simultaneous Flow of Oil and Gas*, Oil & Gas J., **53**, pp. 185–195.
[8] Chato, J. C., 1962, "Laminar Condensation Inside Horizontal and Inclined Tubes," ASHRAE J., **4**, pp. 52–60.
[9] Suo, M., and Griffith, P., 1963, "*Two Phase Flow in Capillary Tube*," Technical Report No. 8581-24, Mass. Institute of Technology.
[10] Griffith, P., and Lee, K. S., 1964, "The Stability of an Annulus of Liquid in a Tube," Trans. ASME, pp. 666–668.
[11] Soliman, H. M., and Azer, N. Z., 1971, "Flow Patterns During Condensation Inside a Horizontal Tube," ASHRAE Trans., **77**, Part 1, pp. 210–224.
[12] Traviss, D. P., and Rohsenow, W. M., 1973, "Flow Regimes in Horizontal Two-Phase Flow With Condensation," ASHRAE Trans., **79**, pp. 31–39.
[13] Mandhane, J. M., Gregory, G. A., and Aziz, K., 1974, "A Flow Pattern Map for Gas-Liquid Flow in Horizontal Pipes," Int. J. Multiphase Flow, **1**, pp. 537–553.
[14] Taitel, Y., and Dukler, A. E., 1976, "A Model for Predicting Flow Regime Transitions in Horizontal and Near Horizontal Gas-Liquid Flow," AIChE J., **22**, No. 1, pp. 47–55.
[15] Jaster, H., and Kosky, P. G., 1976, "Condensation Heat Transfer in a Mixed Flow Regime," Int. J. Heat Mass Transf., **19**, pp. 95–99.
[16] Weisman, J., Duncan, D., Gibson, J., and Crawford, T., 1979, "Effects of Fluid Properties And Pipe Diameter On Two-Phase Flow Patterns In Horizontal Lines," Int. J. Multiphase Flow, **5**, pp. 437–462.
[17] Palen, J. W., Breber, G., and Taborek, J., 1979, "Prediction of Flow Regimes in Horizontal Tube-Side Condensation," Heat Transfer Eng., **1**, No. 2, pp. 47–57.
[18] Breber, G., Palen, J. W., and Taborek, J., 1980, "Prediction of Horizontal Tubeside Condensation of Pure Components Using Flow Regime Criteria," ASME J. Heat Transfer, **102**, pp. 471–476.
[19] Tandon, T. N., Varma, H. K., and Gupta, C. P., 1982, "A New Flow Regimes

Map for Condensation Inside Horizontal Tubes,'' ASME J. Heat Transfer, **104**, pp. 763–768.
[20] Soliman, H. M., 1982, ''On the Annular-to-Wavy Flow Pattern Transition During Condensation Inside Horizontal Tubes,'' Can. J. Chem. Eng., **60**, pp. 475–481.
[21] Barnea, D., Luninski, Y., and Taitel, Y., 1983, ''Flow Pattern in Horizontal and Vertical Two Phase Flow in Small Diameter Pipes,'' Can. J. Chem. Eng., **61**, pp. 617–620.
[22] Soliman, H. M., 1983, ''Correlation of Mist-to-Annular Transition During Condensation,'' Can. J. Chem. Eng., **61**, pp. 178–182.
[23] Soliman, H. M., 1986, ''The Mist-Annular Transition During Condensation and Its Influence on the Heat Transfer Mechanism,'' Int. J. Multiphase Flow, **12**, No. 2, pp. 277–288.
[24] Rahman, M. M., Fathi, A. M., and Soliman, H. M., 1985, ''Flow Pattern Boundaries During Condensation: New Experimental Data,'' Can. J. Chem. Eng., **63**, pp. 547–552.
[25] Fathi, A. M., 1980, *Analysis of Two-Phase Flow Patterns of Condensing Steam Inside a Horizontal Tube*, M.Sc. thesis, University of Manitoba, Winnipeg, Canada.
[26] Damianides, C. A., and Westwater, J. W., 1988, ''Two-Phase Flow Patterns in a Compact Heat Exchanger and in Small Tubes,'' *Proceedings of the 2nd U.K. National Conference on Heat Transfer*, **2**, pp. 1257–1268.
[27] Galbiati, L., and Andreini, P., 1992, ''The Transition Between Stratified and Annular Regimes for Horizontal Two-Phase Flow in Small Diameter Tubes,'' Int. Commun. Heat Mass Transfer, **19**, pp. 185–190.
[28] Palen, J. W., Kistler, R. S., and Yang, Z. F., 1993, ''What We Still Don't Know About Condensation in Tubes, Condensation and Condenser Design,'' *ASME Proceedings of the Engineering Foundation Conference on Condensation and Condenser Design*, pp. 19–53.
[29] Dobson, M. K., Chato, J. C., Hinde, D. K., and Wang, S. P., 1994, ''Experimental Evaluation of Internal Condensation of Refrigerants R-12 and R-134a,'' ASHRAE Trans., **100**, No. 1, pp. 744–754.
[30] Carey, V. P., 1992, *Liquid-Vapor Phase-Change Phenomena: An Introduction to the Thermophysics of Vaporization and Condensation Processes in Heat Transfer Equipment*, Taylor & Francis, Bristol, PA.
[31] Zivi, S. M., 1964, ''Estimation of Steady State Steam Void-Fraction by Means of the Principle of Minimum Entropy Production,'' ASME J. Heat Transfer, **86**, pp. 247–252.
[32] Wallis, G. B., 1965, *One Dimensional Two-Phase Flow*, Wiley, New York.
[33] Baroczy, C. J., 1965, ''Correlation of Liquid Fraction in Two-Phase Flow With Applications to Liquid Metals,'' *Chemical Engineering Progress Symposium Series*, **61**, No. 57, pp. 179–191.
[34] Thom, J. R. S., 1964, ''Prediction of Pressure Drop During Forced Circulation Boiling of Water,'' Int. J. Heat Mass Transf., **7**, pp. 709–724.
[35] Lockhart, R. W., and Martinelli, R. C., 1949, ''Proposed Correlation of Data for Isothermal Two-Phase, Two-Component Flow in Pipes,'' Chem. Eng. Prog., **45**, No. 1, pp. 39–48.
[36] Smith, S. L., 1969–70, ''Void Fraction in Two-Phase Flow: A Correlation Based Upon an Equal Velocity Head Model,'' Proceedings of the Institution of Mechanical Engineers, Thermodynamics and Fluid Mechanics Group, Vol. **184**, Pt. 1, No. 36, pp. 647–657.
[37] Wedekind, G. L., Bhatt, B. L., and Beck, B. T., 1978, ''A System Mean Void Fraction Model For Predicting Various Transient Phenomena Associated With Two-Phase Evaporating and Condensing Flows,'' Int. J. Multiphase Flow, **4**, pp. 97–114.
[38] Levich, V. G., 1962, *Physicochemical Hydrodynamics*, Prentice-Hall, Englewood Cliffs, N. J.

Surface Chemistry and Characteristics Based Model for the Thermal Contact Resistance of Fluidic Interstitial Thermal Interface Materials

Ravi S. Prasher
Associate Mem. ASME
Sr. Packaging Engineer,
Assembly Technology Development,
CH5-157, Intel Corporation,
5000 W. Chandler Blvd.
Chandler, AZ 85226-3699
e-mail: ravi.s.prasher@intel.com

Microprocessor powers are increasing at a phenomenal rate, which requires very small thermal resistance between the die (chip) and the ambient, if the current economical methods of conduction and convection cooling are to be utilized. A typical thermal solution in flip chip technology utilizes two levels of thermal interface materials: between the die and the heat spreader, and between the heat spreader and the heat sink. Phase change materials and thermal greases are among the most prominent interstitial thermal interface materials (TIM) used in electronic packaging. These TIMs are typically polymeric matrix loaded with highly conducting filler particles. The dwindling thermal budget has necessitated a better understanding of the thermal resistance of each component of the thermal solution. Thermal conductivity of these particle-laden materials is better understood than their contact resistance. A careful review of the literature reveals the lack of analytical models for the prediction of contact resistance of these types of interstitial materials, which possess fluidic properties. This paper introduces an analytical model for the thermal contact resistance of these types of interstitial materials. This model is compared with the experimental data obtained on the contact resistance of these TIMs. The model, which depends on parameters such as, surface tension, contact angle, thermal conductivity, roughness and pressure matches very well with the experimental data at low pressures and is still within the error bars at higher pressures. [DOI: 10.1115/1.1388301]

Keywords: Contact Resistance, Heat Transfer, Materials, Packaging, Rheology

Introduction

Thermal management of microelectronics is becoming a bigger challenge every day, particularly if the industry wants to push the current economical methods of conduction and convection cooling to its limits. A typical thermal solution of a microelectronic system utilizes a thermal interface material (TIM) between the die and the heat spreader, and between the heat spreader and the heat sink. The thermal resistance of these TIMs is a major portion of the thermal budget. A thermal interface material is used to reduce the contact resistance (R_c) arising from the incomplete contact between two solid surfaces. Thermal contact resistance is not only important in microelectronics thermal management but also in other applications such as, space vehicle systems and cryogenic applications [1]. The reduction of the thermal contact resistance is achieved by the use of various materials as TIMs, such as solder, metallic foils, metallic coatings, elastomeric pads and etc [2–4]. Another class of materials which are widely used, as TIMs are particle laden polymeric interstitial materials which possess fluid like properties [1,2]. Common examples of these types of materials are thermal greases and phase change materials (PCM). Thermal greases and PCMs are typically polymeric materials loaded with highly conducting filler particles. The effective thermal resistance at the interface after inserting a TIM between the solid surfaces will have two components: the bulk resistance (R_{bulk}) of the TIM arising from its thermal conductivity, and R_c between the TIM and the adjoining solids as shown in Fig. 1. Considerable amount of research, both analytical and experimental has been done in the past on the modeling of contact resistance [2]. These models and experiments have been very successful in explaining the physics behind the phenomenon of contact resistance for bare metal contacts, metallic foils, coatings and elastomers [2–4]. For polymeric fluidic TIMs such as the greases and PCMs the thermal conductivity is better understood than their contact resistance. Thermal conductivity of these particle-laden polymeric interstitial TIMs can be accurately predicted for various parameters such as, the volume fraction and the thermal conductivity of the fillers by different methods such as the percolation model [5]. Thermal contact resistance of these interstitial materials possessing fluid like properties is not very well understood [2]. Fletcher [6] introduced a parameter to judge the performance of interstitial materials. This parameter has two limitations:

1 it does not separate R_c of the TIM with the substrate and R_{bulk} of these TIMs
2 this parameter is empirical in nature

On the experimental front, one of the reasons for not separating R_c and the R_{bulk} of these TIMs is the inadequacy of most of the experimental methods to measure the bond line thickness (BLT) of these materials [4]. On the other hand there is no theoretical tool available for the prediction of R_c of these interstitial polymeric TIMs [2] because the analytical models for R_c available in literature are based on solid mechanics [2]. These models use properties such as, the hardness or the Young's modulus for predicting R_c [2]. These models are not suitable for polymeric TIMs because they posses fluidic properties. Therefore properties such as, the hardness or Young's modulus on which the current models are based can not be defined for these types of TIMs. Another peculiarity of these interstitial TIMs is that they stick to the sub-

Contributed by the Heat Transfer Division for publication in the JOURNAL OF HEAT TRANSFER. Manuscript received by the Heat Transfer Division August 28, 2000; revision received February 27, 2001. Associate Editor: H. Bau.

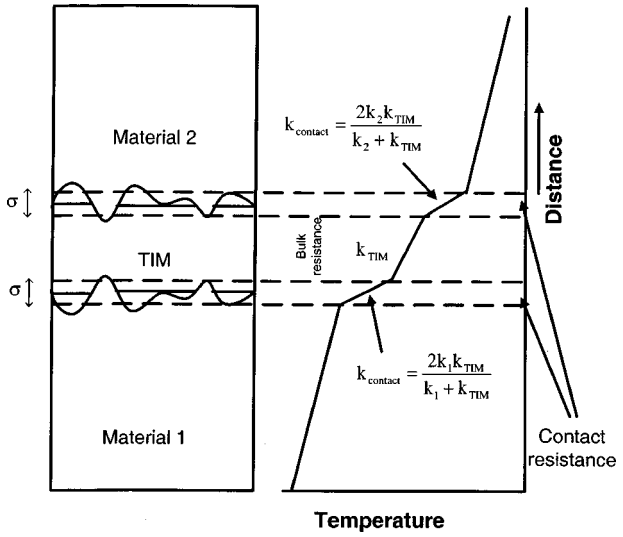

Fig. 1 Schematic showing the origin of contact resistance

strate even without applying any external pressure, which suggests that inter-atomic forces, which depend on the surface energy difference between the substrate and the TIM are present.

This paper introduces an analytical model for the prediction of R_c for this class of fluidic interstitial materials. This model is based on the surface chemistry to account for the surface energy difference and surface characteristics to account for the surface roughness of the substrate. This model is further compared with the experimental results. The experimental setup used was able to separate R_c and R_{bulk}.

Modeling of Thermal Contact Resistance

Figure 1 schematically shows the origin of contact resistance. If one applies a simple one dimensional heat conduction analysis to the zone in Fig. 1, which gives rise to contact resistance an effective thermal conductivity of the contact zone arising due to the roughness can be defined as [11]

$$k_{\text{contact}} = \frac{2k_1k_2}{k_1 + k_2}. \tag{1}$$

Note that other researchers obtained same result by applying an extensive heat conduction analysis to circular discs for solid spot conductance [2]. Equation (1) reveals that k_{contact} is the harmonic mean thermal conductivity of the two sides. While deriving k_{contact} for the contact zone in Eq. (1), it was assumed that the real area of contact is same as the nominal area of contact, but microscopically this is never the case [2]. The real area of contact is always less than the macroscopic nominal area of contact [2]. Assuming that k_{contact} is given by Eq. (1), R_c of any pair of materials, assuming they are nominally flat and there is negligible contribution of the trapped air to the interfacial heat transfer can be written as [11]

$$R_c = \frac{k_1 + k_2}{2k_1k_2}\left(\frac{A_{\text{nominal}}}{A_{\text{real}}}\right)\sigma, \tag{2}$$

where σ is the rms roughness of the interface and A_{nominal} is the nominal area, and A_{real} is the actual microscopic area of contact. The derivation of R_c in Eq. (2) assumes a linear increase in the observed contact resistance due to incomplete area of contact versus that calculated by assuming macroscopic nominal area. The same relation has been derived by applying extensive analysis to multiple spot conductance phenomena [2] in earlier publications. The expression for R_c in Eq. (2) is independent of the material type. For example whether side 1 and side 2 are phase change materials or metal, R_c will be given by Eq. (2). The trick is to find

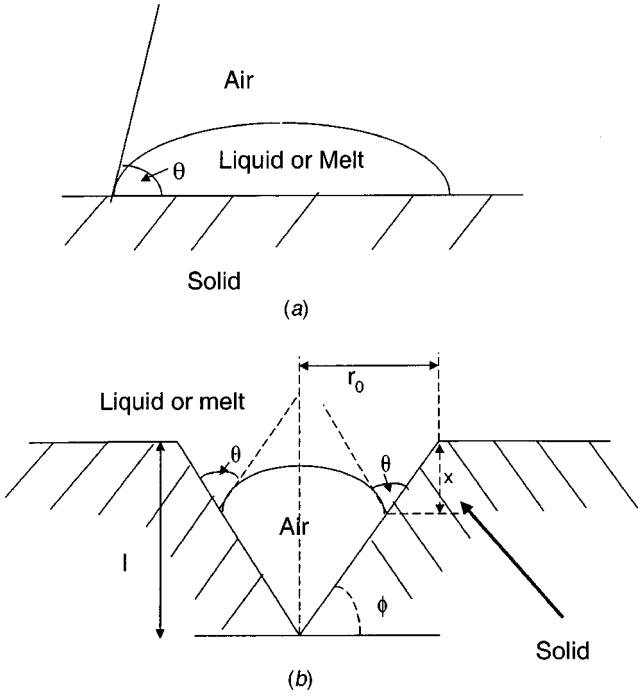

Fig. 2 (*a*) Spreading of a liquid or melt on a microscopically smooth solid surface; and (*b*) liquid/melt interface for notch in the solid/substrate.

the ratio of A_{nominal} and A_{real}. This ratio depends on the material type and is different for different classes of materials. For example, for bare metallic contacts under plastic deformation (no TIM in between) this ratio is given by [2]

$$\frac{A_{\text{nominal}}}{A_{\text{real}}} = \frac{H}{P}, \tag{3}$$

where c is a constant, m the mean absolute slope, H the hardness, P the pressure, and n is another constant. Similar relations have been derived for elastic deformation of bare metallic contacts, metallic foils, elastomeric TIM [2–4], but a model for TIM such as, PCM and grease is not available in the literature [2]. One of the main reasons of difficulty in modeling R_c of fluidic polymers and metallic interface is that all the models for $A_{\text{nominal}}/A_{\text{real}}$ are primarily based on either the theory of plastic or elastic deformation of surfaces [2]. Thus these models depend on properties such as hardness or Young's modulus, whereas for polymers possessing fluid behavior these properties can not be defined.

These fluidic materials also have a distinct difference from other TIMs in that they adhere to the substrate even in the absence of external pressure. This adherence to the substrate indicates the presence of inter-atomic bonding between the substrate and the TIM, which is the result of the difference in the surface energy of the two surfaces. The model developed in this paper is based on this difference in surface energy. Keeping this in view, the surface chemistry of polymer interfaces is briefly discussed here.

When a liquid or melt comes in contact with a solid surface, it spreads out owing to the difference in the surface energy of the liquid/melt and the solid substrate [7]. For a microscopically smooth surface, a drop of liquid takes the shape as shown in Fig. 2(*a*), where θ is the contact angle of the liquid on the substrate [7]. θ is given by the Young Eq. [7]

$$\gamma_{LV}\cos\theta = \gamma_{SV} - \gamma_{SL}, \tag{4}$$

where γ_{LV} is the surface tension of the liquid in equilibrium with its saturated vapor, γ_{SV} the surface tension of the solid in equilibrium with the saturated vapor of the liquid, and γ_{SL} is the interfacial tension between the solid and the liquid. γ_{LV} and γ_{SV} are

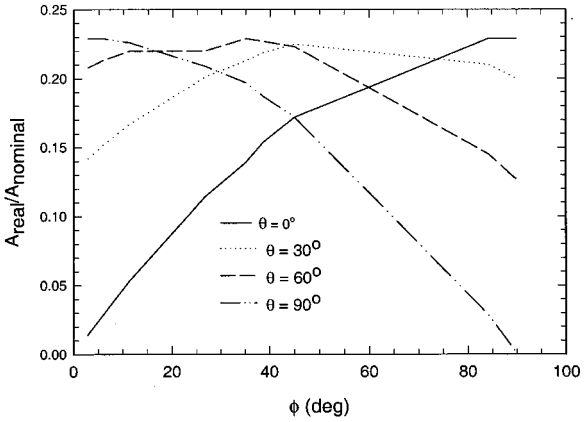

Fig. 3 Ratio of A_{real} and $A_{nominal}$ obtained through exact solution for different values of ϕ and θ

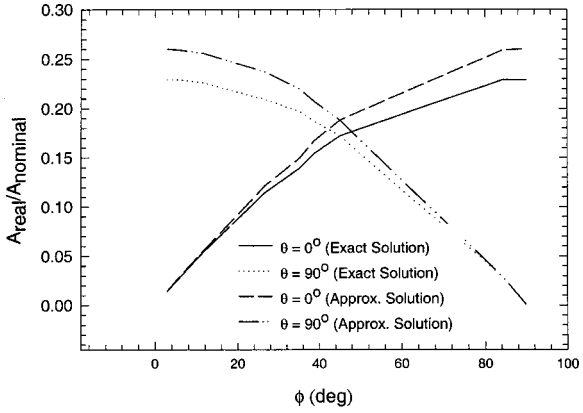

Fig. 4 Comparison of the ratio of $A_{nominal}$ and A_{real} calculated by the exact solution and the approximate solution for different values of ϕ and θ

normally equal to γ_L and γ_S respectively, where γ_L and γ_S are the surface energy of the solid and the liquid respectively [7]. With this assumption, Eq. (4) is rewritten as

$$\gamma_1 \cos\theta = \gamma_2 - \gamma_{12}, \tag{5}$$

where 1 refers to the fluid/melt and 2 refers to the substrate. For a microscopically smooth surface A_{real} and $A_{nominal}$ are same as shown in Fig. 2(*a*), as the liquid is covering the whole area under it on the substrate. If there is a notch in the substrate, the fluid and the substrate interface takes the form shown in Fig. 2(*b*). The notch considered in Fig. 2(*b*) is assumed to be conical in shape. The shape of the fluid/substrate interface is governed by Eq. (5) [7]. The shape of the dome in Fig. 2(*b*) is spherical [8]. The surface energy of the fluid and the small radius of the notch give rise to a capillary force. This capillary force will try to push the liquid into the notch. The capillary pressure is given by [8]

$$F_c = \frac{2\gamma_1 \sin(\theta+\varphi)}{r_0 - x\cot\phi}, \tag{6}$$

where F_c is the capillary pressure, r_0 is the radius of the notch, x the penetration depth of the liquid (shown in Fig. 2(*b*)) and ϕ the angle of the notch with the horizontal as shown in Fig. 2(*b*). If it is assumed that (1) the air is not allowed to escape, i.e., the notch is not open to atmosphere, (2) ideal gas law holds for the trapped air and, (3) the volume of the spherical dome is negligible compared to the conical volume in which the air is trapped, then at equilibrium the applied pressure and the capillary pressure balances the back pressure of the trapped air leading to the following equation:

$$P + \frac{2\gamma_1 \sin(\theta+\varphi)}{r_0 - x\cot\phi} = P_0 \frac{r_0^3}{(r_0 - x\cot\varphi)^3}, \tag{7}$$

where P is the externally applied pressure, and P_0 is the atmospheric pressure. Equation (7) is a polynomial of third degree in x. This equation can be solved for x. The area of contact of the liquid with the substrate in the notch is the area of the frustum of the cone of height x as shown in Fig. 2(*b*). This area can be written as

$$A_{real} = \pi\sqrt{x^2 + (x\cot\varphi)^2}(2r_0 - x\cot\phi). \tag{8}$$

This is the area of the liquid in contact with the notch walls. The area of the conical surface of the notch is given by

$$A_{nominal} = \pi r_0 \sqrt{r_0^2 + 1^2}, \tag{9}$$

where 1 is the depth of the notch. Equations (8) and (9) will give the ratio of the A_{real} and $A_{nominal}$ for the liquid in the notch. This simple model for the notch will be applied to a real rough surface later.

Figure 3 shows the ratio of A_{real} and $A_{nominal}$ for various values of θ and ϕ. The calculation in Fig. 3 are done for $P = P_0$ and γ_1 of $40\times10^{-3}\,\mathrm{N\,m^{-1}}$, which is the typical value for all polymers [7]. The shape of the curve will remain same for different values of P. This figure shows the dependence of $A_{real}/A_{nominal}$ on the notch dimension and the fluid contact angle. For example a larger value of $\tan(\phi)$ for same r_0 means a rougher/bigger notch. This could refer to a rough surface. Figure 3 shows that $A_{real}/A_{nominal}$ is substantially lower than 1 at atmospheric pressure. This figure can be used to find the value of $A_{real}/A_{nominal}$ at atmospheric pressure for a typical polymer. Figure 3 also shows that behavior of the curves change at $\tan\phi = 1$. The behavior of the curves in Fig. 3 is difficult to comprehend directly from Eqs. (7), (8), and (9). To understand the dependence of $A_{real}/A_{nominal}$ on θ and ϕ an approximate solution of x in Eq. (7) can be obtained by using binomial expansion on the right hand side of Eq. (7) by noting that for small pressures such as, for $P = P_0$, $x\cot\phi$ is very small compared to r_0. This reduces Eq. (7) from a third-degree equation to a quadratic equation as follows:

$$\frac{3P_0}{r_0}(x\cot\phi)^2 - 3P_0(x\cot\phi) + 2\gamma_1\sin(\theta+\phi) = 0. \tag{10}$$

If it is further assumed that the quadratic term is negligible compared to other terms in Eq. (10), then x is given by

$$x = \frac{2\gamma_1 \sin(\theta+\varphi)}{3P_0\cot\phi}. \tag{11}$$

$A_{real}/A_{nominal}$ calculated by the approximate solution from Eq. (11) and that by exact solution from Eq. (7) are compared in Fig. 4 for two values of θ. Figure 4 shows that approximate solution given by Eq. (11) is very close to the exact solution. Equation (11) helps in understanding the dependence of $A_{real}/A_{nominal}$ on various parameters. For example at $\tan\phi = 1$, and $\theta = 0$ deg and 90 deg, x remains same as shown by Eq. (11). Figure 3 obtained from the exact solution shows that $A_{real}/A_{nominal}$ is same for $\theta = 0$ deg and 90 deg for $\tan\phi = 1$. Rest of Figs. 3 and 4 can be explained similarly for other values of $\tan\phi$ and θ with the help of Eq. (10).

Equation (7) deserves a closer look in the context of composite interfaces discussed in the classical treatment of interfaces of liquids and solids [9]. In their treatment of rough surfaces, Johnson and Dettre [9], by applying basic thermodynamic principles concluded that a fluid/solid interface changes its behavior from a non-composite to a composite interface only if $\theta + \phi \geq 180$ deg. They did not apply the capillary equation (Eq. (7)) to arrive at this conclusion. From Eq. (7) it is seen that for $\theta + \phi = 180$ deg, the capillary pressure is zero and for atmospheric pressure, no pen-

etration of the liquid will take place, which classically means that the interface has changed from non-composite to composite [9]. This indicates that either a very rough surface or a liquid with a very high contact angle or a combination of both will not result in any penetration of the liquid at atmospheric pressures. It is also worth noting that any combination of $\theta+\phi>180$ deg will result in a negative backpressure. This indicates that a TIM with a large θ can give a very large R_c.

Application of the Notch Model to a Real Rough Surface

A real surface looks like that shown in Fig. 5(*a*). Figure 5(*a*) shows the actual measurement of the surface profile of a bead blasted surface. The measurement of successive points was done at an interval of 2 μm. This real surface profile is simplified for analysis. The peaks and valleys are uniformly distributed for the model surface as shown in Fig. 5(*b*). The spacing of the peaks and valleys in the model surface is assumed to be same as that obtained from actual measurement. Furthermore it is also assumed that the height of the peaks and valleys is same as the r.m.s roughness obtained from the actual measured surface profile. With these assumptions, the model surface is nothing but a series of notches. $A_{\text{nominal}}/A_{\text{real}}$ for this model surface will remain same as that for the single notch given by Eqs. (7), (8), and (9). Tan (ϕ) in Eqs. (6), (7), and (8) for the rough surface is given by

$$\tan\phi=\frac{\sigma}{r_0} \tag{12}$$

and $1=\sigma$ in Eq. (9). It is to be noted here that the modeling of the rough surface as series of notches has been done to simplify the calculation of $A_{\text{nominal}}/A_{\text{real}}$ as the idea in this paper is to show the validity of the surface chemistry model. In rigorous terms one can apply statistical arguments while calculating $A_{\text{nominal}}/A_{\text{real}}$ for real rough surfaces, as has been done for other models for R_c [2], but this does not change the physics behind the surface chemistry model introduced in this paper.

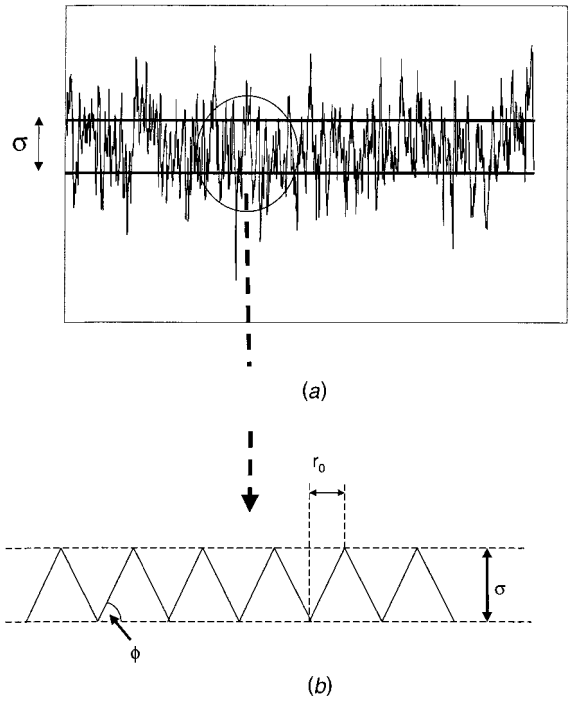

Fig. 5 (*a*) Actual measurement of roughness (in μm) on a bead blasted rough block; and (*b*) modeling of a rough surface as series of notches for the prediction of R_c.

Measurement of the Surface Energy and the Contact Angle

The surface energy of the TIMs and the copper substrate was measured with standard 2 liquid method using water and methyl iodide [7]. The surface energy is calculated by the geometric mean method [7], which gives:

$$(1+\cos\theta)\gamma_L=2\sqrt{(\gamma_{Lp}\gamma_{Sp}+\gamma_{Ld}\gamma_{Sd}}, \tag{13}$$

where the subscript L refers to the liquid, S the substrate, p and d refers to the polar and the dispersion component of the surface energy, respectively [7]. The total surface energy is the sum of the polar and the dispersion component [7]. In the two liquid technique, the material for which surface energy is being measured is used as the substrate and the contact angle of Water and methyl iodide (CH_2I_2) is measured on the substrate. γ_d and γ_p of the water and CH_2I_2 are very well known [7]. Thus by measuring of the contact angle of these two liquids and using Eq. (13), γ_{Sp} and γ_{Sd} can be calculated. For the PCMs considered in this paper the surface energy was measured without melting the PCM. For most of the polymers surface energy of the melt and liquid are nearly same [7]. The surface energy has temperature dependence, but it is normally very weak [7]. Keeping this in view, for the modeling of the contact resistance, it is assumed that the surface energy of the un-melted PCM is same as the melted one. Same method was used to measure the surface energy of the copper blocks and silicone based greases. The data on the measured surface energy and its various components are shown in Table 1. For each surface three measurements were taken and the data reported here is the average of the three measurements.

Table 1 shows that various TIMs have approximately the same surface energy. The values reported here match the typical values of surface energy obtained on these types of polymers in the literature [7]. Due to the low value of surface energy, these materials are also called low energy surfaces [7]. Copper and metallic surfaces are supposed to be high-energy surfaces. Their surface energy is normally of the order of 1 N m^{-1} [7]. Table 1 shows that this is not the case for the experiments considered here. Initially, it was thought that there was some error in the measurement of the surface energy of copper. Therefore, the experiments were repeated on other copper blocks, leading to the same conclusion. Other research groups have found similar number for the surface energy of copper [10]. The main reason for very low surface energy of copper is that it absorbs moisture, hydrocarbons and other low energy materials as soon as it is exposed to the environment owing to its high surface energy [7]. This absorption of low energy materials considerably reduces the surface energy of copper. Table 1 also shows that γ_p for all the TIMs and the copper is negligibly small compared to γ_d.

Contact angle of the PCM was also directly measured on the copper substrate. The values are shown in Table 1. The PCM were melted and the contact angle of the molten liquid was measured by sessile drop method [7]. In this method a drop of the liquid is dispensed on the substrate with the help of a syringe. The measurement of the contact angle was done on the mirror finish copper blocks as rough blocks can give rise to metastable contact angle [7], whereas the model developed here is based on intrinsic contact angle (Eq. (3)), which is a thermodynamic property of the interface [7]. Owing to the extremely high viscosity of the silicone

Table 1 Surface energy of TIMs and the copper blocks, and the contact angle of the TIMs on the copper block

	Phase Change Material A	Phase Change Material B	Silicone Based Thermal Grease	Copper Block
γ (N/m)	42.85 X 10^{-3}	27.13 X 10^{-3}	36.19 X 10^{-3}	29.31X10^{-3}
γ_d (N/m)	41.59 X 10^{-3}	27.12 X 10^{-3}	35.22 X 10^{-3}	29.30 X 10^{-3}
γ_p (N/m)	1.26 X 10^{-3}	0.01 X 10^{-3}	0.97 X 10^{-3}	0.01 X 10^{-3}
θ (deg)	34.3	23.0	36.0 (calculated)	

Table 2 Experimental program for the measurement of R_C

Variables		PCM (Paraffin based)	Grease (Silicone based)
Materials		**Two different materials** • PCM A: With filler k = 0.7 W/mk • PCM B: Without the filler (only the matrix) k = 0.2 W/mk	**Four different materials** • Grease 1 k = 3.1 W/mk • Grease 2 k = 0.4 W/mk • Grease 3 k = 0.25 W/mk • Grease 4 k = 0.2W/mk
Copper Blocks	Roughness	No. of pair of blocks of different roughness used per TIM and the type of TIM tested for each roughness	No. of pair of blocks of different roughness used per TIM and the type of TIM tested for each roughness
	• Bead blasted (3.5 μm)	• No. of pair of blocks: 3 • Type of TIM: PCM A and PCM B	• No. of pair of blocks: 1 • Type of TIM: Grease 1, 2, 3 and 4
	• Regular machined surface (1 μm)	• No. of pair of blocks: 1 • Type of TIM: PCM A	• No. of pair of blocks: 1 • Type of TIM: Grease 1, and 2
	• Mirror Finish (0.12 μm):	• No. of pair of blocks: 2 • Type of TIM: PCM A	• No. of pair of blocks: 1 • Type of TIM: Grease 1

grease, the syringe for dispensing the drop of the grease could not be used. For grease the contact angle on the copper substrate is calculated by using Eq. (13) as all the required variables are known as shown in Table 1. This indirect method of calculation of the contact angle illustrates that if the direct contact angle measurement is not possible, then γ_d and γ_p of the liquid/melt should be measured and Eq. (13) should be used for the calculation of the contact angle with different substrates. This method provides a very strong tool for the calculation of the contact angle without direct measurement of contact angle, as γ_d and γ_p of different materials are normally available in the literature [7]. The calculated values of q for PCM A and B are 49 deg and 0 deg respectively. This does not compare very well with the measured value of θ, but this is not surprising as the measurement of θ is very sensitive to various factors such as surface residue and etc. [7]. This does not affect the results of the model adversely as the cosine of 49 deg and 0 deg are very close to the cosine of the measure measured values for material A and B respectively (Table 1) and the ratio of A_{real} and A_{nominal} for various roughness is also not very sensitive to θ for the combination of roughness and material considered in this paper (Fig. 3 and Table 2).

Experimental Program for the Measurement of R_c

The parameters which were studied in the experiments on R_c were as follows: (1) classes of materials, PCM versus Grease; (2) roughness: highly rough (bead blasted), machined surface, and mirror finish; and (3) different thermal conductivity for the same class of materials. The details of the experimental structure are discussed by Prasher et al. [11].

The experimental program is shown in Table 2. In the experiment the following combinations of upper and lower blocks were used: *Rough/Rough; Machined/Machined; and Smooth/Smooth*.

The blocks were made of copper. Experiments with spacers were conducted to find out the thermal conductivity of the TIM. The BLT (Bond line thickness) of the TIM was measured using a camera [12]. Contact resistance is obtained by using the following equation:

$$R = \frac{\text{BLT}}{k_{\text{TIM}}} + R_{c_{1+2}}, \tag{14}$$

where R is the total resistance, and $R_{c_{1+2}}$ is the sum of the contact resistance of the TIM with both the upper and lower copper blocks. The experiments were performed for different TIMs and different roughness as discussed by Prasher et al. [11]. There were two types of paraffin based PCM considered in this experiment. The only difference between them is that PCM *B* has no fillers in it, which results in a lower k compared to TIM *A*, which has conducting fillers in it. The silicone-based greases also have different k as shown in Table 2. In their earlier study Prasher et al. [11] did not vary the pressure. For the current study contact resistance of TIM *A* is also measured as a function of pressure for the rough blocks.

Error Analysis

The error in the contact resistance with the help of Eq. (14) can be written as [13]

$$\frac{\Delta R_{c_{1+2}}}{R_{c_{1+2}}} = \sqrt{\left(\frac{\Delta R}{R - \text{BLT}/k_{\text{TIM}}}\right)^2 + \frac{1}{k_{\text{TIM}}^2}\left(\frac{\Delta \text{BLT}}{R - \text{BLT}/k_{\text{TIM}}}\right)^2}. \tag{15}$$

The error in R for the PCM is $3\times10^{-6}\,\text{K m}^{-2}\,\text{W}^{-1}$ and for the grease is $2\times10^{-6}\,\text{K m}^{-2}\,\text{W}^{-1}$ [11]. For error analysis of R, the readers are advised to read reference [11] by Prasher et al. [11]. The error in the BLT is 3.3 μ, which is size of the pixel of the camera.

Comparison of Experimental Data With the Model

As discussed earlier for simplicity, the actual rough surface is assumed to be an idealized rough surface of uniform peaks and valleys, which are equally placed as shown in Fig. 5(*b*). The successive data points in Fig. 5(*a*) were measured at an interval of 2 μ for the rough and the machined surfaces, and at 0.7 μ for the smooth surface. The roughness was measured with the help of a non-contact laser beam profilometer made by UBM corporation. The resolution of the profilometer is 0.01 μm if the measurement area is 50 μm and is 0.1 μm if the measurement area is 500 μm. The radius of the cone in the model surface in Fig. 5(*b*) is assumed to be 2 μ for the rough and machined surfaces, and 0.7 μ for the smooth surface which are same as the measurement intervals used to characterize the roughness of the rough and the smooth blocks respectively by the profilometer. The height of the peaks and the valleys is assumed to be same as the r.m.s roughness of the surface.

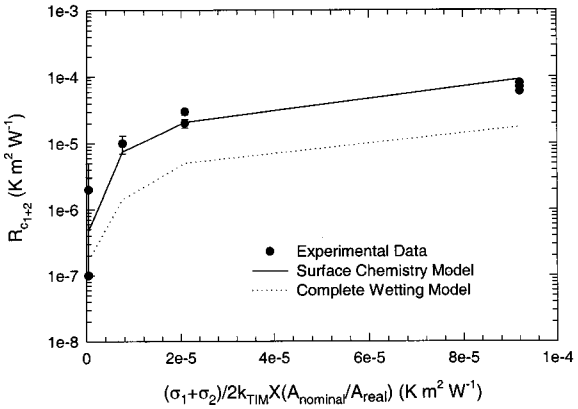

Fig. 6 Comparison of the surface chemistry model with experimental results for Phase change materials

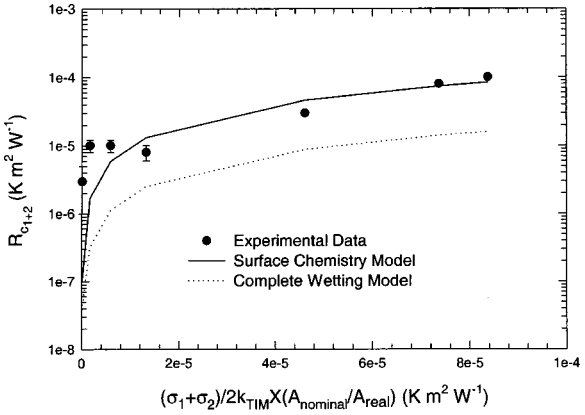

Fig. 7 Comparison of the surface chemistry model with experimental results for Silicon based greases

Owing to the very low thermal conductivity of TIMs compared to copper, and with the help of Eq. (2), $R_{c_{1+2}}$ can be written as

$$R_{c_{1+2}} = \left(\frac{\sigma_1+\sigma_2}{2k_{\mathrm{TIM}}}\right)\left(\frac{A_{\mathrm{nominal}}}{A_{\mathrm{real}}}\right), \tag{16}$$

where σ_1 and σ_2 are roughness of the two copper blocks. Figure 6 shows the $R_{c_{1+2}}$ data for the PCM at a pressure of 1 atm. The data is plotted against the model as shown by Eq. (16). Equations (7), (8), and (9) are used to calculate the $A_{\mathrm{nominal}}/A_{\mathrm{real}}$. The model developed in this paper is called the surface chemistry model. k and σ data are used from Table 2. The model matches very well with the experimental data within experimental error. Figure 7 shows the $R_{c_{1+2}}$ results for different greases at a pressure of 1 atm. Again the model matches very well with the data. Figures 6 and 7 indicate that this model, which is based on the surface chemistry and the characteristics is very successful in predicting R_c for PCM and grease types of polymeric TIM, and is able to explain the underlying phenomenon behind R_c. The surface chemistry model matches very well with the data in spite of the fact that the roughness of the surface was modeled as uniformly distributed peaks and valleys; thus notch model for surface roughness is not a very bad assumption. Both Figs. 6 and 7 also show the contact resistance results for the case where $A_{\mathrm{nominal}}/A_{\mathrm{real}} = 1$. This model is called the complete wetting model, which means that the TIM is completely able to wet the surface. This is theoretically the lowest possible value of the sum of contact resistances of the two interfaces in any sandwich of metal/polymer/metal, and is given by

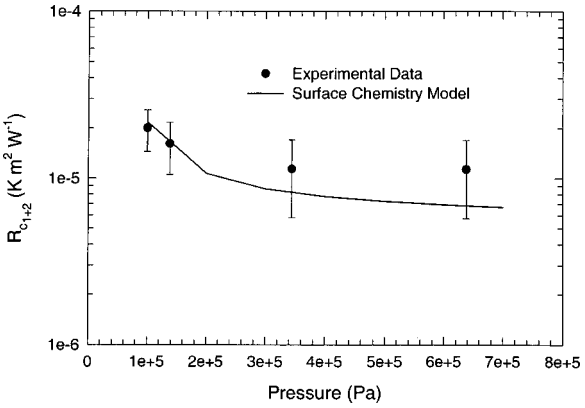

Fig. 8 R_c of PCM A versus pressure for bead blasted rough blocks

$$R_{c_{1+2_{\mathrm{lowest}}}} = \frac{\sigma_1+\sigma_2}{2k_{\mathrm{TIM}}}, \tag{17}$$

where $R_{c_{1+2_{\mathrm{lowest}}}}$ is the lowest possible value of the contact resistance. This assumes that $k_{\mathrm{TIM}} \ll k_{\mathrm{metal}}$. The complete wetting model indicates that even if $A_{\mathrm{nominal}}/A_{\mathrm{real}} = 1$, R_c can be nonzero, depending on the σ and k_{TIM}.

Figure 8 is the comparison of the surface chemistry model with experimental data on PCM *A* for different pressures for the rough blocks. The model matches very well at lower pressures but tends to deviate slightly at higher pressures. At higher pressures, the percentage error in BLT measurement is significantly higher as the BLT is very thin. This could be one of the reasons of the deviation of the model from the experimental data.

Conclusion

This paper introduces a novel model for R_c of fluidic interstitial polymeric TIMs. The model matches very well with the experimental data. The model indicates that thermal contact resistance of polymeric interstitial materials depends on surface tension and the contact angle of the polymer, surface roughness of the substrate, thermal conductivity of the polymer, and the pressure. Roughness of the substrate, surface energy of the polymers and the substrate, the contact angle of the PCM on the substrate, and contact resistance were measured to validate the model. A method is also suggested to indirectly calculate the contact angle of the TIM with any substrate, in lieu of direct measurement of the contact angle. Although the model is currently based on simplified notch model for an actual rough surface, it is able to capture the effects of various critical parameters, which affect the contact resistance.

Acknowledgment

The author would like to acknowledge the support of Dr. Jin-lin Wang for measuring the surface energy and the contact angle of various materials. The author would also like to thank George Berdine for providing critical comments on editing and technical contents of the manuscript.

Nomenclature

A_{nominal} = nominal area (m^2)
A_{real} = real area (m^2)
BLT = bond line thickness (m)
c = constant in Eq. (3)
F_c = capillary pressure (N m^{-2})
H = hardness (N m^{-2})
k = thermal conductivity (W m^{-1} K^{-1})
l = depth of the notch (m)
n = constant in Eq. (3)
P = pressure
P_0 = atmospheric pressure (N m^{-2})
PCM = phase change material
R = thermal resistance (K m^2 W^{-1})
r_0 = radius of the notch (m)
R_c = thermal contact resistance (K m^2 W^{-1})
$R_{c_{1+2}}$ = sum of the thermal contact resistance with the upper and lower blocks (K m^2 W^{-1})
$R_{c_{1+2_{\mathrm{lowest}}}}$ = lowest theoretical R_c of any two materials (K m^2 W^{-1})
TIM = thermal interface material
x = penetration depth of the TIM (m)

Greek

θ = contact angle (rad)
ϕ = angle of the notch with the horizontal (rad)
γ = surface energy (N m^{-1})
σ = surface roughness (m)

ΔBLT = error in measurement of BLT (m)
ΔR = error in measurement of R (K m^2 W^{-1})

Subscript

1, 2 = sides
d = dispersion component of surface energy
L = liquid
p = polar component of surface energy
S = solid or substrate
V = vapor

References

[1] Snaith, B., O' Callaghan, P. W., and Probert, S. D., 1984, ''Use of Interstitial Materials for Thermal Contact Conductance Control,'' Proc. AIAA 22nd *Aerospace Sciences Meeting*, Jan. 9–12, 1984, Reno, Nevada, pp. 1–8.

[2] Madhusudana, C. V., 1996, *Thermal Contact Conductance*, Springer-Verlag, New York.

[3] Snaith, B., O'Callaghan, Snaith, B., and Probert, S. D., 1982, ''Minimizing the Thermal Resistance of Pressed Metallic Contacts,'' J. Mech. Eng. Sci., **24**, No. 4, pp. 183–189.

[4] Zhao, L., and Phelan, P. E., 1999, ''Thermal Contact Conductance Across Filed Polyimide Films at Cryogenic Temperatures,'' Cryogenics, **39**, pp. 803–809.

[5] Devpura, A., Phelan, P. E., and Prasher, R. S., 2000, ''Percolation Theory Applied to the Analysis of Thermal Interface Materials in Flip-Chip Technology,'' *Proc. of ITHERM*, May 23–26, Las Vegas, Nevada, Vol. 1, pp. 21–28.

[6] Fletcher, L. S., and Peterson, G. P., 1986, ''The Effect of Interstitial Materials on the Thermal Contact Conductance of Metallic Junctions,'' *Heat Transfer in Systems Seminar-Phase II*, National Cheng University, Tainan, January 13–14.

[7] Wu, S., 1982, *Polymer Interface and Adhesion*, Marcel Dekker, New York.

[8] de Bruyne, N. A., 1956, ''The Extent of Contact Between Glue and Adherend,'' *Aero Research Technical Notes*, The Technical Service Department, Aero Research Limited, CIBA Company, Duxford, Cambridge.

[9] Johnson, R. E., and Dettre, R. H., 1969, ''Wettability and Contact Angles,'' *Surface and Colloid Science*, Matijevic, E., ed., Willey-Interscience, New York, pp. 338–401.

[10] Jager-Lezer, N., Feutelais Y., Jager-Lezer, N., Doucet, J., Tranchant, A., Baszkin, A., and Grossiord, J. L., 1999, ''Influence of the Chemical Nature of Various Geometries on the Rheological Behavior of Lamellar Lyotropic Phase,'' J. Rheol., **43**, Issue 5, pp. 1067–1082.

[11] Prasher, R. S., Simmons, C., and Solbrekken, G., 2000, ''Thermal Contact Resistance of Phase Change and Grease Type Polymeric Materials,'' *Proc. of International Mechanical Engineering Congress and Exposition*, Orlando, Florida, November, MED-Vol. 11, pp. 461–466.

[12] Solbrekken, G., Chiu, C.-P., Byers, B., and Reichenbacher, D., 2000, ''The Development of a Tool to Predict Package Level Thermal Interface Material Performances,'' *Proc. of ITHERM*, May 23–26, Las Vegas, Nevada, Vol. 1, pp. 48–54

[13] Kline, S. J., and McClintock, F. A., 1953, ''Describing Uncertainties in Single Sample Experiments,'' Mech. Eng. (Am. Soc. Mech. Eng.), **75**, pp. 3–8.

Enhancing Small-Channel Convective Boiling Performance Using a Microporous Surface Coating

C. N. Ammerman[1]
Mem. ASME,
The University of Texas at Arlington,
Department of Mechanical
and Aerospace Engineering,
Box 19023-0023,
Arlington, TX 76019

S. M. You
Mem. ASME,
Seoul National University,
School of Mechanical
and Aerospace Engineering,
San 56-1, Shinrim-Dong, Kwanak-GU,
Seoul 151-742, KOREA

Performance characteristics are experimentally determined for enhanced convective boiling of FC-87 in a horizontal, small-cross-sectional-area, single-channel heater. The channel tested has a square cross section with a side length of 2 mm and a heated length of 8 cm. The heated surface of the channel is tested both with, and without, a microporous surface coating. Although few studies have been performed to quantify the effects of internal porous coatings on flow boiling, their application in this area is promising. The coating is shown to provide increases in both heat transfer coefficient and critical heat flux. Convective boiling curves are generated for mass fluxes from 500 to 5000 kg/m^{2}s and for inlet subcooling levels ranging from 2 to 31°C. [DOI: 10.1115/1.1388300]

Keywords: Boiling, Convection, Enhancement, Heat Transfer

Introduction

Heat removal in flow boiling can be classified either as boiling-dominated or convection-dominated. Convection-dominated heat transfer is a strong function of either mass flux or quality and a weak function of heat flux. Boiling-dominated heat transfer is a strong function of heat flux and a weak function of either mass flux or quality. When dominated by boiling, heat transfer coefficients are generally higher than if boiling were not present. It is desirable, therefore, to generate conditions that promote boiling and avoid geometries that suppress it.

To increase the efficiency of flow boiling compact heat exchangers, research has been performed involving modification of the flow passage surface geometry. This research includes studies by Carey and co-workers on offset strip fins and ribbed channels (Carey and Mandrusiak [1], Mandrusiak and Carey [2,3], Xu and Carey [4]), and Westwater and co-workers on offset strip fins (Panitsidis et al. [5], Chen et al. [6], Chen and Westwater [7]). Offset strip fins or ribs in channels provide enhancement by conducting heat away from the primary surface and by breaking up the developing boundary layer on channel walls. However, results from these studies indicate that these modifications can lead to increased pressure drop, suppression of nucleate boiling, and uneven flow distribution.

Channel Size Reduction. Flow boiling studies have shown that small channels remove heat efficiently and support high heat flux levels (Lazarek and Black [8], Orozco and Hanson [9], Moriyama and Inoue [10], Wambsganss et al. [11], Cornwell and Kew [12], Bowers and Mudawar [13], Xia et al. [14], and Ammerman and You [15]). Heat transfer coefficients are enhanced with decreases in channel diameter, as long as channel dimensions are not made too small. Some of these studies indicate the existence of a critical channel dimension where heat transfer performance is maximized. In addition, boiling-dominated heat transfer has been frequently observed in small channels. Reducing channel size is a favorable method of enhancing performance compared with modifying the channel geometry with the addition of fins or ribs. This is because channel geometry modifications can lead to negative impacts on performance, as mentioned previously.

Addition of Microporous Surface Coating. Porous surfaces containing re-entrant-type cavity geometries have been shown in several studies to enhance boiling heat transfer. Many commercial enhanced surfaces have been shown to provide these geometries, such as ECR-40 of Furukawa Electric, GEWA series of Wieland-Werke, High-Flux of UOP, Thermoexcel series of Hitachi and Turbo-B of Wolverine. As summarized by Thome [16], studies have shown that these surfaces provide boiling enhancement.

Systematic pool boiling investigations have been performed with a microporous coating developed at the University of Texas at Arlington to assess performance of various fluids and heater configurations and to determine surface microstructure for optimum boiling enhancement. O'Connor and You [17] tested a 0.51 cm$\times$1.65 cm flat heater with both a smooth and microporous-coated surface immersed in saturated FC-72. Their surface coating was a novel paint mixture composed of 3–10 μm silver flakes and thermal epoxy with isopropyl alcohol as a carrier. The application of this coating in a 25 μm layer reduced incipient superheat by 85 percent, enhanced nucleate boiling heat transfer coefficient by 70 to 80 percent, and increased CHF by nearly 110 percent. O'Connor et al. [18] developed and tested a dielectric version of this boiling enhancement paint by substituting 8–12 μm diamond particles for the silver flakes. This dielectric coating could be directly applied to the surfaces of immersion-cooled microelectronic devices. Chang and You [19,20] performed detailed studies of paint composition including particle type and size, epoxy type, and paint application method. These tests were conducted on flat heaters immersed in saturated FC-72. Their results showed that regardless of the particle and epoxy types tested, their coatings reduced incipient superheat by 80 to 90 percent, increased nucleate boiling heat transfer coefficient by approximately 330 percent, and raised CHF by approximately 100 percent compared with a smooth reference surface.

The excellent performance of the coating results from an increase in both the number of nucleation sites and the bubble departure frequency. As initial vaporization occurs within the paint structure, the embryonic bubble grows rapidly and vapor generated from one individual liquid-vapor interface is divided into many tiny bubbles. The resulting effect at low heat fluxes is high bubble departure frequencies and small bubble departure sizes

[1]Presently at Los Alamos National Laboratory, Los Alamos, NM 87545.

Contributed by the Heat Transfer Division for publication in the JOURNAL OF HEAT TRANSFER. Manuscript received by the Heat Transfer Division November 8, 1999; revision received February 12, 2001. Associate Editor: C. Beckermann.

(<0.2 mm). For untreated surfaces, bubble sizes of approximately 0.7 mm were observed. The increase in CHF is a result of the persistence of isolated small bubbles adjacent to the heated surface throughout the entire boiling curve, including just prior to CHF. This contrasts with the observed behavior of the untreated surface. Just prior to CHF, the untreated surface exhibited large vapor bubbles and localized regions of film boiling.

Although few studies have been performed to quantify the effects of internal porous coatings on flow boiling, their application in this area is promising. Thome [16] reported on two such studies. The first, by Czikk et al. [21], was performed using liquid oxygen, ammonia, and R-22 inside a vertically oriented 18.7 mm diameter tube internally covered with the commercially available High Flux coating. They reported that the heat transfer coefficient for the porous-coated tube was insensitive to quality and mass flux and was typically an order of magnitude greater than that for smooth-tube data. Czikk et al. [21] also tested ammonia inside a horizontally oriented porous-coated tube with a 25 mm outside diameter. For this tube, however, they did report a mass flux dependence on heat transfer. This might be expected due to the relatively large tube diameter. The second study reported by Thome [16] was performed by Ikeuchi et al. [22] who plated 0.115 mm diameter copper particles inside a 17.05 mm internal diameter tube. Using R-22, their enhanced-tube heat transfer coefficient was approximately 5 times better than plain-tube performance for exit qualities between 70 and 95 percent. These studies indicate that internal porous coatings can dramatically improve flow boiling performance.

The present study is a continuation of a flow boiling investigation that examined enhancement mechanisms that do not require the use of fins or ribs within the channel. Previously, Ammerman and You [15] reported on heat transfer enhancement generated simply by reducing channel cross-sectional area. In the investigation described here, enhancement is obtained with the application of a thin, microporous surface coating. A single-channel test section is examined to prevent the dynamics of multiple-channel interaction from confounding the test results. Average heat transfer coefficients, as well as test section pressure drop, are measured for two-phase operation. Tests are conducted to examine the effects of velocity, subcooling, and heater surface condition on heat transfer and pressure drop performance. The present research using a small channel diameter combined with a dielectric working fluid is relevant to electronics cooling applications.

Experimental Apparatus and Procedure

The closed-loop flow boiling test facility used for this experimental effort is shown in Fig. 1. A shell-and-tube heat exchanger is used both as a condenser and as a working-fluid reservoir. Fluid passes from the condenser through a variable-speed pump followed by a filter. Fluid flow rate can be measured with either a variable-area flowmeter (0.005 to 0.04 lpm) or a turbine flowmeter (0.04 to 2 lpm). Upon exiting the flowmeter, the fluid passes through three pre-conditioning heaters that enable control of test section inlet quality. Fluid then passes through the test section and flows back to the shell side of the condenser, completing the loop. The tube side of the condenser is connected to a chiller. The condenser is also connected to a degassing tank that is equipped with a cartridge heater. The degassing tank is used to aid in degassing the test fluid and to set the reference pressure for the facility. More detailed information regarding the design of this loop can be found in Ammerman [23].

Description of Single-Channel Test Section. A 2 mm, square cross-section channel was investigated. The heated section of this channel was 8 cm in length and was oriented horizontally. Joule heating was supplied along the length of the lower channel

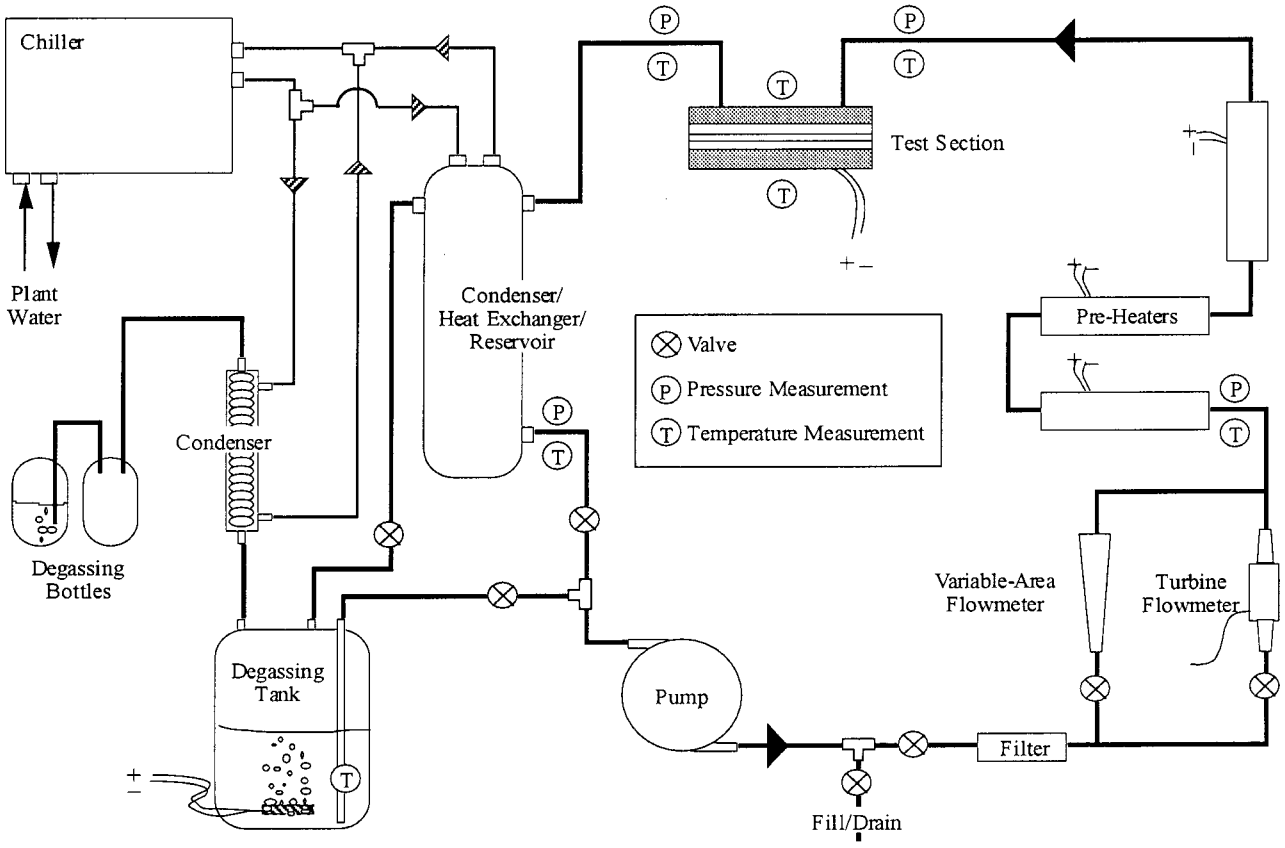

Fig. 1 Flow boiling test facility

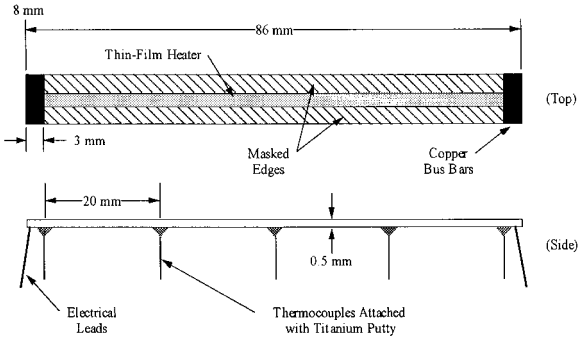

Fig. 2 Thin-film heater on silicon substrate

wall with a thin-film resistive heater. Thermocouples were installed to enable the measurement of local wall and fluid temperatures within the channel.

A thin-film resistive heater was sputtered directly onto a silicon substrate. The silicon substrate measured 8 mm wide by 86 mm long by 0.5 mm thick, as shown in Fig. 2. A mask was applied exposing the silicon where the heater and bus bars were to be sputtered. The width of the heater layer corresponded to the channel width. After the heater layer had been applied, copper was sputtered onto the top, ends, and bottom of the 3 mm end sections to act as bus bars. The heater was instrumented with five, 30 gauge, type-T thermocouples attached to the bottom side of the silicon substrate. The thermocouples were evenly spaced 20 mm apart across the 80 mm heated length and were attached using titanium putty. For steady-state operating conditions, the estimated temperature difference between the heated surface and the bottom side of the substrate was negligible.

The test section was made using a ''sandwich'' design with multiple layers, as shown in Fig. 3. The silicon heater rested on a

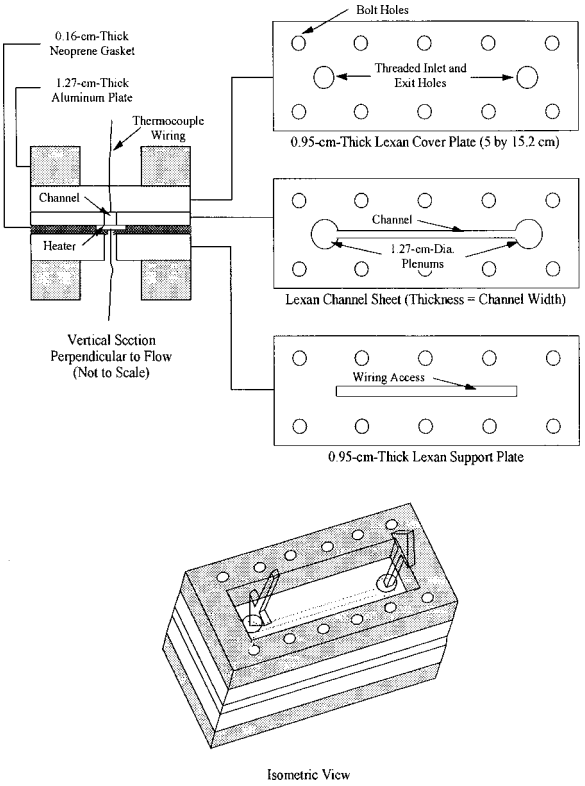

Fig. 3 Drawing of single-channel test section

neoprene gasket layer in the middle of the test section. This gasket layer had a narrow section removed to allow the heater thermocouple wires to pass through the bottom of the test section and to allow the electrical leads to reach the heater. The thin, flat, copper electrical leads were placed between the bottom of each end of the silicon heater and the neoprene gasket. The leads were held in place with mechanical force. Beneath the neoprene gasket was a lexan base plate. This base plate also had a narrow section removed to allow wires to pass through to the silicon heater. Above the silicon heater was a lexan flow channel sheet. This sheet had a thickness equivalent to the channel width and had the flow channel cut out of its center. This sheet, therefore, formed the flow channel side walls.

On either end of the flow channel were inlet and outlet plenums also cut out of the flow channel sheet. Above the flow channel sheet was a lexan plate. This plate formed the top wall of the flow channel. Five, 1 mm holes were drilled into the top of this plate to accommodate 30-gauge, type-T thermocouples. The thermocouple beads were mounted flush with the inner wall of the plate. The holes were sealed with silicone. These thermocouples were located directly above the heater thermocouples, thus enabling local heat transfer coefficient measurements. Two aluminum plates were bolted above and below this stack to provide rigidity to the test section. More information about the design of test section can be found in Ammerman [23].

Microporous Surface Coating. The small-channel heater was tested both with, and without, the application of a microporous surface coating. The coating consisted of enhancement particles, a binder, and a carrier. The coating used in this study is the ''DOA'' coating characterized by Chang and You [19] with methyl-ethyl-ketone (MEK) as a carrier instead of alcohol. The particles were 8–12 μm industrial diamond powder. Diamond is electrically non-conducting which enables the particles to be attached directly to the thin-film heater. The binder is Omega 101 epoxy and is used to glue the particles to the heater. The carrier is MEK, which evaporates quickly after application leaving only the particles and the binder on the surface. A uniform layer was obtained by dripping the paint onto the heater surface and gently shaking the heater from side-to-side to evenly distribute the paint. This painting method resulted in a coating thickness of approximately 100 μm. From SEM images of the coating, Chang and You [19] observed a wide range of pore sizes with a maximum on the order of the particle diameter. They were unable to measure porosity of the coating directly but did estimate porosity of the diamond power alone to be 41 percent. Additional details on the mixing and application of this coating are given by Chang and You [19].

Chang and You [20] also investigated alternate painting methods and performed both durability and adhesion tests. To make the enhancement coating more widely applicable, a spray method of application was developed. The epoxies investigated by Chang and You [20] were selected because they are known to be inert to toxic chemical attack. Durability tests showed little or no degradation in coating performance. Adhesion tests revealed that the coatings have a strong bond strength based on accepted ASTM test methods.

Uncertainty Analysis. A single-sample uncertainty analysis was performed for the test facility and test section based on the method of Kline and McClintock [24]. For the calculation of heat flux uncertainty, the uncertainties in the following parameters were considered: voltage ($\pm$0.009 percent), current ($\pm$0.86 percent), heater surface area ($\pm$3.5 percent). To estimate heat losses to external surroundings, a two-dimensional, steady-state conduction solution was obtained for the test section (perpendicular to the flow) using a finite-difference-based conduction code. This heat loss calculation was conservative assuming a surface heat flux of 500 W/cm^2, which resulted in a heater surface temperature of 250°C. The external heat loss for this condition was estimated

Table 1 Convective boiling uncertainty results

Parameter	Uncertainty
Test Heater Heat Flux	±3.6%
Test Section Pressure Drop	±3.5 kPa
Mass Flow Rate	±5.5%

to be less than 1 percent of the total heat dissipated within the channel. Heat loss through the 30 gage, insulated, thermocouple wires was negligible. Detailed calculations for this uncertainty analysis can be found in Ammerman [23]. The results of this analysis are shown in Table 1.

To ensure that no significant measurement variation existed between the ten, test section thermocouples, a qualification run was performed for each heater. The flow loop was allowed to remain idle for a minimum of 12 hours. The data acquisition system was then used to record and average 30 readings from each of the five test heater thermocouples and the five channel fluid thermocouples. The maximum variation in the average of these 30 temperature readings from thermocouple to thermocouple was within 0.1°C.

Test Procedure. The liquid chosen for this convective boiling study was FC-87. Relevant properties for FC-87 are listed in Table 2 (Fluorinert Product Manual [25]). Liquid FC-87 can absorb a significant volume of air at atmospheric conditions. Hong et al. [26] showed that dissolved gas could greatly affect boiling heat transfer coefficient. For this study, therefore, the FC-87 was degassed prior to each series of experimental runs. Information on the degassing procedure can be found in Ammerman [23].

Two runs were performed for each flow velocity/inlet subcooling test case. Prior to the initiation of a test run for a new case, the pump flow rate was adjusted to provide the desired test section velocity and the pre-heaters were turned on and adjusted to provide the desired level of inlet subcooling. Volume flow rate, test section inlet temperature, and other temperatures within the loop were monitored until steady-state conditions were achieved (typically around 30 minutes).

Steady state was achieved using a computer program that incrementally advanced the heat flux to the test section and monitored test section temperatures. Upon advancing the heat flux, the program continuously monitored heater temperatures for 60 seconds to watch for burnout due to overheating. The program was designed to shut the power supply off in the event of dryout or CHF.

Table 2 Saturation properties of FC-87 at 1 atm (Fluorinert Product Manual [25])

Chemical Formula	C_5F_{12}
Boiling Point (°C)	30
Liquid Density (kg/m^3)	1572
Vapor Density (kg/m^3)	12.38
Liquid Specific Heat (J/kg·°C)	1103
Heat of Vaporization (J/kg)	98970
Liquid Thermal Conductivity (W/m·°C)	0.0550
Liquid Viscosity (kg/m·s)	0.000669
Surface Tension (N/m)	0.00890

At the end of this 60 second period, the monitored temperature readings were averaged. Then the program continuously acquired and averaged heater temperatures for subsequent 20 second durations. At the end of each monitoring period, all five average temperatures were compared with the averages from the previous monitoring period. When all five values were within 0.2°C of their previous values, steady state was assumed to be achieved. Upon reaching steady state, detailed temperature, pressure, and heat flux readings were acquired and written to an output file. After recording output, the heat flux was advanced and the cycle was repeated. Upon occurrence of CHF, a waiting time of at least 5 minutes was allowed prior to initiation of the second run for a given case.

Critical heat flux was assumed to occur when the temperature measured with any one of the five test heater thermocouples increased by 15°C or more for a corresponding increase in heat flux (approximately 1 to 2 W/cm^2). In these circumstances, temperature increased steadily, not achieving a steady-state condition. These increases represented significant departures from the temperature versus heat flux trend for a given run. For a normal operating condition in the convective boiling regime, the typical increase in temperature for an increase in heat flux was approximately 1 to 2°C. This definition of CHF includes cases where local dryout within the flow channel may have caused the heater temperature excursions instead of the classical vapor blanketing of the heater. The value for CHF was computed by adding one-half of the heat flux increment to the heat flux value from the steady-state point just prior to CHF. Data shown for each channel are averages of the CHF values for each of the two runs executed.

All tests were conducted with the degassing tank vented to atmospheric conditions (via the degassing tank condenser). This plumbing configuration resulted in a test section exit reference pressure of approximately 100 kPa for all tests. As test section pressure drop increased during the course of a run (due to increased vaporization), test section inlet pressure would rise. This increase in pressure drop required a corresponding increase in pumping power to maintain a constant flow rate. During a test run, therefore, the flow rate was monitored and adjusted as necessary to maintain a constant flow to the test section. The increase in test section inlet pressure during the course of a run also affected the inlet subcooling level. Maintaining a constant test section inlet temperature while allowing inlet pressure to increase resulted in a corresponding increase in inlet subcooling level during the run.

Results and Discussion

The effects of flow velocity, inlet subcooling, and surface coating on heat transfer and pressure drop were examined. The small channel was horizontally oriented and had a square cross section, therefore, the channel side length also represented hydraulic diameter. Three different mass fluxes were investigated. These mass fluxes were 500, 2,000, and 5,000 kg/s·m^2, which corresponded to single-phase flow velocities of 0.31, 1.25, and 3.15 m/s, respectively. Three levels of inlet subcooling were examined at each flow velocity. Inlet subcooling was defined as the difference between the saturation temperature (evaluated at the inlet pressure) and the actual inlet temperature. As mentioned previously, inlet pressure typically increased during the course of a run due to increasing test section pressure drop. The inlet subcooling level, therefore, was calculated at the beginning of a run prior to the initiation of test section heating. At a velocity of 0.31 m/s, the subcooling levels examined were 2, 12, and 22°C. At a velocity of 1.25 m/s, subcooling levels examined were 3, 15, and 24°C. At a velocity of 3.15 m/s, subcooling levels examined were 9, 21, and 31°C. During a typical run, inlet temperatures were kept to within approximately ±1°C.

Pressure drop values for the cases tested at a velocity of 0.31 m/s were less than 5 kPa which were below the measurement resolution of the diaphragm installed in the pressure transducer. These pressure drop data, therefore, are not available for comparison.

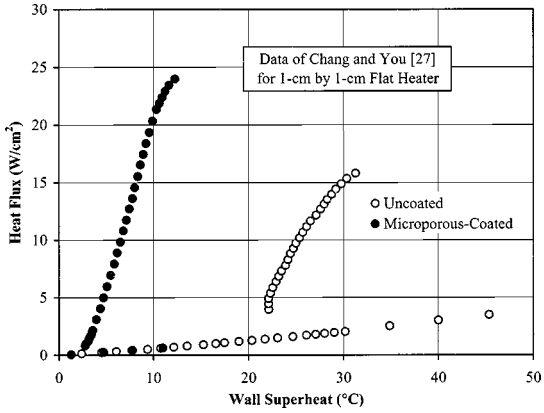

Fig. 4 Pool boiling performance of microporous coating in saturated FC-87

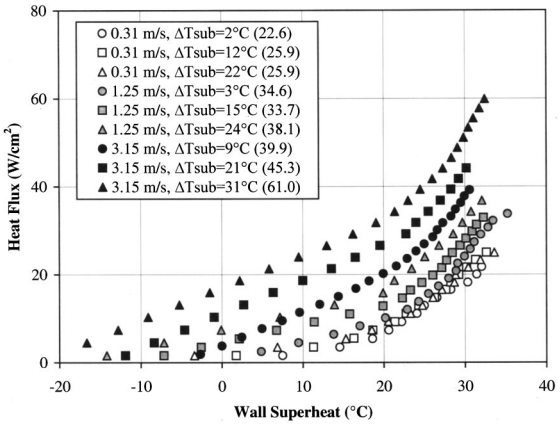

Fig. 5 Convective boiling curves for the uncoated channel

Single-Phase Results. Single-phase pressure drop and heat transfer characteristics were determined for the uncoated channel. Test section pressure drop along with local and average heat transfer coefficients were measured at combinations of low heat flux, high inlet velocity, and high inlet subcooling levels to avoid vaporization.

Single-phase pressure drop data were acquired at Reynolds numbers ranging from approximately 5,000 to 16,000. These experimental, single-phase pressure drop data were larger than those predicted based on the Moody friction factor for turbulent flow in smooth pipes. This is due to difficulties in instrumenting the test section, which caused the measured pressure drop to include effects of additional losses (four 90 deg elbows, an area reduction, and an area expansion). A loss factor was estimated to provide the best match between the experimental and predicted pressure drop. Using the estimated loss factor, all of the experimental pressure drop data were corrected to remove the effects of the inlet and outlet losses.

Single-phase, local, heat transfer data were measured for each of the channels. There was good agreement between the local and average heat transfer coefficients. This agreement is indicative of a minimal thermal entry region, which is typical for turbulent flow. In addition, the single-phase heat transfer data compared favorably with the single-phase correlation of Xu and Carey [4] for flow of methanol and n-butanol in small, rectangular, cross-ribbed channel with one wall heated. Additional information concerning single-phase pressure drop and heat transfer can be found in Ammerman [23].

Microporous Coating Effect on Convective Boiling. As mentioned previously, porous surface coatings have been shown in several studies to enhance boiling heat transfer. Test results of a coated surface (1 cm by 1 cm) pool boiling in saturated FC-87 revealed significant heat transfer enhancement over the entire boiling curve, as illustrated in Fig. 4 (Chang and You [27]). Three important characteristics of the boiling curve were affected: (1) boiling incipience superheat was reduced by 75 percent, (2) nucleate boiling heat transfer coefficient was increased by over 300 percent, and (3) CHF was increased by 50 percent.

Comparison of Uncoated and Coated 2 mm Channels. Subcooled convective boiling curves are shown for the uncoated, 2 mm channel in Fig. 5 for different velocities and various levels of subcooling. These data are plotted on the traditional boiling axes of heat flux versus wall superheat. Heat flux values for this, and subsequent plots, are the average over the heater surface. Wall superheat for this, and subsequent plots, is defined as follows:

$$\Delta T_{\text{sat}} = \overline{T}_{\text{wall}} - T_{\text{sat},m}, \qquad (1)$$

where $\overline{T}_{\text{wall}}$ is the average heater wall temperature and $T_{\text{sat},m}$ is the average of the saturation temperature at the test section inlet and outlet. Critical heat flux values in units of W/cm^2 are supplied in the legend in parentheses for each case on this and subsequent plots of boiling curves.

Each boiling curve in Fig. 5 has two fairly distinct heat transfer regimes as indicated by the two different boiling curve slopes. The lower slope corresponds to prevalence of the single-phase, liquid convection regime. The positive change in slope indicates the onset of boiling. The region with higher slope primarily corresponds to subcooled boiling. The 0.31 m/s data also include regions of saturated boiling.

There is minimal subcooling effect on the 0.31 m/s data in the subcooled boiling regime. This low impact of subcooling indicates that boiling dominates convection. In general, the effects of velocity and subcooling on convective boiling are prevalent in the single-phase and subcooled boiling regions. In the absence of velocity, however, subcooled boiling curves will have a tendency to collapse. Apparently, the 0.31 m/s velocity is too low in this channel to significantly impact the subcooled boiling region.

The subcooling effect is more obvious in the 1.25 and 3.15 m/s data as seen in Fig. 5. At these velocities, convection is playing a substantial role in overall heat dissipation. Also noticeable in these data is the positive effect of velocity and subcooling on CHF.

A plot of coated, 2 mm channel boiling curves for all velocities and subcooling levels tested is shown in Fig. 6. The coated-channel data show a remarkable insensitivity to velocity and subcooling effects. This insensitivity indicates that the heat transfer performance is primarily boiling dominated. The coating provides

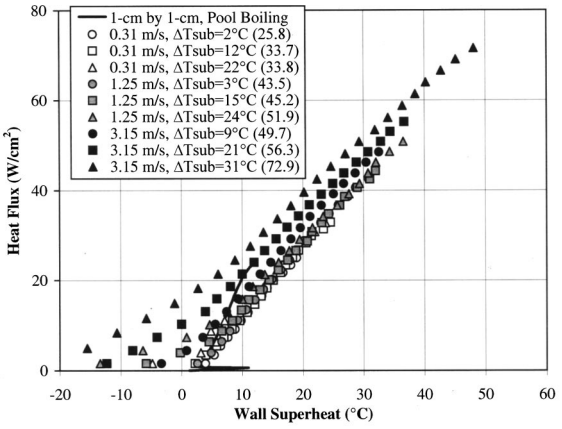

Fig. 6 Boiling curves for the coated channel at all velocities

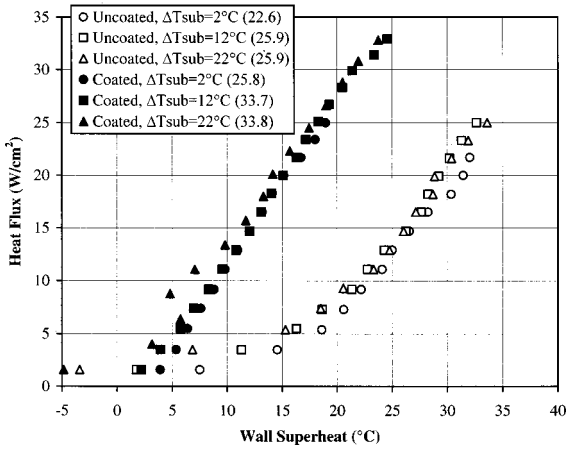

Fig. 7 Boiling curves showing coating effects at 0.31 m/s

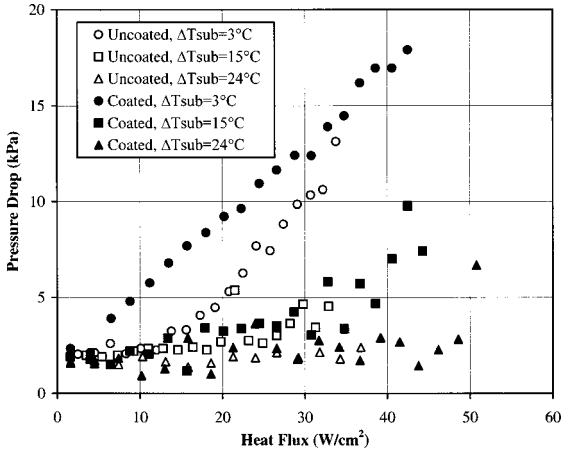

Fig. 9 Pressure drop for the uncoated and coated channels at 1.25 m/s

such a large number of active nucleation sites that there is no place on the heater surface where traditional convection can take place. The competition between convection and boiling begins to become evident at 3.15 m/s, however, as indicated from the slight variation in coated-channel boiling curves versus level of subcooling at this velocity. As mentioned previously, the coating thickness for the 2 mm channel was approximately 100 μm. The slope of these boiling curves, therefore, is adversely affected by the added conductive resistance of the coating layer.

Also shown in Fig. 6 is a solid line representing the pool boiling data of Chang and You's [27] coated 1 cm by 1 cm flat heater. This pool boiling curve's agreement in magnitude and slope with the convective boiling data further support the presence of boiling-domination within the coated channels.

A side-by-side comparison of boiling curves for the uncoated and microporous-coated channels are shown in Fig. 7 at a velocity of 0.31 m/s. Considerable enhancement can be seen in both heat transfer coefficient and CHF due to the application of the microporous coating. At a heat flux of 20 W/cm^2, for example, heat transfer coefficient is doubled. Widespread boiling for the coated channels occurs at much lower wall superheats (3 to 5°C) as compared with those of the uncoated channel (15 to 20°C).

Boiling curves for uncoated and coated channels are shown for a velocity of 1.25 m/s in Fig. 8. The coated channel shows substantial heat transfer and CHF enhancement over the uncoated channel. At a heat flux of 30 W/cm^2, for example, the coated-channel heat transfer coefficient is approximately 1.5 times that of the uncoated. As in the case of the 0.31 m/s data, widespread boiling occurs at much lower wall superheats for the coated channel, even though it is primarily within the subcooled boiling regime.

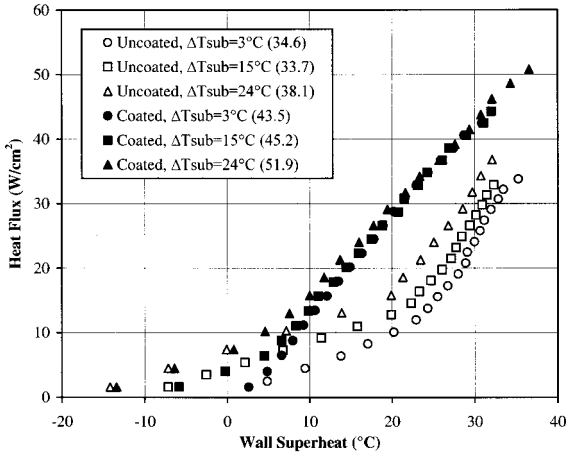

Fig. 8 Boiling curves showing coating effects at 1.25 m/s

Pressure drop data for the uncoated and coated channels at 1.25 m/s is shown in Fig. 9 versus heat flux. The effects of measurement uncertainty in pressure drop are evident in this figure. The presence of the coating does not have much, if any, of an effect on pressure drop for subcooling levels of 15 and 24°C. For the 3°C subcooled case, however, the coated-channel pressure drop exceeds that of the uncoated channel in the lower heat flux range. Test results showed that the test section exit quality for this subcooling level is primarily saturated. Boiling occurring at a lower heat flux combined with saturated conditions within the channel results in a larger void fraction in the coated channel. This increased vapor volume results in a higher contribution from acceleration to the total pressure drop in the lower heat flux region. As boiling becomes more widespread within the uncoated channel, its pressure drop begins to approach that of the coated channel.

Based on a qualitative comparison of heat transfer and pressure drop, application of the coating clearly provides an advantage. For higher subcooling levels, significant heat transfer enhancement is accompanied by little or no pressure drop penalty. The widespread subcooled boiling generated by the presence of the coating does not increase void fraction because boiling vapor is rapidly condensed. At 3°C subcooling, however, early initiation of boiling results in an immediate increase in pressure drop, tending to diminish the advantage of the heat transfer enhancement.

Boiling curves for uncoated and coated channels are shown in Fig. 10 for a velocity of 3.15 m/s. The single-phase regions in Fig. 10 are comparable, as expected. The single-phase region for the coated-channel cases is followed by a gradual transition to subcooled boiling (indicated by the minor change in slope) which provides modest enhancement in heat transfer over the uncoated-channel cases. For the 9°C subcooled case at 30 W/cm^2, for instance, the coated-channel heat transfer coefficient is approximately 1.4 times that of the uncoated channel. This enhancement is diminished relative to that seen for lower velocities. This reduction in enhancement is a result of the increase in efficiency of the uncoated channels with increasing velocity. As seen in Fig. 6, the coated-channel data are relatively insensitive to velocity effects. The uncoated-channel data, however, show a steady increase in heat transfer rate with increasing velocity (Fig. 5). Once subcooled boiling is established in the uncoated channels, their boiling-curve slopes exceed those of the coated channel curves. At a wall superheat of approximately 30°C, this difference in slope causes the uncoated heat transfer rate for the 31°C subcooled case to exceed the coated heat transfer rate.

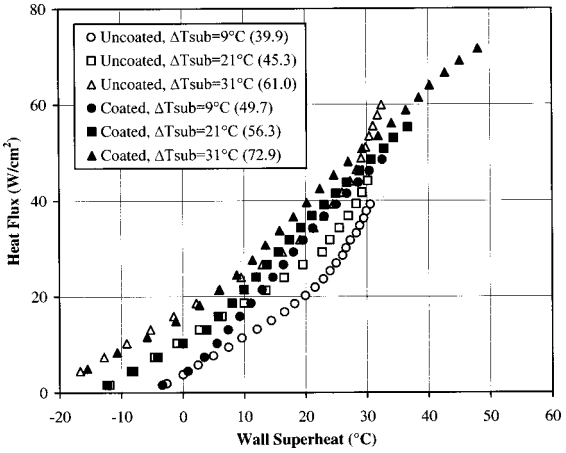

Fig. 10 Boiling curves showing coating effects at 3.15 m/s

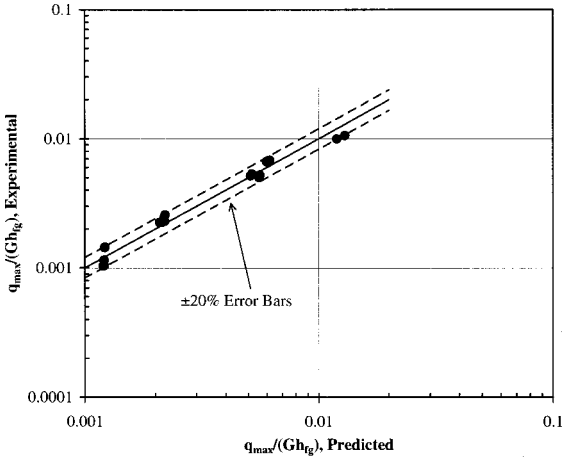

Fig. 12 Coated-channel critical heat flux correlation

This transition in heat transfer superiority from the coated to the uncoated channel may be due to a combination of two effects. First, boiling dominance within the coated channels suggests that, for a given heat flux, wall superheat has a fixed value regardless of velocity (within the velocity range tested). Alternatively, convection dominance within the uncoated channels results in a heat transfer dependence on velocity (and subcooling). For a given heat flux, therefore, wall superheat within the uncoated channel will continue to decrease as velocity increases, thus shifting the boiling curves to the left. Secondly, the coating layer becomes an added conductive resistance in the heat path. This added resistance has the effect of decreasing the boiling curve slope. Minimizing the coating thickness, therefore, is desirable.

A comparison of uncoated- and coated-channel pressure drop for 3.15 m/s is shown in Fig. 11 versus heat flux. A general trend can be seen in which the coated channel pressure drop departs from its single-phase value at lower heat fluxes than the uncoated channel due to early initiation of boiling. This was also observed in Fig. 9 for the 1.25 m/s case. There is a noticeable single-phase pressure drop difference between the uncoated and coated channels. It is possible that the application of the porous coating roughens the surface causing an increase in the turbulent friction factor.

A qualitative comparison of heat transfer and pressure drop indicates that addition of the coating produces only minor benefits at this velocity. At heat fluxes below 20 W/cm^2, boiling is suppressed and no heat transfer benefit is seen for the coated channels. Between approximately 20 and 40 W/cm^2, the coated channels appear to have an advantage as long as increases in pressure drop do not occur. At heat fluxes above 40 W/cm^2, the benefit of the coating appears to come only in the form of increased CHF.

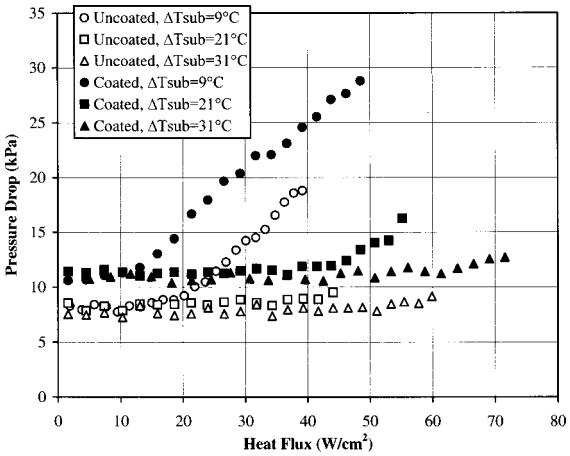

Fig. 11 Pressure drop for the uncoated and coated channels at 3.15 m/s

Critical Heat Flux. The microporous coating effect on CHF can be seen in the comparison plots shown in Figs. 7, 8, and 10. The CHF values shown for each channel are averages of the CHF values for each of the two runs executed. The increase in CHF due to application of the coating ranged from approximately 14 to 36 percent. This is somewhat less than the 50 percent achieved by Chang and You [27] for their flat heater in pool boiling (Fig. 4). This is not surprising since a limited amount of liquid exists within the small-diameter channel.

The coated-channel CHF data were compared against the CHF correlation developed for the uncoated-channel data by Ammerman and You [15]:

$$\frac{q_{\max}}{Gh_{fg}} = 0.45\mathrm{We}_D^{-0.37}(-x_i)^{0.1}\left(\frac{\rho_g}{\rho_f}\right)^{0.6}, \tag{2}$$

where $q_{\max}$ is the critical heat flux, G is the mass flux, h_{fg} is the latent heat of vaporization, We_D is the Weber number based on channel hydraulic diameter, x_i is the equilibrium inlet quality, and ρ_g and ρ_f are the vapor and liquid densities, respectively. This correlation performed well in illustrating the trend of the coated channel data. A better fit for the coated channel data was found by increasing the leading constant in Eq. (2) by a factor of 1.15 as follows:

$$\frac{q_{\max}}{Gh_{fg}} = 0.52\mathrm{We}_D^{-0.37}(-x_i)^{0.1}\left(\frac{\rho_g}{\rho_f}\right)^{0.6}. \tag{3}$$

The coated-channel CHF data are plotted against this prediction in Fig. 12. The added factor of 1.15 represents the mean, approximate CHF increase of the coated-channel data relative to the uncoated-channel data for the conditions tested.

Summary and Conclusions

An experimental investigation into convective boiling heat transfer enhancement was performed. The purpose of this investigation was to develop a fundamental understanding of the advantages and disadvantages of application of a microporous coating to the boiling surface. The present research using a small channel diameter combined with a dielectric working fluid is directly applicable to electronics cooling. The following conclusions are made:

1 Application of the microporous coating produced considerable heat transfer enhancement for nearly all conditions tested.

Similar to the pool boiling case shown in Fig. 4, use of the coating in convective boiling resulted in initiation of boiling at lower wall superheats, increased heat transfer coefficients, and elevated CHF levels. Based on previous pool boiling studies, the present authors theorize that the mechanism of enhancement attributable to the coating is the increase in number of nucleation sites and bubble departure frequency. Thus, the coating provides a means of extending the range over which boiling dominates convection.

2 Application of the coating produced remarkable heat transfer insensitivity to variations in velocity and subcooling. For the uncoated channel, however, the heat transfer performance steadily increased with increases in velocity, eventually surpassing the performance of the coated channel. The coated channel's insensitivity to velocity effects, therefore, is a benefit that diminishes with increasing flow velocity.

3 Comparisons of heat transfer and pressure drop revealed that benefits of the coating are optimum at higher subcooling levels where subcooled boiling prevails. Even though subcooled, the presence of the additional nucleation sites promotes widespread boiling at lower wall superheats. The vapor generated from these sites is quickly condensed due to subcooling, however, and leads only to minor impacts on pressure drop. For these subcooled boiling cases, the coating provides a significant, penalty-free heat transfer enhancement. This attribute of the coating makes it superior to current compact heat exchanger enhancement methods such as the addition of fins or ribs inside channels.

4 Application of the coating provided favorable enhancement in CHF. The increase ranged from 14 to 36 percent, which is slightly lower than the pool boiling CHF enhancement of 50 percent shown by Chang and You [27].

Nomenclature

D = channel hydraulic diameter (m)
G = mass flux (kg/m^{2}s)
h_{fg} = latent heat of vaporization (J/kg)
$q_{\max}$ = maximum heat flux (W/cm^2)
$T_{\text{sat},m}$ = mean saturation temperature at channel inlet and exit (°C)
$\overline{T}_{\text{wall}}$ = average heater wall temperature (°C)
ΔT_{sat} = wall superheat based on saturated fluid conditions (°C)
We_D = Weber number based on channel diameter ($G^2D/\rho_f\sigma$)
x_i = equilibrium inlet quality

Greek Symbols

ρ_f = liquid density (kg/m^3)
ρ_g = vapor density (kg/m^3)
σ = surface tension (N/m)

References

[1] Carey, V. P., and Mandrusiak, G. D., 1986, "Annular Film-Flow Boiling of Liquids in a Partially Heated, Vertical Channel With Offset Strip Fins," Int. J. Heat Mass Transf., **29**, No. 6, pp. 927–939.

[2] Mandrusiak, G. D., and Carey, V. P., 1988, "Pressure Drop Characteristics of Two-Phase Flow in a Vertical Channel with Offset Strip Fins," Exp. Therm. Fluid Sci., **1**, pp. 41–50.

[3] Mandrusiak, G. D., and Carey, V. P., 1989, "Convective Boiling in Vertical Channels With Different Offset Strip Fin Geometries," ASME J. Heat Transfer, **111**, pp. 156–165.

[4] Xu, X., and Carey, V. P., 1987, "Heat Transfer and Two-Phase Flow During Convective Boiling in a Partially-Heated Cross-Ribbed Channel," Int. J. Heat Mass Transf., **30**, No. 11, pp. 2385–2397.

[5] Panitsidis, H., Gresham, R. D., and Westwater, J. W., 1975, "Boiling of Liquids in a Compact Plate-Fin Heat Exchanger," Int. J. Heat Mass Transf., **18**, pp. 37–42.

[6] Chen, C. C., Loh, J. V., and Westwater, J. W., 1981, "Prediction of Boiling Heat Transfer Duty in a Compact Plate-Fin Heat Exchanger Using the Improved Local Assumption," Int. J. Heat Mass Transf., **24**, No. 12, pp. 1907–1912.

[7] Chen, C. C., and Westwater, J. W., 1984, "Application of the Local Assumption for the Design of Compact Heat Exchangers for Boiling Heat Transfer," ASME J. Heat Transfer , **106**, pp. 204–209.

[8] Lazarek, G. M., and Black, S. H., 1982, "Evaporative Heat Transfer, Pressure Drop and Critical Heat Flux in a Small Vertical Tube With R-113," Int. J. Heat Mass Transf., **25**, No. 7, pp. 945–960.

[9] Orozco, J., and Hanson, C., 1992, "A Study of Mixed Convection Boiling Heat Transfer in Narrow Gaps," HTD-Vol. 206-2, pp. 81–85.

[10] Moriyama, K., and Inoue, A., 1992, "The Thermohydraulic Characteristics of Two-Phase Flow in Extremely Narrow Channels (The Frictional Pressure Drop and Heat Transfer of Boiling Two-Phase Flow, Analytical Model)," Heat Transfer-Jpn. Res., **21**, No. 8, pp. 838–856.

[11] Wambsganss, M. W., France, D. M., Jendrzejczyk, J. A., and Tran, T. N., 1993, "Boiling Heat Transfer in a Horizontal Small-Diameter Tube," ASME J. Heat Transfer, **115**, pp. 963–972.

[12] Cornwell, K., and Kew, P. A., 1993, "Boiling in Small Parallel Channels," in *Energy Efficiency in Process Technology*, Elsevier Applied Science, London, pp. 624–640.

[13] Bowers, M. B., and Mudawar, I., 1994, "High Flux Boiling in Low Flow Rate, Low Pressure Drop Mini-Channel and Micro-Channel Heat Sinks," Int. J. Heat Mass Transf., **37**, No 2, pp. 321–332.

[14] Xia, C., Weilin, H., and Zengyuan, G., 1996, "Natural Convective Boiling in Vertical Rectangular Narrow Channels," Exp. Therm. Fluid Sci., **12**, pp. 313–324.

[15] Ammerman, C. N., and You, S. M., 1998, "Enhanced Convective Boiling of FC-87 in Small, Rectangular, Horizontal Channels: Heat Transfer Coefficient and CHF," ASME HTD-Vol. 357-4, pp. 225–233.

[16] Thome, J. R., 1990, *Enhanced Boiling Heat Transfer*, Hemisphere, New York.

[17] O'Connor, J. P., and You, S. M., 1995, "A Painting Technique to Enhance Pool Boiling Heat Transfer in Saturated FC-72," ASME J. Heat Transfer, **117**, pp. 387–393.

[18] O'Connor, J. P., You, S. M., and Price, D. C., 1995, "A Dielectric Surface Coating Technique to Enhance Boiling Heat Transfer from High Power Microelectronics," IEEE Trans. Compon., Packag. Manuf. Technol., Part A, **18**, pp. 656–663.

[19] Chang, J. Y., and You, S. M., 1997, "Boiling Heat Transfer Phenomena from Micro-Porous and Porous Surfaces in Saturated FC-72," Int. J. Heat Mass Transf., **40**, No. 18, pp. 4437–4447.

[20] Chang, J. Y., and You, S. M., 1997, "Enhanced Boiling Heat Transfer from Micro-Porous Surfaces: Effects of Coating Composition and Method," Int. J. Heat Mass Transf., **40**, No. 18, pp. 4449–4460.

[21] Czikk, A. M., O'Neill, P. S., and Gottzmann, C. F., 1981, "Nucleate Pool Boiling From Porous Metal Films: Effect of Primary Variables," in *Advances in Heat Transfer*, HTD-Vol. 18, pp. 109–122.

[22] Ikeuchi, M., Yumikura, T., Fujii, M., and Yamanaka, G., 1984, "Heat-Transfer Characteristics of an Internal Micro-Porous Tube With Refrigerant-22 Under Evaporating Conditions," ASHRAE Trans., **90**, (Part 1A), pp. 196–211.

[23] Ammerman, C. N., 1997, "Experimental Investigation of Enhanced Convective Boiling in Small Channels," Ph.D. thesis, The University of Texas at Arlington, Arlington, TX.

[24] Kline, S. J., and McClintock, F. A., 1953, "Describing Uncertainties in Single-Sample Experiments," Mech. Eng. (Am. Soc. Mech. Eng.), **75**, pp. 3–8.

[25] *Fluorinert Product Manual*, 1987, Fluorinert Electronic Liquids, Commercial Chemical Products Division, 3M Company, St. Paul, Minnesota.

[26] Hong, Y. S., Ammerman, C. N., and You, S. M., 1997, "Boiling Characteristics of Cylindrical Heaters in Saturated, Gas Saturated, and Pure-Subcooled FC-72," ASME J. Heat Transfer, **119**, pp. 313–318.

[27] Chang, J. Y., and You, S. M., 1997, "Enhanced Boiling Heat Transfer from Micro-Porous Cylindrical Surfaces in Saturated FC-87 and R-123," ASME J. Heat Transfer, **119**, pp. 319–325.

Simultaneous Heat and Mass Transfer in Film Absorption With the Presence of Non-Absorbable Gases

Hamza M. Habib
Assistant Professor
College of Engineering,
El-Menoufia University,
Shebin El-Kom, Egypt

Byard D. Wood
Professor and Chairman
Department of Mechanical Engineering,
University of Nevada, Reno
Reno, Nevada, USA

Numerical solutions are presented for the effect of a non-absorbable gas on the heat and mass transfer rates during the absorption of water vapor by a falling laminar smooth film of an aqueous lithium bromide or aqueous lithium chloride solution (absorbent). The geometry consists of a vertical channel with two walls, one of which is isothermal and the other adiabatic. The liquid film of an absorbent flows down over the isothermal wall, while a mixture of water vapor and air flows between the liquid free-surface and the adiabatic wall. The whole system is kept under vacuum pressure. Water vapor is absorbed by the film and air is the non-absorbable gas. The momentum, energy, and concentration equations are written with a set of interfacial and boundary conditions and solved numerically for the two phases. Variable property effects are included, as well as the interfacial shear. Heat and mass transfer results are presented over a wide range of inlet air concentrations. The average mass fluxes showed a continuous reduction with an increase in the amount of air for a concentration of air as high as 40 percent by weight. But the local mass fluxes showed a different behavior from the absorption of a pure vapor case. The decrease was much higher at the entrance than in a pure vapor case. The numerical results are in good agreement with the experimental data available for lithium chloride. The model has promise as means of predicting the heat and mass transfer characteristics of falling film absorber. [DOI: 10.1115/1.1370523]

Introduction

Absorption of vapors or gases into a falling liquid film is an important chemical process for many applications and has been studied widely in chemical technology. It is complicated by the hydrodynamics of the film, the heat generated at the interface, the equilibrium relation, and the presence of a non-absorbable gas in the gas phase. Usually the liquid (absorbent) has a strong affinity for the vapor (adsorbate), and the driving potential for the absorption is the difference between the adsorbate pressure and the vapor pressure of the absorbent corresponding to its concentration and temperature. The heat generated in this exothermic process causes a temperature gradient in both phases and increases the vapor pressure of the solution. Consequently the absorption rate is reduced.

Previous Work

Two types of investigations have been performed in the field of film absorption. One is concerned with the isothermal film absorption, i.e., the heat of absorption generated in the process is small and the process can be considered isothermal. The other is exothermic, i.e., the effect of heat transfer cannot be neglected. The high heat of absorption is a result of non-ideal mixing. This usually happens when highly polar molecules are absorbed such as water and ammonia or Libr water vapor, so the coupling between heat and mass must be considered. Studies of the effect of non-absorbable gases on the heat and mass transfer in film absorption is relatively little in the literature, but much has been published on the effect of non-condensibles in film condensation because of its importance in power plants. It is worth noting the difference between film absorption and film condensation. The condensation problem requires only temperature-pressure equilibrium relation at the interface; whereas the absorption problem requires concentration, temperature and pressure condition equilibrium at the interface. This extra condition significantly complicates the problem.

Nakoryakov and Griger'eva [1] were the first to model the simultaneous heat and mass transfer in film absorption. In their model they assumed a linear temperature profile across the film. To obtain a similarity solution they assumed a uniform velocity profile across the film; essentially, this assumption overestimates the bulk temperature and concentration on the liquid. Later in [2] they improved their model by solving the temperature field rather than assuming it. Further in [3] the same authors studied the combined heat and mass transfer in the entrance region. They used boundary layer equations, and assumed that a thermal layer is formed on the solid wall and thermal and diffusion layers on the film free surface. The authors drew conclusions about the relative lengths of the entrance effects for each process. A convenient set of non-dimensional parameters to describe experimental results for their initial region on the plate were also found.

Yih and Seagrave [4] studied the effect of shear stress and variable properties on laminar film absorption, using a linear temperature profile across the film. They concluded that the heat transfer and interfacial shear could have a profound influence on the mass transfer rate. A co-current gas shear was found to decrease the film thickness and increase the mass transfer rate.

Andberg et al. [5] solved the combined heat and mass transfer in laminar film absorption numerically. They concluded that absorption is dominated by different mechanisms along the film as the temperature and concentration profiles developed at their separate rates. These separate regions were distinguished by both temperature and concentrations developing, developing concentration profile, and both profiles fully developed. Grossman [6] improved the model used by Nakoryakov [2] by assuming a parabolic velocity profile; he also extended by model by studying the adiabatic

Contributed by the Heat Transfer Division for publication in the JOURNAL OF HEAT TRANSFER. Manuscript received by the Heat Transfer Division September 13, 1999; revision received December 4, 2000. Associate Editor: D. A. Kaminski.

wall. He concluded that the heat and mass transfer coefficients depend on the Peclet and Lewis numbers as well as the equilibrium characteristics of the working materials.

The problem of combined heat and mass transfer in a liquid film in the presence of non-absorbable gas has only recently begun to receive attention. Nakoryakov and Grigor'eva [7] showed analytically, by a smooth film model, that for only one percent air in vapor, the mass transfer coefficient was reduced by 75 percent, and 10 percent air reduced the mass transfer by 90 percent. However, their model is only applicable for the entrance region. Burdkov et al. [8] in their experiment with absorption of water vapor by a thin layer of lithium bromide in presence of air, reported that an air content of 0.5 percent in water vapor reduces the mass transfer coefficient almost 50 percent. Yang [9] in his experiment for a laminar wavy film of lithium chloride solution found that the non-absorbables depress heat and mass transfer at low concentrations of air. He also found that the absorption reduction was significantly lower than that reported by Burdkov [8] and reported that the reduction was continuous for up to 30 percent of air content. Similar experiments were conducted by Ameel [10] with better measuring equipment and better analysis. He was able to obtain data for low concentration of non-absorbable gas varied from 0 to 10 percent by volume. The experimental results indicate that significant increase in heat and mass transfer rates can be obtained by reducing the non-absorbable gas concentration to levels approaching 0 percent. For Re=60, the mass transfer rate is enhanced 35 percent by reducing the non-absorbable gas concentration from 5 to 0.5 percent.

Absorption can be enhanced by adding a small amount of surfactants, or wetting agents which act to reduce the surface tension, [11]. It could also be enhanced by changing the surface configuration by mounting disturbances in the base plate [12].

In summary, it appears that a considerable effort has been made to understand the physical phenomena of falling liquid films and the absorption into the same. However, both of these general problem areas still require further study, the problem of combined heat and mass transfer in a liquid film in the presence of non-absorbable gas has only recently begun to receive attention. It is hoped that this study will further our understanding of this interesting process.

Analysis

Consider a thin film of aqueous solution of lithium bromide flowing downward over a vertical isothermal plate under the action of gravity. The film is in contact with a mixture of water vapor and air. The mixture of the water vapor and air is pumped between the liquid free surface and an adiabatic wall. As the vapor flows towards the interface, the non-absorbable gases are swept along with it. Since the interface is impermeable to the non-absorbables, air accumulates there resulting in a reduction of the water vapor pressure. Thus, we have a pair of interacting regions, one in the liquid phase and the other is in the gas phase. It is necessary to formulate the governing equations for the two phases and then couple them by applying the interfacial relations. A schematic representation of the physical model is shown in Fig. 1. The coordinates along and normal to the wall are y and x, respectively, and the corresponding velocity components are v and u, respectively. At the entrance, the vapor and air are introduced into the channel at a velocity and temperature of v_{0g} and T_{0g}. The concentration of the non-absorbable gas (air) is W_{02}. The liquid absorbent has an initial concentration and temperature of C_0 and T_{01} and an average velocity of the film is v_{01} determined from the mass flow rate of the liquid absorbent. The film thickness δ is determined from the relation, Nusselt [13]

$$\delta=\left\langle \frac{3\mu_1 v_{01}}{\rho_1 g}\right\rangle \qquad \text{for} \quad \text{Re}\leqslant 1500.$$

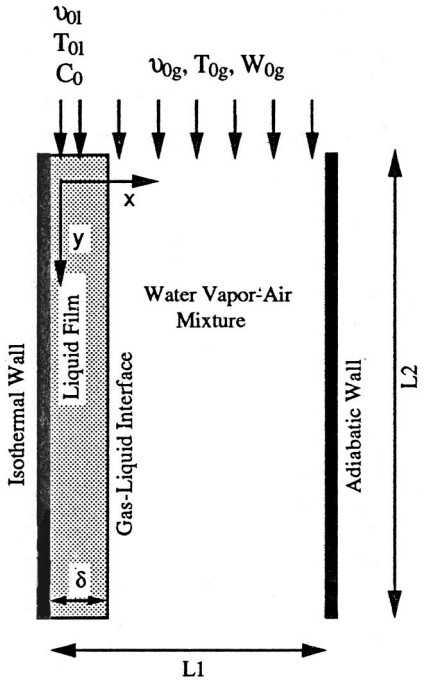

Fig. 1 Schematic of the physical situation

Along the liquid-gas interface the temperature and concentration of the liquid absorbent and the concentration of the non-absorbables are unknown and are determined in the course of analysis.

The following assumptions are used: the flow is laminar in both liquid and gas. The mass of the vapor absorbed at the interface is small compared to the mass flow rate of the liquid, but it is included. The film thickness however is considered constant. There is no slip between the two phases. Diffusion-thermo and thermal diffusion effects are negligible in the liquid film. Finally thermodynamic equilibrium exists at the liquid gas interface.

Governing Equations for the Liquid Phase.

$$\frac{\partial}{\partial x}(\rho_1 u)+\frac{\partial}{\partial y}(\rho_1 v)=0 \tag{1}$$

$$\rho_1 u\frac{\partial u}{\partial x}+\rho_1 v\frac{\partial u}{\partial y}=-\frac{\partial p}{\partial x}+\frac{\partial}{\partial x}\left(\mu_1\frac{\partial u}{\partial x}\right)+\frac{\partial}{\partial y}\left(\mu_1\frac{\partial u}{\partial y}\right) \tag{2}$$

$$\rho_1 u\frac{\partial v}{\partial x}+\rho_1 v\frac{\partial v}{\partial y}=-\frac{\partial p}{\partial y}+\frac{\partial}{\partial x}\left(\mu_1\frac{\partial v}{\partial x}\right)+\frac{\partial}{\partial y}\left(\mu_1\frac{\partial v}{\partial y}\right)+\rho_1 g \tag{3}$$

$$\rho_1 c_{p,1} u\frac{\partial T}{\partial x}+\rho_1 c_{p,1} v\frac{\partial T}{\partial y}=\frac{\partial}{\partial x}\left(k_1\frac{\partial T}{\partial x}\right)+\frac{\partial}{\partial y}\left(k_1\frac{\partial T}{\partial y}\right) \tag{4}$$

$$\rho_1 u\frac{\partial C}{\partial x}+\rho_1 v\frac{\partial C}{\partial y}=\frac{\partial}{\partial x}\left(\rho_1 D_1\frac{\partial C}{\partial x}\right)+\frac{\partial}{\partial y}\left(\rho_1 D_1\frac{\partial C}{\partial y}\right) \tag{5}$$

Governing Equations for the Gas Phase.

$$\frac{\partial}{\partial x}(\rho_g u)+\frac{\partial}{\partial y}(\rho_g v)=0 \tag{6}$$

$$\rho_g u\frac{\partial u}{\partial x}+\rho_g v\frac{\partial u}{\partial y}=-\frac{\partial p}{\partial x}+\frac{\partial}{\partial x}\left(\mu_g\frac{\partial u}{\partial x}\right)+\frac{\partial}{\partial y}\left(\mu_g\frac{\partial u}{\partial y}\right) \tag{7}$$

$$\rho_g u\frac{\partial v}{\partial x}+\rho_g v\frac{\partial v}{\partial y}=-\frac{\partial p}{\partial y}+\frac{\partial}{\partial x}\left(\mu_g\frac{\partial v}{\partial x}\right)+\frac{\partial}{\partial y}\left(\mu_g\frac{\partial v}{\partial y}\right) \tag{8}$$

$$\rho_g c_{p,g} u \frac{\partial T}{\partial x} + \rho_g c_{p,g} v \frac{\partial T}{\partial y} = \frac{\partial}{\partial x}\left(k_g \frac{\partial T}{\partial x}\right) + \frac{\partial}{\partial y}\left(k_g \frac{\partial T}{\partial y}\right) \quad (9)$$

$$\rho_g u \frac{\partial W_2}{\partial x} + \rho_g v \frac{\partial W_2}{\partial y} = \frac{\partial}{\partial x}\left(\rho_g D_g \frac{\partial W_2}{\partial x}\right) + \frac{\partial}{\partial y}\left(\rho_g D_g \frac{\partial W_2}{\partial y}\right) \quad (10)$$

Boundary Conditions and Interfacial Relations.

$$u=0, \quad v=0 \quad \text{at} \quad x=0 \quad \text{and} \quad x=L_1$$

$$T=T_{01}, \quad v=v_{01} \quad C=C_0 \quad \text{at} \quad y=0 \quad \text{and} \quad 0<x<\delta$$

$$T=T_{0g}, \quad v=v_{0g} \quad W_2=W_{02} \quad \text{at} \quad y=0 \quad \text{and} \quad \delta<x<L_1 \quad (11)$$

$$T=T_W \quad \text{at} \quad x=0 \quad (12)$$

$$\frac{\partial C}{\partial x}=0 \quad \text{at} \quad x=0 \quad (13)$$

$$\frac{\partial T}{\partial x}=0, \quad \frac{\partial W_2}{\partial x}=0 \quad \text{at} \quad x=L_1 \quad (14)$$

$$\mu_1 \left.\frac{\partial v}{\partial x}\right|_{x=\delta} = \mu_g \left.\frac{\partial v}{\partial x}\right|_{x=\delta} \quad (15)$$

$$\rho_2 u|_{x=\delta} - \rho_g D_g \left.\frac{\partial W_2}{\partial x}\right|_{x=\delta} = 0 \quad (16)$$

$$k_1 \left.\frac{\partial T}{\partial x}\right|_{x=\delta} = k_g \left.\frac{\partial T}{\partial x}\right|_{x=\delta} - Ha \rho_1 D_1 \left.\frac{\partial C}{\partial x}\right|_{x=\delta} \quad (17)$$

$$-\rho_1 D_1 \left.\frac{\partial C}{\partial x}\right|_{x=\delta} = -\rho_g D_g \left.\frac{\partial}{\partial x}(1-W_2)\right|_{x=\delta} + \rho_1 u|_{x=\delta} \quad (18)$$

$$\frac{\partial u}{\partial y}=0, \quad \frac{\partial v}{\partial y}=0, \quad \frac{\partial T}{\partial y}=0, \quad \frac{\partial C}{\partial y}=0, \quad \frac{\partial W_2}{\partial y}=0 \quad \text{at} \quad y=L2 \quad (19)$$

Equations (1)–(5) represent the continuity, the *x*-momentum, the *y*-momentum, the energy, and concentration equations, respectively, in the liquid phase. The body forces in the gas phase are neglected due to the presence of forced flow. Equations (6)–(10) represent their counterpart in the gas phase. Condition (14) shows that the wall at $x=L_1$ is adiabatic and impermeable to the mass transfer. Condition (15) confirms the continuation of the shear forces at the interface. Condition (16) represents the impermeability of the interface to the non-absorbable gases. Condition (17) represents the continuity of energy through the interface. Condition (18) represents the continuity of mass for the absorbate through the interface. Conditions (19) assume that at the exit of the channel there are no significant changes in the velocity, concentration, and the temperature.

To close the problem an extra equation is needed to relate the water vapor partial pressure, the solution concentration of LiBr/LiCl and the temperature at the interface at equilibrium conditions. Siebe [14] has fitted the experimental data of Lower [15] for LiBr-water solutions and of Uemura [16] for LiCl-water solutions at a specified pressure and temperature in the form of Eq. (20) given below.

$$\mathrm{Log}_{10} P = A + B/T + D/T^2, \quad (20)$$

where

$$A = a_0 + a_1 C + a_2 C^2 + a_3 C^3$$

$$B = b_0 + b_1 C + b_2 C^2 + b_3 C^3$$

$$D = d_0 - d_1 C + d_2 C^2 + d_3 C^3.$$

Given the vapor pressure and temperature; Eq. (20) can be solved iteratively to determine the equilibrium concentration that is required at the interface.

Numerical Method

The governing equations were discretized using the control volume formulation. The control volume formulation ensures an overall energy balance even for very coarse grid. The computer code based on the mathematical model above and the SIMPLER method [17] are validated for the case of zero concentration of nonabsorbable gas and the results are published elsewhere [18].

Due to the large gradients at the entrance and the liquid-gas interface, a non-uniform grid was used with 30 grid points through the film thickness and 20 points through the gas phase in the crosswise direction. The grid was clustered around the interface from both sides of the interface and gradually stretched away from the interface. The grid size in the streamwise direction was 38 points with a gradual decrease in grid density in the flow direction.

Independence of solution on the grid size was studied for various cases for instance, for the case of 1 percent concentration of nonabsorbable gas the grid size of 50×38 was found to be best. The grid independence was achieved within 0.5 percent variation, which also resulted in a favorable C.P.U. computation time. It was observed that further refining the mesh produced a negligible effect on the results.

A relative error of no greater than 10^{-4} in all the variables at all grid points was used as the convergence criterion.

Results and Discussions

To validate the simulation the effect of non-absorbable gas on the mass transfer rate, as determined in this study, is compared to the experimental data of Yang [9] and Ameel [10] in Fig. 2, for lithium chloride solution.

Due to the complexity of the equilibrium relation (20), it is difficult to present the results in a non-dimensional form. A case study is selected for typical operating parameters for an absorber [14]. The operating parameters are: inlet solution temperature, 44°C, inlet solution concentration of lithium bromide, 0.6; liquid film Reynolds number, 30; wall temperature, 35°C; absorber vapor pressure, 7.02 mm Hg; inlet gas temperature, 20°C; inlet concentration of the non-absorbable gas, 3 percent; gas Reynolds number, 30.

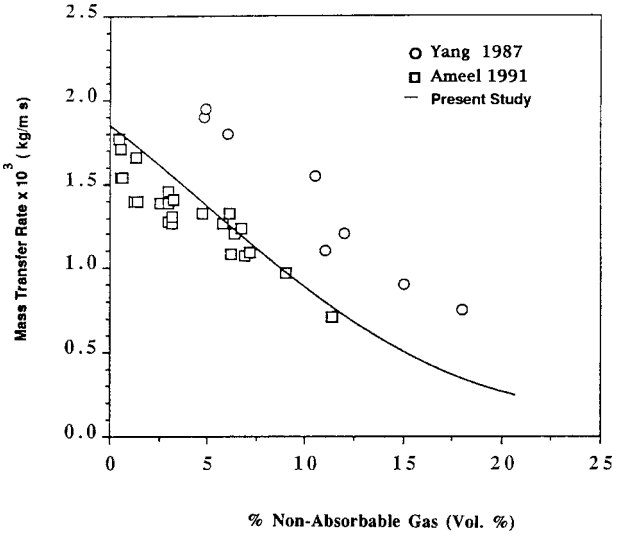

Fig. 2 Comparison of the mass transfer rate at the interface as a function of the non-absorbable gas with previously reported data

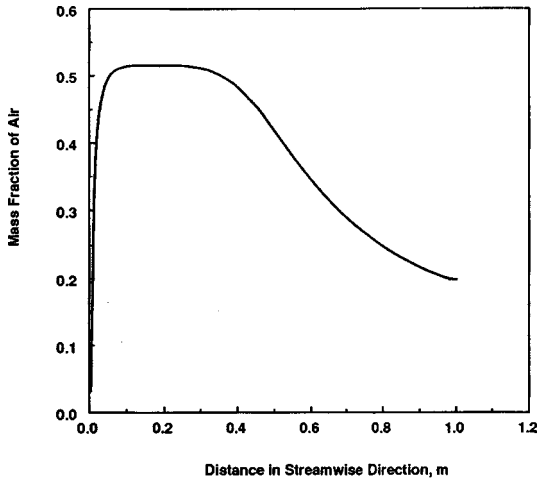

Fig. 3 Local distribution of the non-absorbable gas along the interface

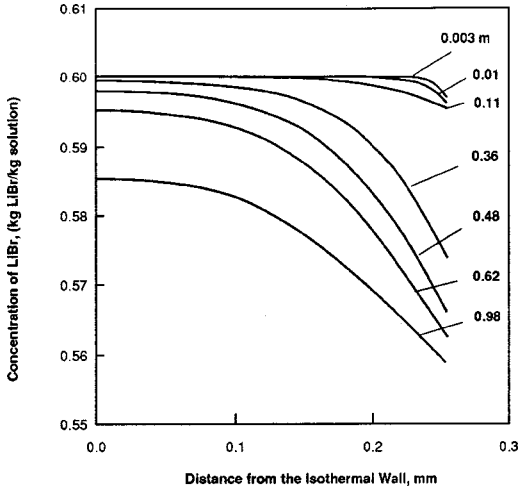

Fig. 5 Effect of the non-absorbable gas on the concentration profiles across the film

The absorption of water vapor by a liquid absorbent decreases the concentration of water vapor at the interface on the gas side. Thus the concentration of air increases. However, this also decreases the driving gradient for water vapor absorption, and eventually, an equilibrium is reached at some distance downstream. This is shown in Fig. 3, where the local distribution of the non-absorbable gas along the interface is plotted against the streamwise distance. Figure 4 shows the local distribution of the non-absorbable gas across the gas phase for different locations. We notice that the concentration of the non-absorbables increases sharply at the interface and approaches its initial value at the adiabatic wall. This can be explained as follows: due to the absorption process water vapor is carried from the bulk to the interface by convective flow, which carries with it the non-absorbable gas. However, since the interface is impermeable to the non-absorbables, it must be removed from the interface at the same rate at which it arrives. The removal is accomplished by a diffusive backflow into the bulk. It is evident that the interfacial concentration of the non-absorbable gas must build up to the level sufficient for the balance between the convective inflow and the diffusive backflow. There will be a consequent reduction of the interface temperature and concentration of the absorbate.

Figure 5 shows the concentration profiles of LiBr across the liquid film for different locations. As the flow progresses along the wall, the interface concentration of LiBr continues to drop because absorption at the interface occurs faster than the water may be transported into the interior of the film. This dropping of interface concentration leads to a drop in interface temperature through the equilibrium conditions that are imposed at the interface. This drop in interface temperature decreases the driving force for heat transfer through the film, and therefore slows down the absorption process as the fluid progresses along the wall.

Figure 6 shows the temperature profiles across the film for different locations. The inlet region of the liquid film is governed by boundary layer growth at the cold wall and a diffusion layer at the interface. Once both heat transfer and mass transfer boundary layers are fully developed, there is no latent heat release, and the temperature becomes flat, at the temperature of the cold wall.

Figure 7 shows the local mass flux as a function of the concentration of the non-absorbables. It is worth noting the difference between an absorption process with a pure vapor and an absorption process with a non-absorbable gas. As one expects from absorption of a pure vapor, at some distance down the plate, the mass transfer decreases continuously, because the driving potential for mass transfer and associated heat transfer decreases, but in

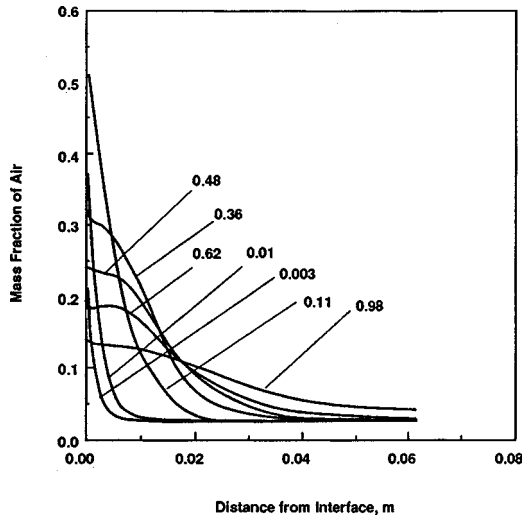

Fig. 4 Local distribution of the non-absorbable gas across the gas phase for various locations

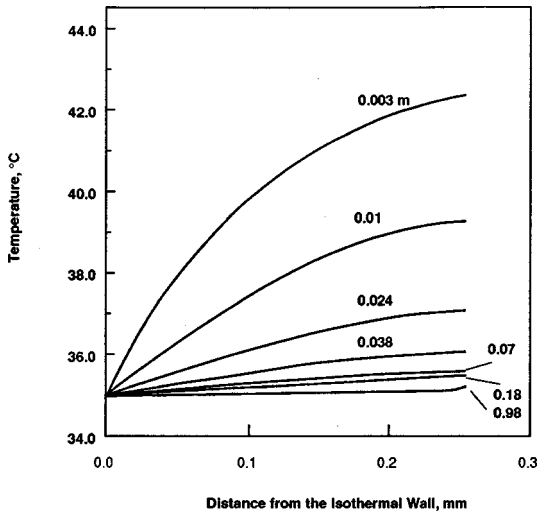

Fig. 6 Effect of the non-absorbable gas on the temperature profiles across the film

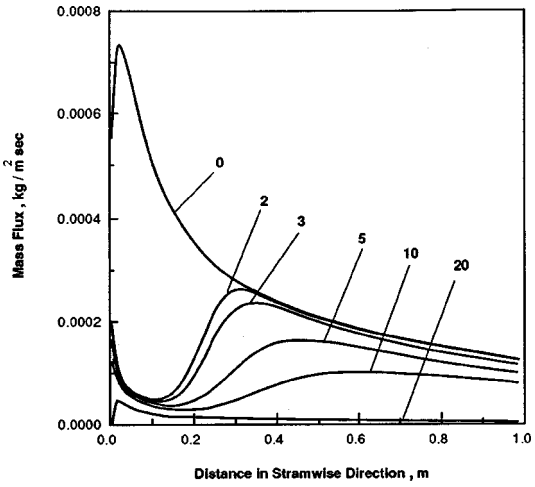

Fig. 7 Local distribution of the mass flux at the interface as function of the concentration of the non-absorbable gas

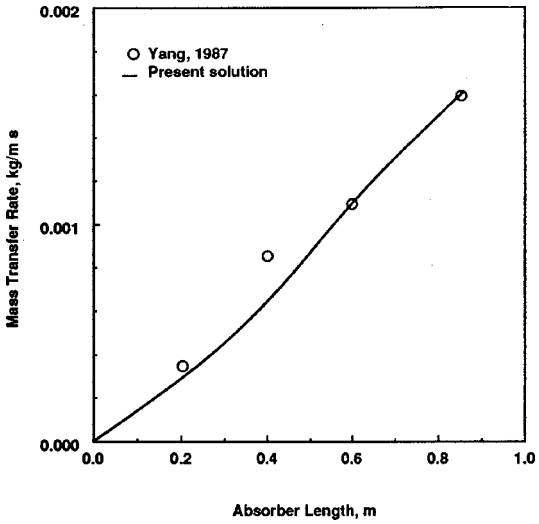

Fig. 9 Comparison of the axial contact length on mass transfer rate

absorption with a presence of a non-absorbable gas in the gas phase the decrease is much higher at the entrance than in a pure vapor case. But at some distance when the concentration of the non-absorbable starts to decrease the local mass flux starts to increase. We notice that the local mass flux approaches the curve of a pure vapor case.

Figure 8 shows the average mass flux as function of the inlet concentration of the non-absorbable gas, for the same parameters given. It is clear that the reduction is continuous up to 30 percent and that the larger the initial concentration of the non-absorbable the smaller the mass flux.

Figure 9 shows the effect of the axial contact length on mass transfer rate with the experimental data given by Yang [9]. The mass transfer rate was calculated for four different lengths, 20, 40, 60, and 85 cm, for the following conditions: inlet solution temperature, 35°C; inlet solution concentration of lithium chloride, 0.44; liquid film Reynolds number, 30; wall temperature, 30°C; absorber vapor pressure, 8.5 mm Hg; inlet gas temperature, 20°C; inlet concentration of the non-absorbable gas, 5 percent (by volume); gas Reynolds number, 30. The numerical solution is in a good agreement with the data except for the low contact lengths. The mass transfer rate increases with increasing the contact length and should approach an asymptotic value when the equilibrium condition is established at a very long distance.

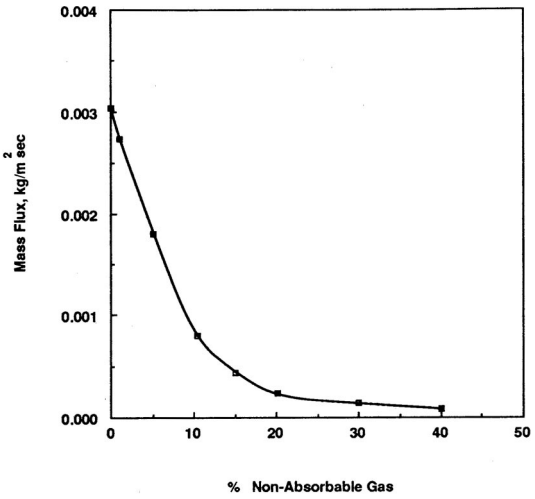

Fig. 8 Average mass flux absorbed at the interface as function of the concentration of the non-absorbable gas

Conclusions

A numerical study of the governing equations for the absorption of water vapor from a mixture of water vapor and air during the absorption of water vapor by a falling film of an aqueous lithium bromide or aqueous lithium chloride solution (absorbent) has been presented. The results cover a wide range of concentrations of the non-absorbable gas. The average mass fluxes showed a continuous reduction with an increase in the amount of air for a concentration of air as high as 40 percent by weight. But the local mass fluxes showed a different behavior from the absorption of a pure vapor case. The decrease was much higher at the entrance than in a pure vapor case. At some distance when the concentration of the non-absorbable gas starts to decrease, the local mass flux starts to increase. Finally the local mass flux approaches the curve of a pure vapor case down the channel. The numerical results are in good agreement with the experimental data. The numerical results indicate that significant increases in heat and mass transfer can be obtained by reducing the the non-absorbable gas concentration to levels approaching 0 percent.

Nomenclature

C = concentration of adsorbate in solution, kg water/kg solution
C_n = equilibrium concentration at the interface
C_p = specific heat, kj/kg c°
D_1 = diffusion coefficient of adsorbate in liquid, m^2/s
D_g = diffusion coefficient of air in water vapor-air mixture, m^2/s
Ha = heat of absorption, kj/kg
k = thermal conductivity, kj/(m.s.°C)
Le = Lewis Number
$L1$ = width of the channel, m
$L2$ = length of the channel, m
P = total pressure of the absorber, mm-Hg
P_v = vapor pressure in the gas phase, mm-Hg
Pr = Prandtl Number
Re_1 = film Reynolds Number $= 4v_{0l}\delta/v_l$
Re_g = gas Reynolds Number $= v_{0g}L1/v_g$
T = temperature, °C
u = velocity in the transverse direction, m/s

v = velocity in the streamwise direction, m/s
W_2 = mass fraction of air
x = coordinate perpendicular to flow direction
y = coordinate in flow direction

Greek Letters

α = thermal diffusion coefficient, m^2/s
Γ = mean volumetric flow rate
δ = film thickness, m
μ = dynamic viscosity, $kg/(m^3.s)$
ν = kinematic viscosity, s^{-1}
ρ = density, kg/m^3

Subscripts

1 = water vapor
2 = air
g = gas phase
l = liquid phase
n = interface
0 = inlet

References

[1] Nakoryakov, V. E., and Grigor'eva, N. I., 1977, "Combined Heat and Mass Transfer During Absorption in Drops and Films," Inzh.fiz.zh., **32**, pp. 399–405.

[2] Nakoryakov, V. E., and Grigor'eva, N. I., 1977, "Exact Solution of Combined Heat and Mass Transfer Problem during Film Absorption," Inzh.fiz.zh., **33**, pp. 893–898.

[3] Nakoryakov, V. E., and Griger'eva, N. I., 1980, "Combined Heat and Mass Transfer in Film Absorption," Heat Transfer-Sov. Res., **72**, pp. 108–117.

[4] Yih, S. M., and Seagrave R. C., 1980, "Mass Transfer in Laminar Falling Liquid Films with Accompanying heat transfer and Interfacial Shear," Int. J. Heat Mass Transf., **23**, pp. 749–758.

[5] Andberg, J. W., 1982, "Non-Isothermal Absorption of Gases into Falling Liquid Films," M.S. thesis, University of Texas at Austin, Austin, TX.

[6] Grossman, G., 1983, "Simultaneous Heat and Mass Transfer in Absorption Under Laminar Flow," Int. J. Heat Mass Transf., **26**, pp. 357–371.

[7] Nakoryakov, V. E., and Griger'eva, N. I., 1980, "Calculation of Heat and Mass Transfer in Non-Isothermal Absorption in the Entrance Region of Falling Film," Teor. Osn. Khim. Tekhnol., **14**, pp. 483–488.

[8] Burdukov, A. P., Bufetov, N. S., Deriy, N. P., Dorokhov, A., and Kazakov, V. I., 1980, "Experimental Study of the Absorption of Water Vapor by Thin Films of Aqueous Lithium Bromide," Heat Transfer-Sov. Res., **12**, pp. 118–123.

[9] Yang, R., 1987, "Heat and Mass Transfer in Laminar Wavy Film Absorption with the Presence of Non-Absorbable Gases," Ph.D. dissertation, Arizona State Univ., Tempe, AZ.

[10] Ameel, T., 1992, "Heat and Mass Transfer in Laminar Wavy Film Absorption with the Presence of Low Concentration of Non-absorbable Gases," Ph.D. dissertation, Arizona State Univ., Tempe, AZ.

[11] Kwang, J. K., 1992, "Heat and Mass Transfer Enhancement in Absorption Cooling," Ph.D. dissertation, Arizona State Univ., Tempe, AZ.

[12] Jiang, Y., 1995, "Enhancement of Heat and Mass Transfer in Film Absorption and Desorption," Ph.D. dissertation, University of Illinois at Chicago, Chicago, IL.

[13] Nusselt, W., 1916, "Die Oberflachen-Kondensation," Zeitshrift Vereins Deutscher Ingenieur, **60**, pp. 541–546.

[14] Siebe, D. A., 1986, "Evaluation of Air-Conditioning Systems Utilizing Liquid Absorbents Regenerated by Solar Energy," Ph.D. dissertation, Arizona State University, Tempe, AZ.

[15] Lower, H., 1960, "Thermodynamische and Physikalische Eigenschaften der Wassrigen Lithiumbromid-Losung," Ph.D. dissertation, Karlsuhe.

[16] Uemura, T., 1967, "Studies on the Lithium Chloride-Water Absorption Refrigeration Machines," *Technology Reports of the Kansai Uni.*, **9**, pp. 71–88.

[17] Patankar, S. V., 1980, *Numerical Heat Transfer and Fluid Flow*, Hemisphere Publishing Corporation, New York.

[18] Habib, H., and Wood B., "Simultaneous Heat and Mass Transfer for a Falling Film Absorber; The two-Phase Flow Problem," Proceedings of the 1990 ASME International Solar Energy Conference, Miami, Florida, USA.

Bridgman Crystal Growth of an Alloy With Thermosolutal Convection Under Microgravity Conditions

James E. Simpson

Suresh V. Garimella

School of Mechanical Engineering,
Purdue University,
West Lafayette, IN 47907-1288
e-mail: sureshg@ecn.purdue.edu

Henry C. de Groh III
NASA Glenn Research Center,
Cleveland, OH 44135

Reza Abbaschian
Department of Materials Science and Engineering,
University of Florida,
Gainesville, FL 32611

The solidification of a dilute alloy (bismuth-tin) under Bridgman crystal growth conditions is investigated. Computations are performed in two dimensions with a uniform grid. The simulation includes the species concentration, temperature and flow fields, as well as conduction in the ampoule. Fully transient simulations have been performed, with no simplifying steady state approximations. Results are obtained under microgravity conditions for pure bismuth, and for Bi-0.1 at.% Sn and Bi-1.0 at.% Sn alloys, and compared with experimental results obtained from crystals grown in the microgravity environment of space. For the Bi-1.0 at.% Sn case the results indicate that a secondary convective cell, driven by solutal gradients, forms near the interface. The magnitude of the velocities in this cell increases with time, causing increasing solute segregation at the solid/liquid interface. Finally, a comparison between model predictions and results obtained from a space experiment is reported. The concentration-dependence of the alloy melting temperature is incorporated in the model for this case. Satisfactory correspondence is obtained between the predicted and experimental results in terms of solute concentrations in the solidified crystal. [DOI: 10.1115/1.1389058]

Introduction

The synthesis of advanced materials, especially for electronics and biomedical applications, demands high-quality crystals. The compositional uniformity (and hence the quality) of such crystals can be profoundly influenced by the transport phenomena which occur in the melt during solidification. The primary transport mechanism causing these deleterious effects is natural convection. The low-gravity environment of space offers an opportunity to suppress the strength of this natural convection. Hence there is a great deal of interest in the study of directional solidification of crystals in space.

The MEPHISTO project [1] is a collaborative program of space experiments aimed at understanding the fundamental processes involved in crystal growth. The space-borne experimental apparatus is a Bridgman-type furnace with an isothermal hot zone, an isothermal chill zone, and an insulated gradient zone. The furnace contains three ingots inside fused silica ampoules with a maximum 6 mm inner diameter and a 10 mm outer diameter. All three samples are solidified simultaneously under identical thermal conditions. After flight, the samples are extracted and analyzed. Four MEPHISTO space experiments have taken place; the most recent, MEPHISTO-4, flew in November 1997. The MEPHISTO-2 and -4 experiments examined the faceted solidification of bismuth doped with tin (Bi-Sn).

The experimental data from the MEPHISTO-2 mission (with a Bi-0.1 at.% Sn alloy) resulted in a greater understanding of the dominant role of interface kinetics on morphological stability. Stability phenomena were observed that had not been previously predicted by theory or measured in terrestrial experiments [2]. The MEPHISTO-4 experiments built on to the previous results, and used a Bi-1.0 at.% Sn alloy.

The MEPHISTO project includes a program of computational modeling of the crystal growth process; in particular, computational techniques are being used to investigate the role of convection, since accurate experimental determination of convection in metallic melts is very difficult to achieve due to the opacity and chemical reactivity of the melts. Furthermore, the computational models themselves are to be improved by a process involving prediction of, and comparison with, the experimental results. The aim of this procedure is to develop effective *fully transient* computer simulations of fluid flow related effects. Previous computations of Bridgman growth had been limited to steady-state growth cases [3–5].

Convection effects for MEPHISTO-4 space experiments were modeled by means of a transient, two-dimensional FIDAP finite-element model by Yao et al. [6]. A fixed-grid approach was adopted, with the enthalpy method being employed to model the phase change. Temporal averaging was used for the apparent heat capacity in the discretized equations. Due to computational difficulties introduced by the small partition coefficient for Bi-Sn, the presence of solute was ignored in Yao et al. [6]. Preliminary scaling arguments by de Groh and Nelson [7] implied that solutal convection effects on solute segregation may be significant. However, only recently has it been possible to include solutal convection into numerical simulations involving phase change for MEPHISTO-4. This inability to include solutal convection was attributed to difficulties with obtaining convergence in front-tracking methods as well as the low partition coefficient for Bi-Sn [6,8]. This has led to the use of a fixed-grid approach in the present work.

Many simulations of Bridgman crystal growth processes, both under terrestrial and microgravity conditions, are available in the literature. The majority of these simulations can be classified as *pseudo steady state* models. The key assumption in such models is that a ''steady-state'' mode of alloy solidification exists, i.e., the concentration of the dopant in the solid which forms at the interface is equal to the initial dopant concentration in the liquid [9]. Such models vary in complexity from simple two-dimensional analyses that consider the interface to be flat [8,10,11] to much more complex formulations that are able to handle interface curvature and wall conduction [12] and fully three-dimensional simu-

Contributed by the Heat Transfer Division for publication in the JOURNAL OF HEAT TRANSFER. Manuscript received by the Heat Transfer Division October 25, 1999; revision received March 13, 2001. Associate Editor: R. Mahajan.

lations [13]. However, because of the low partition coefficient for Bi-Sn alloys, a steady-state mode of solidification is never achieved during the MEPHISTO experiments. Thus pseudo steady state models are not appropriate; recently developed fully transient simulations, such as those of Simpson and Garimella [14] and Timchenko et al. [15] need to be employed and improved in order to faithfully model this process.

The computational modeling presented in this paper is intended to examine the effects of thermosolutal natural convection on the MEPHISTO-4 solidification experiments. This will be achieved using a *fully transient* two-dimensional model, which includes most of the effects of binary alloy solidification, such as convection driven by both thermal and solutal gradients, distinct thermal properties in the solid and liquid phases, conduction through the ampoule wall and the effects of interface curvature. The dependence of melting temperature on concentration is also considered for the numerical results that are compared with experimental data. It must be stressed that for the growth rates and applied thermal gradients encountered during the highly controlled directional solidification experiments modeled in this paper, the liquid/solid interface was experimentally found to be *stable* and *non-dendritic* like that for a pure metal. Consequently, the solid/liquid interface modeled in our numerical analysis is also stable and non-dendritic.

Mathematical Formulation

The problem under consideration is the directional solidification of a binary alloy by the Bridgman process, as shown schematically in Fig. 1. The gravity vector is perpendicular to the furnace axis (horizontal Bridgman growth configuration). The melt region is considered to be a viscous Newtonian fluid subject to thermosolutal convection. Thermophysical properties are considered as constant but distinct for the solid and liquid phases. Density variations are considered to be subject to the Boussinesq approximation. The equation for conservation of momentum and mass are

$$\frac{\partial \tilde{u}}{\partial t}+(\tilde{\nabla}\times\tilde{u})\times\tilde{u}=-\beta_T(T-T_C)\tilde{g}-\beta_C(C-C_0)\tilde{g}-\frac{\tilde{\nabla}P}{\rho_0}+v\nabla^2\tilde{u} \tag{1}$$

$$\tilde{\nabla}\cdot\tilde{u}=0. \tag{2}$$

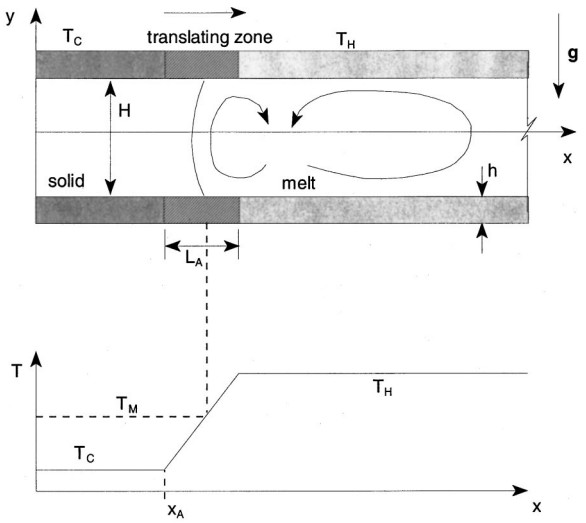

Fig. 1 Schematic of the Bridgman crystal growth process and furnace temperature profile

For calculating nondimensional constants (such as thermal Rayleigh number, *Ra*) the ampoule inside diameter H is selected to be the reference length. The characteristic time and velocity become $t'(=H^2/\alpha)$ and $v'(=H/t'=\alpha/H)$.

The governing equation for the conservation of energy is

$$A(T,C_L)\frac{\partial T}{\partial t}+\rho c_{pL}\tilde{\nabla}\cdot(\tilde{u}T)=\tilde{\nabla}\cdot(k\tilde{\nabla}T)+B(T,C_L). \tag{3}$$

It will be seen below that effective heat capacity A and source term B may be specified in this way for calculating phase-change. An initial temperature equal to T_H is applied throughout the flow field. The temperatures at the $x=0$ and $x=L$ walls are set to be T_H and T_C, respectively.

The thermal boundary conditions along $y=\pm(H/2+h)$ are a function of time and are shown schematically in Fig. 1. There is a translating zone (considered an "adiabatic" zone if the temperature profile is unknown) between the hot and cold regions of the furnace, in which the temperature linearly increases from the cold furnace temperature to the hot furnace temperature. The melting temperature of the material occurs somewhere within this zone, which translates with time at a constant x-velocity, known as the *translation velocity*, u_t. This is what facilitates the directional growth of the crystal. Defining the x location where the translating zone meets the cold furnace temperature zone to be at $x_A(t)$, the boundary condition for temperature may be expressed as

$$y=\pm\left(\frac{H}{2}+h\right):$$

$$T=\begin{cases} T_C, & x<x_A(t) \\ T_C+\Delta T\dfrac{x-x_A(t)}{L_A}, & x_A(t)\leqslant x\leqslant(x_A(t)+L_A). \\ T_H, & (x_A(t)+L_A)<x \end{cases} \tag{4}$$

In principle, the solution of the energy Eq. (3) coupled with the solution of the momentum and mass conservation equations (1 and 2) would yield the temperature and velocity distribution throughout the simulation domain. However, the problem of modeling the physics of the propagation of the solidification front and determining its location remains to be addressed. We choose to do this by employing the phase-transformation model of Zeng and Faghri [16]. In this model, apparent heat capacity A and source term B are given as

$$A(T,C_L)=\rho c_p+a(T,C_L)\frac{\partial f_L}{\partial T}$$

$$B(T,C_L)=-\tilde{\nabla}\cdot(\rho h_0\tilde{u})+\tilde{\nabla}\cdot[\rho f_S(h_0+(c_{pL}-c_{pS})T)\tilde{u}_S]-a(T,C_L)\frac{\partial f_L}{\partial C_L}\frac{\partial C_L}{\partial t}$$

$$a(T,C_L)=\rho\left[(c_{pL}-c_{pS})T+\frac{(\rho_L-\rho_S)c_pT+\rho_Lh_0}{\rho_L-f_L(\rho_L-\rho_S)}\right] \tag{5a}$$

$$c_p=c_{pL}+c_{pS}g_S$$

$$\rho=\rho_Sf_S+\rho_Lf_L.$$

For the present study, the density of each phase is assumed to be equal, and there is no dispersion of solid phase moving in the liquid. For the results shown where the melting temperature is considered dependent on concentration, the full expressions for A and B (Eq. 5a) simplify to become:

$$A(T,C_L)=\rho c_p+a(T)\frac{\partial f_L}{\partial T}$$

$$B(T,C_L)=-a(T)\frac{\partial f_L}{\partial C_L}\frac{\partial C_L}{\partial t} \tag{5b}$$

$$a(T)=\rho[(c_{pL}-c_{pS})T+h_0].$$

For the pure bismuth and dilute alloy results, concentration-dependence on temperature is neglected, and the expressions for A and B simplify further to

$$A(T)=\rho c_p+a(T)\frac{\partial f_L}{\partial T}$$

$$B(T)=0 \tag{5c}$$

$$a(T)=\rho[(c_{pL}-c_{pS})T+h_0].$$

The equation for conservation of solute throughout the computational domain is

$$\frac{\partial C_L}{\partial t}+\tilde{\nabla}\cdot(\tilde{u}C_L)=D\nabla^2 C_L+S(T,C_L). \tag{6}$$

This equation is analogous to the energy equation. We impose an initial solute concentration throughout the solution domain. At the boundaries no solute may exit the solution domain. Thus,

$$\begin{aligned} t=0 \quad & C_L=C_0 \\ x=0,L \quad & \partial C_L/\partial x=0 \\ y=0,H \quad & \partial C_L/\partial y=0. \end{aligned} \tag{7}$$

Again, in principle, solution of Eq. (6) along with energy Eq. (4) and the fluid velocities all subject to the relevant boundary and initial conditions is enough to determine the solute, temperature and velocity values throughout the solution domain. However, the more general problem involving phase change demands that solute redistribution at the advancing solid/liquid interface be addressed. At the interface, new solid material forms at a concentration lower than at the adjacent liquid, in accordance with the partition coefficient [9]:

$$C_s^*=k_pC_L^*. \tag{8}$$

For the Bi-Sn system under consideration in this work, the partition coefficient k_p has a value of 0.029. This small value indicates that the solid forms at a concentration very poor in solute, and thus there is rapid and significant build-up of solute in the liquid region ahead of the interface. Source term S accounts for solute rejection at the interface into the bulk fluid resulting from the effect of the solid material forming at the lower concentration. Following the work of Swaminathan and Voller [17] and Voller et al. [18] source term S may be written as the differential

$$S(T,C_L)=\frac{\partial(f_LC_L)}{\partial t}+k_pC_L\frac{\partial f_S}{\partial t}. \tag{9}$$

Numerical Analysis

The numerical scheme is explained in detail in Simpson and Garimella [14,19]; only salient details are provided here. The computational domain is primarily discretized using regularly spaced finite difference mesh points. Superimposed on this grid are finite volumes which are used for the solution of the energy and species concentration equations. The finite volume centers are staggered with respect to the finite difference mesh point locations. Vorticity, velocity and vector potential are calculated at the finite difference mesh points. Temperature and solute concentration are evaluated using the finite volumes.

For solving velocities, the vorticity-streamfunction representation of the Navier-Stokes and continuity equations (1 and 2) is used. The numerical approach applied here is modified from a program [20] written for the solution of natural convection in a rectangular cavity. The essential details are that the discretized equation for the vorticity transport equation is solved using an Alternating Direction Implicit scheme [21]. The discretized equation for streamfunction is solved using the conjugate gradient method. Once the values of streamfunction are known, the nodal velocities can be determined. Boundary conditions are explicitly applied on the advancing solid/liquid interface which is arbitrarily oriented and so the boundary conditions require special handling. The location and slope of the interface is calculated using a Hirt and Nichols [22] type front reconstruction; the boundary conditions may then be applied once the slope and position of the front are known.

The energy (4) and solute conservation (6) equations are discretized using the finite volume mesh, with an upwind scheme incorporated for the treatment of convective heat fluxes. The discretized equations are solved using iterative solvers—either Gauss-Seidel iteration or Stone's strongly implicit procedure [23]. For the general case where melting temperature is dependent on interface concentration, the concentration and energy equations are highly coupled and are solved simultaneously.

Results and Discussion

Validation. A grid-independence study was undertaken to determine the appropriate spatial and temporal discretization scheme to be used. This study involved examining the solution fields from a test matrix of simulations performed using four different discretization schemes. Four mesh sizes of increasing spatial and temporal refinement were examined. The mesh selected on the basis of this grid independence study was a regularly spaced 300×35 mesh, with 25 of the 35 y-direction cells being in the sample and the remaining 10 in the ampoule walls. The time step size was $\Delta t=0.1338$ s. Detailed results from the grid-independence study, including plots of key field variables, are available in Simpson and Garimella [19]. The key points are as follows:

- The thermal field results were almost identical for all four meshes.
- The difference between the velocities predicted by the mesh adopted in this study and those from a finer mesh was less than 3 percent.
- Particular attention was given to the concentration values in the solidified material. The concentrations in the solid are completely dependent on the solutal, thermal and flow fields in the melt, and so, are very sensitive to any changes in these fields. Concentration traces in the solid for the mesh employed in this study had a maximum discrepancy of only 3.2 percent (with the majority of values being less than 1 percent) compared to results at the finer mesh.

These results make it clear that (*a*) all the field variables converge to a single result as the mesh becomes increasingly fine, and (*b*) the mesh employed in this work is fine enough to obtain meaningful results while keeping computational costs reasonable.

Pure Bismuth. Simulations for the Bridgman crystal growth of pure bismuth were performed. The cold and hot furnace temperatures were $T_C=50°C$ and $T_H=700°C$, respectively. Thermophysical properties from Yao et al. [8] were used, and are shown in Table 1. The gravity level used for this and subsequent cases was $g=10\,\mu g$. This gravity level is a conservative ''worst-case'' estimate of the residual gravity value experienced during the flight experiments [7]. Key nondimensional parameters describing thermal transport are Gr=113.6 and Pr=0.01144. For this pure Bismuth case, there is no solute, so the dilute model for phase chance (Eq. 5*c*) was used.

In order to start each of the crystal growth simulations, the following procedure was carried out. The initial position of the translating zone was flush with the $x=0$ wall. This zone is immobilized for the first 3000 time steps. During this time, the velocity and concentration field solution schemes are switched off while solid rapidly chills in the portion of the translating zone which is lower than the melting temperature. This new state is then taken to

Table 1 Thermophysical properties. The properties (except the solutal diffusion coefficient *D*) for solid and liquid bismuth were evaluated at the mean solid and the mean liquid temperatures of 160.7 and 485.7°C, respectively. The solutal diffusion coefficient was evaluated at a position halfway into a typical solute boundary layer, since solute diffusion occurs mainly in this region. The reference density was considered to be equal for both phases.

Property	Units	Value
Reference density, ρ_0	kg/m^3	10070
Thermal conductivity of the solid, k_S	W/mK	6.872
Thermal conductivity of the liquid, k_L	W/mK	14.66
Specific heat of the solid, c_{pS}	J/kgK	132.6
Specific heat of the liquid, c_{pL}	J/kgK	135.3
Enthalpy of freezing, ΔH	kJ/kg	52.3
Viscosity of the liquid, μ	Ns/m	1.240×10^{-3}
Melting temperature, T_m	°C	271.3
Thermal expansion coefficient, β_T	K^{-1}	-1.25×10^{-4}
Thermal conductivity of the (fused silica) ampoule, k_w	W/mK	2.10
Density of the (fused silica) ampoule, ρ_w	kg/m^3	2020
Specific heat of the (fused silica) ampoule, c_{pw}	J/kgK	1066.8
Partition (or segregation) coefficient, k_p	—	0.029
Diffusivity of liquid Sn in liquid Bi, D	m^2/s	3.50×10^{-9}
Solutal expansion coefficient, β_C	$(vol.\%)^{-1}$	-0.305
Prandtl number, Pr	—	0.01144
Lewis number, Le	—	3074
Slope of liquidus line, m	K/(vol%)	-2.547

be at time $t=0$. After this, simulations proceed with the entire solution scheme enabled and the insulated zone moving at the translation velocity u_t.

Figure 2(*a*) shows a plot of velocity vectors and isotherms after 3000 s have elapsed. Isotherms are shown in the ampoule wall as well as in the liquid and solid bismuth. The thick line at $x=16$ mm represents the solid/liquid interface. The dominant feature of this plot is the counter-clockwise convective cell in the translating zone ($16<x<40$ mm). For clarity, velocity vectors are plotted on every third mesh point in the *x*-direction in this figure. The maximum velocity in this convective cell is 3.47 μm/s at (24.75, −1.8 mm). The ratio of this velocity to the translation velocity, u_t, is 1.03, which compares to the value of 1.12 found from the finite-element, variable-property simulation of the same process by Yao et al. [6]. Velocities in the negative *y*-direction at the interface are constrained and concentrated by the presence of the solid whereas velocities in the positive *y*-direction at the opposite (hot) end of the translating zone are much more diffuse.

The other main feature of this plot is the isotherms throughout the solution domain. On the outside edge of the ampoule, the (imposed) linear temperature profile within the translating zone is witnessed by the regularly spaced isotherms on the outer edge. In the low-conductivity ampoule the isotherms are dramatically distorted, and the thermal field on the inside of the ampoule wall differs from that imposed on the outside. For $x \leqslant 24$ mm, the temperature in the ampoule is greater than the applied temperature (the isotherms distort sharply to the left); for $x \geqslant 24$ mm, the converse is true. In the bismuth region the isotherms exhibit the same trend, and have a gentle, crescent-shaped curvature. The isotherms and the interface appear to be symmetric about the centerline ($y=0$) and thus have not been influenced by convective transport in the melt. The solid-liquid interface, which is an isotherm, is discernibly curved such that the solid is concave. The total deflection of the interface is about 0.5 mm which compares to a value of ~0.46 mm found in Yao et al. [6]. This curvature is primarily a result of the difference in thermophysical properties for the solid and liquid phases. Translation of the thermal boundary condition also contributes slightly to this effect.

Figures 2(*b*) and 2(*c*) are plots of velocity vectors and isotherms at 6000 and 9000 s, respectively. The progression of the translating zone (and thus of the solidification front) is obvious from these figures. After 6000 s, the front is at $x \approx 26$ mm, and the nature of the convective motions is unchanged. The magnitude of the maximum velocities at these later times is identical to that at the previous time (Fig. 2(*a*)). This indicates that end effects are not influencing the results. The curvature of the interface also remains the same.

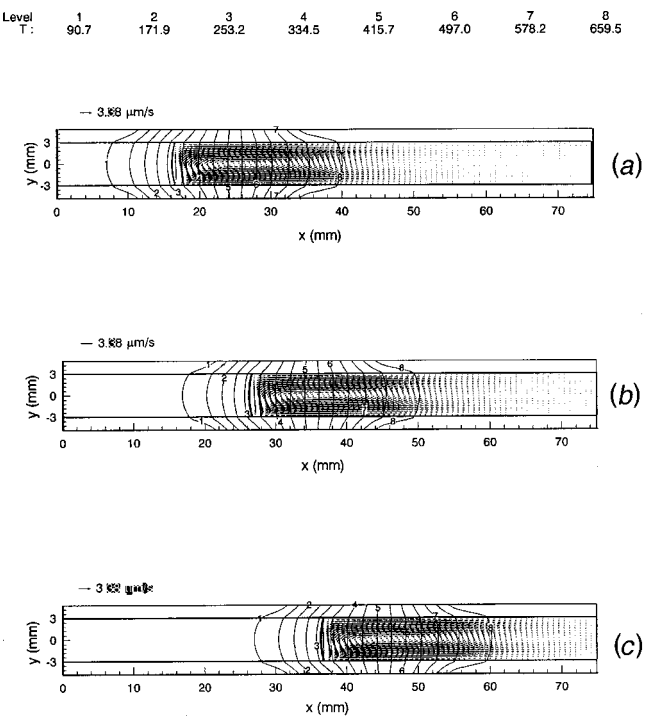

Fig. 2 Velocity vectors and isotherms for the Bridgman growth of pure bismuth at (*a*) 3000, (*b*) 6000, and (*c*) 9000 s. The thick solid line indicates the location of the solid/liquid interface. The velocity vectors are shown at every third location in the *x*-direction.

Bi-0.1 at.% Sn Alloy (MEPHISTO-2). The growth of a Bi-0.1 at.% Sn (0.08185 vol.% Sn) alloy was considered next. The velocity, thermal and solute fields were solved subject to the dilute alloy model (Eq. 5*c*), and the dimensionless parameters for solute transport are $Gr_s=0.349$ and $Le=3074$. Simulations were performed using the same spatial discretization and time step as for pure bismuth.

The nature of the convective flow for this alloy (results not shown) is similar to that for pure bismuth. A single counter-clockwise thermally driven convective cell dominates the domain. The maximum *u*-velocity is slightly less than for pure bismuth, and is at the same location. However, the magnitude of the maximum *v*-velocity is −1.77 μm/s at (17.75, 0 mm) acting in the negative *y*-direction, which is lower in magnitude than for pure bismuth (−1.87 μm/s). Solute rejected at the interface acts to oppose the thermally driven convective motion, resulting in retarded velocities near the interface. The thermal field is not distorted by the action of convection. As time progresses to 6000 and 9000 s, the maximum *v*-velocity decreases to −1.72 μm/s and −1.65 μm/s respectively, as a result of continuing solute rejection at the interface.

Solute concentration profiles across the height of the solidified alloy in the domain are shown in Fig. 3. Three different *x*-locations (16.18, 26.30, 36.41 mm) are considered, corresponding to the location of the interface at $y=0$ at times of 3000, 6000, and 9000 s, respectively. To aid in visualizing the influence of

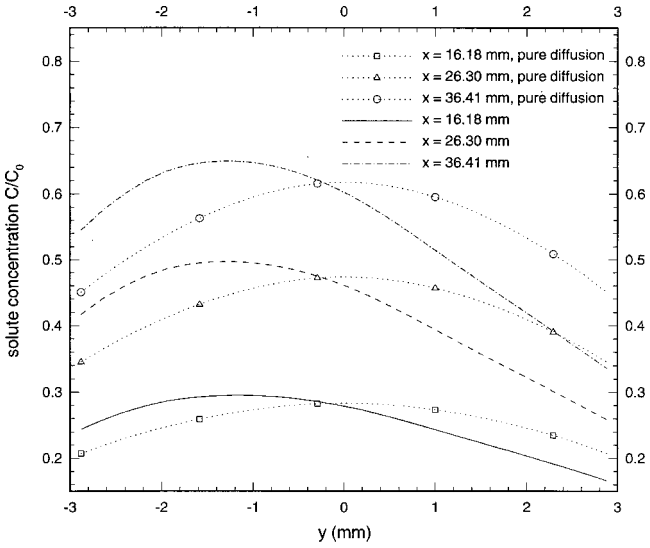

Fig. 3 Traces of solute concentration across the solidified material at various *x*-locations for Bi-0.1 at.% Sn. The dotted lines correspond to diffusion only (no convection) results.

convection, results for a simulation involving diffusion only (no convection) are superimposed on this plot. Note that these pure diffusion results indicate that significant radial segregation arises due to interface curvature [12,13] such that the solute concentrations at the centerline are larger than those at the edges. The level of curvature-induced radial segregation remains almost constant, with values of $\xi = 29.1$ percent (based on the mean concentration) at $x = 16.18$ mm and 29.4 percent at $x = 26.30$ and 36.41 mm. The inclusion of convection into the calculations causes the following effects. Solute levels are increased for low values of y and decreased for higher values of y. The y-location for the maximum solute concentration is also shifted from the centerline to $y = -1.23$ mm for all the traces. This is a consequence of the convective flow sweeping solute "down" the interface in the direction of decreasing y and away from the interface in the direction of increasing x. The maximum values for solute concentration are $C_{max}/C_0 = 0.30$, 0.50, 0.65 for the traces at $x = 16.18$, 26.30, and 36.41 mm, respectively. The radial segregation values increase slightly from $\xi = 50.1$ percent at $x = 16.18$ mm to 56.3 percent at $x = 36.41$ mm.

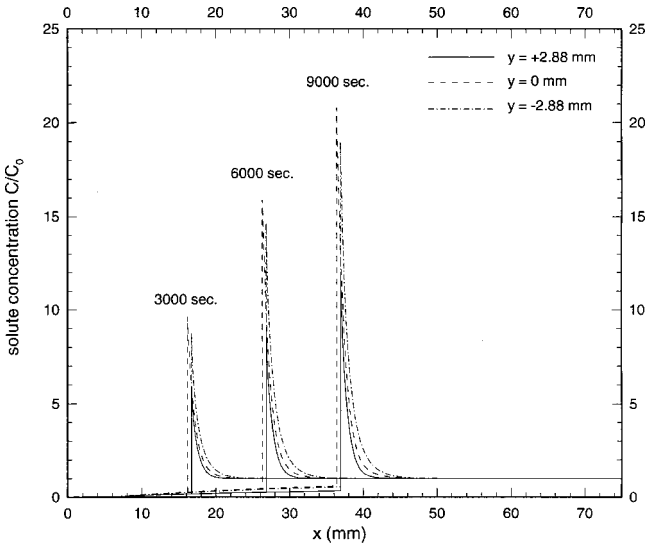

Fig. 4 Longitudinal solute concentration traces at three different *y*-locations for Bi-0.1 at.% Sn

Traces of solute concentrations in the solid and melt at the different times are shown in Fig. 4. These traces run longitudinally along the ampoule for three different heights of $y = -2.88$, 0 and 2.88 mm. Note that the interface location on the centerline ($y = 0$) trace lags slightly behind the value for the other traces since the interface is curved. Solute build-up near the interface, and the exponential profile characteristic of binary-alloy solute rejection [24] are clearly evident. The concentration at the centerline increases from $C/C_0 = 9.62$ at 3000 s to 20.79 at 9000 s. The impact of convection can also be seen in this plot. Warm, solute-poor fluid impinges on the top section of the interface. This fluid, cooled by the interface, falls toward the bottom wall and then returns to the bulk. This convective transport causes a thinner solute boundary layer and lower interface concentration value for $y = 2.88$ mm and, conversely, a thicker solute boundary layer and higher interface concentration value for $y = -2.88$ mm. The interface concentrations along the centerline remain larger than those found at the periphery for all the times shown. This effect is due to interface curvature (see Fig. 3). The axial segregation in the solidified crystal is seen to increase with time; the radial segregation evident in Fig. 3 is also seen in Fig. 4.

For the low-concentration alloy, the solute concentration profiles are governed by solute rejection at the (curved) interface and by thermal convection only. The action of solutal convection is limited at these low concentrations. The velocity field indicates that thermal convection decreases slightly with time.

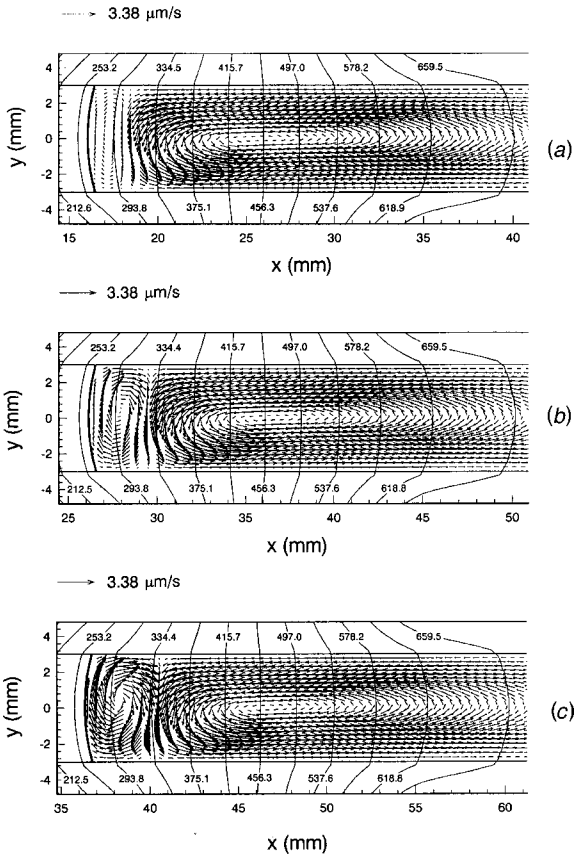

Fig. 5 Velocity vectors and isotherms for the Bridgman growth of Bi-1.0 at.% Sn at (*a*) 3000, (*b*) 6000, and (*c*) 9000 s. The thick solid line indicates the location of the solid/liquid interface. A primary counter-clockwise convective cell is evident in all three panels. A secondary clockwise cell, driven by solutal gradients, develops with time.

Bi-1.0 at.% Sn Alloy (MEPHISTO-4). A richer alloy was simulated next. The initial liquid composition was taken to be at a uniform 1.0 at.% Sn (0.8185 vol.% Sn) increasing the value of Gr_s to 3.49. The dilute model (Eq. 5*c*) was retained for this initial investigation; the validity of this is commented upon later.

Velocity vectors and isotherms at three different times are shown in Fig. 5. At 3000 s (Fig. 5*a*) the velocities indicate a primary counter-clockwise convective cell in the translating zone, along with a weak secondary, clockwise cell driven by solute gradients adjacent to the interface. The two-cell convective motion is in contrast to that observed for pure bismuth and for the more dilute alloy. The maximum v-velocity in the secondary convective cell near the interface at (16.5, 0 mm) is 0.57 μm/s. The nature of the maximum velocities for this case is also different due to the higher levels of solute rejection and the presence of the secondary cell. The maximum u-velocity for this case is slightly lower than that for pure bismuth. The maximum v-velocity is identical to the value for pure bismuth but is located further from the interface ($x=19.25$ versus $x=17.75$ mm for the pure and Bi-0.1 at.% Sn cases).

At a later time (Fig. 5(*b*)), the secondary convective cell has increased in size and strength as solute—the driving force for this cell—continues to build up at the interface. The maximum v-velocity in the secondary convective cell near the interface at (27.00, 0.48 mm) is 1.75 μm/s. Later in the growth process (Fig. 5(*c*)), the front has advanced to $x\approx 36$ mm, and the secondary convective cell has become quite strong. The maximum v-velocity in the secondary cell (and in the domain) is 2.88 μm/s at (37.00, 0.36 mm).

Traces of solute concentration across the height of the solidified alloy, along with pure diffusion results, are shown in Fig. 6. This plot provides a stark contrast with the results shown for the more dilute alloy in Fig. 3; the formation and growth of the secondary cell causes segregation to occur in the opposite sense (such that concentration values near the top of the domain are higher than at the bottom). At $x=16.18$ mm, the concentrations are close to those for pure diffusion; the maximum value is $C/C_0=0.28$ at $y=0.059$ mm with a segregation value of $\xi=28.9$ percent. This serendipitous result is a consequence of segregation arising from the influence of the secondary cell balancing the segregation caused by the thermally driven cell when solidification has proceeded to this location. At lower values of x ($t<3000$ s), segregation is such that the maximum value occurs at $y<0$ (similar to the Bi-0.1 at.% Sn alloy result, see Fig. 3) while at higher values of x ($t>3000$ s) this maximum is shifted to a more positive y value. The traces at $x=26.30$ and 36.41 mm show that increasing solutal convection leads to increasing radial segregation. The maximum values are $C/C_0=0.51$ and 0.75 with radial segregation levels of $\xi=54.7$ and 82.2 percent, respectively. This behavior is different from the case shown in Fig. 3, where the convective field remained almost steady with respect to the interface resulting in only a slight increase in segregation.

Figure 7 is a plot of longitudinal solute concentrations at domain heights of $y=-2.88$, 0 and 2.88 mm for the Bi-1.0 at.% Sn case at the three different times. As for the case shown in Fig. 4 there is significant solute buildup, with liquid solute concentrations C/C_0 at the interface along the centerline being 9.70, 15.59, and 19.20, respectively. Note, however, that this corresponds to much higher concentrations than for the case shown in Fig. 4 due to the higher initial concentration C_0. Near the interface, the solute concentrations in the liquid are higher at $y=2.88$ mm than at $y=-2.88$ mm. Further from the interface, but still within the solute boundary layer, concentration increases with decreasing y. This is due to the interaction of the two convective cells. Close to the interface, the secondary cell circulates solute-rich material within the boundary layer, acting to accumulate solute-rich material in this region. Further from the interface (see Fig. 5), the primary convective cell influences the solute distribution, sweeping solute from the bottom of the domain into the bulk and thickening the solute boundary layer in this region. In general, the solute boundary layers are more compact for the Bi-1.0 at.% Sn (Fig. 7) when compared to the Bi-0.1 at.% Sn case (Fig. 4). Note that concentration values of this magnitude would be sufficient to lower the melting temperature of the alloy by a significant amount. This implies that the constant melting temperature assumption made in these simulations is not valid. This effect will be addressed in the next subsection.

For the higher alloy concentrations, solutal convection plays a much larger role, as can be seen in the concentration profiles discussed above. As growth proceeds, the level of solutal convection grows, with a corresponding increase in radial segregation. The maximum concentration increases much more rapidly than the minimum value.

Figure 8 is a plot of *average* solute concentrations in the solid at 3000, 6000, and 9000 s for both the dilute and rich alloy. Averaging is performed across the height of the solidified material ($y=-3$ to 3 mm). For comparison purposes, average concentra-

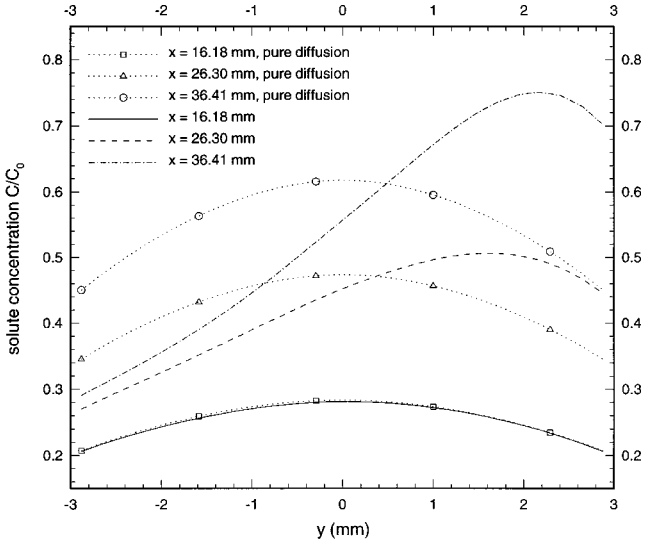

Fig. 6 Traces of solute concentration across the solidified material at various *x*-locations for Bi-1.0 at.% Sn. The dotted lines correspond to diffusion only (no convection) results.

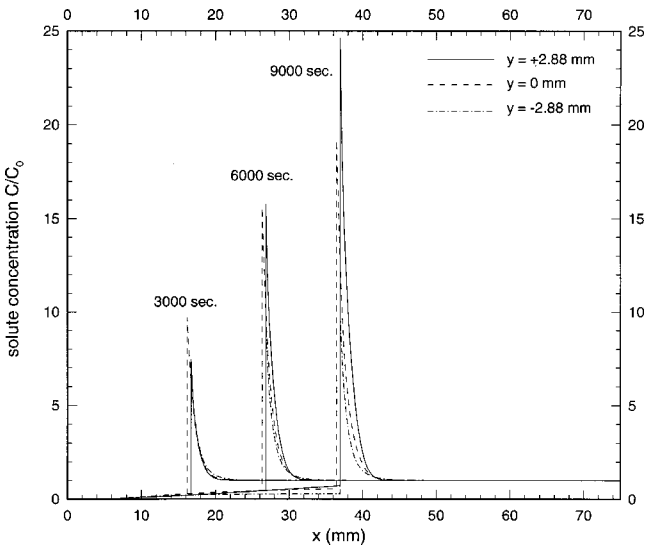

Fig. 7 Longitudinal solute concentration traces at three different *y*-locations for Bi-1.0 at.% Sn

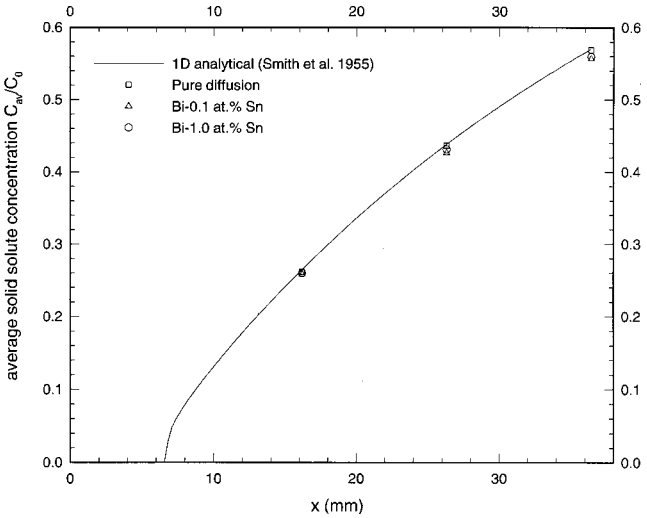

Fig. 8 A comparison of average concentration values in the solidified material. The solid line is the one-dimensional analytical result of Smith et al. [24].

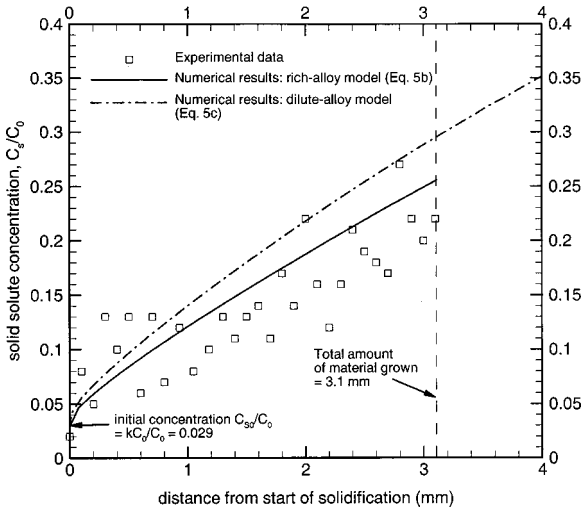

Fig. 9 A comparison of numerically predicted and experimentally measured concentration values for the Bridgman growth of Bi-1.0 at.% Sn. The numerical results are shown for simulations with and without the effect of concentration-dependent melting temperature being included. Reasonable agreement is observed between experimental data and numerical results including concentration-dependent melting temperature.

tions C_{av}/C_0 for the pure diffusion case as well as those calculated from an analytical expression for solid solute concentrations under one-dimensional pure diffusion growth conditions [24] are also shown. The pure diffusion results exhibit good agreement with the one-dimensional analytical result; the largest difference between these results is 1.2 percent at 3000 s. The lowest average normalized solid concentrations are found for the dilute alloy (Bi-0.1 at.% Sn). After 3000 s the dilute alloy concentration is 1.3 percent less than for pure diffusion. With time, this deficit increases to 2.2 percent after 6000 s and 2.1 percent after 9000 s. The average solute concentrations for the richer alloy (Bi-1.0 at.% Sn) lie between those found for the pure diffusion and Bi-0.1 at.% Sn results. These concentrations are 0.76, 1.2, and 1.7 percent lower than the pure diffusion values after 3000, 6000, and 9000 s, respectively. For the dilute alloy, the single convective cell acts, on average, to increase the size of the solute boundary layer (Fig. 5) by transporting solute from the interface out into the melt (Fig. 3). This results in a corresponding decrease in the average solid concentration levels when compared to the pure diffusion case, for a given *y*-location. For the richer alloy, the solute boundary layers are shaped by a more complicated convection pattern (Fig. 6). In general, this convection pattern for the Bi-1.0 at.% Sn alloy acts to make the solute boundary layers more compact than for the dilute alloy case, resulting in slightly higher average concentrations C_{av}/C_0. The difference between the average concentration found for the pure diffusion and Bi-1.0 at.% Sn cases increases with increasing solutal convection levels.

Comparison With Experiment. An actual solidification process carried out during the MEPHISTO-4 space experiment was modeled using the rich-alloy model (Eq. 5*b*) which accounts for the effect of concentration-dependent melting temperature. The main difference in this simulation compared to those above is that the solidification cycle selected was conducted at a furnace translation rate of 11.997 μm/s for a duration of 334 seconds, resulting in a total furnace translation of 4 mm. The gravity level for this case was reduced to 1 μg, which is more typical of residual gravity levels during the experiment [7]. Under these conditions, the process is diffusion-dominated although there is some discernible convection-induced segregation [19].

Figure 9 is a plot of concentration values along the centerline of the sample. The square symbols are experimental data points obtained via a post-flight microprobe analysis of the solidified sample. Although there is scatter in the experimental data, a clear trend of increasing concentration values can be discerned. The solidification process depicted starts at a location 143.5 mm along the ampoule; on Fig. 9, this location is taken as the origin $x=0$ at $t=0$. Then, in order to grow solid from the melt, the furnaces are moved at a constant velocity. As the furnaces begin to move and new solid is formed, solute begins to pile up at the interface. As the concentration at the interface increases, the local melting temperature decreases. Hence the front slowly ''melts back'' with respect to the furnaces and thus moves at a speed that is *slower* than the furnace translation velocity. After 334 seconds have elapsed, the furnaces have traversed 4 mm, however, the solid/liquid interface has moved only 3.1 mm, and so only 3.1 mm of crystal is grown. The results from the numerical simulation, using the rich alloy model (Eq. 5*b*) that includes the effect of concentration-dependent melting temperature, are superimposed on this plot as the thick solid line. The experimental and numerical results are shown for a transverse location of $y=0$. These results agree reasonably well with the experimental data both in terms of the predicted values of concentration and in terms of predicting the total amount of material grown. Results of a simulation using the dilute model (Eq. 5*c*, no concentration-dependence of melting temperature) are also shown as a dashed line on the figure. This simulation clearly cannot handle the ''melt back'' of the interface and is therefore not able to predict the correct final location of the solid-liquid interface or accurate values of concentration.

The effect of the inclusion of concentration-dependent melting temperature in the calculations is to predict less net solute rejection into the liquid at a given time, since the front moves at an overall slower rate. If this concentration-dependence was incorporated into the results considered in Figs. 5, 6 and 7 for Bi-1.0 at.% Sn above, the primary differences would be twofold. First less net solute would be rejected, so that the gradients in the liquid region near the interface would be less steep, resulting in lower levels of convection and hence lower levels of segregation at a given time. The other main effect would be to alter the shape of the interface slightly, such that it would be flatter in regions of higher liquid solute concentrations at the interface.

Conclusions

A series of fully transient simulations of horizontal Bridgman crystal growth under microgravity conditions have been per-

formed. The pure bismuth simulation was found to agree reasonably well with a similar simulation of the process [6], in terms of the convection level and the interface curvature.

For the dilute alloy simulation (Bi-0.1 at.% Sn), a single dominant counter-clockwise convective cell is percent for the entire duration of the process. As time proceeds, solute is rejected at the interface and the level of solute near the interface increases. Due to the presence of thermal convection, radial solute segregation occurs with preferentially higher concentrations at the bottom of the solid. The level of segregation increases slightly with time. The maximum values of concentration are small and so the assumption of constant alloy melting temperature is realistic.

For the richer alloy (Bi-1.0 at.% Sn), the convective field is much more complex. Higher levels of solute rejection at the interface cause higher levels of solute convection. Initially, a single, thermally driven, counter-clockwise rotating cell is present. As time proceeds and solute accumulates at the interface, a secondary, solute-driven clockwise rotating cell develops. The effect of this convective pattern is to yield significant levels of segregation in the solute at the interface (and hence in the solid). This segregation is such that the values towards the top of the domain are highest. The higher values of concentration near the interface would result in a significant change in the melting temperature for the alloy. For this richer alloy, solute build-up is significant and so the concentration-dependence of the melting temperature becomes important.

Finally, simulations of Bridgman crystal growth in microgravity, incorporating the effects of a concentration-dependent melting temperature were performed. The results agree well with data obtained from the flight experiment. The combination of numerical simulations and experimental data presented here has validated the numerical approach used and provided insight into the role of thermosolutal convection during directional solidification.

Acknowledgments

Partial funding for this work from NASA (Coop. Agreement # NCC3-557) is gratefully acknowledged. JES was funded by a UW-Milwaukee Graduate School Fellowship. The insightful help of Dr. M. Yao of the Ohio Aerospace Institute is much appreciated. Professors G. de Vahl Davis and E. Leonardi and Dr. V. Timchenko of the University of New South Wales are thanked for kindly providing their code, FRECON3V, which was the basis for the velocity solution scheme used in this work.

Nomenclature

c_p = specific heat at constant pressure
C = species concentration
D = species diffusion coefficient in liquid
f = volume fraction
g = mass fraction
$\tilde{g}$ = acceleration due to gravity
Gr = Grashof number, $g\beta_T(T_H-T_C)H^3/\nu^2$
Gr_s = solutal Grashof number, $g\beta_c C_0 H^3/\nu^2$
h = ampoule thickness (outside radius—inside radius)
h_0 = reference enthalpy$=\Delta H/\rho$
H = ampoule inside diameter; reference length
k = thermal conductivity
k_p = partition coefficient, C_S^*/C_L^* (Eq. 8)
L = length of simulation domain
L_A = translating zone length
Le = Lewis number, α/D
Pr = Prandtl number, ν/α
t = time
T = temperature
u, v = velocities in x and y directions

Greek Symbols

α = thermal diffusivity
β = expansion coefficient
ΔT = temperature difference, T_H-T_C
ΔH = enthalpy of freezing
ν = kinematic viscosity
ξ = radial segregation, $(C_{\max}-C_{\min})/C_{\text{average}}$
ρ = density

Subscripts

0 = initial condition
C = cold furnace temperature condition
H = hot furnace temperature condition
L = liquid
m = at solidification front
S = solid
w = ampoule wall

Superscripts

$\sim$ = vector
$'$ = reference quantity
$*$ = at solid/liquid interface

References

[1] Abbaschian, R., Gokhale, A. B., Favier, J. J., and Coriell, S. R., 1992, "In-Situ Monitoring of Crystal Growth Using MEPHISTO," NASA Science Requirements Document (SRD), NASA.
[2] Abbaschian, R., 1996, In-Situ Monitoring of Crystal Growth Using MEPHISTO: Revised Science Requirements Document (RSRD) for the Reflight of MEPHISTO aboard USMP-4, NASA.
[3] Yeoh, G. H., de Vahl Davis, G., Leonardi, E., de Groh, III, H. C., and Yao, M., 1997, "A Numerical and Experimental Study of Natural Convection and Interface Shape in Crystal Growth," J. Cryst. Growth, **173**, pp. 492–502.
[4] Yao, M., and de Groh, III, H. C., 1993, "Three-Dimensional Finite Element Method Simulation of Bridgman Crystal Growth and Comparison With Experiments," Numer. Heat Transfer, Part A, **24**, pp. 393–412.
[5] de Groh III, H. C., and Yao, M., 1994, "Numerical and Experimental Study of Transport Phenomena in Directional Solidification of Succinonitrile," *Transport Phenomena in Solidification*, ASME HTD-Vol. 284, pp. 227–243.
[6] Yao, M., de Groh III, H. C., and Abbaschian, R., 1997, "Numerical Modeling of Solidification in Space With MEPHISTO-4 (Part 1)," *35th Aerospace Sciences Meeting and Exhibit*, Reno, NV, Paper AIAA 97-0449.
[7] de Groh III, H. C., and Nelson, E. S., 1994, "On Residual Acceleration During Space Experiments," *Heat Transfer in Microgravity Systems*, ASME HTD-Vol. 290, pp. 23–33.
[8] Yao, M., Raman, R., and de Groh III, H. C., 1995, "Numerical Simulation of Heat and Mass Transport During Space Crystal Growth With MEPHISTO," NASA Technical Memorandum 107015, NASA.
[9] Kurz, W., and Fisher, D. J., 1989, *Fundamentals of Solidification*, Trans Tech Publications.
[10] Alexander, J. I. D., Ouazzani, J., and Rosenberger, F., 1989, "Analysis of the Low Gravity Tolerance of Bridgman-Stockbarger Crystal Growth," J. Cryst. Growth, **97**, pp. 285–302.
[11] Simpson, J. E., Yao, M., de Groh III, H. C., and Garimella, S. V., 1998, "Numerical Modeling of Solidification in Space With MEPHISTO-4 (Part 2)," NASA Technical Memorandum TM-1998-206630, NASA.
[12] Adornato, P. M., and Brown, R. A., 1987, "Convection and Segregation in Directional Solidification of Dilute and Non-Dilute Binary Alloys," J. Cryst. Growth, **80**, pp. 155–190.
[13] Liang, M. C., and Lan, C. W., 1996, "Three-Dimensional Convection and Solute Segregation in Vertical Bridgman Crystal Growth," J. Cryst. Growth, **167**, pp. 320–332.
[14] Simpson, J. E., and Garimella, S. V., 1998, "An Investigation of the Solutal, Thermal and Flow Fields in Unidirectional Alloy Solidification," Int. J. Heat Mass Transf., **41**, pp. 2485–2502.
[15] Timchenko, V., Chen, P. Y. P., Leonardi, E., de Vahl Davis, G., and Abbaschian, R., 2000, "A Computational Study of Transient Plane Front Solidification of Alloys in a Bridgman Apparatus Under Microgravity Conditions," Int. J. Heat Mass Transf., **43**, pp. 963–980.
[16] Zeng, X., and Faghri, A., 1994, "Temperature-Transforming Model for Binary Solid–Liquid Phase-Change Problems: Part 1—Mathematical Modeling and Numerical Methodology," Numer. Heat Transfer, Part B, **25**, pp. 467–480.
[17] Swaminathan, C. R., and Voller, V. R., 1997, "Towards a General Numerical Scheme for Solidification Systems," Int. J. Heat Mass Transf., **30**, pp. 2859–2868.
[18] Voller, V. R., Brent, A. D., and Prakash, C., 1989, "The Modeling of Heat, Mass and Solute Transport in Solidification Systems," Int. J. Heat Mass Transf., **32**, pp. 1719–1731.
[19] Simpson, J. E., and Garimella, S. V., 2000, "The Influence of Gravity Levels on the Horizontal Bridgman Crystal Growth of an Alloy," Int. J. Heat Mass Transf., **43**, pp. 1905–1923.
[20] Timchenko, V., Leonardi, E., and de Vahl Davis, G., 1997, "FRECON3V User's Manual," University of New South Wales, School of Mechanical and

Manufacturing Engineering, Report 1997/FMT/1, and FRECON3V Programmer's Manual, Report 1997/FMT/2.
[21] Samarskii, A. A., and Andreyev, V. B., 1963, ''On a High-Accuracy Difference Scheme for an Elliptic Equation With Several Space Variables,'' USSR Comput. Math. Math. Phys., **3**, pp. 1373–1382.
[22] Hirt, C. W., and Nichols, B. D., 1981, ''Volume of Fluid (VOF) Method for the Dynamics of Free Boundaries,'' J. Comput. Phys., **39**, pp. 210–225.
[23] Ferziger, J. H., and Perić, M., 1996, *Computational Methods for Fluid Dynamics,* Springer-Verlag, New York.
[24] Smith, V. G., Tiller, W. A., and Rutter, J. W., 1955, ''A Mathematical Analysis of Solute Redistribution During Solidification,'' Can. J. Phys., **33**, pp. 723–743.

Assessment of Overall Cooling Performance in Thermal Design of Electronics Based on Thermodynamics

Ken Ogiso
Tokyo University of Technology,
Department of Mechatronics,
1404-1, Katakura-cho, Hachioji-city,
Tokyo, 192-0982, Japan
e-mail: ogiso@cc.teu.ac.jp

A method of assessing the overall cooling performance in the thermal design of electronics is presented. The method is based on the optimization concept proposed by A. Bejan, whose original idea was related to the trade-off between heat transfer enhancement and pressure loss increase based on an assessment of entropy generation rate. The present report summarizes the research conducted to date and presents a study on the optimization of cooling systems. [DOI: 10.1115/1.1387025]

Keywords: Thermal Design, Heat Transfer, Pressure Loss, Entropy Generation

Introduction

In recently produced notebook computers, the cooling system is designed such that the user can select either performance mode or silent mode, corresponding to high CPU speed with continuous fan cooling, or quiet operation with low CPU speed and restrained fan operation, respectively. This design criterion is in accordance with the trade-off between cooling capacity and fluid pressure loss based on the entropy generation method [1], and is a concept that the present author has been proposing since the 1980s. The above example is a simple choice between performance (CPU speed) or silent (restrained fan operation) modes. However, if the design is extended to allow the parameters (e.g., coolant velocity) to be changed continuously, the design may be optimized by an overall performance assessment using the entropy generation rate.

In electronic equipment, the temperature of each component must be kept within an allowable upper limit, specified for each component, from the viewpoint of operating performance and reliability.

The power density in electronic systems is increasing due to the high speed of operation and the miniaturization of equipment. For example, most of the heat generated in LSI/VLSI components can be transmitted from the component surface to a fluid flowing through the equipment. Among the cooling techniques available, forced-air cooling is the most widely used because it produces a good balance between cooling capacity, reliability and economy.

To enhance the cooling capacity of forced-air cooling, thermal resistance must be kept as low as possible by improving the heat transfer coefficient of component surfaces through increasing surface roughness or increasing flow velocity, for example. However, increasing surface area, surface roughness and flow velocity gives rise to an increase in flow friction loss, which in turn brings about increased fan/blower power consumption and wind noise. Consequently, an overall assessment of cooling performance must trade-off improvements in cooling capacity with the corresponding increase in disadvantageous factors.

In assessing the cooling capacity of forced-air cooling, the cooling efficiency factor, defined as the ratio of allowable equipment power consumption to blower power consumption, was once used as the design standard [2]. However, this method had numerous failings and alone cannot properly assess overall cooling performance.

Contributed by the Heat Transfer Division for publication in the JOURNAL OF HEAT TRANSFER. Manuscript received by the Heat Transfer Division December 7, 1999; revision received February 20, 2001. Associate Editor: H. Bau.

In this study, method is proposed in which convective cooling performance is assessed comprehensively, trading-off improvements in cooling capacity with the degradation in the accompanying parameters. The assessment index is connected to the entropy generation rate, which is derived from the irreversible loss of available energy through thermal resistance and fluid friction in convective cooling systems.

The idea of using an entropy generation rate to estimate heat transfer enhancement was first proposed [1] as a performance assessment criterion for thermal systems. Since then, many papers relating to the entropy method have been published [3–8]. These papers were based on the Second Law of Thermodynamics and the main theme was that overall performance can be assessed using the entropy generation rate or the rate of loss of available energy.

Performance Assessment and Related Issues

Generally, in electronic equipment, the allowable temperature elevation limit $\Delta T_{al}(K)$ of any component is defined relative to the temperature profile inside the equipment. If P(W) is the power to be applied to components and while remaining within the prescribed temperature limit, then the cooling capacity of the cooling system for that component can be said to be high when P becomes large. To establish this, let an overall thermal resistance from a heat source to a heat sink, such as ambient air, be R_t(°C/W). Then, from the following inequality:

$$\Delta T_{al} \geqq R_t \cdot P,$$

the smaller R_t is, the larger P becomes, which means a higher cooling capacity. Consequently, the primary prerequisite for thermal resistance is that R_t be as low as possible.

As conductive thermal resistance, determined by the properties of the materials composing the heat path inside a component, is usually sufficiently low, convective thermal resistance is the main consideration here.

Reducing the overall thermal resistance by enhancing the heat transfer coefficient is usually accompanied by an increase in fluid friction loss. This is due to phenomena such as roughening of the surface or increase in flow velocity. As a result, blower power consumption increases.

Let the blower power of the cooling system be P_b(W), including the blower's overall efficiency. A cooling performance factor $\varepsilon = P/P_b$ has been defined as a yardstick of cooling performance, in terms of the ratio of allowable power dissipation for the equipment to the power required for cooling devices such as fans or

blowers [2]. This can be considered as a kind of performance/cost ratio in the engineering domain. In the ε-assessment method, the target is to maximize ε. However, when the flow velocity becomes sufficiently small, P_b becomes very small and P, attributable exclusively to forced convection, also becomes very small. When P_b tends to zero, P also tends to zero and ε tends to 0/0 (undefined). When the flow velocity becomes very large, then in spite of the increase in P, ε deteriorates due to the steep increase in P_b. In this situation, assessment by ε alone is inadequate. To overcome this, an assessment criterion has been proposed in which both ε and P are made as large as possible [9]. However, even by that proposal it remains unclear how these two factors should be theoretically related. Furthermore, it is still an issue that ε tends to 0/0 when P_b tends to 0.

Assessment by Entropy Generation Rate

In the present report, a method to assess the relationship between thermal resistance and fluid friction loss is discussed within the context of the Second Law of Thermodynamics.

Thermal resistance is defined as the temperature drop per unit heat flow. Thermodynamically, when heat is transmitted across a path having a temperature difference, an irreversible loss in available energy occurs, the magnitude of which increases as thermal resistance increases. Furthermore, fluid friction results in an irreversible conversion of useful flow work to heat, which again gives rise to an irreversible loss in available energy. This fact justifies an assessment criterion in which the above two irreversible losses are added and the resultant sum is minimized. The following describes a method to express these irreversible quantities by the entropy generation rate.

In Fig. 1, let T_H(K) be the component heat source temperature, T_L(K) be the fluid temperature surrounding the component, P(W) be component power dissipation as heat flows from a hotter to a colder place, and let p_f(W) be the fluid friction power loss per component. Out of the heat flowing from a hotter to a colder reservoir, a part of the heat could be converted to useful work and the maximum work would be obtained, thermodynamically, by an imaginary Carnot process between the hot and cold sources.

The maximum work obtainable per unit time would then be given by the formula

$$Q_W = P(1 - T_L/T_H) = P \times \eta_C, \tag{1}$$

where $\eta_C = 1 - T_L/T_H$ is the reversible Carnot cycle efficiency. Q_W would be, thermodynamically, the available energy. In an electronic device however, Q_W is wholly transmitted to a lower temperature sink as heat and hence lost, producing an entropy generation rate $\dot{s}_1$, where

$$\dot{s}_1 = Q_W/T_L. \tag{2}$$

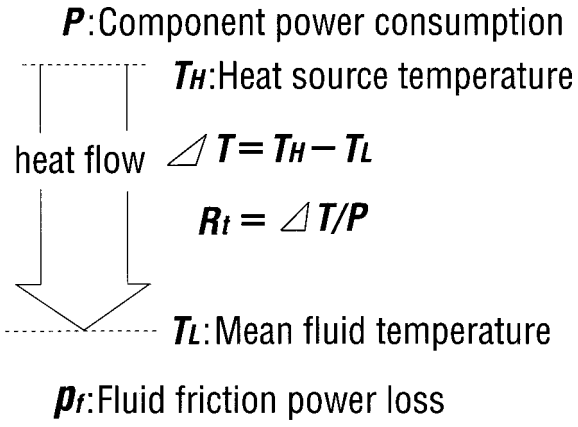

Fig. 1 Heat flow in forced convection cooling

That is, the entropy generation rate is proportional to the irreversible work loss. Expression (2) is identical to another formula for entropy generation, usually expressed as

$$-P/T_H + P/T_L = P(-1/T_H + 1/T_L). \tag{3}$$

From (1) and (2), after some transformation, we obtain

$$\dot{s}_1 = P/T_L(1 + T_L/\Delta T) = P/T_L \cdot \{1 + T_L/(R_t \times P)\}, \tag{4}$$

where $\Delta T = T_H - T_L$. R_t is the thermal resistance of the component and is defined as $\Delta T/P$. As can be seen from Eq. (4), an increase in R_t gives rise to an increase in $\dot{s}_1$, and when $R_t \to 0$, $\dot{s}_1 \to 0$.

Moreover, p_f is also lost to the sink as heat, giving rise to the entropy generation rate $\dot{s}_2$, given by

$$\dot{s}_2 = p_f/T_L. \tag{5}$$

Consequently, the overall entropy generation rate becomes

$$\dot{s} = \dot{s}_1 + \dot{s}_2. \tag{6}$$

Making Eq. (6) nondimensional, we obtain the expression

$$\Gamma = T_L \times \dot{s}/P = 1/\{1 + T_L/(R_t \times P)\} + p_f/P$$
$$= 1/(1 + T_L/\Delta T) + p_f/P, \tag{7}$$

where Γ is the proposed entropy generation rate index number. In Eq. (7), keeping T_L and P constant, if p_f is increased by augmenting the velocity, for example, the first term $(1/(1 + T_L/\Delta T))$ decreases due to the lowering of R_t. That is, the first term and the second term (p_f/P) in Eq. (7) run counter to each other relative to the change in p_f. As R_t is a function of p_f, when p_f changes while P is kept constant, ΔT must change by $\Delta T = R_t \times P$, and if ΔT is fixed as the temperature constraint, then P must change. Accordingly, both ΔT and P cannot be kept constant at the same time. Usually, R_t is a function not only of p_f, but also of the structural dimensions and thermal properties of the cooling systems. Thus, it may be possible to assess overall performance by including the influence of these parameters. However, for the present report, only p_f and the related parameters such as fluid velocity and heat transfer surface area will be considered.

Analysis of a Flow Model Inside a Circular Pipe

In Fig. 2, which shows a flow model inside a circular pipe for the convective cooling of electronic equipment, the outlet temperature rise with respect to the inlet is given by

$$T_{Lo} - T_{Li} = [P + \{(\lambda/d)(1/2)\rho u_m^3 LS\}]/(S u_m \rho c_p), \tag{8}$$

where T_{Lo}: outlet air temperature; T_{Li}: inlet air temperature; λ: friction loss coefficient; D: diameter of pipe; ρ: density; u_m: mean fluid velocity; L: duct length; S: cross-sectional area; and c_p: specific heat of air.

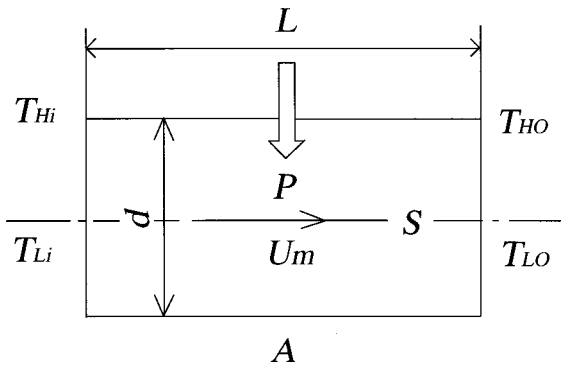

Fig. 2 Flow model inside a circular pipe

In Eq. (8), the first term gives the fluid temperature rise due to transferred heat and the second term that by fluid friction loss.

The mean fluid temperature is defined as

$$T_{Lm}=(T_{Li}+T_{Lo})/2. \tag{9}$$

To estimate T_{Lm}, the first and second terms in Eq. (8) were calculated for practical and typical conditions. The values obtained were as low as (1~10) K. Thus T_{Lm} may be kept almost constant at 300 K, 320 K, 340 K, etc., because T_{Li} is typically room temperature and $T_{Lo}-T_{Li}$ is not very large, as seen above. Next, the entropy generation rate $\dot{s}$ is to be calculated using Eq. (7).

$$\dot{s}/P=(\dot{s}_1+\dot{s}_2)/P$$

$$=[1/\{1+(T_{Lm}hA/P)\}+\{(\lambda/d)(1/2)\rho u_m^3 LS\}/P]/T_{Lm}, \tag{10}$$

where h: heat transfer coefficient; and A: heat transfer surface area. In Eq. (10), h is calculated using Kay's formula for gas ($0.5<\mathrm{Pr}\leqq 1$);

$$\mathrm{Nu}=0.02\,\mathrm{Re}^{0.8}\mathrm{Pr}^{0.5}=(hd)/k. \tag{11}$$

Numerical Examples

Using Eq. (10), the entropy generation rate was calculated for a fluid velocity change with heat load P as a parameter. The results are shown in Fig. 3, where λ is chosen to be 0.072 as it is assumed there are components inside the tube and consequently the inside wall is very rough. The parameters L and d are chosen to be $L=1.0$ m and $d=0.06$ m respectively, considering the actual dimensions of a typical electronic device.

Next, rewriting the second term in Eq. (10) using heat transfer area A, the following expression is obtained:

$$\dot{s}/P=\{1/(1+T_{Lm}hA/P)+\lambda(1/8)\rho u_m^3 A/P\}/T_{Lm}. \tag{12}$$

As Eq. (12) includes a parameter A/P, the calculation of $\dot{s}/P$ versus $\beta=A/P$ gives Fig. 4, plotted with u_m as a parameter. As is seen in Fig. 3 and Fig. 4, there exist minimum points of entropy generation rates for changes in u_m or β. In Fig. 3, in the domain where u_m is small, the pressure drop is small while the temperature difference is large because of small h. Consequently, the first term in Eq. (10) $(1/\{1+(T_{Lm}hA/P)\})$ is large and the second term $(\{(\lambda/d)(1/2)\rho u_m^3 LS\}/P)$ is small. In the domain where u_m is large, the relation is just the opposite. In Fig. 4, we can see the same behavior regarding the relationship between the increase and decrease of the first term and the second for the change of β. Because of this behavior, both in Fig. 3 and in Fig. 4, the entropy generation rates have a minimum at moderate values of u_m or β.

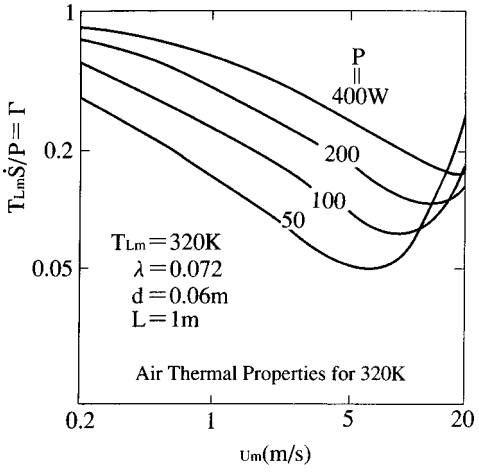

Fig. 3 Entropy generation rate versus flow velocity

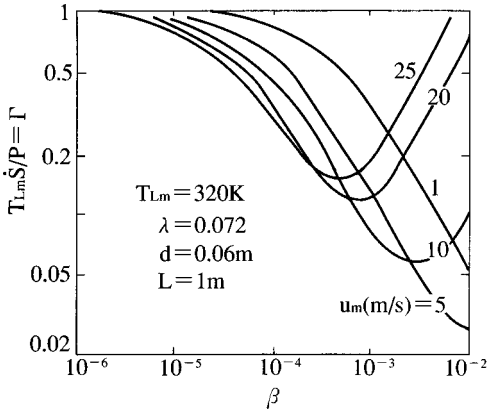

Fig. 4 Entropy generation rate versus heat transfer area

Experimental Data

The results obtained by applying the method described in the foregoing sections to the experimental heater module are presented in the following. Here, R_t, a function of p_f and required for computing Γ, is used (Fig. 5).

The thermal resistance R_t was obtained by experiment [9]. The module was constructed on a 75×75 mm^2 alumina substrate, 1.2 mm thick, on which 18 cooling fins, 70 mm long and 20 mm high of 0.25 mm-thick Cu were attached. The total heat transfer area including the substrate was 5.57×10^{-2} mm^2.

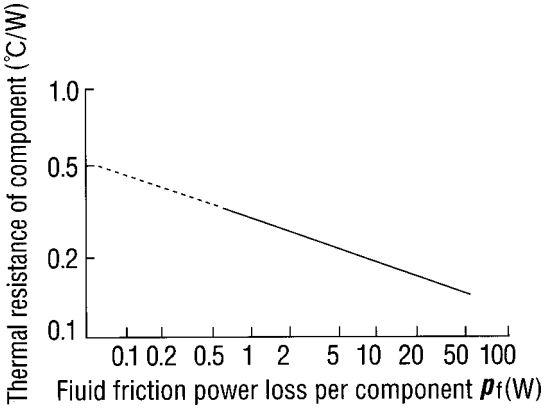

Fig. 5 Example of experimental thermal resistance

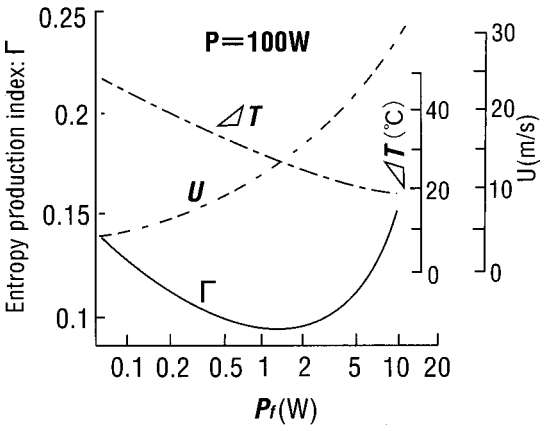

Fig. 6 Entropy generation rate and related parameters

Using the above results, Γ was calculated with $P=100$ W and $T_L=328$ K, giving Fig. 6, which includes ΔT, u_m, and ε (cooling performance factor). Here, the value of p_f was increased by increasing u_m.

Discussion

In Fig. 6, a minimum point for Γ is clearly seen to exist. This means that the optimum trade-off between thermal resistance and pressure loss can be obtained in the sense that the entropy generation rate is at its minimum. Here, we examine in Fig. 6 the variation in ΔT, u_m, and ε relative to the increase in p_f. For P constant, ΔT decreasing, and u_m increasing, ε decreases. The decrease in ε is due to the fact that, in the term P/P_b (P_b: blower power), roughly stating, P is proportional to $u^{0.5\sim1}$, and P_b is proportional to u^3 [2]. From this, the point at which Γ is minimized is the point at which ΔT is traded-off with u, or, since the blowing acoustic noise power is roughly proportional to u^5, it can also be the point at which temperature elevation (and consequently failure rate) is traded-off with acoustic blower noise. In the region away from that point, there arise problems such as excessive temperature elevation and excessive blower noise.

In other words, determining the point of minimum entropy generation seems to mean trading-off temperature elevation or thermal resistance with blower noise, and finally with any other accompanying demerit factors.

Heat Sink Assessment by Entropy Method

The performance of heat sinks (cooling fins) for electronics use is, usually, indicated by thermal resistance, depending on the application objective. Another important factor is size. However, in forced convection cooling, a crucial parameter is pressure loss, from the point of view of blower power consumption. A report on the assessment of pressure loss for electronics-use heat sinks has been made by Biber and Belady [10]. Usually, pressure loss in heat exchange systems has been assessed independently of heat transfer capacity. By the entropy method, however, heat transfer and pressure loss can be integrated into a unique index; the entropy generation rate, and overall performance assessment including advantages (heat transfer) and disadvantages (pressure loss) is possible. In the present report, the entropy assessment for the fin type heat sinks described by Biber et al., which are in practical use in electronics, is calculated. Fin types and sizes are shown in Fig. 7 and in Table 1. For each type, fixing the sizes in Table 1 and changing only the numbers of fins $n=2\sim65$ (number of fin channels: $n'=1\sim64$), the entropy generation rate is calculated, assuming that both the base thickness and fin thickness are zero. This assumption has been adopted in the present report for clarity of theoretical thinking, considering that it will not significantly degrade the accuracy of the analytical results. The parameters are the mean flow velocities. The results are shown in Fig. 8, along with changes in the thermal resistance R_t(°C/W) and pressure drop Δp(Pa) for each type of heat sink, at $u_m=8$ m/s. As can be seen clearly, for each type and for each u_m, the EGR (entropy generation rate) takes the minimum at a certain number of fins. When the number of fins is small, Δp is small while R_t is large due to the small surface area. Thus the EGR due to temperature difference is large while that due to flow resistance is small. When the number of fins is large, the situation is the opposite. As a consequence, the total EGR takes a minimum value at an intermediate number of fins.

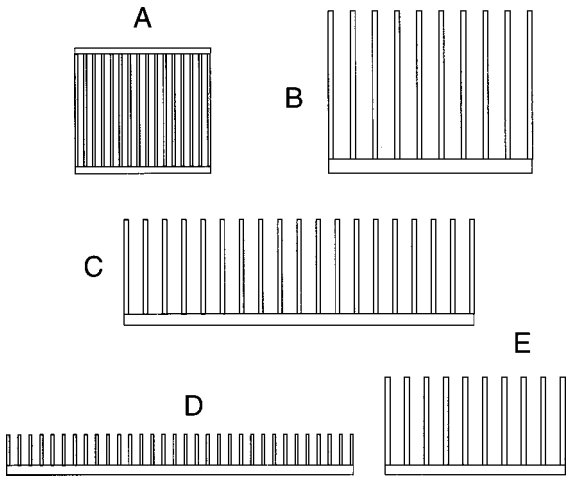

Fig. 7 Fin types [10]

Table 1 Fin geometries [10]

(in mm)	A	B	C	D	E
Flow width	43.7	66	117	117	66
Flow length	25.4	25.4	61	61	58.4
Base thickness	2.5	4.3	3.2	3.2	3.2
Fin thickness	0.5	1.9	1.5	1.4	1.5
Fin height	38.1	50.8	31.8	10.8	31.8

Heat Transfer Enhancement and Performance Assessment

An overview of performance assessment for heat transfer enhancement in heat exchange systems was published by Shah [11]. Most of the criteria are defined as the combination of heat transfer (e.g., j factor) and fluid friction (e.g., f factor), or more directly, the relationship between transferred heat and pumping power. Various other criteria may be considered to be variations to this definition. In practical industrial design, different criteria are chosen, depending on whether the primary objective is to maximize transmitted heat, minimize pumping power, or obtain the minimum volume or weight under the prescribed constraints such as component size and time.

These criteria have been verified thus far, from both academic and industrial viewpoints, with respect to the development of heat exchange system design. However, from a theoretical (thermodynamic) viewpoint, it must be recognized that the field remains largely unclear. For the sake of a clear and simple explanation, the theoretical limit of thermal efficiency in an engine system may be considered. As is well known, the Carnot efficiency is the thermodynamic limit of heat engine thermal efficiency and is derived from the Second Law of Thermodynamics. However, it is not so clear in heat exchange systems as in an engine, what the theoretical limit is to the overall performance including both of thermal resistance and pressure loss. One clue to this issue will be the entropy assessment criterion.

Comparison of Competitive Criteria and Related Issues

Performance assessment using an entropy method means theoretical consideration from the standpoint of the Second Law of Thermodynamics, and neither conforms to conventional assessment criteria nor totally opposes them. The conventional, practical assessments are multi-faceted, and it is normally recommended that the best possible criterion be chosen depending on the heat exchange systems under consideration. Therefore, the entropy method may be said to be a guide for optimum design from the standpoint of theoretical thermodynamics. However, issues related to the size (or volume) of heat exchangers have been pointed out [12,13]. By the entropy method, the size of a heat exchanger becomes very large at the minimum entropy generation point,

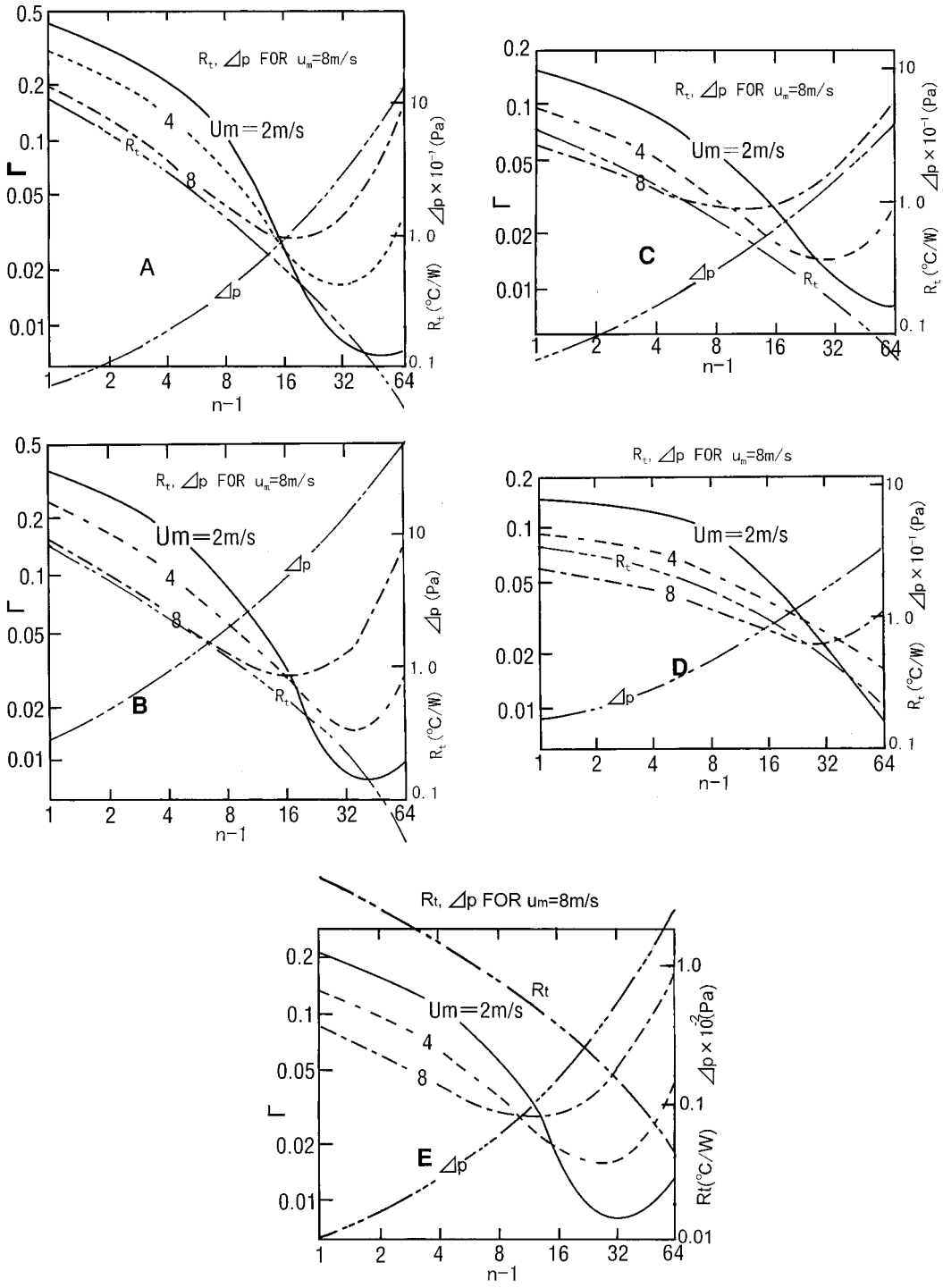

Fig. 8 Entropy generation rates for heat sinks (*A*-*E*)

which is a disadvantage as it is then also very heavy and expensive. This was also pointed out by Ranasinghe et al. [14].

Bejan discussed the volume constraint, which is a common restriction for the design of heat exchangers [15]. He pointed out that the characteristic length l is proportional to $1/N_s$ (N_s: entropy generation index number defined by Bejan), and because the volume is proportional to l^3, a heat exchanger that generates a small EGR becomes inappropriately large.

The present author's idea on this issue is as follows: The major parameters that characterize heat exchanger performance are heat transfer, pressure loss, and size; therefore there are three primary assessment parameters. If two of these parameters, heat transfer and pressure loss, are converted into a single index, the entropy generation rate, we can assess the overall performance of a heat exchange system using the two new parameters of entropy generation rate and size. Thus, the number of primary assessment parameters is reduced from 3 to 2.

Some other significant observations should be mentioned. In Figs. 3, 4, 6, and 8, the characteristic curves indicate the point of minimum entropy generation rate for each parameter value. However, information about performance enhancement by improving the cooling system mechanism itself is not explicitly shown. Any

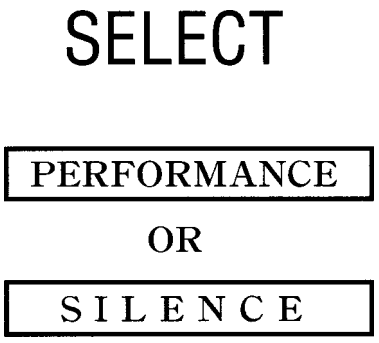

Fig. 9 User selection for "PC" cooling

improvement in cooling performance, by enhancing the heat transfer coefficient for example, will be recognized when such improvement causes the group of EGR curves to shift downwards in the entropy generation graphs.

Another important implication of this approach is the balance between system performance (e.g., computer CPU speed) and environmental assessment criteria (e.g., silence) (Fig. 9). For example, in recent notebook-type personal computers, as described previously, cooling control gives the user the option of either performance (noisy) mode or quiet (low performance) mode. This statement implies that there is a trade-off between performance and fan power consumption; the latter attributable to pressure loss in the cooling channel.

The author makes the observation that this cooling design conform to the entropy assessment criterion in the sense that two parameters, which run counter to each other, are adjusted such that the performance and environmental requirements are harmonized to suit the device user.

Concluding Remarks

In conclusion, the entropy assessment method not only provides thermodynamic basis for heat transfer system design, but also has the practical significance of reducing the number of primary assessment parameters. One important implication is that the size parameter is, naturally, linked most directly to volume and weight and should be considered to be one of the design constraints within which the EGR should be minimized.

In general, the sole objective of improving the cooling of electronic systems is to increase cooling capacity, whereas the consideration of accompanying demerit factors such as pressure loss increase does not seem very important. It is commonly considered to be sufficient to take them as subordinate constraints. However, in forced convective cooling specifically, increases in cooling capacity can never be accomplished without corresponding increases in fluid friction loss, which induces an increase in fan/blower power consumption and acoustic noise level, both of which are disadvantageous in electronic systems. The assessment of the overall performance of electronic equipment including heat transfer and pressure loss by a single index (EGR) can be considered to give a guide to an optimum design for an electronic equipment cooling system from the standpoint of a balance between cooling capacity and acoustic fan/blower noise and power consumption.

With the present trend toward low acoustic noise requirements, this is highly significant as shown in the previous example. If size is chosen as a primary constraining factor, then two parameters; entropy generation rate and size, will make well-balanced optimized design between thermodynamic and technical considerations possible.

Furthermore, in practical applications, the bypass flow around heat sinks affects cooling performance. However, for the present report, the effect of bypass flow on the heat transfer and pressure loss characteristics are not considered.

Nomenclature

A = heat transfer area, m^2
c_p = specific heat of air, J/kg·K
D = diameter, m
d = (hydraulic) diameter, m
h = heat transfer coefficient, $W/m^2 \cdot K$
j = Colburn's j factor
k = thermal conductivity, W/K·m
L = duct length, m
l = characteristic length, m
N_s = entropy generation index number
Nu = Nusselt number
n = number of fins
n' = $n-1$ number of fin channels
P = power consumption, transferred heat, W
p_f = fluid friction power, W
Pr = Prandtl number
Q_W = available work (imaginary), W
R_t = thermal resistance, K/W
Re = Reynolds number
S = cross sectional area, m^2
$\dot{s}$ = entropy generation rate, W/K
T = temperature, K
u = fluid velocity, m/s

Greek Symbols

β = A/P
Δ = difference
Γ = entropy generation index number
ε = performance factor
η = thermal efficiency
λ = friction loss coefficient
ρ = density of air, kg/m^3

Subscripts

al = allowable
b = blower
C = Carnot
f = flow friction
H = high
i = inlet
L = low
m = mean
o = outlet
t = thermal
W = work
1 = first term
2 = second term

References

[1] Bejan, A., 1977, "The Concept of Irreversibility in Heat Exchanger Design: Counterflow Heat Exchanger for Gas-to-Gas Application," ASME J. Heat Transfer, **99**, pp. 374–380.
[2] Ogiso, K. and Sasaki, E., 1977, "Design of Forced Air Cooling based on Power Performance Factor," IECEJ Technical Report, CPM-77-51, pp. 49–56.
[3] Bejan, A., 1978, "Criterion for Rating Heat Exchanger Performance," Int. J. Heat Mass Transf., **21**, pp. 655–658.
[4] Oullete, W. R., and Bejan, A., 1980, "Conservation of Available Work (Exergy) by using Promotors of Swirl Flow in Forced Convection Heat Transfer," Energy, **5**, pp. 587–596.
[5] Bejan, A., and Pfister, Jr., P. A., 1980, "Evaluation of Heat Transfer Augmentation Techniques," Lett. Heat Mass Transfer, **7**, pp. 97–106.
[6] Webb, R. I., 1981, "Performance Evaluation in Criterion for Use of Enhanced Heat Transfer Surface in Heat Exchanger Design," Int. J. Heat Mass Transf., **24**, No. 4, pp. 715–726.
[7] London, A. L., 1982, "Economics and the Second Law: An Engineering View and Methodology," Int. J. Heat Mass Transf., **75**, No. 6, pp. 743–751.
[8] Bejan, A., 1979, "A Study of Entropy Generation in Fundamental Convective Heat Transfer," ASME J. Heat Transfer, **101**, pp. 718–725.
[9] Kishimoto, T., Sasaki, E., and Moriya, K., 1984, "Gas Cooling Enhancement-

Technology for Integrated Circuit Chips,'' IEEE Trans. Compon., Hybrids, Manuf. Technol., **7**, pp. 286–293.
[10] Biber, C. R., and Belady, C. L., 1997, ''Pressure Drop Prediction For Heat Sinks: What is the Best?'' *Proc. INTERpack*, EEP-Vol. 19-2, pp. 1829–1835.
[11] Shah, R. K., 1978, ''Compact heat Exchanger Surface Selection Method,'' *Proc. 6th IHTC*, pp. 193–199.
[12] Yang, W. J., 1985, private communication.
[13] Nishikawa, K., 1994, private communication.
[14] Ranasinghe, J., and Reistad, G. H., 1990, ''Irreversibility in Heat Exchanger-Design and Optimization,'' in *Compact Heat Exchangers*, Hemisphere, Bristol, PA, pp. 365.
[15] Bejan, A., *Entropy Generation Minimization*, CRC PRESS, pp. 121–122.

Three-Dimensional Visualization and Measurement of Temperature Field Using Liquid Crystal Scanning Thermography

P. M. Lutjen[1]

D. Mishra

V. Prasad
e-mail: prasad@pml.eng.sunysb.edu
Fellow ASME

Department of Mechanical Engineering,
State University of New York at Stony Brook,
Stony Brook, NY 11794-2300

A Liquid Crystal Scanning Thermography (LCST) technique is developed and implemented to visualize and measure three-dimensional temperature fields. Results are reported for natural convection in a differentially heated vertical cavity. Experiments are conducted under steady state conditions at Rayleigh numbers of about 10^4 with glycerin as the working fluid. The scanning arrangement is described in detail together with the calibration scheme, and image processing routines that enable the processing of the thermographs and extraction of quantitative temperature information from them, including local and global heat transfer rates. The resultant temperature fields and Nusselt number values are computed and validated against both standard empirical relations and numerical predictions. To date, LCT has not been used to determine Nusselt number for enclosed fluid systems. The ability of LCST to perform this task makes this novel experimental technique a useful tool. [DOI: 10.1115/1.1370514]

Keywords: Experimental, Heat Transfer, Measurement Techniques, Non-Intrusive Diagnostics, Visualization

1 Introduction

In recent years significant attention has been given to the development of precise experimental techniques, ones which incorporate such features as: end effects, heat transfer through boundary layers, and full, three-dimensional velocity and temperature field measurements. Such measurements are necessary to develop a better understanding of complex temperature and flow fields, and their coupling. A three-dimensional, experimental database is also needed for the validation of advanced fluid dynamics and heat transfer computer codes. This paper presents the development and implementation of Liquid Crystal Thermography (LCT) to three-dimensional measurement of temperature field. The scanning system involves a reduction in complexity compared to earlier attempts [1] and most importantly that the test cell in the present scheme is stationary. Any attempt to translate the cavity to acquire three-dimensional data is unacceptable for measurements related to flow field.

Liquid crystals are a class of organic material that possesses a unique mesostable phase between the solid and liquid phases. It is while in the mesostable phase that the unusual optical properties of liquid crystals arise that allow for LCT. The material absorbs and emits light at particular frequencies, as a function of its temperature. Depending upon the angle from which it is viewed, one will detect a unique frequency, a single hue, within the spectrum. From an angle perpendicular to the plane of illumination, the frequency of detection is a continuous function of temperature through the visible spectrum from red to blue (as temperature increases). From a different angle, a different progression would be perceived. Hence, the view angle becomes an important parameter for LCT. It must be held constant macroscopically (frame to frame) and furthermore, it needs to be consistent over the viewing of the image (pixel to pixel in each frame). Farina et al. [2] reported an upper limit of 25 deg for accurate color detection. It has now become a standard practice to keep the subject within 7.5 deg of a perpendicular viewing axis [3].

Liquid crystals have been used in a variety of temperature field and flow visualization experiments. Rhee et al. [4] developed a scheme for simultaneous visualization of velocity and temperature fields of Taylor-Gortler-like vortices in a recirculating flow. Nishimura et al. [5] utilized liquid crystals in a saline solution to study the density inversion and flow structure during solidification. Dabiri and Gharib [6] used liquid crystals to study vortex rings, showing that even in turbulent flow, liquid crystals provide the necessary time response and offer excellent spatial resolution. Kimura et al. [7] and Ashforth-Frost and Jambunathan [8] quantified velocity fields using Liquid crystals as tracer particles. Ozawa et al. [9] used liquid crystals in a Hele-Shaw cell to measure temperature and flow fields. Mukherjee et al. [10,11] applied LCT to study temperature fields in a simulated Czochralski crystal growth system. Kowalewski et al. [12] employed LCT in a study of internal natural convection with solidification.

Application of LCT to the study of three-dimensional flows has been left largely unpursued. Sakakibara and Adrian [13] have presented a laser scanning technique, using fluorescence dye to measure the three-dimensional temperature distribution in water. A scanning mirror was used to direct a laser sheet into the measurement area and a fixed CCD camera grabs the scattered light from the temperature-sensitive fluorescent dye. Some researchers have attempted to capture three-dimensionality by illuminating multiple planes and/or several perpendicular planes using LCT. Braun et al. [1] used an experimental arrangement that had a ten-piece optical train, including a 1 kW Xenon lamp. This optical train produced a light sheet that was reportedly 0.5 to 1 mm thick. In order to illuminate different vertical slices within the cavity the entire optical train was set upon a positioning rail, which was then translated. The authors focused upon the acquisition of the temperature and velocity fields; no mention was made of heat transfer coefficient measurements. Hiller et al. [14,15] and subsequently Kowalewski et al. [12] and Wisniewski et al. [16] have made use of three translation stages to acquire images at different locations. From the experimental arrangement reported by these authors, it

[1]Presently with: Pratt & Whitney, East Hartford, Connecticut 06108.

Contributed by the Heat Transfer Division for publication in the JOURNAL OF HEAT TRANSFER. Manuscript received by the Heat Transfer Division Feb. 1, 2000; revision received Jan. 8, 2001. Associate Editor: D. Poulikakos.

appears that the cavity is mobile, as well as the camera. The choice to translate the cavity, as was done in these works, can disturb the flow. In the present work the cavity is physically isolated from all mobile components. Therefore, the possibility of disturbing the flow pattern is eliminated. As a consequence of these improvements in image acquisition, reduction in the complexity of the number of optical components, as compared with Braun et al. [1], enables a rapid acquisition of multiple, parallel images, with potential application in the study of transient systems.

2 Experimental Arrangement

A sketch of the experimental setup, along with a sketch of the top view of the arrangement is presented in Fig. 1. Light emitted by a Xenon arc lamp is filtered and shaped as it passes through an optical train to form a vertical sheet of light. A mirror mounted on a translation stage reflects the light sheet perpendicularly. This translation stage allows the vertical light sheet to be located at any position across the cavity that is parallel to its front face. The light sheet excites the liquid crystal particles within the fluid causing a variety of colors to be emitted in all directions. A camera, mounted on a second translation stage that moves parallel to the optical train, acquires images of the illuminated plane.

2.1 Experimental Apparatus. A differentially heated cubic enclosure is a classic geometry for heat transfer research, particularly in the field of buoyancy-driven convection. It has inherent three-dimensionality, even at low Rayleigh numbers, but there is a dominant two-dimensional appearance under many controlled conditions. For this reason, a cubic cavity with 76.2 mm sides (internal dimension) was selected for the present experiment.

Four of the walls of the cavity are 25.4 mm thick, acrylic. The remaining two walls are aluminum plates maintained at constant temperatures by recirculating water. Each of the isothermal plate assemblies is comprised of two aluminum plates and a gasket. One piece has a U-shaped channel milled in the central region

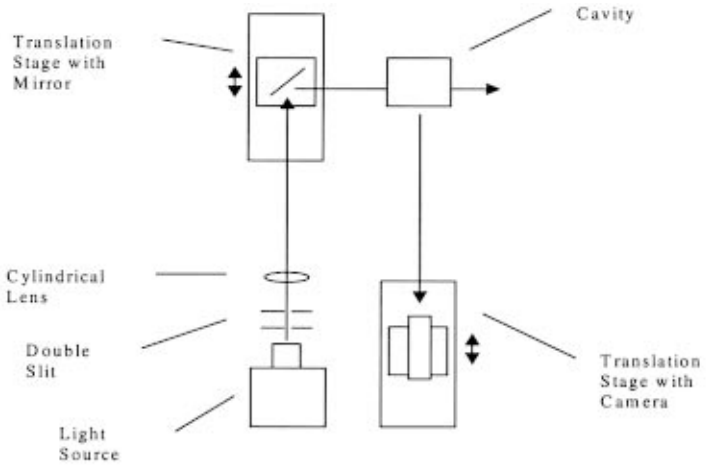

Fig. 1 (*a*) Top view of the experimental setup; (*b*) schematic of experimental arrangement.

Table 1 Properties of the working fluid at 25°C

Coefficient of Thermal Expansion (1/K)	4.81×10^{-4}
Kinematic Viscosity (m/s^2)	840×10^{-6}
Prandtl Number	8940

leading from one corner to the opposite corner by an S-like path. Four copper-constantium thermocouples are embedded in shallow channels in the aluminum near the surface in contact with the working fluid. The top of the U-shaped channel is sealed with a gasket and clamped by the second aluminum plate. As a result of the high thermal conductivity of aluminum and the water flow capacity of at least 14 liter/min a uniform temperature is obtained across the aluminum plate, generally to within 0.05°C of a mean value. The working fluid used for the present experiments is glycerin. The thermophysical properties of the fluids are provided in Table 1 for a temperature of 25°C, which is the approximate, mean temperature of the fluid in all the experiments.

The liquid crystals used in this study are manufactured by Hallcrest, Inc. They have a mean diameter of 40 μm with a diameter range of 20–80 μm. They are active (visible when illuminated) in a temperature region of roughly 5°C starting at approximately 24°C. The specific gravity is within a range of 1.0 to 1.1.

2.2 Optical Arrangement. A Spectral Energy 1 kW Xenon arc lamp with a two-inch diameter condenser assembly is used for the current experiments. It produces stable, consistent emission in the visible spectrum. Upon exiting the lamp condenser assembly, the light encounters a pair of metal plates in series that have vertical slits. Experiments showed that slits of width 0.64 mm and 1.14 mm set at distances of 11 cm and 16.5 cm from the lamp housing provide a well collimated light sheet when used in conjunction with a 310 mm cylindrical lens, set 67 cm from the lamp housing. The long focal length of this cylindrical lens gives the exiting light sheet a width that is consistent as it travels. This lens has a coating that reflects back the UV radiation. This restricts the amount of unnecessary energy input to the system. Following this is two planar mirrors to send the light sheet into the test cell. The first mirror is mounted on a linear translation stage (discussed later). The mirror is roughly 130 cm from the lamp housing. It directs the light sheet perpendicular to its previous direction (still in the horizontal plane). The cavity is located approximately 50 cm from the first mirror. A second mirror is positioned above the cavity at a 45 deg angle, such that the light is directed downward into the cavity. In this orientation the cavity rests approximately 15 cm below the second mirror. Throughout the experiments reported here, the beam width remains within 2 mm.

A Sony DXC-9000, 3-CCD camera with a 50 mm Nikkor lens is used throughout the course of the present experiments. The camera has a pixel density of $659(H) \times 494(V)$. The automatic white balance is deactivated and the ''color temperature'' setting used is 5600 K. The output of the CCD camera is component RGB-sync in NTSC format. The NTSC format has 640 vertical lines and 480 horizontal lines refreshed at a rate of 30 frames per second. These comprise the input to the framegrabber which discretizes the three separate signals into 256 levels (8 bit).

Because the light sheet to illuminate the cavity is mobile the camera must also be mobile to maintain focus over the length of each scan. The index of refraction of the fluid requires that the camera be moved a distance less than the distance the light sheet is traversed. Hence, the camera is mounted on a second translation stage that is geared to the first by the ratio of the index of refraction of the working fluid. The two stages used are Aerotech ATS02020 units with DC-servo motors. The U500 controller card from Aerotech, Inc. has output channels that trigger the framegrabber. The Programmable Logic Control code written for the experiment contains variable inputs for the number of dwell locations and the index of refraction of the fluid, the latter of which is the gear ratio for the two stages. When the stages come to rest, a dwell is initiated that lasts for the time of 6 frames (180 ms). After 66 ms, an output channel is modified from its normal, high output to a low output. A logic level converter circuit monitors this signal and outputs a signal of proper voltage for receipt by the framegrabber software.

The program is written such that the stages take 0.25 s for each motion. The stage controller has a 3 ms ramp to an appropriate top speed and a 3 ms ramp from top speed to rest. In spite of this there is still some vibrations emanating from the stages. To inhibit any effects on the experimental system the camera stage is set upon its own table with at least 1.5 mm of rubber gasket material beneath the legs thereof. The stage carrying the (first) mirror is separated from the underlying table by rubber gasket material as well. The other components of the optical arrangement are placed on this table as well. The cavity rests upon its own table, again with rubber gasket material beneath it. Furthermore, cinder blocks are set against the legs with Styrofoam between to inhibit vibrations from the floor from having any effects on the cavity.

The emf of each of the type-T thermocouples on the interior of the plates and in the ambient is acquired manually by use of a hand-held thermometer (Omega HH23, a resistance thermometer). It is common with the current system to see thermocouple fluctuations of only 0.1°C across an aluminum plate with no correlation to the direction of water flow within the channel or fluid flow within the cavity. The temperature readings on the plates become steady within ten minutes of beginning an experiment, and remain stable (within ± 0.1°C) for the duration.

3 Image Processing and Calibration

Image processing is essential to suppress noise from the original images. The noise in these images is due largely to pixels being void of liquid crystals, though it may also be from nonuniform liquid crystal structure and material defects in the optical components including the walls, lens, and mirrors. The following procedures are used to remove large portions of the noise and then enhance the image.

Each of the red, green, and blue arrays is operated upon by a Fourier filter in the two dimensions of the acquired images to remove high frequency components which are mostly noise. The resulting RGB arrays are each subjected to a further averaging operation using a 5×5 window (spot size), to remove localized noise. The 5×5 window is a matrix of all elements having a weight of 1.0. The resultant filtered images appear ''out of focus.'' To bring back some of the sharpness that has been lost, an image enhancement procedure is applied to the image. This is called a high boost image preparation [17]. The scheme employed for this experiment uses an amplifier of (9A-1) on the center pixel inside of a 3×3 window with the other 8 pixels having an amplifier of -1, where A is the weight factor, set at 1.5. A detail study of the image processing parameters and their effects on the liquid crystal thermographs is presented in [18].

The smoothed color images are used to produce two-dimensional temperature fields. First, the RGB values are converted to the HSI color space, wherein the calibration is performed. With calibration equations determined, a second algorithm converts the hue values to their corresponding temperature values. Even after improving the contrast of the images, the saturation and intensity is low (<0.2) at some pixels to correctly determine the hue at that point. Such pixels at this stage are as-

signed a temperature of 0.0, which are to be assigned a correct temperature value based on an average of acceptable local values in subsequent step.

Because of the conservative approach taken in assigning the operational parameters in the above algorithms local anomalies still exist in some cases. As a result, a cubic spline is fitted through the temperature data along the horizontal lines from the hot wall to the cold wall. The resulting images have smooth transitions in temperature and are free of erroneous data points. The calibration images used to determine the color-to-temperature relationship and the images captured from convection experiments are subjected to the same image processing parameters (Fourier cutoff, and averaging window size etc.).

Each slice (acquired images) provides the x and y data, and successive slices comprise the third dimension. The data is then visualized using the IBM Data Explorer software. This software allows for three-dimensional visualization of regularly and irregularly spaced grid data, and generates intermediate points by linear interpolation.

An accurate relationship between the perceived color and temperature must be established for quantitative measurements. In situ calibration helps to reduce the effects of systemic error in the experiment, by way of it being incorporated in the calibration. By setting the constant temperature aluminum plates horizontally, where the upper plate is at a higher temperature than the lower, a stably stratified conduction profile is obtained. Several other parameters allow one to describe the stratified profile as linear. Foremost, over the temperature range of the crystals the thermal conductivity of glycerin is constant at 0.286 W/mK. Secondly, the low thermal conductivity of the acrylic walls provide a relatively large, though not perfect, thermal resistance. Furthermore, the ambient temperature is maintained near the mean temperature of the plates during each calibration by heating an enclosed space around the test section. Therefore, the conduction profile is not only stable, but also linear (at least in most part of the cavity). As a result, the vertical location of each pixel can be associated with a known temperature. A median value of hue for each row (height) is then related to the temperature for that height as described below.

The middle fifth of the conduction image is investigated more closely (avoiding any possible end effects). The hue, saturation, and intensity values for each horizontal segment are provided as inputs to a median filter. The result is the single median hue, saturation, and intensity value for a given vertical position. The hue value is then plotted as a function of position/temperature. Results are presented based on two calibration experiments for which the temperature of the top and bottom plates are 29.95°C and 23.4°C, and 25.2°C and 23.5°C, respectively. There is a reasonable agreement (within the uncertainty of the thermocouples, ±0.1°C) between the data of the two experiments for a slice at the center of the cavity as represented in Fig. 2.

Another issue relates to the spatial location of the calibration images. There is close agreement between the data for $z=19$ mm, $z=38$ mm, and $z=57$ mm slices for the calibration experiments as demonstrated in Fig. 3. The hue-temperature curve shows a discontinuity, a property of the used liquid crystals. The region where a few scattered points are visible are in the region of purple color. These points are solely due to the camera registering a wrong color at that spatial location, which can be related to the fact that the crystals are not sensitive in that temperature range. Since the calibration equations are decided by fitting a least square curve through the points shown in Fig. 3, and these scattered points are eliminated, from the curve fitting process, they do not affect the measurement. Figure 3 suggests that one set of calibration equations is applicable at any spatial location throughout the span of the cavity. This is extremely important for three-dimensional LCT as it greatly reduces the computational load.

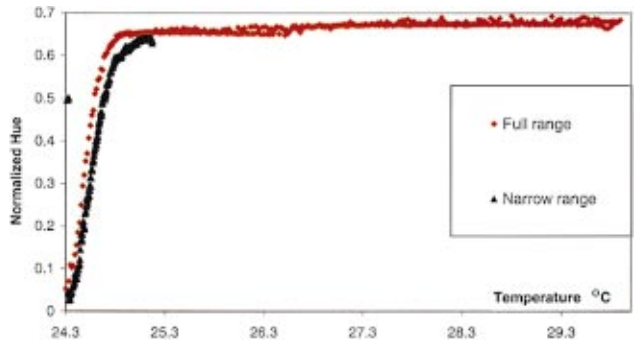

Fig. 2 Hue versus temperature relationship for two separate calibration experiments

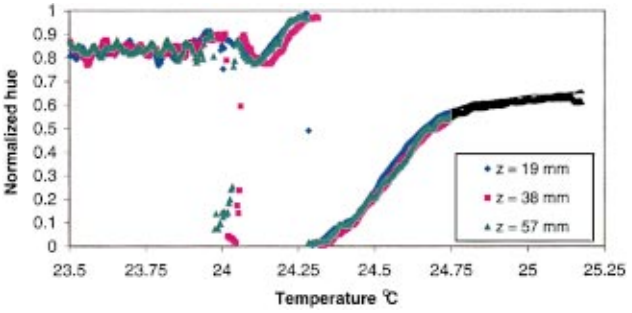

Fig. 3 Hue versus temperature at three *Z* locations in the narrow range calibration

In order to fit the data as closely as possible the following strategy is adopted; the function is separated into four regions. Examining Fig. 2, one can see that there is a region of high sensitivity from red to aqua, hue {0.0, 0.649} and a second region of relative insensitivity, hue {0.649, 0.66}. There is a third region in which the intensity and saturation curves are such that they warrant hue values be disregarded, hue {0.66, 0.95}. The fourth region, hue {0.95, 1.0}, is set to a single value of temperature, 24.25°C. The correlation equations obtained are as follows:

$$T=6.03h^3-4.95h^2+1.76h+24.29 \quad \text{for} \quad h\leqslant 0.6485 \tag{1}$$

$$T=212.71h-112.95 \quad \text{for} \quad 0.6485\leqslant h\leqslant 0.660 \tag{2}$$

$$T=24.25 \quad \text{for} \quad 0.95\leqslant h\leqslant 1.0 \tag{3}$$

For the first region, third order polynomial provides the best fit through the data. The fitted curve, Eq. 1 has a correlation coefficient of 0.98 and a standard deviation of 0.035 with the supplied data. The second region has a first order equation fitted. There are other relationships that provide only marginally better fits, but the linear equation is simplest to implement. The fitted line, Eq. 2, has a correlation coefficient of 0.95 and a standard error of 0.48 with the supplied data.

4 Measurement Uncertainty

The uncertainty in temperature measurements is due to four quantifiable sources: the thermocouple reading, machining tolerance, the manual cropping operation, and construction. The thermometer has an uncertainty of ±0.05°C. Since both the top and bottom plates are monitored by this device there is an uncertainty of ±0.1°C in the liquid crystal temperature reading as a direct result of the thermometer.

The machining tolerance, manual cropping operation and the construction of the cavity each affect the accuracy of the calibration of the liquid crystals. The error in the distance between the two plates affects the linear temperature profile to which the hues are matched. The machining tolerance is ±0.13 mm. This repre-

sents an uncertainty of only 0.85 percent. The construction of the cavity, with the inherent uncertainty in the thickness of the compressed gasket material, also affects the true distance between the controlled plates. This is approximated at ± 1 mm, an uncertainty of 1.3 percent. In the cropping procedure, it is assumed that the image is square. Cropped images are only accepted if the x dimension matches the y dimension to within 4 pixels. The uncertainty is therefore taken as ± 4 pixels. Since the size is generally 440 pixels square, this represents an uncertainty of only ± 0.9 percent. Under the most narrow temperature difference in the calibration experiments (1.68°C) these three sources of error, combined, can contribute an additional uncertainty of ± 0.05°C. Hence, the overall quantifiable sources of uncertainty in the data sum to ± 0.15°C.

Other sources of uncertainty exist which are relatively insignificant or unquantifiable. There exists ''dark current'' on the CCD arrays. This is a matter of local defects and can also be a function of the temperature of the camera. The presence of dark current becomes increasingly apparent as frames are compiled (added) in the multiple exposure mode of the camera. However, even while operating in NTSC mode with exposure times of 1/60 second the signal-to-noise ratio is extremely high under the well-illuminated conditions.

It would be fruitless to use a non-invasive technique like LCT only to disturb the flow field with the introduction of a powerful light source such that the fluid media is volumetrically heated. To restrict the amount of energy imparted to the fluid by the lamp, foremost, the scan time is only ten seconds. Furthermore, the spectral absorptivity of the glycerin-liquid crystal mixture averages less than 8 percent relative to pure water for the visible spectrum. Infrared light is emitted at low levels from the light source. The special coating on the cylindrical lens reflects much of the ultraviolet emissions. Therefore the effect that the light source may have on the flow field is considered insignificant.

The view angle, as mentioned earlier, is an important parameter in LCT. The minimum distance from the illuminated plane to the camera was calculated as 28 cm in order to maintain an appropriate angle for the given geometry. For the duration of the experiments, the camera to plane distance was approximately 125 cm. As a result, uncertainty due to view angle is also considered negligible.

The experiments performed with a vertical cavity and the calibration experiments show no appreciable difference between the consecutive scans. The uncertainty of the arrangement and procedures is negligible, especially with respect to the uncertainty due to thermocouple and cropping. As a whole the three components produces a total of about ± 0.15°C uncertainty in the measurement reported here.

Errors in measurement introduced due to image processing operations, which might have altered the information originally recorded by the camera is a tricky issue. Since a standard set of operations with exactly same parameters are applied to both the calibration and other experiments, errors due to modification of any hue value is expected to be taken care of at the calibration stage itself. However it can not be quantified in the present work since no point measurements in the bulk of the fluid is recorded for the present set of data. It is expected that once the feasibility and applicability are demonstrated future studies will focus on quantifying these errors.

5 Results and Discussion

In bouyancy-driven, internal, convective flows the developing boundary layer of the finite fluid volume must contend with both physical limitations as it circulates and with the coupling of its own motion and the motion of the fluid in the core region. The velocity boundary layer grows as it ascends the lower half of the warm wall, entraining fluid as it progresses. Above the centerline, the boundary layer expels fluid and is reduced while the thermal boundary layer continues to expand. The core region is almost stagnant and is stratified. Strong three-dimensionality as demonstrated by Hiller et al. [15] is thought to arise from two sources [19]: (i) kinematic interaction of the recirculating fluid with the stationary end walls, and (ii) thermally driven flow resulting from a temperature gradient perpendicular to the end walls.

The experimental results obtained here are compared with two separate sources, literature and an in-house numerical model. The literature serves as quantitative comparison of the Nusselt number with two-dimensional experimental techniques compiled over years of research [20]. As a result of the two-dimensional origin of the correlation, it is expected that the experimentally obtained results will be lower due to end-effects. The numerical model serves as both a quantitative and qualitative data source and, as a result of having been tailored to mirror the physical realities of the test section, may provide more meaningful results.

A description of the numerical model follows below. Reconstructed images from the numerical results directly related to one of the sets of experimental conditions are provided as a means of qualitative comparison. The numerical model used to generate comparable results, an in-house computer code based on MASTRAP3d[2] [21,22], provides both temperature data for reconstruction and local Nusselt numbers on the controlled surfaces. The physical properties of the fluid and solid materials are actual values at an approximate mean temperature for the experiments of 25°C. The physical domain is well represented in the model, but does not have a perfect correspondence. The two controlled surfaces are represented as isothermal surfaces as in the experiment. However, the four acrylic walls are treated as though they were adiabatic on the external surface when, indeed, there is convective transfer to/from the ambient. These surfaces are able to conduct heat laterally in the model. The no-slip boundary condition is enforced, which gives rise to the three-dimensionality in the results. The grid employed for the calculations is $33\times33\times33$, which is sufficient for the present cases. In the experiment a grid a $440\times440\times21$ is obtained from each scan. Local Nusselt numbers are calculated at the measured 21 planes at 440×440 points in each plane. The local Nusselt numbers are obtained through the temperature gradient information by fitting a cubic spline across the two walls. From the temperature field obtained, an average temperature profile from hot to cold wall is also obtained. The slopes of this profile at the two walls are used to compute the average Nusselt number. The slopes of the profile at the walls are computed using only one pixel width first order finite differencing.

The particular case for which comparison is presented has a high temperature of 25.43°C and a low temperature of 24.05°C. The Rayleigh number is 3.7×10^4. Rayleigh number is defined as follows:

$$\mathrm{Ra}=g\beta\Delta TL^3/\gamma\alpha,$$

where g is acceleration due to gravity, β is the coefficient of thermal expansion of the fluid, γ is its kinematic viscosity, α is the thermal diffusivity, ΔT is the temperature difference imposed, and L is the internal dimension of the cavity. Figures 4(a)–(g) are Data Explorer images of numerical data. Figure 4(a) is an image in the orientation and position of data that is directly recorded from the experiment at the $z=38$ mm slice location. The symmetry exhibited in this plane is precisely what one expects from such conditions. The three-dimensionality becomes apparent in the other reconstructed images. It is most clearly seen in Fig. 4(c); notice the curvature of the yellow and aqua regions near the hot and cold wall, respectively. Figures 4(f) and (g), represent vertical planes 10 mm (0.125 cavity) from the hot and cold wall, respec-

[2]Multizone Adaptive Scheme for Transport and Phase Change Processes—three-dimensional

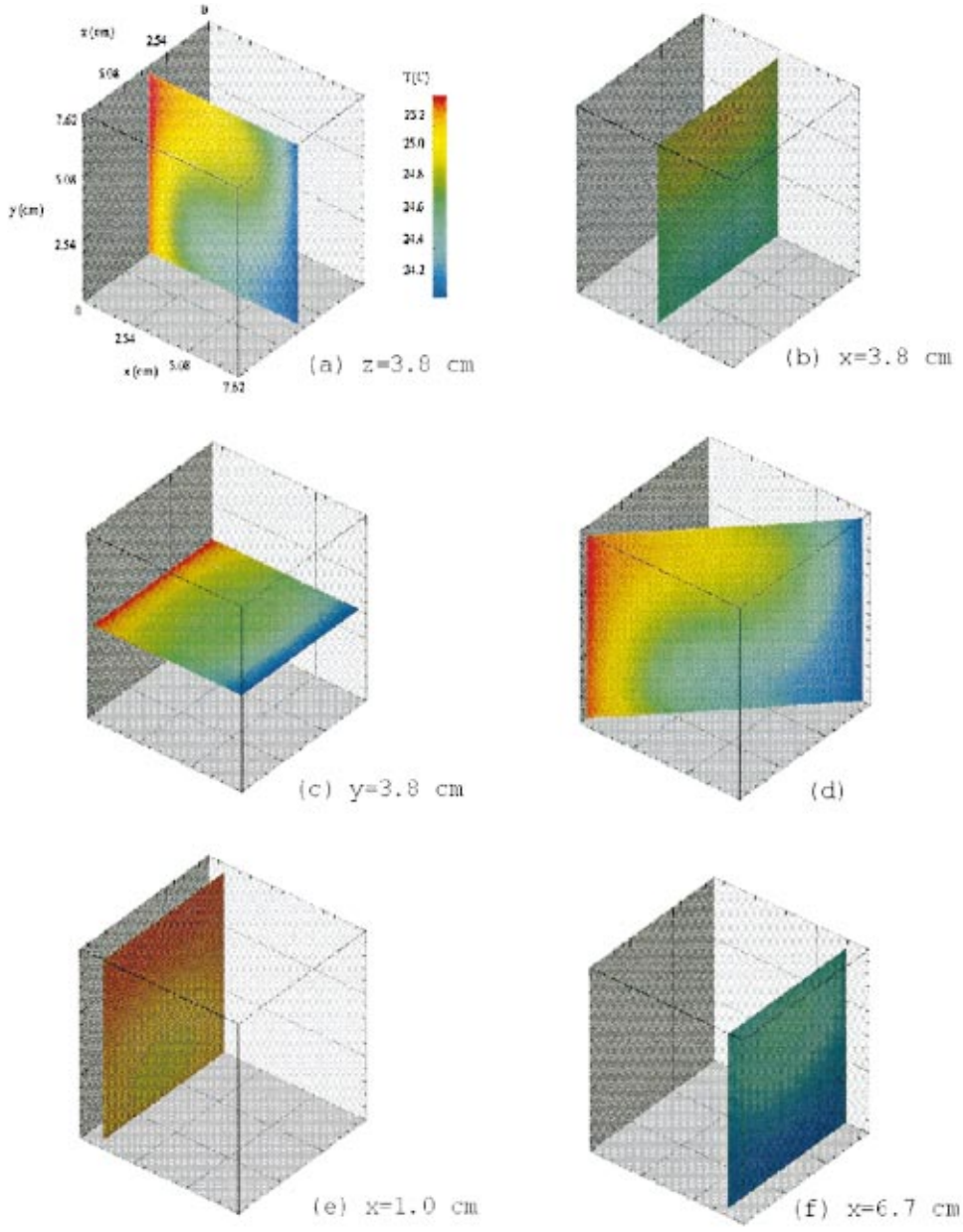

Fig. 4 Temperature fields obtained from numerical calculations: (*d*) is the diagonal plane.

tively, also exhibit three-dimensional behavior. If the flow within the cavity were two-dimensional the temperature distribution in these last two images and the local Nusselt number on the hot and cold walls would be a function of *y* only. Figure 5 demonstrates that the local Nusselt number is a function of both *x* and *y*, indicating three-dimensionality in the temperature field.

5.1 Convection at Ra=3.7×10^4. Figures 6(*a*)–(*g*) are Data Explorer images of the experimentally acquired and processed data for the previously stated boundary conditions. The transitions from one color to another are not as smooth in the experimental data as they are in the numerical data. However, on the whole, one can see similarity in the trends for the colored regions. There is, perhaps, greater penetration of the boundary layers as they exit from the walls. More convincing evidence can be demonstrated via a comparative examination of Fig. 6(*c*) with Fig. 4(*c*), and Fig. 6(*d*), with Fig. 4(*d*). One can see strong similarity between the numerical and experimental data sets particularly along the hot wall. This is an encouraging result

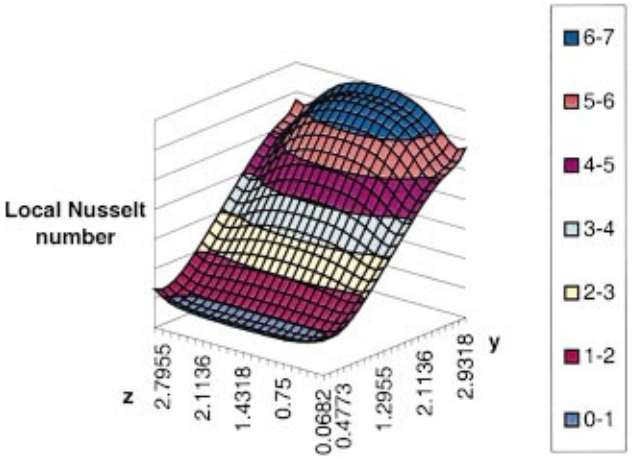

Fig. 5 Distribution of local Nusselt number on hot wall obtained from the numerical results (the *y* and *z*-axis are marked in the units of cm)

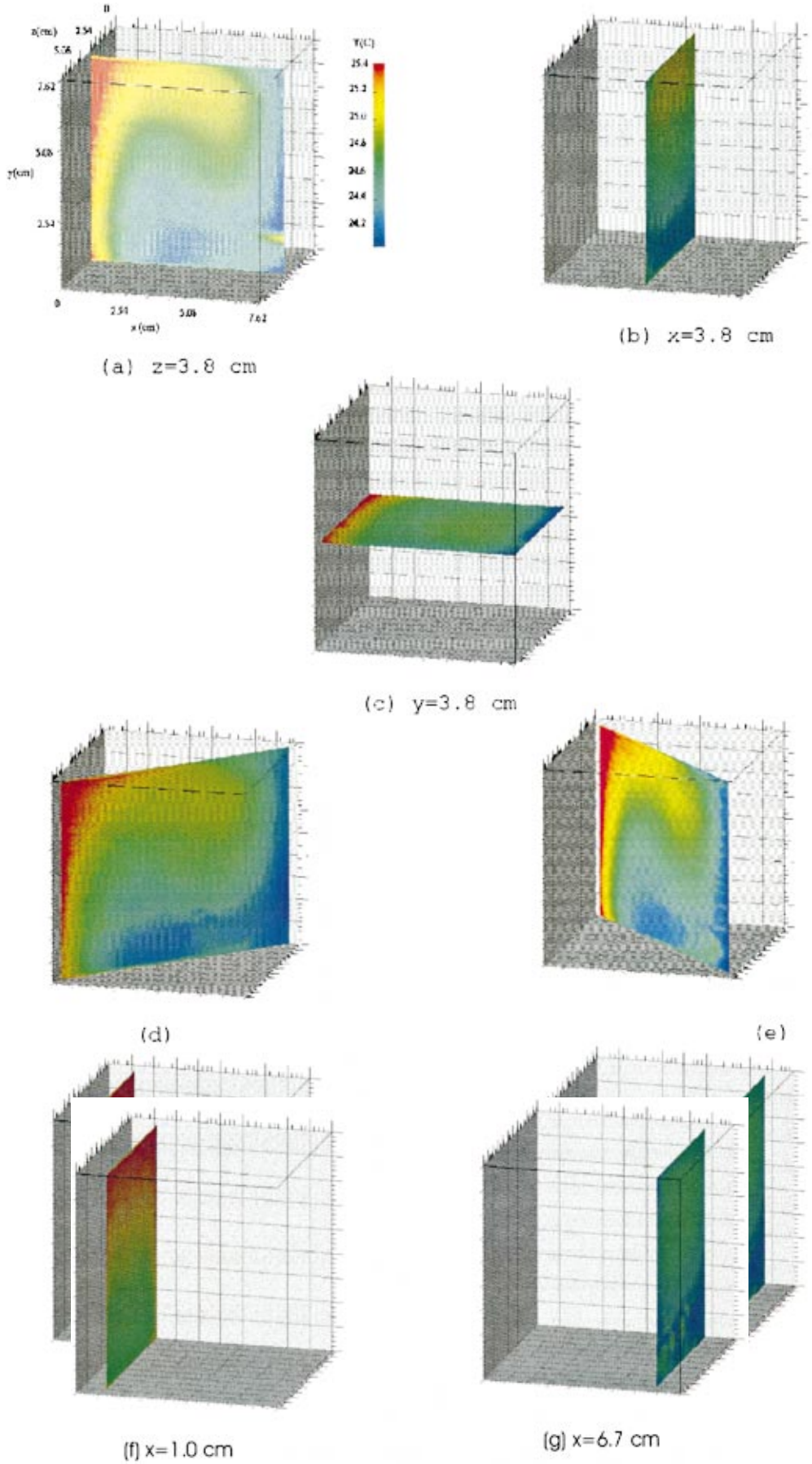

Fig. 6 Reconstruction of experimental temperature field for Ra=3.7×10^4 (*d*) and (*e*) are the diagonal planes

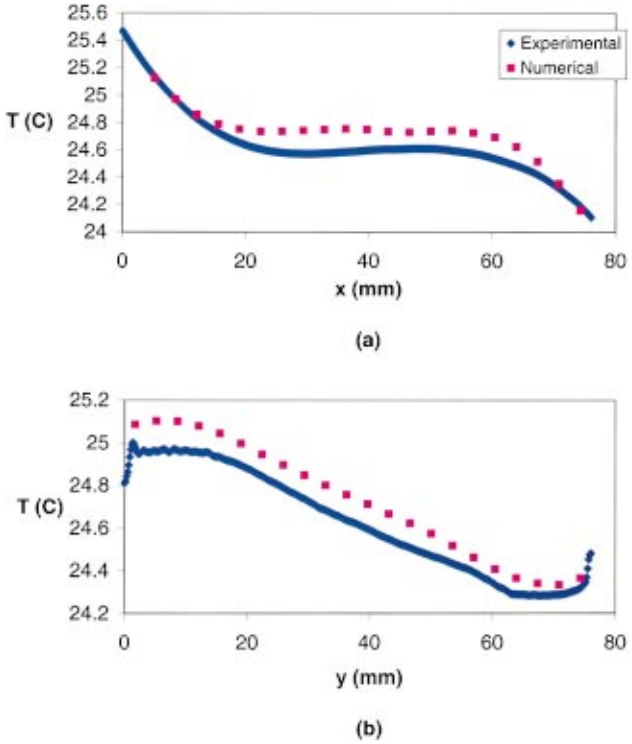

Fig. 7 Comparison of numerical and experimental median temperature value

since these figures are comprised of experimentally acquired data from all 21 slices. Notice the temperature distributions in Figs. 6(*d*) and (*e*). Apart from the green region on the right hand side, there is remarkable similarity as would be expected. Moreover, in viewing Figs. 6(*f*) and (*g*) one can see the same oval shaped regions and surrounding regions that are visible in Figs. 4(*f*) and (*g*).

A comparison of the numerically and experimentally obtained temperature fields is provided in Fig. 7. To obtain Fig. 7(*a*) the vertical slices of constant x value have been processed by a median filter to obtain the temperature as a function of x only. Figure 7(*b*) is obtained by performing the same operation on the horizontal slices of constant y value. The comparison is within the uncertainty of the calibration at all points (± 0.15°C). The data comprising Fig. 7(*a*) has been smoothed by the cubic spline routine in the direction corresponding to the abscissa. The data in Fig. 7(*b*), however shows the sensitivity of the results to the various sources of uncertainty in the measurement data. There are the issues of image acquisition and cropping compounding the discrepancy in the boundary conditions between the model and experiment. Considering the temperature difference for which this experiment has been constructed, 1.38°C, and the difficulty in resolving temperature very close to the wall, this agreement can be considered reasonable.

The local Nusselt number on the hot wall has the same dominant trend in the vertical direction as the numerical results and has a parabolic shape in the horizontal direction less than that which appears in the numerical results (see Fig. 8). The Nusselt number on the hot and cold walls is determined experimentally to be 3.68 and 2.57, respectively. The average of these two numbers, 3.12, has an 18 percent error from the value in literature and 12 percent error from the numerical model (Table 2). Recall the anticipated over-prediction by literature and consider the ambient conditions on the four acrylic walls are not fully characterized in the numerical model. These strong similarities serve to validate the acquired data over the entire span of the cavity, be they symmetry within the experimental data or qualitative, direct comparison with numerically generated data.

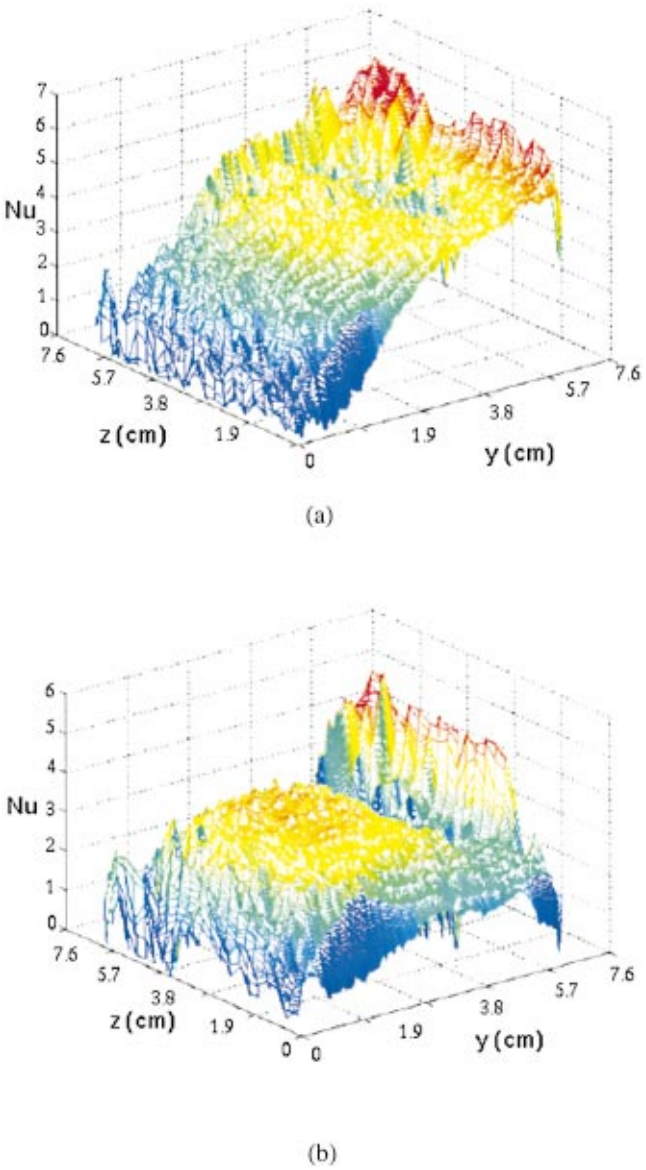

Fig. 8 Local distribution of Nusselt number on (*a*) hot wall and (*b*) cold wall

The second case listed in Table 2, in which glycerin is the working fluid, has similar boundary condition to the first case. With the isothermal boundaries at 24.25 and 25.32°C, the Rayleigh number is 2.84×10^4. Similar results are obtained. The average Nusselt number on the two plates is 2.81, 15 percent lower than the 3.29 predicted by the model, and 20 percent less than the value (3.51) as determined from the relationship in literature [20].

Table 2 Average Nusselt numbers as obtained from literature, numerical model, and the LCST experiment

Experiment	Hot wall Nu	Cold wall Nu	Average Nu	Average Nu from,Gebhart et al. 1988	Average Nu from Numerical model
Vertical, Ra=3.7×10^4	3.68	2.57	3.12	3.79	3.55
Vertical, Ra=2.8×10^4	2.89	2.73	2.81	3.51	3.29

6 Conclusions

LCT, traditionally only used for two-dimensional temperature measurement, has been shown to be a reliable technique for the measurement of three-dimensional temperature fields by the newly developed LCST technique. Herein, the experimental arrangement has been described in detail as well as the capabilities and limitations of the acquisition system. The salient features of the in-house developed image processing software have been disclosed. This work demonstrates that the single in situ calibration, has an uncertainty of ± 0.15°C, is applicable throughout the cavity. Of greatest importance, it has been shown that it is possible to calculate local temperature gradients as well as average Nusselt number within 20 percent variations from reported values as shown by the comparison with results from both a numerical model and empirical relations from literature. To the best of our knowledge, this is the first time LCT images have been used to compute the local Nusselt number for an enclosed fluid system.

Although the scan time is currently 10 seconds for 21 images spanning 76 mm, this is sufficiently fast for the study of many transient, three-dimensional, convection systems. Future work should include the reduction of the scan time for wider applicability by electro-mechanical means and reconstruction methods. Improvement in scanning time will allow the technique to probe time dependent flow systems. This technique may also prove useful in two-phase systems to map the temperature field and solidification interface in three dimensions.

To further improve the accuracy of the technique, it is suggested that the following modifications in designing the experiment will help. Lighting is a major factor in LCT experiments since this determines the quality of images, which finally yields the temperature measurement. Plexiglas containers used by the present investigators and many of the researchers in this field can be improved to optical quality glass materials which has a still better light transmission properties and minimum reflection compared to Plexiglas materials. Since glass has a better thermal conductivity than Plexiglas, one may use two layers of glass with a vacuum in between. For validation of the experimental technique, however, such a high precision construction of sidewall is unnecessary. Void in liquid medium (absence of liquid crystal), gives rise to noise in the final image. This can be controlled by using further small size encapsulated liquid crystals. This will result in more number of particles in the fluid and fill up the voids. Although this will improve the image quality, theoretically speaking it can introduce more seeds into the flow and comparatively more disturbance to the medium. Resolution of color band near the walls, which are at the two extreme ends of the color spectrum can be increased by using two different bands of liquid crystals. This will stretch the color spectrum near the walls and may result in better approximation of the wall heat transfer calculations.

Acknowledgments

This work has been supported by the NSF Division of Design, Manufacturing and Industrial Innovation, and by an AFOSR (ASSERT) grant. Ackknowledgements are also due to Dr. D. K. Mukherjee (Microstrategy, Vienna, USA) for his help in experimental setup and discussions.

References

[1] Braun, M. J., Dzodzo, M., and Lattime, S. B., 1993, ''Automatic Computer Based Non-Intrusive Temperature Measurements in Laminar Natural Convection Using TLC in Enclosures with Variable Aspect Ratio,'' *Experimental and Numerical Flow Visualization*, ASME, FED-Vol. 172, pp. 111–119.

[2] Farina, D. J., Hacker, J. M., Moffat, R. J., and Eaton, J. K., 1994, ''Illuminant Invariant Calibration of Thermochromatic Liguid Crystals,'' Exp. Therm. Fluid Sci., **9**, pp. 1–12.

[3] Parsely, M., 1993, company literature, Hallcrest Products Inc., Glenview IL.

[4] Rhee, H. S., Koseff, J. R., and Street, R. L., 1984, ''Flow Visualization of a Recirculating Flow by Rheoscopic Liquid and Liquid Crystal Techniques,'' Exp. Fluids, **2**, pp. 57–64.

[5] Nishimura, T., Fujiwara, M., and Miyashita, H., 1992, ''Visualization of Temperature Fields and Double-Diffusive Convection Using Liquid Crystals in an Aqueous Solution Crystallizing Along a Vertical Wall,'' Exp. Fluids, **12**, pp. 245–250.

[6] Dabiri, D., and Gharib, M., 1991, ''Digital Particle Image Thermometry: The Method and Implementation,'' Exp. Fluids, **11**, pp. 77–86.

[7] Kimura, I., Takamori, T., Ozawa, M., Takenaka, N., and Sakaguchi, T., 1990, *Simultaneous Measurement of Flow and Temperature Fields Based on Color Image Information, Flow Visualization*, R. Reznicek, ed. Hemisphere Publishing, Washington, pp. 29–34.

[8] Ashforth-Frost, S., and Jambunathan, K., 1993, *Flow Visualization Using Liquid Crystals, SPIE*, Vol. 2005, pp. 237–245.

[9] Ozawa, M., Müller, U., Kimura, I., and Takamori, T., 1992, ''Flow and Temperature Measurement of Natural Convection in a Hele-Shaw Cell Using a Thermo-Sensitive Liquid-Crystal Tracer,'' Exp. Fluids, **12**, pp. 213–222.

[10] Mukherjee, D. K., 1999, ''Computer-Assisted Liquid Crystal Thermography in a Rotating System: Application to Czochralski Crysal Growth,'' Ph.D. thesis, State University of New York at Stony Brook.

[11] Mukherjee, D. K., Prasad, V., Dutta, P., and Yuan, T., 1996, ''Liquid Crystal Visualization of the Effects of Crucible and Crystal Rotation on CZ Melt Flows,'' J. Cryst. Growth, **169**, pp. 136–146.

[12] Kowalewski, T. A., and Stasiek, J., 1998, ''Thermochromic Liquid Crystals in Heat Transfer Research, X'' *Heat Mass Transfer Symposium*, Swieradow, **1**, pp. 407–424.

[13] Sakakibara, J., and Adrian, R. J., 1999, ''Whole Field Measurement of Temperature in Water Using Two-Color Laser Induced Fluorescence,'' Exp. Fluids, **26**, pp. 7–15.

[14] Hiller, W. J., and Kowalewski, T. A., 1987, *Simultaneous Measurement of Temperature and Velocity Fields in Thermal Convective Flows, Flow Visualization IV*, Claude Veret, ed. Hemisphere Publishing, New York, pp. 617–622.

[15] Hiller, W. J., and Kowalewski, T. A., 1989, ''Three-Dimensional Structures in Laminar Natural Convection in a Cubic Enclosure,'' Exp. Therm. Fluid Sci., **2**, pp. 34–44.

[16] Wisniewski, T. S., Kowalewski, T. A., and Rebow, M., 1998, ''Infared and LCT in Natural Convection,'' *8th Int. Symposium on Flow Visualization*, Sorrento, G. M. Carlomagno and I. Grant, eds. CD ROM Proceedings ISBN 0953399109, pp. 212.1–212.8, Edinburgh.

[17] Gonzalez, R. C., and Woods, R. E., 1993, *Digital Image Processing*, Addison-Wesley Publishing Company, Reading, MA.

[18] Lutjen, P. M., 1999, ''Three Dimensional Measurement of Temperature Fields Using Liquid Crystal Scanning Tomoscopy,'' Master thesis, State University of New York at Stony Brook.

[19] Mallinson, G. D., and de Vahl Davis, G., 1977, ''Three-Dimensional Natural Convection in a Box: A Numerical Study,'' J. Fluid Mech., **83**, pp. 1–31.

[20] Gebhart, B., Jaluria, Y., Mahajan, R. L., and Sammakia, B., 1988, *Buoyancy-Induced Flows and Transport*, Hemisphere Publishing Corp., New York.

[21] Chatterjee, A., 1998, ''Three-Dimensional Adaptive Finite Volume Scheme for Transport Phenomena in Material Processing: Application to Czochralski,'' *Doctorate dissertation*, State University of New York at Stony Brook, NY.

[22] Chen, Q. S., Prasad, V., and Chatterjee, A., 1999, ''Modeling of Fluid Flow and Heat Transfer in a Hydrothermal Crystal Growth System: Use of Fluid Superposed Porous Layer Theory,'' Journal of Heat Transfer , **121**, pp. 1049–1058.

Journal of Heat Transfer

Technical Note

This section contains shorter technical papers. These shorter papers will be subjected to the same review process as that for full papers.

Electrochemical Mass Transfer at Moderate Rayleigh Numbers

R. J. Goldstein
Department of Mechanical Engineering, University of Minnesota, 111 Church St. S. E., Minneapolis, MN 55455

A. S. Fleischer
Assistant Professor Assoc. Mem. ASME Villanova University, Department of Mechanical Engineering, 800 Lancaster Avenue, Villanova, PA 19085
e-mail: amy.fleischer@villanova.edu

P. B. Hogerton
3M Center, St. Paul, MN 55144

Introduction

Natural convection in a horizontal enclosure heated from below (Rayleigh-Benard flow) arises from density instabilities within the fluid if a body force, normally gravitational, is present. Density gradients occur in many natural environments and may result from non-uniform temperature or concentration distributions. If the density instability exceeds a critical value, characterized by the Rayleigh number (Ra), the buoyancy forces are able to overcome the viscous forces, and convective motion begins. A comprehensive review of Rayleigh-Benard flow is available in Koschmieder [1].

As the Rayleigh number is increased beyond the critical value, the motion of a Boussinseq fluid will take the form of two-dimensional rolls. Rossby [2], Krishnamurti [3] and Willis, Deardorff and Somerville [4] have shown that the roll diameter increases with the Rayleigh number. As the Rayleigh number is increased further, the fluid motion evolves from two-dimensional through three-dimensional steady state flow to time-dependent flow before becoming turbulent. The occurrence of these transitions is strongly affected by Prandtl number (Pr) (Krishnamurti [5], Busse [6]).

The relationship between the Nusselt number (Nu) or Sherwood number (Sh) and the Rayleigh number is of both engineering and scientific significance, and has been the focus of many theoretical and experimental studies. The classical scaling of $Nu \sim Ra^{1/3}$ is predicted by mixing-length theory assuming the thermal boundary layer is independent of the cell height. Several experiments support the $Ra^{1/3}$ relationship, including Goldstein and Tokuda [7] and Goldstein, Chiang and See [8]. However, many other experimental studies, including Garon and Goldstein [9], Heslot et al. [10], and Castaing et al. [11] reveal a scaling law relationship $Nu \sim Ra^{2/7}$.

The advantages of an electrochemical system over conventional heat transfer include better control of boundary conditions, elimination of sidewall conduction and radiation effects allowing more precise measurements, and the direct determination of mass transfer rates from the electrical current. Electrochemical systems use high Schmidt number (Sc) fluids and using the heat-mass transfer analogy, these results can be extended to high Prandtl number heat transfer situations.

The present investigation was undertaken to provide a link between the high Schmidt number/high Rayleigh number mass transfer experiments of Goldstein, Chiang and See [8] and the high Prandtl number heat transfer data available at lower Rayleigh numbers. Mass transfer data is taken in the range $10^4 < Ra < 10^8$ and compared to the high Prandtl number data of Rossby [2] and the moderate Prandtl number data of Garon and Goldstein [9], Rossby [2] and Goldstein and Tokuda [7]. A relationship in the form $Nu \sim Ra^n$ is developed and cathodic deposition patterns are analyzed for flow patterns.

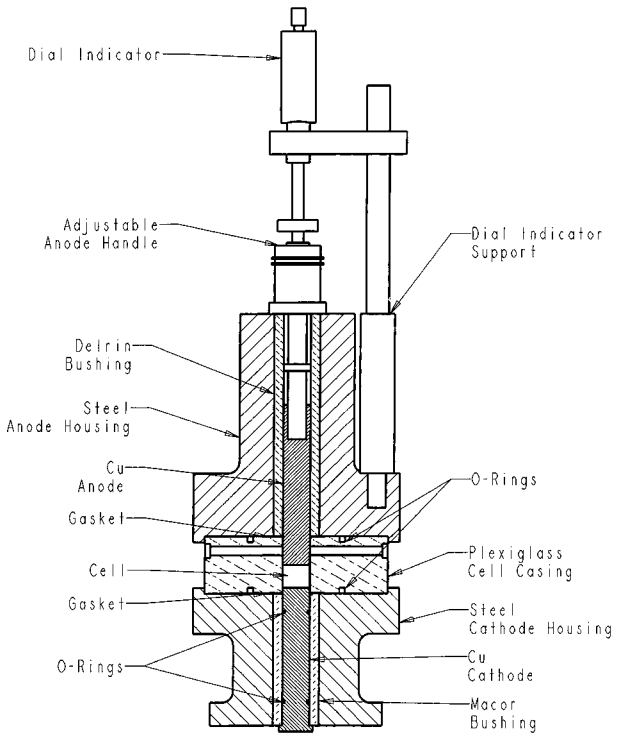

Fig. 1 Experimental apparatus

Contributed by the Heat Transfer Division for publication in the JOURNAL OF HEAT TRANSFER. Manuscript received by the Heat Transfer Division November 9, 2000; revision received March 20, 2001. Associate Editor: R. Mahajan.

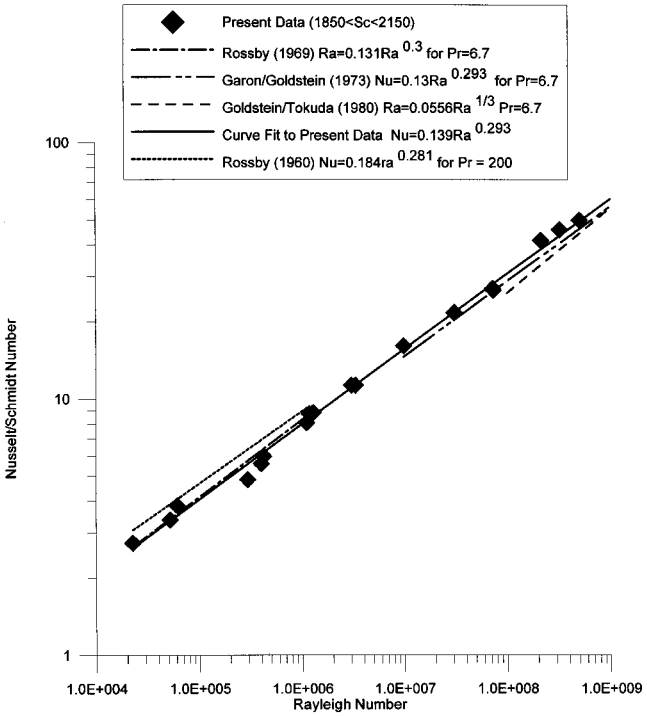

Fig. 2 Comparison of present data to high and moderate Prandtl number studies

Electrochemical Mass Transfer Technique

Electrochemical systems use an externally applied potential across two electrodes, the anode and cathode, to induce current flow through an electrolytic solution. The current system is similar to that of Goldstein, Chiang and See [8]. The electrolytic fluid is $CuSO_4$, and the passage of current through this aqueous solution is caused by chemical reactions creating Cu^{++} ions indicating the dissolution of the copper anode and the deposition of copper onto the cathode. The sulfate ions remain essentially inactive.

The mass transfer data is correlated using the Sherwood, Schmidt and mass transfer Rayleigh numbers,

$$\mathrm{Sh}=\frac{hL}{D} \tag{1}$$

$$\mathrm{Sc}=\frac{\mu}{\rho D} \tag{2}$$

$$\mathrm{Ra}=\frac{g\Delta\rho L^3}{\rho\nu D}, \tag{3}$$

which are analogous to the Nusselt, Prandtl, and Rayleigh numbers for heat transfer, respectively. The Sherwood number is calculated using h, the mass transfer coefficient,

$$h=\frac{(1-t_i)I}{n_i F\Delta C_i}. \tag{4}$$

Figure 1 shows a schematic of the apparatus used in the present study. The test cell consists of two flat and horizontally oriented copper rod electrodes separated by a plexiglass disc with a circular hole reamed through its thickness. The rods are each 11.7 mm in diameter and fabricated of OFHC copper. The longitudinal surfaces of the rods were rendered inactive with a 0.018 mm thick coating of Paralene, an organic film known for its resistance to chemical attack.

The plexiglass disk is 114 mm in diameter and 31.8 mm thick. A circular hole with a diameter of 11.8 mm running through the thickness forms the electrochemical test cavity. The electrode spacing can be varied from zero to 18 mm. The clear sidewalls allow the inspection of the test cell for entrapped air prior to operation. A horizontal channel drilled in the plexiglass cell casing permits the injection of the electrolytic solution.

The power supply is a fixed current source providing a 9.0 V DC current, stable to within 0.03 percent. Temperature measurements are made with a calibrated Teflon coated iron-constantin

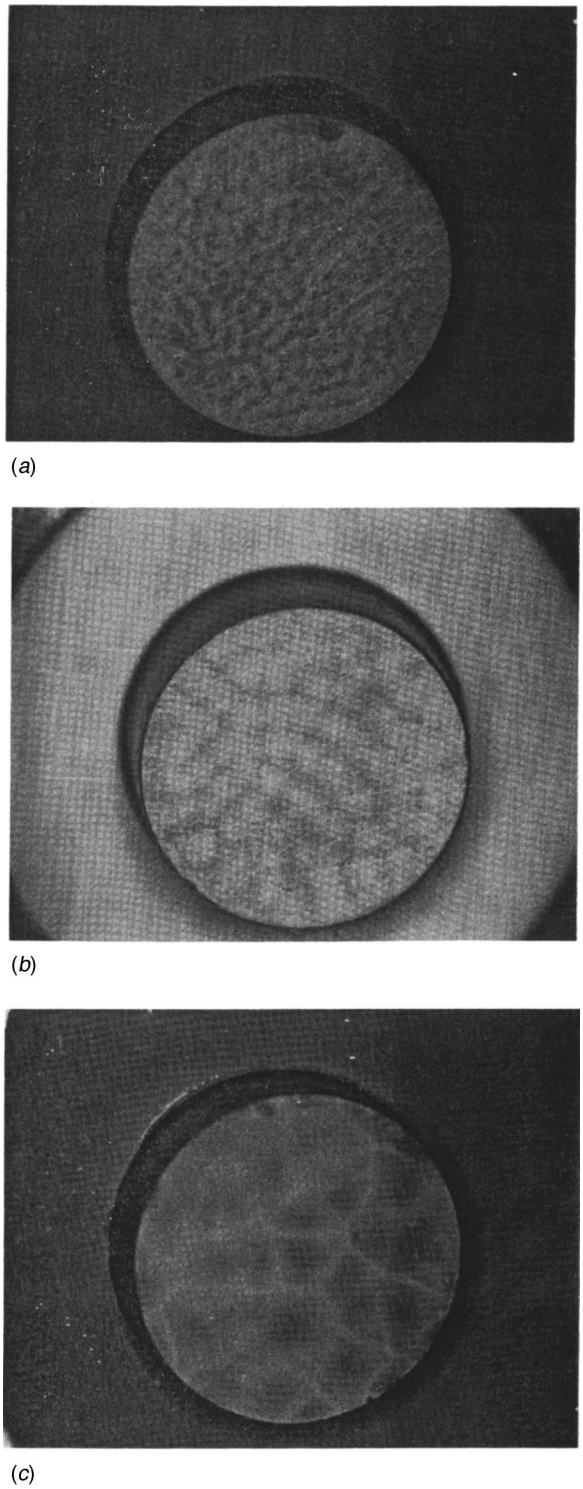

(*a*)

(*b*)

(*c*)

Fig. 3 Cathodic deposition patterns: (*a*) Ra=2.0×10³; (*b*) Ra =1.0×10⁴, and (*c*) Ra=1.2×10⁶.

thermocouple located within 0.76 mm of the test cell wall in the plexiglass casing. The post-test copper concentration differs from the initial concentration by 5 percent and is determined using atomic absorption analysis. The estimated uncertainty is ± 1 percent.

Each run is started at low current levels and progresses to higher currents. At each current setting, convection in the test cavity is allowed to come to steady-state and the value of potential and current are recorded. The characteristic diffusion time of the experiments ranges from 2–5 minutes, and in most cases, one diffusion time is sufficient to get a steady-state signal. At the lowest Rayleigh numbers, the post-test copper concentration may change over the test period by up to 5 percent and is determined using post-test atomic absorption analysis. Longer test periods may result in larger changes in copper ion concentrations, so tests are terminated immediately after the limiting current has been reached.

Results

A total of 19 runs are reported, covering the range $2.26\times 10^4 \leqslant \mathrm{Ra} \leqslant 5.03\times 10^8$ and $1800 \leqslant \mathrm{Sc} \leqslant 2150$. Electrode spacing varies from 0.635 mm to 17.78 mm. Since Ra is varied by changing the electrode spacing, aspect ratio is not an independent parameter in this experiment.

A least squares fit ($\mathrm{Sh}=c\mathrm{Ra}^m$) to the data yields the following:

$$\mathrm{Sh}=0.139\mathrm{Ra}^{0.293} \tag{5}$$

with a standard deviation of 2.8 percent. Considering the uncertainties of the measured parameters, (± 4.6 percent in Ra, ± 4.0 percent in Sh), a 95 percent confidence limit is set for the coefficient of Eq. (5) at $0.112 \leqslant c \leqslant 0.190$ and $0.277 \leqslant m \leqslant 0.302$. This corresponds closely to a 2/7 power law relationship.

The data for the present experiment is compared to the high Prandtl/Schmidt number experiment of Rossby [2] in Fig. 2. The present data and fit compare favorably to Rossby's correlations for $\mathrm{Pr}=200$ ($\mathrm{Ra}=0.184\mathrm{Ra}^{0.281}$). Rossby's fit is consistently higher than the current data, but remains parallel to it throughout the entire range. Figure 2 also shows a comparison of the current data to the moderate Prandtl number studies of Tokuda and Goldstein [7], Garon and Goldstein [9], and Rossby [2]. Despite the large difference in Prandtl (Schmidt) number, the correlations agree well, indicating only a weak effect of Prandtl number on heat transfer.

For $\mathrm{Ra}<2\times 10^6$, deposit patterns which illustrate the flow pattern appear on the cathode. As can be seen in Fig. 3, the size of the two-dimensional cellular pattern increases with Rayleigh number, as would be expected according to the work of Rossby [2], Krishnamurti [3] and Willis, and Deardorff and Somerville [4]. The patterns are quantitatively similar to those observed by Rossby [2]. As the Rayleigh number is increased further, the fluid motion evolves from two-dimensional through three-dimensional steady state flow to time-dependent flow before becoming turbulent. This more chaotic flow does not leave a discernible deposit pattern.

Summary

A series of experiments was conducted to study electrochemical mass transfer across a horizontal fluid layer at moderate Rayleigh numbers. The use of an electrochemical system allows direct analysis of mass transfer rates and the precise control of the boundary conditions. In addition, using the heat-mass transfer analogy, the high Schmidt numbers (Sc), 1800–2150, provides information on high Prandtl number (Pr) convection for which there is limited data. The resultant data provides a link between the high Schmidt number/high Rayleigh number work of Goldstein, Chiang and See [10] and the high Prandtl number heat transfer data available at lower Rayleigh numbers.

For $10^4<\mathrm{Ra}<10^8$, the relationship between Sherwood number and Rayleigh number is given by $\mathrm{Sh}=0.139\mathrm{Ra}^{0.293}$. These results agree well with both the existing high and moderate Prandtl number data in the range $10^4<\mathrm{Ra}<10^9$.

The observation of cathodic deposit patterns for $\mathrm{Ra}<2\times 10^6$ provides qualitative evidence of the similarity between flow structures in the heat transfer and mass transfer processes. Distinct cellular patterns, which increase diameter with Ra, are formed on the cathode.

Nomenclature

ΔC_i = concentration difference in species i
D = diffusion coefficient of copper sulfate
F = Faraday's constant
g = gravitational constant
h = mass transfer coefficient
I = current density
L = electrode spacing
n_i = valence of the transferred ion
Nu = Nusselt number
Pr = Prandtl number
Ra = Rayleigh number
Sc = Schmidt number
Sh = Sherwood number
μ = dynamic viscosity
ρ = density
ν = kinematic viscosity

References

[1] Koschmieder, E. L., 1993, *Benard Cells and Taylor Vortices*, Cambridge University Press.
[2] Rossby, H. T., 1969, "A Study of Benard Convection With and Without Rotation," J. Fluid Mech., **36**, pp. 309–335.
[3] Krishnamurti, R., 1970, "On the Transition to Turbulent Convection. Part 1. The Transition From Two to Three Dimensional Flow," J. Fluid Mech., **42**, pp. 295–307.
[4] Willis, G. E., Deardorff, J. W., and Somerville, R. C., 1972, "Roll Diameter Dependence in Rayleigh Convection and its Effects Upon the Heat Flux," J. Fluid Mech., **54**, pp. 351–367.
[5] Krishnamurti, R., 1973, "Some Further Studies on the Transition to Turbulent Convection," J. Fluid Mech., **60**, pp. 285–303.
[6] Busse, F. H., 1981, "Transition to Turbulence in Rayleigh-Benard Convection," in *Topics in Applied Physics*, H. L. Swinney and J. P. Gollub, eds., **45**, pp. 97–137.
[7] Goldstein, R. J., and Tokuda, S., 1980, "Heat Transfer by Thermal Convection at High Rayleigh Numbers," Int. J. Heat Mass Transf., **23**, pp. 738–740.
[8] Goldstein, R. J., Chiang, H. D., and See, D. L., 1990, "High-Rayleigh-Number Convection in a Horizontal Enclosure," J. Fluid Mech., **213**, pp. 111–126.
[9] Garon, A. M., and Goldstein, R. J., 1973, "Velocity and Heat Transfer Measurements in Thermal Convection," Phys. Fluids, **16**, pp. 1818–1825.
[10] Heslot, F., Castaing, B., and Libchaber, A., 1987, "Transitions to Turbulence in Helium Gas," Physical Review A, **36**, pp. 5870–5873.
[11] Castaing, B., Gunaratne, G., Heslot, F., Kadanoff, L., Libchaber, A., Thomae, S., Wu, X.-Z., Zaleski, S., and Zanetti, G., 1989, "Scaling of Hard Thermal Turbulence in Rayleigh-Benard Convection," J. Fluid Mech., **204**, pp. 1–30.